

*COPY 1*

**UNITED STATES AIR FORCE**

**SUMMER RESEARCH PROGRAM -- 1992**

**SUMMER RESEARCH EXTENSION PROGRAM  
FINAL REPORTS**

**VOLUME 4A**

**WRIGHT LABORATORY**

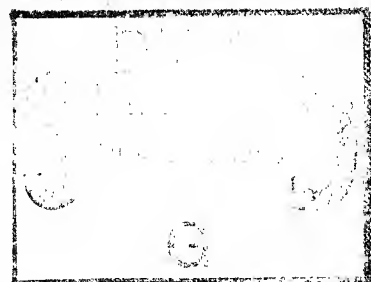
**RESEARCH & DEVELOPMENT LABORATORIES**

**5800 UPLANDER WAY**

**CULVER CITY, CA 90230-6608**

**SUBMITTED TO:**

**LT. COL. CLAUDE CAVENDER  
PROGRAM MANAGER**



**AIR FORCE OFFICE OF SCIENTIFIC RESEARCH**

**BOLLING AIR FORCE BASE**

**WASHINGTON, D.C.**

**MAY 1993**

## REPORT DOCUMENTATION PAGE

Form Approved  
OMB No. 0704-0183

Public reporting burden for this collection of information is estimated to average 1 hour per response, including the time for reviewing instructions, searching existing data sources, gathering and maintaining the data needed, and completing and reviewing the collection of information. Send comments regarding this burden estimate or any other aspect of this collection of information, including suggestions for reducing this burden, to Washington Headquarters Services, Directorate for Information Operations and Reports, 1215 Jefferson Davis Highway, Suite 1204, Arlington, VA 22202-4302, and to the Office of Management and Budget, Paperwork Reduction Project (0704-0183), Washington, DC 20503.

1. AGENCY USE ONLY (Leave blank)	2. REPORT DATE 28 Dec 92	3. REPORT TYPE AND DATES COVERED Annual 1 Sep 91 - 31 Aug 92
4. TITLE AND SUBTITLE  1992 Summer Faculty Research Program (SFRP) Volume: Vol 4A (SRED)		5. FUNDING NUMBERS  F49620-90-C-0076
6. AUTHOR(S)  Mr Gary Moore		
7. PERFORMING ORGANIZATION NAME(S) AND ADDRESS(ES)  Research & Development Laboratoreis (RDL) 5800 Uplander Way Culver City CA 90230-6600		AFOSR-TR-95  0735
9. SPONSORING / MONITORING AGENCY NAME(S) AND ADDRESS(ES) AFOSR/NI 110 Duncan Ave., Suite B115 Bldg 410 Bolling AFB DC 20332-0001 Lt Col Claude Cavender		10. SPONSORING / MONITORING AGENCY REPORT NUMBER
11. SUPPLEMENTARY NOTES		
12a. DISTRIBUTION / AVAILABILITY STATEMENT  UNLIMITED		12b. DISTRIBUTION CODE  G

## 13. ABSTRACT (Maximum 200 words)

The purpose of this program is to develop the basis for continuing research of interest to the Air Force at the institution of the faculty member; to stimulate continuing relations among faculty members and professional peers in the Air Force to enhance the research interests and capabilities of scientific and engineering educators; and to provide follow-on funding for research of particular promise that was started at an Air Force laboratory under the Summer Faculty Research Program.

During the summer of 1992 185 university faculty conducted research at Air Force laboratories for a period of 10 weeks. Each participant provided a report of their research, and these reports are consolidated into this annual report.

19951127 024

14. SUBJECT TERMS		15. SECURITY CLASSIFICATION OF THIS PAGE UNCLASSIFIED		16. SECURITY CLASSIFICATION OF ABSTRACT UNCLASSIFIED		17. SECURITY CLASSIFICATION OF ABSTRACT UNCLASSIFIED		18. SECURITY CLASSIFICATION OF ABSTRACT UL	
-------------------	--	--	--	---	--	---	--	---	--

UNITED STATES AIR FORCE  
SUMMER RESEARCH PROGRAM -- 1992  
SUMMER RESEARCH EXTENSION PROGRAM FINAL REPORTS

VOLUME 4A  
WRIGHT LABORATORY

RESEARCH & DEVELOPMENT LABORATORIES  
5800 Uplander Way  
Culver City, CA 90230-6608

Accession For	
NTIS	<input checked="" type="checkbox"/>
CRA&I	<input checked="" type="checkbox"/>
DTIC	<input type="checkbox"/>
TAB	<input type="checkbox"/>
Unannounced	<input type="checkbox"/>
Justification .....	
By .....	
Distribution /	
Availability Codes	
Dist	Avail and/or Special
A-1	

Program Director, RDL  
Gary Moore

Program Manager, AFOSR  
Lt. Col. Claude Cavender

Program Manager, RDL  
Scott Licoscas

Program Administrator, RDL  
Gwendolyn Smith

Submitted to:

AIR FORCE OFFICE OF SCIENTIFIC RESEARCH  
Bolling Air Force Base  
Washington, D.C.

May 1993

DTIC QUALITY INSPECTED 8

## **PREFACE**

This volume is part of a five-volume set that summarizes the research of participants in the 1992 AFOSR Summer Research Extension Program (SREP). The current volume, Volume 4A of 5, presents the final reports of SREP participants at Wright Laboratory.

Reports presented in this volume are arranged alphabetically by author and are numbered consecutively -- e.g., 1-1, 1-2, 1-3; 2-1, 2-2, 2-3, with each series of reports preceded by a 22-page management summary. Reports in the five-volume set are organized as follows:

<b>VOLUME</b>	<b>TITLE</b>
1A	Armstrong Laboratory (part one)
1B	Armstrong Laboratory (part two)
2	Phillips Laboratory
3	Rome Laboratory
4A	Wright Laboratory (part one)
4B	Wright Laboratory (part two)
5	Air Force Civil Engineering Laboratory, Arnold Engineering Development Center, Frank J. Seiler Research Laboratory, Wilford Hall Medical Center



## 1992 SUMMER RESEARCH EXTENSION PROGRAM FINAL REPORTS

1992 Summer Research Extension Program Management Report . . . . . INTRODUCTION - 1

### Wright Laboratory

<u>Report Number</u>	<u>Report Title</u>	<u>Author</u>
<b><u>VOLUME 4A</u></b>		
1	Multiresolution Electro-Optic Sensor Models	Raj S. Acharya
2	Design and Performance Evaluation of Submicron-Gate-Length Transistors	Vijay K. Arora
3	A Hybrid Method for Three-Dimensional Interferometric Tomographic Reconstruction of High-Speed Aerodynamic Flows	Soyoung Stephen Cha
4	Orientation Estimation with Application in Target Recognition	D. V. Satish Chandra
5	Signal Processing for High Speed Video Technology	Eugene R. Chenette
6	Light-Gas Gun Firing Cycle Optimization for High Velocity and Moderate Projectile Accelerations	Robert W. Courter
7	A Study of Decentralized Control of a Flexible Structure with Uncertain Interconnections	George T. Flowers
8	Direct Measurements of Turbulent Dissipation Rate Using Dual Laser Doppler Velocimeters	Richard D. Gould
9	Polarization Spectra for Infrared Materials and Elements	Randy Grove
10	Computational Study of Factors Contributing to Tire Wear	Manjriker Gunaratne
11	The Effect of Electric Fields on Propane/Air Flames	Harold H. Harris
12	Anisotropic Plastic Deformation of Metals	Steven L. Hatfield
13	Investigation of the Combustion Characteristics of Confined Coannular Swirling Jets with a Sudden Expansion [Task 150 Combustor]	Paul O. Hedman
14	Two Dimensional Simulation of Arc Plasmas in Electromagnetic Rail Launchers	Manuel A. Huerta

### **VOLUME 4B**

15	Effects of Damage on Vibration Frequency and Damping Behavior of Cantilevered Laminated Plates	David Hui
16	High Temperature Elastohydrodynamic Lubrication	Michael M. Khonsari

## Wright Laboratory (cont'd)

<u>Report Number</u>	<u>Report Title</u>	<u>Author</u>
<u>VOLUME 4B (cont'd)</u>		
17	Study of Damage Accumulation and Fatigue Fracture Mechanisms of Cord-Rubber Composites	B. L. Lee
18	(Report not received)	
19	Textural Characterization of Deformed Metals	Jessica L. Mayes
20	Tolerance Reasoning for a Generative Process Planner	Joseph H. Nurre
21	Jacobian Update Strategies for Quadratic and Near-Quadratic Convergence of Newton and Newton-Like Implicit Schemes	Paul D. Orkwis
22	A Molecular Modeling System for Prediction of Siloxane Liquid Crystalline Polymer Microstructures	Steven K. Pollack
23	Analytic Models for the Detection and Interception of Low Probability of Intercept (LPI) Communication Signals	Glenn E. Prescott
24	Robust Low Order Control Design for Uncertain Systems	Jenny L. Rawson
25	Conformational Structure and Dynamics in Perfluoropolyalkylether Lubricants	Martin Schwartz
26	Use of Thresholded Speckle in Testing CCDS	Martin Sensiper
27	Gain-Scheduled Missile Autopilot Design	Jeff S. Shamma
28	Fuzzy and Neural Learning: A Comparison	Thomas Sudkamp
29	Photoreflectance from GaAs/AlGaAs Structures	Michael Sydor
30	Measurements of Droplet Velocity and Size Distributions	Richard S. Tankin
31	Oxidation and Reduction of Carbonous Impediments to the Low Temperature Growth of Diamond Films	Fred V. Wells
32	Superplastic $Y_3Al_5O_{12}$ (YAG)	Jeff Wolfenstine
33	Pattern Theory: Extensions and Applications	James S. Wolper
34	The Identification of Nonlinearity in Structural Systems	Lawrence D. Zavodney
35	A Report on an Investigation of a Sensor Design for Strata Identification by an Earth Penetrating Device	Wayne J. Zimmermann

# **1992 SUMMER RESEARCH EXTENSION PROGRAM (SREP) MANAGEMENT REPORT**

## **1.0 BACKGROUND**

Under the provisions of Air Force Office of Scientific Research (AFOSR) contract F49620-90-C-0076, September 1990, Research & Development Laboratories (RDL), an 8(a) contractor in Culver City, CA, manages AFOSR's Summer Research Program. This report is issued in partial fulfillment of that contract (CLIN 0003AC).

The name of this program was changed during this year's period of performance. For that reason, participants' cover sheets are captioned "Research Initiation Program" (RIP), while the covers of the comprehensive volumes are titled "Summer Research Extension Program" (SREP). The program's sponsor, the Air Force Office of Scientific Research (AFOSR), changed the name to differentiate this program from another which also bore its original name.

Apart from this name change, however, the program remained as it has been since its initiation as the Mini-Grant Program in 1983. The SREP is one of four programs AFOSR manages under the Summer Research Program. The Summer Faculty Research Program (SFRP) and the Graduate Student Research Program (GSRP) place college-level research associates in Air Force research laboratories around the United States for 8 to 12 weeks of research with Air Force scientists. The High School Apprenticeship Program (HSAP) is the fourth element of the Summer Research Program, allowing promising mathematics and science students to spend two months of their summer vacations at Air Force laboratories within commuting distance from their homes.

SFRP associates and exceptional GSRP associates are encouraged, at the end of their summer tours, to write proposals to extend their summer research during the following calendar year at their home institutions. AFOSR provides funds adequate to pay for 75 SREP subcontracts. In addition, AFOSR has traditionally provided further funding, when available, to pay for additional SREP proposals, including those submitted by associates from Historically Black Colleges and Universities (HBCUs) and Minority Institutions (MIs). Finally, laboratories may transfer internal funds to AFOSR to fund additional SREPs. Ultimately the laboratories inform RDL of their SREP choices, RDL gets AFOSR approval, and RDL forwards a subcontract to the institution where the SREP associate is employed. The subcontract (see Attachment 1 for a sample) cites the SREP associate as the principal investigator and requires submission of a report at the end of the subcontract period.

Institutions are encouraged to share costs of the SREP research, and many do so. The most common cost-sharing arrangement is reduction in the overhead, fringes, or administrative changes institutions would normally add on to the principal investigator's or research associate's labor. Some institutions also provide other support (e.g., computer run time, administrative assistance, facilities and equipment or research assistants) at reduced or no cost.

When RDL receives the signed subcontract, we fund the effort initially by providing 90% of the subcontract amount to the institution (normally \$18,000 for a \$20,000 SREP). When we receive the end-of-research report, we evaluate it administratively and send a copy to the laboratory for a technical evaluation. When the laboratory notifies us the SREP report is acceptable, we release the remaining funds to the institution.

## 2.0 THE 1992 SREP PROGRAM

**SELECTION DATA:** In the summer of 1991, 170 faculty members (SFRP associates) and 142 graduate students (GSRP associates) participated in the summer program. Of those, 147 SFRPs and 10 GSRPs submitted SREP proposals; 88 SFRP SREPs and 7 GSRP SREPs were selected for funding (total: 95).

	Summer 1991 Participants	Submitted SREP Proposals	SREPs Funded
SFRP	170	147	88
GSRP	142	10	7

The funding was provided as follows:

Contractual slots funded by AFOSR	75
Laboratory-funded	13
Additional funding from AFOSR	<u>7</u>
Total	95

Seven HBCU/MI associates from the 1991 summer program submitted SREP proposals; five were selected (one was lab-funded; four were funded by additional AFOSR funds).

By laboratory, the applications submitted and selected show in the following table:

	Applied	Selected
Air Force Civil Engineering Laboratory	6	4
Armstrong Laboratory	34	20
Arnold Engineering Development Center	12	2
Frank J. Seiler Research Laboratory	5	3
Phillips Laboratory	30	18
Rome Laboratory	16	11
Wilford Hall Medical Center	1	1
Wright Laboratory	53	36
TOTAL	157	95

Note: Phillips Laboratory funded 2 SREPs; Wright Laboratory funded 11; and AFOSR funded 7 beyond its contractual 75.

ADMINISTRATIVE EVALUATION: The administrative quality of the SREP associates' final reports was satisfactory. Most complied with the formatting and other instructions RDL provided to them. In the final days of December 1992 and in the first two months of 1993, several associates called and requested no-cost extensions of up to six months. After consultation with our AFOSR Contracting Officer's Representative, RDL approved the requests but asked that all such associates provide an interim report to be included in this volume. That caused an AFOSR-approved delay beyond the 1 April 1993 submission of this report. The subcontracts were funded by \$1,893,616 of Air Force money. Institutions' cost sharing amounted to \$948,686.

TECHNICAL EVALUATION: The form we used to gather data for technical evaluation and the technical evaluations of the SREP reports are provided as Attachment 2. This summary evaluation is shown by SREP number. The average rating range was from 3.1 to 5.0. The overall average for those evaluated was 4.6 out of 5.00. The three rating factors with the highest average scores were:

- o The USAF should continue to pursue the research in this RIP report.
- o The money spent on this RIP report was well worth it.
- o I'll be eager to be a focal point for summer and RIP associates in the future.

Thus it is clear that the laboratories place a high value on AFOSR's Summer Research Program: SFRP, GSRP, and SREP.

### 3.0 SUBCONTRACTS SUMMARY

Table 1 lists contractually required information on each SREP subcontract. The individual reports are published in volumes as follows:

<u>Laboratory</u>	<u>Volume</u>
Air Force Civil Engineering Laboratory	5
Armstrong Laboratory	1
Arnold Engineering Development Center	5
Frank J. Seiler Research Laboratory	5
Phillips Laboratory	2
Rome Laboratory	3
Wilford Hall Medical Center	5
Wright Laboratory	4

TABLE 1: SUBCONTRACTS SUMMARY

Researcher's name	Highest Subcontract Degree	Number	Duration
Institution	Department		
Location	Amount		Sharing
Abbott, Ben A Vanderbilt University Nashville, TN 37235	MS	135	01/01/92-12/31/92 Dept of Electrical Engineering 19966.00 0.00
Acharya, Raj State University of New York, Buffalo Buffalo, NY 14260	PhD	151	01/01/92-12/31/92 Dept of Electrical & Comp Engrg 20000.00 0.00
Adams, Christopher M Oklahoma State University Stillwater, OK 74078	PhD	68	01/01/92-12/31/92 Dept of Chemistry 20000.00 0.00
Anderson, Richard A University of Missouri, Rolla Rolla, MO 65401	PhD	50	01/01/92-12/31/92 Dept of Physics 20000.00 5000.00
Arora, Vijay K Wilkes University Wilkes-Barre, PA 18766	PhD	3	10/01/91-09/30/92 Dept of Electrical & Comp Engrg 19996.00 36208.00
Ball, William P Duke University Durham, NC 27706	PhD	71	01/01/92-12/31/92 Dept of Civil & Environmental Eng 20000.00 26747.00
Battles, Frank P Massachusetts Maritime Academy Buzzard's Bay, MA 025321803	PhD	152	01/01/92-12/31/92 Dept of Basic Sciences 20000.00 22000.00
Bieniek, Ronald J University of Missouri, Rolla Rolla, MO 65401	PhD	147	01/01/92-12/31/92 Dept of Physics 19945.00 4000.00
Blystone, Robert V Trinity University San Antonio, TX 78212	PhD	127	01/01/92-12/31/92 Dept of Biology 20000.00 14783.00
Cha, Soyoung S University of Illinois, Chicago Chicago, IL 60680	PhD	011	01/01/92-12/31/92 Dept of Mechanical Engineering 20000.00 3842.00
Chandra, D. V. Satish Kansas State University Manhattan, KS 66506	PhD	89	01/18/92-10/17/92 Dept of Electrical Engineering 20000.00 11170.00
Chenette, Eugene R University of Florida Gainesville, FL 32611	PhD	106	01/01/92-12/31/92 Dept of Electrical Engineering 20000.00 0.00
Christensen, Douglas A University of Utah Salt Lake City, UT 84112	PhD	83	01/01/92-12/31/92 Dept of Electrical Engineering 19999.00 5000.00

Chubb, Gerald P Ohio State University Columbus, OH 43235	PhD 26 Dept of Aviation 20000.00	01/01/92-12/31/92 7600.00
Courter, Robert W Louisiana State University Baton Rouge, LA 70803	PhD 8 Dept of Mechanical Engineering 20000.00	10/01/91-09/30/92 445.00
Dey, Pradip P Hampton University Hampton, VA 23668	PhD 120 Computer Science Department 19921.00	01/01/92-12/31/92 0.00
Draut, Arthur W Embry Riddle Aeronautical University Prescott, AZ 86301	PhD 133 Computer Science Dept 19431.00	01/06/92-05/08/92 0.00
Dreisbach, Joseph University of Scranton Scranton, PA 185104626	PhD 108 Dept of Chemistry 20000.00	12/01/91-12/01/92 4000.00
Dror, Itiel Harvard University Cambridge, MA 02138	BS 76 Dept of Psychology 20000.00	01/01/92-12/31/92 0.00
Drost-Hansen, W. University of Miami Coral Gables, FL 33124	PhD 124 Dept of Chemistry 20000.00	12/01/91-12/01/92 12000.00
Dunleavy, Lawrence P University of South Florida Tampa, FL 33620	PhD 41 Dept of Electrical Engineering 20000.00	01/01/92-12/31/92 6463.00
Evans, Joseph B University of Kansas Lawrence, KS 66045	PhD 96 Dept of Electrical & Comp Engrg 20000.00	01/01/92-12/31/92 0.00
Flowers, George T Auburn University Auburn, AL 368495341	PhD 73 Dept of Mechanical Engineering 19986.00	01/01/92-12/30/92 12121.00
Gantenbein, Rex E University of Wyoming Laramie, WY 82071	PhD 22 Dept of Computer Science 20000.00	01/01/91-12/31/92 26643.00
Garcia, Ephrarim Vanderbilt University Nashville, TN 37235	PhD 32 Dept of Mechanical Engineering 20000.00	12/01/91-11/30/92 9659.00
German, Fred J Auburn University Auburn University, AL 36830	PhD 49 Dept of Electrical Engineering 20000.00	01/01/92-12/31/92 0.00
Gould, Richard D North Carolina State University Raleigh, NC 276957910	PhD 87 Dept of Mech and Aerospace Engrg 20000.00	01/01/92-12/31/92 14424.00
Gove, Randy L University of Alabama, Huntsville Huntsville, AL 35899	MS 122 Dept of Physics 20000.00	01/01/92-12/31/92 3469.00
Grabowski, Marek University of Colorado, Colorado Springs Colorado Springs, CO 809337150	PhD 92 Dept of Physics 19700.00	01/01/92-12/31/92 0.00

Gunaratne, Manjriker  
University of South Florida  
Tampa, FL 33620

PhD 90 01/01/92-12/31/92  
Dept of Civil Engrg & Mechanics  
19994.00 10062.00

Hall, Ernest L  
University of Cincinnati  
Cincinnati, OH 452210072

PhD 134 01/01/92-12/31/92  
Dept of Robotics Research  
19975.00 0.00

Hamilton, William L  
Salem State College  
Salem, MA 01970

PhD 47 01/01/92-12/31/92  
Dept of Geography  
20000.00 32000.00

Hamilton, Kirk L  
Xavier University of Louisiana  
New Orleans, LA 70125

PhD 57 01/01/92-12/31/92  
Dept of Biology  
20000.00 16100.00

Harris, Harold H  
University of Missouri, St.Louis  
St. Louis, MO 63121

PhD 94 01/01/92-12/31/92  
Dept of Chemistry  
19300.00 8600.00

Hartung, George H  
University of Hawaii  
Honolulu, HI 96822

PhD 46 01/01/92-12/31/92  
Dept of Physiology  
20000.00 7530.00

Hatfield, Steven L  
University of Kentucky  
Lexington, KY 40506

BS 23 01/01/92-12/31/92  
Dept of Materials Science & Engrg  
20000.00 28625.00

Hedman, Paul O'Dell  
Brigham Young University  
Provo, UT 84602

PhD 17 01/01/92-12/31/92  
Dept of Chemical Engineering  
19999.00 6928.00

Heister, Stephen D  
Purdue University  
West Lafayette, IN 47907

PhD 5 01/01/92-12/31/92  
School of Aero & Astronautics  
20000.00 4419.00

Hess, David J  
University of Texas, Austin  
Austin, TX 78713

BA 149 01/01/92-12/31/92  
Dept of Psychology  
19914.00 8784.00

Hoffman, R. W  
Case Western Reserve University  
Cleveland, OH 44106

PhD 99 01/01/92-12/31/92  
Dept of Physics  
19770.00 0.00

Huerta, Manuel A  
University of Miami  
Coral Gables, FL 33124

PhD 62 01/01/92-12/31/92  
Dept of Physics  
20000.00 1207.00

Hui, David  
University of New Orleans  
New Orleans, LA 70148

PhD 116 01/01/92-12/31/92  
Dept of Mechanical Engineering  
20000.00 0.00

Iyer, Ashok  
University of Nevada, Las Vegas  
Las Vegas, NV 89154

PhD 74 01/01/92-12/31/92  
Dept of Electrical & Comp Engrg  
20000.00 18549.00

Khonsari, Michael M  
University of Pittsburgh  
Pittsburgh, PA 15260

PhD 53 01/01/92-12/31/92  
Dept of Mechanical Engineering  
20000.00 32958.00

Kibert, Charles J  
University of Florida  
Gainesville, FL 32611

PhD 2 01/01/92-12/31/92  
Dept of Fire Testing & Research  
20000.00 6928.00



Klarup, Douglas G University of Montana Missoula, MT 59812	PhD 84 Dept of Chemistry 20000.00	01/01/92-12/31/92 0.00
Koblasz, Arthur J Georgia Institute of Technology Atlanta, GA 30332	PhD 145 Dept of Civil Engineering 19956.00	01/01/92-09/30/92 0.00
Kornreich, Philipp Syracuse University Syracuse, NY 13244	PhD 35 Dept of Electrical & Comp Engrg 20000.00	10/01/91-09/30/92 0.00
Kuo, Spencer P Polytechnic University Farmingdale, NY 11735	PhD 59 Dept of Electrical Engineering 20000.00	01/01/92-12/31/92 9916.00
Langhoff, Peter W Indiana University Bloomington, IN 47402	PhD 115 Dept of Chemistry 20000.00	01/01/92-12/31/92 35407.00
Lee, Byung-Lip Pennsylvania State University University Park, PA 16802	PhD 93 Dept of Engrg Science & Mechanics 20000.00	01/01/92-12/31/92 8173.00
Leigh, Wallace B Alfred University Alfred, NY 14802	PhD 118 Dept of Electrical Engineering 19767.00	01/01/92-12/31/92 18770.00
Liddy, Elizabeth Syracuse University Syracuse, NY 132444100	PhD 104 Dept of Information Studies 20000.00	01/01/92-12/31/92 0.00
Liu, Cheng University of North Carolina, Charlotte Charlotte, NC 28270	PhD 6 Dept of Engineering Technology 20000.00	11/01/99-12/31/92 0.00
Main, Robert G California State University, Chico Chico, CA 959290504	PhD 28 Dept of Communication Design 20000.00	01/01/92-06/30/92 7672.00
Mains, Gilbert J Oklahoma State University Stillwater, OK 74078	PhD 52 Dept of Chemistry 19071.00	01/01/92-12/31/92 8746.00
Marathay, Arvind S University of Arizona Tucson, AZ 85721	PhD 51 Dept of Optical Sciences 20000.00	01/01/92-12/31/92 0.00
Martin, Charlesworth R Norfolk State University Norfolk, VA 23504	PhD 125 Dept of Physics & Engineering 20000.00	01/01/92-12/31/92 0.00
Mayes, Jessica L University of Kentucky Lexington, KY 405034203	BS 16 Dept of Material Science & Engrng 20000.00	01/01/92-12/31/92 28625.00
Mulligan, Benjamin E University of Georgia Athens, GA 30602	PhD 54 Dept of Psychology 19895.00	01/01/92-12/31/92 13677.00
Munday, Edgar G University of North Carolina, Charlotte Charlotte, NC 28223	PhD 38 Dept of Mechanical Engineering 20000.00	10/01/91-10/30/92 11638.00

Nurre, Joseph H Ohio University Athens, OH 45701	PhD 56 Dept of Electrical & Comp Engrg 19842.00	01/01/92-12/31/92 15135.00
Orkwis, Paul D University of Cincinnati Cincinnati, OH 452210070	PhD 14 Dept of Engineering Mechanics 19966.00	10/01/91-10/30/92 23017.00
Patra, Amit L University of Puerto Rico Mayaguez, PR 00681	PhD 69 Dept of General Engineering 20000.00	01/01/92-12/31/92 2750.00
Peters II, Richard A Vanderbilt University Nashville, TN 37235	PhD 160 Dept of Electrical Engineering 20000.00	01/01/92-12/31/92 0.00
Pollack, Steven K University of Cincinnati Cincinnati, OH 452200012	PhD 31 Dept of Materials Sci & Engrg 20000.00	01/01/92-12/31/92 14877.00
Prescott, Glenn E University of Kansas Lawrence, KS 66045	PhD 72 Dept of Electrical Engineering 20000.00	01/01/92-12/31/92 8000.00
Price, James L University of Iowa Iowa City, IA 52242	PhD 48 Dept of Sociology 20000.00	01/01/92-12/30/92 8600.00
Qazi, Salahuddin SUNY, Utica Utica, NY 13504	PhD 129 Dept of Electrical Engineering 20000.00	01/01/92-12/31/92 25000.00
Rappaport, Carey M Northeastern University Boston, MA 02115	PhD 58 Dept of Electrical & Comp Engrng 19999.00	01/01/92-06/30/92 0.00
Rawson, Jenny L North Dakota State University Fargo, ND 58105	PhD 144 Dept of Electrical Engineering 19997.00	01/01/92-12/31/92 19826.00
Riccio, Gary E University of Illinois, Urbana Urbana, IL 61821	PhD 80 Dept of Human Perception 20000.00	01/01/92-12/31/92 0.00
Rotz, Christopher A Brigham Young University Provo, UT 84602	PhD 136 Dept of Manufacturing Engineering 20000.00	12/01/91-12/31/92 11814.00
Schwartz, Martin University of North Texas Denton, TX 762035068	PhD 55 Dept of Chemistry 20000.00	01/01/92-12/31/92 18918.00
Senseman, David M University of Texas, San Antonio San Antonio, TX 78285	PhD 77 Dept of Information 20000.00	12/01/91-11/30/92 19935.00
Sensiper, Martin University of Central Florida Orlando, FL 32816	BS 15 Dept of Electrical Engineering 20000.00	11/01/91-05/31/92 0.00
Shamma, Jeff S University of Texas, Austin Austin, TX 78713	PhD 70 Dept of Electrical Engineering 20000.00	01/01/92-12/31/92 0.00

Shively, Jon H California State University, Northridge Northridge, CA 91330	PhD 140 Dept of CIAM 20000.00	01/01/92-12/31/92  14553.00
Singh, Sahjendra N University of Nevada, Las Vegas Las Vegas, NV 89014	PhD 79 Dept of Electrical Engineering 20000.00	01/01/92-12/31/92  20595.00
Smith, Gerald A Pennsylvania State University University Park, PA 16802	PhD 63 Dept of Physics 20000.00	07/01/92-07/01/93  0.00
Stephens, Benjamin R Clemson University Clemson, SC 29634	PhD 114 Dept of Psycology 19988.00	01/01/92-12/31/92  4250.00
Sudkamp, Thomas Wright State University Dayton, OH 45435	PhD 97 Dept of Computer Science 20000.00	01/01/92-08/31/92  18739.00
Sydor, Michael University of Minnesota, Duluth Duluth, MN 55804	PhD 11 Dept of Physics 20000.00	01/01/92-12/31/92  0.00
Tankin, Richard S Northwestern University Evanston, IL 60208	PhD 44 Dept of Mechanical Engineering 20000.00	01/01/92-12/31/92  29103.00
Taylor, Michael D University of Central Florida Orlando, FL 32816	PhD 141 Dept of Mathematics 20000.00	05/01/92-07/31/92  1587.00
Teegarden, Kenneth J University of Rochester Rochester, NY 14627	PhD 98 Dept of Optics 20250.00	01/01/92-12/31/92  60600.00
Tew, Jeffrey D Virginia Polytech Instit and State Univ Blacksburg, VA 24061	PhD 137 Dept of Industrial Engineering 17008.00	03/01/92-09/30/92  4564.00
Tipping, Richard H University of Alabama Tuscaloosa, AL 35487	PhD 81 Dept of Physics & Astronomy 20000.00	01/01/92-05/31/92  15000.00
Tripathi, Ram C University of Texas, San Antonio San Antonio, TX 78249	PhD 105 Dept of Mathematics 20000.00	01/01/92-12/31/92  2274.00
Wells, Fred V Idaho State University Pocatello, ID 83209	PhD 155 Dept of Chemistry 20000.00	01/01/92-12/31/92  8000.00
Whitefield, Phillip D University of Missouri, Rolla Rolla, MO 65401	PhD 25 Dept of Chemistry 19991.00	01/01/92-12/31/92  25448.00
Wolfenstine, Jeffrey B University California, Irvine Irvine, CA 92717	PhD 18 Dept of Mechanical Engineering 20000.00	01/01/92-12/31/92  11485.00
Wolper, James S Idaho State University Pocatello, ID 83209	PhD 138 Dept of Mathematics 20000.00	01/15/92-09/30/92  4828.00

Zavodney, Lawrence D  
Ohio State University  
Columbus, OH 43210

PhD 148 01/01/92-12/31/92  
Dept of Engineering Mechanics  
20000.00 0.00

Zimmerman, Wayne J  
Texas Women University  
Denton, TX 76204

PhD 111 01/01/92-12/31/92  
Dept of Mathematics  
19990.00 8900.00

**ATTACHMENT 1:**  
**SAMPLE SREP SUBCONTRACT**

AIR FORCE OFFICE OF SCIENTIFIC RESEARCH  
1993 SUMMER RESEARCH EXTENSION PROGRAM SUBCONTRACT 93-36

BETWEEN

Research & Development Laboratories  
5800 Uplander Way  
Culver City, CA 90230-6608

AND

University of Delaware  
Sponsored Programs Admin.  
Newark, DE 19716

REFERENCE: Summer Research Extension Program Proposal 93-36  
Start Date: 01/01/93 End Date: 12/31/93  
Proposal amount: \$20000.00

- (1) PRINCIPAL INVESTIGATOR: Dr. Ian W. Hall  
Materials Science  
University of Delaware  
Newark, DE 19716
- (2) UNITED STATES AFOSR CONTRACT NUMBER: F49620-90-C-09076
- (3) CATALOG OF FEDERAL DOMESTIC ASSISTANCE NUMBER (CFDA): 12.800  
PROJECT TITLE: AIR FORCE DEFENSE RESEARCH SOURCES PROGRAM
- (4) ATTACHMENTS 1 AND 2: SREP REPORT INSTRUCTIONS

\*\*\* SIGN SREP SUBCONTRACT AND RETURN TO RDL \*\*\*

1. **BACKGROUND:** Research & Development Laboratories (RDL) is under contract (F49620-90-C-0076) to the United States Air Force to administer the Summer Research Programs (SRP), sponsored by the Air Force Office of Scientific Research (AFOSR), Bolling Air Force Base, D.C. Under the SRP, a selected number of college faculty members and graduate students spend part of the summer conducting research in Air Force laboratories. After completion of the summer tour participants may submit, through their home institutions, proposals for follow-on research. The follow-on research is known as the Research Initiation Program (RIP). Approximately 75 RIP proposals annually will be selected by the Air Force for funding of up to \$20,000; shared funding by the academic institution is encouraged. RIP efforts selected for funding are administered by RDL through subcontracts with the institutions. This subcontract represents such an agreement between RDL and the institution designated in Section 5 below.
2. **RDL PAYMENTS:** RDL will provide the following payments to RIP institutions:
  - 90 percent of the negotiated RIP dollar amount at the start of the RIP Research period.
  - the remainder of the funds within 30 days after receipt at RDL of the acceptable written final report for the RIP research.
3. **INSTITUTION'S RESPONSIBILITIES:** As a subcontractor to RDL, the institution designated on the title page will:
  - a. Assure that the research performed and the resources utilized adhere to those defined in the RIP proposal.
  - b. Provide the level and amounts of institutional support specified in the RIP proposal.
  - c. Notify RDL as soon as possible, but not later than 30 days, of any changes in 3a or 3b above, or any change to the assignment or amount of participation of the Principal Investigator designated on the title page.
  - d. Assure that the research is completed and the final report is delivered to RDL not later than twelve months from the effective date of this subcontract. The effective date of the subcontract is one week after the date that the institution's contracting representative signs this subcontract, but no later than January 15, 1992.
  - e. Assure that the final report is submitted in the format shown in Attachment 1.

- f. Agree that any release of information relating to this subcontract (news releases, articles, manuscripts, brochures, advertisements, still and motion pictures, speeches, trade association meetings, symposia, etc.) will include a statement that the project or effort depicted was or is sponsored by: Air Force Office of Scientific Research, Bolling AFB, D.C.
- g. Notify RDL of inventions or patents claimed as the result of this research in a format specified in Attachment 1.
- h. RDL is required by the prime contract to flow down patent rights and technical data requirements in this subcontract. Attachment 2 to this subcontract contains a list of contract clauses incorporated by reference in the prime contract.

4. All notices to RDL shall be addressed to:

RDL Summer Research Program Office  
5800 Uplander Way  
Culver City, CA 90230-6608

5. By their signatures below, the parties agree to the provisions of this subcontract.

\_\_\_\_\_  
Abe S. Sopher  
RDL Contracts Manager

\_\_\_\_\_  
Date

\_\_\_\_\_  
Signature of Institution Contracting Official

\_\_\_\_\_  
Typed/Printed Name

\_\_\_\_\_  
Title

\_\_\_\_\_  
Institution

\_\_\_\_\_  
Date/Phone



**Attachment 1**  
**Final Report Format**

1. All RIP Principal Investigators will submit a final report of the research conducted.
2. One copy of the report is due to RDL no later than twelve months after the effective date of the RIP subcontract. At the same time, submit one copy to the Air Force laboratory focal point.
3. The title page should contain the title of the research, the Principal Investigator and or other co-investigators, the month and year of issue, the university with department and address, and acknowledgement of sponsorship by AFOSR (see clause 3f of this subcontract).
4. For text, use a font that is 12 characters per inch (elite) and as close to letter quality as possible. Start with the title in all caps one and one-half inches from the top of the first page; if the title requires two or more lines, single space it. Double space below the title, and then center and type the researcher's title and name. Then space twice and begin the double-spaced text.

Use a one-and-one-half-inch left margin and a one-inch right margin for the body of the text. Center page numbers at the foot of each page, one inch from the bottom. Each page should have a one-inch margin at the top. The format should be that of a standard research paper: it should begin with a one-paragraph abstract (on its own page) summarizing your work and should be followed by an introduction, a discussion of the problem, a results section, and a conclusion. Since multiple copies of your report may be required, assure that all pages can be readily copied to a black-and-white 8 1/2" by 11" page. (No colors, such as blue or green, that don't photocopy well, and no foldouts, please.)

5. The report must be accompanied by a separate statement on whether or not any inventions or patents have resulted from this research. If yes, use a DD Form 882 (supplied by RDL on request) to indicate the patent filing date, serial number, title, and a copy of the patent application, and patent number and issue date for any subject invention in any country in which the subcontractor has applied for patents.

**Attachment 2**  
**Contract Clauses**

This contract incorporates by reference the following clauses of the Federal Acquisition Regulations (FAR), with the same force and effect as if they were given in full text. Upon request, the Contracting Officer or RDL will make their full text available (FAR 52.252-2).

<b><u>FAR CLAUSES</u></b>	<b><u>TITLE AND DATE</u></b>
52.202-1	DEFINITIONS (APR 1984)
52.203-1	OFFICIALS NOT TO BENEFIT (APR 1984)
52.203-3	GRATUITIES (APR 1984)
52.203-5	COVENANT AGAINST CONTINGENT FEES (APR 1984)
52.304-6	RESTRICTIONS ON SUBCONTRACTOR SALES TO THE GOVERNMENT (JUL 1985)
52.203-7	ANTI-KICKBACK PROCEDURES (OCT 1988)
52.203-12	LIMITATION ON PAYMENTS TO INFLUENCE CERTAIN FEDERAL TRANSACTIONS (JAN 1990)
52.204-2	SECURITY REQUIREMENTS (APR 1984)
52.209-6	PROTECTING THE GOVERNMENT'S INTEREST WHEN SUBCONTRACTING WITH CONTRACTORS DEBARRED, SUSPENDED, OR PROPOSED FOR DEBARMENT (MAY 1989)
52.212-8	DEFENSE PRIORITY AND ALLOCATION REQUIREMENTS (MAY 1986)
52.215-1	EXAMINATION OF RECORDS BY COMPTROLLER GENERAL (APR 1984)
52.215-2	AUDIT - NEGOTIATION (DEC 1989)
52.222-26	EQUAL OPPORTUNITY (APR 1984)
52.222-28	EQUAL OPPORTUNITY PREAWARD CLEARANCE OF SUBCONTRACTS (APR 1984)
52.222-35	AFFIRMATIVE ACTION FOR SPECIAL DISABLED AND VIETNAM ERA VETERANS (APR 1984)
52.222-36	AFFIRMATIVE ACTION FOR HANDICAPPED WORKERS (APR 1984)

52.222-37	EMPLOYMENT REPORTS ON SPECIAL DISABLED VETERANS AND VETERANS OF THE VIETNAM ERA (JAN 1988)
52.223-2	CLEAN AIR AND WATER (APR 1984)
52.232-6	DRUG-FREE WORKPLACE (MAR 1989)
52.224-1	PRIVACY ACT NOTIFICATION (APR 1984)
52.224-2	PRIVACY ACT (APR 1984)
52.225-13	RESTRICTIONS ON CONTRACTING WITH SANCTIONED PERSONS (MAY 1989)
52.227-1	AUTHORIZATION AND CONSENT (APR 1984)
52.227-2	NOTICE AND ASSISTANCE REGARDING PATENT AND COPYRIGHT INFRINGEMENT (APR 1984)
52.227-10	FILING OF PATENT APPLICATIONS - CLASSIFIED SUBJECT MATTER (APR 1984)
52.227-11	PATENT RIGHTS - RETENTION BY THE CONTRACTOR (SHORT FORM) (JUN 1989)
52.228-6	INSURANCE - IMMUNITY FROM TORT LIABILITY (APR 1984)
52.228-7	INSURANCE - LIABILITY TO THIRD PERSONS (APR 1984)
52.230-5	DISCLOSURE AND CONSISTENCY OF COST ACCOUNTING PRACTICES (SEP 1987)
52.232-23	ASSIGNMENT OF CLAIMS (JAN 1986)
52.237-3	CONTINUITY OF SERVICES (APR 1984)
52.246-25	LIMITATION OF LIABILITY - SERVICES (APR 1984)
52.249-6	TERMINATION (COST-REIMBURSEMENT) (MAY 1986)
52.249-14	EXCUSABLE DELAYS (APR 1984)
52.251-1	GOVERNMENT SUPPLY SOURCES (APR 1984)

<u>DoD FAR CLAUSES</u>	<u>TITLE AND DATE</u>
252.203-7001	SPECIAL PROHIBITION ON EMPLOYMENT (MAR 1989)
252.203-7002	STATUTORY COMPENSATION PROHIBITIONS AND REPORTING REQUIREMENTS RELATING TO CERTAIN FORMER DEPARTMENT OF DEFENSE (DoD) EMPLOYEES (APR 1988)
252.223-7500	DRUG-FREE WORK FORCE (SEP 1988)
252.225-7001	BUY AMERICAN ACT AND BALANCE OF PAYMENTS PROGRAM (APR 1985)
252.225-7023	RESTRICTION ON ACQUISITION OF FOREIGN MACHINE TOOLS (JAN 1989)
252.227-7013	RIGHTS IN TECHNICAL DATA AND COMPUTER SOFTWARE (OCT 1988)
252.227-7018	RESTRICTIVE MARKINGS ON TECHNICAL DATA (OCT 1988)
252.227-7029	IDENTIFICATION OF TECHNICAL DATA (APR 1988)
252.227-7034	PATENTS - SUBCONTRACTS (APR 1984)
252.227-7037	VALIDATION OF RESTRICTIVE MARKINGS ON TECHNICAL DATA (APR 1988)
252.231-7000	SUPPLEMENTAL COST PRINCIPLES (APR 1984)
252.231-7001	PENALTIES FOR UNALLOWABLE COSTS (APR 1988)
252.231-7003	CERTIFICATION OF INDIRECT COSTS (APR 1986)
252.251-7000	ORDERING FROM GOVERNMENT SUPPLY SOURCES (APR 1984)
252.271-7001	RECOVERY OF NONRECURRING COSTS ON COMMERCIAL SALES OF DEFENSE PRODUCTS AND TECHNOLOGY AND OF ROYALTY FEES FOR USE OF DoD TECHNICAL DATA (FEB 1989)

7 November 1991

AFOSR/PKO  
Bldg. 410, Room C-124  
Bolling AFB, DC 20332-6448

Attn: Ms. Kathleen Wetherell

Dear Ms. Wetherell:

Enclosed for your approval is the model subcontract for the Research Initiation Program under the Summer Research Programs (Contract F9620-90-C-0076). The blanks will be filled by merging information from our dBase IV database.

Sincerely,

Abe S. Sopher  
Contracts Manager

cc: AFOSR/NI (Lt. Col. Cavendar)

**ATTACHMENT 2:**  
**SAMPLE TECHNICAL EVALUATION FORM AND TECHNICAL**  
**EVALUATION SUMMARY**

## 1992 RESEARCH INITIATION PROGRAM TECHNICAL EVALUATION

RIP NO: 92-2  
RIP ASSOCIATE: Dr. Charles Kibert

Provided are several evaluation statements followed by ratings of (1) through (5). A rating of (1) is the lowest and (5) is the highest. Circle the rating level number you best feel rates the statement. Document additional comments on the back of this evaluation form.

Mail or fax the completed form to:

RDL  
Attn: 1992 RIP TECH EVALS  
5800 Uplander Way  
Culver City, CA 90230-6608  
(Fax: 310 216-5940)

- |  |           |
|--|-----------|
| 1. This RIP report has a high level of technical merit                           | 1 2 3 4 5 |
| 2. The RIP program is important to accomplishing the lab's mission               | 1 2 3 4 5 |
| 3. This RIP report accomplished what the associate's proposal promised           | 1 2 3 4 5 |
| 4. This RIP report addresses area(s) important to the USAF                       | 1 2 3 4 5 |
| 5. The USAF should continue to pursue the research in this RIP report            | 1 2 3 4 5 |
| 6. The USAF should maintain research relationships with this RIP associate       | 1 2 3 4 5 |
| 7. The money spent on this RIP effort was well worth it                          | 1 2 3 4 5 |
| 8. This RIP report is well organized and well written                            | 1 2 3 4 5 |
| 9. I'll be eager to be a focal point for summer and RIP associates in the future | 1 2 3 4 5 |
| 10. The one-year period for complete RIP research is about right                 | 1 2 3 4 5 |

\*\*\*\*USE THE BACK OF THIS FORM FOR ADDITIONAL COMMENTS\*\*\*\*

LAB FOCAL POINT'S NAME (PRINT): \_\_\_\_\_

OFFICE SYMBOL: \_\_\_\_\_ PHONE: \_\_\_\_\_

# TECHNICAL EVALUATION SUMMARY

## Technical Evaluation Questionnaire Rating Factors

Subcontract no.	1	2	3	4	5	6	7	8	9	10	Average
135	5	4	5	4	4	4	4	4	5	5	4.4
50	4	4	5	4	4	4	4	3	5	5	4.2
3	4	3	3	3	3	3	3	3	3	4	3.2
71	4	4	4	4	3	5	5	4	5	5	4.3
152	3	4	3	4	4	3	4	3	4	5	3.7
147	5	5	5	5	5	5	5	5	5	4	4.9
011	4	4	5	4	5	5	5	4	5	4	4.5
106	5	5	4	5	5	5	5	5	5	5	4.9
83	5	4	5	5	5	5	5	5	5	4	4.8
26	5	4	4	5	5	5	5	5	4	4	4.6
8	5	3	4	4	5	5	5	3	5	5	4.4
120	1	5	2	4	5	3	2	1	4	4	3.1
133	3	2	4	5	5	4	3	4	3	5	3.8
108	5	4	4	5	5	5	5	5	5	5	4.8
76	5	5	5	5	5	5	5	5	5	3	4.8
122	5	5	5	5	5	4	5	5	5	5	4.9
92	4	5	5	5	5	5	5	5	5	5	4.9
47	5	5	5	5	5	4	4	5	5	5	4.8
57	4	4	4	5	5	4	4	4	4	2	4.0
17	5	5	5	5	5	5	5	5	5	5	5.0
5	5	3	4	4	4	5	5	5	4	3	4.2
62	5	4	5	4	4	5	5	5	5	5	4.7
74	4	3	4	4	4	4	5	4	4	5	4.1
53	4	3	4	4	3	4	3	5	3	4	3.7
84	5	4	4	5	5	5	5	5	5	4	4.7
145	4	4	5	4	5	5	5	5	5	4	4.6
35	5	5	5	5	5	5	5	5	5	5	5.0



# Technical Evaluation Questionnaire Rating Factors

Subcontract no.	1	2	3	4	5	6	7	8	9	10	Average
59	5	4	5	5	5	5	5	5	5	5	4.9
115	5	5	5	5	5	5	5	5	5	5	5.0
118	4	5	5	5	5	5	5	4	5	4	4.7
104	5	3	4	3	5	4	5	5	4	5	4.3
6	3	5	5	5	3	5	5	4	5	3	4.3
28	5	4	5	5	5	4	5	4	4	4	4.5
51	5	5	4	5	5	5	5	5	5	4	4.8
16	5	5	5	5	5	4	5	5	5	5	4.9
54	5	4	5	4	5	4	5	5	5	5	4.7
56	3	3	5	4	5	3	4	5	5	5	4.2
69	4	5	4	5	5	4	5	5	5	5	4.7
72	5	5	5	5	5	5	5	5	5	5	5.0
129	5	5	5	5	5	5	5	5	5	5	5.0
58	3	4	5	4	3	4	5	4	4	4	4.0
144	5	5	5	5	5	5	5	5	5	5	5.0
80	5	5	5	5	5	5	5	5	4	4	4.8
136	5	4	5	5	5	5	5	5	5	4	4.8
55	5	5	5	5	5	5	5	5	5	4	4.9
77	5	4	3	4	3	4	4	4	5	4	4.0
15	5	4	5	5	5	5	5	4	5	5	4.8
70	5	4	4	5	5	5	5	5	5	4	4.7
140	5	5	5	5	5	5	5	5	5	5	5.0
79	4	3	5	4	5	4	5	5	4	5	4.4
63	5	5	5	5	5	5	5	5	5	5	5.0
97	5	4	4	5	5	5	5	5	5	5	4.8
11	5	4	4	4	4	5	4	4	5	3	4.2
44	5	5	5	5	5	5	5	5	5	5	5.0
141	5	4	5	4	4	5	5	5	5	4	4.6
98	5	5	5	5	5	5	5	5	5	5	5.0

Technical Evaluation Questionnaire Rating Factors

Subcontract no.	1	2	3	4	5	6	7	8	9	10	Average
81	4	4	3	4	4	4	4	5	5	4	4.1
105	5	5	5	5	5	5	5	5	5	5	5.0
25	4	4	4	5	5	5	4	5	4	2	4.2
18	5	3	5	5	5	3	5	5	5	4	4.5
138	5	4	5	5	5	5	5	3	5	3	4.5
111	5	5	5	5	5	5	5	5	5	5	5.0
Avg by factor:	4.5	4.2	4.5	4.6	4.7	4.6	4.7	4.6	4.7	4.4	4.6

MULTIRESOLUTION ELECTRO-OPTIC SENSOR MODELS

Raj S. Acharya  
Associate Professor  
Department of Electrical and Computer Engineering

State University of New York at Buffalo  
Buffalo, NY 14260

Final Report for:  
Research Initiation Program  
Wright Laboratory

Sponsored by:  
Air Force Office of Scientific Research  
Bolling Air Force Base, Washington, D.C.

and

State University of New York at Buffalo

March 1993

## **Abstract**

### **Multiresolution Electro-Optic Sensor Models**

**Raj S. Acharya**

Electrical and Computer Engineering  
State University of New York at Buffalo  
Buffalo, NY 14260  
acharya@eng.buffalo.edu

In this research we propose a Nonlinear Multiscale approach to the Analysis of FLIR Images. We implement Nonlinear Pyramids with the aid of Mathematical Morphology. We construct the Nonlinear Scale Space with the aid of Alternating Sequential Filters (ASF). ASFs involve sequential application of Opening-Closing filters with increasing size of the Structuring Elements. Our research is based on the premise that Nonlinear Scale Space is better than Linear Scale Space (Such as Wavelet Scale Space) as it provides Multiresolution representations without distorting the desired features.

We analyze the FLIR features in the ASF generated Scale Space. We study the features as a function of the time of the day. The graphs of the edge fractal measures provide diurnal thermal signatures, and show the thermal behavior of the materials. These features are used to obtain relative thermal behavior of target substructures which in turn are used to obtain Target Sensor Models.

## Multiresolution Electro-Optic Sensor Models

We have studied two specific tasks:

- (1) **Development of Multiresolution Representations for FLIR Image Analysis using Nonlinear Scale Space.**
- (2) **FLIR Image Analysis using a Nonlinear Multiresolution Representation.**

### Hypothesis/Rationale

1. Multiresolution analysis of FLIR images is not only optimal but also practical.
2. Nonlinear Scalespace (unlike Wavelet representation) provides a multiresolution representation without blurring the features.
3. Relative thermal behavior of target substructures can be used to develop Target Sensor Models.

## I. INTRODUCTION

In this report, we use the Nonlinear Scalespace for Multiresolution FLIR image analysis. The Nonlinear Scalespace is generated with the aid of Mathematical Morphology. Specifically, we propose the use of Alternating Sequential Filters( ASF) for Nonlinear Scalespace generation. We present some preliminary results on FLIR image analysis using nonlinear scalespace.

We have proposed a nonlinear multiresolution approach to image analysis(11). We implement the multiresolution pyramid within the framework of Mathematical Morphology. **We propose the use of ASF(Alternating Sequential Filters) for nonlinear scale space generation.** In the following section, we briefly review some important concepts of Mathematical Morphology.

The image pyramid paradigm provides a computational framework that is well suited for implementing an efficient computer vision system. This hierarchical structure supports a wide variety of fast and robust algorithms [1], [2]. On the other hand, recent papers in mathematical morphology [3],[19],[20], specifically the ones related to morphological sampling theorem [7],[8],[9],[11] permit the development of new pyramid algorithms. In general, a pyramid structure can be obtained by low pass filtering and then sampling an image to generate the next lower resolution level of the pyramid. The analysis of a morphological pyramid requires a morphological sampling theorem which explains how an appropriately morphological filtered and sampled image relates to the unsampled image. It also explains the relationship between performing a less costly morphological operation on the sampled image and performing the more costly equivalent morphological filtering operation on the original image.

We relate alternating sequential filters (ASF) [15],[17] to the morphological sampling theorem [7],[8]. One of the main reasons behind this approach is to take advantage of

the computational efficiency offered by the MST to implement morphological operations, specifically ASF's. An alternating sequential filter is an iterative application of openings and closing with structuring elements of different sizes. Transformations which apply products of openings and closings are less severe and introduce less distortion than individual openings or closings. It has been shown in [13] that alternating sequential filters are the best in preserving crucial structures of binary images in the "least difference sense". Due to the nonlinearities found in mathematical morphology, there may be limitations in the performance of a single structuring element [16],[18]. Therefore, we consider alternating sequential filters with a combination of structuring elements. The proofs are done for binary images operated with binary structuring elements. Using the threshold decomposition theorem, they are easily extended to gray scale images operated with binary structuring elements.

## II. BACKGROUND

In this section, we briefly review definitions of morphological transformations (see also [5],[6],[11]). Let  $E$  denote the set of integers. Binary discrete images are represented by 2-D sets in the discrete plane  $E^2$ . Given a set  $F$  and a set  $B$ , called the structuring element, two primitive operations are defined by knowing how the structuring element  $B$  interacts with the set  $F$ . The first operation, dilation is defined as

$$F \oplus B = \{x : B_x \cap F \neq \phi\} = \bigcup_{y \in B} F_y = \bigcup_{x \in F} B_x \quad (1)$$

where  $B_x$  is the translation of  $B$  by  $x$ . Dilation can be seen as an operation that expands the original set. The other operation, erosion, is defined as

$$\begin{aligned} F \ominus B &= \{x : B_x \subset F\} = \bigcap_{y \in B_0} F_{-y} \\ &= \bigcap_{-y \in B_0} F_y \end{aligned} \quad (2)$$

where  $B_0$  denotes the structuring element associated with the origin. This is the dual operation of dilation and it can be viewed geometrically as an operation that shrinks the original set. In practice, dilations and erosions are usually employed in pairs, either dilation followed by the erosion or an erosion followed by a dilation.

The opening of an image  $F$  by a structuring element  $B$  is defined as

$$F \circ B = (F \ominus B) \oplus B \quad (3)$$

Similarly closing

$$F \bullet B = (F \oplus B) \ominus B \quad (4)$$

Define now the compound opening-closing mapping (opening followed by closing) as

$$M_B(F) = (F \circ B) \bullet B \quad (5)$$

An alternating sequential filter (ASF) is an iterative application of  $M_B(F)$

$$ASF(F) = M_{B_N} M_{B_{N-1}} \cdots M_{B_1}(F) \quad (6)$$

where  $N$  is an integer,  $B_N, B_{N-1}, \dots, B_1$  are structuring elements with different sizes and  $B_N \supseteq B_{N-1} \supseteq \cdots B_1$ . Transformations which apply products of openings and closing are less severe and introduce less distortion than an individual closing or opening. In addition, it has been shown that Alternating Sequential Filters are the best in preserving crucial structure of binary images [13].

Next, we review a unifying theory of morphological filters developed in [5],[10],[14]. This unification establishes that any morphological transformation that is translation invariant (TI) and increasing can be characterized by a special collection of input images. This set of images is called the kernel.

**Definition 1.** The kernel of any transformation  $\psi$  that is TI and increasing is defined by  $Ker(\psi) = \{F : \bar{0} \in \psi(F)\}$ , where  $F$  is the input image and  $\bar{0}$  denotes the origin  $(0, 0)$ .

Using the above definition, one of the classic results of mathematical morphology has been derived (see [5],[10],[14]). This theorem states that any morphological filter can be represented as a union of erosions by elements in the filter's kernel. In its dual form, it states that the erosion representation can be replaced by an intersection of dilations with elements of the dual filter's kernel.

**Matheron's Theorem I** If  $\psi$  is an increasing morphological transformation, then for any image or signal  $F$

$$\psi(F) = \bigcup_{B \in Ker(\psi)} F \ominus B$$

It is possible also to represent a filter using its dual form

$$\psi(F) = \bigcap_{B \in Ker(\psi^d)} F \oplus B$$

However, these realizations, except for their theoretical interest, are impractical because they require an infinite number of kernel elements. On the other hand, one can

exploit the redundancy in these kernel elements. This has lead to the concept of basis functions [5],[10].

**Definition 2.** The basis functions are the minimal elements of  $Ker(\psi)$ . The system  $(Ker(\psi), \subseteq)$  is a partially ordered set; an element  $B \in Ker(\psi)$  is minimal if and only if for each  $A \in Ker(\psi)$ ,  $A \subseteq B \Rightarrow A = B$ . These elements exist if  $\psi$  is TI and increasing.

Thus, Matheron's Theorem I is modified in the sense that now  $B$  belongs to the basis function representation which is a smaller set than the Kernel. The basis representation of any of morphological transformation yields a single *local operation* rather than a cascade of operations that introduce delays and require additional storage. This aids in the VLSI implementation of opening and closing [10].

### III. Morphological Sampling Theorem (MST)

A multiresolution representation (or pyramid) is referred as a hierarchy of images where copies of the original ( or base image) are transformed and sampled in regular steps. In multiresolution morphology the transformations are basically morphological operations. In order to set up the framework of our work it is necessary to review the morphological sampling theorem (MST) developed by Haralick *et. al.* Detailed definitions of morphological concepts in this paper can be found in Haralick *et al.* [7], [8]. There are four basic structures utilized in the MST

- the original set  $F$
- the sampling set  $S$
- the reconstruction structuring element  $K$
- the structuring element  $B$

Sampling a set is accomplished by taking the intersection of the original set  $F$  with the sampling set  $S$ . The sampling set  $S$  is defined as  $S = \{(x, y) | x, y \text{ integers}\}$ . Example:  $S = \{(x, y) | x \text{ and } y \text{ even}\}$ . Reconstruction of a sampled set can be done by either dilating the sampled set or closing the sampled set with the reconstruction structuring element  $K$ . These provide maximal and minimal reconstruction respectively. Relationships between the sampling set  $S$  and the reconstruction structuring element  $K$  are given by the following conditions:

1.  $S = S \oplus S$
2.  $S = \check{S}$
3.  $K \cap S = \{0\}$
4.  $K = \check{K}$
5.  $a \in K_b \rightarrow K_a \cap K_b \cap S \neq \emptyset$

Conditions 1 and 2 imply that  $S$  is an infinite set, conditions 3 and 4 mean that the



reconstruction structuring element is symmetric, contains the origin and is small enough so that its intersection with the sampling set  $S$  is reduced to  $\{0\}$ . Condition 5 states that the sampling space must be small enough such that the diameter of  $K$  contains two sample intervals but not three. Finally, conditions 3,4 and 5 imply that  $S \oplus = E^2$  ( See [7],[8] for details).

### The Distance Relationships

The set bounding relationships states that the closing reconstruction is contained in the set itself, which in turn is contained in its dilation reconstruction. In order to measure inclusion or in other words how far from each other these reconstructions are, the following distances are used

**Definition 3** Define the radius of a set  $B$  denoted by  $r(B)$  as

$$r(B) = \min_{x \in B} \max_{y \in B} \|x - y\| \quad (7)$$

**Definition 4** For a set  $A$  which contains  $B$  define a pseudo-distance from set  $A$  to  $B$  as

$$\rho(A, B) = \max_{x \in A} \min_{y \in B} \|x - y\| \quad (8)$$

$\rho(A, B)$  is the radius of the smallest disk which when used as a structuring element to dilate  $B$  produces a result which contains  $A$ .

**Definition 5** Define the **Hausdorff metric** as the following distance

$$\rho_m(A, B) = \max\{\rho(A, B), \rho(B, A)\} \quad (9)$$

It has been shown in [8] that the distance between the minimal reconstruction and the maximal reconstruction which differs only by a dilation by  $K$  is not greater than the size of the reconstruction structuring element, i.e.,

$$\rho_m([F \cap S] \bullet K, [F \cap S] \oplus K) \leq \rho_m(F \cap S, [F \cap S] \oplus K) \leq r(K)$$

This distance relationship means that just as the standard sampling theorem cannot produce a reconstruction with frequencies higher than the Nyquist rate, the morphological sampling theorem cannot produce a reconstruction whose positional accuracy is better than the radius of the reconstruction structuring element [8].

## IV. Alternating Sequential Filters and The MST

Equipped with the previous definitions, in this section we will provide answers to the questions raised in section II. For the sake of completeness, let's restate these questions: Are the operations equivalent if we decrease the size of the image or if we increase the size of the structuring element? If they are not, how different are these operations? Under

what circumstances will we have equivalent results? The main reason to answer these questions is to exploit the computational efficiency offered by the morphological sampling theorem. We will provide some relationships between working in the computationally more efficient morphological operations in sampled domain vs. the less efficient operations in the unsampled domain. Due to the advantages of alternating sequential filters [13],[17], we generate a morphological pyramid with these operators rather than just using opening or closing [8]. We recall from section II that an ASF is defined as

$$ASF(F) = M_{B_N} M_{B_{N-1}} \cdots M_{B_1}(F)$$

Alternating sequential filters are less severe and introduce fewer distortions when a small structuring element is used before a larger one. Generally speaking, these filters can be categorized as low pass filters. The properties of alternating sequential filters have been studied in [13],[15],[17].

In order to find a relationship between opening-closing in the sampled and unsampled domain we first show, using basis functions, an alternative proof for propositions 1 and 2. Although these proofs were presented in [8] (propositions 16 and 17), they were done using the sequential nature of opening (closing) which is an erosion (dilation) followed by a dilation (erosion). The proofs carried out here are done using the basis functions implementation of opening and closing. From the hardware point of this is very important because the proofs of propositions 1 and 2 show that these operations can be done in one step procedure rather the classical two-step procedure of opening (closing).

**Proposition 1**

$$(F \cap S) \circ (B \cap S) = [F \circ (B \cap S)] \cap S$$

**Proof :** Using basis functions [8], it is known that

$$(F \cap S) \circ (B \cap S) = \bigcup_i [(F \cap S) \ominus (B_i \cap S)]$$

where  $B_i \cap S$  is the basis representation of opening in the sampled domain. One important point is that the  $B_i$ 's contain the origin thus the intersection  $B_i \cap S$  is never empty. If we let  $A_i = B_i \cap S$ , then :

$$\bigcup_i [(F \cap S) \ominus (B_i \cap S)] = ((F \cap S) \ominus A_1) \bigcup ((F \cap S) \ominus A_2) \cdots$$

But

$$((F \cap S) \ominus A_1) = (F \ominus A_1) \cap (S \ominus A_1)$$

Note that by definition  $S$  is an infinite set and since all  $A_i$ 's are sampled sets then

$$S \ominus A_i = S$$

It follows

$$\begin{aligned}
(F \cap S) \circ (B \cap S) &= [(F \ominus A_1) \cap S] \bigcup [(F \ominus A_2) \cap S] \dots \\
&= [(F \ominus A_1) \cup (F \ominus A_2) \dots] \bigcap S \\
&= [\bigcup_i (F \ominus (B_i \cap S))] \bigcap S
\end{aligned}$$

But

$$\bigcup_i (F \ominus (B_i \cap S)) = F \circ (B \cap S)$$

Therefore

$$(F \cap S) \circ (B \cap S) = [F \circ (B \cap S)] \cap S$$

**Q.E.D.**

**Proposition 2**

$$(F \cap S) \bullet (B \cap S) = [F \bullet (B \cap S)] \cap S$$

**Proof :** By using basis functions [8], we know that the closing representation can be done using intersection of dilations.

$$(F \cap S) \bullet (B \cap S) = \bigcap^i (F \cap S) \oplus (B_i \cap S)$$

Decompose the intersection as follows

$$\bigcap^i (F \cap S) \oplus (B_i \cap S) = [(F \cap S) \oplus (B_1 \cap S)] \bigcap [(F \cap S) \oplus (B_2 \cap S)] \dots$$

By lemma

$$(F \cap S) \oplus (B_i \cap S) = [F \oplus (B_i \cap S)] \cap S$$

Substituting in the previous equation,

$$\begin{aligned}
(F \cap S) \bullet (B \cap S) &= ([F \oplus (B_1 \cap S)] \bigcap S) \bigcap \dots \\
&= ([F \oplus (B_1 \cap S)] \bigcap \dots) \bigcap S \\
&= [\bigcap^i (F \oplus (B_i \cap S))] \bigcap S
\end{aligned}$$

But

$$[F \bullet (B \cap S)] \cap S = [\bigcap^i (F \oplus (B_i \cap S))] \bigcap S$$

**Q.E.D.**

These two important relationships show that opening or closing can be obtained at any level of the morphological pyramid in one step rather than the traditional two-step procedure. By using the two previous propositions, we now derive the first relationship for opening-closing in the sampled and unsampled domain.

**Proposition 3**

$$[(F \cap S) \circ (B \cap S)] \bullet (B \cap S) = [F \circ (B \cap S)] \bullet (B \cap S) \cap S$$

**Proof :** By proposition 1

$$[(F \cap S) \circ (B \cap S)] = [F \circ (B \cap S)] \cap S$$

Let now

$$[F \circ (B \cap S)] = A$$

Then

$$\begin{aligned} (A \cap S) \bullet (B \cap S) &= [A \bullet (B \cap S)] \cap S \\ &= [F \circ (B \cap S)] \bullet (B \cap S) \cap S \end{aligned}$$

**Q.E.D.**

Proposition 3 shows that one can sample the original image and then perform the open-close operation or equivalently one can perform the open-close in the original image and then sample. The two results are similar. However, the first procedure is more efficient.

**Proposition 4**

$$[F \circ ((B \cap S) \oplus K)] \bullet ((B \cap S) \oplus K) \cap S \subseteq (F \cap S) \circ (B \cap S) \bullet (B \cap S) \subseteq [[(F \cap S) \oplus K] \circ B \bullet B] \cap S$$

**Proof :** It can be shown that

$$(F \cap S) \circ (B \cap S) \bullet (B \cap S) = [[F \circ (B \cap S)] \cap S \bullet (B \cap S)] \cap S$$

By a previous theorem [7],[8], we have that

$$([F \circ (B \cap S)] \cap S) \subseteq [(F \cap S) \oplus K] \circ B$$

Since closing is an increasing operation and

$$(B \cap S) \subset B$$

Then

$$[[F \circ (B \cap S)] \cap S \bullet (B \cap S)] \cap S \subseteq [(F \cap S) \oplus K] \circ B \bullet B] \cap S$$

The lower set containment can be proved in similar way. Since opening is anti-extensive we have that

$$F \circ ((B \cap S) \oplus K) \subseteq F \circ (B \cap S)$$

Let

$$A = F \circ ((B \cap S) \oplus K)$$

Consider

$$[A \bullet (B \cap S) \oplus K] \cap S$$

There exists a  $x$  such that

$$x \in A \bullet ((B \cap S) \oplus K) \text{ and } x \in S$$

By definition of closing

$$x \in A \cap [(B \cap S) \oplus K]_y \neq \emptyset \text{ and } x \in S$$

As  $S$  is an infinite set, the above condition means that

$$x \in A \cap [(B \cap S) \oplus K]_y \cap S \neq \emptyset$$

Because  $x \in S$ ,  $y$  should be such that  $S_y \cap S = S$ , and

$$x \in A \cap [((B \cap S) \oplus K) \cap S]_y \cap S \neq \emptyset$$

$$x \in A \cap (B \cap S) \cap S$$

since

$$A = F \circ ((B \cap S) \oplus K) \subseteq F \circ (B \cap S)$$

and closing is an increasing operation

$$x \in [F \circ (B \cap S) \bullet (B \cap S)] \cap S$$

**Q.E.D.**

This proposition establishes that the operation in the sampled domain is limited by maximally reconstructing the image and then transforming it by open-close or by maximally reconstructing the structuring element and then open-close the original image. In practice, this proposition may be used in generating band-pass pyramids.

**Proposition 5** Suppose that  $B = (B \cap S) \oplus K$ , if  $F = (F \cap S) \oplus K$ , then

$$(F \cap S) \circ (B \cap S) \bullet (B \cap S) = (F \circ B \bullet B) \cap S$$

**Proof :** The bounding relationship of proposition 4 becomes

$$[(F \circ B) \bullet B] \cap S \subseteq (F \cap S) \circ (B \cap S) \bullet (B \cap S) \subseteq [(F \circ B) \bullet B] \cap S$$

Then it follows that:

$$(F \cap S) \circ (B \cap S) \bullet (B \cap S) = [(F \circ B) \bullet B] \cap S$$

**Q.E.D.**

Proposition 5 shows that if the maximal reconstructions of  $F$  and  $B$  are the same as the original sets, then opening-closing in the sampled and unsampled domain are equivalent. However, it is clear that the operation in the sampled domain is faster. This result is very important from the theoretical point of view but in practice one has to prove that  $F = (F \cap S) \oplus K$  and  $B = (B \cap S) \oplus K$  which tends to be time consuming. Of more practical importance are the results shown next.

**Proposition 6** If  $K \subseteq B$  then

$$[(F \circ B \bullet B) \cap S] \bullet K \subseteq F \circ B \bullet B \subseteq [(F \circ B \bullet B) \cap S] \oplus K$$

**Proof** From [18] and from proposition 5 in [8],  $F \circ B \bullet B$  is both open and close with respect to  $K$ .

**Q.E.D.**

Propositions 6 states very interesting limits to be used in band- pass pyramids. A band pass pyramid can be obtained by reconstructing any level of the pyramid either by dilation or closing with the reconstruction structuring element. This proposition can be used to implement a good edge detector as will be shown in the examples provided in section VI.

These 6 propositions have shown how to relate an alternating sequential filter and the morphological sampling theorem. However, due to the nonlinear nature of mathematical morphology there may be limitations in the performance of only one structuring element [16],[18]. Thus, we also consider morphological operators with multiple structuring elements, like the union of openings and intersection of closings. Mathematical Morphology provides representations that allows us to build complicated algorithms in terms of simpler ones (like basis representation). Next, we show applications of another powerful theorem due also to G. Matheron [14] :

**Matheron's Theorem II :** An image mapping  $\psi$  is an algebraic opening ( i.e. increasing, anti-extensive, idempotent and translation invariant) if and only if there exist a class  $\beta$  such that

$$\psi(X) = \bigcup_{B_i \in \beta} X_B = \bigcup_i (X \circ B_i)$$

where  $\beta$  is a sub-collection of images called *base* ( there is a difference between *base* and *basis*. See [5],[14] for details). There is also a dual representation of  $\psi$  using the intersection of closing. Thus, if we want to construct a filter which is anti-extensive, increasing, idempotent and translation invariant, we need to apply the properties of openings (closing). In others words a union of openings (intersection of closing) is still a morphological opening (closing). We will show the application of the above theorem with the following propositions

**Proposition 7**

$$a) \quad \bigcup_j [(X \cap S) \circ (B_j \cap S)] = \{ \bigcup_j [X \circ (B_j \cap S)] \} \cap S$$

$$b) \quad \bigcap_i [(X \cap S) \bullet (B_i \cap S)] = \{ \bigcap_i [X \bullet (B_i \cap S)] \} \cap S$$

**Proof :** a) Decompose the union of openings as follows

$$[(X \cap S) \circ (B_1 \cap S)] \bigcup [(X \cap S) \circ (B_2 \cap S)] \dots$$

By proposition 1

$$(X \cap S) \circ (B_1 \cap S) = [X \circ (B_1 \cap S)] \cap S$$

The union of closings can be written as

$$\{ [X \circ (B_1 \cap S)] \cap S \} \bigcup \{ [X \circ (B_2 \cap S)] \cap S \} \dots$$

which is

$$\{ \bigcup_j [X \circ (B_j \cap S)] \} \cap S$$

**Q.E.D.**

b) The proof is similar to the previous one.

This representation is similar to proposition 1 (2), i.e., if we had had only one opening (closing).

An equivalence to proposition 3 can also be shown by using union of openings (intersection of closings) as follows:

**Proposition 8**

$$\bigcap_i \left\{ \bigcup_j [F \cap S] \circ (B_j \cap S) \bullet (B_i \cap S) \right\} = \left[ \bigcap_i \left\{ \bigcup_j [F \circ (B_j \cap S)] \bullet (B_i \cap S) \right\} \right] \cap S$$

**Proof :** Using proposition 7a, we obtain the left hand side of the equation as

$$\bigcap_i \left\{ \left( \bigcup_j [F \circ (B_j \cap S)] \right) \cap S \bullet (B_i \cap S) \right\}$$

Using proposition 7b, we can obtain

$$\left[ \bigcap_i \left\{ \bigcup_j [F \circ (B_j \cap S)] \bullet (B_i \cap S) \right\} \right] \cap S$$

**Q.E.D.**

Propositions 4 and 5 can also be extended in similar fashion. All the propositions presented so far can be readily extended to gray scale images operated on with binary structuring elements without modification. This is possible by the application of the threshold decomposition theorem.

## V. Some Distance Relationships

In this section we study the distance between pre and post sampled operation. We will establish similar reconstruction bounds as in the standard sampling theorem [7],[8], i.e, we can not morphologically reconstruct an image whose positional accuracy is better than twice the radius of the reconstruction structuring element.

**Proposition 9**

$$\rho_m \{ [(F \cap S) \oplus B] \cap S, (F \cap S) \oplus (B \cap S) \} \leq 2r(K)$$

where  $r(K)$  is the radius of the reconstruction structuring element.

Although this distance relationship is implicit in Haralick's papers [7],[8], we show explicitly that this distance is no greater than  $2r(K)$

**Proof** The previous distance is

$$\begin{aligned} &\leq \rho_m \{ [F \cap S] \oplus B, (F \cap S) \oplus (B \cap S) \} \\ &\leq \rho_m \{ [(F \cap S) \oplus K] \oplus [(B \cap S) \oplus K], (F \cap S) \oplus (B \cap S) \} \\ &\leq \rho_m \{ (F \cap S) \oplus (B \cap S) \oplus 2K, (F \cap S) \oplus (B \cap S) \} \\ &\leq 2r(K) \end{aligned}$$



**Q.E.D.**

The following proposition establishes the distance between post-sampling the opened maximal reconstructed set and opening the set in the sampled domain.

**Proposition 10**

$$\rho_m[\{((F \cap S) \oplus K) \circ B\} \cap S, (F \cap S) \circ (B \cap S)] \leq 2r(K)$$

**Proof :** We know

$$(F \cap S) \circ (B \cap S) \subseteq \{((F \cap S) \oplus K) \circ B\} \cap S = [\{(F \cap S) \oplus K\} \oplus B] \cap S$$

Let  $Y = [(F \cap S) \oplus K] \oplus B$

It is clear that

$$(Y \cap S) \oplus (B \cap S) \subseteq (Y \oplus B) \cap S$$

Let's assume that  $B = B \circ K$  then from [8]

$$(F \cap S) \oplus (B \cap S) = Y \cap S$$

Dilate now both sides with  $B \cap S$

$$(F \cap S) \oplus (B \cap S) \oplus (B \cap S) = (F \cap S) \circ (B \cap S) = (Y \cap S) \oplus (B \cap S) \subseteq (Y \oplus B) \cap S$$

Therefore the distance

$$\rho_m[\{(Y \oplus B) \cap S\}, (Y \cap S) \oplus (B \cap S)] \leq 2r(K)$$

**Q.E.D.**

A similar relationship can be established if we close the maximal reconstructed set

**Proposition 11**

$$\rho_m[\{[(F \cap S) \oplus K] \bullet B\} \cap S, [(F \cap S) \bullet (B \cap S)]] \leq 2r(K)$$

**Proof :** The left hand distance is

$$\begin{aligned} &\leq \rho_m[\{[(F \cap S) \oplus K] \bullet B, (F \cap S) \bullet (B \cap S)\}] \\ &\leq \rho_m[\{[(F \cap S) \oplus K] \bullet (B \cap S) \oplus K, (F \cap S) \bullet (B \cap S)\}] \end{aligned}$$

Using basis functions, we can prove that

$$[(F \cap S) \oplus K] \bullet [(B \cap S) \oplus K] = [(F \cap S) \oplus 2K] \bullet (B \cap S)$$

Then

$$\begin{aligned} &\leq \rho_m \{[(F \cap S) \oplus 2K] \bullet (B \cap S), (F \cap S) \bullet (B \cap S)\} \\ &\leq 2r(K) \end{aligned}$$

**Q.E.D.**

The last proposition establishes the maximum distance between opening-closing the maximal reconstructed set and the opening-closing the set in the sampled domain.

**Proposition 12**

$$\rho_m \{([(F \cap S) \oplus K] \circ B \bullet B) \cap S, (F \cap S) \circ (B \cap S) \bullet (B \cap S)\} \leq 2r(K)$$

**Proof :** The left hand distance is

$$\leq \rho_m [(F \cap S) \oplus K \circ B \bullet B, (F \cap S) \circ (B \cap S) \bullet (B \cap S)]$$

Now since

$$[(F \cap S) \oplus K] \circ B \subseteq (F \cap S) \oplus K \quad (a)$$

$$(F \cap S) \circ (B \cap S) \subseteq (F \cap S) \quad (b)$$

It is fair to assume that the previous inequality is

$$\leq \rho_m \{[(F \cap S) \oplus K] \bullet B, (F \cap S) \bullet (B \cap S)\}$$

This is because the set containment in (a) is bigger than in (b). Then, from proposition 2

$$\begin{aligned} &\rho_m \{([(F \cap S) \oplus K] \circ B \bullet B) \cap S, (F \cap S) \circ (B \cap S) \bullet (B \cap S)\} \\ &\leq \rho_m \{[(F \cap S) \oplus K] \bullet B, (F \cap S) \bullet (B \cap S)\} \leq 2r(K) \end{aligned}$$

**Q.E.D.**

## VI. MULTI RESOLUTION FLIR FEATURE ANALYSIS

We study the diurnal changes of detectable features of tactile targets in infrared images at different resolutions. Twenty four images of tank T3, used in the experiments have been obtained at each hour starting at 8.24pm, 12th October, 1988.

The images were preprocessed using histogram equalization technique [22]. Images at reduced resolutions were derived using morphological scale space[11].

Fig 1 shows Nonlinear Scalespace edges while, Fig 2 shows the linear(Wavelet based) Scalespace edges.

The desired features in the Tank image were wheels, turret, middle thread, tool box, and drive wheel. These features were identified by detecting their boundary edge contours. After thinning, edges were partitioned into edge segments at the intersection points and the corner points. Points where the curvature of the contour changes considerably were marked as corner points[24].

The uncertainty about the features were determined as a fractal measure of boundary edges [25]. Fractal measure of a boundary contour is the percentage of the edge points detected in the contour. The graphs(Figs 3,4,5) show this measure for different features against time at three different resolutions :  $1/2$ ,  $1/4$  and  $1/8$ , of the original resolution. Although these percentage values do not express an absolute measure of uncertainty of features, they are useful in comparing uncertainties of different features and their variations with time.

The graphs of edge fractal measures, or *diurnal thermal signatures*, show the thermal behavior of the materials of the features. Most of the features observed have shown similar thermal properties and have appeared in a constant manner over the day. The invariant behavior of these features are due to their high thermal mass and can be used to distinguish the target from other surrounding objects and terrain patterns. *We believe that diurnal thermal signatures may be successfully used in the detection of tactile targets.*

Since high resolution signals are often affected with noise and redundant information, it is important to examine thermal signatures at different resolutions. We adhere to morphological transforms to obtain the multi scale representation to avoid feature blurring in linear scale space. At low resolution, the signatures display similar variations, while some of the features, such as wheels and the turret, are more prominent than others. **We conclude that confidence of the target detection process can be improved by utilizing the thermal signatures of features that remain significant in scale space.**

Results of our method are exciting and show promise. We plan to further refine the feature extraction procedure.

## VII. REFERENCES

- [1] P. Burt and E. Adelson, "The Laplacian Pyramid as a Compact Image Code", *IEEE Transactions on Communications*. Vol 31, No. 4. April 1983.
- [2] P. Burt, "Smart Sensing within a Pyramid Vision Machine". *Proceedings of the IEEE*. August 1988.
- [3] M. Chen and P. Yan, "A Multiscaling Approach Based on Mathematical Morphology". *IEEE Transactions on Pattern Analysis and Machine Intelligence*. Vol. 11, No. 7, July 1989.
- [4] E. Dougherty, "Optimal Mean-Square N-Observation Digital Morphological Filters", *CVGIP: Image Understanding*. Vol. 55, No. 1, January 1992.
- [5] C. Giardina and E. Dougherty, *Morphological Methods in Image and Signal Processing*, New Jersey, Prentice Hall 1988.
- [6] R. M. Haralick, S. R. Sternberg, and X. Zhuang, "Image Analysis Using Mathematical Morphology", *IEEE Transactions on Pattern Analysis and Machine Intelligence*, vol. PAMI-9, July 1987.
- [7] R. Haralick, J. Lee, C. Lin, and X. Zhuang, "Multi-resolution Morphology". *Proc. IEEE First conference on Computer Vision*. London 1987.
- [8] R. Haralick, X. Zhuang, C. Lin and J. Lee, "The Digital Morphological Sampling Theorem". *IEEE Transactions on Acoustics, Speech, and Signal Processing*. Vol. 37. No. 12, December 1989.
- [9] H.J.A. Heijmans and A. Toet, "Morphological Sampling", *CVGIP: Image Understanding*, Vol. 54, No. 3, November, pp 384-400, 1991.
- [10] P. Maragos and R. W. Schafer, "Morphological Filters-Part II: Their Relations to Median, Order Statistics, and Stack Filters", *IEEE Transactions on Acoustics, Speech and Signal Processing*, Vol. ASSP-35, August 1987.
- [11] A. Morales and R. Acharya, "An Image Pyramid with Morphological Operators", *Proceedings 1991 IEEE Computer Society Conference on Computer Vision and Pattern Recognition*. Lahaina, Maui, Hawaii, June 1991.
- [12] A. Morales and S.J. Ko, "Designing Morphological Composite Operators Based on Fuzzy Systems", *Proc. of SPIE/SPSE Symposium in Electronic Imaging*, January 31 - February 4, 1993. San Jose, California.
- [13] D. Schonfeld and J. Goutsias, "Optimal Morphological Pattern Restoration from Noisy Binary Images". *IEEE Transactions on Pattern Analysis and Machine Intelligence*, Vol. 13. No. 1, January 1991.
- [14] J. Serra, *Image Analysis and Mathematical Morphology*, New York, Academic Press, 1982.
- [15] J. Serra, *Image Analysis and Mathematical Morphology*, Vol. 2, New York, Academic Press, 1988.

- [16] J. Song and E. Delp, " The Analysis of Morphological Filters with Multiple Structuring Elements ". *Computer Vision, Graphics, and Image Processing*. Vol. 50, No. 3, June 1990.
- [17] S. Sternberg, " Grey Scale Morphology", *Computer Vision, Graphics and Image Processing*, Vol. 35, 1986.
- [18] R.L. Stevenson and G.R. Arce, " Morphological Filters: Statistics and Further Syntactic Properties". *IEEE Transactions on Circuits and Systems*, CAS-34, No. 11, November 1987.
- [19] A. Toet. " A Morphological Pyramid Image Decomposition". *Pattern Recognition Letters* 9. May 1989.
- [20] A. Toet. " A Hierarchical Morphological Image Decomposition". *Pattern Recognition Letters* 11. pp 267-274. April 1990.
- [21] S. Wilson, " Training of Object Classes Using Mathematical Morphology ", *Proc. of SPIE/SPSE Symposium on Electronic Imaging*. February 9-14, 1992. San Jose, California.
- [22]. Jain, Anil K., *Fundermentals of Image Processing*, Prentice Hall, Englewood Cliffs, NJ 07632.
- [23]. Mallat, Stephane G, " A Theory of Multiresolution Signal Decomposition, " *IEEE Transaction of Pattern Analysis and Machine Intelligence*, Vol 11, No. 7, July 1989.
- [24]. Freeman, H., and Davis, L., " A corner Finding Algorithm For Chain-Coded Curves, " *IEEE Transaction of Computers*, March, 1977.
- [25]. Stephanou, H. E., and Erkman, A. M., " Evidential Classification of Dexterous Graphs for the Integration of Perception and Action, " *Journal of Robotics Systems*, vol. 5, no. 4, pp. 309-336, 1988.

Nonlinear Scalespace Edges

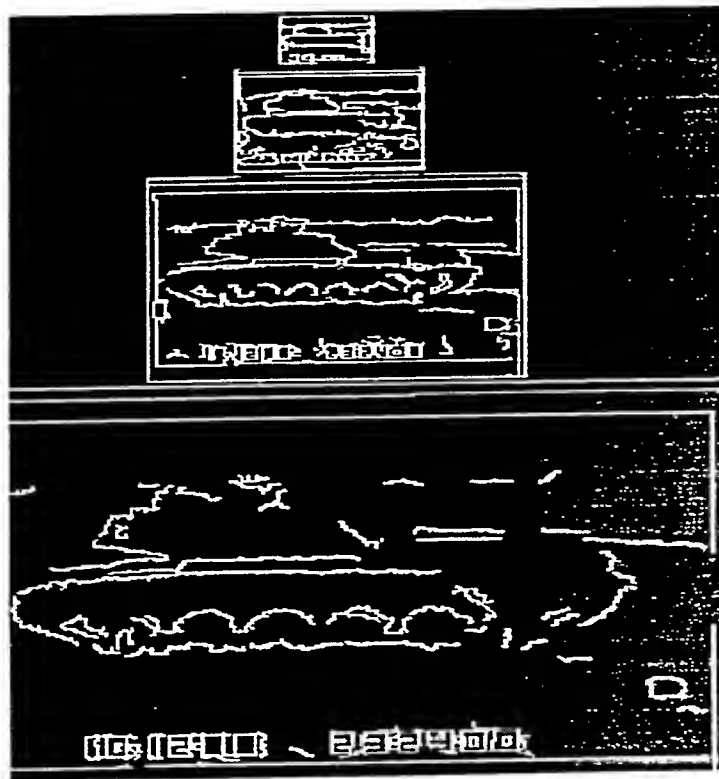


Fig 1

Linear Scalespace Edges

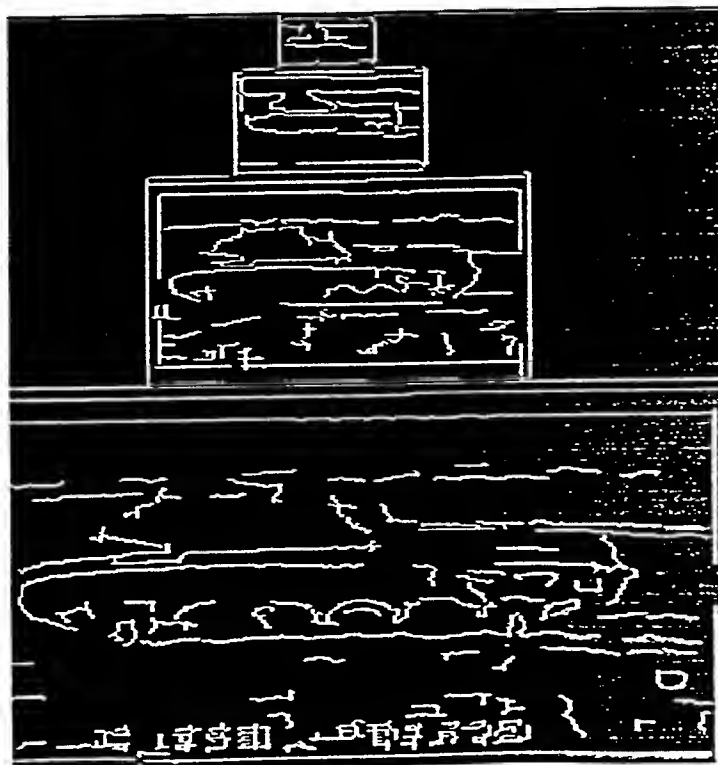
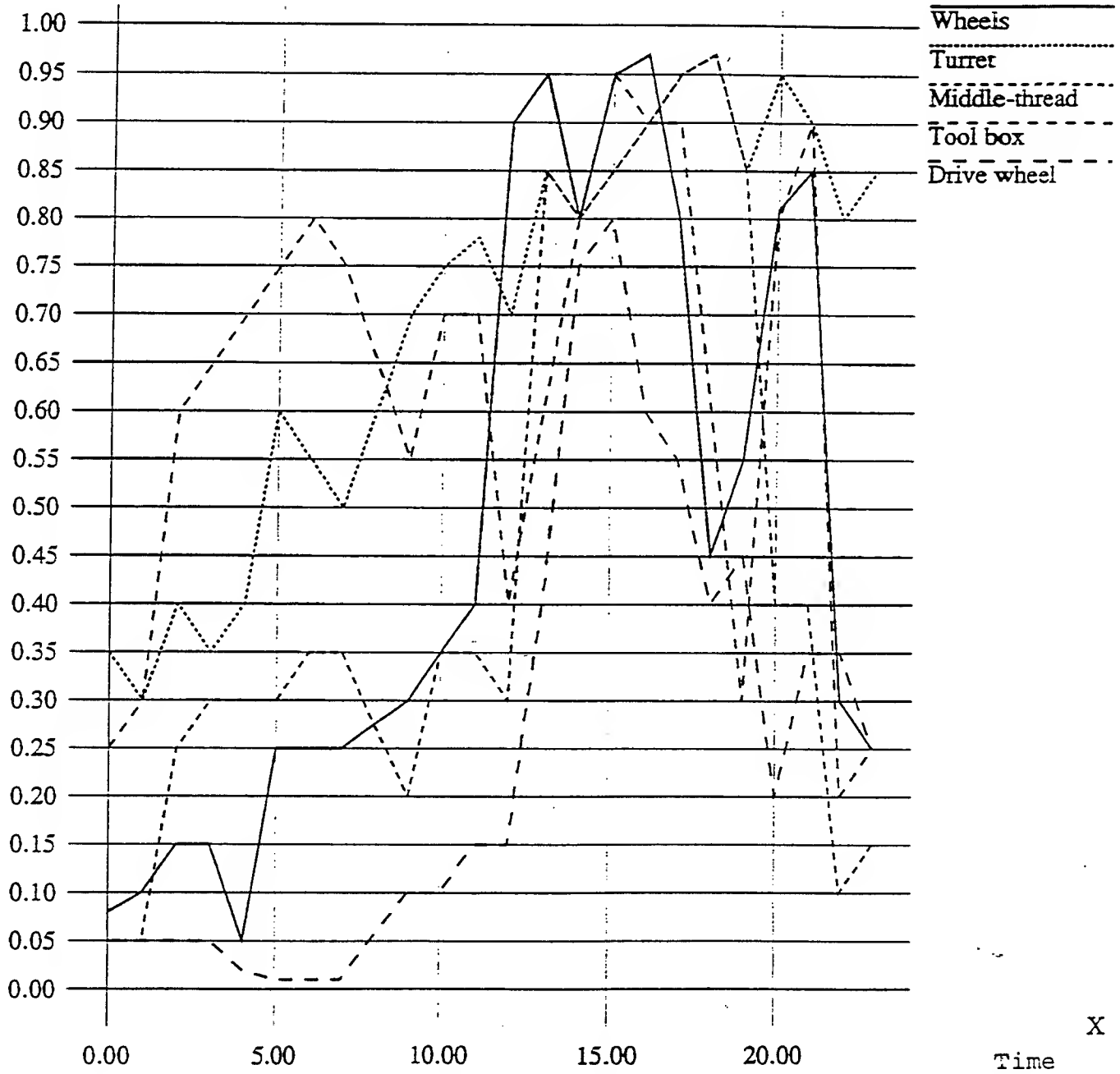


Fig 2

Scale = 0

% of features present  
Y



Features vs Time\_Scale 0

## Features vs Time\_scale 1

Y

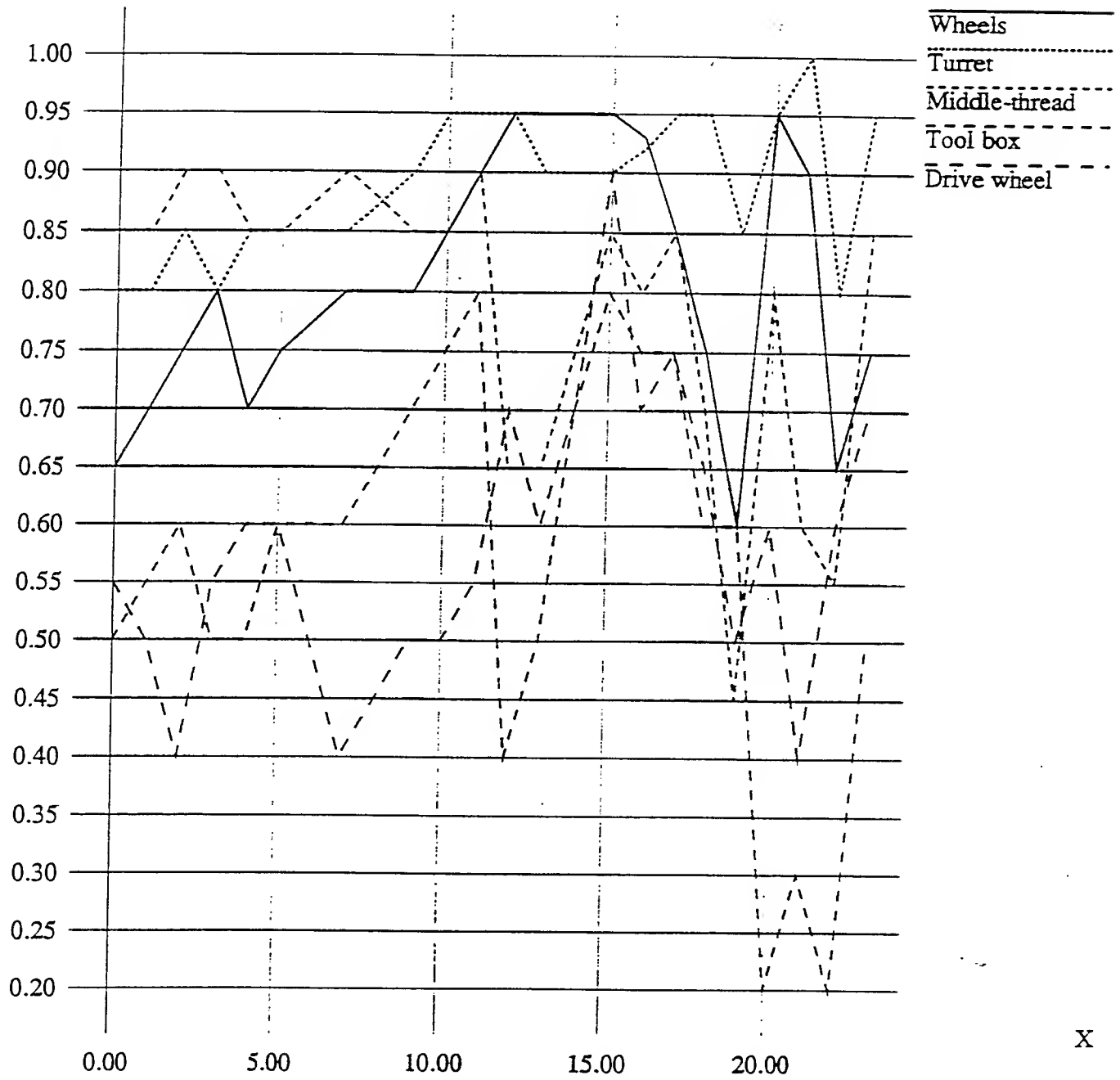
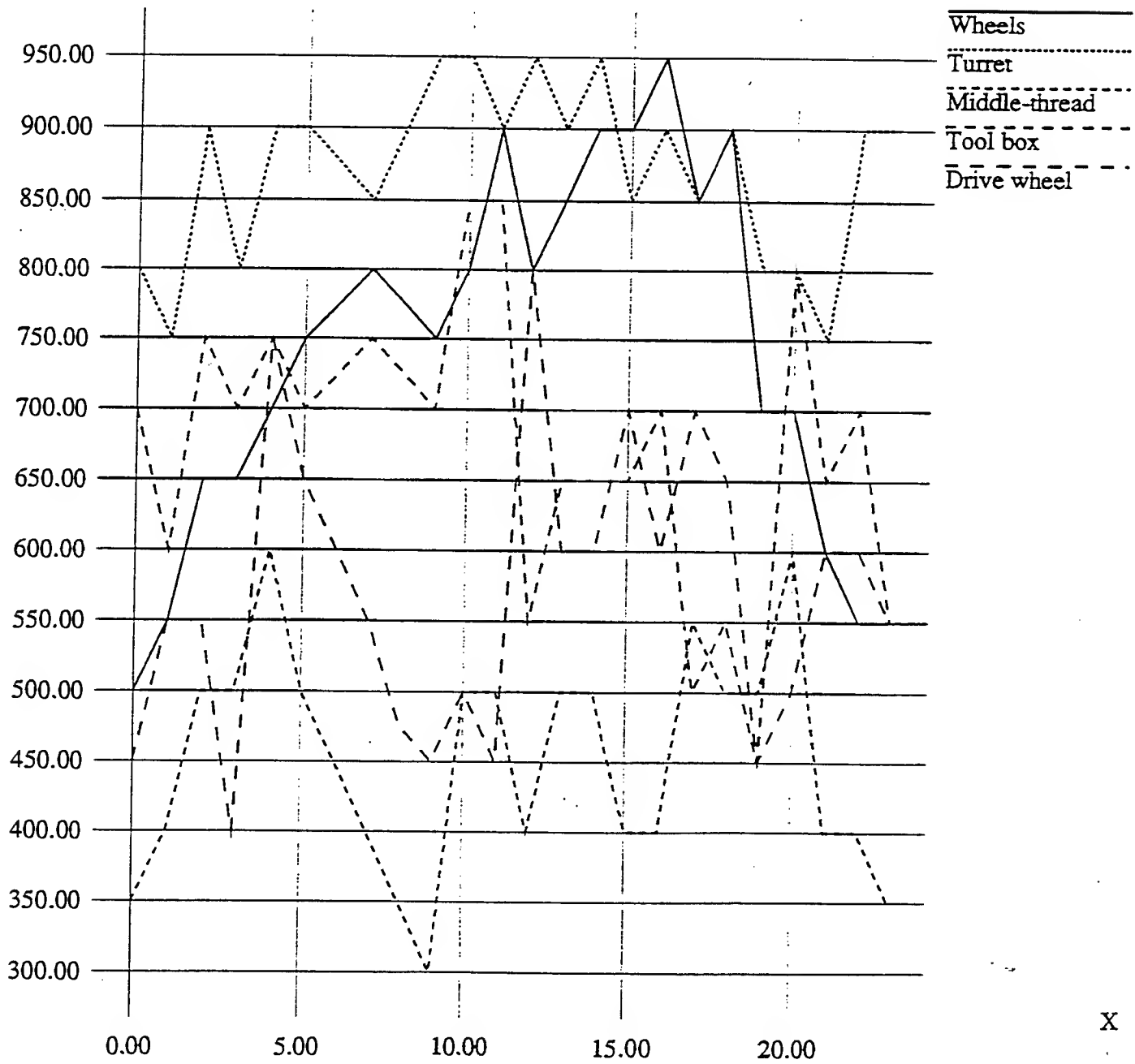


Fig 4



## Features vs Time-scale 2

Features  $\times 10^{-3}$   
 $Y \times 10^{-3}$



X

Fig 5

# **DESIGN AND PERFORMANCE EVALUATION OF SUBMICRON-GATE-LENGTH TRANSISTORS**

Vijay K. Arora  
Professor  
Department of Electrical and Computer Engineering

Wilkes University  
Wilkes-Barre, PA 18766

Final Report for:  
Research Initiation Program  
Solid State Electronics Directorate  
Wright Laboratory

Sponsored by:  
Air Force Office of Scientific Research  
Bolling Air Force Base, Washington, D. C.

and

Wilkes University

December 1992

## DESIGN AND PERFORMANCE EVALUATION OF SUBMICRON-GATE-LENGTH TRANSISTORS

Vijay K. Arora  
Professor  
Department of Electrical and Computer Engineering  
Wilkes University  
Wilkes-Barre, PA 18766

### Abstract

Quantum-well microstructures for the design and performance evaluation of submicron-gate-length field effect transistors were investigated. The density matrix formalism was found to give a distinct advantage over the Boltzmann transport framework, especially when exciting electromagnetic field was polarized in one of the directions of quantum confinement. An understanding of the velocity-limiting mechanism in degenerately-doped 3D, 2D, and 1D microstructures subjected to high electric fields was obtained by using the high-field distribution function which takes into account the strong asymmetry of the carrier velocities, resulting in a drift velocity limited by the Fermi velocity in the strongly degenerate limit. The emission of optical phonons further limits the velocity. The suppression of the emission of optical phonons in a superlattice structure can result in a velocity comparable to the Fermi velocity, which in turn depends on the carrier concentration. The electric field distribution, velocity distribution, carrier distribution, and I-V characteristics of submicron-length transistor were obtained from the velocity-field profiles obtained. The velocity at the drain end of a field effect transistor is always limited by the carrier saturation velocity while it is lower than this limiting velocity at other points in the channel, no matter what the length of the channel. The results so obtained were compared with the experimental results available in the published literature. Three papers based on this research are accepted for journal publication, two papers are in the process of preparation, and four papers were presented at international conferences. A thesis by Mr. David Moss, accompanying graduate student, was approved for award of M. S. degree. These investigations have advanced our understanding of limitations imposed by quantum and high-field effects in quantum well microstructures and possible device design. The expertise so developed can be integrated into electrical engineering curriculum, thereby supporting manpower resource development base of the U. S.

# DESIGN AND PERFORMANCE EVALUATION OF SUBMICRON-GATE-LENGTH TRANSISTORS

Vijay K. Arora

## INTRODUCTION

The advances in the crystal growth, device concepts, and fabrication of electronic and optical devices in GaAs and other III-V semiconductors have inspired the scientists in several laboratories around the world to work on combining both types of devices to create a new, powerful class of high speed optoelectronic integrated circuits for optical communications and many other high speed applications like digital optical computers. Miniaturized quantum well microstructures hold key to the development of Microwave Monolithic Integrated Circuits (MMIC's), including quantum well wires and related superlattice structures. Even though the fabrication of devices based on these microstructures are now being perfected, the high frequency performance of these devices tends to be below one's expectations. This is, perhaps, due to the elusive nature of the limitations imposed by quantum mechanics and high field effects, the understanding of which is the major theme of present investigations.

## VELOCITY-FIELD CHARACTERISTICS

In these days, when microstructures based on MODFET (Modulation-Doped Field Effect Transistor) geometries are being experimented with for high speed applications, several theories to understand the mobility-limiting scattering mechanisms have been developed. These theories, based on the solution of the Boltzmann Transport Equation (BTE), have been very successful in predicting mobility-limiting mechanism in low electric field under the conditions that the field is present in quasi-free classical direction. No such consensus is apparent if the electric field vector (e. g. in optical stimulation) is present in the confinement direction or if the electric field is too high. This prompted us to investigate quantum well microstructures under these far-from-equilibrium conditions.

In the development of quantum transport framework using the density matrix, the average velocity  $\langle v \rangle$  (or currents  $\langle j \rangle = -e \langle v \rangle$ ) for a myriad of electrons in a confined system is evaluated from the quantum-mechanical prescription:

$$\langle v \rangle = \text{Tr} (\rho v_{\text{op}} ), \quad (1)$$

where Tr is the trace of the matrix. The density matrix  $\rho$  is obtained by solving the Liouville's Equation:

$$i \hbar \partial \rho / \partial t = [ \mathcal{H} , \rho ] , \quad (2)$$

with

$$\mathcal{H} = \mathcal{H}_0 + \mathcal{V} + \mathcal{F}. \quad (3)$$

Here,  $\mathcal{H}_0$  is the unperturbed hamiltonian related to the kinetic energy,  $\mathcal{V}$  is the electron-lattice interaction, and  $\mathcal{F}$  is the electron interaction with the applied electric field in the dipole approximation (  $\mathcal{F} = -e \mathbf{E} \cdot \mathbf{r}$  ). In this framework, the central control of the transport behavior lies with the density matrix which is influenced by the external stimulations and scattering interactions. In general, the stimulating field can be a dc or ac, electromagnetic fields (lasers), or transients. The density matrix driven by a sinusoidally varying field of frequency  $\omega$  ( $\omega \rightarrow 0$  for dc electric field) can be assumed to be of the form

$$\rho = \rho_0 + \rho' \exp( s + i\omega )t , \quad s \rightarrow 0^+, \quad (4)$$

where  $\rho_0$  is the equilibrium density matrix which is diagonal, with diagonal matrix elements as the Fermi-Dirac distribution functions at different eigenvalues. The second part in Equation (4) is the modification of the density matrix in response to the external fields of frequency  $\omega$ . When a solution of Equation (2) is attempted by any of the perturbation methods, the result is a coupled equation in  $\rho'$ , which is of the form

$$\begin{aligned} & ( \varepsilon_\alpha - \varepsilon_{\alpha'} + \Delta_{\alpha\alpha'} + \hbar \omega - i \hbar \tau_{\alpha\alpha'}^{-1} ) \langle \alpha | \rho' | \alpha' \rangle \\ & = \langle \alpha | [ \rho_0 , \mathcal{F} ] | \alpha' \rangle + \text{terms containing } \langle \alpha | \mathcal{V} \rho' \mathcal{V} | \alpha' \rangle. \end{aligned} \quad (5)$$

Here,  $\alpha$  is the symbol for the quantum-mechanical state of the unperturbed system (yet unspecified in the generalized framework).  $\Delta_{\alpha\alpha'}$  is the shift in the eigenvalue difference  $\varepsilon_\alpha - \varepsilon_{\alpha'}$  due to the perturbing potential  $\mathcal{V}$ .  $\hbar \tau_{\alpha\alpha'}^{-1}$  is the collision broadening which depends on the frequency and the confinement size of the carriers. In the limit of weak scattering interactions (  $\mathcal{V} \rightarrow 0$  ), zero frequency, and diagonal nature of  $\rho'$ , the expression for  $\tau_{\alpha\alpha'}^{-1}$  is the well-known Fermi golden rule formula extensively used in the carrier transport. But, in several other applications, the strength of the scattering interaction and the frequency dependence in calculating scattering

rates cannot be ignored and should be considered in correct interpretation of the experimental data.

For an isotropic scattering interaction, e.g. the acoustic-phonon scattering, the coupled terms containing  $\langle \alpha | \mathcal{V} \rho' \mathcal{V} | \alpha' \rangle$  (the last terms in Equation (6)) reduce to zero or are negligible and Equation (6) can be solved for  $\langle \alpha | \rho' | \alpha' \rangle$  in a straightforward manner:

$$\langle \alpha | \rho' | \alpha' \rangle = \frac{\langle \alpha | [\rho_0, \mathcal{F}] | \alpha' \rangle}{\epsilon_{\alpha} - \epsilon_{\alpha'} + \Delta_{\alpha\alpha'} + \hbar \omega - i \hbar \tau_{\alpha\alpha'}^{-1}} \quad (6)$$

In this form,  $\hbar \tau_{\alpha\alpha'}^{-1}$  is the familiar Breit-Wigner type of broadening in any interband or intraband transition and  $\Delta_{\alpha\alpha'}$  is the line shift at resonance. Equation (6), in the semiclassical regime, gives results equivalent to those obtained from BTE when  $\langle \alpha | \rho' | \alpha' \rangle$  is diagonal.

For polar semiconductors (e.g. GaAs), the terms containing  $\langle \alpha | \mathcal{V} \rho' \mathcal{V} | \alpha' \rangle$  (the last terms in Equations (5)) are not negligible. In that case, a clear distinction between scattering rates and momentum relaxation rates should be made. In deriving scattering rates,  $\langle \alpha | \mathcal{V} \rho' \mathcal{V} | \alpha' \rangle$  is completely neglected and  $\tau_{\alpha\alpha'}^{-1}$  gives scattering rates. On the other hand, in deriving momentum relaxation rates, some approximation for  $\langle \alpha | \mathcal{V} \rho' \mathcal{V} | \alpha' \rangle$  should be made so that it appears in the form of scattering factor multiplied by  $\langle \alpha | \rho' | \alpha' \rangle$ . For elastic scattering, where  $\rho' \propto k_z$  is assumed, the inclusion of this term gives an additional factor  $(1 - k_z'/k_z)$  in the expression of  $\tau_{\alpha\alpha'}^{-1}$ , and then this becomes a momentum relaxation rate. Here,  $k_z$  is the momentum component (before scattering) in the direction of the electric field, and  $k_z'$  is that after scattering. For inelastic POP scattering, this simplification cannot be made, but may be used as a starting point for a better approximation. This proved to be an excellent testing ground for the validity of relaxation effects normally used in the description of carrier transport using the BTE.

For the ellipsoidal satellite valleys, the band structure resembles that of germanium and silicon. In an ellipsoidal valley, the longitudinal velocity operator  $v_z$  is given by

$$v_z = (\alpha_{13} p_x + \alpha_{33} p_z)/m_0, \quad (7)$$

where  $p_x$  and  $p_z$  are x and z components of the electron momentum, and  $\alpha_{ij} = (m_0/m^*)_{ij}$  are the components of the normalized inverse effective mass. These

anisotropies, as appropriate to silicon-like band structures were studied and results indicated in APPENDIX I (accepted for publication in Journal of Applied Physics)

Another application of the density matrix, which was tried, is in the hot electron transistor where the electrons enter the quantum-well base in the confinement direction by tunneling through the emitter-base barrier, pass through the base, and are collected by base-collector barrier. Since the bulk mean free path of electrons is larger than the base length, the electrons are expected to pass through the base ballistically. There has been several difficulties in utilizing this concept for speed enhancement. The development of the density matrix formalism gave us an excellent platform to view the role and even the possible redefinition of mean free path in microstructures to qualify the term ballistic transport. The same can be said of electron transport in resonant tunneling devices fabricated from the ultra-thin multiple QW superlattices.

In treating high frequency effects, the density matrix formalism gives relaxation rates which are frequency dependent. In optical excitation if the energy of the photon quantum  $\omega$  is comparable to the carrier thermal energy  $k_B T$ , as is usually the case, the effect of frequency on relaxation rates which give the linewidth of various resonances cannot be completely ignored. Moreover, there is found to be an energy shift in interband transitions with the density matrix, which may become comparable to excitonic shift of the bandedge. In such cases, the density matrix technique offers a distinct advantage over the BTE formalism.

In the derivation of Equations (5) and (6), implicit is the assumption of a weak electric field. In a strong electric field, strong asymmetry may change the distribution of electrons in and opposite to the direction of the applied electric field. In addition to the energy gained in-between collisions, the energy gained during the collision process (intracollisional field effect) also becomes important. This makes nonlinear effects appear when electric field is so high that energy gained in-between collisions  $e E \ell$  comparable to the thermal energy  $k_B T$ . The critical field  $E_{cr}$  for the onset of nonlinear behavior is thus given by  $E_{cr} = k_B T / e \ell$ . This is strictly true when  $\ell$  is constant. If  $\ell$  is a function of energy, the saturation regime of the velocity field characteristics will be affected. These effects have been extensively discussed in the papers given in the appendices.

## MODELLING OF FIELD EFFECT TRANSISTORS

In modeling the I-V characteristics, the textbook models assume the mobility to be field-independent. As channels are becoming narrow (and associated electric fields high), the high-field mobility degradation as stated in the previous section becomes important. After evaluating the velocity-field characteristics of layered structures, we

are in a sound position to evaluate the performance of transistors of various dimensionalities. We found that 0.25- $\mu\text{m}$  gate length MESFET could show a superior performance over MODFET under room temperature conditions. This is due to the fact that the saturation velocity of MESFET tends to be higher than that of a MODFET. Noise behavior of MODFET and the quantum-well-wire transistor (QWWT) is expected to be better because of the quantum freeze-out of the intrinsic carriers due to the zero-point quantum energy which extends the bandgap. The role of negative differential resistivity which is so distinct in bulk GaAs was found to be diminished in low-dimensional materials due to change in dimensionality of quantum-confined electrons in the  $\Gamma$ -valley and less-confined (more like bulk electrons) in the higher satellite valleys. Another significant result which emerged from the present comparative studies is the role of parasitic regions. If the transistor current is comparable to the limiting saturation current appropriate to the material properties of parasitic regions, the resistance of the parasitic resistance can become quite high. This may considerably enhance the RC-time constants of the channel, giving diminished frequency response of the transistor. A proper design of parasitic regions of the transistor so that the saturation current of the parasitic region is much higher than the transistor current will tremendously improve the high frequency performance of the transistor.

### OPTICAL PROPERTIES

In order to crystallize our thinking of scattering processes and their effect on the microwave performance of transistors, we considered it important to study the layered structures when these are stimulated by an alternating electric field with polarization in the direction of confinement. In this respect the density matrix formalism explained earlier proved very useful. As of this writing this work is still continuing. We have considered a quantum well with finite boundaries and have obtained its wavefunction in the form of sinusoidal functions with an effective well width which is larger than that of the well assumed to be of infinite barrier height. The matrix elements of the velocity operator, as expected, are diagonal in the confinement direction. We have obtained the expressions of the frequency-dependent conductivity, but calculations for frequency-dependence of the relaxation mechanisms is continuing. Once completed, these results will allow us to see the lineshift and linewidth effects associated with the inter-subband resonance in quantum wells, which can be easily extended to include inter-band transitions and the effect of quantization. At this point, we conjecture that the frequency shift in the interband transitions will give effects very similar to the excitonic shift.



#### PAPERS (ACCEPTED)

1. "High Field Electron Transport for Ellipsoidal Multivalley Band Structure of Silicon," with G. Samudra, S. J. Chua, A. K. Ghatak, Journal of Applied Physics, accepted (see APPENDIX I).
2. "The Role of Optical Phonon Emission in Limiting Velocity in GaAs/AlGaAs Quantum Well Heterostructures," with L. S. Tan and S. J. Chua, Physical Review, accepted (see APPENDIX II).
3. "Velocity Response to High Electric Fields in Submicron Gate Length Field Effect Transistor," Asia Pacific Engineering Journal, accepted (see APPENDIX III).

#### PAPERS PUBLISHED

1. "Quantum Engineering of Modern Optoelectronic Devices and Circuits," with T. C. Chong, IEEE Search (Singapore), Vol 170/7/92, No. MITA(p), pp. 12-17 (August 1992) (see APPENDIX IV).

#### PAPERS PRESENTED

1. "Physics and Technology of Quantum Well Wires and Related Superlattices," with H. Sakaki (U. of Tokyo), invited paper, *Proceedings of the VI<sup>th</sup> International Workshop on the Physics of Semiconductor Devices*, December 2-6, 1991, New Delhi, India (see APPENDIX V).
2. "High-Field Induced Hot-Carrier Temperature, Bandgap Narrowing, and Carrier Multiplication in Bulk Semiconductors," with H. Sakaki (U. of Tokyo), invited paper, *Proceedings of SemCon, the International Conference on Physics and Technology of Semiconductor Devices and Integrated Circuits*, February 5-7, 1992, Madras, India, SPIE Publication, Tata-McGraHill Company, pp. 160-171 (see APPENDIX VI).

3. "Velocity Distribution in a Degenerately Doped 0.25- $\mu$ m GaAs MODFET," with L. S. Tan and S. J. Chua, Proceedings of 1992 International Conference on Semiconductor Electronics, October 6-8, 1992, at Kuala Lumpur, Malaysia (see APPENDIX VII).
4. "Velocity Limiting Mechanism in Quantum-Well-Wire Microstructures and Superlattices," with S. J. Chua and L. S. Tan, Proceedings of 1992 International Electronic Devices and Materials Symposium (EDMS'92), November 1-4, 1992, Taipei (Taiwan), pp. 339-342 (see APPENDIX VIII).

#### THESIS COMPLETED

1. "Development of High Temperature Ohmic Contacts to Gallium Arsenide for VLSI Applications," an M. S. thesis by Mr. David Moss, Wilkes University, August 1992.

#### PAPERS IN PREPARATION

1. "A Density Matrix Theory for Intersubband Optical Transitions in a Quantum Well of Finite Dimensions," with S. J. Chua, and Y. Kiang, IEEE J. Quantum Electronics.
2. "Modelling and Performance Evaluation of 0.25- $\mu$ m InGaAs/AlGaAs MODFET," with L. S. Tan and K. P. Lee, IEEE Transactions on Electron Devices.

## APPENDIX I

“High-Field Transport for Ellipsoidal Multivalley Band Structure of Silicon,” Ganesh Samudra, Soo Jin Chua, Ajoy K. Ghatak, and *Vijay K. Arora.*, Galley proof of the paper to appear in the Journal of Applied Physics.

# High-field electron transport for ellipsoidal multivalley band structure of silicon

Ganesh Samudra, Soo Jin Chua, Ajoy K. Ghatak,<sup>a)</sup> and Vijay K. Arora<sup>b)</sup>

Department of Electrical Engineering, National University of Singapore 10 Kent Ridge Crescent, Singapore 0511

(Received 21 April 1992; accepted for publication 27 July 1992)

High-field electron-transport properties of bulk silicon are studied taking into account the multivalley band structure with ellipsoidal energy surface. A distribution function that takes into account the anisotropy introduced in electron motion by the high electric field is described. This puts some order in the otherwise completely random motion. The transition from linear to nonlinear behavior is obtained when the energy gained by an electron in traversing a mean free path is comparable to the thermal energy. The drift velocity is shown to be limited to the random thermal velocity for nondegenerate electrons and to the Fermi velocity for degenerate electrons. This indicates independence of the saturation velocity on momentum-randomizing scattering events which control the mobility. The emission of an optical phonon is significant when inelastic scattering length is comparable to the momentum randomizing mean free path. This further lowers the saturation velocity. When an electric field is applied along the  $\langle 100 \rangle$  direction in silicon, an intervalley transfer from valleys with lower mean free path to the ones with higher mean free path is obtained. When compared with the experimental data on silicon, an excellent agreement is obtained.

## I. INTRODUCTION

Much attention is presently focused on semiconductor microstructures of submicrometer dimensions because of their widespread use in ultra-large-scale integrated circuits. Since the electric field in these microstructures is very high, the familiar linear velocity-field relationship, as given by Ohm's law, breaks down and the carrier velocity eventually saturates at very high electric fields.<sup>1</sup> This nonlinear response of the carrier velocity to high electric field has been extensively explored, both theoretically and experimentally; however, as of today, no consensus has been reached on the mechanism limiting the velocity and its interdependence on low-field mobility. Recent experiments<sup>2-8</sup> show decisively that the saturation velocity does not sensitively depend on the mobility, in contradiction to long-held views that a higher mobility necessarily leads to a higher saturation velocity. The experiments of Masselink *et al.*<sup>3,7</sup> first showed that the velocity at room temperature is higher than that at 77 K and, therefore, indicated that the velocity-limiting mechanism is not controlled by the mobility of the sample. Therefore, a careful analysis of the mechanism limiting carrier velocity and how it depends on scattering parameters is desirable.

It is well known that the charge carriers drift in response to an electric field that converts their random motion to an ordered motion with an average velocity known as the drift velocity. The free fall of electrons (or free bubbling up of the holes) in a carrier mean free path  $l$  on a tilted band diagram (as shown in Fig. 1) is terminated with a momentum-randomizing scattering event or by the

creation of an optical phonon. All scattering events change carrier momentum, but in an inelastic scattering event energy is lost through the emission of an optical phonon, provided enough energy has been accumulated during its free flight motion. The inelastic scattering length for the emission of an optical phonon of energy  $\hbar\omega_0$  in the presence of an electric field  $E$  is, therefore, given by  $l_{op} = \hbar\omega_0/qE$ . At low electric field  $l_{op} \gg l_0$ , the momentum randomizing mean free path; but, at a high electric field,  $l_{op} \ll l_0$ , and the emission of an optical phonon ( $\hbar\omega_0 = 46.8$  meV for silicon) becomes important, as originally suggested by Lanyon.<sup>9</sup> Therefore, the velocity of carriers in a low electric field is limited by scattering, whereas in a high electric field it is independent of the conventional momentum-randomizing scattering interactions.

## II. DISTRIBUTION FUNCTION

The carrier distribution is determined by the Fermi level. In response to an electric field, the Fermi level and band edges tilt parallel to each other. As a result, the carrier concentration at each point remains the same (neglecting the electron-hole pair generation) as at equilibrium; however, the direction of carrier motion is severely affected. Since the Fermi energy changes by  $qE \cdot l$ , an appropriate distribution function is given by<sup>1</sup>

$$f(\epsilon_k, E) = \frac{1}{e^{(\epsilon_k - \zeta + qEl)/k_B T} + 1}, \quad (2.1)$$

with<sup>10</sup>

$$l = l_0 [1 - \exp(-l_{op}/l_0)], \quad (2.2)$$

and  $\zeta$  is the Fermi energy (electrochemical potential),  $k_B$  is the Boltzmann constant, and  $T$  the temperature.

<sup>a)</sup>Permanent address: Department of Physics, Indian Institute of Technology, Hauz Khas, New Delhi, 110016, India.

<sup>b)</sup>Permanent address: Department of Electrical and Computer Engineering, Wilkes University, Wilkes-Barre, PA 18760.

14p

FIG. 1. Tilted band diagram in an electric field applied from right- to left-hand side. After traversing a mean free path, carriers come closer to the conduction-band edge either by emitting an optical phonon or by randomizing its velocity.

The relevance of this distribution function to other high-field theories is extensively discussed in Ref. 1. Figure 1 shows the band diagram under the influence of an electric field and the changes in the electrochemical potential by  $qE\lambda$  of an electron (or a hole) after traveling a mean free path. Here  $q = -e$  for electrons and  $q = +e$  for holes. An excellent description of carrier motion on a tilted band diagram is given by Böer,<sup>11</sup> both in built-in as well as in external fields. An electron after traveling a mean free path is either scattered by a momentum-randomizing collision or releases its excess energy by emitting an optical phonon<sup>10</sup> and falls closer to the conduction-band edge. The distribution function of Eq. (2.1) takes into account the left-right asymmetry in the direction of motion of carriers in an electric field.

The energy eigenvalue  $\epsilon_k$  for a given ellipsoid, in a six-ellipsoidal model of silicon, is written as<sup>12</sup>

$$\epsilon_k = \frac{\hbar^2 k_x^2}{2m_1^*} + \frac{\hbar^2 k_y^2}{2m_2^*} + \frac{\hbar^2 k_z^2}{2m_3^*}, \quad (2.3)$$

with corresponding eigenfunctions given by

$$\psi_k = e^{i(k_x x + k_y y + k_z z)}, \quad (2.4)$$

where  $\alpha_{ij}$  are the components of the effective-mass tensor for an electron in the ellipsoidal valley represented by the Hamiltonian

$$\mathcal{H} = \frac{\hbar^2}{2m_0} \sum_{ij} \alpha_{ij} k_i k_j. \quad (2.5)$$

The effective-mass tensor is diagonal in the ellipsoidal frame where the  $z$  axis lies along its principal longitudinal axis and  $\alpha_{ij} = \alpha_i \delta_{ij}$ . In the laboratory frame, the electric field is applied along the  $z$  axis. The transformation from the principal longitudinal axis of the ellipsoidal frame to the  $z$  axis of the laboratory frame by a rotation about the  $y$  axis by an angle  $\chi$  results in components  $\alpha_{ij}$  given by the matrix

$$\begin{pmatrix} \alpha_1 \cos^2 \chi + \alpha_3 \sin^2 \chi & 0 & (\alpha_1 - \alpha_3) \sin \chi \cos \chi \\ 0 & \alpha_1 & 0 \\ (\alpha_1 - \alpha_3) \sin \chi \cos \chi & 0 & \alpha_1 \sin^2 \chi + \alpha_3 \cos^2 \chi \end{pmatrix}. \quad (2.6)$$

The principal effective masses are given by

$$m_1^* = (\alpha_3 / \alpha_1 \alpha_3) m_0, \quad m_2^* = m_0 / \alpha_1, \quad m_3^* = m_0 / \alpha_3. \quad (2.7)$$

Here the valley index on  $\alpha$ 's is suppressed for ease in writing the expressions. The density-of-states effective mass is still the same in all ellipsoids, i.e.,  $m_{ds}^* = m_0 / (\alpha_1^2 \alpha_3)^{1/3}$ . For electric fields applied along  $\langle 111 \rangle$  directions, all valleys are equivalent. With  $\alpha_1 = 5.249$  and  $\alpha_3 = 1.091$ ,<sup>13</sup> principal masses are  $m_1^* = 0.675 m_0$ ,  $m_2^* = 0.1905 m_0$ ,  $m_3^* = 0.259 m_0$ . The single-valley density-of-states effective mass is  $0.3216 m_0$ . For  $\langle 100 \rangle$  orientation, two valleys have  $m_1^* = 0.1905 m_0$ ,  $m_2^* = 0.1905 m_0$ ,  $m_3^* = 0.916 m_0$ , the other four valleys have  $m_1^* = 0.1905 m_0$ ,  $m_2^* = 0.916 m_0$ ,  $m_3^* = 0.1905 m_0$ . These effective masses are consistent with those suggested by Green<sup>13</sup> who has extensively surveyed the literature and has resolved inconsistencies among various silicon parameters. The thermal effective mass of  $0.28 m_0$  for the thermal velocity is closer to the  $m_3^* = 0.259 m_0$ . Similarly, the density-of-states effective mass (with all six valleys included) is  $6^{2/3} \times 0.3216 m_0 = 1.06 m_0$ , in close agreement with  $1.09 m_0$  quoted by Green.<sup>13</sup> The ellipsoidal valley model, therefore, is expected to give a more accurate description of electrons in silicon, including anisotropies introduced in the motion of drifting electrons. The anisotropies can be easily included in this formalism by finding the matrix elements of the velocity operator in Hilbert space from the Hamiltonian formulation by using the Heisenberg equation of motion.

### III. DRIFT VELOCITY

For the multivalley band structure, the average drift velocity is calculated as

$$\langle v_z \rangle = \frac{\sum_i \frac{\hbar k_{zi}}{m_i^*} f(\epsilon_i, E)}{\sum_i f(\epsilon_i, E)}. \quad (3.1)$$

Here  $i$  is the valley index for six ellipsoidal valleys of silicon. Using the distribution function of Eq. (2.1), the velocity-field characteristics for  $\langle 111 \rangle$ -oriented electric field are obtained as

$$v_d = \langle v_z \rangle = \frac{1}{\sqrt{\pi}} v_{th} \frac{\int_0^\pi \sin(2\theta) \mathcal{F}_1[H(\theta)] d\theta}{\int_0^\pi \sin(\theta) \mathcal{F}_1[H(\theta)] d\theta}, \quad (3.2)$$

where

$$\mathcal{F}_j(\eta) = \frac{1}{\Gamma(j+1)} \int_0^\infty \frac{x^j}{e^{1+x} - 1} dx \quad (3.3)$$

is the Fermi-Dirac integral.  $H(\theta)$ , the quasi-Fermi level of electron, is defined as

$$H(\theta) = \eta - \delta \cos(\theta) = \frac{\zeta}{k_B T} - \delta \cos(\theta) \quad (3.4)$$

and

$$\delta = eEl/k_B T, \quad (3.5)$$

$$v_{th} = (2k_B T / m_{x(111)}^*)^{1/2}. \quad (3.6)$$

$\theta$  is the angle between the particle velocity and the direction of applied field. The normalized Fermi energy (electrochemical potential)  $\eta$  is obtained from carrier conservation by numerically solving the normalization equation

$$n_v = \left( \frac{\sqrt{\pi}}{\lambda_D} \right)^3 \int_0^\pi \sin(\theta) \mathcal{F}_{1/2}[H(\theta)] d\theta, \quad (3.7)$$

where  $n_v$  is the carrier concentration per unit volume. The quasi-Fermi level  $H(\theta)$  is plotted in Fig. 2 for degeneracy parameter  $N_3 = n_v \lambda_D^3 = 100$ , where  $\lambda_D = \hbar / m^* v_{th}$  is the de Broglie wavelength appropriate for the thermal energy  $k_B T$ . In equilibrium, electrons are uniformly distributed in all directions and the electrochemical potential (Fermi energy) is constant; but, with the applied electric field, the electrons transfer from the parallel ( $\theta = 0^\circ$ ) to antiparallel ( $\theta = 180^\circ$ ) direction, thereby increasing the degeneracy of electron gas in the antiparallel direction. Normalized drift velocity  $v_d/v_{th}$  as a function of normalized electric field  $\delta_0 = eEl_0/k_B T$  for  $N_3 = 1, 10, 100$ , are given in Fig. 3. The solid lines are under the conditions when optical phonon emission is absent or optical phonon energy is much higher than the thermal energy. The dotted lines are for the cases where optical phonon emission is allowed with the value of  $0 = \hbar\omega_{ph}/k_B T = 1.81$  appropriate for the room-temperature value for silicon. The saturation velocity is enhanced with the degeneracy of the electron gas and is limited by the Fermi velocity which depends on the carrier concentration; but, with the presence of optical phonon emission, the carrier velocity is strongly suppressed. This suggests that if we were to enhance the speed of silicon devices, some material engineering along the lines suggested by Sakaki<sup>14</sup> is needed. With the suppression of optical phonon emission, the drift

velocity can be considerably enhanced especially for a strongly degenerate system, with a larger impurity concentration. Also shown in Fig. 3 is the nondegenerate approximation of Eq. (3.2) (dashed lines).

Electrons in silicon are nondegenerate if the carrier concentration is  $0.1N_c$ , where  $N_c$  is the effective density of states for electrons. At room temperature,  $N_c = 2.86 \times 10^{19} \text{ cm}^{-3}$ , as recently evaluated by Green.<sup>13</sup> Thus, the nondegenerate approximation can easily be applied for carrier concentrations less than  $10^{18} \text{ cm}^{-3}$ . In the nondegenerate limit, Eq. (3.2) can be considerably simplified, and the drift velocity is now given by

$$\langle v_z \rangle = \left( \frac{8k_B T}{\pi m_0} \right)^{1/2} \frac{\int_0^\pi \left( \frac{m_0}{m_{x(111)}^*} \right)^{1/2} \left( \frac{\cosh(\delta_i)}{\delta_i} - \frac{\sinh(\delta_i)}{\delta_i^2} \right) \sin(\theta) d\theta}{\int_0^\pi \frac{\sinh(\delta_i)}{\delta_i} d\theta}, \quad (3.8)$$

with

$$\delta_i = \frac{eEl_i}{k_B T}. \quad (3.9)$$

For electric field applied in the  $\langle 111 \rangle$  direction, all valleys are equivalent. Equation (3.8) then simplifies to

$$\langle v_z \rangle = \left( \frac{8k_B T}{\pi m_{x(111)}^*} \right)^{1/2} \left[ \coth(\delta_{(111)}) - \frac{1}{\delta_{(111)}} \right]. \quad (3.10)$$

In low electric field ( $\delta_{(111)} \ll 1$ ), Eq. (3.4) gives the ohmic relationship

$$\langle v_z \rangle = \mu_0 E, \quad \mu_0 = \frac{4}{3} \frac{el_{(111)}}{\sqrt{2\pi m_{x(111)}^* k_B T}}. \quad (3.11)$$

In the high-field limit, if the optical phonon emission is neglected, Eq. (3.4) gives for the saturation velocity

$$v_{sat} = (8k_B T / \pi m_{x(111)}^*)^{1/2}. \quad (3.12)$$

FIG. 2. Electrochemical potential (quasi-Fermi level) in an electric field for degeneracy level  $N_3 = n_v \lambda_D^3 = 100$ . Electrons show a preferential behavior antiparallel to the electric-field direction.  $\delta = eEl/k_B T$ , the ratio of energy gained by an electron in a mean free path and the thermal energy.

FIG. 3. Normalized velocity-field characteristics for various degeneracy conditions, with (dotted lines) and without (solid lines) the optical phonon emission. The dashed lines are for nondegenerate electrons.

When the emission of optical phonons is included, the saturation velocity is given by

$$v_{\text{sat(ph)}} = (8k_B T / \pi m_{\text{eff}}^* \chi_{(111)})^{1/2} [\coth(\Theta) - (1/\Theta)], \quad (3.13)$$

with

$$\Theta = \hbar \omega_{\text{LO}} / k_B T. \quad (3.14)$$

Thus, if the mean free path is known, velocity-field characteristics can be obtained from Eq. (3.10). The carrier mean free path can easily be obtained from ohmic mobility for which reliable experimental data are available. The electrochemical potential  $\zeta$ , in nondegenerate approximation, does not play an active role in the expression of drift velocity; however, for the degenerate case, the drift velocity depends on carrier concentration through  $\zeta$ . The observed velocity-field characteristics for (111) orientation are well described by the empirical relation, originally suggested by Scharfetter and Gummel,<sup>15</sup>

$$v_d = \frac{\mu_0 E}{\sqrt{1 + \frac{N}{(N/S) + N_{\text{ref}}} + \frac{(E/A)^2}{(E/A) + F} + \left(\frac{E}{B}\right)^2}}. \quad (3.15)$$

with  $\mu_0 = 1430 \text{ cm}^2/\text{Vs}$ ,  $N_{\text{ref}} = 3 \times 10^{16} \text{ cm}^{-3}$ ,  $S = 350$ ,  $A = 3.5 \text{ kV/cm}$ ,  $F = 8.8$ , and  $B = 7.4 \text{ kV/cm}$ .  $N$  is the total impurity concentration, which may or may not be equal to carrier concentration depending on compensation in the sample.

With the values of  $\mu_0$  obtained from the zero-field mobility of  $\mu_0 = 1430 \text{ cm}^2/\text{Vs}$  for a relatively pure sample, the velocity-field characteristics, as obtained from Eq. (3.10), are shown in Fig. 4. The dashed line in Fig. 4 shows the velocity-field characteristics when optical phonon emission is forbidden, whereas the dotted line includes the emission of an optical phonon in a scattering event. The solid line is the experimentally observed velocity-field characteristics as given by Eq. (3.15). The emission of optical phonons plays a prominent role in limiting the carrier velocity. Figure 5 shows the comparison of theory (solid lines) to the experimental data (dotted lines) for samples of three different impurity concentrations and hence the mobility. The

14p

FIG. 4. Velocity-field characteristics for nondegenerate electrons in pure silicon, with (dotted line) and without (dashed line) the optical phonon emission. The solid line is the experimental curve.

14p

FIG. 5. Velocity-field characteristics of electrons for samples of various mobilities. Solid lines are the theoretical results and dotted lines are the experimental results.

agreement with the experimental data is good considering experimental uncertainties, the scatter of data taken by different experimental techniques, and the assumption of a parabolic model. Even though the ohmic mobilities are different for various impurity concentrations, the saturation velocity tends to a common value, although the approach towards saturation is much faster for higher mobility materials. A room-temperature saturation velocity value of  $1.0 \times 10^7 \text{ cm/s}$  for electrons is obtained. This indicates that higher mobility does not necessarily lead to higher saturation velocity. Only at moderate electric fields is the velocity of high-mobility materials higher than that of a low-mobility material. Experimental data on quantum-well heterostructures also support this observation. The mobility in a quantum-well heterostructure is much higher than that of bulk materials, but the saturation velocity is lower.<sup>7,8</sup> Velocity measurements on a variety of samples lead to the same saturation velocity at a given temperature.

In (100)-oriented electric fields, the two valleys in the direction of an electric field have  $m_{\text{eff}}^* = 0.916m_0$ , while the other four valleys have  $m_{\text{eff}}^* = 0.1905m_0$ . The mean free path for the lighter-effective-mass valleys (denoted by L) is higher than those with heavier effective mass valleys (denoted by H). In equilibrium two-thirds of the electrons remain in lighter valleys and one-third in heavier valleys; but, at a high electric field and in the absence of phonon emission, the transfer to lighter valleys takes place (solid line in Fig. 6). This transfer is interrupted by the emission of optical phonons (dashed line in Fig. 6). In Fig. 7, the velocity-field characteristics for (100) orientation (dashed line) of the electric field is compared to that in (111) orientation (solid lines). Velocities in (100) orientation are slightly lower than those in (111) orientation, in conformity with the experimental data.<sup>16,17</sup>

#### IV. CONCLUSION

We have given a description of the velocity-limiting mechanism in silicon that is in agreement with the experimental observations. A distribution function, the crux of

15p

FIG. 6. Intervalley transfer in  $\langle 100 \rangle$ -oriented electric field between valleys with lower (L) and higher (H) longitudinal effective mass.

any transport theory, which takes into account the asymmetry introduced by the electric field is described. The deviations from the ohmic behavior are obtained when the energy gained by an electron in a mean free path is comparable to the thermal energy. The electrons in high electric field are transferred from the antiparallel to parallel direction, thereby increasing the degeneracy of the electron gas.

The saturation velocity is limited by the appropriate average of the electron thermal motion, and does not sensitively depend on momentum-randomizing scattering parameters, and hence on mobility. This is in agreement with earlier scaling theory arguments of Thornber<sup>18</sup> in which saturation velocity was found to be invariant under scaling of the magnitude of scattering rates which alters mobility, while mobility is invariant under scaling of the magnitude of momentum which alters the saturation velocity. These observations are in direct contradiction to long-held views that the higher saturation velocity necessarily follows from the higher mobility. The velocity-limiting mechanisms in

14p

FIG. 7. Comparison of velocity-field characteristics for  $\langle 100 \rangle$ - (dotted lines) and  $\langle 111 \rangle$ -oriented (solid lines) electric field.

saturation velocity and ohmic mobility should be considered independent parameters. This is in agreement with experimental observations where high mobility does not necessarily give rise to higher saturation velocity.<sup>3</sup> As collision broadening is much smaller than the thermal energy, the fundamental assumptions of semiclassical character of the electron<sup>19,20</sup> remain intact.

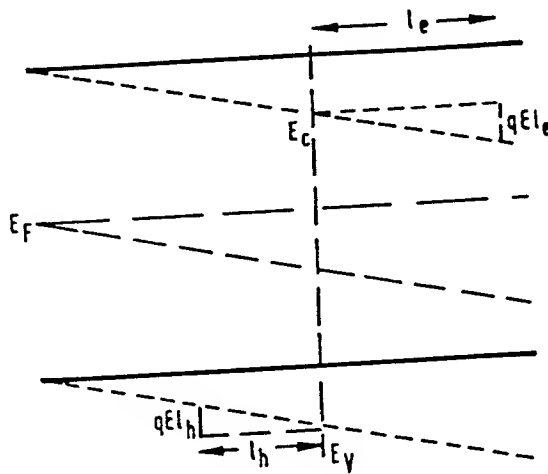
The emission of optical phonons becomes important when inelastic scattering length  $l_{op}$  is comparable to the momentum randomizing mean free path  $l$ . In the high electric field, the emission of optical phonons plays a dominant role in limiting the mobility, in agreement with earlier work of Lanyon, who also predicted scattering rates increasing with the electric field due to this emission process. If somehow this optical phonon emission is contained or eliminated, as suggested by Sakaki,<sup>14</sup> very high electron velocities are possible in silicon. Due to the nonequivalent valley for electric field applied in the  $\langle 100 \rangle$  direction, the intervalley transfer is possible. The velocities in this orientation are not dramatically different from those in the  $\langle 111 \rangle$  orientation. With the ever increasing importance of high speed in devices of submicrometer dimensions where high fields are necessarily present, these results should prove valuable in modeling future silicon devices.

#### ACKNOWLEDGMENTS

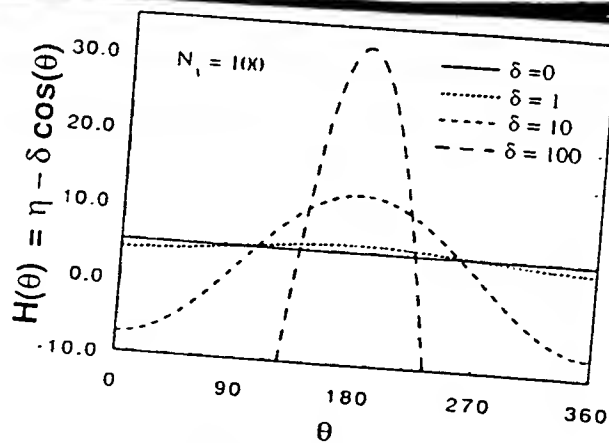
V. K. A. Partially supported by a research initiation grant of the Air Force Office of Scientific Research (AFOSR) and Quantum Wave Project of Japan Research and Development Corporation.

- <sup>1</sup>V. K. Arora, *Jpn. J. Appl. Phys.* **24**, 537 (1985); *J. Appl. Phys.* **54**, 824 (1983).
- <sup>2</sup>K. Hirakawa and H. Sakaki, *J. Appl. Phys.* **63**, 803 (1988).
- <sup>3</sup>W. T. Masselink, T. S. Henderson, J. Klem, W. F. Kopp, and H. Morkoç, *IEEE Trans. Electron Devices* **ED-33**, 639 (1986).
- <sup>4</sup>M. Feng, C. L. Lau, V. Eu, and C. Ito, *Appl. Phys. Lett.* **57**, 1233 (1990).
- <sup>5</sup>J. Laskar, J. Kolodzey, A. A. Ketterson, I. Adesida, and A. Y. Cho, *IEEE Electron Device Lett.* **ED-11**, 300 (1990).
- <sup>6</sup>K. Inoue, H. Sakaki, and J. Yoshino, *Appl. Phys. Lett.* **47**, 614 (1985).
- <sup>7</sup>A. A. Ketterson, W. T. Masselink, J. S. Gdymn, J. Klem, C.-K. Peng, W. F. Kopp, H. Morkoç, and K. R. Gleason, *IEEE Trans. Electron Devices* **ED-33**, 564 (1986).
- <sup>8</sup>W. T. Masselink, N. Braslau, W. I. Wang, and S. I. Wright, *Appl. Phys. Lett.* **51**, 1533 (1987).
- <sup>9</sup>H. P. D. Lanyon, *Solid-State Electron.* **21**, 291 (1978).
- <sup>10</sup>S. A. Schwartz and S. E. Russek, *IEEE Trans. Electron Devices* **ED-30**, 1629 (1983).
- <sup>11</sup>K. W. Böer, *Survey of Semiconductor Physics* (Van Nostrand Reinhold, New York, 1990), pp. 696–725.
- <sup>12</sup>V. K. Arora, C. Munera, and M. Jafarian, *J. Phys. Chem. Solids* **38**, 469 (1977).
- <sup>13</sup>M. A. Green, *J. Appl. Phys.* **67**, 2944 (1990).
- <sup>14</sup>H. Sakaki, *Jpn. J. Appl. Phys.* **28**, L314 (1989).
- <sup>15</sup>D. L. Scharfetter and H. K. Gummel, *IEEE Trans. Electron Devices* **ED-16**, 64 (1982).
- <sup>16</sup>C. Jacoboni, C. Canali, G. Ottaviani, and A. A. Quaranta, *Solid-State Electron.* **20**, 77 (1977).
- <sup>17</sup>C. Canali, C. Jacoboni, F. Nava, G. Ottaviani, and A. Alberigi Quaranta, *Phys. Rev. B* **12**, 2265 (1975).
- <sup>18</sup>K. K. Thornber, *J. Appl. Phys.* **51**, 2127 (1980).
- <sup>19</sup>M. Dresden, *Rev. Mod. Phys.* **33**, 265 (1961).
- <sup>20</sup>F. Capasso, T. P. Pearsall, and K. K. Thornber, *IEEE Electron Device Lett.* **EDL-2**, 295 (1981).

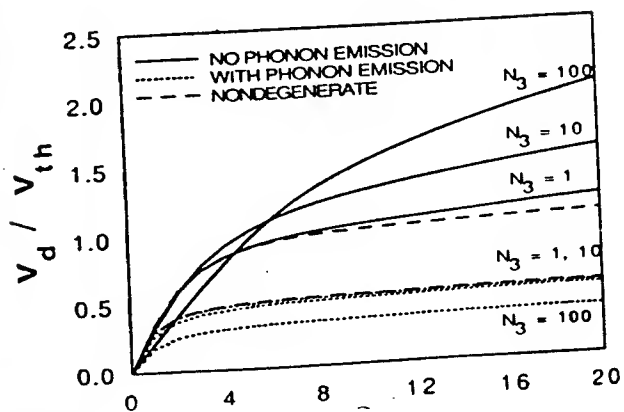


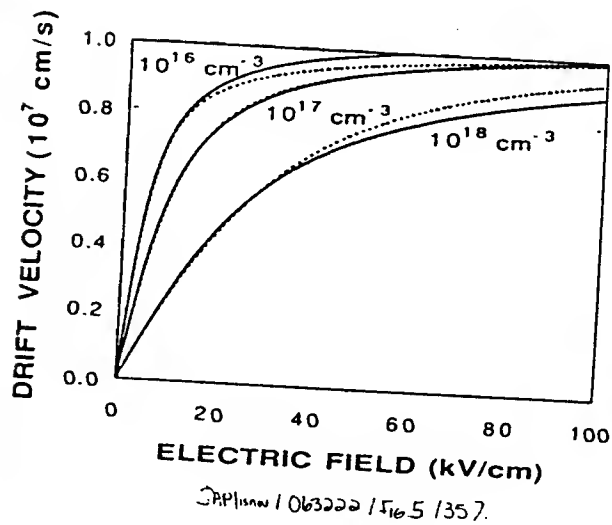
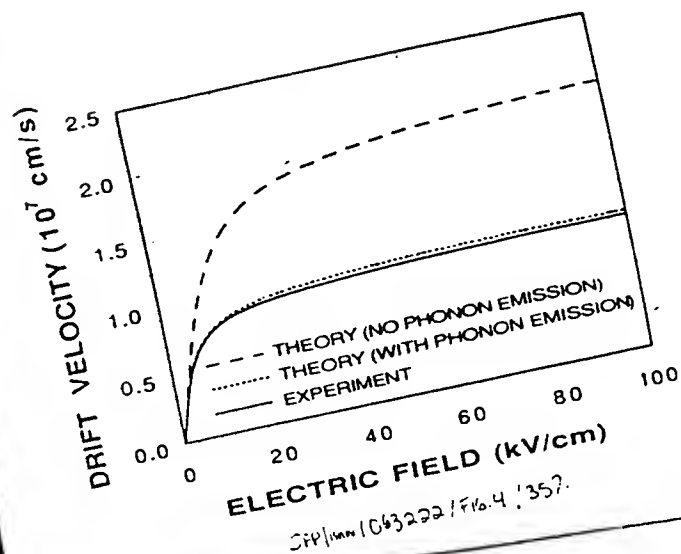


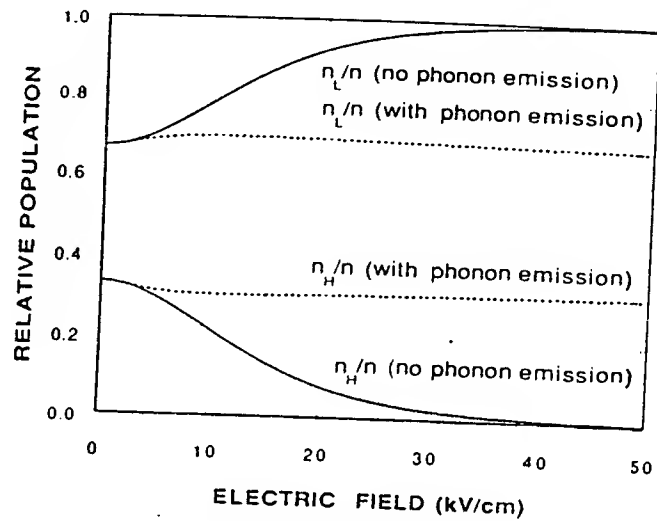
JAP/KAN/063222/FIG.1/507.



JAP/KAN/063222/FIG.2/357.

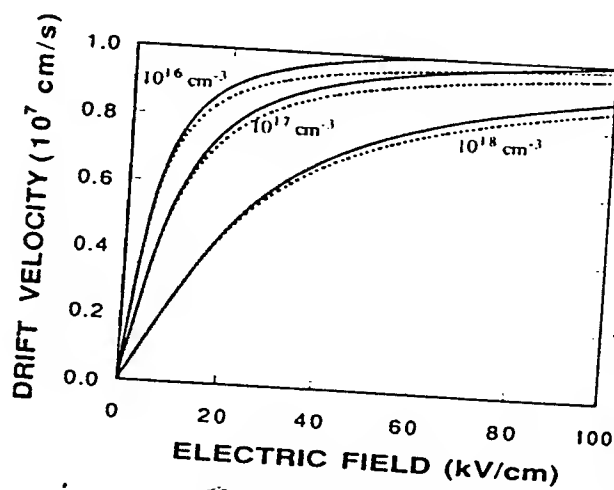






JRP/sem/ 063222 / Fig. 6/ 407.

Fig. 6 original - 2000 10/10/00



JRP/sem/ 063222 / Fig. 7/ 357.

## APPENDIX II

The Role of Optical Phonon Emission in Limiting Velocity in GaAs/AlGaAs Quantum Well Heterostructures," L. S. Tan, S. J. Chua, V. K. Arora, to appear in Physical Review.

# **The role of optical phonon emission in limiting velocity in selectively doped GaAs/AlGaAs quantum well heterostructure\***

L. S. Tan, S. J. Chua, and Vijay K. Arora<sup>†</sup>

Center for Optoelectronics, Department of Electrical Engineering, National University of Singapore, 10 Kent Ridge Crescent, Singapore 0511

## **Abstract**

In the light of recent experimental observations indicating poor correlation between the saturation velocity and the ohmic mobility, a theory for velocity limiting mechanism in quantum well heterostructures is compounded which explains very well the experimental results under wide variety of conditions. The free flight of a carrier during a mean free path is interrupted either by a momentum randomizing collisions (dominant in low electric field) or by the emission of an optical phonon (dominant in high electric field). If optical phonon emission is suppressed, for example as suggested by Sakaki (Jpn. J. Appl. Phys. 28, L314(1989)), considerable enhancement in saturation velocity is obtained. The saturation velocity is then limited by the Fermi velocity under strongly degenerate conditions or by the thermal velocity under nondegenerate conditions.

Recent developments in VLSI and VHSIC programs have indicated an ever-increasing importance of high-field effects which limit the velocity of carriers and hence impose an intrinsic limit on device speed. There have been numerous attempts to identify the mechanism responsible for this saturation of the carrier velocity in high electric field (See Ref. 1,2 for a review). Often a high mobility is cited in the published literature to give higher saturation velocity. But, recent experiments tend to indicate a poor correlation between saturation velocity and mobility.<sup>3,4</sup> In selectively doped heterostructures, the mobility is higher yet the saturation velocity is lower. This absence of correlation was predicted, several years ago, in scaling theory arguments of Thornber.<sup>5</sup> Saturation velocity was found to be invariant under scaling of the magnitude of scattering rates which alters mobility, while mobility was found to be invariant under scaling of the magnitude of momentum which alters saturation velocity. This is further confirmed by recent experimental observations<sup>6,7</sup> where high frequency performance of MESFET or MISFET is equal to or superior than that achieved by HEMT. Independently determined decreases in mobility and increases in electron velocity under similar conditions are observed.<sup>7</sup>

The understanding of the distribution function is essential in any carrier transport study. The equilibrium distribution function is well known to be the Fermi-Dirac distribution function. In equilibrium, the bands are flat unless there is a built-in electric field. The electrons are moving at random with the average velocity in each of the three cartesian directions equal to zero. In low electric field  $\mathcal{E}$ , collisions can be considered point collisions as the energy  $q\mathcal{E}\lambda_D$  (field broadening) absorbed by a carrier of charge  $q$  ( $q = \pm e$  for holes(electrons)) in the de Broglie wavelength  $\lambda_D$  is negligible compared to collision broadening. But, as the electric field becomes larger, the field broadening tends to mask the collision broadening, and hence makes carrier transport virtually independent of scattering. The onset of nonlinear behavior thus takes place when field broadening is comparable to the collision broadening. This condition is equivalent to the condition that the momentum gained by the carrier from the field  $e\mathcal{E}\tau$  in the mean free time  $\tau$  is comparable to its thermal momentum  $m^*v$ . In terms of energy, this condition is equivalent to the condition that the energy gained by an electron in a mean free path  $e\mathcal{E}l$  is comparable to the thermal energy  $k_B T$ . This condition was originally considered by Shockley,<sup>8</sup> but was discarded in favor of the energy balance theories which dominated the high-field arena in those days and are reviewed in Refs. 1 and 2.

In external fields, the Fermi energy (electrochemical potential) and bands are tilted parallel to each other.<sup>9</sup> An excellent description of the carrier transport with the tilted band diagram is given by Böer,<sup>9</sup> who examines the effect of built-in as well as the applied electric field on the distribution of carriers. The carrier distribution is determined relative to the Fermi

level. In zero bias, the distribution is independent of position and the Fermi level (chemical potential) is constant. In an external field, however, Fermi level and bands are tilted. The carrier distribution is now a function of spatial coordinates. When electrons are accelerated in the field, they move from a region of higher density  $n(\epsilon - \zeta)$  to that of lower density  $n(\epsilon - (\zeta - e \mathcal{E} \ell))$ . These electrons can dissipate their drift momentum or net additional energy to the lattice by a momentum randomizing event or by emitting a phonon. The carriers drop close to the conduction band edge and the motion is repeated. From intuitive arguments, as suggested by Böer,<sup>8</sup> a limiting velocity comparable to the random thermal velocity at lattice temperature is expected. The carrier motion in an external field is, therefore, not random. It has a finite component in the field direction. This makes distribution of carriers asymmetric in the direction of applied electric field. The electrons will roll down the energy hill and holes will bubble up the energy hill. The electric field thus tries to organize the otherwise completely random motion. Understandably, the Fermi level will be affected by the applied electric field. All these features are contained in the distribution function originally proposed by Zukotynski and Howlett:<sup>10</sup>

$$f(\epsilon_{nk}, \mathcal{E}, \theta) = \frac{1}{e^{(\epsilon_{nk} - \zeta + e \mathcal{E} \cdot \ell(\epsilon_{nk}))/k_B T} + 1} \quad (1)$$

$\epsilon_{nk}$  is the quantized energy of a quantum well.  $\ell(\epsilon_k) = \tau v$  is the energy-dependent mean free path. This distribution function thus has a very simple interpretation. The electrochemical potential  $\zeta$  during the free flight of carriers changes by  $\pm e \mathcal{E} \cdot \ell$  as electrons tend to sink and holes tend to float on the tilted energy band diagram. This observation may suggest that the applied electric field tends to organize the otherwise completely random motion. Electric dipoles  $e \ell$  due to quasi-free motion of the carriers tend to organize in the direction of electric field for holes and in the opposite direction for electrons. The high-field effects thus become important when the dipole energy  $e \mathcal{E} \cdot \ell$  is comparable to the thermal energy for nondegenerate electrons or the Fermi energy for degenerate electrons. The collisions tend to bring the electron closer to the conduction band edge. If the electric field is strong, this unidirectional motion will give carrier drift comparable to the thermal velocity which is average of the magnitude of electron velocity  $v$ . A quasi-ballistic behavior of the carriers thus follows in strong electric field.

The drift velocity for a QTD gas with the distribution function of Eq. (1) in the quantum limit ( $n=1$ ), is obtained as

$$v_d = \frac{\sqrt{\pi}}{2} v_{th} \frac{\int_0^{2\pi} \cos(\theta) \mathcal{F}_{1/2}(H(\theta)) d\theta}{\int_0^{2\pi} \ln(1+e^{H(\theta)}) d\theta} \quad (2)$$

where

$$H(\theta) = \eta - \delta \cos(\theta) \quad (3)$$

is the quasi-Fermi level which is direction-dependent and  $\eta$  is given by

$$\eta = \frac{\zeta - \varepsilon_o}{k_B T} \quad (4)$$

where  $\varepsilon_o$  is the ground state energy.  $\eta$  is evaluated from the normalization condition

$$n = \lambda_D^{-2} \int_0^{2\pi} \ln(1+e^{H(\theta)}) d\theta \quad (5)$$

In the nondegenerate limit, Eq. (3.2) simplifies to

$$v_d = \frac{\sqrt{\pi}}{2} v_{th} \frac{I_1(\delta)}{I_0(\delta)} \quad (6)$$

where  $I_n(\delta)$  is the modified Bessel function of order  $n$ . Taking the limit of Equation (6) as  $\delta \rightarrow \infty$ , the saturation velocity in the nondegenerate case is

$$v_{d sat} = \frac{\sqrt{\pi}}{2} v_{th} \quad (7)$$

No such simple expression can be obtained under strongly degenerate conditions, as degeneracy increases in the antiparallel direction to the field and electrons tend to be nondegenerate in the direction of the applied electric field.

All scattering events change the carrier momentum. However, only some of them, the inelastic scattering events change the energy of the carriers. Usually several scattering events are followed by one inelastic scattering usually by generating a phonon. But, in high electric field, inelastic scatterings can become frequent, comparable to momentum scattering rate. The



scattering length  $\ell_{op}$  associated with the emission of an optical phonon can be obtained by equating the energy gained by an electron in a mean free path to that of an optical phonon  $\hbar\omega_0$ :

$$\ell_{op} = \hbar\omega_0 / e \mathcal{E} \quad (8)$$

The total scattering length is then given by

$$\ell^{-1} = \ell_0^{-1} + \ell_{op}^{-1} \quad (9)$$

where  $\ell_0$  is the zero-field scattering length obtained from the ohmic mobility.

Fig. 1 shows the comparison of theoretical results obtained from Eq. (2) with the experimental data of Hirakawa and Sakaki.<sup>2</sup> The agreement is as best as is possible considering the experimental uncertainties and single constant mean free path. These experimental results could not be interpreted by a Monte Carlo theory or an approach based on the electron temperature model. The results are also consistent with the measurement of Masselink et. al,<sup>13</sup> who have also shown lack of dependence of saturation velocity on ohmic mobility. Under strong degenerate conditions, the velocity tends to a value of  $2.0 \times 10^7$  cm/s, both for 77 K and 4.2 K. The velocity at room temperature has not yet reached the saturation level at the highest electric field in the experimental setup of Hirakawa and Sakaki.<sup>3</sup> But, as shown in Fig. 2, the saturation velocity as high as  $1.8 \times 10^7$  cm/s is possible, which is considerably higher than the highest measured velocity of  $0.73 \times 10^7$  cm/s reported in Ref. 3. Fig. 2 clearly shows the role of optical phonons in limiting the velocity. If optical phonon scattering is somehow suppressed, considerable improvement in device speed is possible. Sakaki<sup>12</sup> has recently proposed engineering the quantum well wire and quantum box array structures, where the minibands are so designed that the optical phonon emission is avoided. In such microstructures, the velocity at least twice as high is expected from these theoretical considerations. Also, shown in Fig. 2 are the results obtained from the empirical relation commonly used in modelling the transistor<sup>14,15</sup>:

$$v_D = \frac{\mu_0 \mathcal{E}}{1 + \frac{\mathcal{E}}{\mathcal{E}_c}} \quad (10)$$

with  $\mathcal{E}_c = v_{sat} / \mu_0 = 3.1$  kV/cm. This shows that this relation gives a good description of velocity-field characteristics for modelling field effect transistors. In the experiment of Ketterson et. al., an unusual high velocity at room temperature was obtained. In the light of this theory, the saturation velocity is limited by the random thermal velocity under nondegenerate conditions, which explains the discrepancy. At room temperature, the saturation of velocity takes place at very high electric field (Fig. 2) as compared to low-

temperature conditions (Fig. 3) because the ratio of the Fermi velocity to the thermal velocity is much higher at cryogenic temperatures.<sup>17</sup>

In Fig. 3, we show the velocity-field characteristics for strongly degenerate gas at 4.2 K for five samples with varying mobility and carrier concentration, with phonon emission (solid lines) and without the phonon emission (dashed lines). With phonon emission considered, the saturation velocity does not sensitively depend on the mobility. For all samples considered, the saturation velocity is approximately  $2.0 \times 10^7$  cm/s. But, if the phonon emission is suppressed, considerably higher saturation velocity comparable to the Fermi velocity is obtainable. In a recent paper by Shur and coworkers<sup>17</sup>, this idea of obtaining saturation velocity closer to Fermi velocity, which could be as high as  $5-10 \times 10^7$  cm/s has been utilized in designing a novel Schottky diode for millimeter and submillimeter wave applications. For high mobility materials, the approach towards saturation is much faster as compared to the low mobility materials. Thus high mobility materials are more vulnerable to high field effects than the low mobility materials. The saturation velocity does not sensitively depend on carrier concentration or on low-field mobility, in agreement with the experimental deductions of Hirakawa and Sakaki.<sup>3</sup>

To conclude, we have identified a mechanism for velocity saturation as electrons transfer from parallel to antiparallel direction of the electric field, interpreted the experimental results on GaAs/AlGaAs quantum wells under a wide variety of experimental conditions, and given a recipe for enhancement of velocity by quantum engineering of miniband structures.<sup>17</sup> We, therefore, hope that the results presented here will prove useful in understanding the world of future quantum device on miniaturized scale.

### ACKNOWLEDGEMENTS

One of us (V. K. A.) would like to acknowledge the warm hospitality of the Center of Optoelectronics at the National University of Singapore, Quantum Wave Project at the University of Tokyo, and Research Division of the Solid State Electronics Directorate of Wright Laboratory at Wright-Patterson Air Force Base, where fundamental ideas of this work were developed after interaction with active researchers.

## REFERENCES

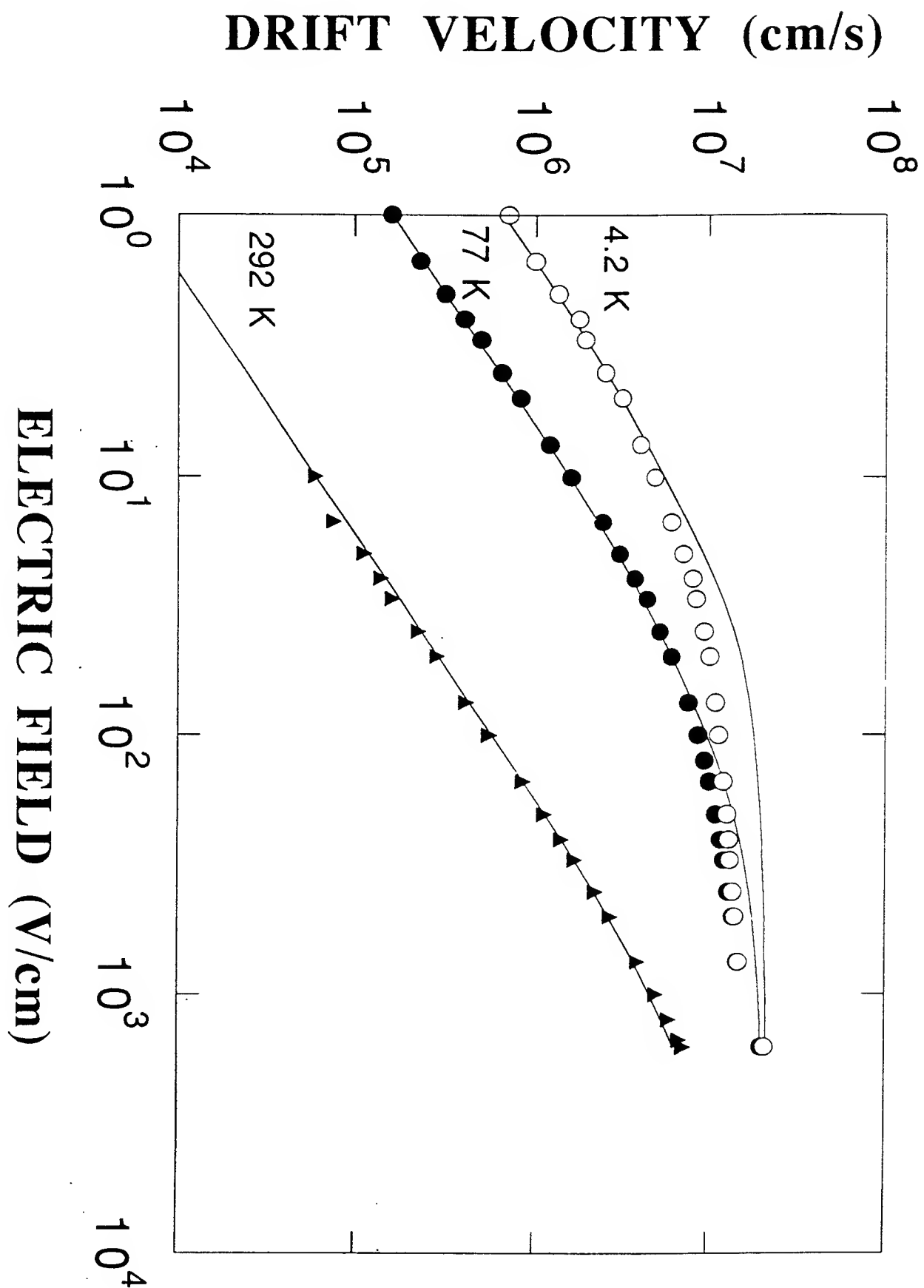
\*Work supported by Research Initiation Grant of the Air Force Office of Scientific Research.

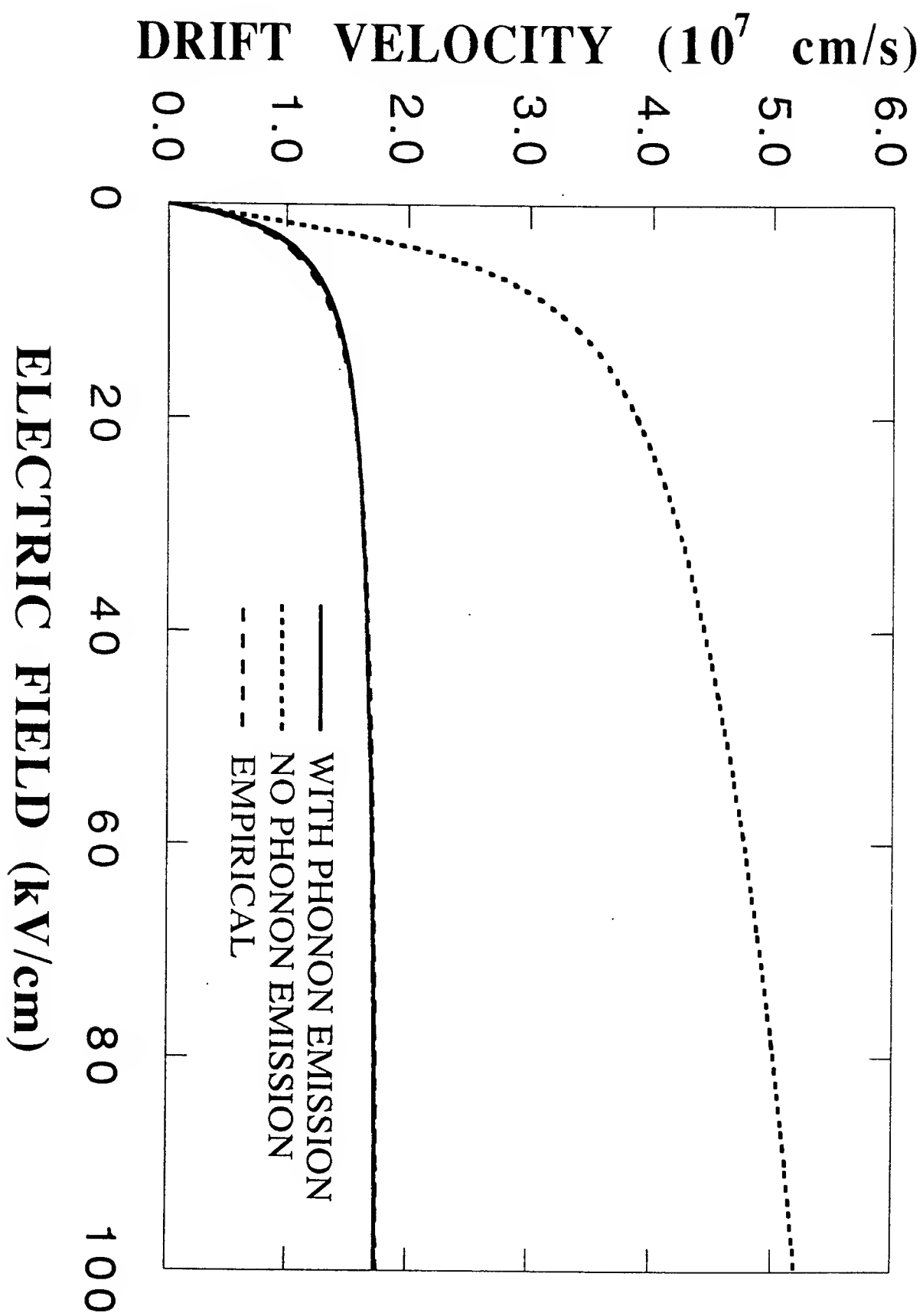
†Permanent Address: Department of Electrical and Computer Engineering, Wilkes University, Wilkes-Barre, PA 18766, U. S. A.

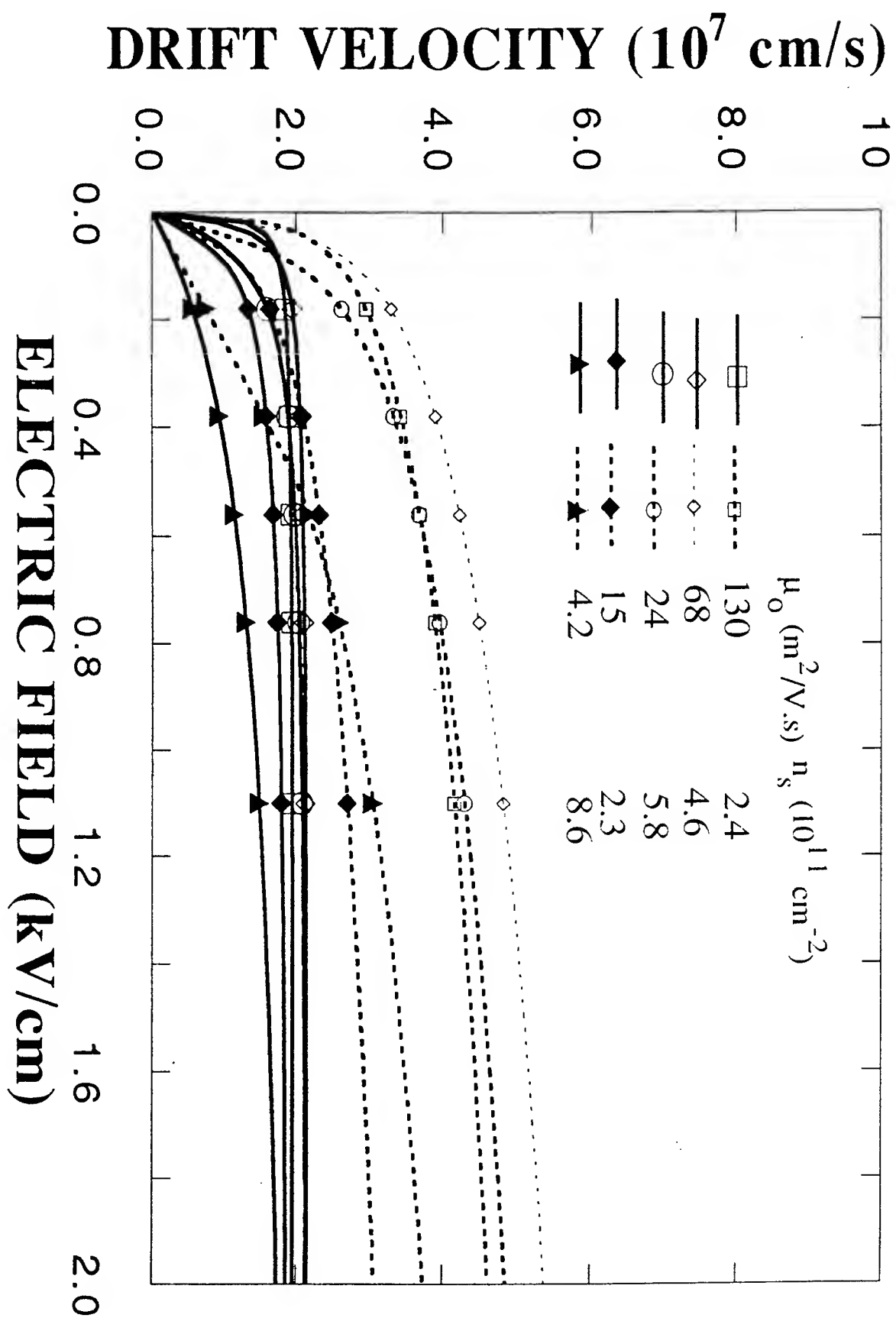
1. V. K. Arora, J. Appl. Phys. **54**, 824(1983).
2. V. K. Arora, Jpn. J. Appl. Phys. **24**, 537(1985).
3. K. Hirakawa and H. Sakaki, J. Appl. Phys. **63**, 803(1988).
4. W. T. Masselink, T. S. Henderson, J. Klem, W. F. Kopp, and H. Morkoç, IEEE Trans. Electron Dev. **ED-33**, 639(1986).
5. K. K. Thornber, J. Appl. Phys. **51**, 2127(1980).
6. M. Feng, C. L. Lau, V. Eu, C. Ito, Appl. Phys. Lett. **57**, 1233(1990).
7. J. Laskar, J. Kolodzey, A. A. Ketterson, I. Adesida, and A. Y. Cho, IEEE Electron Dev. Lett. **11**, 300(1990).
8. W. Shockley, Bell Syst. Tech. J. **30**, 990(1951).
9. K. W. Böer, *Survey of Semiconductor Physics*, Van Nostrand Reinhold, New York, 1990, pp. 696-725.
10. S. Zukotynski and W. Howlett, Solid State Electron. **21**, 35(1978).
11. C. M. Wolfe, N. Holonyak, and G. Stillman, *Physical Properties of Semiconductors*, Prentice-Hall, Englewood Cliffs, N. J., 1989, pp. 112-118.
12. H. Sakaki, Jpn. J. Appl. Phys. **28**, L314(1989).
13. W. T. Masselink, N. Braslau, W. I. Wang, and S. I. Wright, Appl. Phys. Lett. **51**, 1533(1987).
14. V. K. Arora and M. B. Das, Electron. Lett. **25**, 820(1989).
15. V. K. Arora and M. B. Das, Semicond. Sci. & Tech. **5** (1990).
16. A. A. Ketterson, W. T. Masselink, J. S. Gedymin, J. Klem, C.-K. Peng, W. F. Kopp, H. Morkoç, and K. R. Gleason, IEEE Trans Electron Dev. **ED-33**, 564(1980).
17. W. C. B. Peatman, T. W. Crowe, and M. Shur, IEEE Elec. Dev. Lett. **13**, 11(1992).

## FIGURE CAPTIONS

- Fig. 1.** Velocity-field characteristics of GaAs/AlGaAs quantum well heterostructure at 292K, 77K, and 4.2K. The points are the experimental results of Hirakawa and Sakaki (Ref. 3).
- Fig. 2.** Extrapolation of velocity-field characteristics at 292K to much higher electric fields. The solid curve is with optical phonon emission included and dotted curve is when optical phonon emission is ignored. The dashed curve is the empirical relation commonly used in modelling a transistor (Eq. (10)).
- Fig. 3.** The velocity-field characteristics at 4.2 K for five samples of varying mobility and carrier concentration. Solid curves are with optical phonon emission included and dashed curves are with phonon emission ignored.







## **APPENDIX III**

“Velocity Response to High Electric Fields in Submicron Gate Length Field Effect Transistor,” to appear in Asia-Pacific Engineering Journal.



# VELOCITY RESPONSE TO HIGH ELECTRIC FIELDS IN A SUBMICRON GATE LENGTH FIELD EFFECT TRANSISTOR

by

Vijay K. Arora<sup>†</sup>

Center of Optoelectronics, Department of Electrical Engineering, National University of Singapore, 10 Kent Ridge Crescent, Singapore 0511

## Abstract

An analysis of the velocity-limiting mechanism indicates that there is a poor correlation between the saturation velocity and the ohmic mobility. The electron velocity is limited by the average of the random thermal velocity which is further suppressed by the emission of an optical phonon emission. An excellent agreement with the experimental data on GaAs quantum well is obtained. The electric-field distribution, the velocity distribution, carrier distribution, and I-V characteristics in the channel of submicron high electron mobility transistor (HEMT) are evaluated. The *pinchoff* behavior is found to be absent even in the long channel limit.

---

<sup>†</sup> Permanent Address: Department of Electrical Engineering, Wilkes University, Wilkes-Barre, PA 18766, U. S. A.

## 1. INTRODUCTION

The advances in the crystal growth, device concepts, and fabrication of electronic and optical devices in GaAs and other III-V semiconductors have inspired the scientists in several laboratories around the world to work on combining both types of devices to create a new, powerful class of high speed optoelectronic integrated circuits for optical communications and many other high speed applications like digital optical computers. GaAs has a direct band gap necessary for microwave sources. In addition, it has better electron transport properties than the industry's device vehicle, Si. Electrons in GaAs are about five times more mobile than in Si. GaAs is also available in semi-insulating form and, when used as a substrate, substantially reduces the parasitic capacitances. GaAs combined with lattice-matched alloy AlGaAs, has lead to the fabrication of very efficient lasers and many unique heterojunction devices which are not possible in Si. These include modulation-doped field effect transistors (MODFETs), metal-semiconductor field effect transistors (MESFETs), heterojunction bipolar transistors (HBTs), resonant tunneling devices (RTDs) and several variations of hot electron transistors (HETs) and high electron mobility transistors (HEMTs). This new range of laterally patterned nanometer scale devices which are based on MODFET geometries provides many challenges to quantum transport theory. In such devices the quasi-two-dimensional (QTD) electron gas set up in a MODFET is reconfigured by surface patterning of the gate region to produce a variety of structures in the varying low dimensionality and coherence. With the ever increasing need for high-speed device applications, researchers in laboratories around the world are looking for breakthroughs on the conventional design of transistors.

One of the essential factors in the operational design of these microwave devices is the proper understanding of the relationship between velocity and electric field in the channel. A typical velocity-field ( $v$ - $E$ ) relationship for  $\Gamma$ -valley of the GaAs<sup>1</sup> is shown in Fig. 1. At lower electric fields, the relationship is linear. But, at high electric field, the velocity becomes saturated at  $4.2 \times 10^7$  cm/s (as shown by flat dashed line).

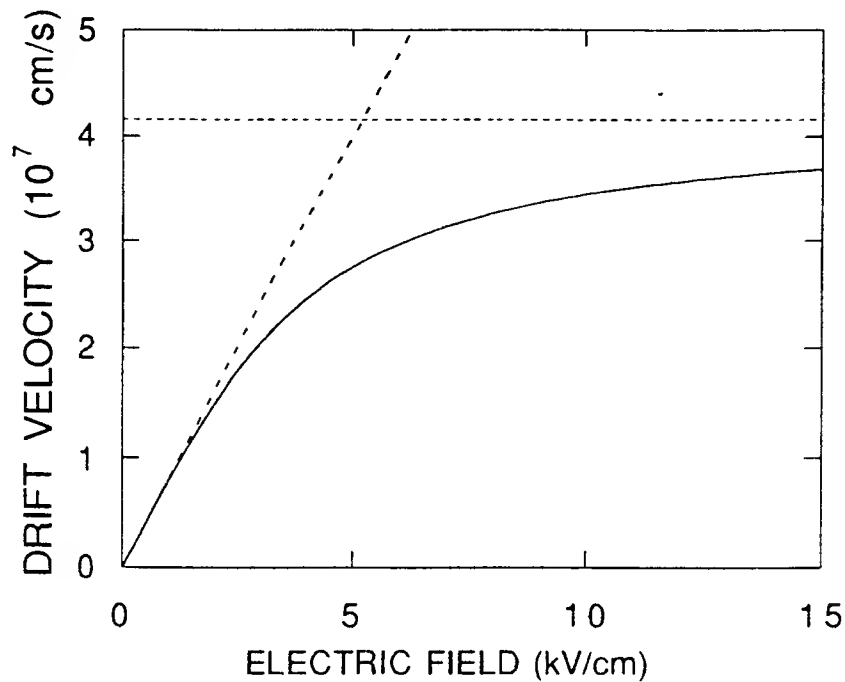


**Fig. 1.** Room temperature velocity-field characteristics of the  $\Gamma$ -valley of nondegenerate bulk GaAs (Ref. 1).

Recent developments in VLSI and VHSIC programs have indicated an ever-increasing importance of high-field effects which limit the velocity of carriers and hence impose an intrinsic limit on device speed. There have been numerous attempts to identify the mechanism responsible for this saturation of the carrier velocity in high electric field (See Ref. 1,2 for a review). Often a high mobility is cited in the published literature to give higher saturation velocity. But, recent experiments tend to indicate a poor correlation between saturation velocity and mobility.<sup>3,4</sup> This absence of correlation was predicted, several years ago, in scaling theory arguments of Thornber.<sup>5</sup> Saturation velocity was found to be invariant under scaling of the magnitude of scattering rates which alters mobility, while mobility was found to be invariant under scaling of the magnitude of momentum which alters saturation velocity, consistent with the predictions of Arora.<sup>1,2</sup>

The primary motivation behind this study is to understand fully the v-E characteristics and the role these characteristics play in

in an inelastic scattering. If this emission is disregarded, the accumulated energy can become very high, necessitating the use of high-energy scattering times, which are central to any successful simulation. The high collision broadening present in these simulations can easily mask the semiclassical behavior of a carrier, as pointed out by Capasso et al.<sup>7</sup> Dresden<sup>8</sup> has reviewed assumptions, implicit and explicit, which are to be satisfied in treating electron as a classical particle. One such assumption is that the collision broadening  $\hbar/\tau$  is much smaller than the thermal energy  $k_B T$  ( $\hbar/\tau \ll k_B T$ ), which is easily satisfied in low-field transport of carriers. But, if high collision broadening is present, this condition can be easily violated. In spite of these conceptual difficulties, the understanding of the physical mechanism responsible for velocity saturation and its interdependence on the ohmic mobility is missing in simulation experiments. As the mean free time  $\tau$  is inversely proportional to the velocity  $v$  of a carrier for deformation potential scattering, a dominant mechanism in simulation experiments, a description of the carrier transport in terms of a constant mean free path  $\ell = v \tau$  appears more appropriate.

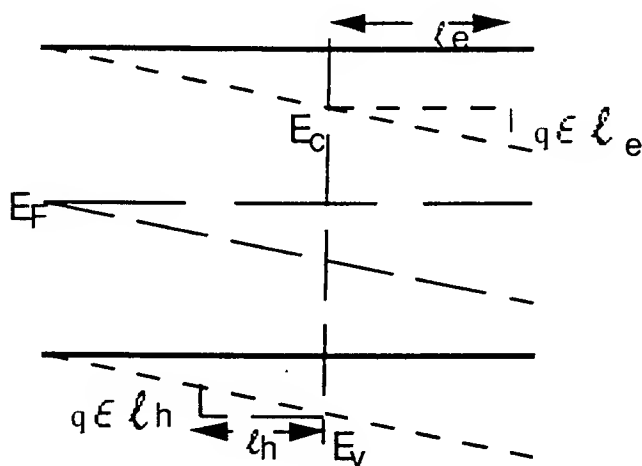


**Fig. 2.** Energy band diagram of an intrinsic semiconductor in an electric field applied in the direction from right to left.

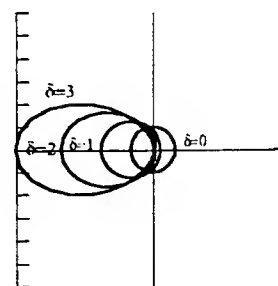


**Fig. 3.** Polar Plot of the normalized distribution function  $f(\epsilon, \ell, \theta) / f(\epsilon, 0, \theta)$  for nondegenerate carriers.

In external fields, the Fermi energy (electrochemical potential) and bands are tilted parallel to each other<sup>9</sup>, as shown in Fig. 2. An

modelling of submicron channels of FET's, where electron gas is predominantly degenerate and exhibits a QTD character.

## 2. DISTRIBUTION FUNCTION

The understanding of the distribution function is essential in any carrier transport study. The equilibrium distribution function is well known to be the Fermi-Dirac distribution function. In equilibrium, the bands are flat unless there is a built-in electric field. The electrons are moving at random with the average velocity in each of the three cartesian directions equal to zero.

In low electric field  $E$ , collisions can be considered point collisions as the energy  $|q| E \lambda_D$  (field broadening) absorbed by a carrier of charge  $q$  ( $q = \pm e$  for holes(electrons)) in the de Broglie wavelength  $\lambda_D$  is negligible compared to collision broadening. But, as the electric field becomes larger, the field broadening tends to mask the collision broadening, and hence makes carrier transport virtually independent of scattering. The onset of nonlinear behavior thus takes place when field broadening is comparable to the collision broadening. This condition is equivalent to the condition that the momentum gained by the carrier from the field  $e E \tau$  in the mean free time  $\tau$  is comparable to its thermal momentum  $m^* v$ . In terms of energy, this condition is equivalent to the condition that the energy gained by an electron in a mean free path  $e E \ell$  is comparable to the thermal energy  $k_B T$ . This condition was originally considered by Shockley,<sup>6</sup> but was discarded in favor of the energy balance theories which dominated the high-field arena in those days.

Recently, due to the availability of supercomputers, Monte Carlo simulations of carrier trajectory have become very popular. In a simulation, the carrier is subjected to the classical laws of motion followed by a scattering event generated by a set of random numbers. The use of complicated energy-balance equations, which are generally difficult to solve for all possible scattering interactions thus can be avoided. Instead at each scattering event, the electron is allowed to keep a portion of energy gained from the field which accumulates as collisions proceed and could be emitted in the form of an optical phonon

excellent description of the carrier transport with tilted band diagram is given by Böer,<sup>9</sup> who examines the effect of built-in as well as the applied electric field on the distribution of carriers. The carrier distribution is determined relative to the Fermi level. In zero bias, the distribution is independent of position and the Fermi level (chemical potential) is constant. In an external field, however, Fermi level and bands are tilted. The carrier distribution is now a function of spatial coordinates. When electrons are accelerated in the field, they move from a region of higher density  $n(\epsilon - \zeta)$  to that of lower density  $n(\epsilon - (\zeta \pm e E \ell))$ . These electrons can dissipate their net additional energy to the lattice by emitting phonons, thereby causing lattice heating. The carriers drop close to the conduction band edge and the motion is repeated. From intuitive arguments, as suggested by Böer,<sup>8</sup> a limiting velocity comparable to the random thermal velocity at lattice temperature is expected. The carrier motion in an external field is, therefore, not random. It has a finite component in the field direction. This makes distribution of carriers asymmetric in the direction of applied electric field. The electrons will roll down the energy hill and holes will bubble up the energy hill. The electric field thus tries to organize the otherwise completely random motion. Understandably, the Fermi level will be affected by the applied electric field.

The distribution function for electrons rolling on a tilted band diagram, following the proposal of Zukotynski and Howlett,<sup>10</sup> is obtained as follows:

$$f(\epsilon_k, E, \theta) = \frac{1}{e^{(\epsilon_k - \zeta + e E \ell(\epsilon_k))/k_B T + 1}} \quad (2.1)$$

For holes  $e$  in Equation (2.1) should be replaced by  $-e$ .  $\ell(\epsilon_k) = \tau v$  is the energy-dependent mean free path. This distribution function thus has a very simple interpretation. The electrochemical potential  $\zeta$  during the free flight of carriers changes by  $\pm e E \ell$  as electrons tend to sink and holes tend to float on the tilted energy band diagram. This observation may suggest that the applied electric field tends to organize the otherwise completely random motion. Electric dipoles  $e \ell$  due to quasi-

free motion of the carriers tend to organize in the direction of electric field for holes and in the opposite direction for electrons. The high-field effects thus become important when the dipole energy  $e \mathcal{E} \cdot l$  is comparable to the thermal energy for nondegenerate electrons or the Fermi energy for degenerate electrons. The collisions tend to bring the electron closer to the conduction band edge. If the electric field is strong, this unidirectional motion will give carrier drift comparable to the thermal velocity which is average of the magnitude of electron velocity  $v$ . A quasi-ballistic behavior of the carriers thus follows in strong electric field.

### 3. QTD Quantum Wells

For a quasi-two dimensional (QTD) quantum well, the energy is given by

$$\epsilon_{n,k_x,k_y} = n^2 \epsilon_0 + \frac{\hbar^2}{2m^*} (k_x^2 + k_y^2) \quad n=1,2,3,\dots \quad (3.1)$$

The drift velocity for a QTD gas with the distribution function of Eq. (2.1), with  $k$  replaced by  $n,k_x,k_y$ , in the quantum limit ( $n=1$ ), is obtained as

$$v_d = \frac{\sqrt{\pi}}{2} v_{th} \frac{\int_0^{2\pi} \cos(\theta) \mathcal{F}_{1/2}(H(\theta)) d\theta}{\int_0^{2\pi} \ln(1 + e^{H(\theta)}) d\theta} \quad (3.2)$$

where

$$H(\theta) = \eta - \delta \cos(\theta) \quad (3.3)$$

and  $\eta$  is now given by

$$\eta = \frac{\zeta - \epsilon_0}{k_B T} \quad (3.4)$$

$\eta$  is now evaluated from the normalization condition

$$n = \lambda_D^{-2} \int_0^{2\pi} \ln(1 + e^{H(\theta)}) d\theta \quad (3.5)$$

In the nondegenerate limit, Eq. (3.2) simplifies to

$$v_d = \frac{\sqrt{\pi}}{2} v_{th} \frac{I_1(\delta)}{I_0(\delta)} \quad (3.6)$$

where  $I_n(\delta)$  is the modified Bessel function of order  $n$ . Taking the limit of Equation (3.6) as  $\delta \rightarrow \infty$ , the saturation velocity in the nondegenerate case is

$$v_{d \text{ sat}} = \frac{\sqrt{\pi}}{2} v_{th} \quad (3.7)$$

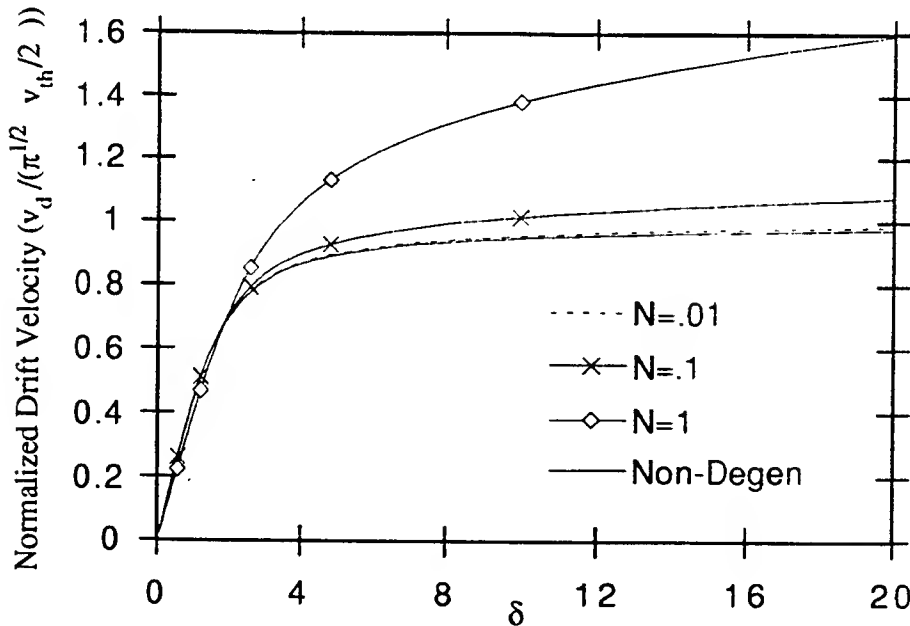


**Fig. 4.** Velocity-field curves obtained from Eq. (3.2) at several values of  $N$ . The velocity-field curve obtained in the non-degenerate approximation (Eq. (3.6)) is included for comparison.

The drift velocity  $v_d$  given by Eq. (3.2) is evaluated for several values of the degeneracy parameter  $N = n\lambda_D^2$  in Fig. 4. It is clear from



the Figure that as  $N$  changes from unity to a small fraction, the simplified results of Eq. (3.6) can be used. Observe also that for the moderate ( $N=.1$ ) to highly ( $N=1$ ) degenerate samples, the drift velocity at high fields clearly exceeds  $v_{dsat}$  as given by Eq. (3.7). These results are in conformity with the published results of experiments performed using a variety of sample preparations.

All scattering events change the carrier momentum. However, only some of them, the inelastic scattering events change the energy of the carriers. Usually several scattering events are followed by one inelastic scattering usually by generating a phonon. But, in high electric field, inelastic scattering can become frequent, comparable to momentum scattering rate. The scattering length  $\ell_{op}$  associated with the emission of an optical phonon can be obtained by equating the energy gained by an electron in a mean free path to that of an optical phonon  $\omega_0$ :

$$\ell_{op} = \omega_0 / e \mathcal{E} \quad (3.8)$$

The total scattering length is then given by

$$\ell^{-1} = \ell_o^{-1} + \ell_{op}^{-1} \quad (3.9)$$

where  $\ell_o$  is the zero-field scattering length obtained from the ohmic mobility. Figure 5 shows the comparison of theoretical results obtained from Eq. (4.2) with the experimental data of Hirakawa and Sakaki.<sup>2</sup> These experimental results could not be interpreted by a Monte Carlo theory.<sup>2</sup>

The multi-valley case of QTD quantum wells is much more complicated since not only the valleys in the GaAs, but also those in the neighboring AlGaAs layer play a critical role. Thus, velocity field characteristics depend strongly on the composition of the neighboring layer. If all valleys are assumed to be quantum-confined, the velocity field characteristics are given by the equation

$$v_d = \left( \frac{\pi k_B T}{2m_o} \right)^{1/2} \frac{\sum_{n,i} e^{-n^2 \epsilon_{\alpha,i}/k_B T} (m_i^*/m_o)^{1/2} I_1(\delta_{n,i}) e^{-\Delta_i/k_B T}}{\sum_{n,i} e^{-n^2 \epsilon_{\alpha,i}/k_B T} (m_i^*/m_o) I_0(\delta_{n,i}) e^{-\Delta_i/k_B T}} \quad (4.8)$$

with  $\delta_{ni} = eE\ell_{ni}/k_B T$ , where  $n,i$  stands for the  $n$ th subband in the  $i$ th valley.  $I_n(x)$  is a Bessel function of order  $n$ . If the mean free path decreases with electron energy, as is the case for phonon scattering, the contribution from higher subbands can be neglected. Intervalley transfer will be affected by the change in energy separation between the valleys because of different effective masses.

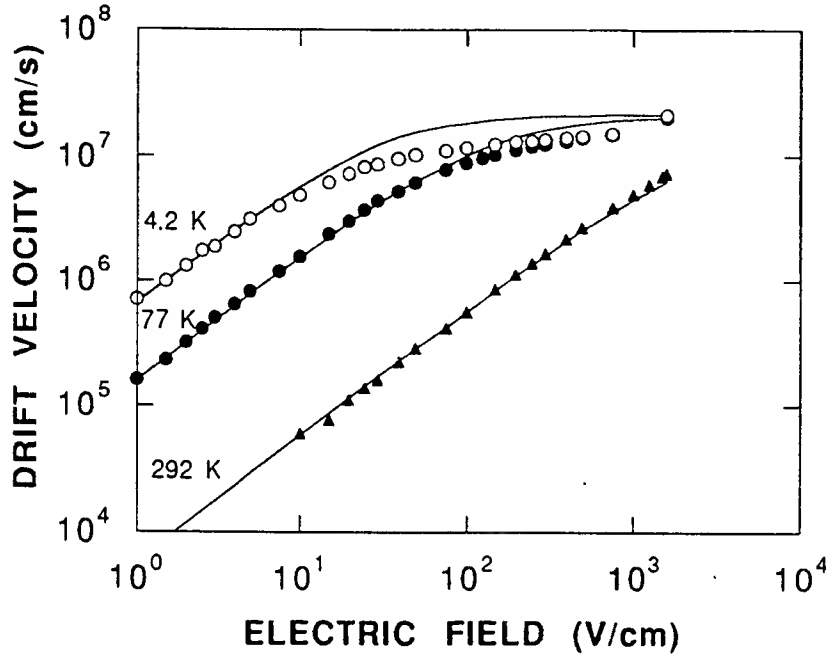


**Fig. 5.** Comparison of velocity-field characteristics obtained from theory and experiment.<sup>2</sup> Solid lines are theoretical curves and scattered points are taken from K. Hirakawa and H. Sakaki, J. Appl. Phys. 63, 803(1985).

Under the condition that the bandgap discontinuity for the higher subband is small, there will be a transition of  $\Gamma$ -valley electrons from 2D quantum-confined states to 3D propagating states in one of the higher valleys. In this case, the velocity-field characteristics are described by

$$v_d = \left( \frac{\pi k_B T}{2 m_\Gamma^*} \right)^{1/2} \frac{I_1(\delta_\Gamma) + e^{-(\Delta_H - \epsilon_{o\Gamma})/k_B T} \frac{2\pi L_z}{\lambda_{DH}} \frac{m_H^*}{m_\Gamma^*} \frac{2}{\pi^{3/2}} (\cosh(\delta_H) - \sinh(\delta_H)/\delta_H)}{I_0(\delta_\Gamma) + e^{-(\Delta_H - \epsilon_{o\Gamma})/k_B T} \frac{2\pi L_z}{\lambda_{DH}} \frac{m_H^*}{m_\Gamma^*} \frac{1}{2\pi^{1/2}} \sinh(\delta_H)/\delta_H} \quad (4.9)$$

Here H stands for a higher valley. If growth conditions are such that  $L_z \ll \lambda_{DH}/2\pi$ , the contributions of the higher valleys can be neglected. In that case an electron will follow the velocity-field characteristics appropriate for the  $\Gamma$ -valley. Otherwise, it will exhibit a 3D behavior at sufficiently high electric fields.

#### 4. MODELLING OF FIELD EFFECT TRANSISTOR

In modelling an FET, e.g. HEMT, commonly used empirical relation given by

$$v_D = \frac{\mu_o E}{1 + \frac{E}{E_c}} \quad (4.1)$$

is found to be quite convenient. The value of  $v_{sat} = \mu_o E_c$  is not normally known, necessitating an estimate of the saturation velocity. For room temperature conditions, the comparison of Eqs. (3.2) and (4.1) for the sample of Hirakawa and Sakaki<sup>2</sup> is shown in Fig. 6. This comparison indicates a value of  $1.8 \times 10^7$  cm/s for the saturation velocity, which is much higher than the highest velocity of  $0.73 \times 10^7$  cm/s reported in the experimental results at the highest practical value of the electric field. Figure 6 indicates that the highest observed velocity in an experimental setup is not necessarily the saturation velocity.

Also shown in Fig. 6 (dashed line) is the velocity field characteristics if optical phonon scattering is suppressed in a superlattice structure such as recently suggested by Sakaki<sup>12</sup>. If that is feasible, a saturation velocity as high as  $3.2 \times 10^7$  cm/s is possible.

Potential and electric field profiles along the length of the channel at the current saturation point can easily be shown to be<sup>14</sup>

$$V(x) = V_{Dsat} - V_{Dsat} (1 - x/L)^{1/2} \quad (4.2)$$

$$\mathcal{E}(x) = (V_{Dsat}/2L) (1 - x/L)^{-1/2} \quad (4.3)$$

with

$$V_{Dsat} = V_c \left[ \left( 1 + \frac{2 V_g'}{V_c} \right)^{1/2} - 1 \right], \quad (4.4)$$

$V_g' = V_g - V_T$  is the gate voltage above the threshold value and  $V_c = E_c L$ .

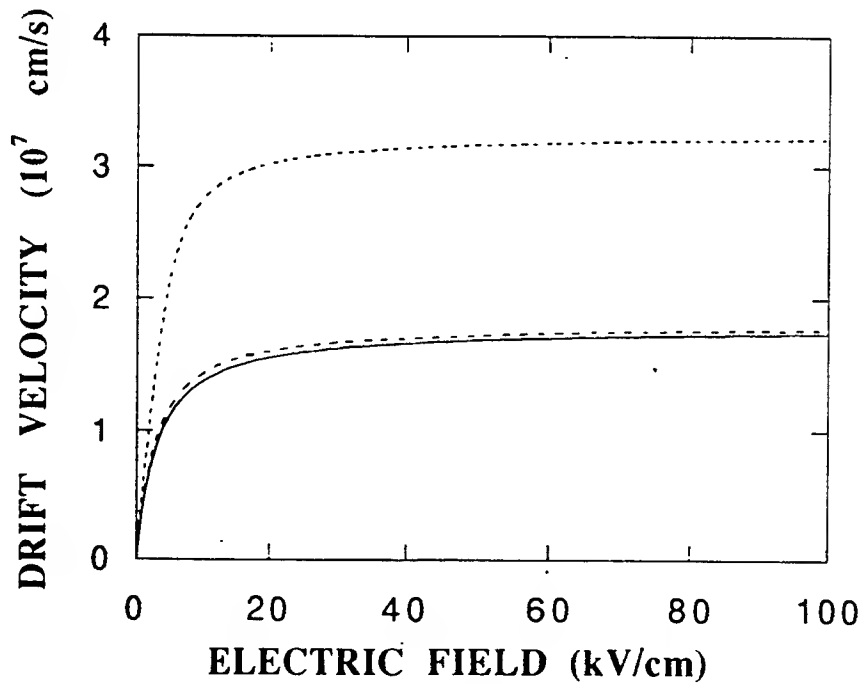


**Fig. 6.** Velocity-field characteristics for QTD electrons in GaAs at room temperature. Velocity field characteristics obtained from Eq. (3.2) are shown by solid line (with optical phonon emission) and dashed line (without optical phonon emission). The broken line represents the empirical relation of Eq. (4.1).

Following these profiles,<sup>14</sup> the velocity distribution in a 0.25- $\mu\text{m}$  gate length FET is shown in Fig. 6. Because of high electric field present at the drain end, the velocity at that end will be at its saturation limit of  $1.8 \times 10^7 \text{ cm/s}$ . It can easily be seen that the carriers are not travelling throughout the channel at the saturation velocity of  $1.8 \times 10^7 \text{ cm/s}$ . The carrier velocity is lower on the source end. Only at the drain end, the carrier velocity is saturated. As channel becomes smaller, velocities tend to reach the saturation velocity. This approach towards saturation is faster for higher mobilities and shorter gate lengths. But, no matter how small is the gate length, the velocity will always be unevenly distributed as Fig. 7 indicates.

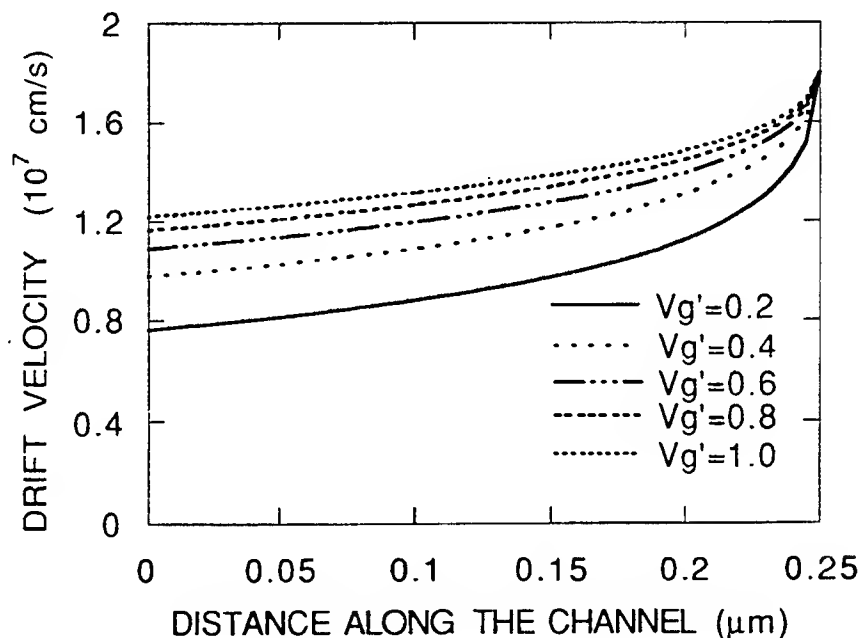


**Fig. 7.** Velocity Distribution in 0.25- $\mu\text{m}$  length channel of GaAs HEMT at room temperature.

Figure 5 indicates that the performance of the HEMT's at 77 K and 4.2 K will not be substantially different as saturation velocity is essentially the same at these temperature. This may be important information for cryoelectronics, as HEMT operating at 77 K may be much more economical than those operating at liquid helium temperature, but still without substantial loss about their performance.

The inclusion of mobility degradation in modelling of HEMT lifts the well-known *pinchoff* condition, which requires the carrier concentration to vanish at the drain end of the channel at the saturation point. This carrier concentration, in fact, saturates to the value given by

$$n_{SD}/n_{SO} = [1 - (V_C/V_{g'}) \{ (1 + 2V_{g'}/V_C)^{1/2} - 1 \}], \quad (4.5)$$

with

$$n_{SO} = (C_O/q) V_{g'}. \quad (4.6)$$

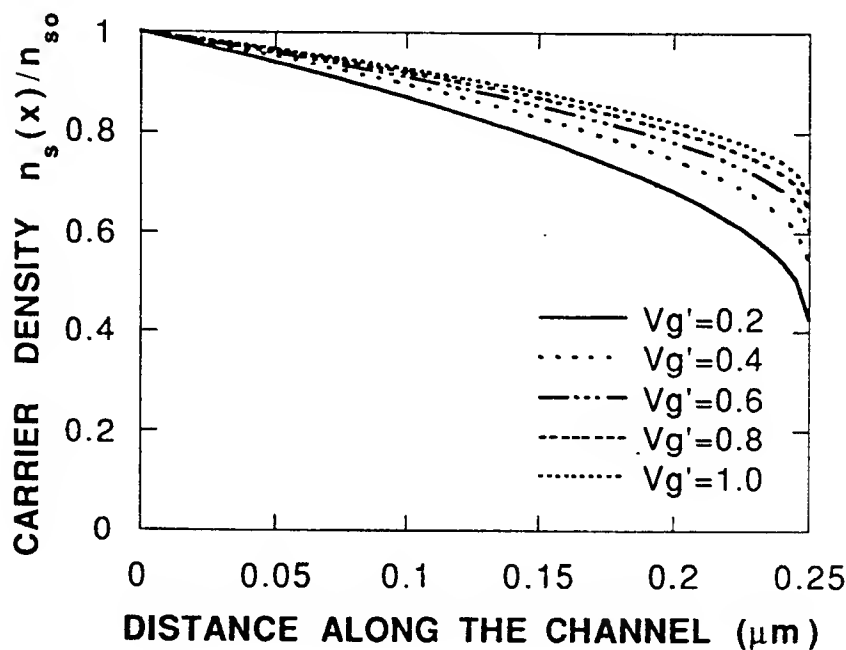


**Fig. 8.** Carrier distribution along the length of channel for a 0.25  $\mu\text{m}$  HEMT at saturation point. The carrier density is nonzero at the saturation point.

Carrier density profile in a 0.25- $\mu\text{m}$  HEMT structure is shown in Fig. 8. Contrary to common belief that the channel pinches off at the drain end at the onset of saturation, the results of Fig. 8 show that the carrier density does not go to zero. The carrier density may drop to as low as 50% for lower gate voltages. But, the channel is always open when current saturates. This conclusion is valid even for long gate-length FET's. The pinch-off phenomenon comes into play only if

velocity saturation effect is ignored which is present in long as well as short channel transistors. In either case, the electric field at the drain end is very high and mobility degradation due to high electric field cannot be ignored. In the long-channel limit the relative density saturates to the value  $n_{SD}/n_{SO} = V_g'/2 V_c$ .

I-V characteristics of HEMT can be described by the equation<sup>14</sup>

$$I_D = \beta_o \frac{2 V_g' V_{Dsat} - V_{Dsat}^2}{1 + \frac{V_{Dsat}}{V_c}} \quad (4.7)$$

with

$$\beta_o = \frac{C_o \mu_o W}{2 L} \quad (4.8)$$

The saturated current as obtained from optimizing Eq. (4.7) is given by

$$I_{Dsat} = \beta_o V_{Dsat}^2. \quad (4.9)$$

A plot of  $I_D/I_c$ , where  $I_c = \beta_o V_c^2$ , is shown in Fig. 9. The curve represented in Fig. 9 is valid for channels of all dimensions. For submicron channels  $V_g'/V_c$  will be very large and so are the values of  $V_{Dsat}/V_c$ . The distinction between a short and a long channel can be made by examining the ratio of  $V_g'/V_c$ . If  $V_g'/V_c \gg 1$ , the channel will exhibit a short-channel behavior. On the other hand, for experimental conditions which make  $V_g'/V_c \ll 1$ , a long-channel behavior is predicted. But, in any case, the channel is not pinched off at the onset of sturation.  $V_c = 0.077$  for a channel of  $0.25\text{-}\mu\text{m}$  gate length. In this regime, the saturation current  $I_{Dsat} = I_c (2 V_g'/V_c)$  is very small.

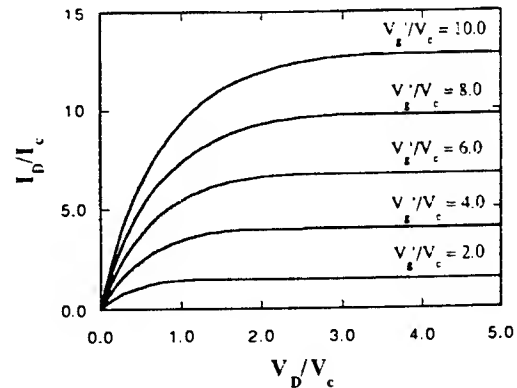


**Fig. 9.** I-V Characteristics of a Submicron Channel FET.

## 5. CONCLUSION

An overview of the velocity-field profiles for submicron-length channels is given. It is shown that under nondegenerate conditions, if a constant mean free path may be assumed, the drift velocity is limited by the appropriate thermal average of the magnitude of the velocity. The presence of an electric field tends to order the otherwise random electronic motion in its direction. For degenerate samples, the numerical calculations show that the saturation velocity tends to overshoot the thermal average of the magnitude of the velocity. This is due to the expansion of the Fermi sphere (or hemisphere in the strong electric field which has now to accommodate twice as many electrons than that in the zero electric field). But due to the experimental conditions present in the sample, the transfer to higher valleys is also possible. Unfortunately, very little is known about the transport parameters of the higher satellite valleys<sup>16</sup>. Moreover, because of the ellipsoidal nature of the valley, the effective mass is a tensor. Anisotropies in this tensor can give anisotropies in the direction of current flow.

A few comments about the intrinsic transport which is directly related to the electron temperature can be made. The concept of hot electron temperature is extensively used in the literature to define electric-field-induced change in energy of the electron. As one can easily see, this concept is valid if the bands remain flat in the electric field. When electric field is applied and the current is flowing, the bands tilt in the sample. Thus an electron after completing a mean free path will sink in the conduction band by an amount  $e E \ell_e$ , and holes tend to float by an amount  $e E \ell_h$ . This decreases the bandgap by an amount equal to  $e E (\ell_e + \ell_h)$ . The decrease in bandgap enhances the number of electron hole pairs in strong electric field (carrier multiplication). If bandgap is assumed to be constant at zero field value, the carrier multiplication can be renormalized in terms of change in temperature, which is perhaps a better definition for an effective electron temperature as it involves both the conduction and the valence band.

When velocity-field profiles are considered in modelling FET's, it is found that the usual pinchoff effect at the onset of current saturation is absent. Actually, pinchoff phenomena appear when



constant mobility, independent of an electric field, is used in modelling a transistor. When the velocity saturation effect, as present in the velocity-field profiles is used, the drain-end carrier density at the onset of saturation is found to be nonzero.<sup>12</sup> For obvious reasons, when the electric field is very high at the drain end, as is the case, the electrons do not follow the linear behavior in velocity-field relationship as predicted by Ohm's law. After the saturation point in I-V characteristics of the FET, carrier multiplication yields a large number of intrinsic carriers, which keep the channel open and current continues to flow. This explanation seems to be closer to the experimental observation than that the flow of carriers is through depletion layers as is modelled in the published literature. This carrier multiplication, perhaps, is also the source of noise which is normally present on the drain end.

These are some of the observations where velocity-field profiles may influence the modelling of modern nanostructure devices. We, therefore, hope that the results presented here will prove useful in understanding the world of future quantum device.

### ACKNOWLEDGEMENTS

The author would like to acknowledge the warm hospitality of the Center of Optoelectronics at the National University of Singapore, Quantum Wave Project at the University of Tokyo, and Research Division of the Solid State Electronics Directorate of Wright Laboratory at the Wight-Patterson Air Force Base, where most of this work was done. Many conversations with David Look have given me some directions for the future, for which I am grateful.

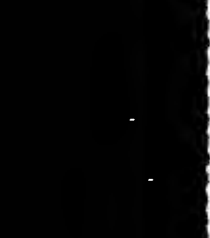
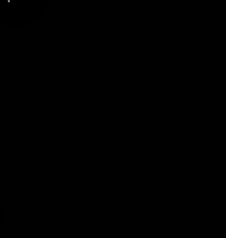
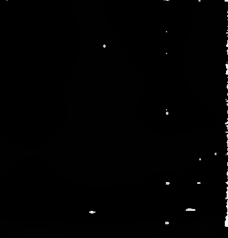
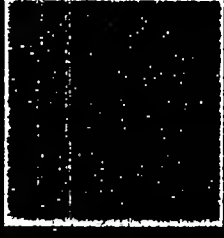
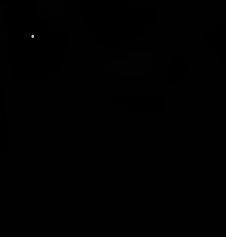
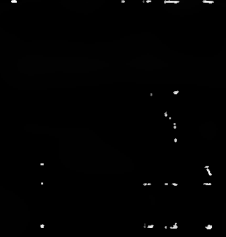
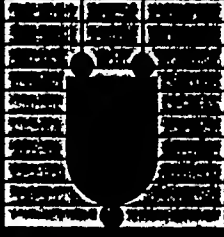
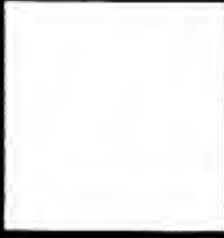
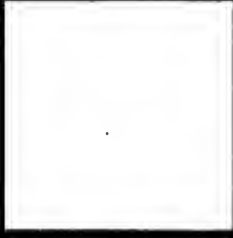
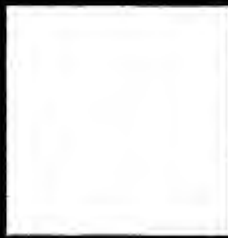
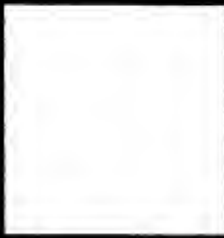
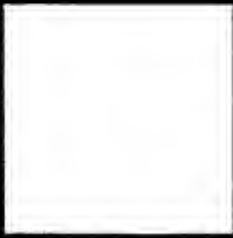
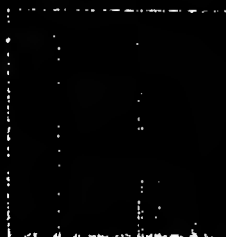
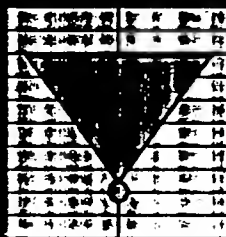
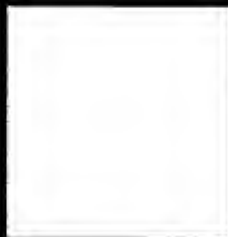
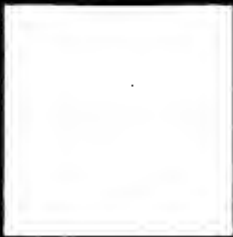
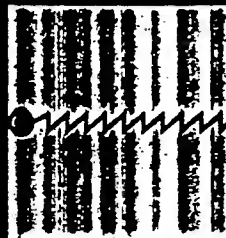
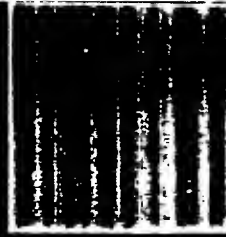
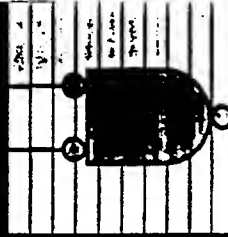
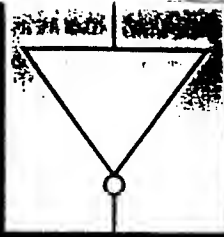
### REFERENCES

1. V. Arora, D. Mui, and H. Morkoc, IEEE Trans on Electron Devices, **ED-34**, 1231(1987)
2. V. K. Arora, Jpn. J. Appl. Phys. **24**, 537(1985); J. Appl. Phys. **54**, 824(1983).
3. K. Hirakawa and H. Sakaki, J. Appl. Phys. **63**, 803(1985).
4. W. T. Masselink, T. S. Henderson, J. Klem, W. F. Kopp, and H. Morkoç, IEEE Trans. Electron Dev. **ED-33**, 639(1986).
5. K. K. Thornber, J. Appl. Phys. **51**, 2127(1980).

6. W. Shockley, Bell Syst. Tech. J. **30**, 990(1951).
7. F. Capasso, T. P. Pearsall, and K. K. Thornber IEEE Electron Dev. Lett. **EDL-2**, 295(1981).
8. M. Dresden, Rev. Mod. Phys. **33**, 265(1961).
9. K. W. Böer, *Survey of Semiconductor Physics*, Van Nostrand Reinhold, New York, 1990, pp. 696-725.
10. S. Zukotynski and W. Howlett, Solid State Electron. **21**, 35(1978).
11. C. M. Wolfe, N. Holonyak, and G. Stillman, *Physical Properties of Semiconductors*, Prentice-Hall, Englewood Cliffs, N. J., 1989, pp. 112-118.
12. H. Sakaki, Jpn. J. Appl. Phys. **28**, L314(1989).
13. W. T. Masselink, N. Braslau, W. I. Wang, and S. I. Wright, Appl. Phys. Lett. **51**, 1533(1987).
14. V. K. Arora and M. B. Das, Electron. Lett. **25**, 820(1989).
15. V. K. Arora and M. B. Das, Semicond. Sci. & Tech. **5** (1990).
16. A. A. Ketterson, W. T. Masselink, J. S. Gedymin, J. Klem, C.-K. Peng, W. F. Kopp, H. Morkoç, and K. R. Gleason, IEEE Trans Electron Dev. **ED-33**, 564(1980).

## APPENDIX IV

“Quantum Engineering of Modern Optoelectronic Devices and Circuits,” V. K. Arora and T. C. Chong, IEEE Search (Singapore), Vol 170/7/92, No. MITA(p), pp. 12-17 (August 1992).



# Quantum Engineering of Modern Optoelectronic Devices and Circuits

by Dr V.K. Arora and Dr T.C. Chong,  
Centre for Optoelectronics,  
Department of Electrical Engineering,  
National University of Singapore

*A new range of optoelectronic devices, based on GaAs and related compound semiconductors, with physical properties very different from multimicron devices of present day integrated circuits are being experimented with in laboratories around the world. The high speed optoelectronics circuits based on these devices are needed for applications in future electronic systems such as supercomputers, high speed signal processors and satellite communication links. At nanometer dimensions of these miniaturized devices, the electrons lose their particle-like properties and behave like waves. Quantum engineering refers to happy marriage of quantum-mechanical ideas from physics and materials and electrical circuit ideas from engineering. On miniaturized scale, the electric fields are very high which give deviations from the well-known Ohm's law. The ways these quantum waves will influence the design of modern optoelectronic devices are discussed.*

## Introduction

The advances in the crystal growth, device concepts, and fabrication of electronic and optical devices in GaAs (Gallium Arsenide) and other III-V semiconductors have inspired the scientists in several laboratories around the world to work on combining both types of devices to create a new powerful class of high speed optoelectronic integrated circuits for optical communications and many other high speed applications like digital optical computers. For example, the U.S. Department of Defence is interested in these devices in order to develop Microwave Monolithic Integrated Circuits (MMIC's) which will make radar, now the size of a building, to fit on the front panel of an aeroplane. In order to develop such capabilities, it has supported the effort of several industries. Japan's Ministry of International Trade and Industry (MITI) and Exploratory Research for Advanced Technology (ERATO) Program have attached a significant importance to this critical area for development of sensitive technology as well as consumer electronics. In Singapore, considering the importance of high density and high performance integrated circuits (IC's), the Centre for Optoelectronics at NUS and Institute of Microelectronics have been established.

GaAs has a direct band gap material which is necessary for several optoelectronic applications. In addition, it has better electron transport properties than the industry's device vehicle silicon. Electrons in GaAs are about six times more mobile than in silicon. There have been attempts to integrate GaAs devices on a silicon substrate. Silicon

is a good conductor of heat and hence can provide a good heat sink for GaAs devices.

As very large scale integration (VLSI) in microcircuitry gives over to ultra-large scale integration (ULSI), the use of a mixed bag of devices, device structures, and materials very different from those of silicon VLSI circuits has led to the birth of nanoelectronics - an allusion to nanometer minimum dimensions required for these modern ICs. Apart from economic and space-saving reasons, these scaled-down devices cut down the transit time of the electron through the active channel. But, this decrease in the channel length makes the driving electric field in the channel very high. This high field substantially degrades the carrier mobility giving rise to saturation of the electron velocity, which limits the device speed. The elusive nature of these high field effects has kept the performance of designed devices below one's expectations. Since most devices now have length considerably smaller than the classical mean free path of the electrons, the concept of ballistic or quasi-ballistic transport is being utilised to enhance the speed limitations. As current-voltage characteristics give only the statistical high electric field is a formidable task. Considering the above facts and technological nanoelectronic devices. The idea that high mobility will necessarily lead to higher device speed is disputed by recent experimental observations. This is due to the fact that familiar Ohm's which gives linear relationship between current and voltage breaks down when high electric fields are encountered in miniaturized devices.

Practical limits in making integrated circuits (IC's) based on these devices are imposed by lithographic tooling, complexity of inter-

connections, and heat dissipation. Optical interconnections promise to relieve bottlenecks in electrical interconnections from projects in this emerging areas of nanoelectronics will necessarily involve engineers and scientists from varied speciality areas, working together to develop complex optoelectronic systems. The specialised system-on-a-chip circuits, normally called Application Specific Integrated Circuits (ASIC's), are being designed for specialised for variety of monitoring actions. Neural networks are being designed to emulate the operations of human brains. Even there have been several successful attempts in integrating micro-motors and micro-sensors on the same chip.

## Quantum Well MODFETS's

When quantum waves (QW) are considered, an electron loses its classical particle-like character in one or more of the three Cartesian directions. Whether an electron will behave like a quantum wave or a classical particle very much depends on the relative size of a device with respect to the de Broglie wavelength  $\lambda_p = h/p$ , where  $h$  is Planck's constant and  $p$  is the momentum of the particle. For thermal electrons with  $E = p^2/2m^* = k_B T = 25.9 \text{ meV}$  at room temperature,  $\lambda_p = 29.5 \text{ nm}$ , with electron effective mass of  $m^* = 0.067 m_0$  (GaAs), where  $m_0 = 9.1 \times 10^{-31} \text{ kg}$  is the free electron mass.

The wave character is well described by solving Schrodinger Equation for a given potential profile. For a simple quantum well of Fig. 1, quantum waves are well described by sinusoidal functions. The quantum-mechanical wave function of the electron can be engineered to obtain desired properties by changing the value and geometry of the confinement potential, and hence the name *quantum engineering* or wave-function engineering as called by Professor H. Sakaki, Director of the Quantum Wave Project of the Japan Research and Development Corporation (JRDC) and Professor of Electronic Engineering at the University of Tokyo.

The QW in Fig. 1 is engineered by sand-

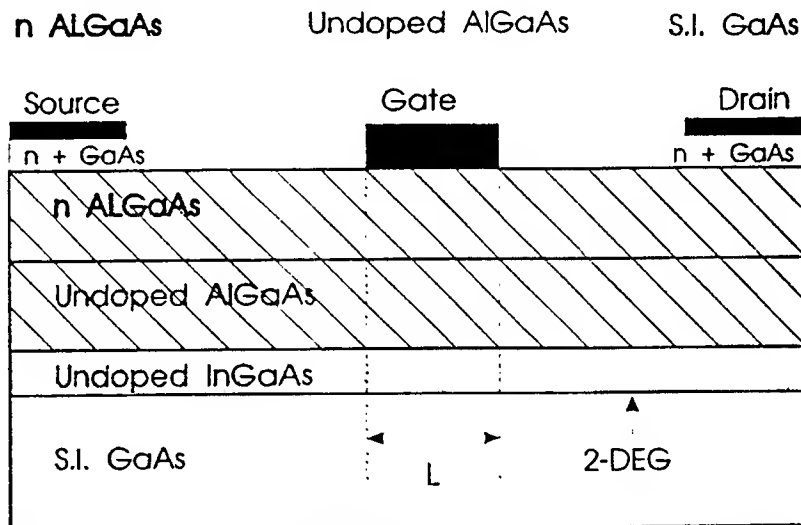
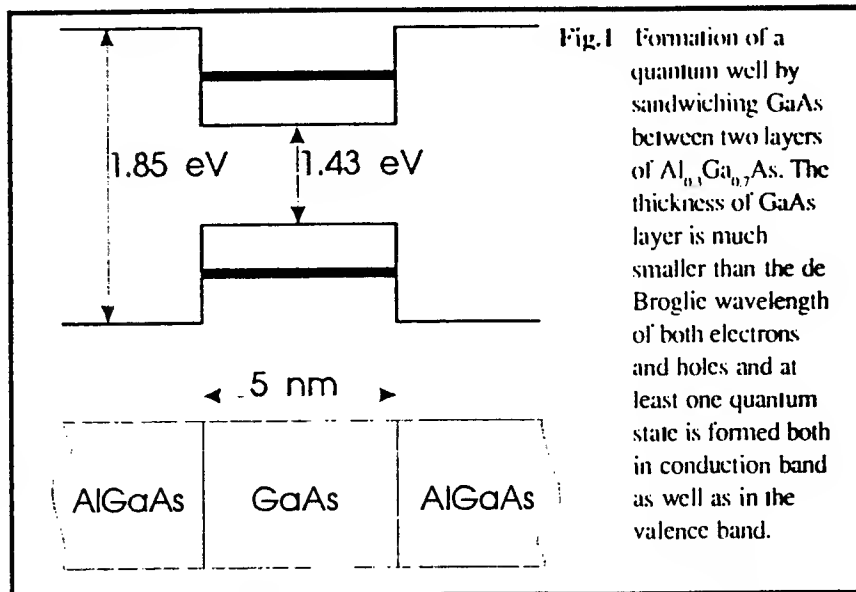


Fig. 2 An example of a pseudomorphic GaAs/InGaAs/AlGaAs Modulation Doped Field Effect Transistor (MODFET). Two-Dimensional Electron Gas (2-DEG) in InGaAs layer is supplied by parent donors in n-AlGaAs layer.

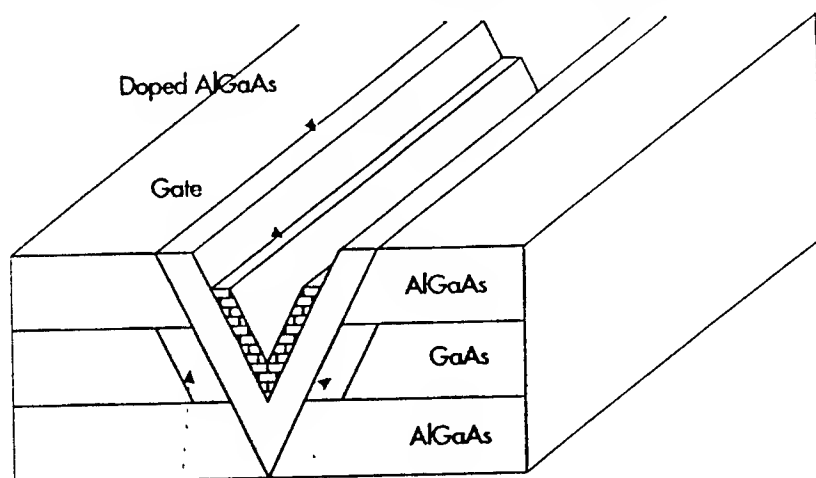
wiching a narrow bandgap material, e.g. GaAs, in between two layers of  $\text{Al}_x\text{Ga}_{1-x}\text{As}$ , an alloy of GaAs with Al.  $\text{Al}_x\text{Ga}_{1-x}\text{As}$  is a wider bandgap material, depending on the value of  $x$ , as compared to the bandgap of GaAs. The QW so designed can become a building block of a modulation-doped field effect transistor (MODFET), quantum well laser, or in the formation of a synthetic crystal by repeating the pattern, etc. Due to the physical separation of electrons in the QW which are supplied by donors placed in AlGaAs, with an undoped spacer layer, the ionized impurity scattering is considerably suppressed, resulting in high mobility of electrons especially at low temperatures. In the last few years, a new type of MODFET, the pseudomorphic or strained QW MODFET, using the InGaAs/GaAs system has been introduced (see Fig. 2). In these nanostructures, InGaAs is thin enough ( $\sim 200 \text{ \AA}$ ) so that the lattice strain can be accommodated by the lattice mismatch

without producing dislocations.

The fabrication of these QW's at submicron scale with excellent material quality and atomically smooth interface is made possible by novel techniques of molecular beam epitaxy (MBE), metal-organic chemical vapour deposition (MOCVD), or more recent combined technology of MO-MBE. A/P S.J. Chua reviews this technology and microstructures (to be exact, we should call them nanostructures because of nanometer scale dimensions) which are needed for development of quantum well lasers in a previous issue to which readers are referred [1]. Here, we will emphasise on the research which is still in its infancy to develop future integrated systems.

### Quantum Well Wires

Presently, devices based on QW wires (QWW's) (see Fig.3) in which electrons are



Quantum Wires

Fig.3 Field-induced quantum well wires in a V-groove of a layered structure of GaAs/AlGaAs

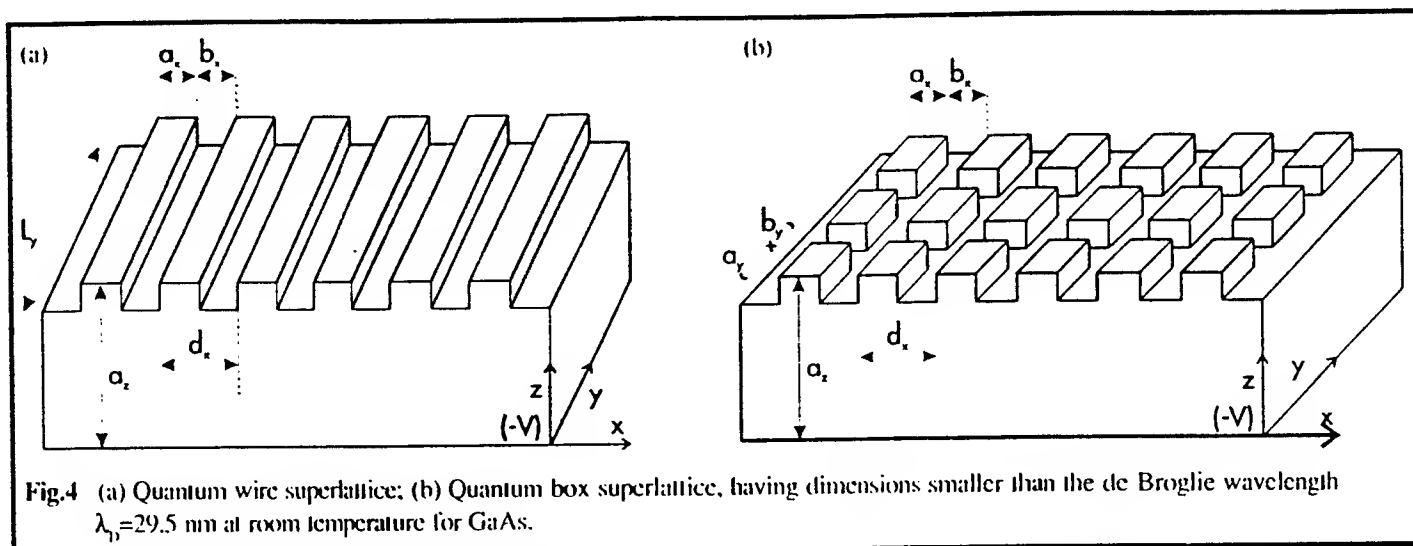
confines in two directions, are also being considered. QWW's and possibly quantum boxes with three-dimensionally confined electrons undoubtedly will occupy researchers and developers in the next decade. The two-dimensional confinement of carriers in QWW nanostructures is a natural extensions of the one-dimensional confinement in MODFET's. Electrons confined in QWW offer several attractive properties. In many

ways, the two-dimensional electron confinement is similar to electrons confined in a strong magnetic field. This correspondence is useful in predicting the behaviour of quantum confined electrons in QWW's where the electron gas can be characterised as quasi-one-dimensional (QOD). This new range of laterally patterned nanometer scale devices and superlattices provide many challenges to quantum theory. When the quasi-two-dimensional (QTD) gas in a quantum well is re-configured by surface patterning of the gate region to produce a variety of structures in the varying low dimensionality and phase coherence, there are endless possibilities of engineering new devices. A quantum wire transistor (also known as Sakaki Transistor [2],[3]) can be fabricated by growing layered structure of AlGaAs/GaAs/AlGaAs (see Fig.3), followed by an anisotropic chemical etch that allows the formation of a V-groove. A regrowth of AlGaAs and metal layer in the V-groove allows the formation of a transistor gate. By further lithographic techniques, source and drain contacts can be deposited at the two ends of the quantum wire. A planar field-effect coupled quantum wire transistor has recently been demonstrated by workers at AT&T Bell Laboratories in the U.S.A. The fabrication conditions of such nanostructures are being perfected for applications in the future range of integrated circuits. Such structures are projected to provide extremely high mobility at cryogenic temperatures.

### Quantum Boxes and Arrays

Further reduction in the dimensionality is possible by confining all three dimensions, i.e. the device dimensions are less than the de Broglie wavelength in all three directions. In such nanostructures, known as quantum box, electron loses its semiclassical character in all directions, and therefore exhibits a quasi-zero-dimensional (QZD) behaviour.

Recently, in quest for enhancing the speed of nanotransistors, Professor H. Sakaki has proposed novel quantum wire and quantum box arrays [3],[4], each with dimensions



less than the de Broglie wavelength (Fig.4). The rationale for engineering these nanostructures is to suppress the emission of optical phonons, the lattice quanta of energy (each quantum has energy  $\hbar\omega = 35$  meV), which substantially limit the velocity of carriers. Such structures also form the possibility of three dimensional integration of future integrated circuits.

With these developments and several others and an ever increasing need for high-speed device applications, researchers at the National University of Singapore and other industrial and academic laboratories are looking for further breakthroughs on the conventional design of transistors.

### Fundamental Processes

As said in the Introduction, there are two set of fundamental processes which govern the design and operation of these devices. First set is due to the reduction of dimensions less than the de Broglie wavelength. For example, the energy of electron confined to a QWW, where confinement dimensions (5-10 nm) are much smaller than the de Broglie wavelength of the electron can be written as [3]

$$\epsilon_{n,k} = \epsilon_n + (\hbar^2 k_x^2) / (2m^*) \quad (1)$$

where  $\epsilon_n$  is the quantised energy in the two confinement directions perpendicular to the quasi-free x-direction, and depends on the cross-sectional geometry of the wire.  $n$  is a set of integers and  $\hbar k_x$  is the momentum of the electron parallel to the quasi-classical direction

of the wire ( $L_y \gg \lambda_D$ ). Thus, when transport properties are averaged using these energy values, summation over quantum numbers and integration over  $k_x$  is encountered, in contrast to three dimensional integrals for conventional bulk devices.

An electron in a cylindrical QWW behaves very much similar to an electron confined to a strong magnetic field, which follows a helical path. In the case of an electron confined to a magnetic field, the quantised energy  $\epsilon_n$  is replaced by Landau energy  $\epsilon_n = (n + \frac{1}{2})\hbar\omega_c$  where  $\omega_c = qB/m^*$  is the cyclotron frequency of the electron orbit perpendicular to the magnetic field  $B$  applied in the x-direction and  $n$  is an integer.

The other set of processes has to do with the dynamics of electrons in response to the applied voltage which results in high electric field in miniaturised devices [5],[6]. With a logic level of 5V, a cm-length device will have an electric field of 5V/cm, at which Ohm's law is obeyed. Velocity is then a linear function of the applied electric field. But, if the dimensions are reduced to submicron range (say 0.5  $\mu\text{m}$ ), a very high electric field of 5V/0.5  $\mu\text{m} = 100$  kV/cm is encountered. At this high electric field, electron velocity varies nonlinearly as shown in Fig.5 (solid line). At electric field less than the critical value  $\epsilon_c = 3.1$  kV/cm, the relationship is linear, but at higher electric field velocity becomes sublinear function of an electric field and eventually saturates to a value of  $1.8 \times 10^7$  cm/s. Fig.5 also shows



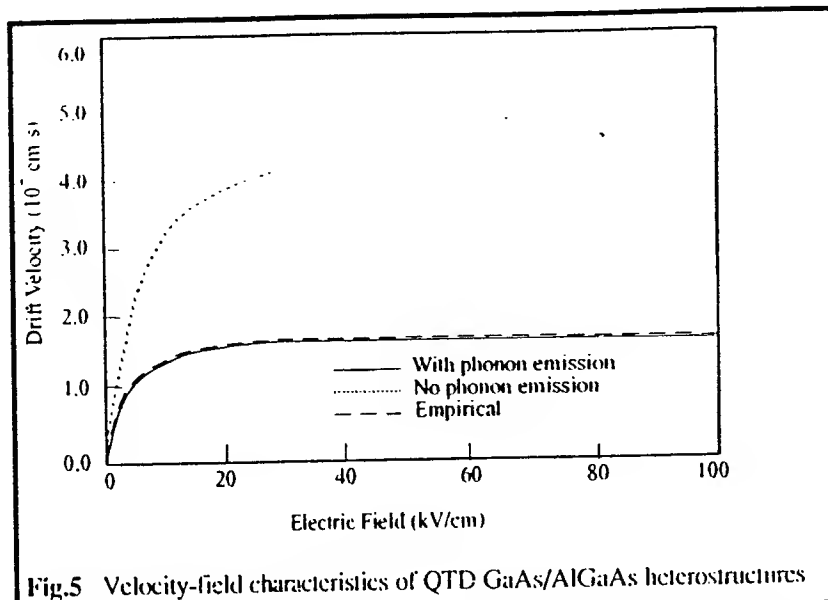


Fig.5 Velocity-field characteristics of QTD GaAs/AlGaAs heterostructures

that is optical phonon emission is suppressed as suggested by Sakaki by engineering the quantum box array structure, substantial improvement in speed is possible (dotted line). This velocity saturation plays a dominant role in modern transistors.

In modelling an FET, e.g. HEMT, an empirical relation given by

$$v_D = \mu_0 E / (1 + E/E_c) \quad (2)$$

is found quite convenient. Here  $\mu_0 = 5800 \text{ cm}^2/\text{V.s}$  and  $E_c = 3.1 \text{ kV/cm}$ . This relationship is plotted by dashed line in Fig.5. Note that when  $E \ll E_c$ , Ohm's law is obeyed. But when  $E \gg E_c$ , substantial deviations from Ohm's law are obtained.

All scattering interactions change the carrier momentum. However, only some of them, inelastic scattering events change the energy of the carriers. Usually several scattering events are followed by one elastic scattering usually by generating an optical phonon. The scattering length is  $l_{\text{op}} = \hbar\omega/qE$  for this inelastic scattering. If this scattering length becomes comparable to or smaller than the momentum randomising mean free path, the probability of optical phonon emission is considerably enhanced. The solid line in Fig.5 includes the optical phonon emission, and dotted line does not.

### To Be Accomplished

As the industrial needs to develop scaled

down optoelectronic systems expand, an understanding of the processes necessary for the development of these complex systems is of paramount importance. As new nanostructures, including superlattices with coupled arrays, are being proposed in academic institutions, it is timely and appropriate to consider processes which will allow fabrication of such complex systems. A well-understood design can save a lot of effort, time and resources, which would otherwise be wasted in fabrication of nonfunctional systems. Therefore, there is a great need to undertake investigations concerning device design, involving optimisation of active and parasitic device parameters, determination of basic material electronic parameters such as mobility  $\mu_0$ , carrier saturation velocity, and the device gain and noise performance with identification of low-frequency and high-frequency noise sources. The following list identifies a number of problems that remain and will form a basis for research for future generations of students to undertake:

- ☐ To design fabrication conditions such that the regrowth takes place in closed chambers with minimum exposure to the atmosphere.
- ☐ To develop lithographic techniques to cut dimensions of the order of nanometer without distortions in geometry of nanostructures.
- ☐ To develop etching processes so that the undercutting under the mask pattern can be reduced in order to increase device density as well as to have better control over the device and circuit topology.
- ☐ To develop a comprehensive transport theory for quantum processes at the nanometer scale.
- ☐ To develop a high-field distribution function which could be utilised for multivalley structures of materials used in the nanofabrication process.
- ☐ To design and optimize the shape and also the size of the quantum well for high frequency applications extending beyond

200GHz.

- To carry out numerical calculations based on the quantum transport framework to understand the role of quasi-ballistic electrons determining the I-V characteristics and high frequency limitations of ultra-submicron gate lengths.
- To investigate the low-frequency and high-frequency noise behaviour and identify the noise sources in nanometer scale quantum wells.
- To study the electric field and velocity distributions in active and parasitic regions of the device.
- To explore the possibility of designing a multi-state logic device by using quantum states in a given quantum well.

These points form a vantage point for global outlook of the arena of future optoelectronics devices and integrated circuits. These studies should significantly advance our understanding of fundamental processes at the interface between physical sciences and quantum engineering of advanced device designs being considered for the future nanofabrication technology. These advance design ideas, hopefully, will be transmitted to the engineering students in classrooms environments in preparing them for the technologies of the 1990's and beyond, thereby contributing significantly to the engineering manpower resource base in Singapore. □

## References

- [1] S.J. Chua, "Semiconductor Lasers and Recent Developments", IEEE Search, pp6-10, August 1991.
- [2] H. Sakaki, "Scattering Suppression and High-Mobility Effect of Size Quantized Electrons in Ultrathin Semiconductor Wire Structures", Jpn J. Appl. Phys., Vol. 19, No. 12, pp. L735-L738 (1980)
- [3] V.K. Arora and H. Sakaki, "Physics and Technology of Quantum Well Wires and Related Superalloys", invited paper, *Proceedings of the International Workshop on Semiconductor Devices*, December 2-6, 1991, Tata-McGraw Hill, New Delhi, pp. 38-45.
- [4] H. Sakaki, "Quantum Wire Superlattices and Coupled Box Arrays: A Novel Method to Suppress Optical Phonon Scattering in Semiconductors", Jpn J. Appl. Phys., Vol. 28, No. 2, pp. L314-L316 (1989).
- [5] V.K. Arora, Dr S.L. Mui, and H. Morkoc, "Mobility Degradation and Transferred Electron Effect in Gallium Arsenide and Indium Gallium Arsenide", IEEE Transactions on Electron Devices, Vol. ED-34, No. 6, pp. 1231-1237 (1987)
- [6] L.S. Tan, S.J. Chua and V.K. Arora, to be published.

## APPENDIX V

"Physics and Technology of Quantum Well Wires and Related Superlattices," with H. Sakaki (U. of Tokyo), invited paper, *Proceedings of the VI<sup>th</sup> International Workshop on the Physics of Semiconductor Devices*, December 2-6, 1991, pp. 38-45, New Delhi, India, Tata-McGrawHill, 1992.

**IWPSD—91**

# **Physics of Semiconductor Devices**

Proceedings of the Sixth International Workshop on  
Physics of Semiconductor Devices,  
New Delhi, India, December 2-6, 1991

**Editors**

**A.K. SREEDHAR • W.S. KHOKLE • SURESH C. JAIN**

*Organised by*

Central Electronics Engineering Research Institute, Pilani  
Solid State Physics Laboratory, Delhi  
Indian Institute of Technology, New Delhi



**Tata McGraw-Hill Publishing Company Limited**  
NEW DELHI

---

*McGraw-Hill Offices*

New Delhi New York St. Louis San Francisco Auckland Bogotá Guatemala  
Hamburg Lisbon London Madrid Mexico Milan Montreal Panama  
Paris San Juan São Paulo Singapore Sydney Tokyo Toronto

# PHYSICS AND TECHNOLOGY OF QUANTUM WELL WIRES AND RELATED SUPERLATTICES

Vijay K. Arora\*

*Department of Electrical Engineering, National University of Singapore, 10 Kent Ridge Crescent, Singapore 0511, and Quantum Wave Project, Research Center for Advanced Science and Technology, University of Tokyo, 4-6-1, Komaba, Meguro-ku, Tokyo 153, Japan*

Hiroyuki Sakaki

*Quantum Wave Project, Research Center for Advanced Science and Technology, University of Tokyo, 4-6-1, Komaba, Meguro-ku, Tokyo 153, Japan, and Institute of Industrial Science, 7-22-1 Roppongi, Minato-ku, Tokyo 106, Japan*

## ABSTRACT

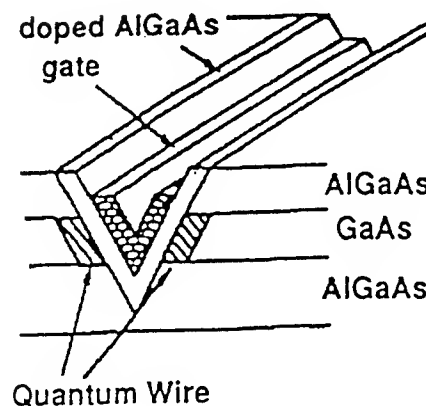
As pointed out by Sakaki/1/, the ionized impurity scattering in quantum well wire (QWW) microstructures which are confined two-dimensionally are drastically suppressed. Recently, a novel method to suppress the optical phonon scattering in QWW superlattices and coupled quantum box arrays has been proposed/2/. In an effort to enhance the intrinsic device speed, these structures are attractive from the device applications point of view. As dimensions in these proposed structures are comparable to or smaller than the deBroglie wavelength of carriers, the scattering interaction depends strongly on the geometry of the QWW. The contribution of various scattering interactions is reviewed. In addition, when potential is applied along the miniaturized dimensions of the device, high fields are encountered which substantially degrade the mobility and hence velocity becomes saturated. Therefore, in the design of a QWW field effect transistor, complete velocity-field characteristics are needed. The conditions necessary for enhancement of the saturation velocity, which limits the intrinsic device speed, are analyzed. The feasibility of preparing such microstructures, physical significance of the mobility-limiting scattering mechanisms in scaled-down dimensions, and optimal criteria for their operations are discussed.

## 1. INTRODUCTION

Recent developments in nanofabrication technology have allowed researchers in laboratories around the world to fabricate structures as small as a fraction of a monolayer/1,2/. In these superfine nanostructures, the electrons exhibit their wavelike character and hence their behavior best described by quantum mechanical principles. This results in reduced dimensionality of the fabricated nanostructure. Quantum well wire (QWW) is an example of such a structure. When confinement length is comparable to or smaller than the de Broglie wavelength of an electron, classical particle-like nature of the electron is preserved only in the direction parallel to the wire, giving it an appearance of a quasi-one-dimensional (QOD) structure/3,4/. An example of this structure, most recently fabricated by Sakaki and others/5/ by using V-

\* Permanent Address: School of Science and Engineering, Wilkes University, Wilkes-Barre, PA 18766, U. S. A.

groove anisotropic etching, is shown in Fig. 1. The theory of quantum transport in QWW's in the ohmic regime is well developed<sup>[3,4]</sup>. The thrust behind the development of QWW's lies in the fact that the ionized impurity scattering is considerably reduced and hence high mobilities could be obtained. To obtain a high speed and high frequency performance of such a transistor, the length of the wire should necessarily be small. At such small lengths, high electric fields along the length of the wire are anticipated. The understanding of these high field effects is crucial to the design of a QWW transistor.



All scattering interactions change the carrier momentum. However, only some of them, inelastic scattering events change the energy of the carriers. Usually several scattering events are followed by one inelastic scattering usually by generating an optical phonon. The scattering length is  $\ell_{op} = \hbar \omega_{op} / qE$  for this inelastic scattering. To suppress the emission of an optical phonon, Sakaki<sup>[2]</sup> suggested QWW array and box structures indicated in Fig. 2. With the development of such arrays, the width and spacing of minibands can be tailored to suppress the emission of optical phonons. This will enhance the saturation velocity and hence provide a prototype structure for high speed applications.

## 2. QUANTUM TRANSPORT

The energy of an electron confined to a QWW, where confinement dimensions are much smaller than the deBroglie wavelength of the electron, can be written as<sup>[3]</sup>

$$\epsilon_{\alpha k} = \epsilon_{\alpha} + \frac{\hbar^2 k_x^2}{2 m^*} \quad (2.1)$$

where  $\epsilon_{\alpha}$  is the quantized energy in the two confinement directions perpendicular to the quasi-free x-direction. An electron in a QWW behaves very much similar to an electron confined to a strong magnetic field. In the case of a magnetic field the quantized energy  $\epsilon_{\alpha}$  is replaced by Landau energy  $\epsilon_n = (n+1/2)\hbar\omega_c$ , where  $\omega_c = qB/m^*$  is the cyclotron frequency of the electron orbit perpendicular to the magnetic field applied in the x-direction.

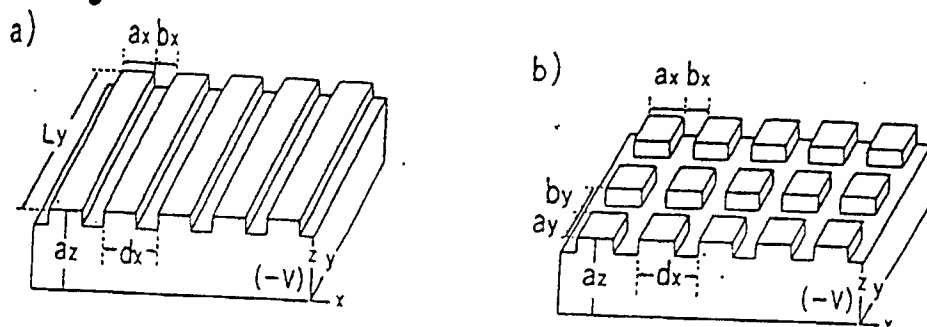


Fig. 2. a) QWW array superlattice; b) quantum box array superlattice [2].

Quantum transport in the presence of a low electric field is discussed in several papers. The ohmic mobility due to isotropic scattering (e.g. acoustic phonon scattering) is proportional to the area of confinement [3], i.e. quantum confinement tends to enhance the isotropic scattering. On the other hand, mobility due to ionized impurity scattering is suppressed due to highly improbable unidirectional momentum change of the electron along the quasi-free direction [1]. The mobility in QWW is shown to exceed  $10^6 \text{ cm}^2/\text{V}\cdot\text{s}$  at liquid helium temperatures and can be optimized at liquid nitrogen temperatures.

High mobilities obtained in QWW's rapidly degrade [6,7] in the presence of a high electric field which is necessarily present in the scaled-down channels. This high-field effect tilts the otherwise flat band structure as shown in Fig. 3. An excellent description of this tilted band diagram is given by Böer [8]. On this tilted band diagram, electrons tend to sink and holes tend to float. The change in energy in a mean free path is given by  $q\mathcal{E}\ell_{e(h)}$ . In the following, we consider the electronic motion limited by a mean free path  $\ell$ .

An electron, in traversing a mean free path of length  $\ell$  which is randomly oriented, finds the electrochemical potential (the Fermi energy) changed by an amount  $e\mathcal{E}\ell$ . This change in Fermi energy results in a distribution function which has forward-backward asymmetry in the direction of an electric field and is given by

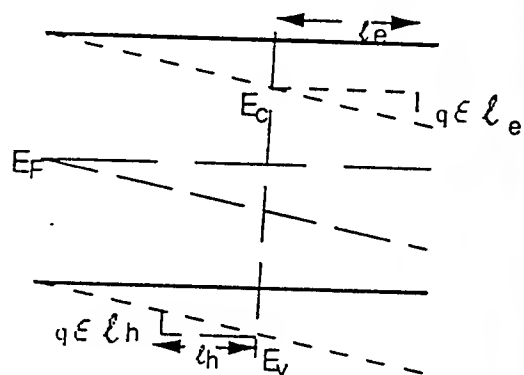


Fig.1. Energy band diagram of an intrinsic semiconductor in an electric field applied in the direction from right to left.

$$f(\epsilon_{\alpha k}, \vec{E}) = \frac{1}{e^{\frac{\epsilon_{\alpha k} - \zeta + q \vec{E} \cdot \vec{\ell}}{k_B T}} + 1} \quad (2.2)$$

The distribution function of Eq. (2.2) can also be derived by following the technique of Lagrange multiplier for a steady state nonequilibrium conditions with an additional constraint that the current density due to electrons having the same frequency is constant/6/.

Following Fig. 3, the distribution of electrons and asymmetry created in the electron gas can be explained as follows. Central to any transport problem is the electron distribution function. For linear transport, the distribution function obtained from the Boltzmann transport equation has been extremely successful in predicting mobility behavior. Thornber/9/ did a study of scattering rate and momentum scaling transformations of the distribution function. It was determined that the saturation velocity is invariant under scaling of the magnitude of scattering rates, which alters mobility, while mobility is invariant under scaling of the magnitude of momentum, which alters saturation velocity. The mobility and saturation velocity are thus independent parameters in velocity-field profiles of heterostructures. In one experiment/10/, an unusually high room temperature saturation velocity was observed. Consistent with the observations of Thornber/9/, the electric field tends to organize in its direction the otherwise completely random motion of the electrons. The electric dipole moment  $q\vec{\ell}$  due to the quasi-free electron motion in a mean free path  $\ell$  between two collisions tends to arrange in a direction antiparallel to the applied field. High field effects thus become important when the dipole energy  $q\vec{E} \cdot \vec{\ell}$  is comparable to the thermal energy (nondegenerate samples) or to the Fermi energy (degenerate samples). At each collision, the randomness is re-established. If the electric field is strong, this randomness is destroyed, and an electron exhibits a quasi-ballistic behavior appropriate to the thermal motion of the electron. Since electrons are confined to move only in x-direction, transport behavior of electrons in QWW's is perhaps easy to understand. In general  $\ell$  can be a very complicated function of energy. But, for degenerate systems, since this is evaluated at the Fermi energy, it can be considered a constant.

Under steady-state nonequilibrium conditions, appropriate for high-field present in QWW's, the Fermi energy  $\zeta$  can be described as electrochemical potential. Its value is obtained from the normalization condition  $\sum_{\alpha k} f(\epsilon_{\alpha k}) = N_e$ . Here  $\alpha$  stands for the two spin states of the electron, and  $N_e$  is the total number of electrons in the sample. In the quantum limit, when only the lowest level  $\epsilon_0$  is appreciably populated, the electrochemical potential can be calculated from the equation



$$\mathcal{F}_{1/2}(\eta + \delta) + \mathcal{F}_{1/2}(\eta - \delta) = \frac{N_1}{\sqrt{\pi}} \quad (2.3)$$

with

$$\eta = (\zeta - \varepsilon_0) / k_B T \quad (2.4)$$

$$\delta = q \mathcal{E} \ell / k_B T \quad (2.5)$$

$$N_1 = n_l \lambda_D \quad (2.6)$$

$$\lambda_D = h / \sqrt{2 m^* k_B T} \quad (2.7)$$

Here  $n_l$  is the electron density per unit length of the wire and  $\lambda_D$  is the de Broglie wavelength of electron at thermal energy  $k_B T$ .  $\mathcal{F}_j(y)$  is the Fermi-Dirac integral of order  $j$ .  $N_1$  is the degeneracy factor which describes the degenerate character of the electron gas in quantum well wire.

In the zero-field case  $\eta = N_1^2 / 16$ . In the nondegenerate limit, Eq. (2.3) can be approximated and  $\eta$  can be calculated from the equation

$$e^\eta = N_1 / 2 \pi^{1/2} \cosh(\delta) \quad (2.8)$$

which shows that the electrochemical potential decreases with the increase in the electric field.

As the distribution function of Eq. (2.2) has forward-backward asymmetry in the direction of the electric field, which increases as the magnitude of the electric field is increased, the fraction of electrons moving antiparallel to the electric field is given by the expression

$$\frac{n(-)}{n_l} = \left[ 1 + \frac{\mathcal{F}_{1/2}(\eta + \delta)}{\mathcal{F}_{1/2}(\eta - \delta)} \right]^{-1} \quad (2.9)$$

This fraction is 0.5 in zero electric field as the electrons are equally likely to move in both directions. In the strong electric field limit, the fraction approaches unity as the electric field forces the electrons to move in antiparallel direction. Figure 4 shows the relative population of electrons moving antiparallel to the electric field as a function of applied electric field for various values of the degeneracy parameter. The Figure clearly exhibits that the electric field has lesser influence on strongly degenerate gas as compared to that on the nondegenerate electron gas. Nondegenerate electrons change their directions easily in the direction of the electric field as the quantum states are

available at relatively low energies. The results of Fig. 4 suggest that the electric field breeds some order in otherwise complete random motion. Following the tilted band diagram of Fig. 3, the electrons moving parallel to the electric field will encounter an energy hill and hence are less likely to move in that direction. The collisions force the electrons to stay energetically close to the conduction band edge. Thus band structure and collision interactions play a central role in the transport of electrons in high electric field.

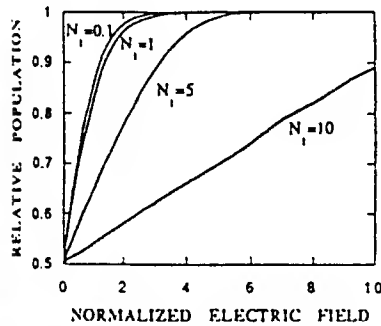


Fig. 4. Relative population of electrons in antiparallel direction to the applied electric field as a function of normalized electric field.  $N_1$  is the degeneracy parameter.

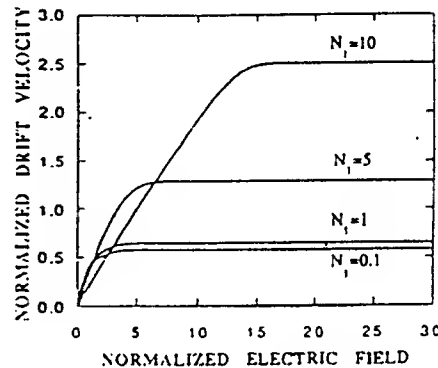


Fig. 5. Normalized drift velocity as a function of normalized electric field for various values of degeneracy parameter.

The drift velocity of an electron, with the distribution function of Eq. (1), can easily be calculated with the result

$$v_D = \frac{v_{th}}{N_1} \ln \left[ \frac{1+e^{\eta+\delta}}{1+e^{\eta-\delta}} \right] \quad (2.10)$$

Figure 5 gives the normalized drift velocity  $v_d/v_{th}$  as a function of normalized electric field for various values of the degeneracy parameter. To observe deviations from the ohmic behavior in strongly degenerate system, much larger values of the electric field are required. Even though the mobilities of degenerate systems are lower, the saturation velocity is enhanced in strong electric field. This can be understood on the basis that the electrochemical potential is enhanced as electrons tend to move in the antiparallel direction to the electric field and high energy quantum states get occupied. For a nondegenerate gas, the relative drift velocity saturates to the value equal to  $1/\pi^{1/2}$  for all concentrations. The complete velocity-field profile under the nondegenerate conditions can be described by the equation

$$v_D = \frac{v_{th}}{\sqrt{\pi}} \tanh(\delta) \quad (2.11)$$

This equation is obeyed for all concentrations for degeneracy factor  $N_1$  less than 0.1.

### 3. OPTICAL PHONON EMISSION

As said in the Introduction, the optical phonon emission can be included in the distribution function by defining a combined mean free path due to momentum and energy relaxation processes. To demonstrate the importance of the optical phonon emission/11/ in limiting the saturation velocity, the case of nondegenerate electrons as depicted in Eq. (2.11) is considered. In this case  $\delta$  in Eq. (2.12) is replaced by

$$\delta = \frac{\delta_o}{1 + \frac{\delta_o}{\Theta}}, \quad \delta_o = \frac{q\epsilon\ell_o}{k_B T}, \quad \Theta = \frac{\hbar\omega_o}{k_B T} \quad (3.1)$$

where  $\ell_o$  is the momentum relaxation scattering length. Velocity-field characteristics for various values of optical phonon energy parameter  $\Theta$  are shown in Fig. 6.  $\Theta = \infty$  curve refers to the case when optical phonon energy is much larger than the thermal energy (no emission). On the other extreme, the saturation velocity limited by the emission of an optical phonon in the high-field limit is given by

$$v_{sat} = \frac{v_{th}}{\sqrt{\pi}} \tanh(\Theta) \quad (3.2)$$

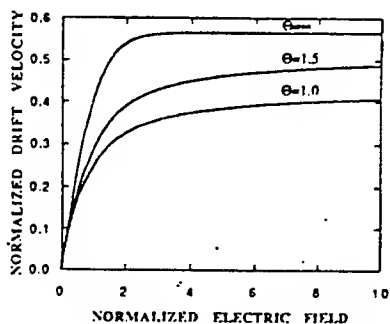


Fig. 6. Velocity-Field Characteristics of nondegenerate QWW.

The mobility in the ohmic regime does not alter appreciably by the emission of an optical phonon. But, optical phonon emission can drastically change the saturation velocity. As optical phonon energy becomes comparable to the thermal energy of the carriers, the saturation velocity decreases. Velocity enhancement is possible by suppression of this optical phonon scattering in a superlattice structure as suggested by Sakaki/2/, for example. Minibands in the superlattice structure can be engineered in such a way that the spacing between minibands is greater than the optical phonon energy. The calculations

for such a superlattice structure indicate a lower mobility. As the saturation velocity is relatively independent of the ohmic mobility, a greater operating speed of a transistor fabricated from such transistors is expected. When the velocity saturation is considered in modelling a transistor, the usual pinchoff effect is found to be absent/12/. The results also show that the saturation velocity does not sensitively depend on the ohmic mobility, in agreement with the recent findings of Hirakawa and Sakaki/13/. The results are also consistent with original idea of Shockley/14/ which was discarded in favor of energy-balance theories.

To conclude, an overview of the physics and possible applications of QWW nanostructures for the development of high speed transistor is given. The presence of an electric field tends to order the otherwise random electronic motion in its direction. It is shown that the drift velocity is limited by the average of the magnitude of the thermal velocity for nondegenerate electrons or by the Fermi velocity in modified Fermi sphere in QWW.

### ACKNOWLEDGEMENTS

One of us (VKA) would like to acknowledge financial support of Japan Research and Development Corporation (JRDC) and that of U. S. Air Force Office of Scientific Research under Faculty Associateship Program. He, also, wishes to acknowledge the useful interaction with researchers at Quantum Wave Project of JRDC, Electronic Research Laboratory at Wright-Patterson Air Force Base, and the Center of Optoelectronics at the National University of Singapore.

### REFERENCES

1. H. Sakaki, IEEE J. Quantum Electronics QE-22, 1845(1986).
2. H. Sakaki, Jpn. J. Appl. Phys. 28, L314(1989).
3. V. K. Arora, J. Phys. C 18, 3011(1985).
4. V. K. Arora, Phys. Stat. Solidi (b) 117, 127(1983).
5. H. Sakaki et. al., to be published.
6. V. K. Arora, Jpn. j. Appl. Phys. 24, 537(1985); J. Appl. Phys. 54, 824(1983).
7. V. K. Arora, D. Mui, and H. Morkoc, IEEE Trans. Elect. Dev. ED-34, 1231(1987)
8. K. W. Boer, *Survey of Semiconductor Physics*, Van Nostrand Reinhold, New York, 1990, pp. 696-725.
9. K. K. Thonber, J. Appl. Phys. 51, 2127(1980).
10. W. T. Masselink, T. S. Henderson, J. Klem, W. F. Kopp, and H. Morkoc, IEEE Trans. Electron Dev. ED-33, 639(1986).
11. D. L. Scharfetter and H. K. Gummel, IEEE Trans. Electron Dev. ED-16, 64(1982)
12. V. K. Arora and M. B. Das, Electron. Lett. 25, 820(1989); Semicond. Sci. & Tech. 5(1990).
13. K. Hirakawa and H. Sakaki, J. Appl. Phys. 63, 803(1985).
14. W. Shockley, Bell Syst. Tech J. 30, 990(1951).

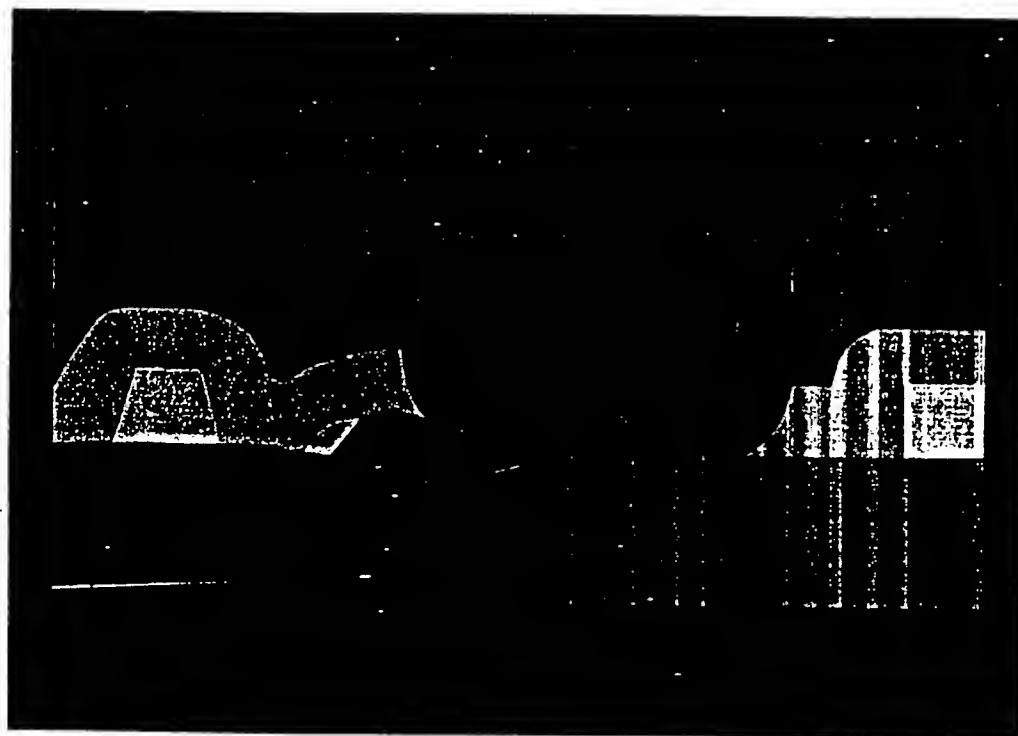
## **APPENDIX VI**

"High-Field Induced Hot-Carrier Temperature, Bandgap Narrowing, and Carrier Multiplication in Bulk Semiconductors," V. K. Arora and H. Sakaki (U. of Tokyo), invited paper, Proceedings of SemCon, the International Conference on Physics and Technology of Semiconductor Devices and Integrated Circuits, February 5-7, 1992, Madras, India, SPIE Publication, Tata-McGraHill Company, pp. 160-171.

**PROCEEDINGS**

# **Conference on the Physics and Technology of Semiconductor Devices and Integrated Circuits**

**5-7 February 1992, Indian Institute of Technology Madras, India**



*Editor*  
**B.S.V. Gopalam**

*Assistant Editor*  
**J. Majhi**

**SPIE PUBLICATION**

2-69



CONFERENCE ON THE  
PHYSICS AND TECHNOLOGY OF SEMICONDUCTOR DEVICES  
AND INTEGRATED CIRCUITS

Volume 1523

**Semiconductor Device  
Performance-Related Effects**

*Chairs*

**P. R. Vaya**

Indian Institute of Technology (India)

**Jan Misiewicz**

Technical University of Wroclaw (Poland)

# High-Field-Induced Hot-Carrier Temperature, Bandgap Narrowing and Carrier Multiplication in Bulk Semiconductors

Vijay K. Arora\* and Hiroyuki Sakaki†

Quantum Wave Project, Research and Development Corporation of Japan, Keyaki House, Komaba 4-3-24-302, Meguro-ku, Tokyo 153, Japan, and Research Centre for Advanced Science and Technology, University of Tokyo, 4-6-1, Komaba, Meguro-ku, Tokyo 153, Japan

## ABSTRACT

The steady state distribution function of charged carriers which takes into account the energy absorbed by the carriers in an electric field is described. Velocity-field characteristics so obtained agree well with the room-temperature experimental data for silicon samples of varying ohmic mobility. In the nondegenerate approximation, the saturation velocity obtained is comparable to the thermal velocity of the carriers ( $1.03 \times 10^7$  cm/s for electrons and  $1.00 \times 10^7$  cm/s for holes), a result which is independent of the low-field mobility of the carriers, consistent with the experimental observations. The asymmetrical distribution function favors holes in the direction of the applied electric field and electrons in the opposite direction. Therefore, on a tilted band diagram, electrons tend to sink and holes tend to float, thereby reducing the effective bandgap. This increases the number of intrinsic carriers with the increase of electric field. An effective hot-electron temperature which accounts for this increase in carrier concentration also increases with the increase in electric field. Effective bandgap, effective hot-electron temperature, and carrier multiplication factor as a function of electric field are analyzed for various doping concentrations. The results so obtained extrapolate well in the limit of zero electric field, when well-known ohmic behavior is reproduced. The implications of this carrier multiplication on pinchoff condition, noise behavior, breakdown characteristics, etc. are discussed.

## 1. INTRODUCTION

Recent developments in VLSI and VHSIC programs have indicated an ever-increasing importance of high-field effects which limit the velocity of carriers and hence impose an intrinsic limit on device speed. There have been numerous attempts to identify the mechanism responsible for this saturation of the carrier velocity in high electric field (See Ref. 1 for a review). Often a high mobility is cited in the published literature to give higher saturation velocity. But, recent experiments tend to indicate a poor correlation between saturation velocity and mobility.<sup>2,3</sup> This absence of correlation was predicted, several years ago, in scaling theory arguments of Thornber.<sup>4</sup> Saturation velocity was found to be invariant under scaling of the magnitude of scattering rates which alters mobility, while mobility was found to be invariant under scaling of the magnitude of momentum which alters saturation velocity, consistent with the predictions of Arora.<sup>1</sup> In low electric field  $\mathcal{E}$ , collisions can be considered point collisions as the energy  $|q| \mathcal{E} \lambda_D$  (field broadening)

\*Permanent Address: School of Science and Engineering, Wilkes University, Wilkes-Barre, PA 18766, U. S. A.

†Also at Institute of Industrial Science, University of Tokyo, 7-22-1 Roppongi, Minato-ku, Tokyo 106, Japan



absorbed by a carrier of charge  $q$  ( $q = \pm e$  for holes/electrons) in the de Broglie wavelength  $\lambda_D$  is negligible compared to collision broadening. But, as the electric field becomes larger, the field broadening tends to mask the collision broadening, and hence makes carrier transport virtually independent of scattering. The onset of nonlinear behavior thus takes place when field broadening is comparable to the collision broadening. This condition is equivalent to the condition that the momentum gained by the carrier from the field  $e \mathcal{E} \tau$  in the mean free time  $\tau$  is comparable to its thermal momentum  $m^* v$ . In terms of energy, this condition is equivalent to the condition that the energy gained by an electron in a mean free path  $e \mathcal{E} \ell$  is comparable to the thermal energy  $k_B T$ . This condition was originally considered by Shockley,<sup>5</sup> but was discarded in favor of the energy balance theories which dominated the high-field arena in those days.

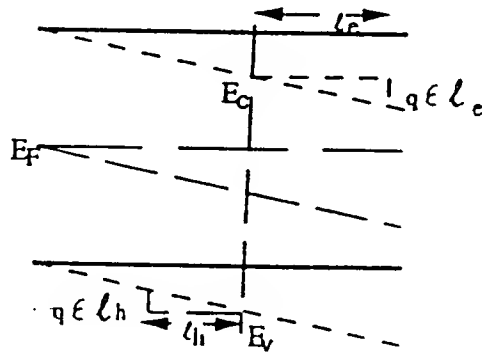


Fig. 1. Energy band diagram of an intrinsic semiconductor in an electric field applied in the direction from right to left.

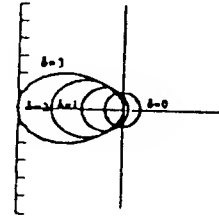


Fig. 2. Polar Plot of the normalized distribution function  $f(\epsilon, \mathcal{E}, \theta) / f(\epsilon, 0, \theta)$  for holes. The electron distribution is the mirror image about the vertical axis.

Recently, due to the availability of supercomputers, Monte Carlo simulations of carrier trajectory have become very popular. In a simulation, the carrier is subjected to the classical laws of motion followed by a scattering event generated by a set of random numbers. The use of complicated energy-balance equations, which are generally difficult to solve for all possible scattering interactions thus can be avoided. Instead at each scattering event, the electron is allowed to keep a portion of energy gained from the field which accumulates as collisions proceed and could be emitted in the form of an optical phonon in an inelastic scattering. If this emission is disregarded, the accumulated energy can become very high, necessitating the use of high-energy scattering times, which are central to any successful simulation. The high collision broadening present in these simulations can easily mask the semiclassical behavior of a carrier, as pointed out by Capasso et al.<sup>6</sup> Dresden<sup>7</sup> has reviewed assumptions, implicit and explicit, which are to be satisfied in treating electron as a classical particle. One such assumption is that the collision broadening  $\hbar/\tau$  is much smaller than the thermal energy  $k_B T$  ( $\hbar/\tau \ll k_B T$ ), which is easily satisfied in low-field transport of carriers. But, if high collision broadening is present, this condition can be easily violated. In spite of these conceptual difficulties, the understanding of the physical mechanism responsible for velocity saturation and its interdependence on the ohmic mobility is missing in simulation experiments. As the mean free time  $\tau$  is inversely proportional to the velocity  $v$  of a carrier for deformation potential scattering, which is considered to be the

dominant mechanism in simulation experiments, a description of the carrier transport in terms of mean free path  $\ell = v \tau$ , a constant for deformation potential scattering, appears more appropriate.

In external fields, the Fermi energy (electrochemical potential) and bands are tilted parallel to each other<sup>8</sup>, as shown in Fig. 1. An excellent description of the carrier transport with tilted band diagram is given by Böer,<sup>8</sup> who examines the effect of built-in as well as the applied electric field on the distribution of carriers. The carrier distribution is determined relative to the Fermi level. In zero bias, the distribution is independent of position and the Fermi level (chemical potential) is constant. In an external field, however, Fermi level and bands are tilted. The carrier distribution is now a function of spatial coordinates. When electrons are accelerated in the field, they move from a region of higher density  $n(e - \zeta)$  to that of lower density  $n(e - (\zeta \pm e \mathcal{E} \ell))$ . These electrons can dissipate their net additional energy to the lattice by emitting phonons, thereby causing lattice heating. The carriers drop close to the conduction band edge and the motion is repeated. From intuitive arguments, as suggested by Böer,<sup>8</sup> a limiting velocity comparable to the random thermal velocity at lattice temperature is expected. The carrier motion in an external field is, therefore, not random. It has a finite component in the field direction. This makes distribution of carriers asymmetric in the direction of applied electric field. The electrons will roll down the energy hill and holes will bubble up the energy hill. The electric field thus tries to organize the otherwise completely random motion. As no new randomness is created, the thermodynamic carrier temperature does not go up. For convenience in interpreting the experimental data, the energy gained by a carrier can be translated in terms of increase in carrier temperature. This gives an apparent decrease in the energy bandgap, which can result in carrier multiplication. Understandably, the Fermi level will be affected by the applied electric field. Because of well-understood transport parameters of silicon in which deformation scattering plays a dominant role, its importance in semiconductor industry, and its potential in silicon-germanium superlattices, we will illustrate the results for this material.

## 2. HIGH-FIELD DISTRIBUTION FUNCTION

The distribution function can be derived from fundamental principles following the proposal of Zukotynski and Howlett.<sup>9</sup> Suppose the quantum states are divided into many cells with  $n_1$  electrons and  $g_1$  states of energy  $\epsilon_1$  in the first cell,  $n_2$  electrons and  $g_2$  states of energy  $\epsilon_2$  in the second cell, and so on. Then the number of ways of arranging the total  $n$  electrons in the  $g$  states is given by

$$W = \prod_i g_i! / n_i! (g_i - n_i)! \quad (2.1)$$

with

$$g = \sum_i g_i \quad (2.2)$$

The total number of electrons is given by

$$n = \sum_i n_i \quad (2.3)$$

and the total energy of the system is

$$\epsilon = \sum_i n_i \epsilon_i \quad (2.4)$$

If there is net carrier current, an additional condition must be added. In this case, the current  $j^m$  due to all electrons having the same collision frequency (or relaxation time  $\tau(\epsilon_m)$ ) is conserved independently. This current is given by

$$j^m = e \sum_{i \in m} n_i v_{Fi} \quad (2.5)$$

where  $v_{Fi}$  is the component of the electron velocity in the direction of the field. This ensures the proper selection of states that are equally probable. Since collisions are, in general, a function of energy, the electrons in a group having the same collision time should be grouped together. Following the standard procedure,<sup>10</sup> the number  $W$  of ways of arranging the electrons is maximized (subject to the constraints of constant total  $n$ ,  $e$ , and  $j^m$ ) using Lagrange multipliers. The energy dependent distribution function, with Lagrange multipliers  $\alpha$ ,  $\beta$ , and  $\gamma(\epsilon_i)$  is obtained as

$$f(\epsilon_i, \theta) = \frac{1}{e^{(\alpha + \beta \epsilon_i + \gamma(\epsilon_i) \cdot v)/k_B T + 1}} \quad (2.6)$$

It is clear that  $\gamma = 0$  in the absence of an electric field. Since  $\alpha$  and  $\beta$  are constants, independent of electric field, their values can be obtained by comparison with the equilibrium Fermi-Dirac distribution function and are determined to be  $\alpha = -\zeta/k_B T$  and  $\beta = 1/k_B T$ . Here,  $\zeta$  is the Fermi energy or chemical potential (or the electrochemical potential when an electric field is applied). The Fermi energy is to be determined from the normalization condition  $\sum_k f(\epsilon_k) = N$ , where  $k = (k_x, k_y, k_z)$  and  $N$  is the total number of carriers in the sample. The multiplier  $\gamma(\epsilon_k)$ , which must be a function of the electric field  $\epsilon$ , can be evaluated by comparing Eq. (2.6) with the linearized solution of the Boltzmann transport equation:

$$f(\epsilon_k, \epsilon, \theta) = f_0 + e \epsilon \cdot v \tau(\epsilon_k) \frac{df_0}{d\epsilon_k} \quad (2.7)$$

Expanding Eq. (2.6) to first order in  $\epsilon$  and comparing with Eq. (2.7), we find  $\gamma(\epsilon_k) = e \epsilon \tau(\epsilon_k)/k_B T$ . Using  $\ell(\epsilon_k) = \tau v$ , an energy dependent mean free path, the distribution function of Eq. (2.6) transforms to

$$f(\epsilon_k, \epsilon, \theta) = \frac{1}{e^{(\epsilon_k \cdot \zeta + e \epsilon \cdot \ell(\epsilon_k))/k_B T + 1}} \quad (2.8)$$

For holes  $e$  in equation (2.8) should be replaced by  $-e$ . This distribution function thus has a very simple interpretation. The electrochemical potential  $\zeta$  during the free flight of carriers changes by  $\pm e \cdot \ell$  as electrons tend to sink and electrons tend to float on the tilted energy band diagram. This observation may suggest that the applied electric field tends to organize the otherwise completely random motion. electric dipoles  $e \cdot \ell$  due to quasi-free motion of the carriers tend to organize in the direction of electric field for holes and in the opposite direction for electrons. The high-field effects thus become important when the dipole energy  $e \cdot \ell$  becomes comparable to thermal energy for nondegenerate electrons or Fermi energy for degenerate electrons. The collisions tend to bring the electron closer to the conduction band edge. If the electric field is strong, this unidirectional motion will give

carrier drift comparable to the thermal velocity which is average of the magnitude of electron velocity  $v$ . A quasi-ballistic behavior of the carriers thus follows in strong electric field.

As said earlier, for deformation potential scattering in bulk samples, a dominant scattering mechanism in silicon, the collision time is inversely proportional to the velocity of the carriers. Therefore,  $\ell$  is constant. In this description, even if the scattering rates increase with the carrier velocity, the mean free path is essentially constant. This is the distinct advantage of using the mean free path over mean free time. The distribution function so obtained is strongly protruded in the direction of electric field and is central to the understanding of velocity-field characteristics. In the non-degenerate approximation (carrier concentration  $n \ll \lambda_D^{-3}$ , where  $\lambda_D = h/(2m^* k_B T)^{1/2}$  is the thermal de Broglie wavelength of the electron), the distribution function can be written as

$$f(\epsilon_k, \epsilon, \theta) = e^{-(\epsilon_k - \zeta)/k_B T - \delta \cos(\theta)} \quad (2.9)$$

with

$$\delta = \frac{e \mathcal{E} \ell}{k_B T} \quad (2.10)$$

In Eq. (2.9), we assume the electric field is along the z-axis. A polar plot of  $f(\epsilon_k, \epsilon, \theta)/f(\epsilon_k, 0, \theta)$  for electrons is shown in Fig. 2. When  $\delta \ll 1$ , the distribution function is spherically symmetric. When  $\delta > 1$ , however, the distribution function deviates considerably from this spherical character and protrudes in the direction opposite to the applied electric field.

### 3. CARRIER TRANSPORT

For a bulk parabolic semiconductor, the energy as a function of the momentum  $\hbar k$  is given by

$$\epsilon_k = \frac{\hbar^2 (k_x^2 + k_y^2 + k_z^2)}{2m^*} \quad (3.1)$$

The drift velocity is obtained from the relationship

$$v_d = \frac{\sum_{k, \mathcal{A}} f(\epsilon_k) (\hbar k / m^*)}{\sum_{k, \mathcal{A}} f(\epsilon_k)} \quad (3.2)$$

Here  $\mathcal{A}$  stands for spin. Converting  $\sum_k$  to integration using the factor  $\Omega/(2\pi)^3$  (where  $\Omega$  is the volume of the crystal), the drift velocity in response to an electric field applied in the polar z-direction is obtained as

$$v_d = \frac{2}{\sqrt{\pi}} v_{th} \frac{\int_0^\pi \sin(2\theta) \mathcal{F}_1(H(\theta)) d\theta}{\int_0^\pi \sin(\theta) \mathcal{F}_{1/2}(H(\theta)) d\theta} \quad (3.3)$$

where

$$\mathcal{F}_j(\eta) = \frac{1}{\Gamma(j+1)} \int_0^\infty \frac{x^j}{e^{(x-\eta)} + 1} dx \quad (3.4)$$

is the Fermi-dirac integral.  $H(\theta)$ , the quasi Fermi level of carrier, is defined as

$$H(\theta) = \eta - \delta \cos(\theta) = \frac{\zeta}{k_B T} - \delta \cos(\theta) \quad (3.5)$$

and

$$v_{th} = (2k_B T/m^*)^{1/2} \quad (3.6)$$

The normalized Fermi energy (electrochemical potential)  $\eta$  is obtained from carrier conservation by numerically solving the normalization equation

$$n_v = (\sqrt{\pi} / \lambda_D)^3 \int_0^\pi \sin(\theta) \mathcal{F}_{1/2}(H(\theta)) d\theta \quad (3.7)$$

where  $n_v$  is the carrier concentration per unit volume. Carriers in silicon are nondegenerate if carrier concentration is  $0.1N_c(v)$ , where  $N_c(v)$  is the effective density of states for electrons (holes). At room temperature,  $N_c = 2.86 \times 10^{19} \text{ cm}^{-3}$  and  $N_v = 3.10 \times 10^{19} \text{ cm}^{-3}$ , as recently evaluated by Green<sup>11</sup>. Thus, nondegenerate approximation can easily be applied for carrier concentrations less than  $10^{18} \text{ cm}^{-3}$ . In the nondegenerate limit, Eq. (3.3) can be considerably simplified, and the drift velocity is now given by

$$v_d = \frac{2}{\sqrt{\pi}} v_{th} L(\delta) \quad (3.8)$$

where

$$L(\delta) = \coth(\delta) - 1/\delta \quad (3.9)$$

Thus if carrier mean free path is known, velocity-field characteristics can be obtained from Eq. (3.8). The carrier mean free path can easily be obtained from ohmic mobility for which reliable experimental data is available. The electrochemical potential  $\zeta$ , in nondegenerate approximation, does not play an active role in the expression of drift velocity. However, for degenerate case, the drift velocity depends on carrier concentration through  $\zeta$ . Expanding Eq. (3.8) for low electric field and writing  $v_d = \mu E$ , the mobility expression is obtained as

$$\mu_{e(h)} = 4 e \mathcal{L}_e(h) / 3 (2 \pi m^* k_B T)^{1/2} \quad (3.10)$$

where  $\mu_{e(h)}$ , the mobility of electrons(holes), which is a function of impurity concentration  $N$ , is given by the empirical relation<sup>9,10</sup> which is found to fit most experimental data:

$$\mu = \frac{\mu_0}{\sqrt{1 + \frac{N}{S + N_{ref}}}} \quad (3.11)$$

The parameters are listed in Table I.

Table I. Carrier Properties of Si at Room Temperature<sup>9,10,11</sup>

	Electron	Holes	Units
$\mu_0$	1430	480	$\text{cm}^2/\text{V}\cdot\text{s}$
$N_{ref}$	$3 \times 10^{16}$	$4 \times 10^{16}$	$\text{cm}^{-3}$
$S$	350	81	
$A$	$3.5 \times 10^3$	$6.1 \times 10^3$	$\text{V}/\text{cm}$
$B$	$7.4 \times 10^3$	$2.5 \times 10^4$	$\text{V}/\text{cm}$
$F$	8.8	1.6	
$m^*$	1.09	1.15	$m_0$
$N_{c(v)}$	$2.86 \times 10^{19}$	$3.10 \times 10^{19}$	$\text{cm}^{-3}$

With the values of  $\mu_{e(h)}$  obtained from Eqs. (3.10) and (3.11), the velocity-field characteristics of electrons and holes, as obtained from Eq. (3.8) are shown by solid lines in Figs. 3 and 4. The dashed lines show the experimentally observed velocity-field characteristics which are well-represented by the equation, originally suggested by Scharfetter and Gummel<sup>9</sup>:

$$v_d = \frac{\mu_0 \mathcal{E}}{\sqrt{1 + \frac{N}{S + N_{ref}} + \frac{(\mathcal{E}/A)^2}{(\mathcal{E}/A) + F} + \left(\frac{\mathcal{E}}{B}\right)^2}} \quad (3.12)$$

The agreement with the experimental data is as good as is possible within the experimental uncertainty, the scatter of data taken by different experimental techniques, and assumption of a parabolic model. Even though, the ohmic mobilities are different for various impurity concentrations, the saturation velocity tends to a common value, although the approach towards saturation is much faster for high mobility materials. Because of the low ohmic mobility of holes, the approach towards saturation is much slower. The experimental hole mobility is lower than the theoretical mobility which considers hole bands to be parabolic with a single effective mass. At high electric fields, electron may transfer to split-off band which may give lower theoretical velocity and hence explain the discrepancy. As transport properties of this split-off band are not known, this inclusion is excluded in the present analysis. Room-temperature saturation values of  $1.03 \times 10^7$  cm/s (electrons) and  $1.00 \times 10^7$  cm/s (holes) are obtained. This indicates that high mobility does not necessarily lead to high saturation velocity. Only at moderate electric fields, the velocity of a high-mobility materials is higher than that of a low-mobility material. Experimental data on quantum-well heterostructures also support this observation. The mobility in quantum well heterostructure is much higher than that of bulk materials, but saturation velocity is lower<sup>14</sup>. Velocity

measurements on a variety of samples lead to the same saturation velocity at a given temperature<sup>2,3</sup>.

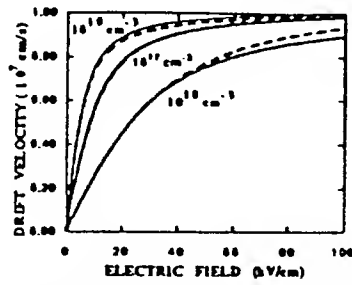


Fig. 3. Velocity-field characteristics of electrons in silicon. The number on each curve is the impurity concentration in the sample.

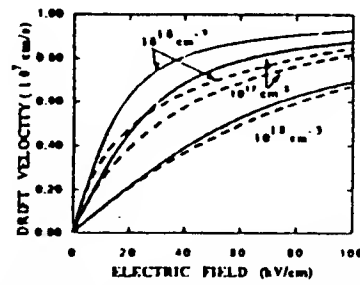


Fig. 4. Velocity-field characteristics of holes in silicon. The number on each curve is the impurity concentration in the sample.

As said in the Introduction, the carrier temperature concept may not be a useful concept as electric field tries to put some order into otherwise completely random motion. If carrier energy is the criteria used, a carrier in its free flight absorbs an energy  $q\mathcal{E}\cdot\ell$  ( $q=+e$  for holes,  $-e$  for electrons), whose average value can be evaluated by the distribution function of Eq. (2.9). When equated to  $(3/2)k_B \Delta T_{e(h)}$ , the relative change in carrier temperature is obtained as

$$\Delta T_{e(h)} / T = (2/3) \delta_{e(h)} L(\delta_{e(h)}) \quad (3.13)$$

The carrier temperatures for both type of carriers are plotted in Figs. 5 and 6. At very low electric field  $\Delta T_{e(h)}$  varies quadratically with the applied electric field, but at very high electric field the dependence is linear. If this linear dependence of the carrier temperature is used in mobility formula for acoustic phonon scattering, a drift velocity proportional to  $\mathcal{E}^{1/2}$ , consistent with earlier dependence predicted by Shockley,<sup>5</sup> is obtained. This indicates that the present theory is consistent with energy-balance theories if this hot-carrier concept is used. Equation (3.13) can be compared with the equation obtained from the energy balance<sup>10</sup>:

$$\Delta T_{e(h)} / T = (2/3) e \mathcal{E} v_{de(h)} \tau_{ee(h)} / k_B T \quad (3.14)$$

where  $\tau_{ee(h)}$  is the energy relaxation time for electrons(holes). When Eqs (3.13) and (3.14) are compared with  $v_d$  given by Eq. (3.8), the energy relaxation time can be shown to be comparable to the momentum relaxation time  $\langle \tau_m \rangle$ :

$$\tau_{ee(h)} = 2 v_{th e(h)} \ell_{e(h)} / \pi^{1/2} = 3 \pi m^* \mu_{e(h)} / 8 e = (3 \pi / 8) \langle \tau_m \rangle \quad (3.15)$$

For relatively pure silicon samples,  $\tau_{ee} = 1.04$  ps and  $\tau_{eh} = 0.37$  ps. The energy of electrons thus relaxes faster than that of holes.

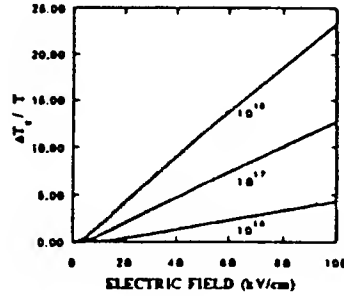


Fig. 5. The relative change in hot-electron temperature for various impurity concentrations.

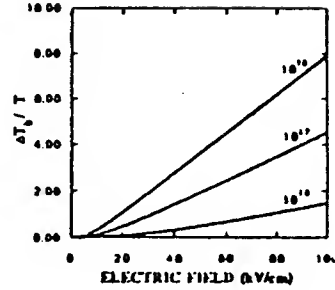


Fig. 6. The relative change in hot-electron temperature for various impurity concentrations.

#### 4. INTRINSIC SEMICONDUCTORS

From device application point of view, intrinsic concentration in silicon is of prime importance. As pointed out by Green,<sup>11</sup> commonly accepted values of intrinsic parameters form an incomplete and often inconsistent set. In this section, the intrinsic case is examined from a point of view to see how the tilting of energy bands can affect intrinsic parameters. Since the Fermi level is very close to the middle of the bandgap for an intrinsic semiconductor, the distribution in this case is predominantly intrinsic. Starting from a point  $E_c(v)$  on the tilted band diagram (Fig. 1), the number of carriers as a function of electric field can easily be calculated from the distribution function of Eq. (2.9). The resulting expression for electrons and holes is given by

$$n = N_c e^{(\zeta - E_c)/k_B T} \frac{\sinh(\delta_e)}{\delta_e} \quad (4.1)$$

$$p = N_v e^{(E_v - \zeta)/k_B T} \frac{\sinh(\delta_h)}{\delta_h} \quad (4.2)$$

with

$$N_{c(v)} = 2 \left( \frac{2 \pi m_{c(h)}^* k_B T}{h^2} \right)^{3/2} \quad (4.3)$$

Since for an intrinsic semiconductor, equal numbers of electrons and holes are generated ( $n=p=n_i$ ), the number of intrinsic carriers as a function of electric field is given by the expression

$$n_i(\mathcal{E}) = n_{i0} \left[ \frac{\sinh(\delta_e) \sinh(\delta_h)}{\delta_e \delta_h} \right]^{1/2} \quad (4.4)$$

with



$$n_{i0} = (N_c N_v)^{1/2} \exp(-E_g / 2 k_B T) \quad (4.5)$$

Here  $E_g = E_c - E_v$  is the material bandgap which at 300 K is 1.1242 eV.<sup>11</sup> The equilibrium intrinsic concentration is calculated to be  $1.08 \times 10^{10} \text{ cm}^{-3}$ . The relative increase in carrier concentration (carrier multiplication  $n_i(\mathcal{E})/n_{i0}$ ) as a function of electric field for various carrier concentrations is given in Fig. 7. This increase in carrier concentration can significantly affect the noise behavior of devices. As expected, the carrier multiplication is lower for low mobility materials.

As carriers multiply, the effective bandgap of the material appears narrow. This bandgap renormalization can be considered if an equation similar to Eq. (4.5) is used for  $n_i(\mathcal{E})$  with  $E_g$  replaced by  $E_g'$ , the effective bandgap, which is given by

$$E_g' = E_g - 2 k_B T \ln(n_i(\mathcal{E})/n_{i0}) \quad (4.6)$$

Figure 8 gives the effective bandgap as a function of electric field for various impurity concentrations. In high mobility materials, the decrease in effective bandgap is faster than that of low-mobility material as the electric field is increased. Therefore, high mobility materials can easily be subjected to carrier avalanche. Of course, this description is valid if the tunneling between the bands is neglected. At very high electric fields, the overlap of electron and hole wavefunctions may increase the tunneling probability.

Another useful concept for intrinsic semiconductors is that of the intrinsic hot-carrier temperature. This concept can be invoked if the carrier concentration  $n_i(\mathcal{E})$  is represented by Eq. (4.5) by replacing  $T$  by  $T_i$ , but leaving the bandgap unchanged. The intrinsic carrier temperature is then obtained by solving the transcendental equation

$$\frac{n_i(\mathcal{E})}{n_{i0}} = \left(\frac{T_i}{T}\right)^{3/2} \exp\left[-\frac{E_g}{2 k_B} \left(\frac{1}{T_i} - \frac{1}{T}\right)\right] \quad (4.7)$$

The relative change in intrinsic temperature  $\Delta T_i/T$  as a function of electric field is shown by solid lines in Fig. 9.

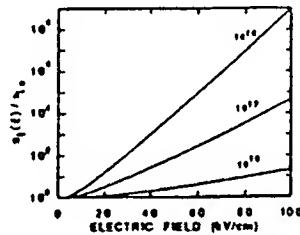


Fig. 7. Carrier multiplication in intrinsic silicon as a function of electric field. The number on each curve represents the total number of compensated impurities.

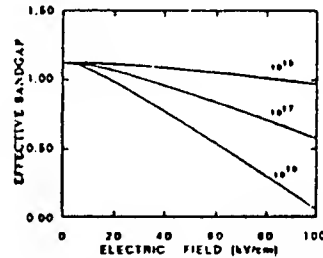


Fig. 8. Effective band gap as a function of electric field. The number on each curve represents the total number of compensated impurities.

## 5. DISCUSSION

A distribution function which explains the experimentally observed behavior of elemental semiconductors, with specific applications to silicon is presented. By including

the energy gained by a carrier in a mean free path in the distribution function, *a priori* assumption of a heated Maxwellian distribution, which is found to be far from correct,<sup>17,18</sup> is avoided. The onset of nonlinear behavior is expected at critical field  $\mathcal{E}^* = k_B T / e \mathcal{L}_{e(h)}$  which can be expressed in terms of ohmic mobility as  $\mathcal{E}^* = v_{sat} e(h) / 3 \mu_{e(h)}$ , where  $v_{sat} e(h)$  is the saturation velocity of electrons(holes). Thus high mobility materials are more vulnerable to high-field effects. The results also show that for nondegenerate samples, there is very little, if any, relationship between the saturation velocity and the ohmic mobility consistent with experimental observation.<sup>2,3,15</sup> When measurements are done for moderately high electric field, the electron velocity for high mobility material may appear higher as high-mobility materials tend towards saturation much faster than low-mobility materials. In the experiments of Ketterson et. al.,<sup>16</sup> an unusual high room temperature velocity comparable to thermal velocity was found, which could not be explained by any of

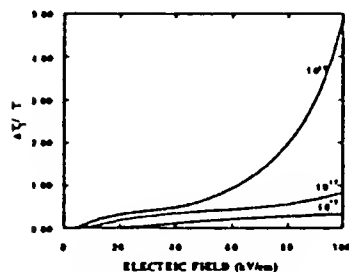


Fig. 9. Intrinsic Electron Temperature

the earlier theories. The results obtained are consistent with the intuitive arguments of Böer,<sup>8</sup> but are in direct contrast with the original explanation<sup>5</sup> which was based on a very rough physical model in which optical phonon emission was alone considered responsible for the saturation of drift velocity in high electric field. Although the detailed analysis is presented for nondegenerate samples, the results can easily be extended to degenerate samples. For degenerate samples, the onset of nonlinear behavior is expected when  $\mathcal{E}^* = \zeta / e \mathcal{L}_{e(h)}$  and the saturation velocity comparable to Fermi velocity is possible in the present framework. The

distribution function of Eq.(2.8) also shows that erroneous results could result if expansion of the distribution function is attempted under the conditions when  $\delta_{e(h)}$  is much larger than unity. The separation of the distribution function into spherically symmetric and antisymmetric parts thus does not appear possible unless it is made for low electric fields when  $\delta_{e(h)} < 1$ . The change in carrier energy on the energy band diagram can lead to apparent change in carrier temperature which varies quadratically in low electric fields and linearly in high electric fields. An energy relaxation time comparable to momentum relaxation time is found. At high electric fields, carrier temperature proportional to electric field is obtained, a prediction in conformity with that of Monte Carlo simulations<sup>13</sup>. Considerable carrier multiplication due to the high fields present can significantly change the carrier concentration in solid state devices as high electric fields are encountered at junctions in bipolar devices and at the drain end in field effect transistors. This should be taken into account while modelling submicron devices.

It is worthwhile to emphasize the electrochemical identity of the Fermi energy  $\zeta$ . In strong electric field,  $\zeta$  depends strongly on the electric field, both for nondegenerate and degenerate materials. If this electric field dependence is ignored, degenerate material can be shown to follow nondegenerate behavior at high electric fields, as is sometimes assumed in interpreting high-field experiments. When this assumption is made in the present theoretical framework, a carrier velocity  $v_d = (v_{th} / \pi^{1/2} \delta_{e(h)}) \exp(\delta_{e(h)})$  is obtained in the high field limit. This can give a velocity runaway condition, which does not appear in present-day experimental results. But, sometimes this behavior can easily be confused with the carrier multiplication which is also a high-field phenomenon.

When velocity-field profiles, similar to those predicted by Eq. (3.8), are considered in modelling FETs, it is found that the usual pinchoff effect at the onset of current saturation is absent<sup>19,20</sup>. Actually pinchoff phenomena appears when constant mobility, independent of an electric field, is used in modelling a transistor. When velocity saturation

effect, as present in the velocity-field profiles is used, the carrier density at the onset of saturation is found to be constant.<sup>17</sup> For obvious reasons, when the electric field is very high at the drain end, as is the case, the electrons do not follow the linear behavior in velocity-field relationship as predicted by Ohm's law, even in long-channel FET's.<sup>19</sup> After the saturation point in I-V characteristics of the FET, carrier multiplication yields a large number of intrinsic carriers, which keep the channel open and current continues to flow. This explanation seems to be closer to the experimental observation than the flow of carriers through depletion layers (channel-length modulation) as is considered in the published literature. This carrier multiplication, perhaps, could also be a source of noise, especially at the drain end where electric field is high.

#### ACKNOWLEDGEMENTS

One of us (VKA) would acknowledge support from ERATO program of Japan Research and Development Corporation. He would like to acknowledge the warm hospitality accorded to him by Professor Hiroyuki Sakaki, Director and Dr. Hiroyuki Kano, Technical Manager of the Quantum Wave Project during his stay at the University of Tokyo. He also wishes to acknowledge the useful conversations he had with Dr. K. Hirakawa of the Institute of Industrial Science at the University of Tokyo, and with Drs. A. Shimizu and M. Tsuchiya of the Quantum Wave Project of JRDC.

#### REFERENCES

1. V. K. Arora, Jpn. J. Appl. Phys. 24, 537(1985); J. Appl. Phys. 54, 824(1983).
2. K. Hirakawa and H. Sakaki, J. Appl. Phys. 63, 803(1985).
3. W. T. Masselink, T. S. Henderson, J. Klem, W. F. Kopp, and H. Morkoç, IEEE Trans. Electron Dev. ED-33, 639(1986).
4. K. K. Thornber, J. Appl. Phys. 51, 2127(1980).
5. W. Shockley, Bell Syst. Tech. J. 30, 990(1951).
6. F. Capasso, T. P. Pearsall, and K. K. Thornber IEEE Electron Dev. Lett. EDL-2, 295(1981).
7. M. Dresden, Rev. Mod. Phys. 33, 265(1961).
8. K. W. Böer, *Survey of Semiconductor Physics*, Van Nostrand Reinhold, New York, 1990, pp. 696-725.
9. S. Zukotynski and W. Howlett, Solid State Electron. 21, 35(1978).
10. C. M. Wolfe, N. Holonyak, and G. Stillman, *Physical Properties of Semiconductors*, Prentice-Hall, Englewood Cliffs, N. J., 1989, pp. 112-118.
11. M. A. Green, J. Appl. Phys. 67, 2944(1990).
12. D. L. Scharfetter and H. K. Gummel, IEEE Trans. Electron Dev. ED-16, 64(1982).
13. C. Jacoboni, C. Canali, G. Ottaviani, and A. A. Quaranta, Solid State Electron. 20, 77(1977).
14. W. T. Masselink, N. Braslau, W. I. Wang, and S. I. Wright, Appl. Phys. Lett. 51, 1533(1987).
15. J. A. Cooper and D. F. Nelson, J. Appl. Phys. 54, 1445(1983).
16. A. A. Ketterson, W. T. Masselink, J. S. Gedymin, J. Klem, C.-K. Peng, W. F. Kopp, H. Morkoç, and K. R. Gleason, IEEE Trans Electron Dev. ED-33, 564(1980).
17. W. Fawcett, A. D. Boardman, and S. Swain, J. Phys. Chem. Solids 31, 1963(1970).
18. C. Canali, C. Jacoboni, F. Nava, G. Ottaviani, and A. Alberigi Quaranta, Phys. Rev. B 12, 2265(1975).
19. V. K. Arora and M. B. Das, Electron. Lett. 25, 820(1989).
20. V. K. Arora and M. B. Das, Semicond. Sci. & Tech. 5 (1990).

## APPENDIX VII

“Velocity Distribution in a Degenerately Doped 0.25- $\mu\text{m}$  GaAs MODFET,” V. K. Arora, L. S. Tan and S. J. Chua, Proceedings of 1992 International Conference on Semiconductor Electronics, October 6-8, 1992, at Kuala Lumpur, Malaysia, pp. 166-175.

**ICSE '92  
PROCEEDINGS**

**1992 IEEE INTERNATIONAL CONFERENCE  
ON SEMICONDUCTOR  
ELECTRONICS**



**OCTOBER 6-8 1992  
PUTRA WORLD TRADE CENTRE  
KUALA LUMPUR  
MALAYSIA  
2-84**

# Velocity Distribution in a Degenerately-Doped 0.25- $\mu\text{m}$ GaAs MODFET

Vijay K. Arora<sup>†</sup>, Leng Scow Tan, and Soo Jin Chua

Department of Electrical Engineering, National University of Singapore,  
10 Kent Ridge Crescent, Singapore 0511  
FAX: (65)779-1103, Phone: (65)772-6474, e-mail: elevka@nusvm.bitnet

## Abstract

The role of velocity saturation on the design and operational characteristics of a submicron transistor is studied. For degenerately doped channels, it is shown that the velocity is limited by Fermi velocity, indicating poor correlation between the saturation velocity and mobility which is strongly controlled by momentum randomizing scattering events. At high electric field, emission of optical phonons further limits the velocity. By decreasing the temperature to cryogenic temperatures, a little improvement in speed is possible. But, a substantial improvement in speed is possible if optical phonon emission is suppressed by mini bandgap engineering of quantum well superlattice. The velocity-field characteristics obtained are used to obtain the electric field distribution, the velocity distribution, the effective saturation velocity, and the maximum internal frequency of 0.25  $\mu\text{m}$  GaAs/AlGaAs transistor. The expression are also analyzed in long-channel and short-channel limits. It is shown that usual long-channel pinchoff effect is absent when velocity saturation is included.

## 1. Introduction

In the design of submicron-gate-length transistors, the high field effects which put a limit on carrier velocity play an important role. The high mobility materials are often projected to yield higher saturation velocity. Recent experiments on short channel transistors tend to indicate that the carrier velocity not the mobility controls the transport in these devices.<sup>1,2</sup> Independently determined decreases in mobility and increases in electron velocity under similar conditions are observed, showing poor correlation between the saturation velocity and ohmic mobility.<sup>2,3</sup> These observations are in agreement with the earlier observations of Arora<sup>4,5</sup> and scaling theory arguments of Thornber.<sup>6</sup> Recently, Sakaki<sup>7</sup> has proposed the suppression of optical phonon emission in quantum well superlattices and arrays with an intention to improve upon the operational speed of a transistor. Considering these latest developments, a theory for studying the velocity response of electron to the high electric fields which are always present in short length channel is worked out.

In low electric field  $\mathcal{E}$ , collisions can be considered point collisions as the energy  $|\mathbf{q}| \mathcal{E} \lambda_D$  (field broadening) absorbed by a carrier of charge  $q$  ( $q = \pm e$  for holes/electrons) in the de Broglie wavelength  $\lambda_D$  is negligible compared to collision broadening. But, as the electric field becomes larger, the field broadening tends to mask the collision broadening, and hence makes carrier transport virtually independent of scattering. The onset of nonlinear behavior thus takes place when field broadening is comparable to the collision broadening. This condition is equivalent to the condition that the momentum gained by the carrier from the field  $e \mathcal{E} \tau$  in the mean free time  $\tau$  is comparable to its thermal momentum  $m^* v$ . In terms of energy, this condition is equivalent to the condition that the energy gained by an electron in a mean free path  $e \mathcal{E} \ell$  is comparable to the thermal energy  $k_B T$ . This condition was originally considered

by Shockley,<sup>12</sup> but was discarded in favor of the energy balance theories which dominated the high-field arena in those days. At room temperature, the mean free path in GaAs/AlGaAs quantum well ( $\mu_0 = 5800 \text{ cm}^2/\text{V.s}$ )<sup>3</sup> is about 100 nm. The transition from linear to nonlinear behavior is thus expected at  $E = k_B T / e \ell = 2.6 \text{ kV/cm}$ , consistent with experimental observations. The free flight of a carrier in a mean free path is interrupted by either the momentum randomizing collision (dominant in low electric field) or emission of an optical phonon (dominant in high electric field). If this phonon emission is suppressed as proposed by Sakaki,<sup>7</sup> considerable improvement in device speed is possible. The velocity is then limited by the Fermi velocity for degenerate gas or by the thermal velocity for a nondegenerate gas as electrons are being transferred from parallel direction of the electric field to the antiparallel direction. Velocity-limiting mechanism and its impact on the operational characteristics of a field effect transistor are discussed in the following sections.

## 2. Velocity-Limiting Mechanism

The understanding of the distribution function is essential in any carrier transport study. The equilibrium distribution function is well known to be the Fermi-Dirac distribution function. In equilibrium, the bands are flat unless there is a built-in electric field. The electrons are moving at random with the average velocity in each of the three Cartesian directions equal to zero. In external fields, the Fermi energy (electrochemical potential) and bands are tilted parallel to each other<sup>13</sup>. An excellent description of the carrier transport with tilted band diagram is given by Böer,<sup>13</sup> who examines the effect of built-in as well as the applied electric field on the distribution of carriers. The carrier distribution is determined relative to the Fermi level. In zero bias, the distribution is independent of position and the Fermi level (chemical potential) is constant. In an external field, however, Fermi level and bands are tilted. The carrier distribution is now a function of spatial coordinates. When electrons are accelerated in the field, they move from a region of higher density  $n(E - \zeta)$  to that of lower density  $n(E - (\zeta - e E \ell))$ . These electrons can dissipate their net additional energy to the lattice by emitting phonons, thereby causing lattice heating. The carriers drop close to the conduction band edge and the motion is repeated. From intuitive arguments, as suggested by Böer,<sup>13</sup> a limiting velocity comparable to the random thermal velocity at lattice temperature is expected. The carrier motion in an external field is, therefore, not random. It has a finite component in the field direction. This makes distribution of carriers asymmetric in the direction of applied electric field. The electrons will roll down the energy hill and holes will bubble up the energy hill. The electric field thus tries to organize the otherwise completely random motion. Understandably, the Fermi level will be affected by the applied electric field. All these features are contained in the distribution function, originally proposed by Zukotynski and Howlett [10] and extensively discussed in Ref. 4, which is given below:

$$f(\epsilon_{nk}, E, \theta) = \frac{1}{e^{(\epsilon_{nk} - \zeta + e E \cdot \ell(\epsilon_{nk})) / k_B T} + 1} \quad (2.1)$$

$\epsilon_{nk}$  is the quantized energy of electron in a quantum well:

$$\epsilon_{n,k_x,k_y} = n^2 \epsilon_0 + \frac{\hbar^2}{2m} (k_x^2 + k_y^2) \quad n = 1, 2, 3, \dots \quad (2.2)$$

$\ell(\epsilon_{nk}) = \tau v$  is the energy-dependent mean free path and  $\epsilon_0$  is the ground state energy in the quantum well. This distribution function thus has a very simple interpretation. The electrochemical potential  $\zeta$  during the free flight of carriers changes by  $\pm e \ell$  as electrons tend to sink and holes tend to float on the tilted energy band diagram. This observation may suggest that the applied electric field tends to organize the otherwise completely random motion. Electric dipoles  $e \ell$  due to quasi-free motion of the carriers tend to organize in the direction of electric field for holes and in the opposite direction for electrons. The collisions tend to bring the electron closer to the conduction band edge. If the electric field is strong, this unidirectional motion will give carrier drift comparable to the Fermi velocity which is average of the magnitude of electron velocity  $v$ . A quasi-ballistic behavior of the carriers thus follows in a strong electric field.

The drift velocity for the electron gas in a quantum well, with the distribution function of Eq. (1) in the quantum limit ( $n=1$ ), is obtained as

$$v_d = \frac{\sqrt{\pi}}{2} v_{th} \frac{\int_0^{2\pi} \cos(\theta) \mathcal{F}_{1/2}(H(\theta)) d\theta}{\int_0^{2\pi} \ln(1 + e^{H(\theta)}) d\theta} \quad (2.3)$$

where

$$H(\theta) = \eta - \delta \cos(\theta) \quad (2.4)$$

is the quasi-Fermi level which is direction-dependent and

$$\delta = e \ell / k_B T, \quad (2.5)$$

$$v_{sat} = (2 k_B T / m^*)^{1/2} \quad (2.6)$$

$$\eta = \frac{\zeta - \epsilon_0}{k_B T} \quad (2.7)$$

$\mathcal{F}_{1/2}(x)$  is the Fermi-Dirac integral [9].  $\eta$  is evaluated from the normalization condition

$$n = \lambda_D^{-2} \int_0^{2\pi} \ln(1 + e^{H(\theta)}) d\theta \quad (2.8)$$

In the nondegenerate limit, Eq. (2.3) simplifies to

$$v_d = \frac{\sqrt{\pi}}{2} v_{th} \frac{I_1(\delta)}{I_0(\delta)} \quad (2.9)$$

where  $I_n(\delta)$  is the modified Bessel function of order  $n$ . Taking the limit of Equation (2.9) as  $\delta \rightarrow \infty$ , the saturation velocity in the nondegenerate case is



the measurements of Masselink et. al.,<sup>14</sup> who have shown lack of dependence of saturation velocity on ohmic mobility. Under strong degenerate conditions, the velocity tends to a value of  $2.0 \times 10^7$  cm/s, both for 77 K and 4.2 K. The highest room temperature velocity reported in Ref. [3] is  $0.73 \times 10^7$  cm/s, which is considerably lower than the predicted saturation velocity of  $1.8 \times 10^7$  cm/s, as shown in Fig. 2. Fig. 2 clearly shows the predominant role of optical phonon emission in limiting the electron velocity. Sakaki<sup>12</sup> has proposed engineering the quantum well wire and quantum box array structures in order to obtain a miniband structure so that the optical phonon emission is eliminated. The elimination of optical phonon emission is expected to give considerable improvement in device speed. In such microstructures, the velocity at least twice as high is expected from these theoretical considerations. Also, shown in Fig. 2 are the results obtained from the empirical relation commonly used in modeling a transistor:<sup>18</sup>,

$$v_D = \frac{\mu_o \epsilon}{1 + \frac{\epsilon}{\epsilon_c}} \quad (2.13)$$

with

$$\epsilon_c = v_{sat} / \mu_o \quad (2.14)$$

For the sample considered,  $\epsilon_c = 3.1$  kV/cm. This shows that this relation gives a good description of velocity-field characteristics for modeling field effect transistors.

It was the experiments of Ketterson et. al.[16] which first showed the velocity at room temperature is higher than that at 77 K and, therefore, indicated that the velocity limiting mechanism is not controlled by the mobility of the sample. In the light of this theory, under nondegenerate conditions, the saturation velocity is limited by the random thermal velocity which is higher at the room temperature. At room temperature, saturation is noticeable at much higher electric fields (Fig. 2) as compared to low-temperature conditions (Fig. 3) because the ratio of the Fermi velocity to the thermal velocity is much higher at cryogenic temperatures.<sup>21</sup>

In a recent paper by Shur and coworkers,<sup>21</sup> the idea of obtaining saturation velocity closer to the Fermi velocity, which could be as high as  $5-10 \times 10^7$  cm/s has been utilized in designing a novel Schottky diode for millimeter and submillimeter wave applications. Similarly, the recently reported experimental observations of Mizutani and Maezawa<sup>22</sup> on AlGaAs/InGaAs can be easily interpreted in the framework of this theory. For high mobility materials, the approach towards saturation is much faster than for the low-mobility materials. Thus high mobility materials are more vulnerable to high field effects than the low mobility materials. The saturation velocity does not sensitively depend on carrier concentration or on low-field mobility, in agreement with experimental deductions.<sup>3</sup>

### 3. MODFET Characteristics

We consider the MODFET structure with gate length  $L$ , gate width  $W$ , and the effective thickness of the AlGaAs layer, assumed insulating, as  $d^*$ . The electron concentration as a function of distance along the length of the channel is given by

$$n_s(x) = (C_0/q) [V_g - V(x)] \quad (3.1)$$

where  $V_g' = V_g - V_{Th}$  is the applied gate voltage above the threshold value,  $V(x)$  is the potential at a point  $x$  along the length of the channel ( $V(0)=0$  at the source end at  $x=0$ , and  $V(L)=V_D$  at the drain end at  $x=L$ ),  $C_0 = \epsilon A/d^*$  is the effective capacitance per unit area. The current along the length of the channel is same at all the points and is given by

$$I_D = q n_s(x) v(x) W, \quad (3.2)$$

where  $v(x)$  is the velocity at a point  $x$  in the channel. Substituting Eqs. (2.13) and (3.1) in Eq. (3.2), with  $\mathcal{E} = dV/dx$ , and integrating from  $x=0$  to  $x$ , the following equations for the potential and field distribution in the channel are obtained:<sup>23</sup>

$$V(x) = [V_g' - (I_D/v_{sat} C_0 W)] - \{ [V_g' - (I_D/v_{sat} C_0 W)]^2 - (2I_D/C_0 W \mu_0) x \}^{1/2} \quad (3.3)$$

$$\mathcal{E}(x) = (I_D/C_0 W \mu_0) \{ [V_g' - (I_D/v_{sat} C_0 W)]^2 - (2I_D/C_0 W \mu_0) x \}^{-1/2} \quad (3.4)$$

with

$$I_D = \beta_0 (2V_g' V_D - V_D^2) / (1 + V_D/V_c), \quad (3.5)$$

$$\beta_0 = C_0 \mu_0 W / 2L \quad (3.6)$$

The drain voltage at the onset of saturation and the saturation current, as obtained by setting  $dI_D/dV_D=0$ , are obtained as

$$V_{Dsat} = V_c \{ (1 + 2V_g'/V_c)^{1/2} - 1 \}, \quad (3.7)$$

$$I_{Dsat} = \beta_0 V_{Dsat}^2. \quad (3.8)$$

At the onset of current saturation, the potential and the electric field distributions along the channel length are given by

$$V(x) = V_{Dsat} - V_{Dsat} (1 - x/L)^{1/2} \quad (3.9)$$

$$\mathcal{E}(x) = (V_{Dsat}/2L) (1 - x/L)^{-1/2} \quad (3.10)$$

This is the same result as is obtained for a long channel MOSFET, except that  $V_{Dsat}$ , in this case, is equal to  $V_g'$  only in the long channel limit ( $V_c \rightarrow \infty$ ). In the short-channel limit ( $V_c \rightarrow 0$ ),  $V_{Dsat}$  can be approximated as  $(2V_g' V_c)^{1/2}$ . Hence the mobility degradation substantially reduces the values of  $V_{Dsat}$  and  $I_{Dsat}$ , but the field distribution follows the same general pattern. The electric field distribution along the length of the channel for a submicron-length channel of  $L=0.25 \mu m$  is plotted in Fig. 3. The associated velocity distribution is plotted in Fig. 4. It is clear from Fig. 3 that not all electrons, as is normally assumed, are traveling at the saturation velocity even in such small gate-length channels. The velocity is lower at the source end than that at the drain end.

The inclusion of mobility degradation in modeling of the MODFET lifts the well-known *pinchoff* condition, which requires the carrier concentration to vanish at the drain end of the channel at the saturation point. This carrier concentration, in fact, saturates to the value given by

$$n_{SD}/n_{SO} = [1 - (V_c/V_g) \{ (1 + 2V_g/V_c)^{1/2} - 1 \}], \quad (3.11)$$

with

$$n_{SO} = (C_0/q) V_g'. \quad (3.12)$$

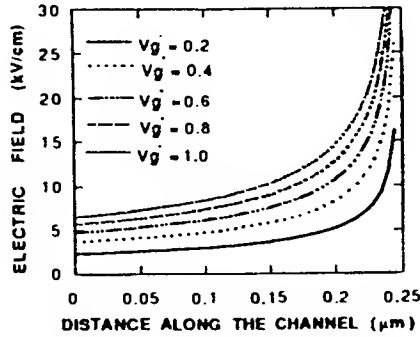


Fig. 3. Electric field profile along the length of channel

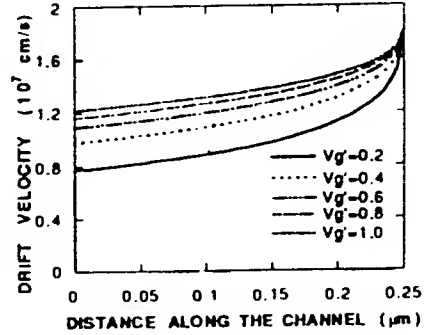


Fig. 4. Velocity distribution along the length of channel

The normalized carrier density profile  $n_s(x)/n_{SO}$  along the length of channel is plotted in Fig. 5 for various gate voltages. The absence of pinchoff effect at the drain end is also true for long-channel devices. In the long-channel approximation, the concentration at the drain end of the long-channel MODFET saturates to the value  $n_{SD} = n_{SO} V_g' / 2V_c = I_{DSat} / Wq v_{sat}$ . This result is in direct contrast to the models which use field-independent mobility and predict  $n_{SD}$  approaching to zero at the saturation point. The present result is consistent with the continuity of the current at both ends of the channel, which gives  $I_{DSat} = q n_{SO} \mu_0 \mathcal{E}(0) W = q n_{SD} v_{sat} W$ . This gives  $\mathcal{E}(0) = (v_{sat}/\mu_0)(n_{SD}/n_{SO}) = V_g' / 2L$ . Obviously, in the long-channel limit, Ohm's law applies at the source end and the velocity is at its saturation limit at the drain end at the onset of current saturation.

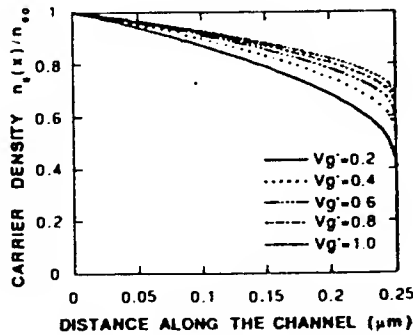


Fig. 5. Carrier distribution along the length of the channel.

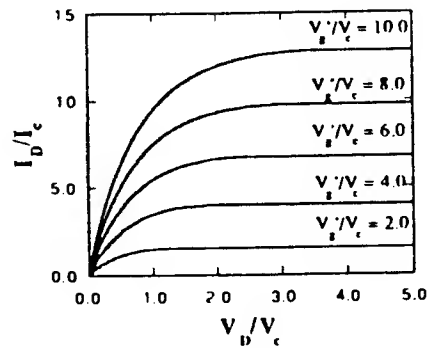


Fig. 6. Normalized current-voltage characteristics

The intrinsic transconductance, in the saturation regime, is given by  $C_0 v_{eff}$ , where  $v_{eff}$  is the effective velocity as a function of the gate length:

$$v_{eff} = v_{sat} [1 - (1 + 2V_g'/V_c)^{-1/2}]. \quad (3.13)$$

In the long channel MODFET ( $L \rightarrow \infty$ ), the effective velocity is  $v_{eff}(\infty) = \mu_0 V_g'/L$ , which corresponds to intrinsic transconductance of  $g_m(\infty) = C_0 \mu_0 V_g'/L$ . On the other hand, in the ultrashort channel MODFET ( $L \rightarrow 0$ ), Eq. (3.13) reduces to  $v_{eff}(0) = v_{sat}$ , which leads to the short-channel limit  $g_m(0) = C_0 v_{sat}$  of the transconductance. This is the reason that as channels are becoming smaller, the effective saturation velocity, as obtained from the transconductance measurements, is increasing. The theoretical limit of the saturation velocity for ultrashort channel is given by  $v_{sat} = 1.8 \times 10^7$  cm/s for the quantum well parameters considered [3]. For a 0.25- $\mu$ m length channel, depending on the gate voltage, effective velocity is considerably lower than the theoretical saturation limit of  $1.8 \times 10^7$  cm/s.

The average velocity  $v_{av}$  of the MODFET is given by the equation

$$v_{av} = (v_{sat} V_{Dsat} / V_c) [1 - (V_{Dsat} / 2 V_c) \ln \{1 + (2V_c / V_{Dsat})\}]. \quad (3.14)$$

For ultrashort channels this velocity will also approach the theoretical limit of  $v_{sat} = 1.8 \times 10^7$  cm/s.

The maximum operating frequency of the MODFET in the saturation regime is determined principally by the transit time of the electron through the channel. For a channel of length  $L$ , this internal channel frequency is calculated to be

$$f_{max} = (v_{sat} / 2\pi L) [1 + (4v_{sat} L / 3\mu_0 V_{Dsat})]^{-1} \quad (3.15)$$

As the length goes into ultra-submicron range, the theoretical limit of  $f_{max}$  is set at  $v_{sat} / 2\pi L$ , which for a 0.25  $\mu$ m channel is obtained as 115 GHz. Of course, the inclusion of time constants associated with parasitic regions will reduce this theoretical limit to much lower value.

The above calculations do not take into account the velocity profile in the parasitic regions. These parasitic effects can considerably reduce the operating characteristics from the maximum values predicted above. Also, the maximum operating characteristics will be affected by the electron transfer to higher valleys in GaAs or AlGaAs layers. In such cases, the saturation velocity will be much smaller than the predicted value of  $1.8 \times 10^7$  cm/s at room temperature. Due to modification of the scattering in quasi-two-dimensional electron gas, the transfer to higher valleys does not seem likely, which is a distinct advantage of quantization and the modulation doping. The presence of high electric fields makes the creation of excess carriers possible and hence is perhaps the major source of noise in the MODFET.

#### 4. Conclusions

The velocity response of carriers to the high electric fields present in submicron length field transistors has puzzled scientists and engineers for the last several years. The breakdown of Ohm's law has been obvious for several years, but the mechanism limiting the carrier velocity and its relationship to ohmic mobility has kept several researchers at bay. The recent experiments of Fang et. al.<sup>1</sup> and others<sup>2</sup> proved decisively that there is a poor correlation between the limiting velocity of carriers and its mobility, contradicting the long held view that the higher ohmic mobility necessarily leads to higher saturation velocity. The maximum frequency of MESFET, which is predominantly three-dimensional in nature with lower ohmic mobility, was found to give comparable to or superior performance than that of MODFET, which is

predominantly quasi-two-dimensional with higher ohmic mobility. This indicates that the momentum randomizing scattering events which control mobility in a channel do not control the limiting velocity of the carriers. We have shown that these experimental observations are consistent with the velocity distribution obtained from the asymmetric distribution function which tends to put some order in the otherwise completely random motion. The saturation velocity can be increased by the appropriate design of miniband structure by quantum engineering of superlattice structures, such as those proposed by Sakaki.<sup>7</sup> This way saturation velocity can be increased to the Fermi velocity which can be very high at cryogenic temperatures for degenerately doped heterostructures.

When these velocity-field profiles are used to study the velocity distribution of carriers, the velocity along the channel of the length is found to be lower than the saturation velocity except at the drain end where it is limited by the saturation velocity at the onset of current saturation. At the onset of current saturation, carriers are always traveling at saturation velocity on the drain end of the channel, no matter what the length of the channel. This eliminates the pinchoff effect which is present in models following Ohm's law where velocity saturation is completely ignored. The reduction to channel length to submicron dimensions does not make all carriers traveling at the saturation velocity, but the approach towards saturation is closer for submicron channels. The reduced transit time is the major reason for enhancement of maximum frequency of the MODFET.

A few comments on parasitic regions of submicron devices are useful in defining the role of parasitic resistances. The parasitic resistances are important in extracting RC time constants and in extracting the external parameter from internal channel parameters or vice versa. These resistances are normally measured under ohmic conditions. But, for current levels when transistor is operating in the saturation regime, there may be an enhancement in the parasitic resistance due to mobility degradation given by Eq. (2.13). When internal transistor current becomes comparable to the saturation current of parasitic region which is limited by velocity saturation, the resistance can become very high for parasitic regions. This requires a careful design of parasitic regions to keep the resistance close to ohmic resistance.

To conclude, we have identified a mechanism for velocity saturation as electrons transfer from parallel to antiparallel direction of the electric field, interpreted the experimental results on GaAs/AlGaAs quantum wells under a wide variety of experimental conditions, and applied these velocity-field profiles to study the velocity distribution and current-voltage characteristics of 0.25- $\mu\text{m}$  MODFET. The velocity can be made closer to the Fermi velocity of the carriers by eliminating emission of optical phonon by quantum engineered miniband structure.<sup>7</sup> We, therefore, hope that the results presented here will prove useful in understanding the world of future quantum devices on miniaturized scale.

## Acknowledgments

One of us (V. K. A.) would like to acknowledge the warm hospitality of the Center for Optoelectronics at the National University of Singapore, Quantum Wave Project at the University of Tokyo, and Research Division of the Solid State Electronics Directorate of Wright Laboratory at the Wright-Patterson Air Force Base, where fundamental ideas of this work were developed after interaction with active researchers.

## References

<sup>†</sup>Permanent Address: *Department of Electrical and Computer Engineering, Wilkes University, Wilkes-Barre, PA 18766, U. S. A. The work was partially supported by the Research Initiation Grant of the U. S. Air Force Office of Scientific Research.*

<sup>1</sup>M. Feng, C. L. Lau, V. Eu, C. Ito, *Appl. Phys. Lett.* 57, 1233(1990).

- <sup>2</sup>J. Laskar, J. Kolodzey, A. A. Ketterson, I. Adesida, and A. Y. Cho, IEEE Electron Dev. Lett. **11**, 300(1990).
- <sup>3</sup>K. Hirakawa and H. Sakaki, J. Appl. Phys. **63**, 803(1988).
- <sup>4</sup>V. K. Arora, Jpn J. Appl. Phys. **24**, 537(1985).
- <sup>5</sup>V. K. Arora, J. Appl. Phys. **54**, 824(1983).
- <sup>6</sup>K. K. Thornber, J. Appl. Phys. **51**, 2127(1980).
- <sup>7</sup>H. Sakaki, Jpn J. Appl. Phys. **28**, L314(1989).
- <sup>8</sup>W. T. Masselink, T. S. Henderson, J. Klem, W. F. Kopp, and H. Morkoç, IEEE Trans. Electron Dev. **ED-33**, 639(1986).
- <sup>9</sup>K. K. Thornber, J. Appl. Phys. **51**, 2127(1980).
- <sup>10</sup>M. Feng, C. L. Lau, V. Eu, and C. Ito, Appl. Phys. Lett. **57**, 1233(1990).
- <sup>11</sup>J. Laskar, J. Kolodzey, A. A. Ketterson, I. Adesida, and A. Y. Cho, IEEE Electron Dev. Lett. **11**, 300(1990).
- <sup>12</sup>W. Shockley, Bell Syst. Tech. J. **30**, 990(1951).
- <sup>13</sup>K. W. Böer, *Survey of Semiconductor Physics*, Van Nostrand Reinhold, New York, 1990, pp. 696-725.
- <sup>14</sup>S. Zukotynski and W. Howlett, Solid State Electron. **21**, 35(1978).
- <sup>15</sup>C. M. Wolfe, N. Holonyak, and G. Stillman, *Physical Properties of Semiconductors*, Prentice-Hall, Englewood Cliffs, N. J., 1989, pp. 112-118.
- <sup>16</sup>H. Sakaki, Jpn. J. Appl. Phys. **28**, L314(1989).
- <sup>17</sup>W. T. Masselink, N. Braslau, W. I. Wang, and S. I. Wright, Appl. Phys. Lett. **51**, 1533(1987).
- <sup>18</sup>V. K. Arora and M. B. Das, Electron. Lett. **25**, 820(1989).
- <sup>19</sup>V. K. Arora and M. B. Das, Semicond. Sci. & Tech. **5**, 967(1990).
- <sup>20</sup>A. A. Ketterson, W. T. Masselink, J. S. Gedymin, J. Klem, C.-K. Peng, W. F. Kopp, H. Morkoç, and K. R. Gleason, IEEE Trans Electron Dev. **ED-33**, 564(1980).
- <sup>21</sup>W. C. B. Peatman, T. W. Crowe, and M. Shur, IEEE Elec. Dev. Lett. **13**, 11(1992).
- <sup>22</sup>T. Mizutani and K. Maezawa, IEEE Elec. Dev. Lett. **13**, 1(1992).

## **APPENDIX VIII**

“Velocity Limiting Mechanism in Quantum-Well-Wire Microstructures and Superlattices,” V. K. Arora, S. J. Chua and L. S. Tan, Proceedings of 1992 International Electronic Devices and Materials Symposium (EDMS’92), November 1-4, 1992, Taipei (Taiwan), pp. 339-342.

***Proceedings***

***e<sup>1992</sup>  
dm<sup>s</sup>***

**1992 International  
Electron Devices and Materials Symposium**

**November 1-4, 1992  
National Taiwan University  
Taipei, Taiwan, ROC**

***Sponsored by*** Ministry of Education  
National Science Council  
Ministry of Economic Affairs  
Industrial Technology Research Institute:  
Electronics Research Service Organization  
Material Research Laboratories  
Opto-Electronics Systems Laboratories

***In Cooperation with*** IEEE Electron Devices Society  
IEEE Taipei Section



*Session 14*

**Quantum Well  
and  
Novel Devices**

1992 International Electron Devices and Materials Symposium

# Velocity Limiting Mechanism in Quantum-Well-Wire Microstructures and Superlattices

Vijay K. Arora<sup>†</sup>, Leng Seow Tan, and Soo Jit Chua

Department of Electrical Engineering, National University of Singapore,  
10 Kent Ridge Crescent, Singapore 0511

FAX: (65)779-1103, Phone: (65)772-6474, e-mail: elevka@nusvm.bitnet

## Abstract

*The quantum-well-wire (QWW) microstructures expected to have extremely high mobilities are evaluated to study the limitations on the drift velocity of the carriers and its relationship with the low-field ohmic mobility and other sample characteristics. We show that a considerable enhancement in electron velocity is possible if optical phonon scattering is suppressed in QWW superlattices. The role of this velocity saturation on the design of a QWW transistor with channel length of submicron dimensions is emphasized.*

## 1 Introduction

It is well-known that the mobility in a quantum-well-wire (QWW) can be considerably enhanced due to the suppression of ionized impurity scattering, especially at low temperatures [1]. The relationship of this high low-field mobility to the device speed is not obvious from the published literature. The high mobility materials are often projected to yield higher saturation velocity. Recent experiments on short channel transistors tend to indicate that the carrier velocity not the mobility controls the transport in these devices [2,3,4]. Independently determined decreases in mobility and increases in electron velocity under similar conditions are observed, showing poor correlation between the saturation velocity and ohmic mobility [2,3]. These observations are in agreement with the earlier observations of Arora [5] and scaling theory arguments of Thornber [6]. Recently, Sakaki [7] has proposed the suppression of optical phonon emission in quantum well superlattices and arrays with an intention to improve upon the operational speed of QWW transistor. Considering these latest developments, a theory for studying the velocity response of an electron to the high electric fields present in short length channels of QWW's is needed.

In low electric field  $\mathcal{E}$ , collisions can be considered point collisions as the energy  $q\mathcal{E}\lambda_D$  (field broadening) absorbed by a carrier of charge  $q$  ( $q = \pm e$  for holes/electrons) in the de Broglie wavelength  $\lambda_D$  is negligible compared to collision broadening. But, as the electric field becomes larger, the field broadening tends to mask the collision broadening, and hence makes carrier transport virtually independent of scattering. The onset of nonlinear behavior thus takes place when the field broadening is comparable to the collision broadening. This condition is equivalent to the condition that

the momentum gained by the carrier from the field  $e\mathcal{E}\tau$  in the mean free time  $\tau$  is comparable to its thermal momentum  $m^*v$ . In terms of energy, this condition is equivalent to the condition that the energy gained by an electron in a mean free path,  $e\mathcal{E}\ell$ , is comparable to the thermal energy  $k_B T$ . The transition from ohmic to nonohmic behavior is thus expected when electric field exceeds  $\mathcal{E}^* = k_B T / e\ell$ . This indicates that the approach towards saturation is faster for high mobility materials, but does not enhance the ultimate velocity, which is limited by the Fermi velocity for strongly degenerate QWW's.

## 2 Drift Velocity

The energy of an electron confined to a QWW, where confinement dimensions are much smaller than the de Broglie wavelength of the electron, can be written as [8]

$$\epsilon_{\alpha k} = \epsilon_{\alpha} + \frac{\hbar^2 k_x^2}{2m^*} \quad (2.1)$$

where  $\epsilon_{\alpha}$  is the quantized energy in the two confinement directions perpendicular to the quasi-free x-direction.

Ohmic transport in the presence of a low electric field is discussed in several papers (see for example Ref. [8]). The ohmic mobility due to isotropic scattering (e.g. acoustic phonon scattering) in QWW is proportional to the area of confinement, i.e., quantum confinement tends to enhance the isotropic scattering. On the other hand, mobility due to ionized impurity scattering is suppressed due to highly improbable unidirectional momentum change of the electron along the quasi-free direction. This highly improbable large momentum change led Sakaki [1] to predict extremely high low-field mobilities (exceeding  $10^6 \text{ cm}^2/\text{V.s}$ ) at liquid helium temperatures.

High mobilities obtained in QWW's rapidly degrade [5] in the presence of a high electric field which is necessarily present in the scaled-down channels. The presence of high electric field tilts the otherwise flat band structure [9]. An electron, in traversing a mean free path of length  $\ell$  which is randomly oriented, finds the electrochemical potential (the Fermi energy  $\zeta$ ) changed by an amount  $e\mathcal{E}\ell$ . This change in

Fermi energy results in a distribution function which has forward-backward asymmetry in the direction of an electric field and is given by

$$f(\epsilon_{\alpha}, \mathcal{E}) = \frac{1}{e^{\frac{\epsilon_{\alpha} - \zeta + q \mathcal{E} \cdot \hat{\ell}}{k_B T}} + 1} \quad (2.2)$$

The distribution function of Eq. (2.2) can also be derived by following the technique of Lagrange multiplier for a steady state nonequilibrium conditions with an additional constraint that the current density due to electrons having the same frequency is constant. The distribution function is central to any transport problem. For linear transport, the distribution function obtained from the solution of the Boltzmann equation describes carrier transport very well. But, no such consensus is reached on high-field distribution function even today, in spite of the fact that it occupied several researchers for decades. The distribution function of Eq. (2.2) has a very simple interpretation. The electric field tends to organize in its direction the otherwise completely random motion of the electrons. The electric dipole moment  $q \hat{\ell}$  due to the quasi-free electron motion in a mean free path  $\ell$  between two collisions tends to arrange in a direction antiparallel to the applied field. High field effects thus become important when the dipole energy  $q \mathcal{E} \cdot \hat{\ell}$  is comparable to the thermal energy (nondegenerate samples) or to the Fermi energy (degenerate samples). At each collision, the randomness is re-established. If the electric field is strong, this randomness is destroyed, and an electron exhibits a quasi-ballistic behavior appropriate to the thermal motion of the electron. Since electrons are confined to move only in  $x$ -direction, transport behavior of electrons in QWW's perhaps is easy to understand. In general,  $\ell$  can be a very complicated function of energy. But, for degenerate systems, since its value is evaluated at the Fermi energy, it can be taken as a constant.

In the quantum limit, when only the lowest level  $\epsilon_0$  is appreciably populated, the electron drift velocity, as calculated from the distribution function of Eq. (2.2), is given by

$$v_D = \frac{v_{th}}{N_1} \ln \left[ \frac{1 + e^{\eta + \delta}}{1 + e^{\eta - \delta}} \right] \quad (2.3)$$

where  $\eta$  is evaluated from the normalization condition

$$\mathcal{J}_{1/2}(\eta + \delta) - \mathcal{J}_{1/2}(\eta - \delta) = \frac{N_1}{\pi^{1/2}} \quad (2.4)$$

with

$$\eta = (\zeta - \epsilon_0) / k_B T \quad (2.5)$$

$$\delta = q \mathcal{E} \ell / k_B T \quad (2.6)$$

$$N_1 = n_l \lambda_D \quad (2.7)$$

$$\lambda_D = h / \sqrt{2 m^* k_B T} \quad (2.8)$$

Here  $n_l$  is the electron density per unit length of the wire and  $\lambda_D$  is the de Broglie wavelength of electron at thermal energy  $k_B T$ .  $\mathcal{J}_j(y)$  is the Fermi-Dirac integral of order  $j$ .  $N_1$  is the degeneracy factor which describes the degenerate character of the electron gas in quantum well wire.

In the zero-field case,  $\eta = N_1^2 / 16$  in the strong degenerate limit. In the nondegenerate limit, Eq. (2.4) can be approximated and  $\eta$  can be calculated from the equation

$$e^\eta = N_1 / 2 \pi^{1/2} \cosh(\delta) \quad (2.9)$$

which shows that the electrochemical potential decreases with the increase in the electric field.

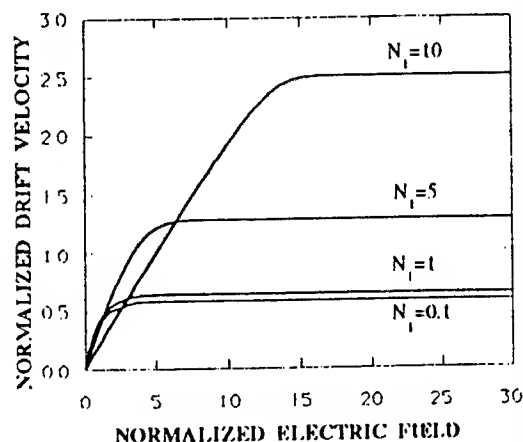


Fig. 1. Normalized drift velocity as a function of normalized electric field for various values of degeneracy parameter

Fig. 1 gives the normalized drift velocity  $v_D/v_{th}$  as a function of normalized electric field  $\delta$  for various values of the degeneracy parameter. To observe deviations from the ohmic behavior in strongly degenerate system, much larger values of the electric field are required. Even though the mobilities of degenerate systems are lower, the saturation velocity is enhanced in strong electric field. This can be understood on the basis that the electrochemical potential is enhanced as electrons tend to move in the antiparallel direction to the electric field and high energy quantum states get occupied. For a nondegenerate gas, the relative drift velocity saturates to the value equal to  $1/\pi^{1/2}$  for all concentrations. The complete velocity-field profile under the nondegenerate conditions can be described by a simpler equation

$$v_D = \frac{v_{th}}{\sqrt{\pi}} \tanh(\delta) \quad (2.10)$$

This equation is obeyed for all concentrations for degeneracy factor  $N_1$  less than 0.1.

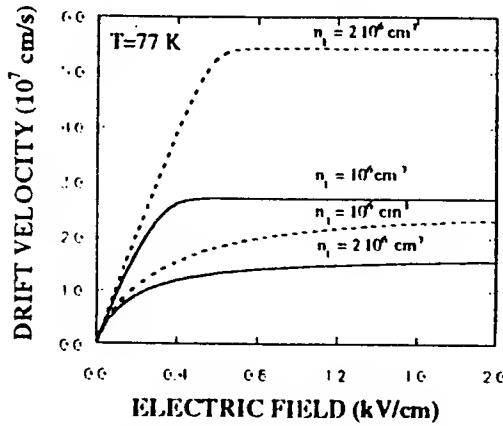


Fig. 2. Velocity-field characteristics of electrons in quantum well wire at 77 K, with (solid curve) and without (dashed curve) the emission of optical phonons.

The optical phonon emission can be included in the distribution function by defining a combined mean free path due to momentum and energy relaxation processes. To demonstrate the importance of the optical phonon emission in limiting the saturation velocity, the normalized electric field is replaced by

$$\delta = \frac{\delta_0}{1 + \frac{\delta_0}{\Theta}}, \quad \delta_0 = \frac{q\epsilon\ell_0}{k_B T}, \quad \Theta = \frac{\hbar\omega_0}{k_B T} \quad (2.11)$$

where  $\ell_0$  is the momentum relaxation scattering length. Velocity-field characteristics for degenerately-doped quantum well wire are shown in Fig. 2, with (solid line) and without (dashed line) the emission of optical phonons.

The mobility in the ohmic regime does not alter appreciably by the emission of an optical phonon. In the strongly degenerate limit, the mean free path  $\ell_0$  is obtained from the ohmic mobility as follows:

$$\ell_0 = \mu_0 m^* v_F / q \quad (2.13)$$

with the Fermi velocity given by

$$v_F = n_1 \hbar / 4 m^* \quad (2.14)$$

where carrier-concentration dependence of the mobility is ignored.  $\ell_0 = 1.03 \times 10^{-3}$  cm for an ohmic mobility of  $10^6 \text{ cm}^2/\text{V.s}$  in GaAs QWW for a carrier concentration of  $10^6 \text{ cm}^{-3}$ .

The optical phonon emission can drastically reduce the saturation velocity. In the absence of optical phonon emission, the saturation velocity is limited by the Fermi

velocity which is  $2.71 \times 10^7$  cm/s for carrier concentration of  $10^6 \text{ cm}^{-3}$ , and twice as much for twice the carrier concentration. But, with the optical phonon emission included, the saturation velocity decreases by substantial amount especially for strongly degenerate samples. Velocity enhancement is possible by suppression of this optical phonon scattering in a superlattice structure as suggested by Sakaki [7], for example. Minibands in the superlattice structure can be engineered in such a way that the spacing between minibands is greater than the optical phonon energy, and the width of each miniband less than the phonon energy. The calculations for such a superlattice structure indicate a lower mobility. As the saturation velocity is relatively independent of the ohmic mobility, a greater operating speed of a transistor fabricated from QWW's is expected.

### 3 QWW Transistor

The velocity saturation effect can easily be implemented in the modelling of a quantum well wire transistor if the empirical relation

$$v_D = \frac{\mu_0 E}{1 + \frac{E}{E_c}} \quad (3.1)$$

is considered. The velocity-field profiles obtained from this equation agrees with those obtained by Eq. (2.3) if  $E_c = v_{sat} / \mu_0 = 54.2$  V/cm for saturation velocity of  $v_{sat} = 5.42 \times 10^7$  cm/s in the absence of optical phonon emission for carrier concentration of  $2 \times 10^6 \text{ cm}^{-3}$  and mobility of  $10^6 \text{ cm}^2/\text{V.s}$ . This shows that the approach towards saturation takes place at much lower values of the electric field for high mobility materials, even though the saturation velocity itself does not depend on the ohmic mobility.

With Eq. (3.1) considered for modelling of the transistor, by following the procedure outlined in Ref. [10], the drain current as a function of the gate voltage and drain voltage is obtained as

$$I_D = \beta \left[ \frac{2 V_g V_D - V_D^2}{1 + \frac{V_D}{V_c}} \right] \quad (3.2)$$

with

$$\beta = \frac{N_{ch} \mu_0 C_o W}{2 L} \quad (3.3)$$

$$V_c = \frac{v_{sat}}{\mu_0} L \quad (3.4)$$

where  $N_{ch}$  is the number of channels in multiple QWW superlattice structure,  $C_o$  the effective gate capacitance,  $W$  the gate width, and  $L$  the effective channel length. For a  $0.25\text{-}\mu\text{m}$  channel length,  $V_c = 1.36$  mV. This shows if the

drain voltage is larger than 1.36 mV, the channel will exhibit a short-channel like behavior. In the presence of optical phonon emission, this value decreases to 0.4 mV. In Eq. (3.2),  $V_g'$  is the gate voltage above the threshold value and  $V_D$  is the drain voltage with source grounded.

At the onset of current saturation, all carriers leave the channel at the saturation velocity where electric field is very high. Therefore, the saturation current is given by

$$I_{Dsat} = v_{sat} WC_o (V_g' - V_{Dsat}). \quad (3.5)$$

When Eq. (3.5) is compared with Eq. (3.2) at the onset of current saturation, the drain voltage at which the current saturated is given by

$$V_{Dsat} = V_c \left[ \left( 1 + \frac{2 V_g'}{V_c} \right)^{\frac{1}{2}} - 1 \right]. \quad (3.6)$$

With this value of  $V_{Dsat}$  substituted in Eq. (3.5), the saturation current is given by

$$I_{Dsat} = I_c \left( \frac{V_{Dsat}}{V_c} \right)^2 \quad (3.7)$$

where

$$I_c = \beta V_c^2. \quad (3.8)$$

Fig. 3 shows the normalized current-voltage characteristics of a transistor with submicron dimensions. In this regime  $V_g' > V_c$ . As  $V_g'$  becomes much larger than  $V_c$ , the steps tend to be equally spaced. An analysis of the velocity distribution in the channel indicates that the velocity throughout the length of the channel is lower than that on the drain end where carriers are moving with the maximum permissible velocity. To have a reasonable value of the current, several multiple channels are available. The equally-spaced step behavior of I-V characteristics is in direct contrast to the behavior expected from long channel transistors ( $V_g' \ll V_c$ ), when steps separation varies quadratically with the adjusted gate voltage  $V_g'$ . In fact, if Eq. (3.6) is expanded to second order in  $V_g' / V_c$ , one can easily notice the complete absence of pinchoff effect. The real strength of QWW transistor lies in elimination of optical phonon scattering, as suggested by Sakaki [7]. If such superlattice structures can be fabricated, it will certainly open a new range of devices where velocity can be considerably enhanced by heavy doping.

High mobility does not influence the saturation velocity of the carriers, although it may accelerate the approach towards saturation as high fields are encountered in submicron-length channels.

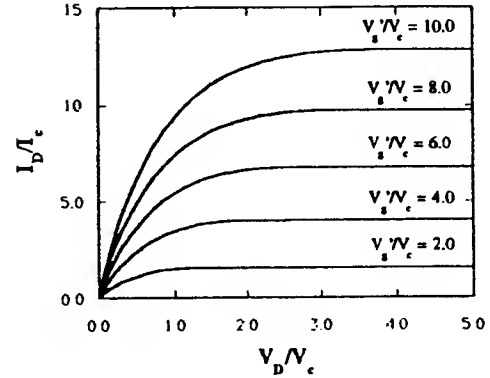


Fig. 3. Normalized Current-Voltage characteristics of QWW transistors.

### Acknowledgements

One of us (VKA) would like to acknowledge financial support of Japan Research and Development Corporation (JRDC) and that of U. S. Air Force Office of Scientific Research under Faculty Associateship Program.

### References

†Permanent Address: Department of Electrical and Computer Engineering, Wilkes University, Wilkes-Barre, PA 18766, U. S. A.

- [1] H. Sakaki, Japanese J. Appl. Phys. **19**, L735(1980).
- [2] M. Feng, C. L. Lau, V. En, C. Ito, Appl. Phys. Lett. **57**, 1233(1990).
- [3] J. Laskar, J. Kolodzey, A. A. Ketterson, I. Adesida, and A. Y. Cho, IEEE Electron Dev. Lett. **11**, 300(1990).
- [4] K. Hirakawa and H. Sakaki, J. Appl. Phys. **63**, 803(1988).
- [5] V. K. Arora, Jpn J. Appl. Phys. **24**, 537(1985).
- [6] K. K. Thornber, J. Appl. Phys. **51**, 2127(1980).
- [7] H. Sakaki, Japanese J. Appl. Phys. **28**, L314(1989).
- [8] V. K. Arora, J. Phys C **18**, 3011(1985).
- [9] V. K. Arora, J. Appl. Phys., to be published.
- [10] V. K. Arora and M. B. Das, Semicond. Sci. Technol. **5**, 967(1990).

## APPENDIX IX

“Development of High Temperature Ohmic Contacts to Gallium Arsenide for VLSI Applications,” abstract of an M. S. thesis by Mr. David Moss, Wilkes University, August 1992.

Wilkes University  
School of Science and Engineering  
Department of Physics

DEVELOPMENT OF HIGH TEMPERATURE  
OHMIC CONTACTS TO GALLIUM ARSENIDE  
FOR VLSI APPLICATIONS

A Thesis in  
Physics

by

David W. Moss

Submitted in Partial Fulfillment  
of the Requirements  
for the Degree of

Master of Science in Physics

August 1992

## ABSTRACT

Fabrication of electrical contacts to n+ and p+ GaAs was studied using GeMoW, as the refractory ohmic metal; and TiPtAu, and Al were used as the different Schottky metals. The transmission line model (TLM) was used to determine the contact resistance at room temperature. The contacts were annealed with As and InAs over pressure. The samples were annealed at increasing temperatures, then the contact resistance was measured after each anneal. Plots of average contact resistance verses annealing temperature were created to help understand the relation between the two parameters. A GeMoW/TiPtAu contact on p+ GaAs had the lowest average minimum contact resistance of 0.14  $\Omega$ -mm after 550 ° Celsius anneal and remained as an ohmic contact until 650 °. A GeMoW/Al contact on p+ GaAs remained ohmic from 300 ° C to 550 ° C with an average minimum contact resistance of less than 0.4  $\Omega$ -mm. The goal of this work was to increase the operating temperature of GaAs-based HBTs and MESFET devices by eliminating ohmic contact as an impediment.



**A HYBRID METHOD FOR THREE-DIMENSIONAL INTERFEROMETRIC  
TOMOGRAPHIC RECONSTRUCTION OF  
HIGH-SPEED AERODYNAMIC FLOWS**

Soyoung Stephen Cha  
Associate Professor  
Department of Mechanical Engineering

University of Illinois at Chicago  
P.O. Box 4348  
Chicago, IL 60680

Final Report for:  
Research Initiation Program  
Wright Laboratory

Sponsored by:  
Air Force Office of Scientific Research  
Bolling Air Force Base, Washington, D.C.  
and  
University of Illinois at Chicago

December 1992

# **A HYBRID METHOD FOR THREE-DIMENSIONAL INTERFEROMETRIC TOMOGRAPHIC RECONSTRUCTION OF HIGH-SPEED AERODYNAMIC FLOWS**

Soyoung Stephen Cha  
Associate Professor  
Department of Mechanical Engineering  
University of Illinois at Chicago

## **Abstract**

Interferometric reconstruction of three-dimensional flow fields, that is, interferometric tomography, can be a very useful flow diagnostic tool in many engineering applications. It is noninvasive and can capture gross fields; however, it frequently confronts a challenging problem of reconstructing flow fields from insufficient data. In most cases, flow-field interferometric data are sparse, nonuniform, noisy, and incomplete in projection and scanning due to opaque objects present either inside or outside the field. Recently, we have developed and tested a new approach in an effort to improve reconstruction under these ill-posed conditions. In essence, the method incorporates distinct features of flow field data, being based on natural pixel decomposition of the field to be reconstructed. It employs rectangular grid elements of different sizes and aspect ratios. It thus reflects intrinsic spatial resolution information contained in the measured data, and allows reconstruction with better resolution and accuracy in the region with more probing rays scanned. It also can efficiently utilize a priori information on the field. Computer simulation of experiments involving a flow field has demonstrated the superiority of the developed method to the conventional fixed grid method. In simulation, the temperature field of a three-dimensional gravity-driven flow of two interacting cubic heat sources, which is produced from a numerical code, is tested. Both of the maximum and average reconstruction errors are reduced appreciably. Especially, the reconstruction demonstrates substantial improvement in the region of interest.

# A HYBRID METHOD FOR THREE-DIMENSIONAL INTERFEROMETRIC TOMOGRAPHIC RECONSTRUCTION OF HIGH-SPEED AERODYNAMIC FLOWS

Soyoung Stephen Cha

## 1. Introduction

The development of the hybrid method as outlined in the proposal is very extensive and requires a long-term commitment. Due to the very limited funding during a short period of one year, only the most important part of the hybrid method, that is, the variable grid method (VGM), was investigated as explained in this report.

Interferometric tomography of flow fields confronts ill-posed problems due to the limited data that are sparse, nonuniform, noisy, and incomplete in projection and angular scanning. For these types of ill-posed problems, series expansion methods are good candidates since they allow direct reconstruction from limited data, that is, it does not require full information of uniformly sampled data and entire angular scanning.

In a series expansion method, an object field  $f(x,y)$  is approximated by a finite series expansion of either local or nonlocal basis functions.

$$f(x,y) = \sum_{i=1}^K c_i b_i(x,y) \quad (1)$$

where  $b_i(x,y)$  are the series basis functions and  $c_i$  are the corresponding coefficients. The reconstruction needs to determine the coefficients  $c_i$  by solving a system of linear algebraic equations.

$$g(\rho, \theta) = \sum_{i=1}^K c_i a_i(\rho, \theta) \quad (2)$$

where  $g(\rho, \theta)$  and  $a_i(\rho, \theta)$  are the line integral transforms of the field and the basis function

$b_i(x,y)$ , respectively. Subscript  $j$  represents measured data points. Series expansion methods are convenient in incorporating a priori information, i.e., boundary, positiveness, etc.

In the local basis function approach, the basis (domain of support) of an individual series term is confined to a local region in the field. The line integral transform is linear. Hence, the transform and its inversion can be accomplished on a term-by-term basis. One simple approach is to consider the domain occupied by the object field, divided into discrete uniform rectangular-pulse basis functions of dimension  $\Delta x$  by  $\Delta y$  ( $\Delta x = \frac{L_x}{M}$  and  $\Delta y = \frac{L_y}{N}$ ), as shown in Figure 1. Each basis is considered to have a uniform refractive index.  $a_i(\rho_j, \theta_j)$  which is the length of the segment or the  $j$ th ray which lies in the  $i$ th element can be determined geometrically [1]. This approach is the well-known conventional fixed grid method (CM). In tomographic reconstruction, the number of local basis functions,  $K$ , which is the number of unknowns in Equation (2) is usually different from the number of measurement data,  $K_{\text{data}}$ . If  $K_{\text{data}} < K$ , the system of linear algebraic equations is underdetermined. While for  $K_{\text{data}} > K$ , it is overdetermined. The algebraic reconstruction technique (ART) [2,3,4] is an iterative method for solving the underdetermined as well as the overdetermined systems according to the criterion of minimum variance. It treats the problem as one of solving an underdetermined set of equations and attempts to obtain the best possible solution consistent with the given data. The ART is efficient in solving large system of equations, especially the underdetermined one.

To reconstruct the flow field more accurately, an overdetermined system of linear equations is desirable in practical applications. Since some measurement errors in optical pathlength data always exist, the system of linear equations will be inconsistent and have no exact solution. Enough redundant data should be used to reduce the effects of these errors by averaging several measured data. Thus, the redundancy is one of the important requirements

for good reconstruction. Certain data redundancy can be obtained by increasing the number of data points or by suitably choosing the number of local basis functions. Fine reconstruction resolution requires large number of bases, which is in turn limited by the number of data points and the requirement of redundancy. There should be some trade-off between the number of unknowns and the number of data point. The least square method [5,6] can also be used to solve a system of linear algebraic equations. This method works well for small or medium-size overdetermined systems. Hence, it was incorporated into the developed computational reconstruction computer code for its relative accuracy and efficiency.

Interferometric data under ill-posed conditions lead to nonuniform scanning of a field. This nonuniform scanning should provide nonuniform reconstruction resolution with greater accuracy in the region where the rays scan more closely. In general, we are interested in the region with a large density gradient. This region, producing dense fringes, allows close sampling. In practice, some regions can be intentionally heavily scanned to extract more information. Smoothed and uniformly sampled data may be obtained through interpolation after the initial data acquisition. However, this post processing does not enhance the intrinsic resolving power contained in the original data. When a field is reconstructed by a series expansion method, a system of redundant linear algebraic equations can be formed. The redundancy is related to the weighing factors in solving the coefficient matrix. Consequently, the uniformly interpolated data may cause heavier weighing in the region that was originally scanned sparsely. This eventually leads to the loss of reconstruction resolution in the region with dense sampling. When the CM is employed, a relatively large number of well-conditioned data is required in order for individual grid elements to have a sufficient number of rays crossing through them. In this way, a well-behaved coefficient matrix can be formulated but it limits the

number of grid elements and thus the resolution. To reflect the intrinsic spatial resolution information contained in the data while producing a well-behaved coefficient matrix for a stable solution, a new computational reconstruction technique termed the variable grid method (VGM) was studied as explained hereafter.

## 2. Variable Grid Method

The VGM employs nonuniform rectangular-pulse local basis functions. In this method, the field is divided into rectangular bases of different sizes and aspect ratios. A constant value is then assigned to an individual basis. During this project, two VGM were investigated, termed the VGM and new VGM, respectively; the former is the one developed originally [7] and the latter is an improved version of the former.

The implementation procedure for forming nonuniform bases for the VGM is as follows. Initially, the entire field is taken as an element (basis). Each element is then continuously divided in half either horizontally or vertically until the criteria in Equation (3) are met.

$$S_h = \sum_{m=1}^{N_d} \ell_h > C$$

$$S_v = \sum_{m=1}^{N_d} \ell_v > C \quad (3)$$

In Equation (3),  $\ell_h$  and  $\ell_v$  represent the normalized lengths in the horizontal and vertical directions, respectively, as shown in Figure 2. They are the ratios of horizontal and vertical components of a ray segment in a basis to its width and height, respectively. The cumulative normalized lengths,  $S_h$  and  $S_v$ , can be found by adding the normalized lengths of all rays of  $N_d$

contained in the basis. The redundancy parameters  $C$  in Equation (3) controls basis sizes and aspect ratios in such a way that cumulative normalized lengths become reasonably equal for all bases. An appropriate choice of the parameters  $C$  allow sufficient redundancy of coefficients in the linear algebraic equations.

The new VGM was formulated in order to reconstruct flow fields under ill-posed conditions more accurately and to extend its application scope to more severe cases, i.e., zero view angle. The implementation procedure for the new VGM is as follows. Initially, the entire field is divided into four elements (bases). If there is an opaque object in the field, however, the corresponding region that has no rays passing through is not considered. That is, only the remaining region is divided into four elements. Each element is then continuously divided in half either horizontally or vertically until the following criteria are met:

$$S_h = \sum_{m=1}^{N_d} \ell_h > C$$

$$S_v = \sum_{m=1}^{N_d} \ell_v > C \quad (4)$$

Similarly, the redundancy parameters  $C_h$  and  $C_v$  in Equation (4) control basis sizes and aspect ratios in such a way that cumulative normalized lengths become reasonably equal for all elements. It allows sufficient redundancy in the resulting linear algebraic equations if chosen properly. Both of the original and new VGMs are expected to have the following characteristics. First, the bases of a field are adjusted so an appropriate number of rays pass through each of them. This allows a reasonably uniform degree of redundancy to an individual coefficient in the linear algebraic equations. The resulting well-behaved matrix is believed to

yield a stable solution of the coefficients. Second, the algorithm also enables the region of interest, scanned more heavily with probing rays, to contain finer bases and thus to be reconstructed with better accuracy and resolution. In the case where data interpolation is necessary, the interpolation intervals can be proportional to the original data intervals. In this way, the spatial resolution information can be preserved. Both VGMs can also easily incorporate a priori information such as boundary value, positiveness, etc. Past experiences indicate that these types of a priori information are very valuable in improving reconstruction. In summary, both VGMs can allow high reconstruction resolution and accuracy with a larger number of approximating series terms even under ill-posed conditions and local undersampling.

### **3. Reconstruction Examples For Ill-Posed Problems**

Tests of the studied algorithms were conducted through computer simulation of experiments and reconstruction of various fields under the ill-posed conditions. Due to the lengthy time involved and unknown nature of values in experiments, this may be the most efficient way for evaluating the synergistic effects of various algorithmic procedures and input parameters. In computer simulation of experiments, interferometric data were generated from known fields through the line integral transformation with different degrees of view angle and incomplete projection. The adequacy of the methods was then studied by reconstructing the fields from the computer generated data and comparing them with the originally-known fields. The reconstruction accuracy and performance were also compared against those of the CM. In all comparisons, the input data points employed were the same for all methods. All the discussions here correspond to the optimum reconstruction by either the VGMs or the CM. For a given data set, the optimum reconstruction can be found by adjusting the number of bases and



choosing the best reconstruction. In real applications, the field to be reconstructed is not known. The exact evaluation of the optimum reconstruction conditions is thus not possible. An approximate field, however, can be reconstructed with a relatively small number of bases that allow sufficient redundancy of the data and thus provide stability in the solution. The optimum reconstruction can then be found through computer simulation of experiments with this approximate field. The reconstruction error  $\epsilon$  was defined as the percent of the maximum absolute value of the exact field;

$$\epsilon = 100 \frac{|f(x,y) - f_r(x,y)|}{\max \{|f(x,y)|\}} \quad (5)$$

where  $f(x,y)$  and  $f_r(x,y)$  are the exact and reconstructed fields, respectively. Since step functions were used in reconstruction, the field was smoothed by the B-spline interpolation. The center values of the bases were employed for this purpose. Reconstruction errors were then calculated at uniform mesh nodes excluding the opaque object region.

### 3.1 Test Fields

In the study, the test fields which are defined in a square domain ( $|x| < 1$  and  $|y| < 1$ ) were reconstructed through computer simulation of experiments. Two of the test fields consisting of three-dimensional gravity-driven flows are realistic, being generated from numerical flow solutions. The plots of the absolute value of these test fields at two different planes are shown in Figures 3, and 4, respectively. The field in Figure 3 was used as a test field for the ill-posed problem of limited view angle. The field in Figure 4 was used as a test field for the ill-posed problem of incomplete projection as well as limited view angle. The square region of constant temperature in the field represents an opaque object. The opaque

object is fairly large when compared with the field and has steep gradients along the wall.

### **3.2 Comparison of the New Variable Grid Method with the Conventional Method**

The computer simulation of experiment have been conducted for the new VGM with the fields and then compared to those of the CM and VGM. The first test field was a double hump three-dimensional field, as shown in Figure 3. The simulated projection data consisted of sixteen equally-spaced data points for each twenty projections for either full or limited scanning. The optimum number of bases and corresponding errors are plotted in Figure 5 as functions of view angle. As shown in the diagrams, the new VGM outperformed the CM at a reduced view angle and even at the full angle scanning. As the degree of ill-posedness increased, the new VGM produced a larger number of appropriately-adjusted bases. This led to finer resolution in the region of interest and thus less errors. Also the new VGM results showed that the reconstructions with limited view angle up to  $90^\circ$  are comparable to that of full angle scanning. These results can manifest our claim that new VGM can compensate for the deficiencies associated with limited data by employing the appropriately-adjusted bases. Figures 6 and 7 are plots of the reconstruction by the new VGM and CM at a view angle of  $90^\circ$ , respectively. The new VGM reconstructed the flow field very close to the original field. We can notice that the two humps, original and reconstructed, are quite similar in shape. However, noticeable distortion around the humps can be detected in the CM reconstruction. The maximum and average errors by the CM were 28.3 and 5.4%, respectively. These were reduced to 10.3 and 0.8% when new VGM was applied. As shown in the plots, a substantial improvement occurred near the region where the field obtains a local maximum.

The next test field was a three-dimensional field having an opaque object, as shown in Figure 4. This field can be a good example of the ill-posed problem of incomplete projection as well as limited view angle reconstruction. Similarly, twelve equally-spaced data points were generated per each projection, excluding the region blocked by the opaque object. A total of twenty projections were collected to cover the entire view angle which varied from  $180^\circ$  to  $60^\circ$ . The trends of optimum number of bases and corresponding errors as the view angle changes are plotted in Figure 8. As shown in the diagram, the new VGM outperforms the CM at reduced view angles as well as at the full angle scanning; especially the maximum errors by the CM were reduced by half when the new VGM was applied. Similarly to the reconstructions of two previous test fields, the new VGM results showed that the reconstructions with limited view angle up to  $90^\circ$  are comparable to that of full angle scanning. Figures 9 and 10 are plots of the reconstructions by the new VGM and the CM at a view angle of  $180^\circ$ , respectively. The new VGM produced twice more bases than the CM. As shown in the figure, the new VGM reconstructed the hump at the left of the opaque object, but the CM failed to do so. The maximum and average errors by the CM were 37.2 and 3.0%, respectively. These were reduced to 19.6 and 2.1% when the new VGM was applied. Figures 11 and 12 are plots of the reconstructions by the new VGM and the CM at a view angle of  $90^\circ$ , respectively. As shown in the figure, new VGM could still reconstruct the hump at the left of the opaque object successfully. The maximum and average errors were 20.7 and 2.4% for the new VGM and 48.8 and 6.3% for the CM, respectively. The corresponding numbers of bases were 76 and 36, respectively. The reconstruction of the upward flow on the left of the opaque object was of our interest. Figure 13 shows reconstruction errors versus view angle when only the left half of the field was reconstructed with the same bases and coefficients as those used for Figure 8. As

shown in the figure, the average errors remained fairly constant but the maximum errors were reduced substantially for both of the new VGM and CM. This means that the maximum errors appeared near the wall where the field obtains a local maximum or has steep gradients. They might result from the resolution limit of the sampled data. If a finer sampling had been adopted, they would be reduced more. Also, they would be further reduced by applying the complementary field method [8,9]. In the computer simulation of experiments maximum errors were reduced mostly in the areas with large field values or steep gradients. Optimum values of  $C_h$  and  $C_v$  ranged from 5.6 to 11.8 and from 5.2 to 11.8 in this study, respectively.

### **3.3 Comparison of Both Variable Grid Methods**

Both of the original and new VGMs improved the reconstructions over the CM for several test fields. It may be interesting to see how the new VGM can improve reconstruction over the VGM.

Similarly to the previous comparison of the new VGM against the CM, the reconstruction data points and input parameters that were employed for comparison of the two VGMs are the same or at least equivalent. First, the performances of the two VGMs were compared by using the reconstruction results with single hump test fields. For comparison, the improvement in reconstruction, i.e., the difference of the reconstruction error by the CM and the reconstruction error by either the VGM or the new VGM, were compared as shown in Figure 14. The reconstruction improvement by the new VGM was little greater than those by the VGM in most cases. While, the VGM improved the reconstruction appreciably only near a very restricted view angle, the new VGM could improve it over a wide range of view angle. Second, both of the VGM and the new VGM were also compared against the test field shown in Figure 4 to

compare their performances more reasonably. The hump on the left half of the test field was reconstructed by both of the methods. The reconstruction errors were compared in Figure 15. As shown in the figure, the new VGM reconstructed the field more accurately than the VGM in most cases. In addition to the different redundancy criteria of the two methods, that is, Equation (3) and Equation (4), respectively, their remaining implementation procedures are different. For example, there was a hypothetical grid element having no rays passing through, called a blind element in the region of an opaque object for the new VGM. To see this effect, one more new VGM which employed the same implementation procedure as the new VGM but incorporated the redundancy criteria of Equation (3) for the VGM was tested. This modified version was termed new VGM1. For the convenience, the new VGM was called by the new VGM2. A whole field shown in Figure 4 was reconstructed by three reconstruction methods, that is, the VGM, new VGM1, and new VGM2. The reconstruction errors by these methods were compared in Figure 16. The VGM failed to reconstruct the flow field having an opaque object in it like the CM. These results were shown here for the comparison purpose only. Obviously, both of the new VGM1 and new VGM2 reconstructed the field much more accurately than the VGM. Furthermore, the new VGM2 could improve the reconstruction of the field more than the new VGM1. Keeping in mind that the redundancy criteria of both the VGM and the new VGM1 were same, we can realize that the way to decompose the pixels to generate variable grid elements is also an important factor.

#### **4. Conclusion**

In summary, the following general interpretations can be drawn. The performance of the VGM is better than that of the CM. For complete data, the performance of the two methods

including the number of bases, was fairly comparable. They produced the almost same number of bases. However, as the degree of the ill-posedness increased, especially limited view angle, the VGM produced a larger number of appropriately-adjusted bases. The new VGM also outperformed the CM for the ill-posed problems of both limited view angle and incomplete projections as well as limited view angle only. The performance of the new VGM was even better than the VGM. General performance characteristics were quite similar between the two VGMS. For the both VGMS, it was easier to incorporate a priori information due to its changeable basis sizes. They produced finer resolution and thus less errors in the region of interest, and compensated for the deficiencies associated with measured data to produce less reconstruction errors. In general, maximum errors were reduced mostly in the areas with large field values or steep gradients. Overall results indicated that the performance of the VGMS was better than that of that of the CM under all circumstances considered.

#### 4. References

1. Sweeney, D.W. and Vest, C.M.: Reconstruction of three dimensional refractive index fields from multidirectional interferometric data. Appl. Opt. 12, 2649-2664, 1973.
2. Oppenheim, B.E.: Reconstruction tomography from incomplete projections. In Reconst. Tomography in Diagnostic Radiology and Nuclear Medicine, eds. Terpogossian, et al., pp. 155-183, Baltimore, University Park Press, 1977.
3. Gordon, R., Bender, R., and Herman, G.T.: Algebraic reconstruction techniques (ART) for three-dimensional electron microscopy and X-ray photography. J. Theor. Biol. 29: 471, 1970.
4. Herman, G.T., Lent, A., and Rowland, S.W.: ART: mathematics and applications: a report on the mathematical foundations and on the applicability to real data of the algebraic reconstruction techniques. J. Theor. Biol. 42: 1, 1973.
5. Lawson, C.L. and Hanson, R.J.: Solving least square problems. Englewood Cliffs, NJ, Prentice-Hall, 1974.
6. Wilkinson, J.H. and Reinsch, C.: Linear Algebra. New York, Springer-Verlag, 1971.
7. Cha, D.J. and Cha, S.S.: Interferometric Reconstruction of Three-Dimensional Flow Fields through Natural Pixel Decomposition. AIAA Paper 90-1517, 1990.
8. Cha, S.S. and Sun, H.: Interferometric tomography of continuous fields with incomplete projections. Opt. Lett. 14: 299-301, 1989.
9. Cha, S.S. and Sun, H.: Tomography for reconstructing continuous fields from ill-posed multidirectional interferometric data. Appl. Opt. 29: 251-258, 1990.

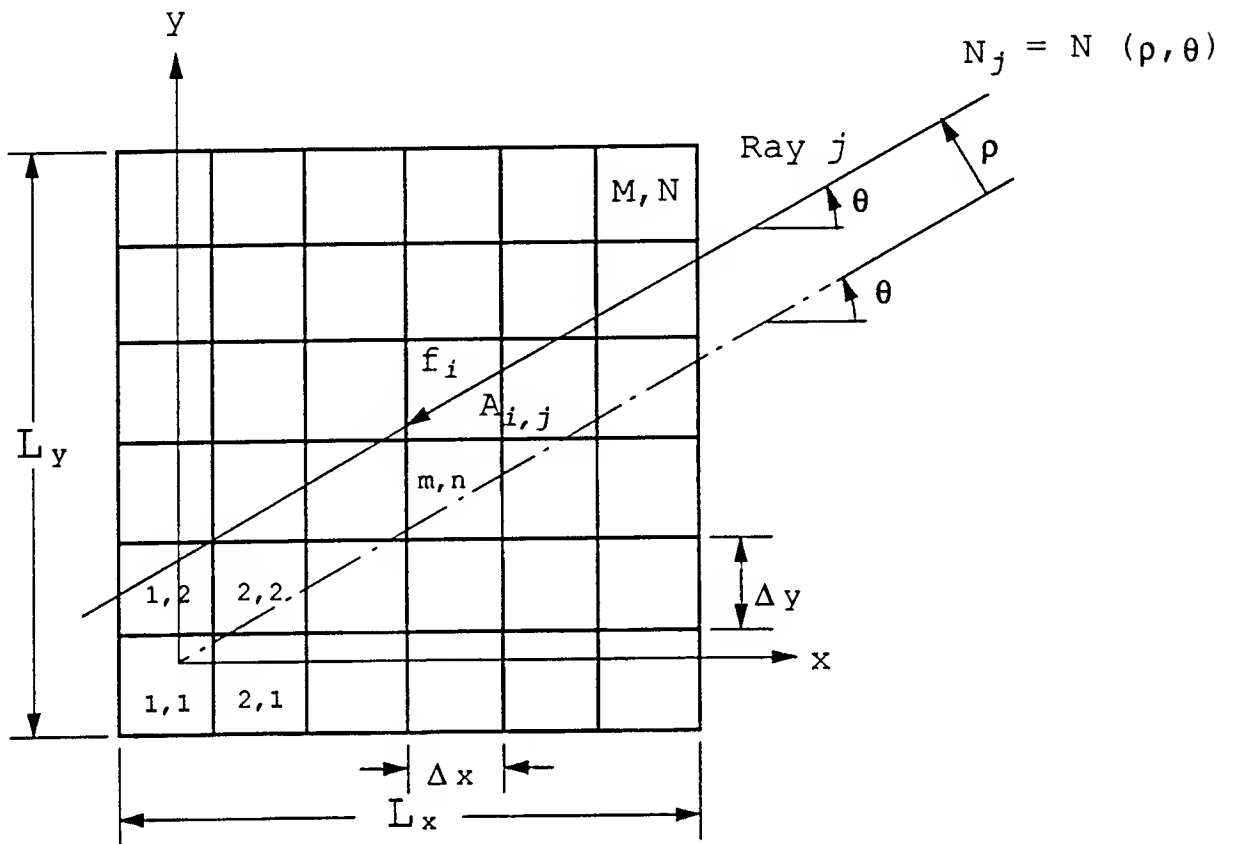
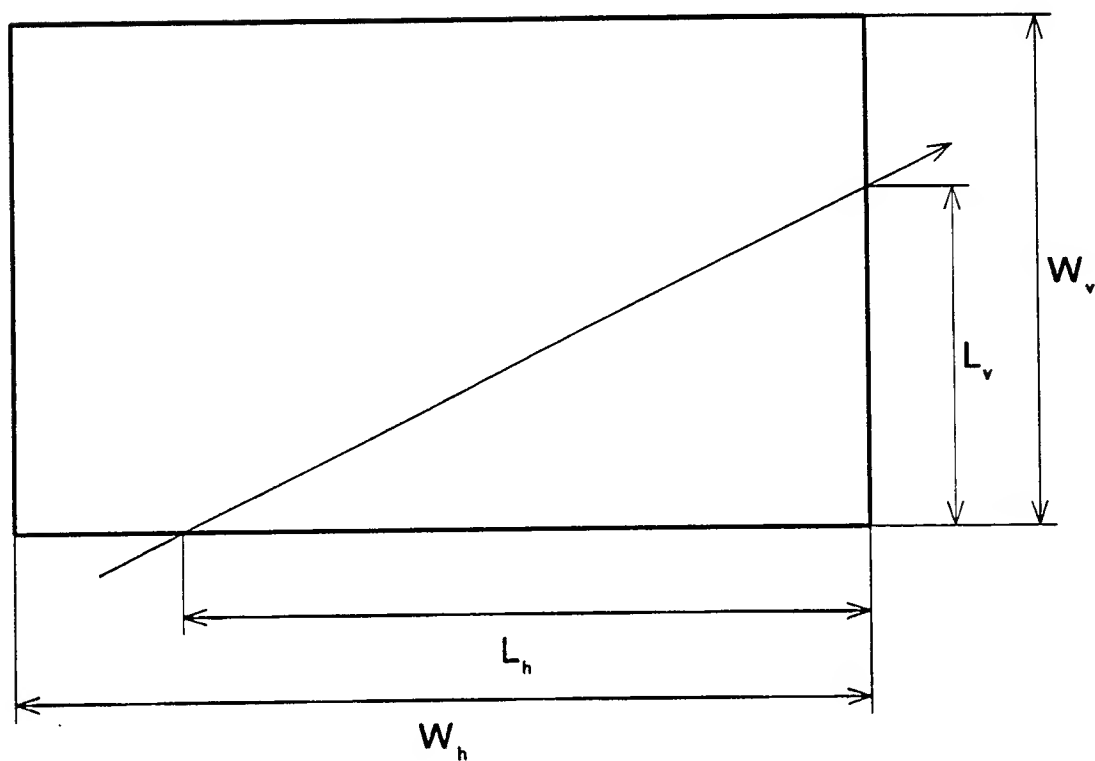


Figure 1

Discrete uniform rectangular-pulse basis functions of dimension  $\Delta x \times \Delta y$ . A typical probing ray, denoted by the index  $j$ , is shown traversing the object.





$$l_h = L_h / W_h$$

$$l_v = L_v / W_v$$

Figure 2 Vertical and horizontal normalized lengths of a ray in an element.

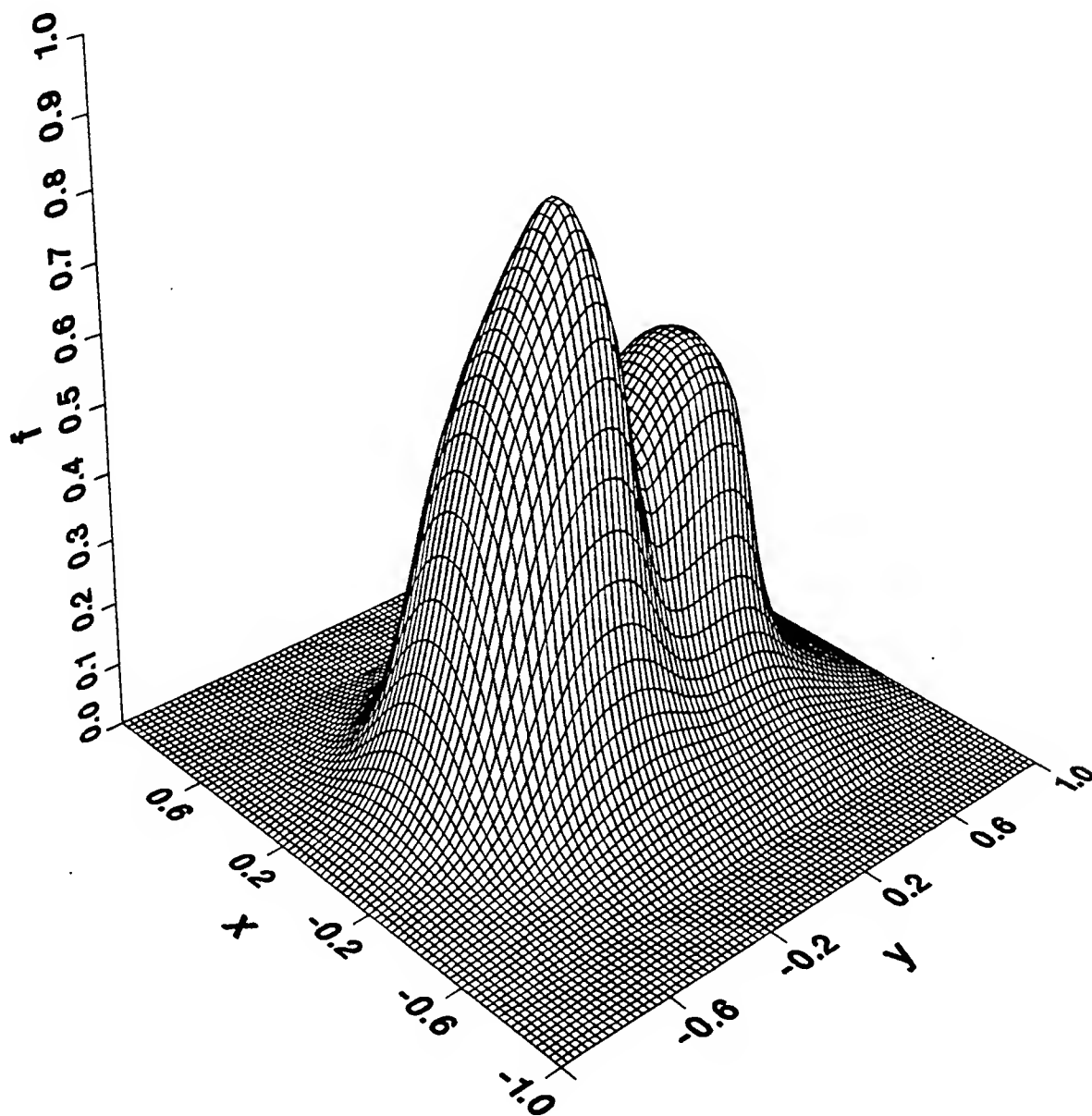


Figure 3                      Double hump three-dimensional test field.

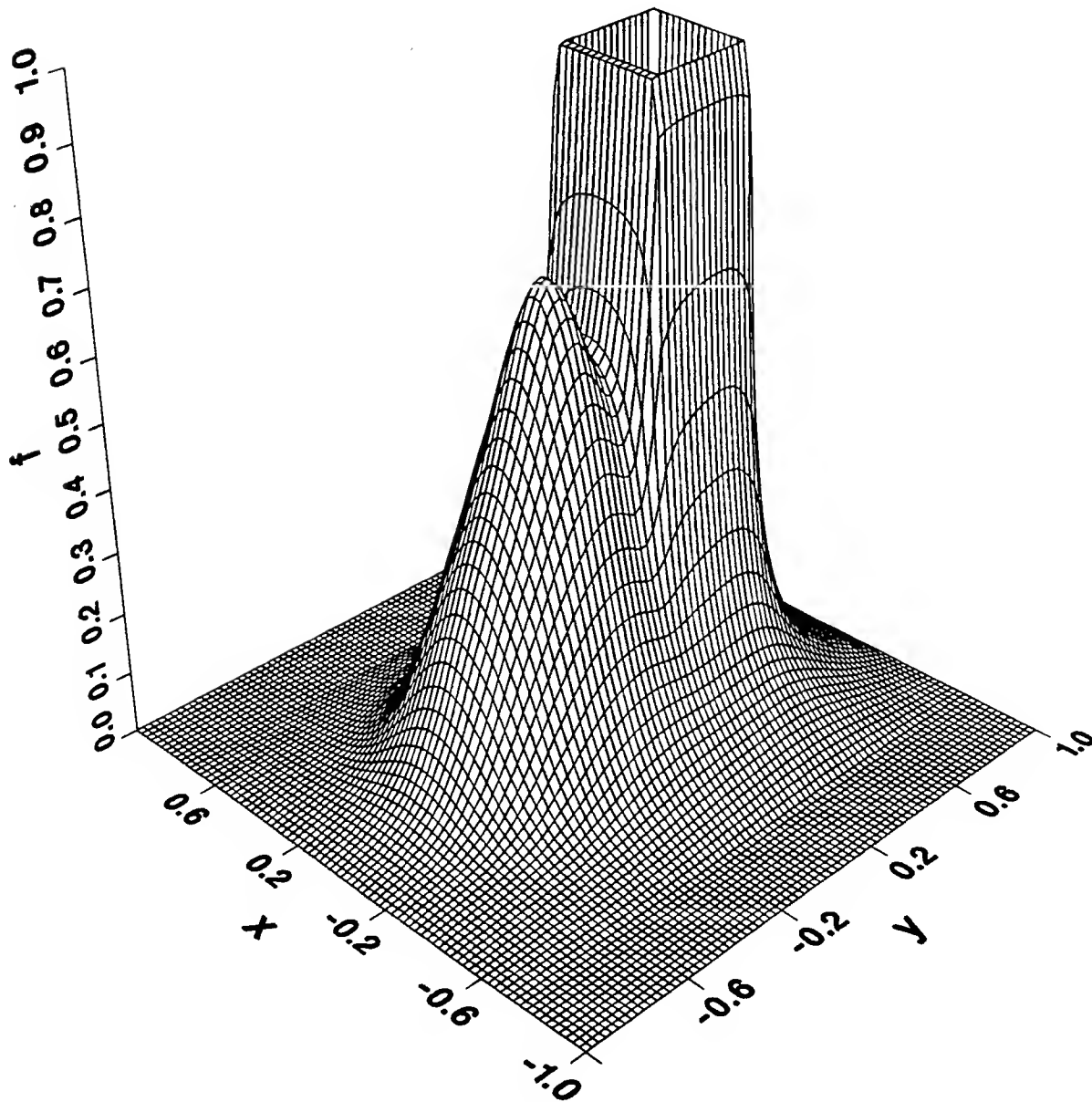


Figure 4

Three-dimensional test field having an opaque object.

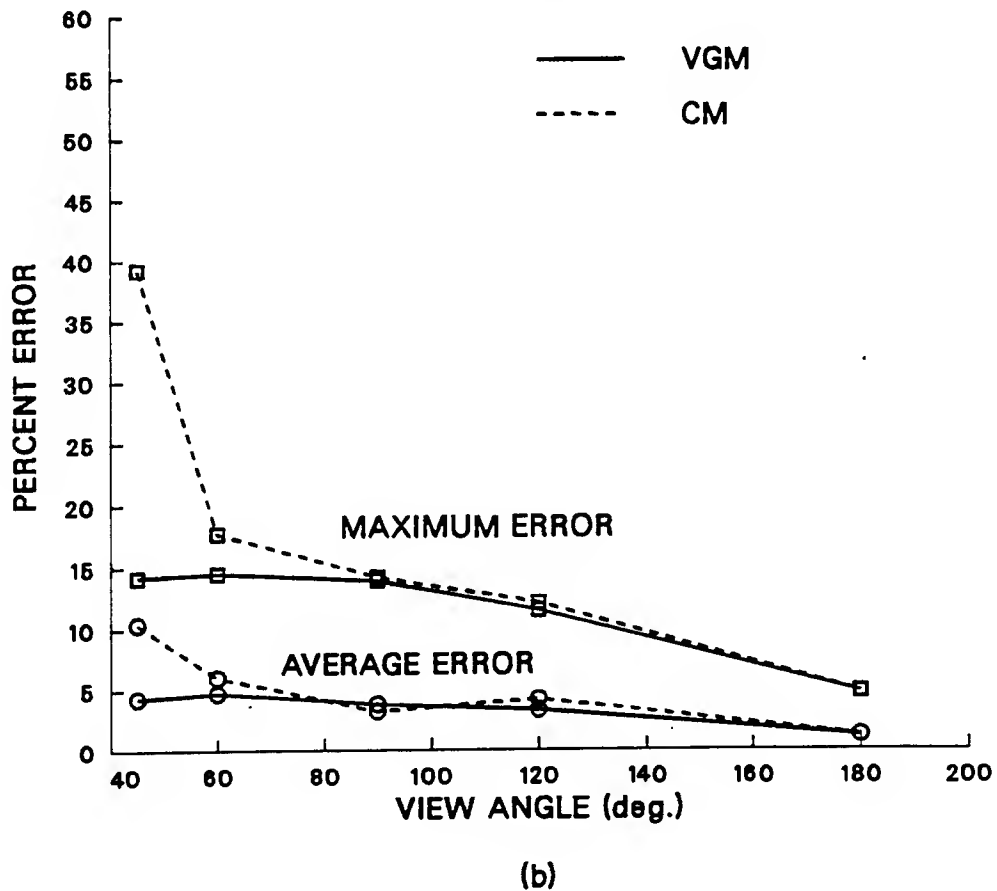
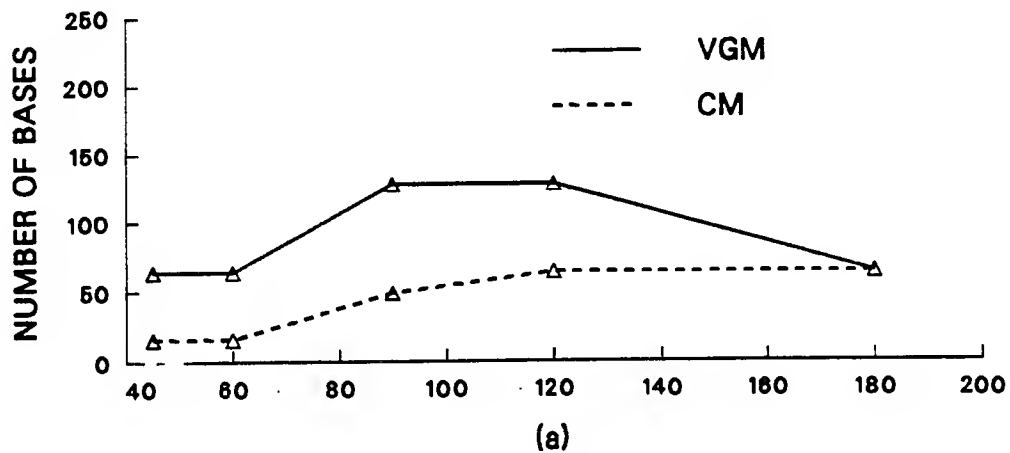


Figure 5

Effects of the view angle on the optimum reconstruction of the double hump test field shown in Figure 3: (a) number of bases; (b) percent reconstruction error.

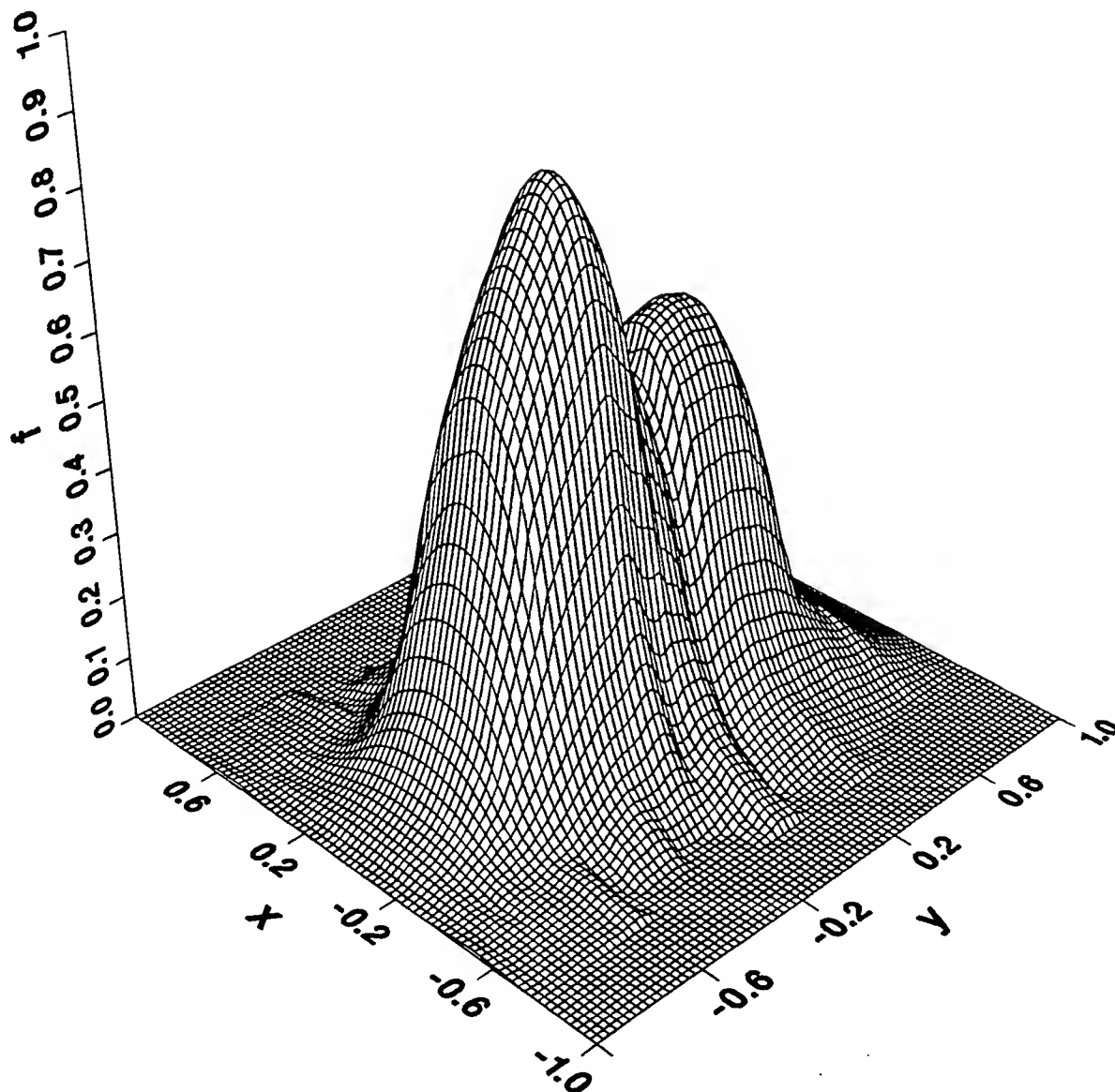


Figure 6

Reconstruction by the new VGM of the double hump test field shown at the view angle of  $90^\circ$ .

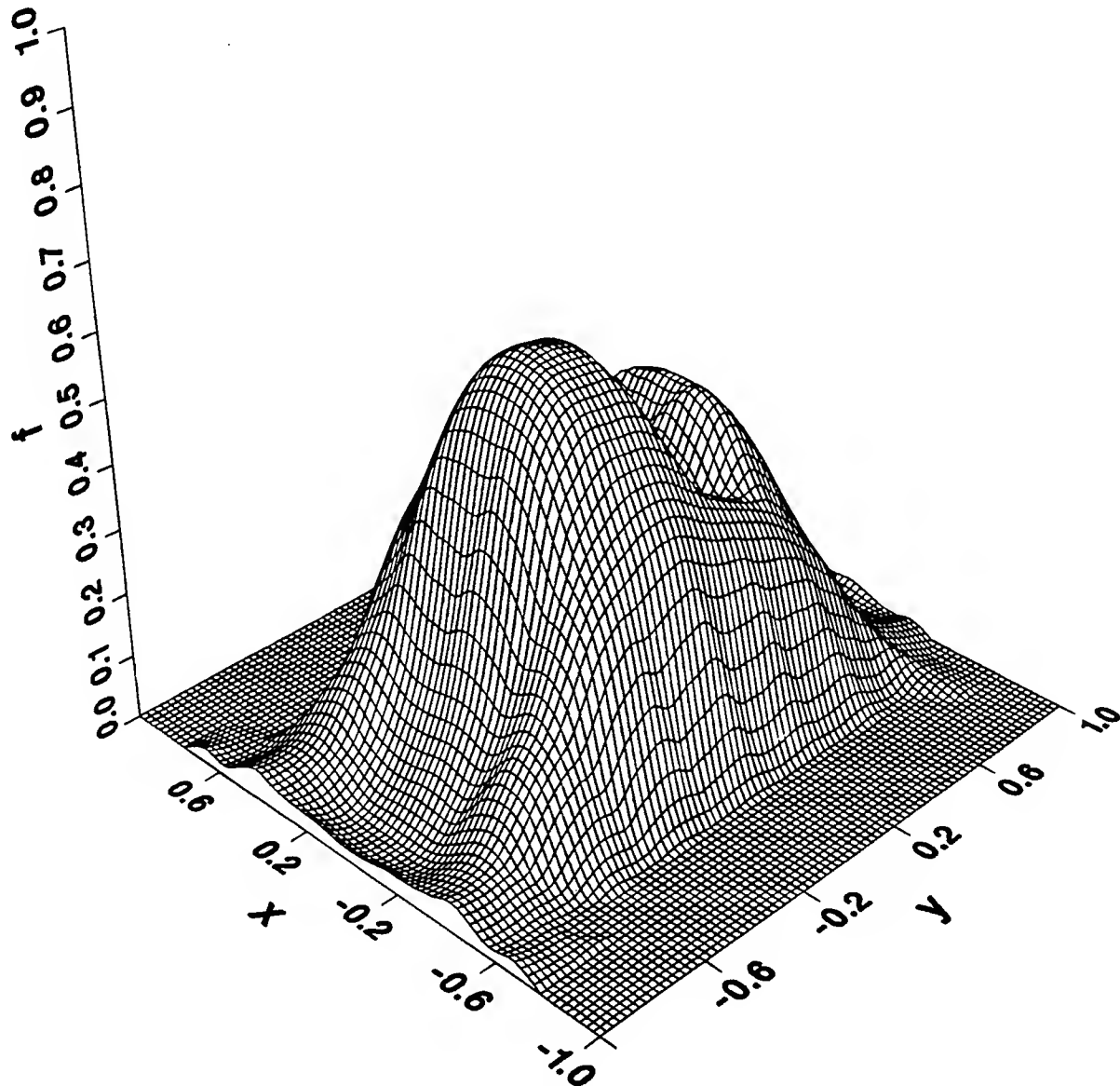
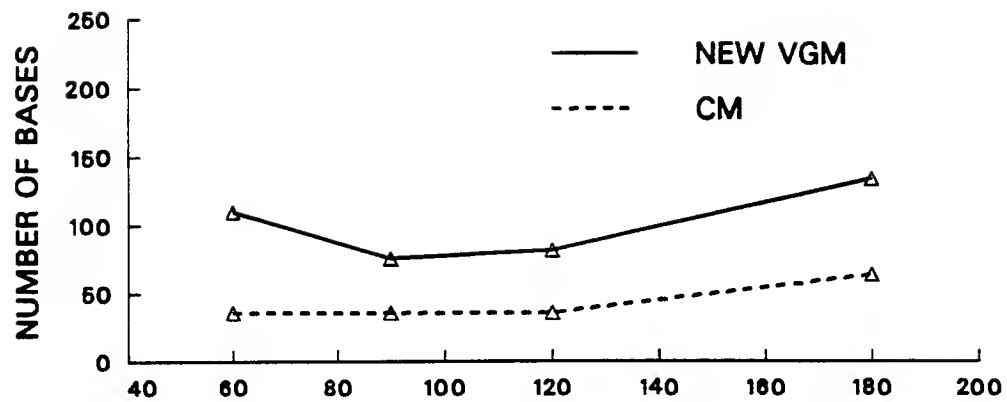
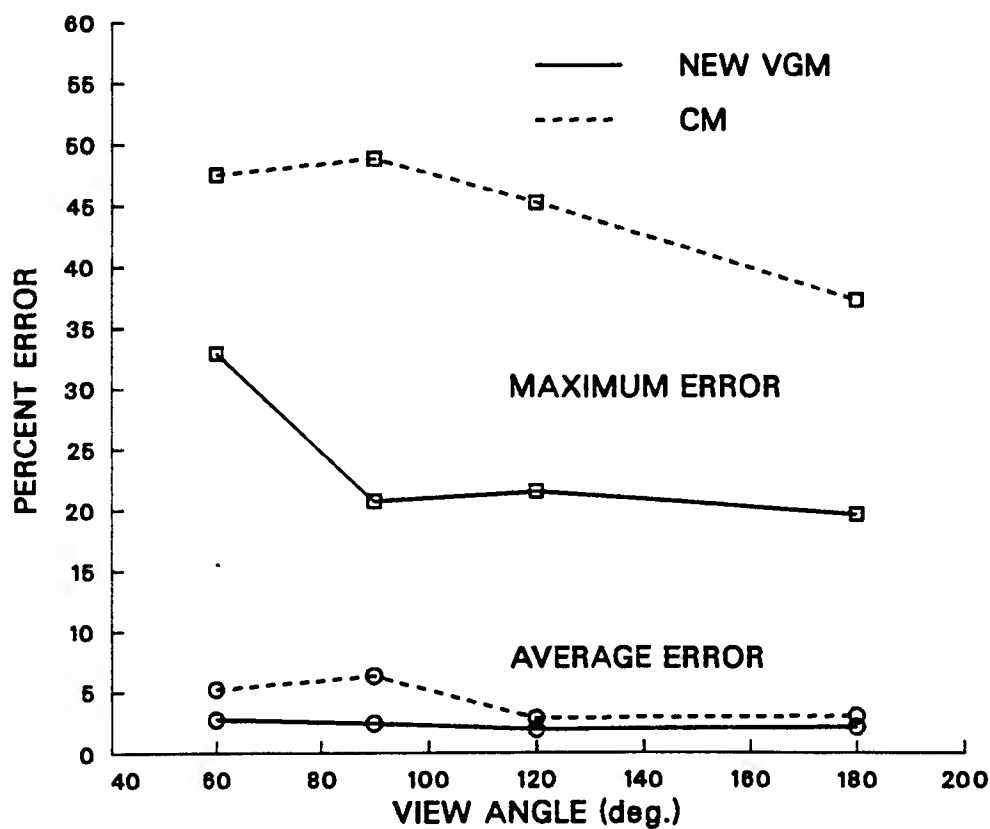


Figure 7

Reconstruction by the CM of the double hump test field at the view angle of  $90^\circ$ .



(a)



(b)

Figure 8

Effects of the view angle on the optimum reconstruction of the test field in Figure 4: (a) number of bases; (b) percent reconstruction error.

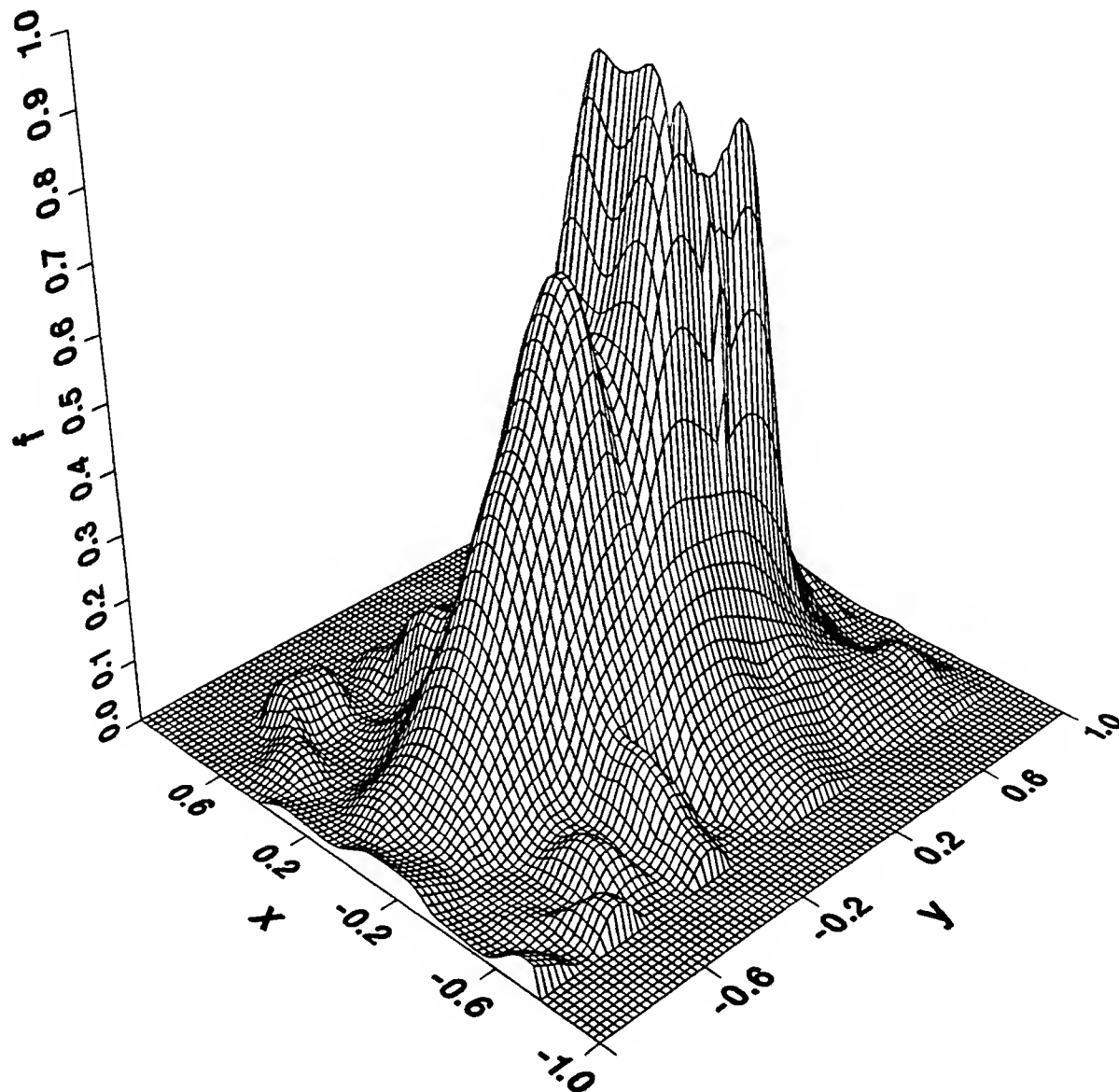


Figure 9

Reconstruction by the new VGM of the test field in Figure 4 at the full view angle.



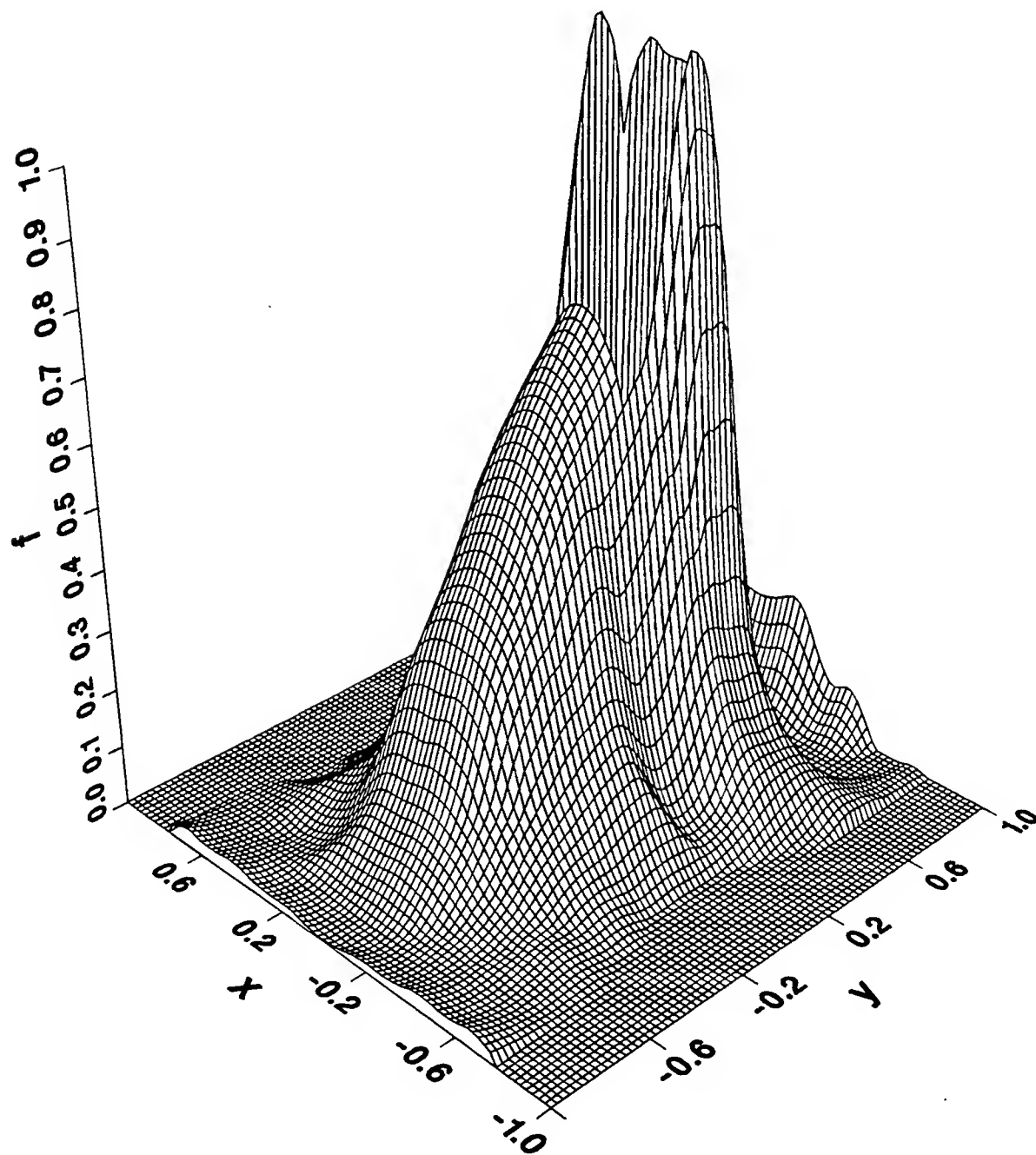


Figure 10

Reconstruction by the CM of the test field in Figure 4 at the full view angle.

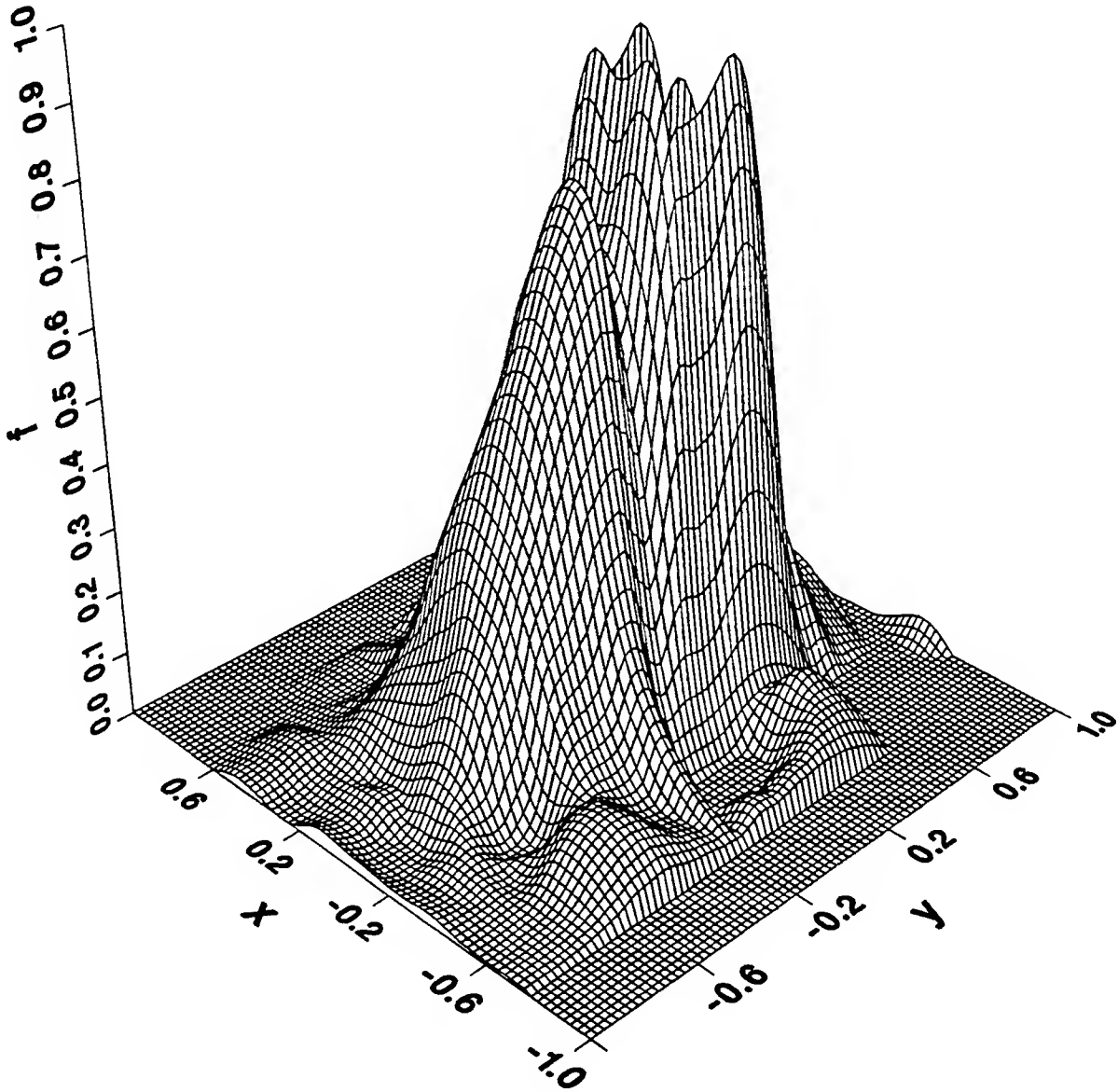


Figure 11

Reconstruction by new VGM of the test field in Figure 4 at the view angle of  $90^\circ$ .

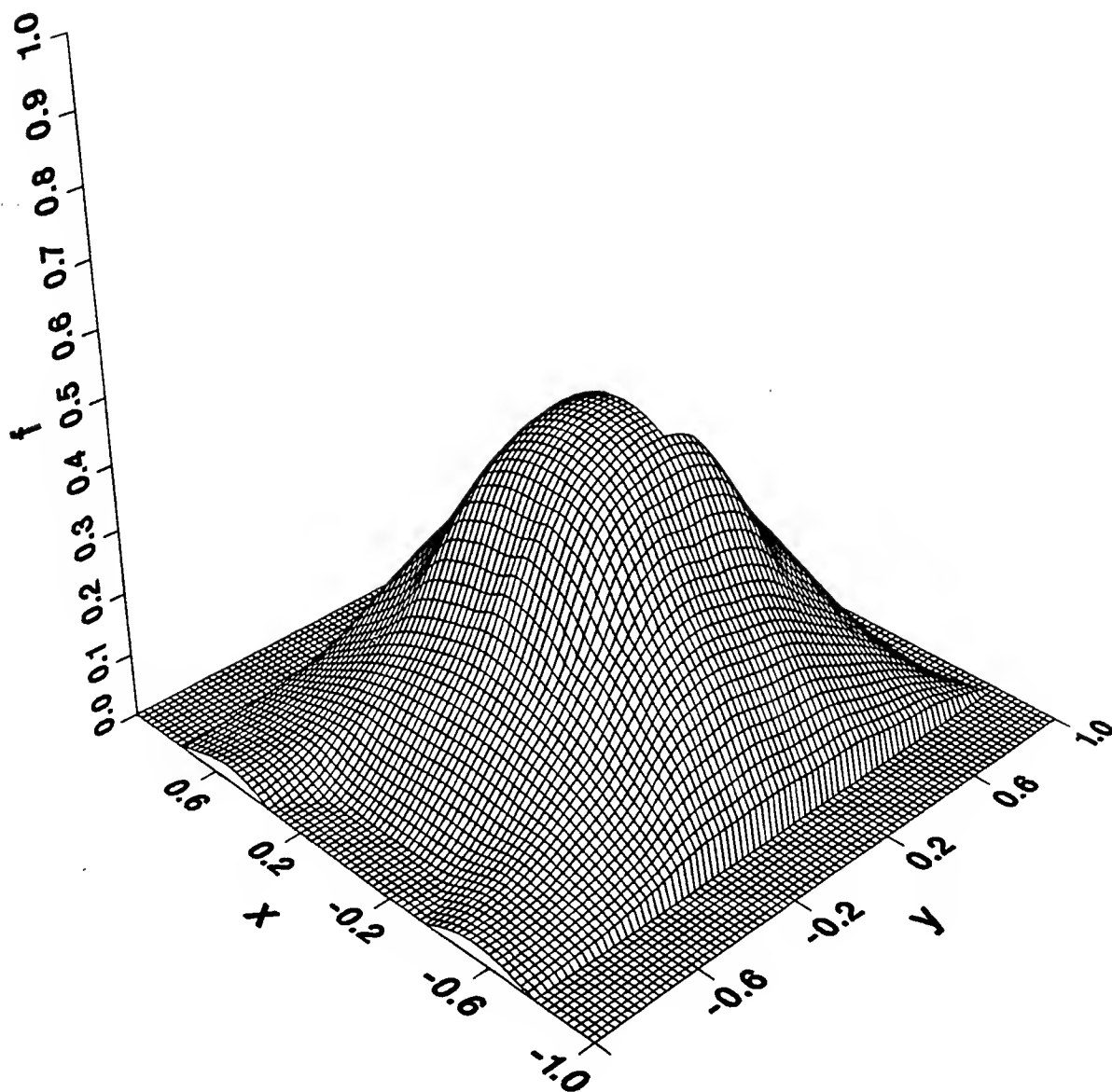


Figure 12

Reconstruction by the CM of the test field in Figure 4 at the view angle of  $90^\circ$ .

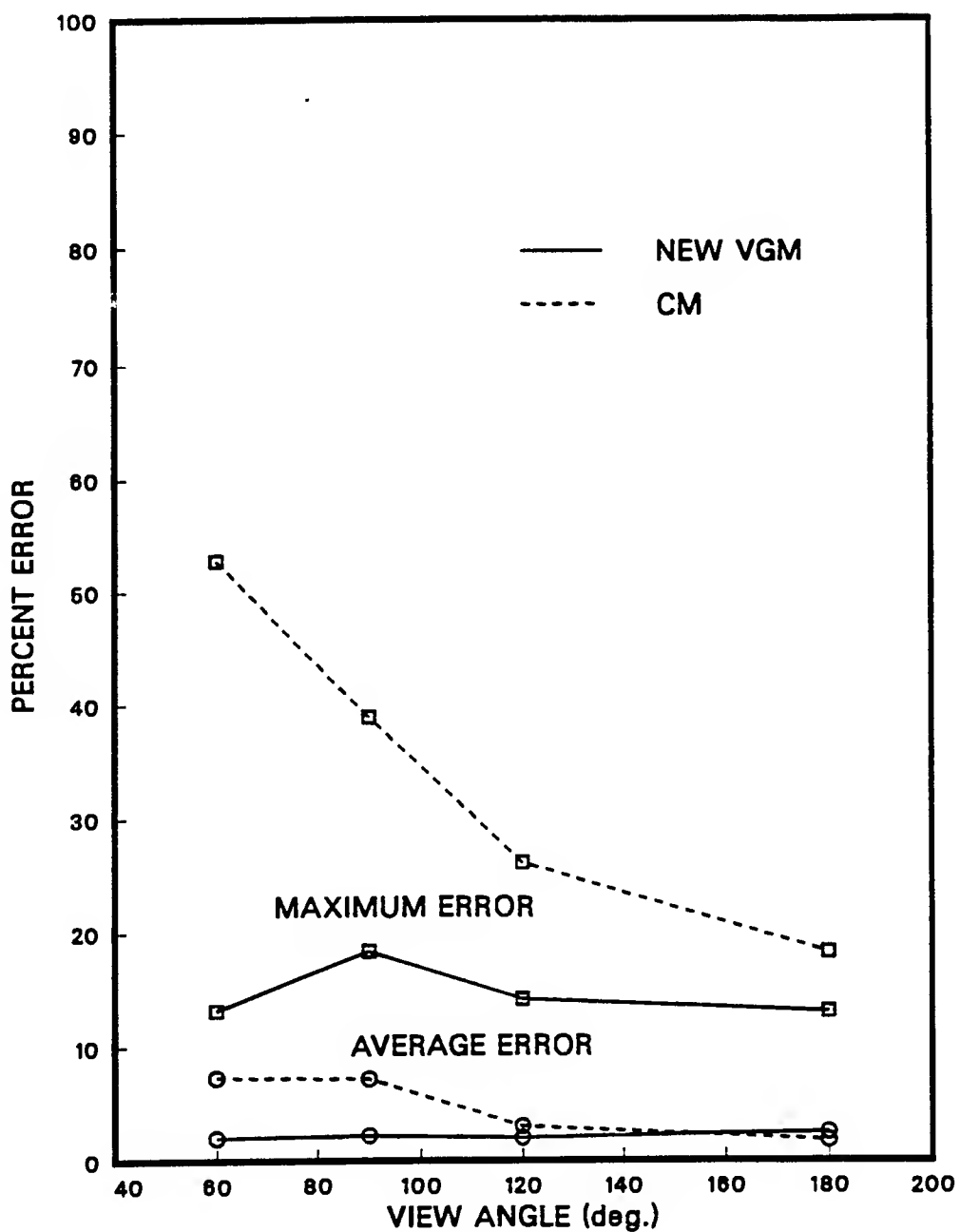
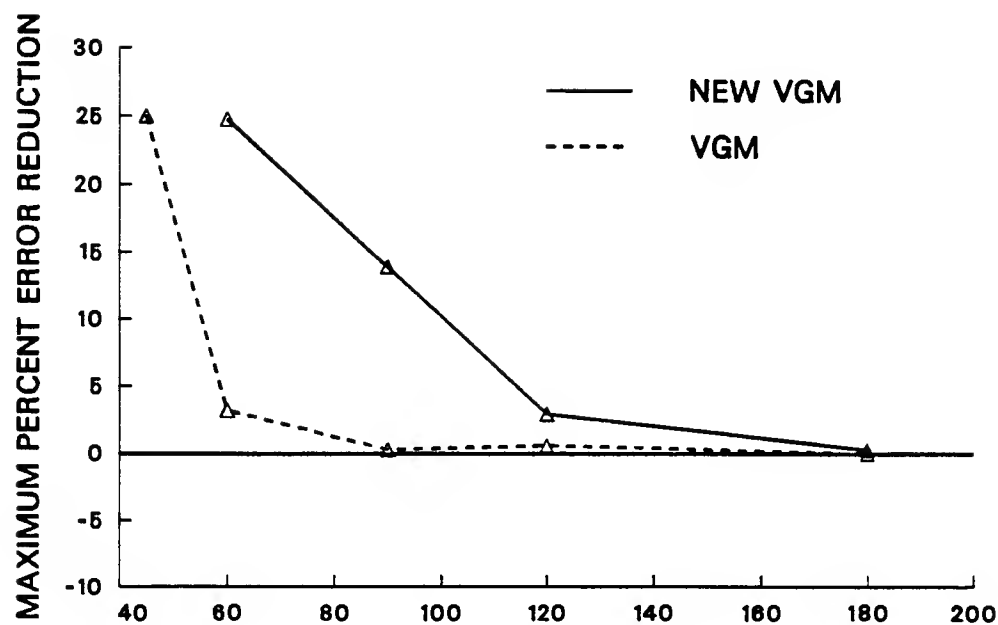
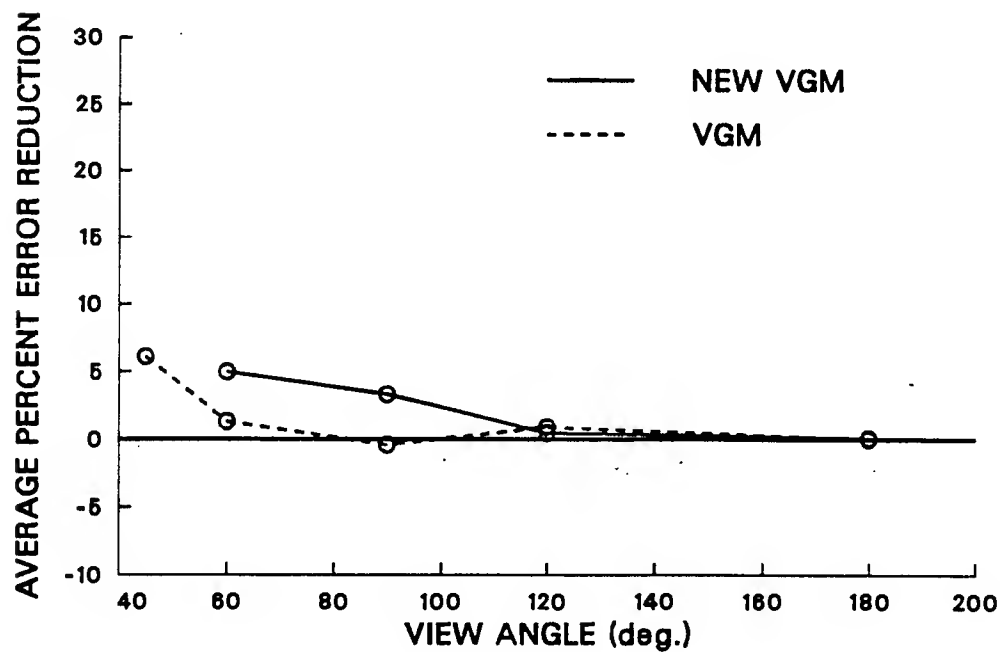


Figure 13

Reconstruction error versus the view angle when only left half of the test field in Figure 4 was reconstructed.



(a)



(b)

Figure 14

Reconstruction improvement by the VGM and the new VGM over the CM reconstruction: (a) reduction in the maximum error; (b) reduction in the average error.

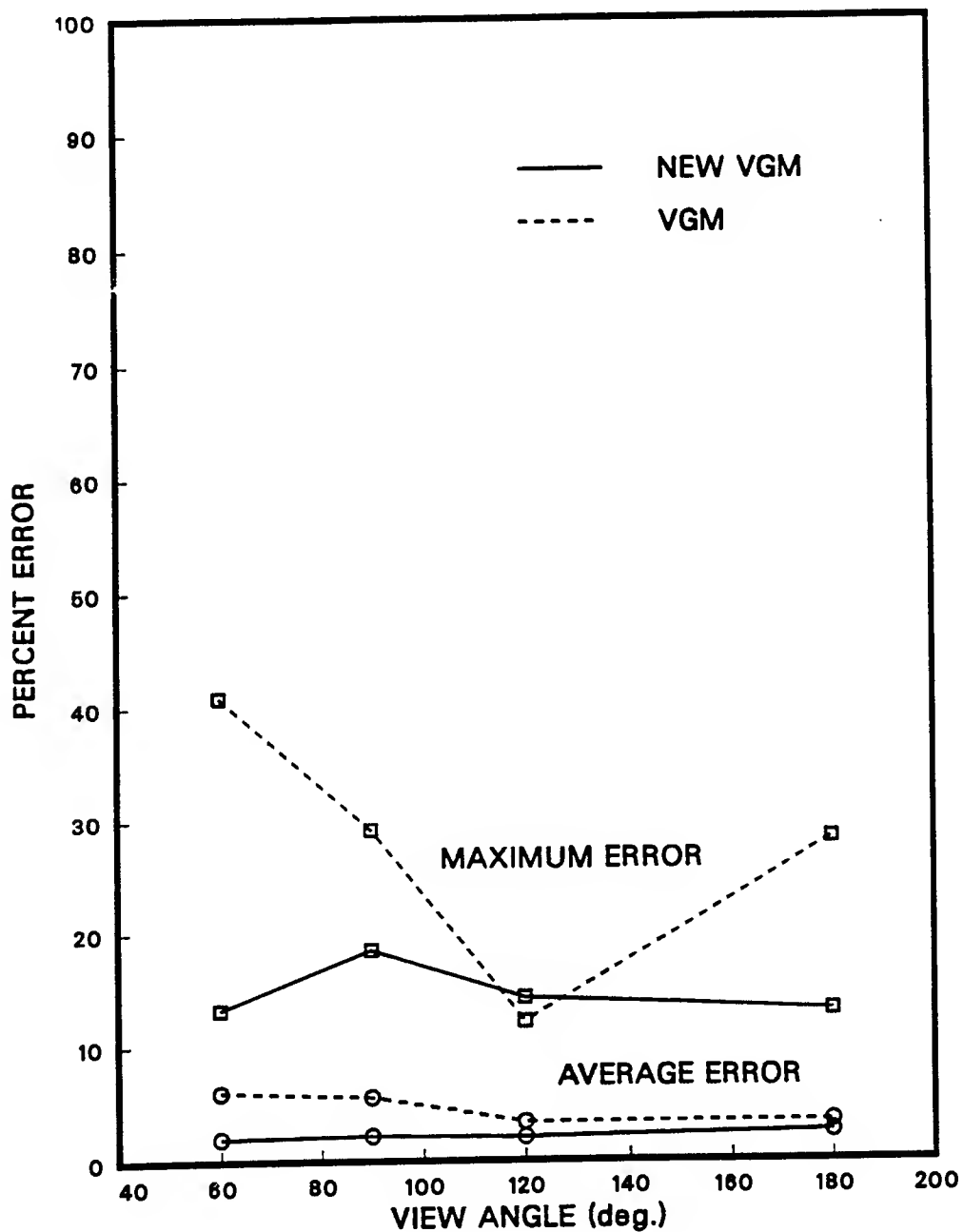


Figure 15

Reconstruction error versus the view angle when the only left half of the test field in Figure 4 was reconstructed.

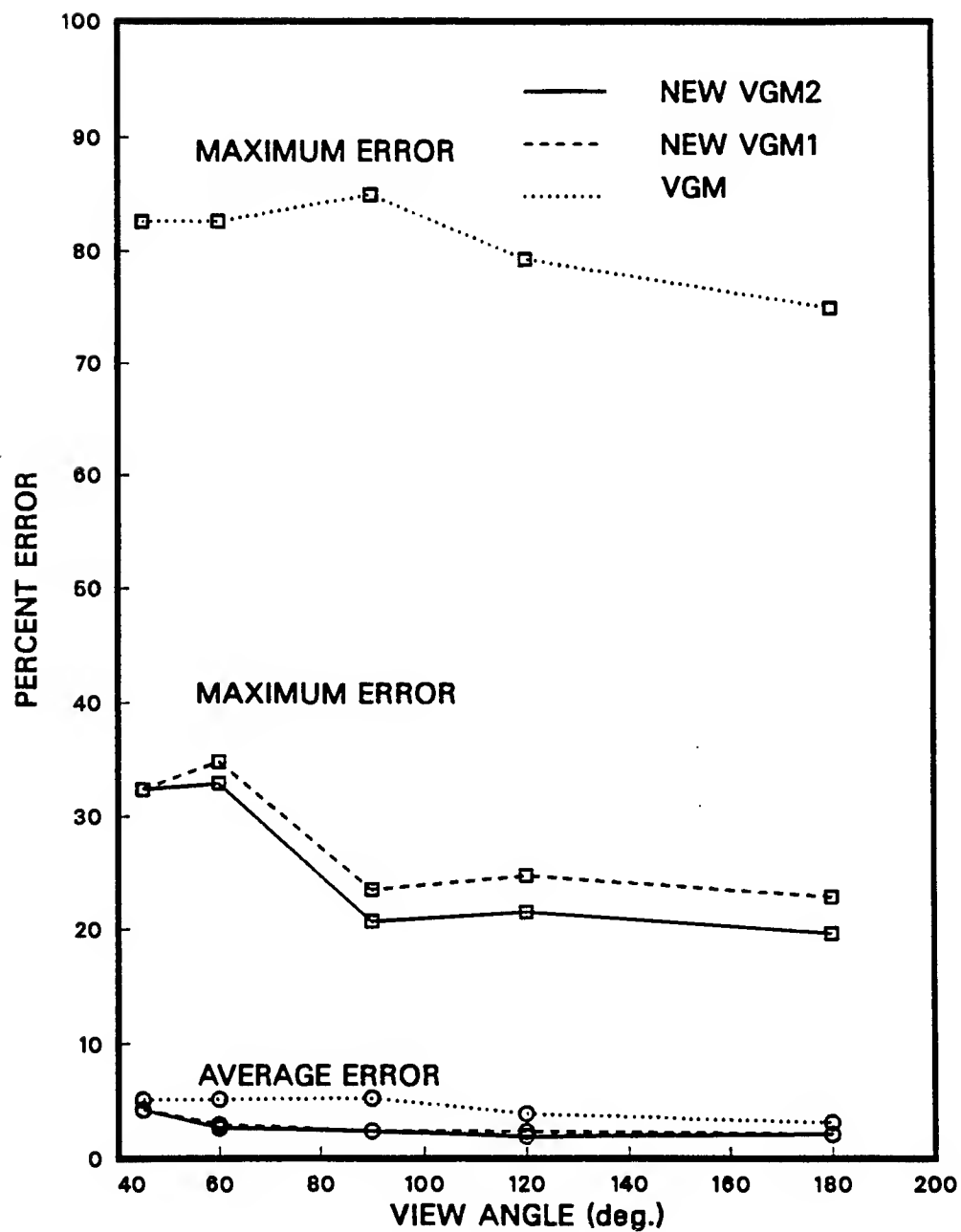


Figure 16 Reconstruction error versus the view angle when the whole test field in Figure 4 was reconstructed.

ORIENTATION ESTIMATION WITH APPLICATION  
IN TARGET RECOGNITION

D.V. Satish Chandra  
Associate Professor  
Department of Electrical and Computer Engineering

Kansas State University  
Manhattan, KS 66506

Final Report for:  
Research Initiation Program  
Avionics Laboratory

Sponsored by:  
Air Force Office of Scientific Research  
Wright-Patterson Air Force Base, Ohio

and

Kansas State University

December 1992



ORIENTATION ESTIMATION WITH APPLICATION  
IN TARGET RECOGNITION

D.V. Satish Chandra  
Associate Professor  
Department of Electrical and Computer Engineering  
Kansas State University

Abstract

A fundamental task in many computer vision applications is the determination of the position and orientation of objects in space. In target recognition, orientation information can be used to select relevant target models from the model database for matching purpose, or local dominant orientations can be used as features in the recognition process. In this report, a procedure is presented to estimate the target orientation using spectral energy distribution in the Fourier domain. The performance of this technique is determined by conducting simulation experiments on a set of infrared images consisting of military targets at different orientations. Experimental results indicate that the nonuniqueness of the location of the target, target size, and target aspect angle, causes no significant problems in the determination of orientation.

## ORIENTATION ESTIMATION WITH APPLICATION IN TARGET RECOGNITION

D.V. Satish Chandra

### INTRODUCTION

The problem of orientation detection arises in many situations in image processing and computer vision. In target recognition, local dominant orientations can be used as features in the recognition process. Model based target recognition requires that the orientation of the target be determined before a corresponding target model can be chosen for matching purpose. The most natural approach to determine the orientation of targets consists of matching all possible rotated positions of a target model to an observed target position. While this method is straightforward to implement, it is computationally very expensive. The generation and comparison of templates for all possible orientations and positions are infeasible. One way to reduce the computational complexity is to extract features on the target that capture information about target's orientation. These features are then compared with the similar features extracted from the target model to estimate the unknown orientation of the target.

One of the objectives of this research is to investigate various methods of extracting features that are sensitive to the orientation of the target. In the following section a brief review of several approaches that aid in the solution of orientation determination problem will be given. Next, an orientation estimation procedure based on Fourier transform will be presented. The effectiveness of this algorithm in estimating the target orientation is determined by conducting simulation experiments on a set of infrared images containing military targets at different orientations.

### OVERVIEW OF DIFFERENT APPROACHES

A number of different model-based techniques have been used to estimate the orientation of an object in an image, including searching for possible

correspondences of model and image features, and alignment of a model with an object. In model-based approach to object orientation estimation, a set of geometric features from an object model are compared against like features from an image of a scene. This comparison generally involves determining a valid correspondence between a subset of the model features and a subset of the image features.

Feature-based orientation estimation methods fall generally into two categories: global and local approaches. In global approaches orientation is determined from the global properties of the parameters that depend on the entire object. In local feature-based approaches orientation is determined by establishing a correspondence between local features extracted from the sensory data and the corresponding local features of the object model. Local approaches have been found to perform better than global approaches under cluttered environments, occlusion and spurious data.

Other methods used to aid in the solution of orientation estimation problem are based on affine transformation, the generalized Hough transform, and image moments. In affine transformation approach [7] estimation of pose is based on a series of transformations required to bring the standard view of the object into alignment with the object of unknown orientation. However, when using this approach, it is more convenient to apply the transformation to features such as contours of planar areas extracted from the target rather than the entire image.

A popular method of object orientation recognition is the generalized Hough transform [5], which works on the object's boundary. This technique, being a local one, has the advantage of handling partial occlusion, but requires management of a high dimensional parameter space. Another problem with Hough transforms is that they compress information obtained from the image or the object model in a nonunique way.

The use of image moments computed on the object's boundary greatly reduces the computation required for object orientation determination. Recently, affine invariants [12] have been defined and found to be more

efficient than Euclidean moment invariants in reducing the amount of computation required in the implementation of algorithms for object recognition and for indexing into a library of object models. A major drawback of these approaches is that they are either computationally intensive or rely on the accurate extraction of geometric features. The orientation estimation procedure presented in the next section uses Fourier transform to determine the target's orientation.

#### METHODOLOGY

In this study, in order to obtain a measure of orientation of targets, features are extracted in the frequency domain using Fourier transform. The linearity and rotational properties of the Fourier transform can be used to decompose an image into components lying in different directions. The spectral energy,  $S(\theta)$ , of a Fourier spectrum for each radial direction  $\theta$  can be calculated according to the equation

$$S(\theta) = \sum_{r=1}^R S(r, \theta) \quad (1)$$

where  $S(r, \theta)$  represents the Fourier spectrum in polar coordinates and  $R$  is the radius of a circle centered at the origin of the two-dimensional spectrum. For an  $N \times N$  spectrum  $R$  is typically chosen as  $N/2$ . This spectral energy plot can be used to obtain a measure of the target's orientation.

The Gaussian operator [13] has been suggested as an optimal smoothing filter, whose impulse response in two dimensions is given by

$$g(x, y, \sigma) = \frac{1}{2\pi\sigma^2} \exp\left[-\frac{x^2+y^2}{2\sigma^2}\right] \quad (2)$$

where  $\sigma$  is the standard deviation of the Gaussian function,  $(x, y)$  represents the image cartesian coordinates. Applying Gaussian filters of different  $\sigma$  (scale) to images results in a set of images with different levels of smoothness. It was also observed [13] that significant intensity changes occur at different scales (resolution) in an image. Detection of edges at different scales can be achieved by using the Laplacian of the Gaussian (LOG)

as a filter and locating the zero crossings. The filtered image is given by

$$\nabla^2 [g(x,y) * f(x,y)] = \nabla^2 g(x,y) * f(x,y) \quad (3)$$

where  $\nabla^2$  represents the orientation-independent second-order Laplacian differential operator. The mask for the LOG operator can be obtained by sampling the kernel

$$A[1 - B \frac{x^2 + y^2}{\sigma^2}] \exp[-\frac{x^2 + y^2}{2\sigma^2}], \quad (4)$$

at integer row column coordinates (x,y). The constants A and B are selected so as to make the sum of the resulting weights in the mask zero. Fourier energy spectrum computed using images with zero crossings can be used to estimate the orientation of objects. One advantage of this approach is that the scale factor,  $\sigma$ , can be chosen so as to eliminate weak edges in order to improve the accuracy of orientation determination.

A set of steerable filters tuned to arbitrary angles, synthesized from a linear combination of basis filters, can be used in the orientation analysis. Orientation map of segmented target images derived by measuring the oriented energy along different directions using steerable filters can be analyzed to obtain a measure of orientation of the target in the input image. Steerable filters can be constructed from Gaussians and their derivatives. It is also known that a filter tuned to a narrow range of spatial orientations about some preferred orientation  $\theta$  must have its amplitude spectrum concentrated about a line through the origin with orientation  $\theta + \pi/2$  in the frequency space. This property can be used to analyze the frequency in the Fourier domain to extract the orientation information.

Filters of arbitrary orientations can be synthesized from the first derivative of the Gaussian [9]. The first derivative of the Gaussian in the x direction is given by

$$G_x = \frac{\partial g(x,y,\sigma)}{\partial x} = \frac{-2x}{4\pi\sigma^4} \exp[-\frac{x^2 + y^2}{2\sigma^2}] \quad (5)$$

The first derivative in the y direction is given by

$$G_y = \frac{\partial g(x, y, \sigma)}{\partial y} = \frac{-2y}{4\pi\sigma^4} \exp\left[-\frac{x^2+y^2}{2\sigma^2}\right] \quad (6)$$

The gradient operator in any arbitrary orientation  $\theta$  can be obtained according to

$$G_\theta = G_x \cos \theta + G_y \sin \theta \quad (7)$$

The filters  $G_x$  and  $G_y$  can be regarded as basis filters as they span the set of all  $G_\theta$  filters. Since convolution is a linear operation, image filtered at any arbitrary orientation  $\theta$  is given by

$$G_\theta * f(x, y) = G_x * f(x, y) \cos \theta + G_y * f(x, y) \sin \theta \quad (8)$$

Oriented energy can be computed by measuring the orientation strength along a particular direction  $\theta$  by combining the responses of quadrature pair filters as indicated by (8). Oriented energies at different  $\theta$  are used to construct Orientation profiles which aid in the orientation analysis.

#### RESULTS

The test images used in the orientation estimation experiment consist of a set of forward looking infrared (FLIR) images containing military tank targets at different orientations. These FLIR images are selected from the Abordean TI image data supplied by the Automatic Target Recognition section of the Avionics Laboratory. All the images in the data set had a very low contrast between target and background. Therefore, as an initial processing step all the images were histogram equalized to enhance the target/background contrast. A subimage consisting of a military tank was extracted from one of the images (AP770) from the preprocessed Abordean data set and used as the model image. The orientation of the target in this model image was assumed to be zero degrees and is shown in Fig. 1. The original image from which the target model was selected was rotated in increments of 10 degrees and subimages containing the target were extracted from the rotated images. These images, along with the model image, were used in the initial orientation estimation simulation experiment. A set of nine images, consisting of the

targets oriented from 10 through 90 degrees at 10 degree intervals, obtained as described above is shown in Fig. 2. Notice that the size of the targets in this set is the same as that in the model image, but differs in orientation and position.

The procedure used to determine the target orientation involves computation of the spectral energy of images containing the target according to (1). Using the histogram enhanced images shown in Figs. 1 and 2, gradient images were generated by applying the Sobel gradient operator. The spectral energy,  $S(\theta)$ , was computed for each of the gradient image, and normalized by representing the minimum and maximum values by 0 and 1, respectively, and linearly scaling all the intermediate values to lie within this range. The normalized spectral energy plot for the model tank image of Fig. 1 is shown in Fig. 3. Since the spectrum of a real image is symmetric about the origin only half the frequency plane needs to be considered. The normalized spectral energy plots obtained as described above for the test images of Fig.2 are shown in Fig. 4.

An estimate of the orientation of the target was obtained by correlating cyclically shifted versions of the model image spectral energy distribution with the spectral energy distribution of the test image. The correlation plots thus obtained for the nine test images of Fig.2 are shown in Fig.5. The orientation of the target can be determined from these plots by locating the angle at which the peak correlation value occurs. It is easily seen from Fig. 5 that, for all the nine test images the correlation peak occurs at or very close to the actual orientation of the target.

The targets in the image set shown in Fig.2 have the same size and aspect angle as the target model, but differs only in orientation and position within the image. The performance of this approach was also determined using another set of images containing targets that differ not only in position and orientation but also in size and aspect angle. These images were also extracted from the Abordean data set. A subset of these images with targets oriented at 30 degrees with reference to the model target



Figure 1. Model tank image ( $0^\circ$  orientation)



(a)  $10^\circ$



(b)  $20^\circ$



(c)  $30^\circ$



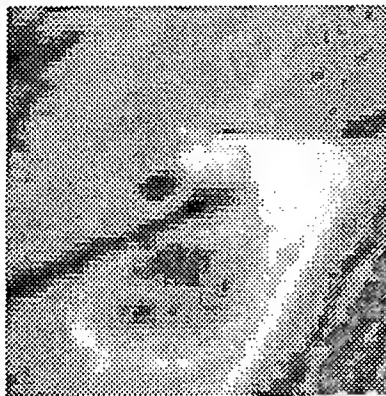
(d)  $40^\circ$

Figure 2. Test images at different orientations





(e)  $50^\circ$



(f)  $60^\circ$



(g)  $70^\circ$



(h)  $80^\circ$



(i)  $90^\circ$

Figure 2. (continued.)

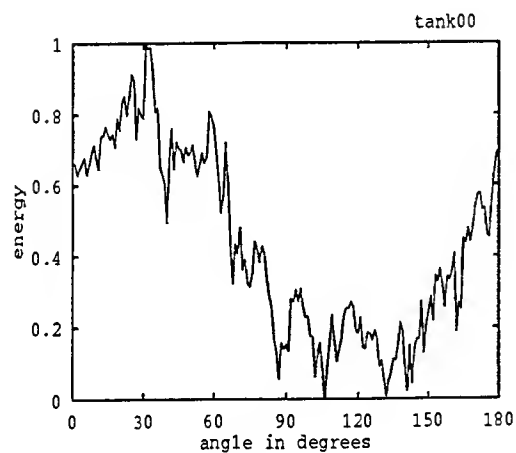
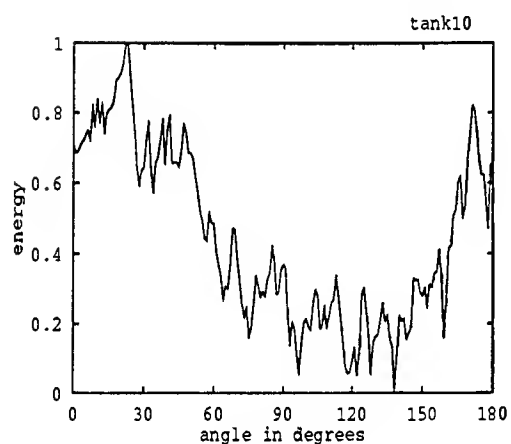
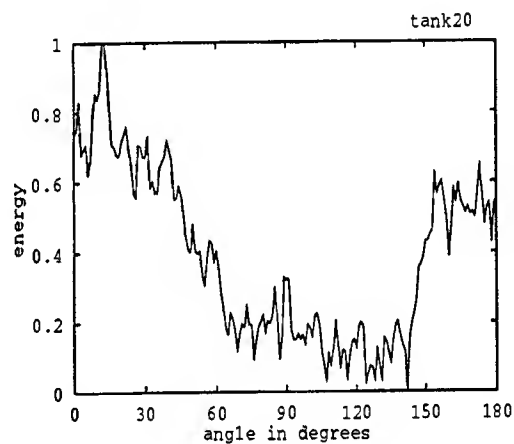


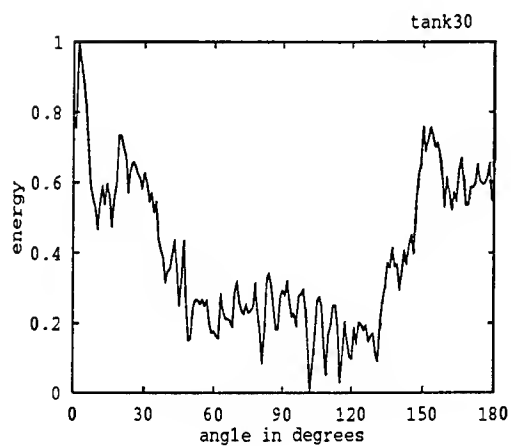
Figure 3. Plot of  $S(\theta)$  for the model tank image.



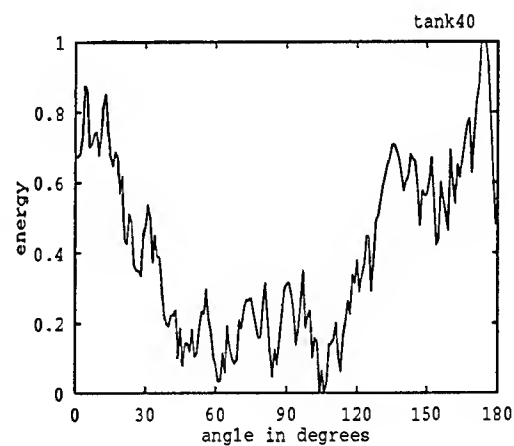
(a)  $10^\circ$



(b)  $20^\circ$

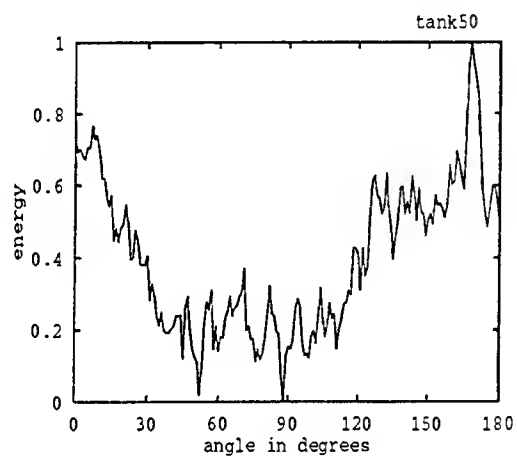


(c)  $30^\circ$

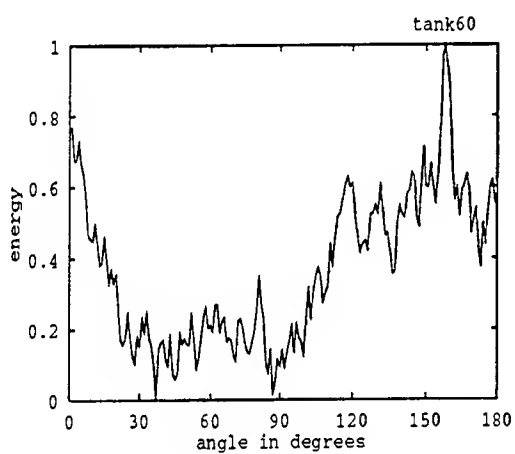


(d)  $40^\circ$

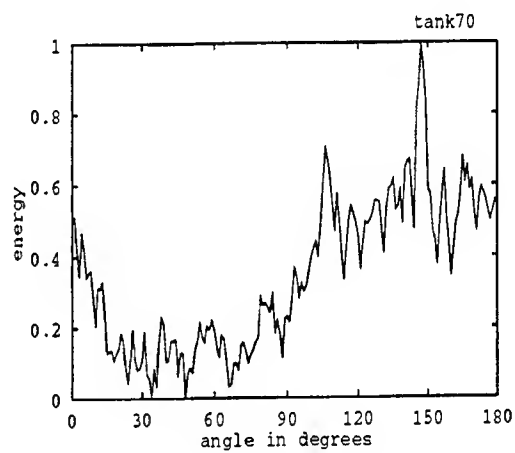
Figure 4. Plot of  $S(\theta)$  for test images.



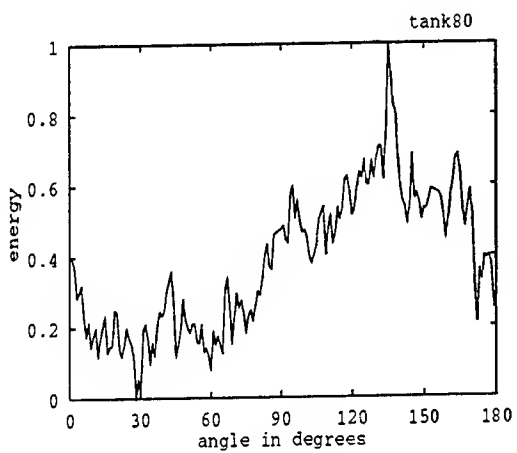
(e)  $50^\circ$



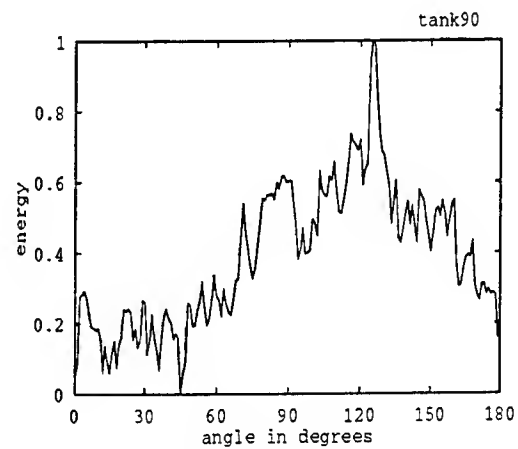
(f)  $60^\circ$



(g)  $70^\circ$

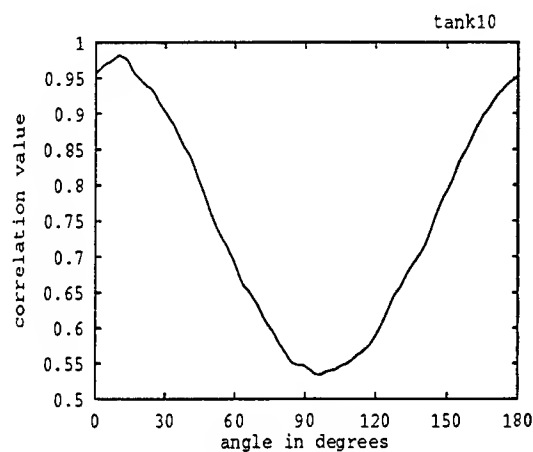


(h)  $80^\circ$

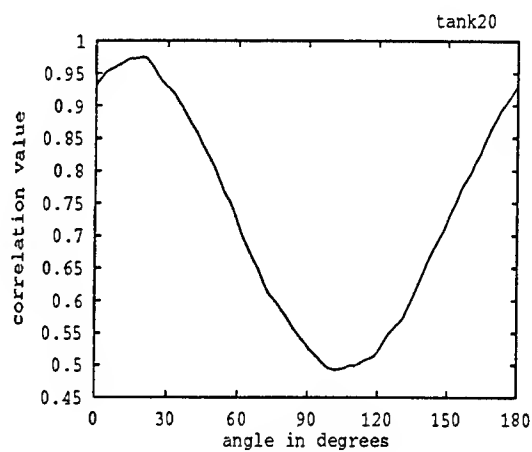


(i)  $90^\circ$

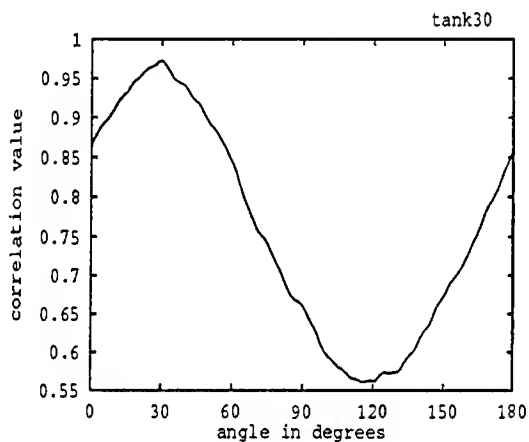
Figure 4. (continued.)



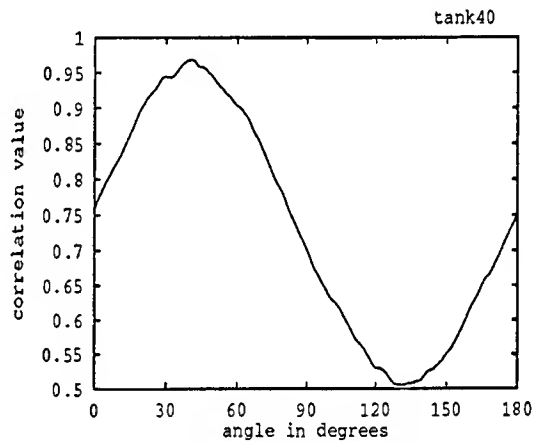
(a)  $10^\circ$



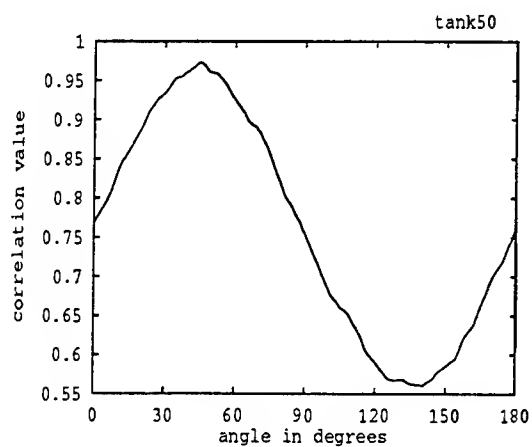
(b)  $20^\circ$



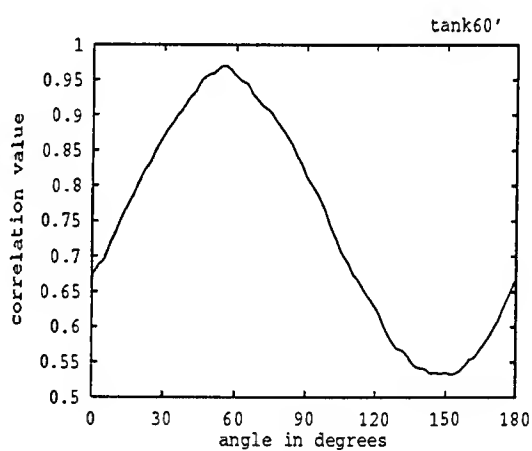
(c)  $30^\circ$



(d)  $40^\circ$



(e)  $50^\circ$



(f)  $60^\circ$

Figure 5. Correlation plots for the test images of Fig. 2.

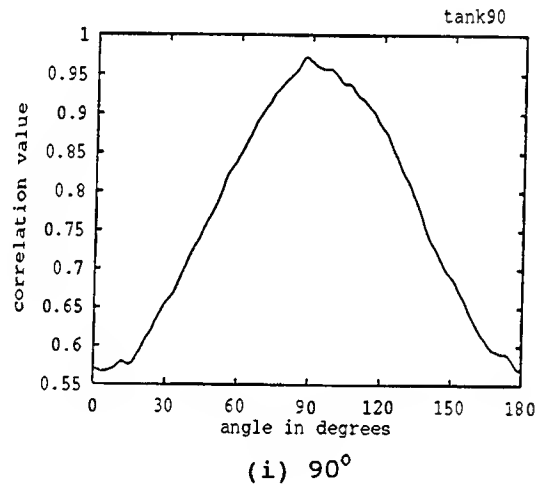
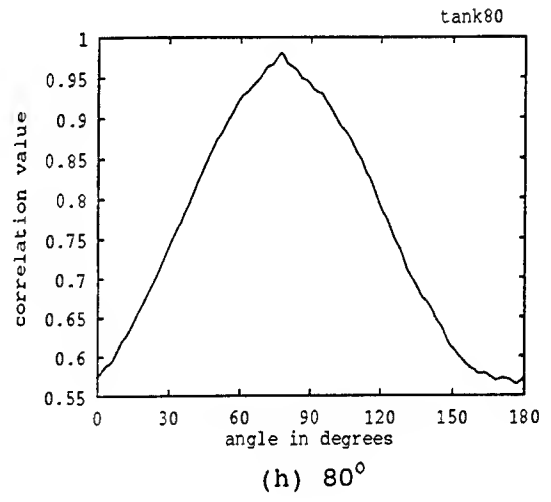
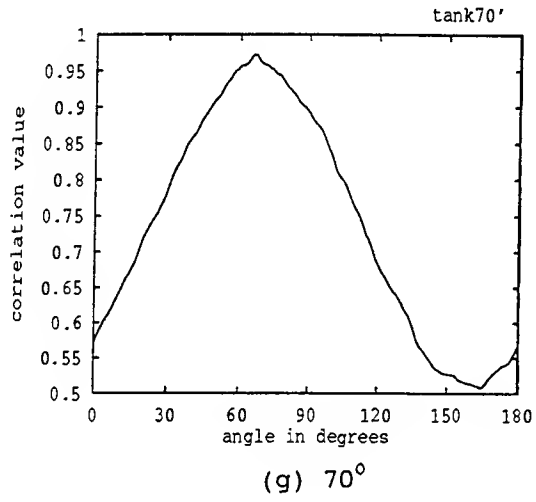


Figure 5. (Continued.)

of Fig. 1 are shown in Fig. 6. The correlation plots obtained, according to the procedure outlined above, for these images are shown in Fig. 7. It is readily seen from these plots that the peak correlation value occurs near  $30^\circ$  angle for all the images, indicating that this approach is fairly robust for the type of images considered.

Simulation experiments were also conducted on test images without computing the Sobel gradient. The orientation estimates obtained were comparable to that obtained when gradient images were used. However, the use of Sobel gradient images resulted in sharper correlation peaks. Further improvement in the orientation estimation accuracy was achieved by using edge images obtained by detecting zero crossings from the images filtered by the LOG operator according to (3). LOG operator masks of size  $11 \times 11$ , obtained by sampling the kernel (4) with filter scale  $\sigma$  ranging from 4.4 to 4.6, were used in the simulation. The performance of this method, however, depends greatly on the size of the LOG operator mask and  $\sigma$  used to generate the edge image. In addition, this technique requires considerable computational resources.

Simulations were also conducted on the test images to determine the orientation by constructing orientation profiles using (8). The orientation profiles of test images were compared with that of the model image to determine a measure of target orientation. Even though the initial results looked promising, they were not fully satisfactory and are not reported.

#### SUMMARY

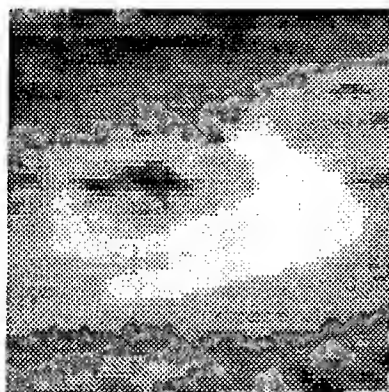
The experiments described above confirm that spectral energy distribution in the Fourier domain can be used successfully in determining the orientation of a known target to a reasonable degree of accuracy. The nonuniqueness of the location of the target, target size, and target aspect angle, causes no significant problems in the determination of orientation. However, the ability of this technique in estimating the orientation independent of target type needs further investigation.



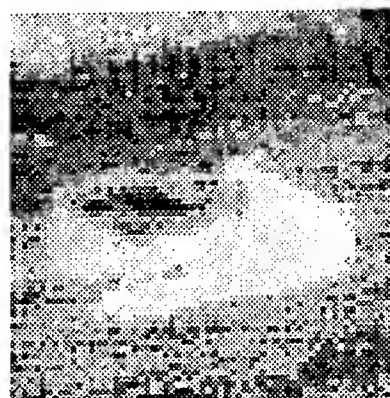
(a) tank830



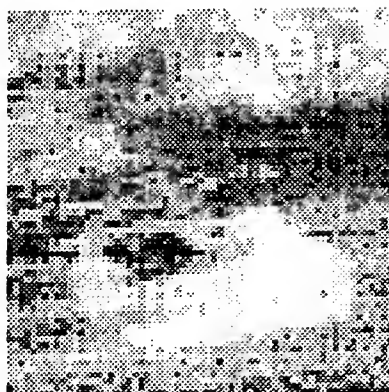
(b) tank930



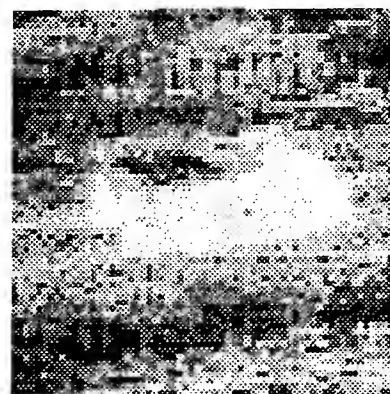
(c) tank990



(d) tank1050



(e) tank1110

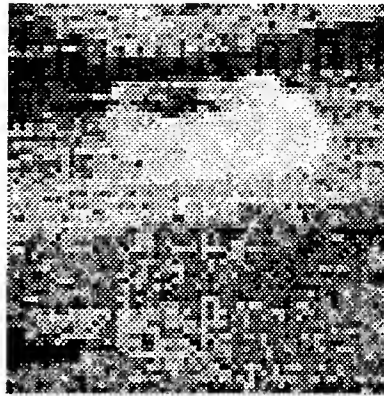


(f) tank1170

Figure 6. Test images with targets at  $30^\circ$  orientation.

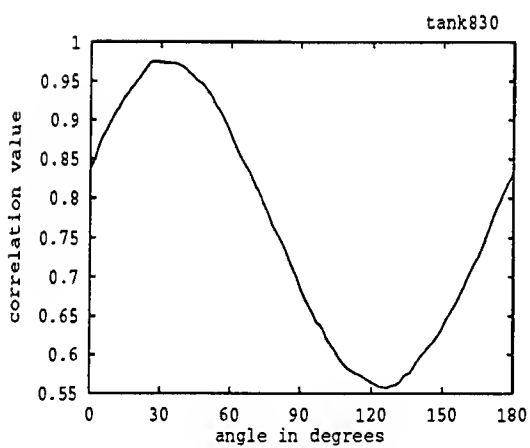


(g) tank1230

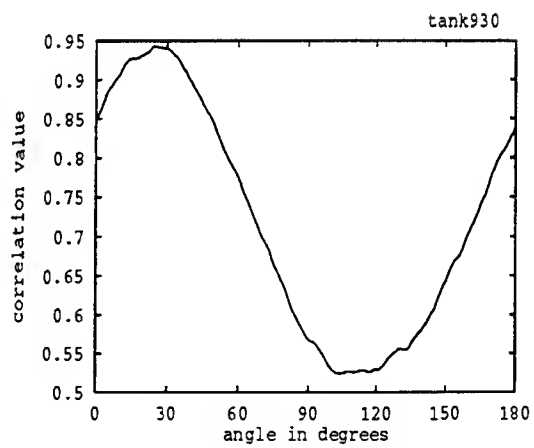


(h) tank1290

Figure 6. (Continued.)



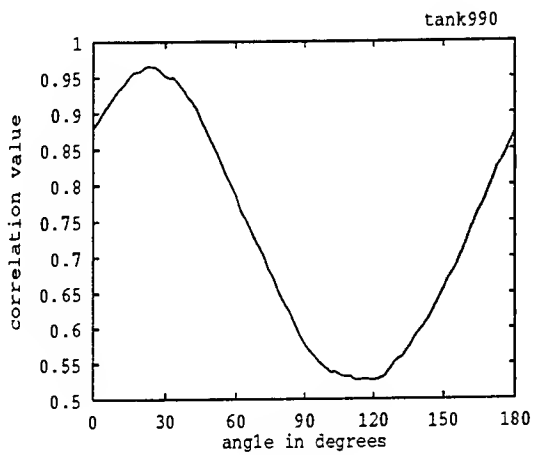
(a)



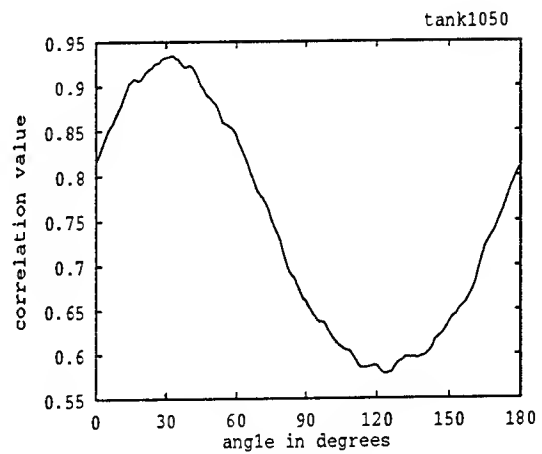
(b)

Figure 7. Correlation plots for images in Fig. 6.

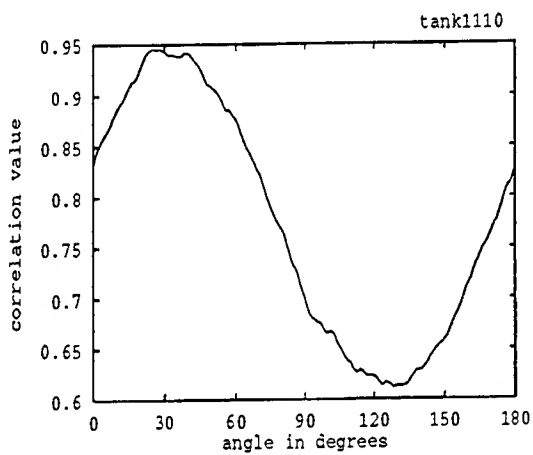




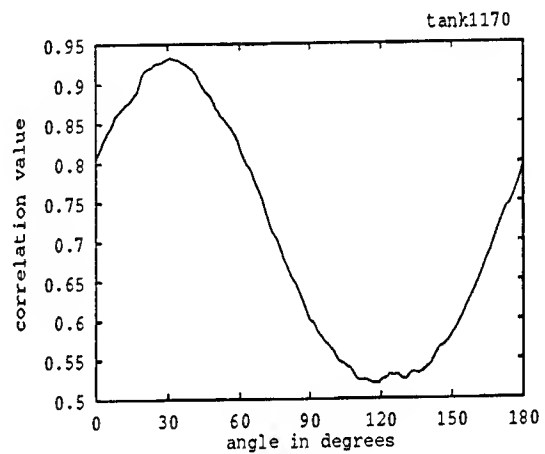
(c)



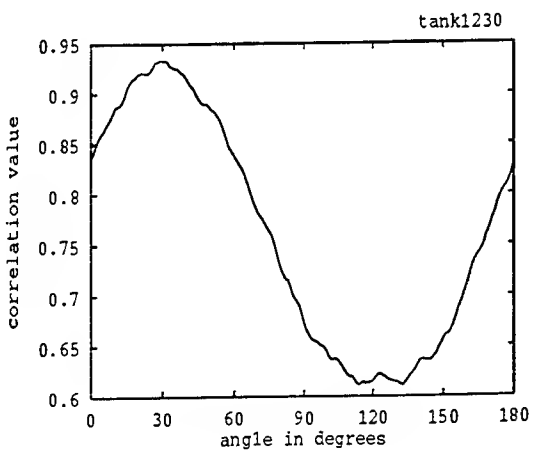
(d)



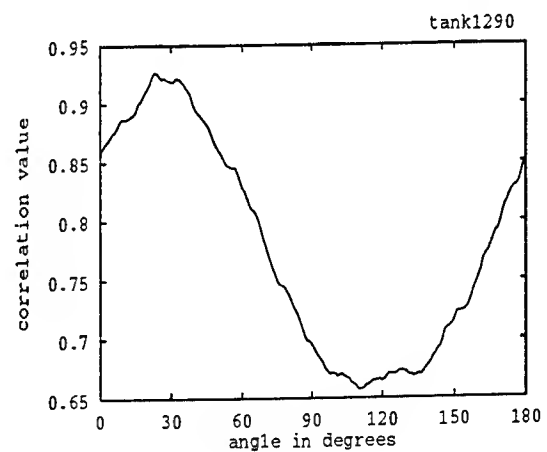
(e)



(f)



(g)



(h)

Figure 7. (Continued.)

Most of the current target recognition systems try to match each database object consisting of all possible rotated positions of a target model against the viewed target in a scene. In order to avoid repeated matching of all database objects against the scene, target orientation information can be used as an index to the database to select only the relevant models for matching purpose. Such an indexing approach can significantly reduce the workload of a target recognition algorithm by focussing only on those poses which are suggested by the orientation estimation algorithm.

#### Acknowledgements

I wish to thank the Air Force Systems Command and the Air Force Office of Scientific Research for sponsorship of this research and the Research Development Laboratories for their concern and help to me in all the administrative and directional aspects of this program. I am sincerely grateful to my Effort Focal Point Mr. Ed Zelnio and Mr. Vince Velten.

#### REFERENCES

- [1] B. Bamieh, and R.J.P. Figueriedo, "A General Moment Invariants-/Attributed-graph Method for Three-Dimensional Object Recognition from a Single Image," IEEE J. Robotics Automation, vol.2, pp. 31-41, Jan 1986.
- [2] R.H. Banberger and M-J. T. Smith, "A Filter Bank for Directional Decomposition of Images: Theory and Design," IEEE Trans. ASSP-40, pp. 882-893, Apr. 1992.
- [3] J. Bigun, G.H. Granlund, and J. Wiklund, "Multidimensional Orientation Estimation with Applications to Texture Analysis and Optical Flow," IEEE Trans. Patt. Anal. Machine Intell., vol. PAMI-13, pp. 775-790, Aug. 1991.
- [4] R.C. Bolles, and P. Horland, "3DPO: A Three Dimensional Part Orientation System," Int. J. Robotics Res., vol. 5, no. 3, pp. 3-26, Fall 1986.
- [5] P. Brou, "Using the Gaussian Image to Find the Orientation of Objects," Int. J. Robotics Res., vol. 3, no. 4, pp. 89-175, 1984.

- [6] H.H. Chen, "Pose Determination from Line-to-Plane Correspondences: Existence Condition and Closed-Form Solutions," IEEE Trans. Patt. Anal. Machine Intell., vol. PAMI-13, pp. 530-541, June 1991.
- [7] D. Cyganski, and J.A. Orr, "Applications of Tensor Theory to Object Recognition and Orientation Determination," IEEE Trans. Patt. Anal. Machine Intell., vol. PAMI-7, pp. 662-673, Nov. 1985.
- [8] D.J. Fleet, and A.D. Jepson, "Hierarchical Construction of Orientation and Velocity Selective Filters," IEEE Trans. Patt. Anal. Machine Intell., vol. PAMI-11, pp. 315-324, March 1989.
- [9] W.T. Freeman, and E.H. Adelson, "The Design and Use of Steerable Filters," IEEE Trans. Patt. Anal. Machine Intell., vol. PAMI-13, pp. 891-906, Sep. 1991.
- [10] W.E.L. Grimson, Object Recognition by Computer: The Role of Geometric Constraints, The MIT Press, Cambridge, Massachusetts, 1990.
- [11] R.M. Haralick, H. Joo, et. al., "Pose Estimation from Corresponding Point Data," IEEE Trans. Syst. Man Cybern., vol. SMC-19, pp. 1426-1446, Nov. 1989.
- [12] J.E. Hopcroft, D.P. Huttenlocher, and P.C. Wayner, "affine Invariants for Model-Based Recognition," in Geometric invariance in Computer Vision, J.L. Mundy, and A. Zisserman (Eds.), MIT Press, Massachusetts, 1992.
- [13] D. Marr and E. Hildreth, "Theory of Edge Detection," Proc. Royal Soc. London, ser. B, vol. 207, pp. 187-217, 1980.
- [14] C.A. Rothwell, A. Zisserman, et. al., "Relative Motion and Pose from Arbitrary Plane Curves," Image and Vision Computing, vol. 10, pp. 250-262, May 1992.
- [15] S. Shekhar, O. Khatib, and M. Shimojo, "Object Localization with Multiple Sensors," Int. J. Robotics Res., vol. 7, no. 6, pp. 34-44, Dec. 1988.
- [16] G.C. stockman and S-W. Chen, "Detecting the Pose of Rigid Objects: a Comparision of Paradigms," Proc. SPIE, Jan 1987.

- [17] R. Wilson, and A.H. Bhalerao, Kernel designs for Efficient Multiresolution Edge Detection and Orientation Estimation, IEEE Trans. Patt. Anal. Machine Intell., vol. PAMI-14, pp. 384-390, March 1992.
- [18] J. S.-C. Yuan, "A General Photogrammetric Method for Determining Object Position and Orientation," IEEE J. Rob. Autom., vol. RA-5, pp. 129-142, Apr. 1989.

SIGNAL PROCESSING  
FOR  
HIGH SPEED VIDEO TECHNOLOGY

Eugene R. Chenette  
Professor  
Department of Electrical Engineering

University of Florida  
Graduate Engineering and Research Center  
Second Street and D Avenue  
Eglin Air Force Base, FL 32542

Final Report for:  
Research Initiation Program  
Wright Laboratories/MNGI

Sponsored by  
Air Force Office of Scientific Research  
Bolling Air Force Base, Washington DC

and

The University of Florida

December 1992

## Signal Processing for High Speed Video Technology

Eugene R. Chenette, Professor  
Department of Electrical Engineering  
University of Florida Graduate Engineering Research Center

### Abstract

The work reported here is concerned with the design of a Test Bed for High Speed Video Technology. Research on signal processing for HSVT, learning to deal with the vast amounts of data has led to the idea that what is really needed is a unique test bed to evaluate the imaging arrays and the necessary support electronics. Hence of this report deals mostly with the design of test bed for HSVT which is being built in the WL/MNGI Special Projects Laboratory at Eglin Air Force Base. This is a versatile system, designed to enable the operation of many different photo imaging arrays; to investigate the performance and limitations of the arrays under a way range of operating conditions; to determine the timing and shape of clock waveforms which yield the highest charge transfer efficiency and the fastest charge transfer rates; to produce video signals with the greatest possible dynamic range and/or signal to noise ratio; to investigate the performance of both analog and digital signal processing systems; to determine the effect of various data compression systems and algorithms on the data; and many other experiments not yet defined. The test bed includes a workstation dedicated to data analysis and the generation of highest quality images, and of course it will include facilities to review video in RS-170 format.

## SIGNAL PROCESSING FOR HIGH SPEED VIDEO TECHNOLOGY

Eugene R. Chenette,

### Introduction:

The greatest barrier to the success of High Speed Video Technology (HSVT) as a tool for scientific and engineering research is also the greatest asset. HSVT will be capable of collecting enormous amounts of information. Storing the data digitally will require very large high speed memories and transmission of the video signals in real time will require very large bandwidths. Memory/bandwidth/ time delay tradeoffs become part of the design problem, a problem which is application and image dependent. Requirements for performance are different for a video system intended to collect data for machine-aided analysis of motion than when the data are to be used primarily to generate images for viewing by humans; they are also different when generating images for precise scientific evaluation than when generating images intended for entertainment.

Figure 1 shows a simplified block diagram of test test bed being developed in the Wright Laboratories/MNGI Special Projects Lab at Eglin Air Force Base. The purpose of this test bed is to evaluate the performance of different components such as focal plane arrays, analog to digital converters, specialized digital signal processing arrays designed to compress the data; to determine the timing and shape of the many signals required to achieve maximum possible signal to noise performance, and to achieve maximum accuracy of the data collected.

It is important to remember, while reading the discussions which follow, that no format or timing standards have been defined for HSVT. The existing ad hoc definition is that HSVT is a video system capable of megapixel resolution with frame rates on the order of 1000 frames per second. Workers at Wright Laboratories/MNGI at Eglin Air Force Base have documented the need for a system with video resolution of at least 1024(H) by 512(V) pixels; a frame rate of 920 frames per second; and exposure time for each frame of not more than 220 microseconds and as short as 100 microseconds. [1,2] While this system cannot be assembled with off-the-shelf components, it provides useful numbers to guide the design of the test bed

The discussion which follows deals briefly with each of the major components of the test bed

### Test Scene and Optics

Accurate measurements of the performance of an imaging array require precise knowledge about the characteristics of the image incident upon the array. To this end the facilities of the test bed include a variety of calibrated optical sources, precision test patterns, and a laser speckle pattern generator to allow testing of the performance of the imaging array, of all other components, and of the total system under a wide variety of operating conditions.

### The Focal Plane Array

The work related to this report has been much more concerned with problems related to enabling the performance of a CCD imaging array and processing the signals which they produce than with the details of the array itself. CCD imaging arrays work and work very well. They have become the imaging element of choice for most high performance professional and industrial video camera. Several laboratories are marketing imaging arrays with much higher resolution than the 1024(H) by 1024(V) pixel array being used in this discussion. For example, the Sony Corporation and the the Toshiba Corporation have announced two million pixel CCD image sensors for HDVT [3, 4]. Kodak markets a still camera with an imaging array of 8 million pixels. Ford-Loral produces a 1024(H) by 1024(V) array which was designed and used originally to be read in 100 milliseconds (to operate at the rate of 10 frames per second with a single video output. This is the array which Bredthauer has modified, converting it to a set of 64 sub-arrays with 64 video outputs [5].

A number of manufacturers are marketing somewhat smaller arrays with multiple outputs. Examples are found in the high speed television camera and video tape recording system for motion analysis reported by Bixby [6]; the EG&G/Reticon MCMC4256 Modlar Matrix Camera which uses a Reticon RA2568N 256x256 pixel photo-diode array with frame rate of 500 frames per second; and the EEV CCD13 VERY HIGH SPEED CCD IMAGE SENSOR.

This brief list is not comprehensive, it's intended only to document that high resolution high performance CCD imaging arrays are readily available. . The use of parallel architecture, arranging the 1024(H) by 1024(V) 1000 frame per second array so that it operates as 64 subarray, reduces the active pixel rate for each output to 16,384,000 pixels per second, a rate comparable to that of standard RS-170 video cameras. This report includes the results of some measurements on the performance of an evaluation system provided by EG&G. The evaluation board includes analog signal processing for all eight ooutputs of the RA2568N photodiode array. The pixel rate of each output is only about five MHz.

Bredthauer has modified the Ford-Loral array and produced and delivered prototype samples which have 64 outputs. Operation of the array requires three phase clock signals to enable both the horizontal and vertical charge transfer systems. Preliminary tests of this array have been made by Dereniak and others [7] and operation of the parallel systems have been verified at low frame rates. Data obtained during those test are used in the discussion which follow.

Figure 2 shows a sketch block diagram of the array. The 1024(H) x 1024(V) array has become a set of 64 sub-arrays, each 32(H) by 512(V). Each of the sub-arrays has a separate output shift register and charge sensing system. All 64 arrays must be clocked synchronously, and the net data output for every frame is a data stream of 512 active lines with 32 active pixels per line, a total of 16,384 pixels per frame. This figure includes several blocks which represent the line drivers required to provide the relatively large signals required to operate the CCD charge transport system. The Ford-Loral array is designed to use three-phase clock signals. The blocks indicate that the total clock load is divided among four sets of vertical drivers, one for each quadrant of the array, and two



sets of horizontal drivers, one to operate the 32 shift registers at the top of the figure and the other to operate the 32 shift registers at the bottom of the figure.

#### Driving the Focal Plane Array

An imaging array is a relatively complex electronic system and requires that operating conditions of a number of elements be accurately controlled by applying some fixed and some time varying signals. Table 1 shows a list of the names of the various parameters which, in addition to clocking signals, must be controlled for a typical large scale array.

**TABLE 1. LIST OF OPERATING VOLTAGES FOR A TYPICAL CCD FPA**

<u>Symbol</u>	<u>Description</u>	<u>Typical value</u>
$V_{SS}$	Substrate	0 (Adjust to control dark current)
$V_{OG}$	Output Gate	-1 to 2 volts
$V_{CS}$	Current Source	$V_{SS}+1$
$V_{RD}$	Reset Drain	13 to 16 volts
$V_{DD}$	First stage Drain	18.5 to 20 volts
$V_{OD}$	Output Drain	20 volts
$V_{BLD}$	Antiblooming Drain	20 volts
$V_{BLG}$	Antiblooming Gate	-4 to 10 volts
$V_{SSF}$	Source bias on Source Follower	4 volts
$V_{GSF}$	Gate bias on Source Follower	3 volts
$V_{CLOCK}$	Clock voltage waveforms (Horizontal and Vertical Transfers)	Peak to peak, 10 to 20 volts Offset -10 to zero volts.
$V_{HB}$	Horizontal blanking	
$V_{VB}$	Vertical blanking	

The most challenging and most interesting problem is that of providing the signals required to enable operation of the various transfer shift registers. Details of this problem depend upon the characteristics of the imaging array, but principles can be illustrated by investigating the performance of a generic system. Here it's convenient to use numbers which were obtained from an early prototype of the Ford-Loral array, and to use that array as the generic example.

Figure 3 shows a set of timing diagrams for clock signals which could be used to enable the operation of this array at the rate of 1000 frames per second. Many arbitrary decisions were made in drawing these diagrams, and they are presented here with some misgivings. Some of the most experiments made possible by the Test Bed will have to do with investigating the effect of clock parameters (timing, voltage and current waveforms, etc.) on the performance of various imaging arrays

The diagrams of Figure 3 show the period of the horizontal transfer clock to be 42 nanoseconds and the period for every vertical transfer to be 168 microseconds. Each horizontal line includes a "four pixel equivalent" inactive period, the time required allowed for clocking the vertical array. Thus the time required for each horizontal line is  $36 \times 42 \text{ nanoseconds} = 1.512 \text{ microseconds}$  and the active video period for every frame is  $512 \times 1.512 \text{ microseconds} = 774 \text{ microseconds}$ . With this scheme 226 microseconds are available every millisecond for resetting the array and collecting photo-generated charge. This is equivalent to choosing a pixel clock frequency of 23.8 megaHertz. The result is a sampled data system with the Nyquist limit of 11.9 megaHertz corresponding to the optical spatial Nyquist frequency of 512 line pairs per optical image (alternating dark and illuminated pixels). The shape of the clock voltage pulses was chosen so that only one of the three phase voltages is changing, rising or falling, at any instant and so that one phase is always changing. Rising and falling slew rates are identical. This allows the smallest possible slew rate for a given clock period and also assure that time varying fields produced by these clock signals within the array are always pointed in the direction required for optimum performance.

Figure 4 shows a block diagram of the system which will be used to generate and control the clock pulses and the many other signals needed to enable the operation of the test bed. The frequency of operation is controlled by a single standard frequency generator. The patterns of waveforms for the various clocks, for electronic control of exposure, and for setting and resetting all the other components which must be synchronously timed come from the 100 MHz pattern generators of the Tektronix Model 9200 Data Acquisition System. A flexible, easily programmed, stable and precise pattern generator is essential to the success of the test bed.

It is likely that the drivers for the interface between the clock control waveforms and the imaging array will be designed and built in the WL/MNGI Special Projects Laboratory. Figure 5 shows the schematic diagram of a "brute force driver" which is being investigated. The merit of the "brute force driver" is that it allows independent control of the driving currents and the peak voltages applied to the imaging array clock lines. The "brute force driver" is intended only for lab use.

The "brute force driver" has a constant current bipolar junction transistor output driving the clock line load which can be represented as an equivalent lumped capacitance,  $C_L$ . The merit of this driver becomes apparent when the clock voltage and current waveforms it delivers are compared with those of an ideal CMOS driver. Figure 6 shows the results of that comparison. The circuits are both generic, using ideal BJT and CMOS device characteristics. Circuit parameters were adjusted to yield almost identical output voltage waveforms. Special attention was given to the times required for the voltage transitions. The peak current required from the BJT driver is much lower than that required from the CMOS driver. What's important about the test bed approach is that it will allow comparison of the effects that the performance of different kinds of drivers have on the performance of the imaging array. Keeping peak currents as small as possible can play an important part in controlling the dissipation of electrical energy in the array.

Figure 7 shows a lumped constant equivalent circuit a set of three phase clock lines for vertical transfer. The numerical values for the capacitors come from the results of measurements on an early prototype of the the Ford-Loral high speed array, and they represent one quadrant of the array.  $C_{12} = C_{23} = C_{31} = 1966 \text{ pF}$

represents the total capacitance between each pair of lines, and  $C_1 = C_2 = C_3 = 393$  pF represents the total pixel charging capacitance seen by each line. Here it has been assumed that drivers are arranged as shown in Figure 2, one for each phase for each quadrant of the array. Two drivers provides drive for 512 sets of lines crossing 1024 pixels. Because of symmetry each line is driven simultaneously from both ends. Hence, each driver delivers current to 512 lines with 512 pixels per line.

The circuit of Figure 7 shows a lumped equivalent resistance,  $r_1$ , in each line and another lumped equivalent resistance,  $r_2$ , in series with each of the  $C'_1$ 's. No values are given for these resistors here because, if the system is going to work, these resistors must be very small. In particular all time constants associated with  $r_1$  and  $r_2$  must be short with respect to risetimes of the clocking voltage waveforms. Volt drops across these resistors must be small with respect to peak clocking voltages.

Also shown on Figure 7 are the set of waveforms of the line currents which result when the voltage waveforms shown below are applied. Note again that the timing and shape of these waveforms were carefully chosen so that only one clock voltage is changing at any one time, that one is always changing. and also so that the sum of all three clock rise times and fall times are equal to the clock period. This results in the lowest peak and average currents for a fixed period and voltage change. One of the voltage waveforms and one of the current waveforms have been emphasized in Figure 7 to help make it possible to interpret the total display. Note the peak value of the current is about 1.6 Amperes. Note that the peak value of the current for each of the line drivers is given by the expression

$$i_{PEAK} = (C_1 + C_{12} + C_{23}) * dV/dt \\ = 4.325nF * (10/28nSec) = 1.54 \text{ Amperes}$$

and the current during other intervals, due to parasitic current through interline capacitance is

$$i_{min} = C_{12} * dV/dt = 1.966nF * (10/28nSec) = .702 \text{ Amperes.}$$

Thus the average current required by the three drivers during a 168 nanosecond clocking period is  $(1.54 + 2*.702)/2 = 1.472$  Amperes.

#### Power requirements for Clocking A Typical Focal plane Array.

Consider first the problem of providing drivers for the horizontal output registers. The clock operates continuously with a clock period of 42 nanoseconds or, equivalently, a clock frequency of 23.8 MegaHertz. clocking a total of  $32 \times 36 = 1152$  horizontal transfer pixels in the in the 32 horizontal output registers at the top of the array and another 1152 pixels in the horizontal shift registers at the bottom of the array. The pixels of the horizontal shift registers are somewhat larger than those of the active photo-array itself. Assume the capacitance per pixel per phase is 3 fF. The equivalent capacitance of 1152 pixels is 3.5pF. The parasitic capacitance of the thin film metal lines connecting the pixels to the external world is probably several times this total. For now, until better data are available, a conservative estimate is that the total load seen by the horizontal shift register drivers is about 25 pF for each phase at the top of the array and another 25 pF for the bottom. The energy required from the power supply, delivered to the horizontal driver for the top half array and again for the bottom half array, for each ten volt clock pulse operation will be  $W_H = C_{eq} V^2$  or

$$W_H = 25 \times 10^{-12} \times 10^2 = 25 \times 10^{-10} \text{ Joules / cycle}$$

Repeating this operation 23,800,000 times a second requires that both drivers dissipate

$$P_H = 25 \times 10^{-10} \times 23.8 \times 10^6 = 59.5 \text{ milliwatts per phase.}$$

The power dissipated in the FPA because of  $i^2 R$  heating will be much less.

The total energy required from a ten volt power supply to enable the operation of a set of three drivers can be estimated because we know the current averages 1.472 amperes for 168 nanoseconds. The total energy required per transfer is

$$W_V = 1.472 \times 168 \times 10^{-9} \times 10 = 2.73 \times 10^{-6} \text{ joules per cycles}$$

and the average power dissipated by each set of drivers is

$$P_V = 2 \times 2.73 \times 10^{-6} \times 512 \times 10^5 = 2.8 \text{ watts.}$$

Four sets of drivers dissipating this power, one for each quadrant, are required. Hence the total power which will be dissipated in vertical drivers is

$$P_{TOTAL} = 4 \times 2.8 = 10.6 \text{ watts.}$$

The numbers used in the discussion above are approximate, but they give useful insight into the problem of designing the clock drivers for a focal plane array. Note that all real drivers will have some minimum voltage drop across the driver itself while delivering current. The sum of supply voltages required will always be greater than the peak to peak value of the clock waveform. The results of the calculations above are the absolute minimums required to enable operation of the array under discussion at the rate being considered.

Providing clock drivers for the test bed in the laboratory is relatively straightforward. The "brute force line driver" is suitable for use in the test bed, but the design problem will become considerably more challenging when the designer is faced with the constraints of high efficiency as required for an HSVT camera for field use.

Accurate estimates of the power which would be dissipated in the focal plane itself required accurate information about loss in the focal plane and in the clocking lines themselves, about the values of  $r_1$  and  $r_2$  in Figure 7. Equally important is the problem of possible thermal coupling between the drivers and the focal plane array. The electrical performance required makes it necessary that drivers be mounted very close to the focal plane array. In the limiting case CMOS drivers could be integrated in the same silicon crystal used for the array. And that must be the worst case thermal problem because then the power dissipated by the drivers would be dissipated in the same silicon wafer as the imaging array.

An important thing to remember when considering power dissipation problems is that there are many occasions when high speed video systems will operate for only very short periods of time. For example the EG&G Modular Matrix Camera mentioned earlier is designed to collect video for 128 frame (about .25 seconds), 256 frames (about .5 second) or for 1024 frames (about 2 seconds).

### Analog Signal Processing:

Video signals from a CCD focal plane array are buried in noise. Fortunately the sources of noise are well understood and techniques for extracting the signals from noise are well established. [8] Some of the cameras which have been investigated (such as the Pulnix Model TM-7) use correlated double sampling.

The operation of the correlated double sampler (CDS) is equivalent to subtracting the instantaneous values of noise at time  $nT$  and  $n(T-T/2)$ . The overall effect is represented by the transfer function

$$H_{CDS} = 1 - z^{-(1/2)}. \text{ In the frequency domain this reduces to}$$
$$H_{CDS}(e^{j\omega T}) = 1 - e^{-j(\omega T/2)} = e^{-j(\omega T/4)} 2j \sin(\omega T/4).$$

What's important here is that the use of a sampling system to extract signals from the noise not only solves the low frequency clock noise and  $1/f$  noise problems but also limits the performance at high frequencies since the transfer function goes to zero when  $(\omega T/4) = \pi$ . Note that for a CDS taking one sample per pixel this  $T$  corresponds to two pixel periods, and the first null occurs at the Nyquist frequency for the clock (which corresponds to the spatial Nyquist frequency of the array.)

Analog signal processing includes conditioning the video signal available from the output of the CDS or a gated integrator and adjusting the dc level and peak to peak amplitude of the signal to that required by the analog to digital converter.

### Analog to Digital Data Conversion:

One of the goals for the ultimate HSVT system is that the dynamic range or signal to noise performance be the maximum possible. The signal to quantizing noise ratio of an A/D converter is given by the expression

$$SNR = 6.02N + 1.76 \text{ db.}$$

Many existing video cameras use imaging arrays with dynamic range on the order of 50 decibels. Eight bit A/D converters are adequate. Video images with an eight bit gray scale are acceptable for many applications.

Here we come to an interesting problem. Many people are working to improve silicon technology, to improve the performance of electronic devices as evaluated by any and all measures. The performance of CCD imaging arrays is improving. Measurements made during the course of this work have shown that even the simplest, lowest cost arrays, such as the Sony array used in the Pulnix TM-7 camera, yield signal to noise performance of more than 60 db over a wide range of operating conditions. This dynamic range suggests the use of a ten bit A/D converter, and hence we have been investigating the performance of high speed 10 bit A/D converters. Some laboratories are reporting high resolution high speed arrays with signal to noise performance greater than 72 db (such as that of the Toshiba array mentioned earlier). Hence the plan that the test bed be designed to accommodate A/D converters with word lengths of at least twelve bits.

The test bed will help answer the question, "Is the additional information collected by using a twelve bit system worth the cost? Right now we think the answer is "Yes!" This problem will be discussed in more detail in the section on memory below, but recognize that increasing the resolution from 8 bits to twelve bits per word will increase memory requirements by 50 %, from 1 million to 1.5 million bytes for every million pixel frame of data.

Figure 8 shows the block diagrams of the systems used for preliminary measurements of the operation and dynamic range of an ADC 9060 and an SPT 7814 high speed 10 bit AD converter. Within the experimental error of the instruments used, the performance of the two units, mounted on evaluation boards provided by the manufacturers, was identical. Signal to noise performance was measured with clock frequencies ranging from 3 MHz to 40 MHz. Figure 9 shows the spectrum of a signal and the noise of a typical recovered signal as obtained with the system shown in Figure 8a. Here the frequency of the input signal was set to 10 kHz and the peak to peak amplitude was adjusted to be exactly 4 volts, the maximum amplitude limitation for the SPT 7814. The magnitude of the signal at the output is, as expected, about 60 db above the noise floor.

Figure 9 was derived from measurements of the small signal gain of the A/D system as a function of the frequency of the input signal. The noise floor remains constant, and the result of frequency dependence of the gain is well represented as a reduction in the Equivalent Number of Bits (ENOB). The performance of both converters tested is consistent with this result. An A/D converter which produces accurate 10 bit data for low frequency signals produces "eight-bit resolution" when the input signal is a 10 MHz sinusoid.

#### Memory Requirements

The greatest barrier that stands in the way of practical HSVT is the memory (and bandwidth) requirement. Each frame of the proposed FPA contains one million picture elements. Information about the photo-generated charge of each picture element must be represented digitally. As mentioned above there is still some question about the resolution required, but the SNR of the FPA itself suggests the use of 12 bit words. Then the memory required for every frame would be  $1024 \times 1024 \times 1.5 = 1,572,864$  bytes per frame. With 64-channel parallel architecture memory required for each of the 64 parallel channels is reduced to only 24,576 bytes per frame or to 24.6 Megabytes per channel for every second (1000 frames) of operation. The total system, 64 channels, requires almost 1.6 Gigabytes of memory for every second of operation at the 1000 frame per second rate.

One approach to the memory problem was suggested by representative of DATARAM, a manufacturer of large high speed memories. They suggested the architecture shown in Figure 11. The interface blocks on the left side of Figure 11 accept data from 8 sub-array ADCs. The 20-bit width of the eight input paths are the result of a 2-1 de-multiplexer on the output of each sub-array ADC. The total system requires eight of these interface blocks and eight DATARAM WI-508 memories. A single host adapter module would allow communication with all the memories and access to all the data.

The maximum continuous data collection time with this architecture is a function of the amount of memory in each chassis. The largest, based on the use of 4 Mbit DRAMS, with a total memory of 2.56 GB per chassis, would allow maximum collection time of 8.92 seconds. The smallest system discussed with representatives from DATARAM was based on memory array cards using 1 Mbit DRAMS, 320 MB per chassis, and the maximum recording time would then be 1.024 seconds.

Many important experiments to be performed on the test bed are not memory intensive, and the immediate plan is to move ahead with much smaller memories. Many useful experiments can be performed on the output of a single sub-array, and for such experiments memory requirements are relatively modest.

#### Data Compression and Decompression

We come now to the topic which is the central focus of the research of this project, signal processing for the purpose of data compression. Efficient use of data compression is critical to the success of HSVT. This test bed will provide a realistic environment for investigating the performance of signal processing components and algorithms.

Workers at the NASA Space Engineering Research Center at the University of Idaho, working in cooperation with people from Jet Propulsion Laboratories and the Goddard Space Flight Center have developed, manufactured, and delivered a high performance lossless encoder/decoder chip set; a CMOS implementation of Rice Algorithms for lossless compression of digital data. [9, 10, 11] Testing the performance of this chip set is one of the highest priority projects related to the test bed. Design and construction of the electronics required to enable operation of the chip set has been postponed because of work on other phases of this big project, but this goal continues to be of great importance. NASA is moving ahead with plans to implement the use of this chip set in a lossless data compression module in an orbiting video system. [12] Data from typical NASA scenes have been compressed, typically, by ratios as high as 3:1 and compression ratios as high as 7:1 have been reported for high entropy images.

What's important is to evaluate the performance of the encoder with images typical of those of interest to the WL/MNGI scientific and engineering community. The discussion which follows is based upon information found in the "Preliminary Product Specification" for the MRC Universal Source Encoder (USE). The USE can accept image data quantized from 4 to 14 bits per pixel and compresses data by encoding the difference between a predicted pixel and the present pixel. Differences are mapped to a positive integer before being sent to the Rice 12-option entropy coder.

The USE is designed to accept data in blocks that correspond to a continuous string of pixels, and each block is made up of 16 pixels. A reference pixel must be included at the start of a set of blocks of data. A reference pixel is an N bit word of raw data on which succeeding pixel differences are based. Note that references are needed by the Decoder to recover the differenced pixels. The default reference is the word corresponding to the data of the first pixel of a block. When using default prediction, the USE requires that the user/programmer determine how often to insert references. The rate can be varied over the range from one reference per block to one reference every 128 blocks, which corresponds to one reference every 2048 samples. A common choice when dealing with data from RS-170 video is to use one reference per line, typically one reference per 48 blocks (16 pixels per block) of a 768 pixel line. For the HSVT 32(H) x 512(V) sub-array it's reasonable to use one reference

for every 64 blocks (1024 pixels, 32 lines) or for every 128 blocks (2048 pixels, 64 lines). The first choice would give 16 and the second would give 8 reference pixels per sub-array frame.

Output data from the encoder is delivered in a block of 16 bit parallel words. The first word, a header, provides information for a packetizer and is removed from the data stream before the coded block is sent to memory. Data are always sent in the following order:

1. Header word,
2. ID bits,
3. Reference word (if needed),
4. Fundamental sequence data (or default data), and
5. Concatenated k least-significant bits (if present).

Here is an example of a 16 bit header word. [ 0000,000,1,00101110 ]. Commas have been inserted as an aid in recognizing the various components. The first four digits (most significant bits) are the 4 bit ID. They also carry the information that option psi1,0 [0000] was the one of twelve possible options of the Rice algorithm which was selected because it yielded the coded sequence with the lowest bit count. The next three digits [000] are unused bits. Then comes the reference bit [1]. This is [1] if the data stream includes a reference word and is [0] if no reference word is included. The last eight bits [00101110] give the total bit count required to deliver the coded output data.

Table 2 shows an example of a block of pixel data which would produce the above header word. Here, for convenience, base 10 numbers are used for pixel data and for the difference between adjacent pixels. Sigma, a value generated as part of the encoding process, is given in both decimal and binary representation.

Table 2: Pixel data, deltas, sigma data, and resulting code for a "first block which includes a reference pixel."

<u>Pixel</u>	<u>Value</u>	<u>delta</u>	<u>sigma</u>	<u>binary sigma</u>	<u>Coded</u>
1	455	--	--	0111000111	Reference
2	455	0	0	0000000000	1
3	456	1	2	0000000010	001
4	453	-3	5	0000000101	000001
5	454	1	2	0000000010	001
6	454	0	0	0000000000	1
7	454	0	0	0000000000	1
8	454	0	0	0000000000	1
9	455	1	2	0000000010	001
10	455	0	0	0000000000	1
11	455	0	0	0000000000	1
12	454	-1	1	0000000001	01
13	453	-1	1	0000000001	01
14	453	0	0	0000000000	1
15	453	0	0	0000000000	1
16	453	0	0	0000000000	1



Table 3: Coded output data for the input block shown in Table 2.

0000,000,1,00101010	Header word: ID=0, Refbit=1, Count=42
0000,0111000111,1,0	ID, Reference word, Begin FS data
01,000001,001,1,1,1,00	Fundamental sequence data
1,1,1,01,01,1,1,1,xxxxxx	Fundamental sequence data, x's are fill.

The example of Tables 2 and 3 shows lossless compression of the data of a stream of sixteen 10 bit words into an output block of 42 bits, arranged in three 16 bit words with six fill bits added to the third word. Tables 4 and 5 show an example with lossless compression of a similar stream of sixteen 10 bit input words yielding an output stream of 84 data bits plus 12 fill bits arranged in six 16 bit words.

Table 4: Pixel data and mapped data for a second block of data.

Here the bits are split with k=3 which corresponds to "option Psi1,3."

<u>Pixel</u>	<u>Value</u>	<u>delta</u>	<u>sigma</u>	<u>(N-k)bits</u>	<u>kbits</u>	<u>Coded (N-k)bits</u>
17	437	-16	31	0000011111	111	0001
18	444	7	14	0000001110	110	01
19	463	19	39	0000100110	110	00001
20	458	-5	9	0000001001	001	01
21	458	0	0	0000000000	000	1
22	456	-2	3	0000000011	011	1
23	464	8	16	0000010000	000	001
24	463	-1	1	0000000001	001	1
25	460	-3	5	0000000101	101	1
26	459	-1	1	0000000001	001	1
27	448	-11	21	0000010101	101	001
28	447	-1	1	0000000	001	1
29	459	12	24	0000011	000	0001
30	459	0	0	0000000000	000	1
31	460	1	2	0000000010	010	1
32	460	0	0	0000000000	000	1

Table 5: Output data for block two, The N-k sigma bits are coded and the k bits are concatenated. Total length of the data stream is 84 bits.

0011,000,0,01010100	Header word: ID=3, Refbit=0, Count=84
0011,0001,01,00001,0	ID, Begin FS data
1,1,1,001,1,1,1,001,1,000	Fundamental sequence data
1,1,1,1,111,110,110,001,	FS data; begin k bits, k=3
000,011,000,001,101,0	kbits
01,101,001,000,000,01	kbits
0,000,xxxxxxxxxxxxx	end of kbits followed by fill (x=fill=0)

Note that the shortest possible output data stream which would be produced by a block of sixteen pixels with identical values would be 20 bits; the 4 bit ID plus one [1] for each of the sixteen pixels. The longest possible output data stream (with N=10) would be 164 bits, the default when all options fail to reduce the length of the stream below that of the input.

Figure 12 shows a block diagram of the encoder system. Figure 13a shows the timing required from various signals to begin operation of the encoder, and Figure 13b shows a sketch of the relative timings of input and output data blocks and illustrates the 64 clock cycle latency of the encoder. All input and output data delays are referenced to the rising edge of the clock.

Initialization is accomplished by holding Reset low for a minimum of nine clock cycles. The input control signals (N, ExtPre, and InRef) must be present one clock cycle before Reset goes high and must remain stable for two clock cycles following Reset. The encoder must be reinitialized to change input control settings. The ValBlk signal accompanies input data. It must be low during initialization and may go high with the first byte of pixel data after the rising edge of the second clock pulse following Reset going high. Data are then accepted and processed every clock period.

There is no handshaking at the output. The BlkRdy signal goes high when the header for a new block arrives at the output. BlkRdy is the signal to the system at the output of the encoder that it must be accepting data. Each output data transfer takes 1 clock cycle and each 16 bit output word is sent on consecutive clock cycles until the entire block is output. BlkRdy goes low when the last data word (for a block) is at the output and remains low until the header word for the next block is at the output.

Figure 14a shows a block diagram of the decoder, and Figure 15a shows the input/output interface. The various terms are defined on Figure 14. Although the Encoder puts out data in 16 bit words, the Decoder accepts data only in 8 bit words. The solution to this problem is illustrated in Figure 15b. Each 16 bit word of Encoder output is accepted as two 8 bit words by the Decoder; the Encoder's most significant byte becomes the leading word, and the Least-significant byte becomes the immediately following word.

Consider an example of operation of Decoder. Control settings are as follows:

N	10	Bits per sample
ExtPre	Low	Use default nearest neighbor prediction
InRef	4	Insert reference every 4 blocks or 64 samples
BlkPac	4	Blocks per packet
PacMod High		Input data is grouped into packets
Clock	20MHz	Data at rates up to 10 Megasamples/second.

The Decoder has been initialized and is waiting for data: DatReq signal high. When the FIFO is not empty it will assert Nempty high. Note that because PacMod is set to packet data, both Nempty and ValPac must be high for the Decoder to receive compressed data. When ValPac goes high the Decoder will latch in the value at the BlkPac input. BlkPac may change between packets but in this example BlkPac is set to 4--the same setting as InRef.

The first byte the Decoder reads from the FIFO is an ID followed by the 4 most significant bytes of the first 10 bit reference. Each FIFO read takes one clock cycle. The second byte the Decoder reads contains the six

remaining bit of the reference plus two bit of encoded data. The input section of the Decoder continues reading until it fills up its internal FIFO at which time the DatReq signal will go low.

When the Decoder's input FIFO begins to fill with data, the internal decoding section reads and decodes the ID bits, and the strips off the Reference bits. If the ID signifies that the block is default data (sigma data), the bit stream is parsed and the 10 bit sigma data is unmapped and sent to the output.

If the ID specifies that the Fundamental Sequence option with  $k=3$  is the winner, the decoding logic will begin decoding 15 samples. (For a block with reference there are 15 samples to be decoded. When references are not present, there are 16 samples to decode.) The  $k=3$  signifies that the Encoder stripped off the 3 least significant bits from every sigma value and sent them following the coded 7 coded most-significant bit of each sample. The Decoder must first decode the 15 (or 16) samples and then match the least significant bits with the corresponding samples. Complete samples, matched with their least-significant bits, are referred to as sigma values. Each sigma value must be unmapped and then added to the predicted value to obtain the original pixel data.

When the block of data is decoded and ready to be output, the first word will be sent to the output register, accompanied by the BlkRdy signal going high. Because the first block contains a reference the Ref signal will go high for the first clock period that BlkRdy is high. The block of 16 pixels words will be output on the rising edge of 16 consecutive clock pulses. BlkRdy goes low for a period of 10 to 16 clock periods following the last pixel of every block.

The output section of the Decoder outputs 14 bit words. If N is less than 14 the unused most significant bits are filled with zeros. The interface between the Decoder and the memory of the following system must be designed to strip these unneeded leading bits.

Figure 16 shows a more detailed block diagram of the total encoding/decoding system with separate control of the encoding and decoding process. The purpose of encoding is to achieve the efficient storage of noiseless data. Here decoding is considered to be part of the process of image generation or part of the process of producing an array of data which is a noiseless representation of the data originally generated by the focal plane array. Encoding must take place at a rate determined by the pixel rate of the sub-arrays of the focal plane. Decoding can take place at a rate convenient for restoring data to the form required for the image memory. The practical solution to the need for image memory is to use, for that purpose, the memory of one of several commercially available image-processing boards. (Consider, for example, the Imaging Technology Model Visionplus-AT VEG, 1024 x 1024 variable scan frame grabber.)

This report does not include a discussion of the theory of operation of the NASA encoder/ decoder chip set. That information is available in the references as is a comparison of the performance of this chip set with that of Huffman coding. [11] The compression ratio is comparable to that of Huffman coding, and the chip is arithmetically much more efficient.

Lossy compression opens another world. Great progress is being made in lossy compression of digital video. [13] Mellott, Smith, and Taylor have developed a new approach to data compression using wavelets [14]. The only information available at this time is that, although the system is technically "lossy" there is no corruption

of spatial resolution and the system yields compression ratios as high as 50:1 for a wide range of entropies. [15] Other workers have also reported on the development of wavelet-based algorithms for data compression and investigating the performance of chip-sets using these algorithms must be an important topic for future work. [16, 17, 18, 19]

All that will be required to evaluate a new encoder/decoder set on the test bed will be to design and build a pair of evaluation boards, one for the encoder and the other for the decoder. The encoder evaluation board must provide the interface needed to acquire data from ADCs and packetize the data for efficient transmission to and storage in the memory. The decoder card must depacketize the data stream from the memory and produce data in the format required by the data analysis system and/or imaging processing systems.

### Conclusion

The Test Bed for High Speed Video Technology is a major set of laboratory instruments dedicated to an important technological problem. The system is being designed and built to be as flexible as possible. It will allow the evaluation of focal plane arrays ranging in size from 256 x 256 pixels to 2048 x 2048 pixels. It will allow testing the operation of these arrays at frame rates ranging up to 10,000 frames per second. Optical signals available will range from those which offer point source, single pixel, illumination; images from precision optical test patterns, laser speckle sources, and a wide variety of scenes important to scientific and engineering image analysis.

The analog and digital signal processing systems are being designed to be compatible with imaging arrays with 72 db dynamic range. Memory capacity will be expanded over the next several years and maximum sensible use will be made of digital data compression.

The major goal, of course, is the development of HSVT cameras and data processing systems for use in the field. This is a major packaging problem, and the results of experiments which would be impossible without a facility like the test bed will make possible the early development of those systems.

### Acknowledgments

This work was made possible by support from AFOSR and the University of Florida. Thanks to the people of RDL for administering the program. Thanks to Don Snyder for enthusiastic encouragement, to Rod Powell for his interest, and to both for many helpful discussions. Thanks to Howard McCormick and his cohorts in the MNGI Special Projects Lab for great support.

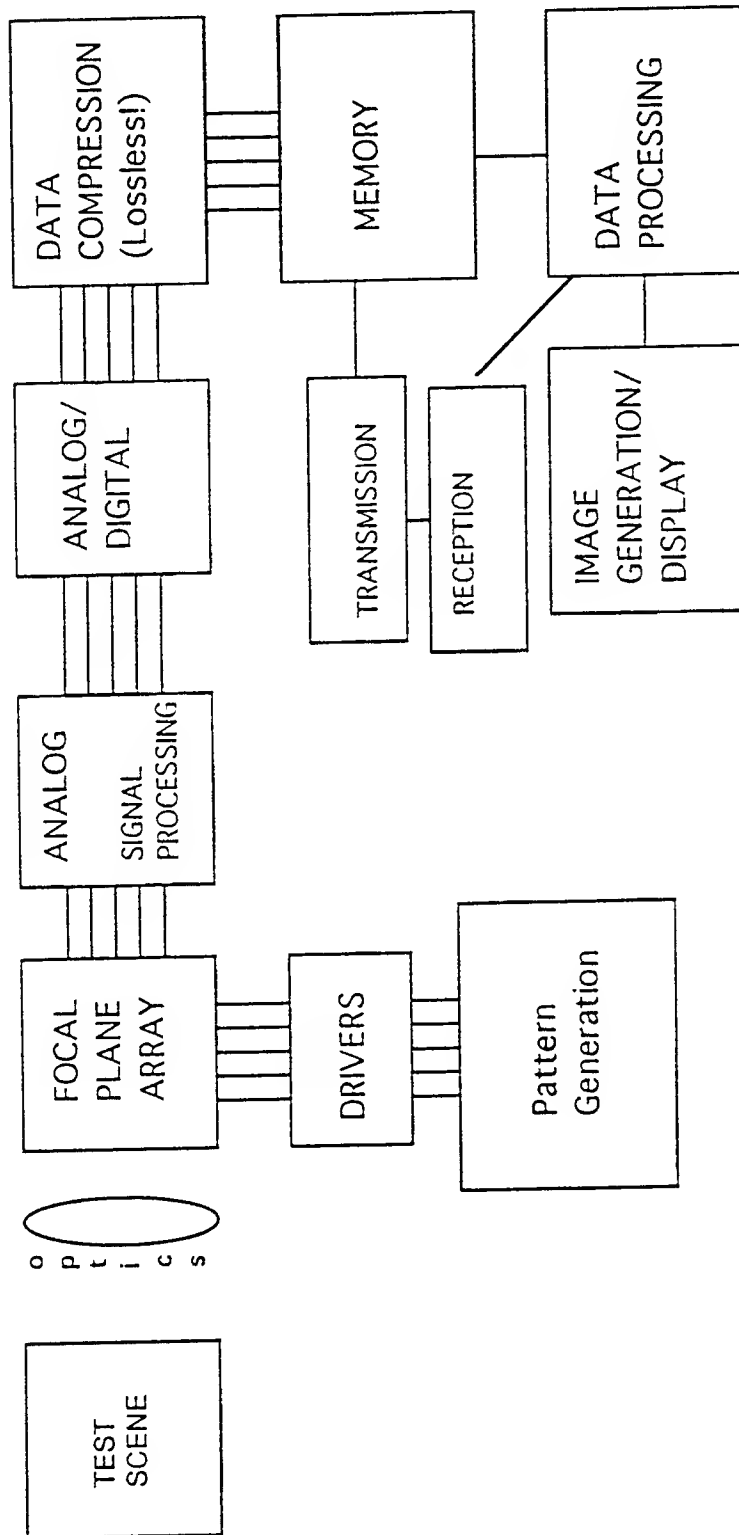


Figure 1. Block diagram of the test bed for high speed video technology

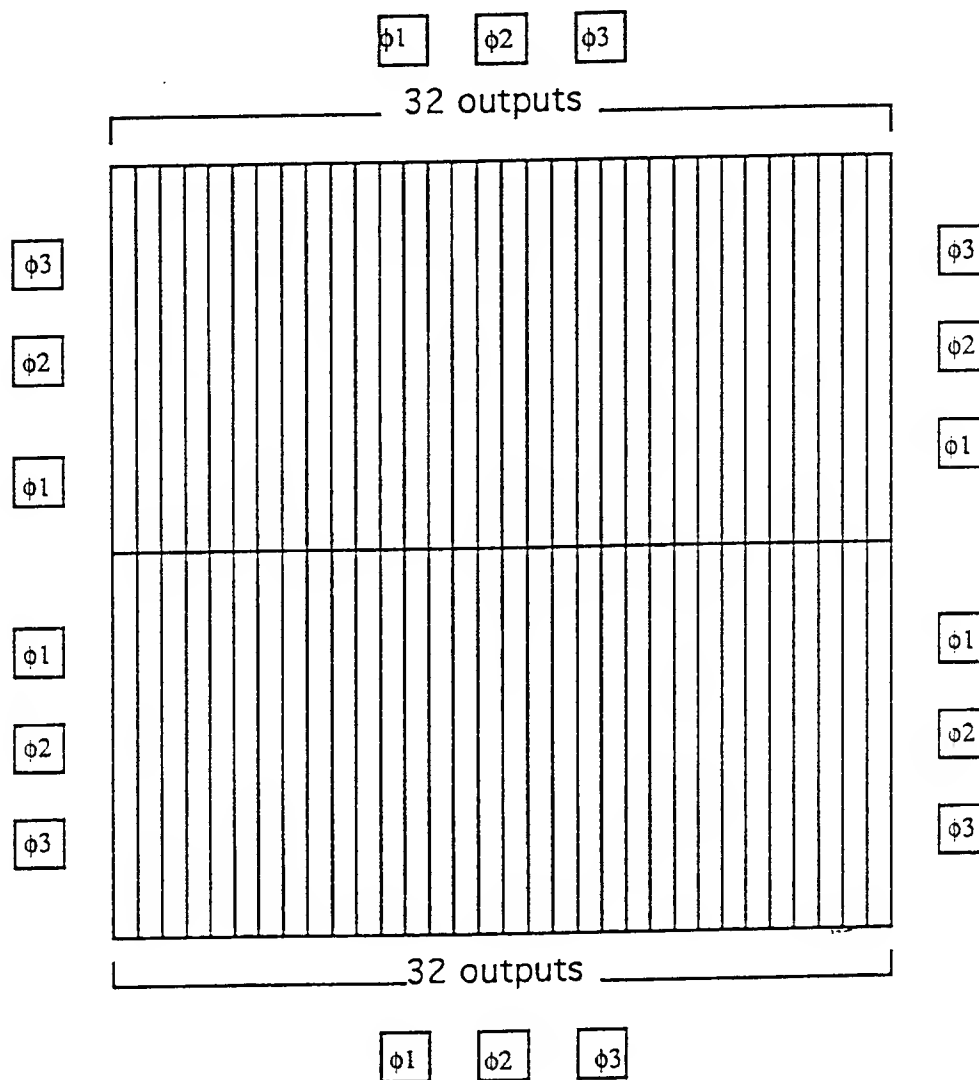
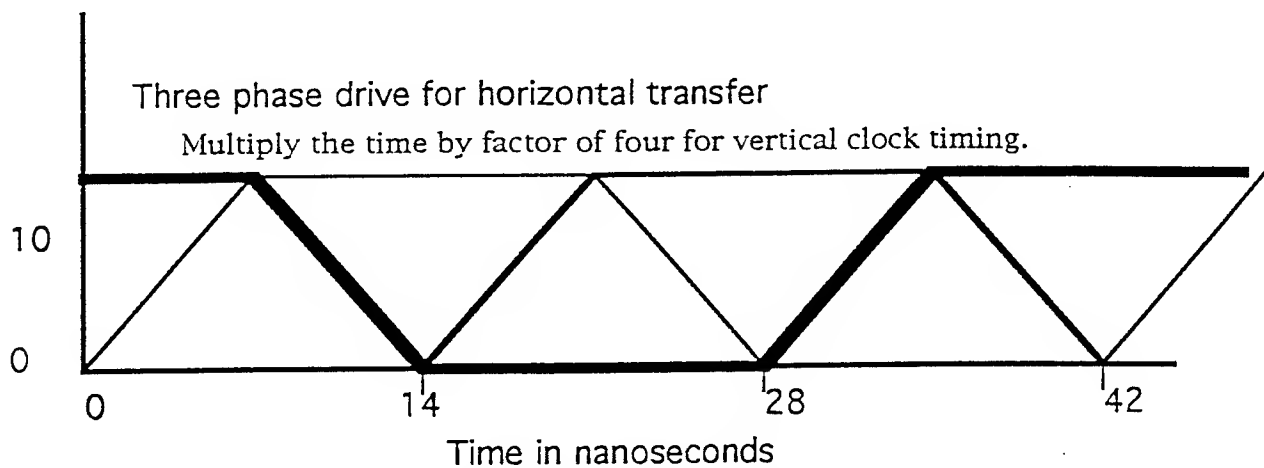


Figure 2. Sketch of the architecture of a 1024(H) x 1024(V) focal plane array. There are 64 sub-arrays. Each sub-array is composed of 32(H) x 512(V) picture elements, 16,384 pixels. All sub-arrays are clocked synchronously. This diagram shows two sets of horizontal clock drivers and four sets of vertical clock drivers. In the accompanying discussion each horizontal transfer requires 42 nanoseconds and each vertical transfer is allowed 168 nanoseconds.



Note: Each clock voltage waveform has a period of 42 nanoseconds.  
Seven nanoseconds have been allowed for every voltage transistion.

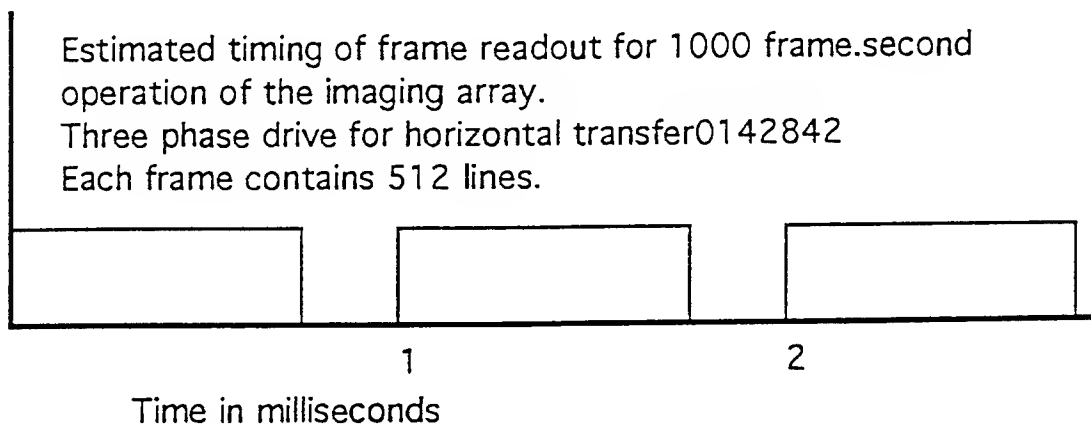
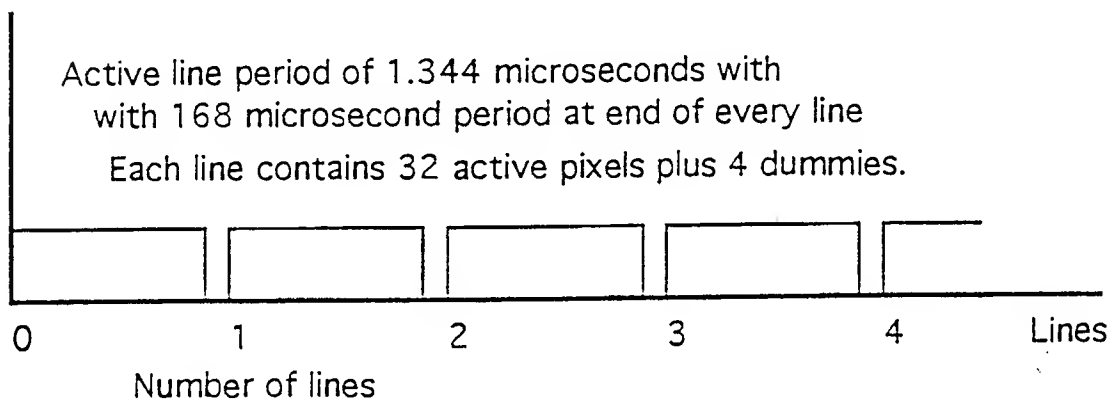


Figure 3. Timing diagrams for clocking the 1024(H) by 1024(V)  
64 output imaging array at 1000 frames per second.

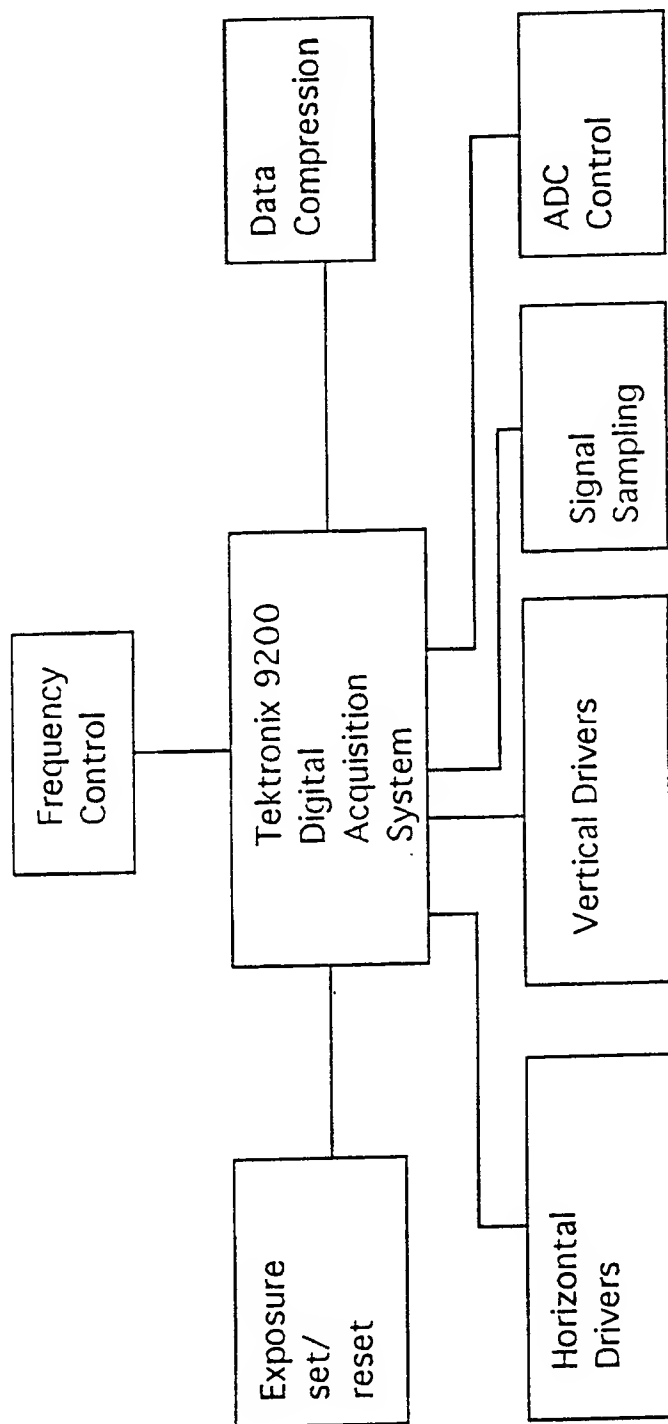


Figure 4. Block Diagram of Test Bed Control.



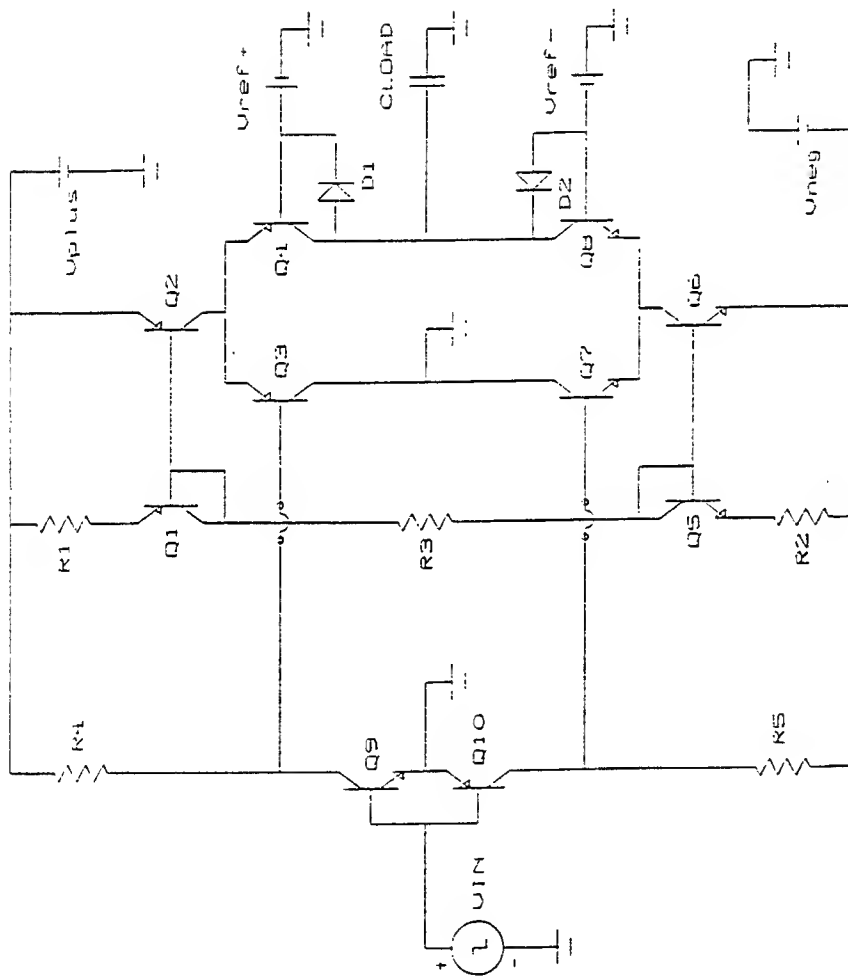


Figure 5 Schematic diagram of generic circuit design of "Brute Force Line Driver for Test Bed. This circuit allows for independent control of clock amplitude and slew rate.

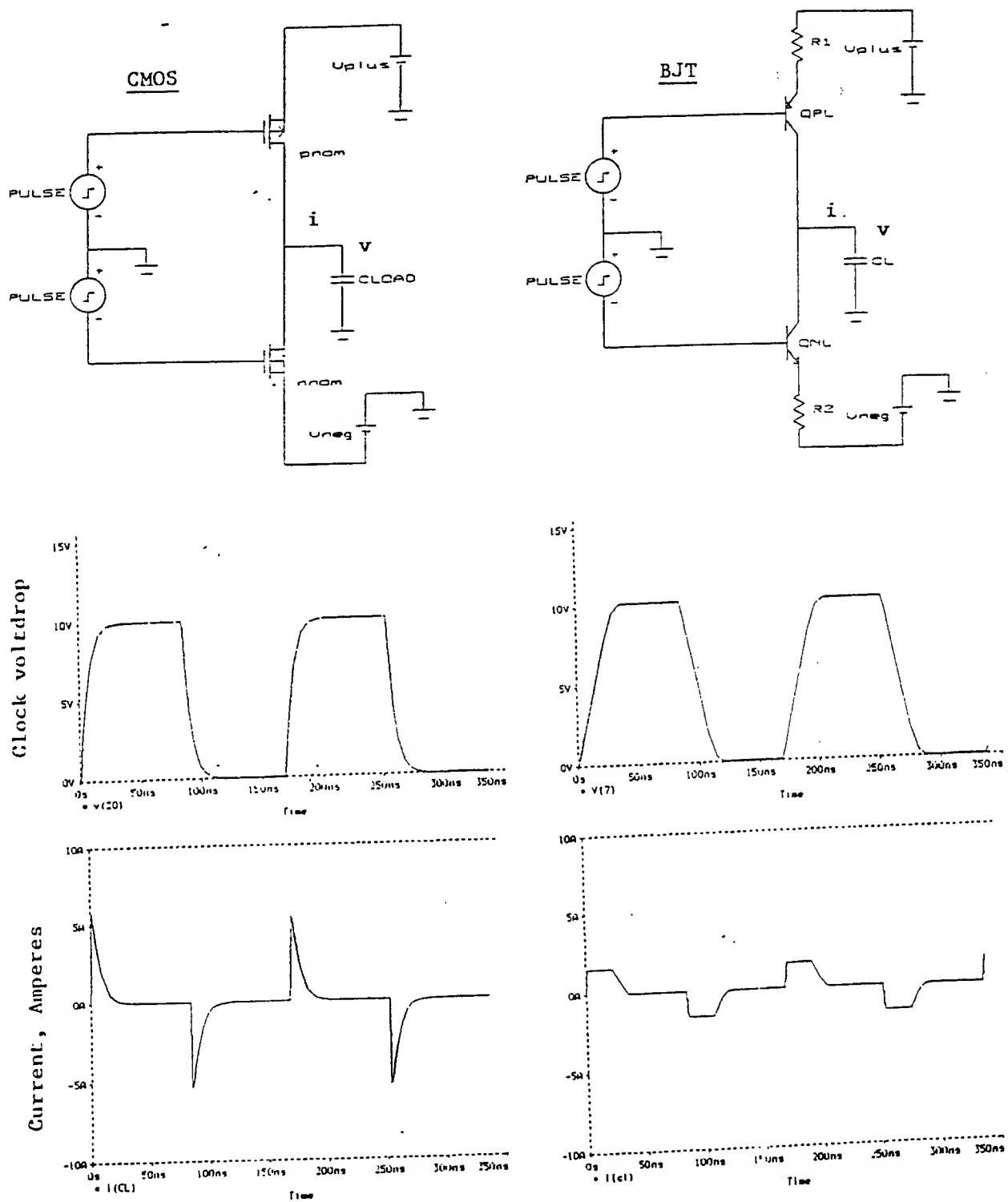


Figure 6: Comparison of the clock voltage and current waveforms produced by the GENERIC CMOS and BJT line drivers shown. Parameter were adjusted to make clock voltage waveforms as similar as possible.  $C_L = 4325$  pF.

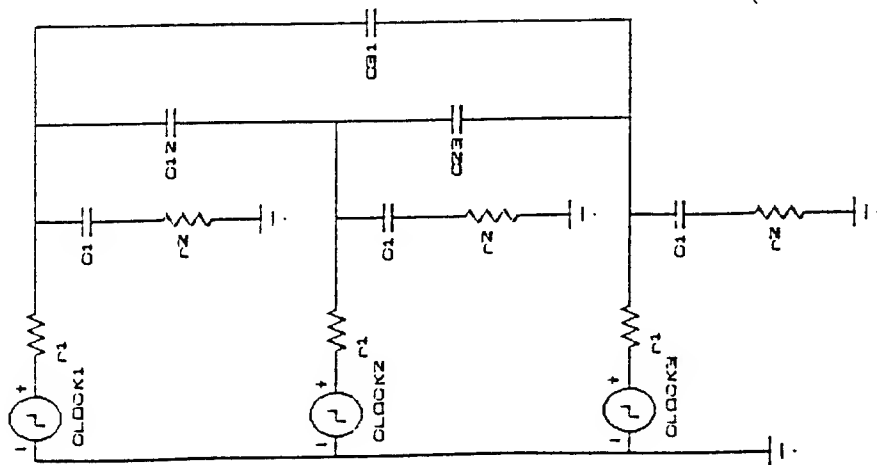
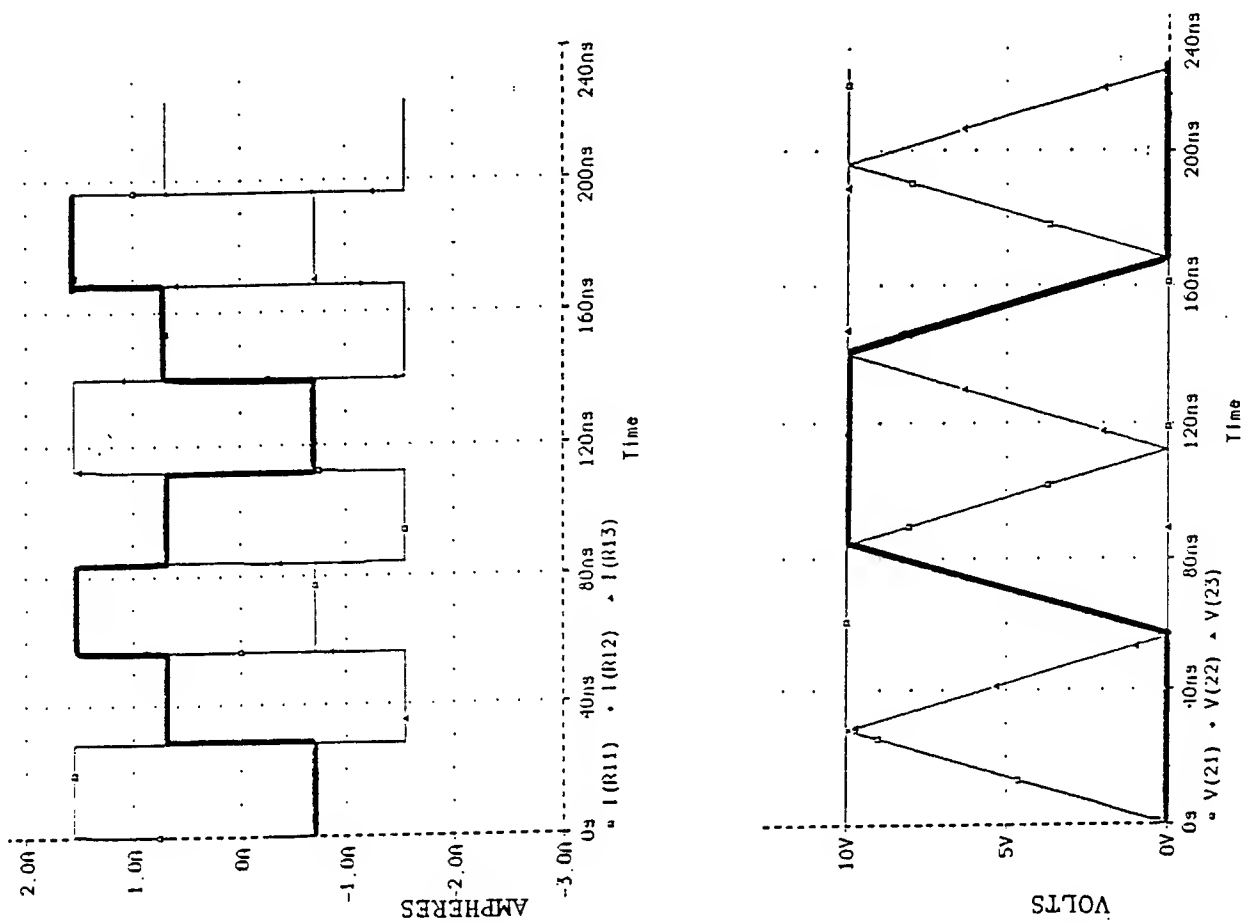


FIGURE 7: Equivalent circuit of a set of 3-phase clock lines. Also shown are a graph of 3-phase voltage waveforms and a graph of the corresponding 3-phase current waveforms.



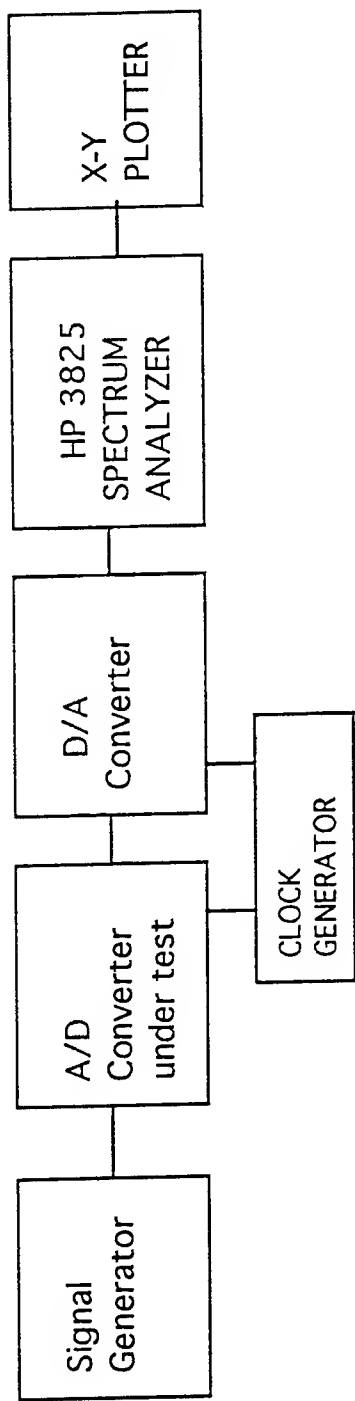


Figure8a: Block diagram of system used to measure dynamic range of A/D Converters at low frequencies.

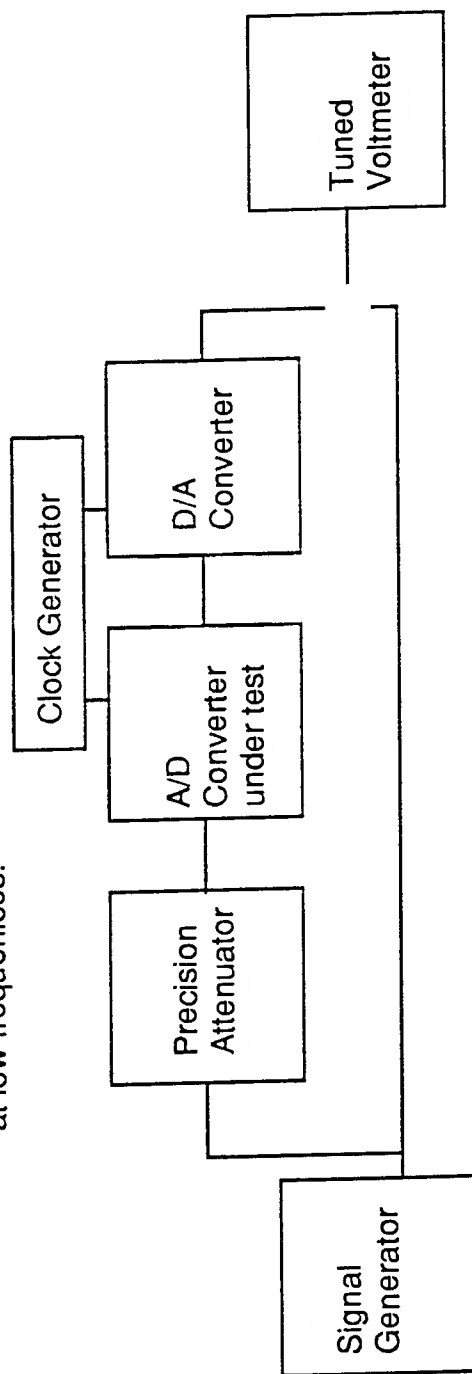


Figure 8b: Block diagram of system used to measure performance at higher frequencies.

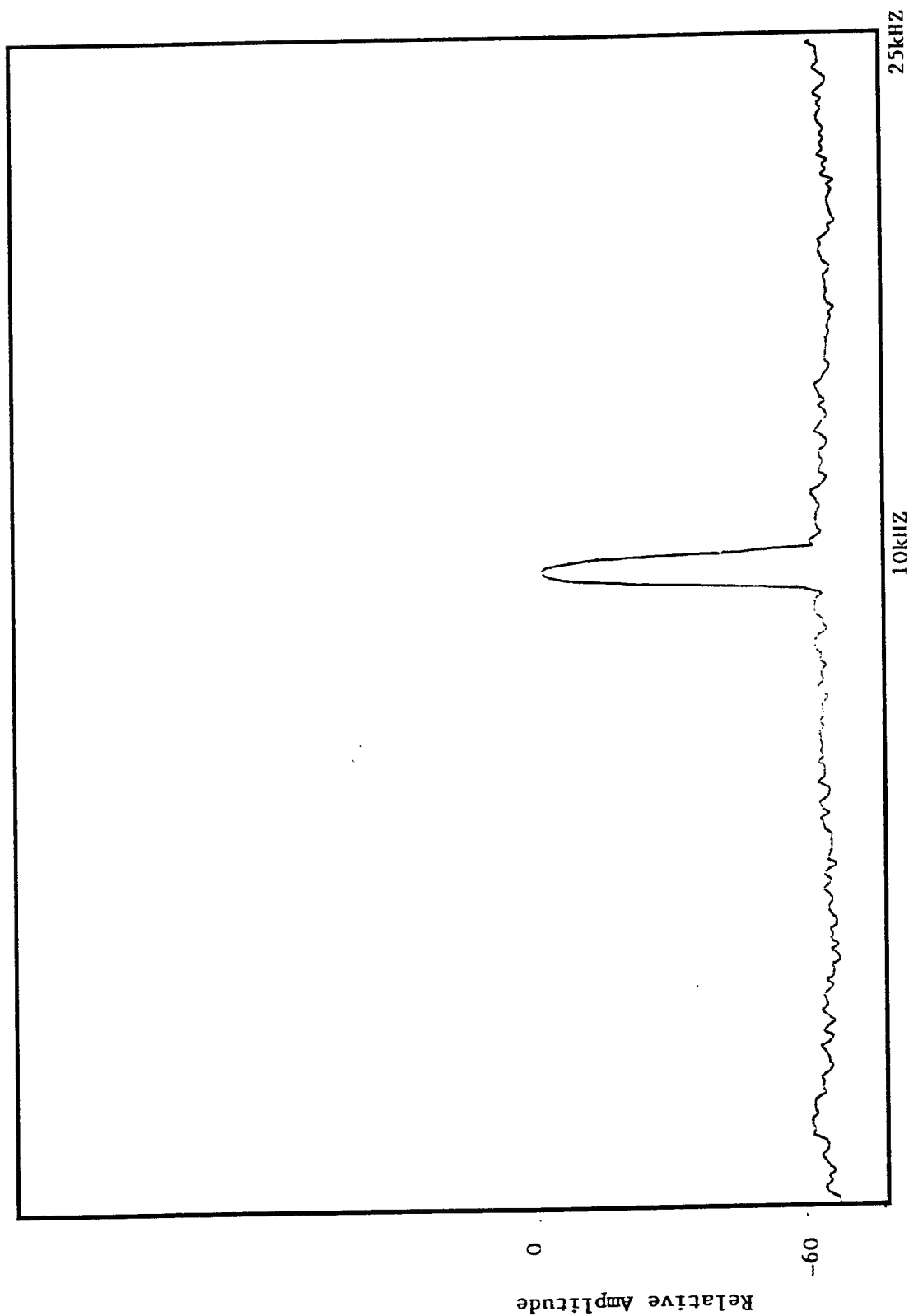


FIGURE 9: Spectrum of the signal recovered at the output of the SPT7814 Evaluation Board. The input signal was a 10kHz sinusoid with peak to peak amplitude of 4 volts.

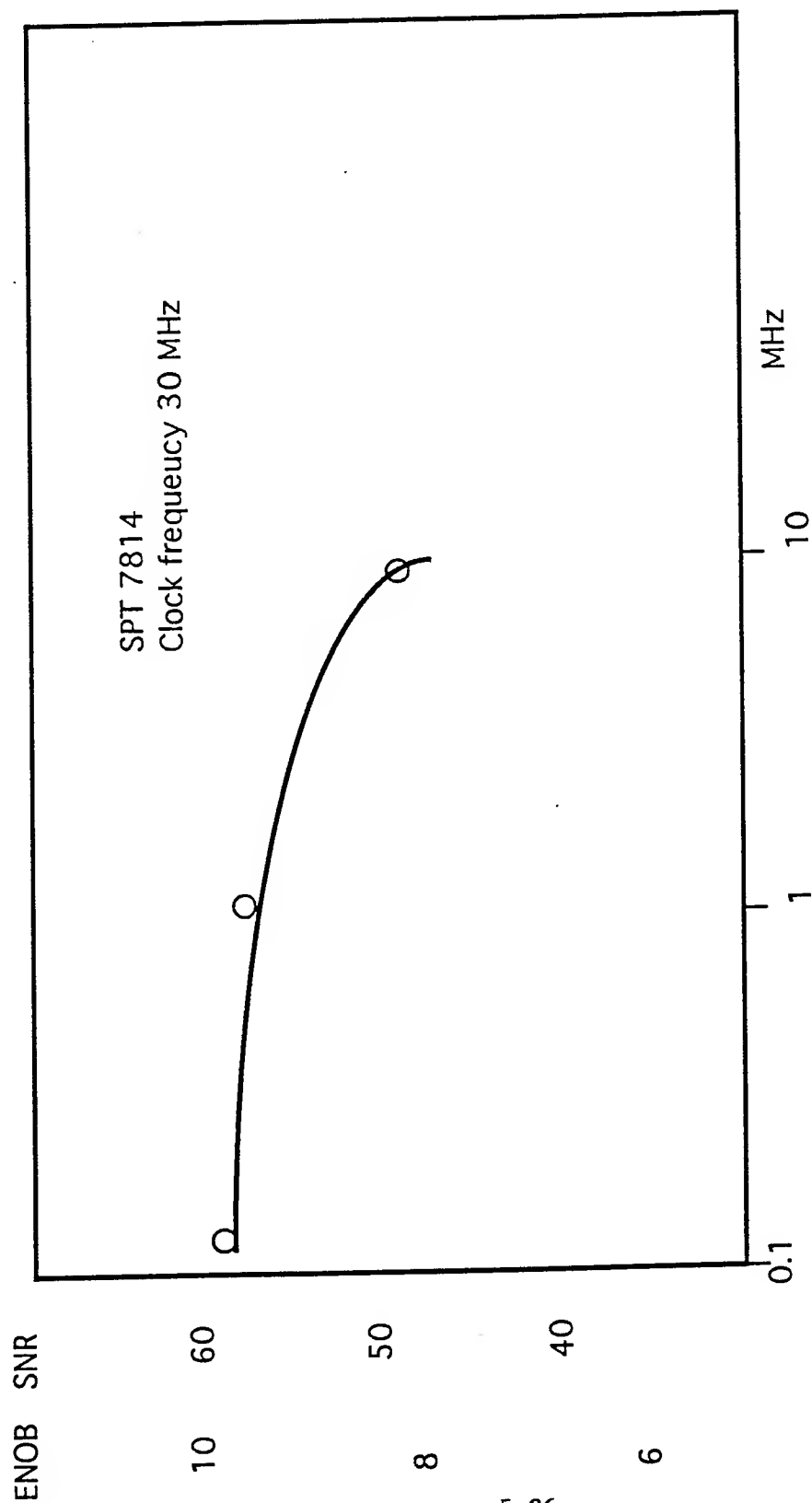
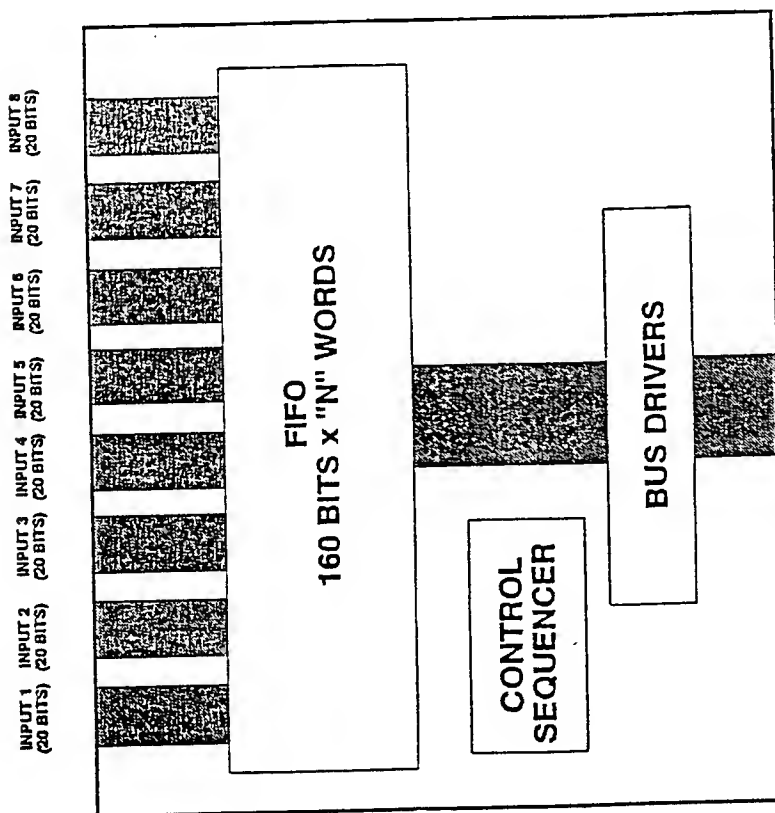


Figure 10 Signal to Noise Ratio and the Equivalent Number of Bits as a function of frequency of the input signal.



## HIGH-SPEED PARALLEL INTERFACE

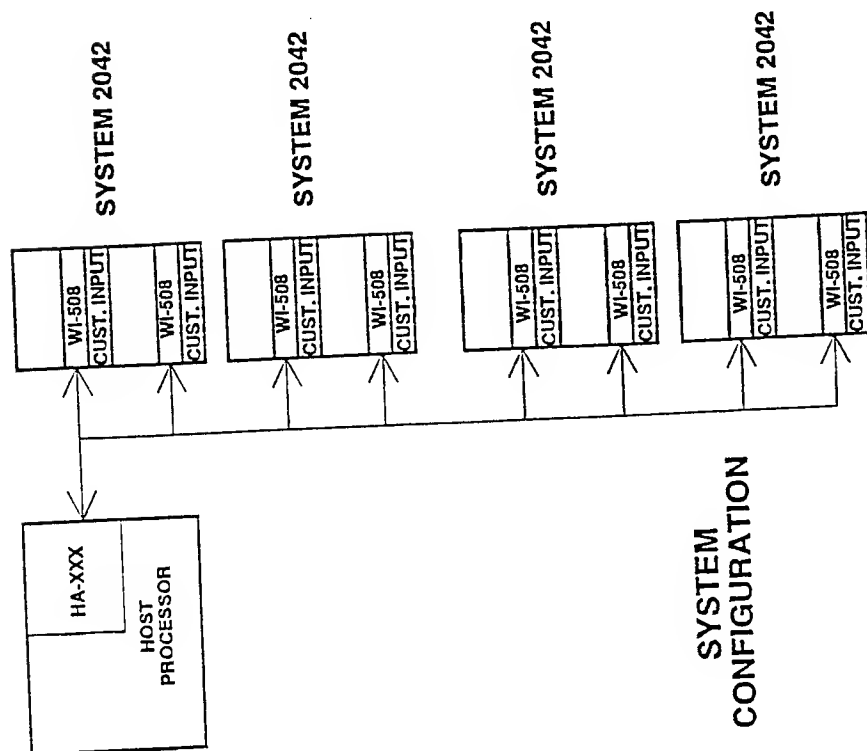


Figure 11. Block diagrams of a memory architecture for HSVT suggested by Representatives of DATARAM. Each high-speed parallel interface accepts data from eight sub-arrays and supplies data to one memory module. A single host processor controls the system.

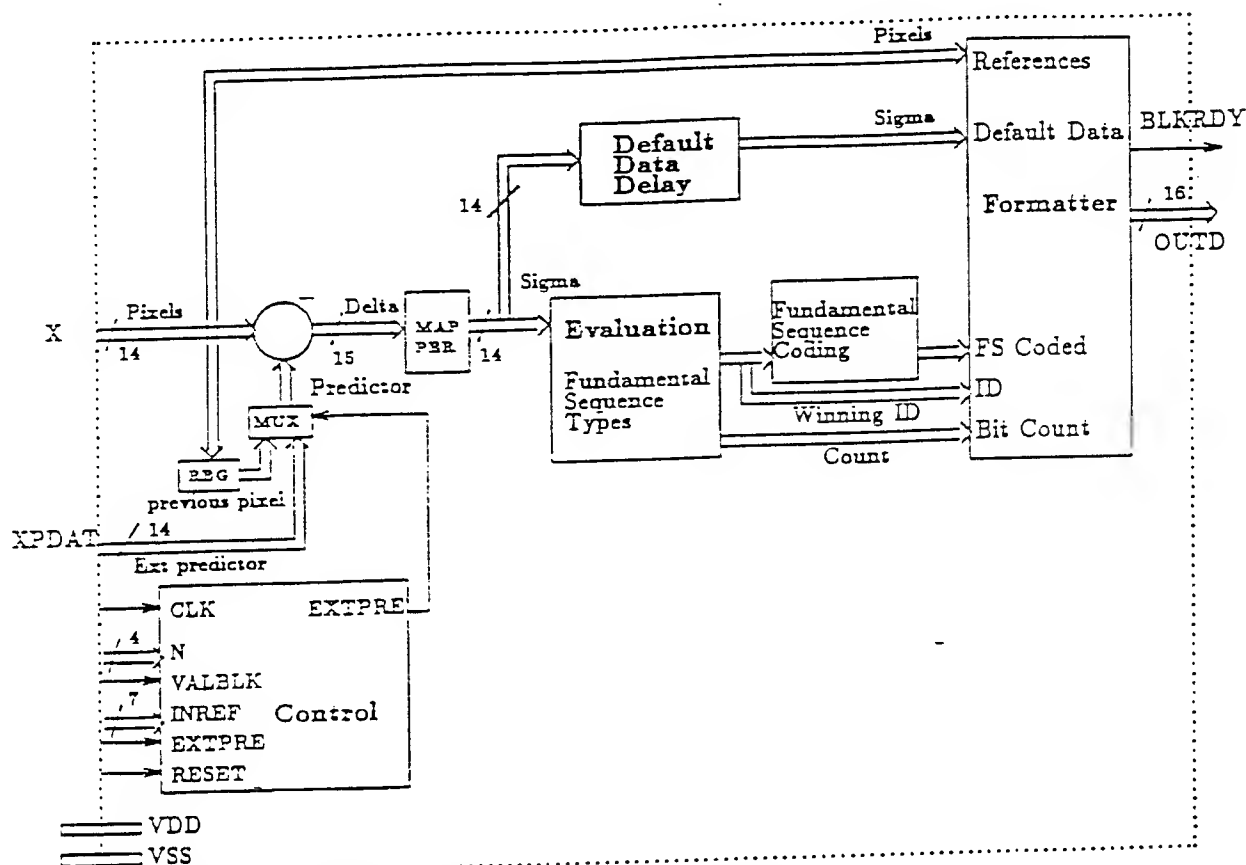


Figure 12 Block diagram of the Encoder

#### Control Signals for the Encoder

CLK	Clock, maximum frequency of 20 Mhz
N	4 bit word, number of bits per pixel
INREF	7 bit word, number of blocks per reference word
ValBlk	Must go high accompanying pixel data.
EXTPRE	Low for nearest neighbor prediction, High for use of external words for prediction.
RESET	Hold RESET low for nine clock cycles to reset encoder.

#### Input related signals

X	Pixel data to be encoded (4 bits to 14 bits.)
XPDATA	External prediction data (4 to 14 bits).

#### Output related signals

OUTD	The output data block. 16 bit words with block length as required by data.
BLKRDY	Goes high as data arrives at the output and remains high for length of block.



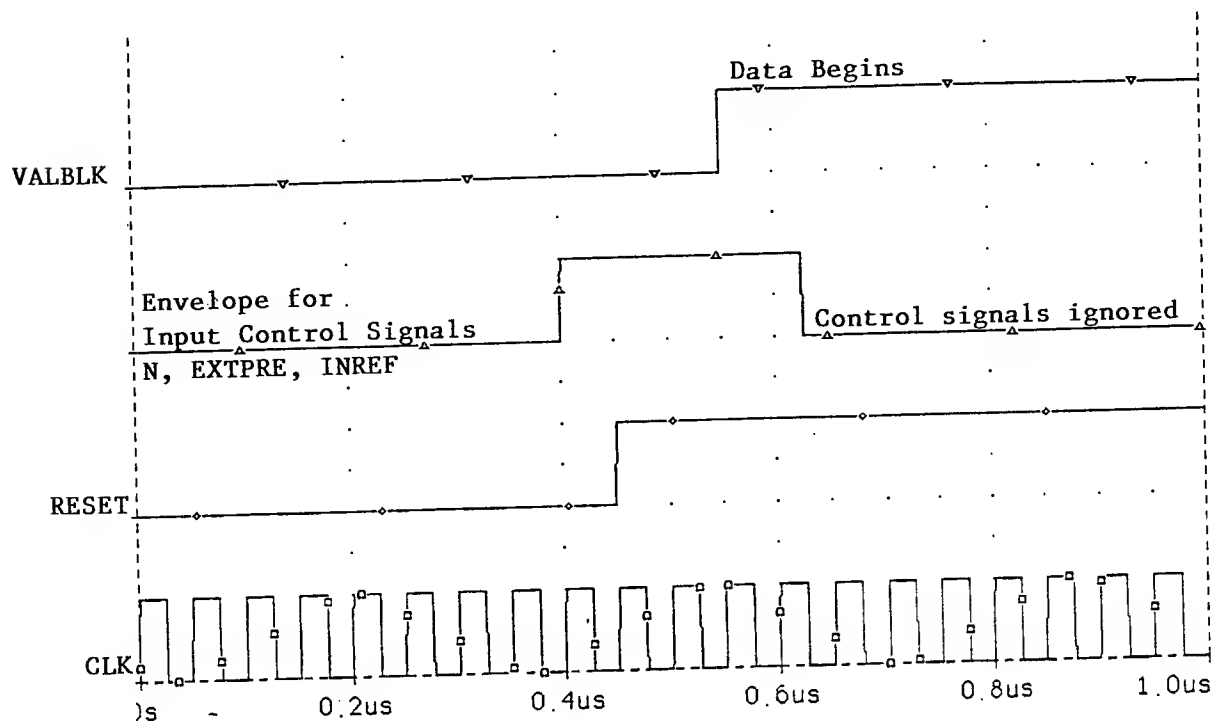


Figure 13a: Timing of control signals to reset encoder.

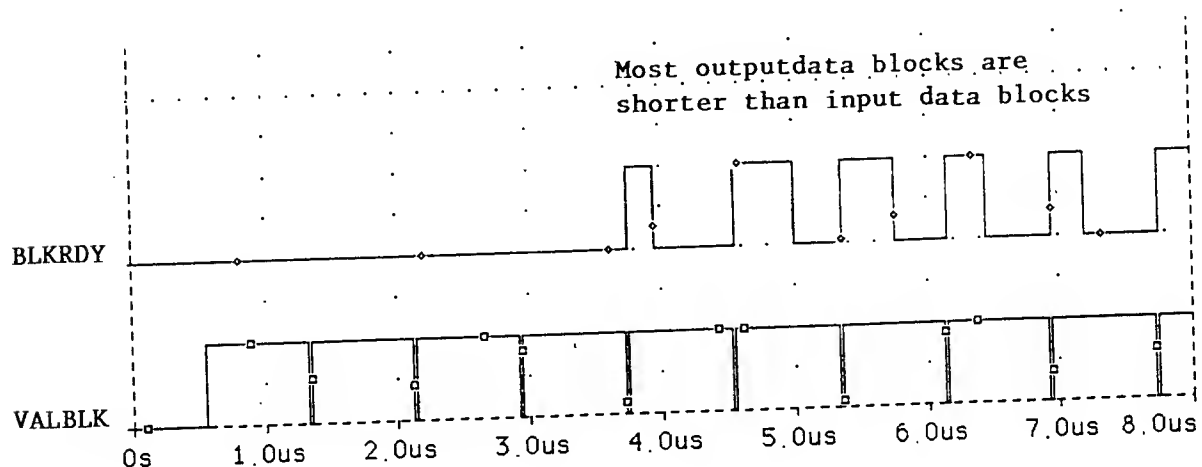


Figure 13b: Relative timing of input and output data blocks

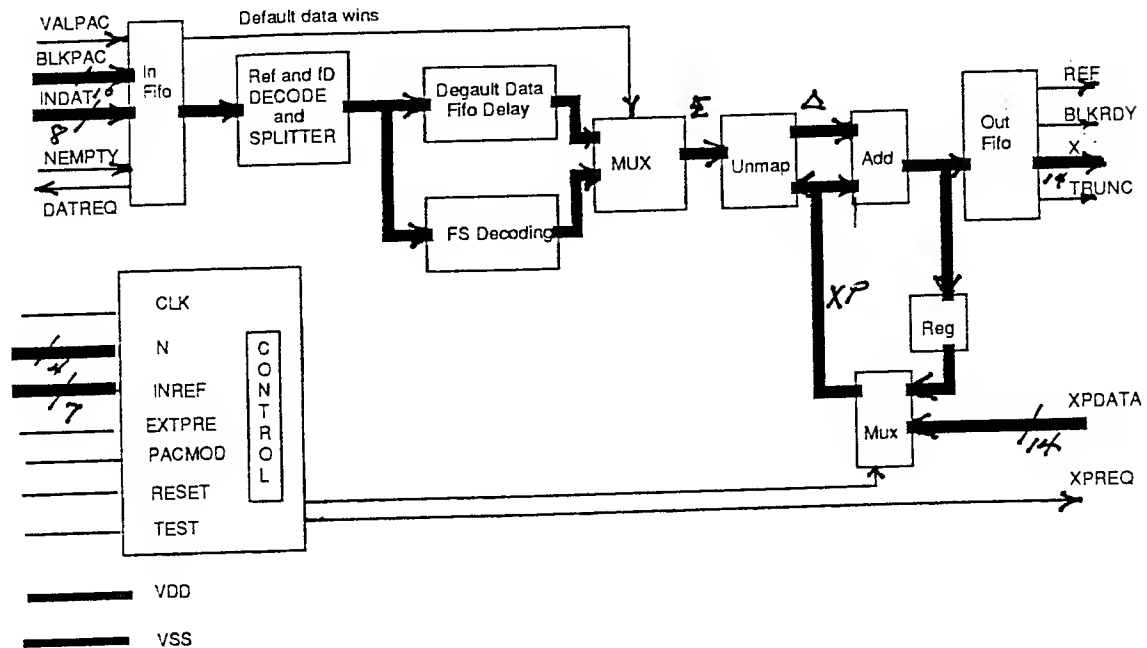


Figure 14: Block diagram of the Decoder

Control Signals for the Decoder:

CLK	Clock, maximum frequency of 20 Mhz
N	Quantization number of bits per pixel (4 to 14 bits)
INREF	Number of blocks between reference pixels
EXTPRE	External predictor option
PACMOD	Packet mode or continuous data stream
RESET	Required to reset the Decoder
TEST	To verify operation of Decoder.

Input related signals:

INDAT	Input data to be decoded, 8 bit words.
VALPAC	Input control. High--valid packet data available at output of external FIFO
BlkPac	10 bit word that specifies number of valid blocks in the packet,
Nempty	When high specifies the external FIFO is not empty.
DATREQ	Goes high when the Decoder is ready to accept data.

Output related signals:

X	The 14 bit decoded pixel data.
BlkRdy	Goes high as the first word of a block arrives at the output and stays high to the end of the block .
Trunc	Goes high if packets are truncated. Decoder produces as many dummy pixels as would be in a packet that was not truncated.

Signals related to external prediction:

XPREQ	Goes high to request external prediction word
XPDAT	External prediction data, 14 bits.

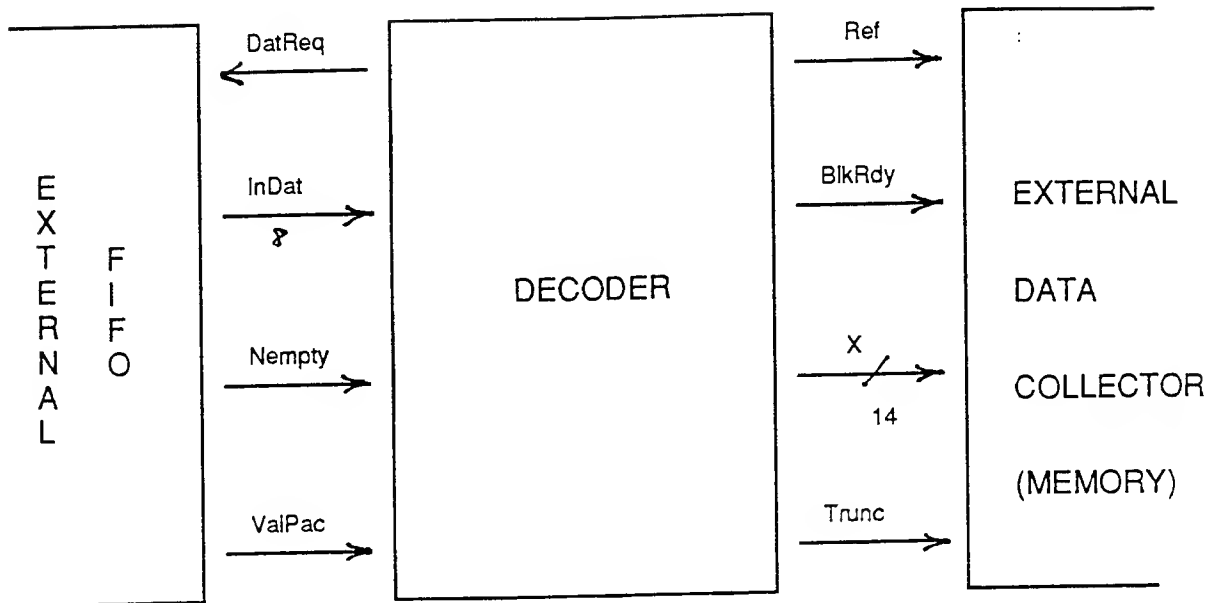


Figure 15a: The Decoder input/output interface.

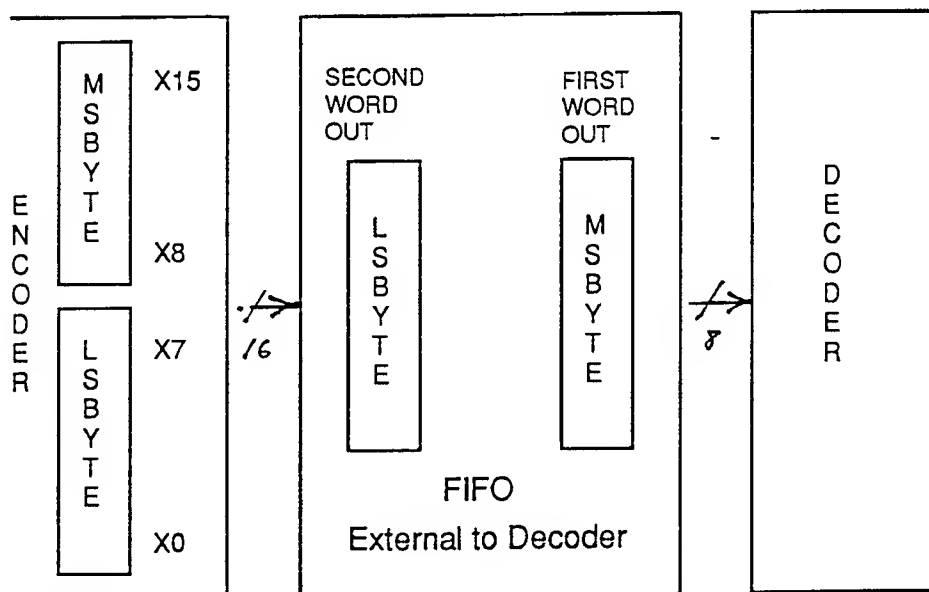


Figure 15b: The external FIFO must provide 16-bit word to 8-bit word transition

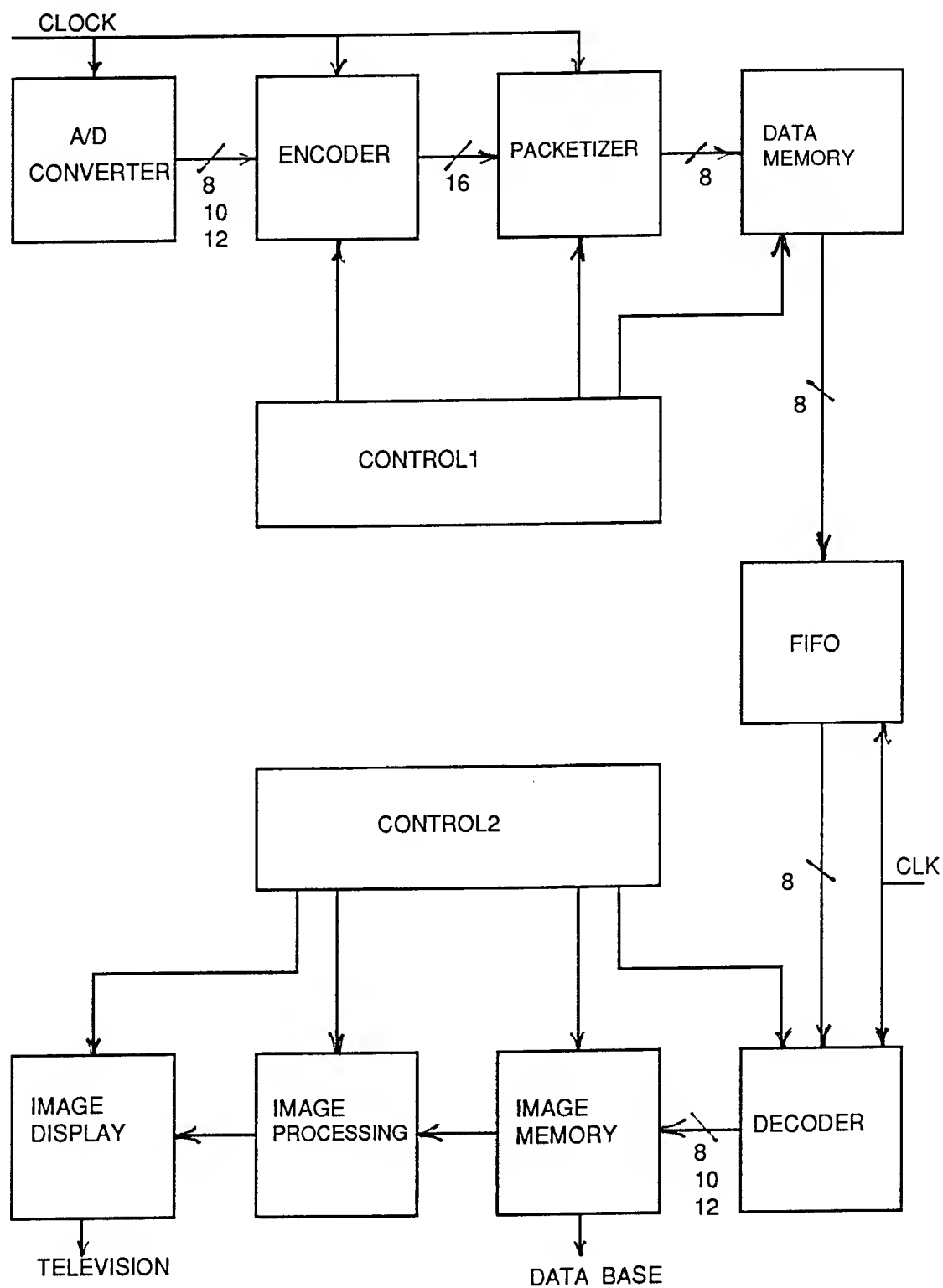


Figure 16: Block diagram of complete encoder/decoder system showing both high speed data memory and memory dedicated to image processing.

**LIGHT-GAS GUN FIRING CYCLE OPTIMIZATION  
FOR HIGH VELOCITY AND MODERATE PROJECTILE ACCELERATIONS**

**Robert W. Courter  
Associate Professor  
Department of Mechanical Engineering**

**Louisiana State University  
Baton Rouge, LA 70803**

**Final Report for:  
Research Initiation Program  
Wright Laboratory**

**Sponsored by:  
Air Force Office of Scientific Research  
Bolling Air Force Base, Washington, D.C.**

**and**

**Louisiana State University**

**December 1992**

# LIGHT-GAS GUN FIRING CYCLE OPTIMIZATION FOR HIGH VELOCITY AND MODERATE PROJECTILE ACCELERATIONS

Robert W. Courter  
Associate Professor  
Department of Mechanical Engineering  
Louisiana State University

## Abstract

An unconventional multiple shock-compression firing cycle for a light gas gun was investigated with a goal of providing high muzzle velocity at moderate levels of projectile acceleration and system pressure. A formal, multi-parameter optimization scheme in conjunction with a one-dimensional interior ballistic simulation procedure was applied to the firing cycle of a conventional powder-driven light gas gun. The purpose of the analysis was to define a set of geometric and physical performance parameters which will produce the desired multiple shock-compression cycle. Sixteen parameters were identified which define gun performance. Optimizations were performed for as many as six and as few as two unconstrained parameters. While some improvements were made in the basic cycle selected, the results were disappointing. A typical result produced an acceleration reduction of approximately 55% at the expense of a corresponding velocity reduction of 13%. It is felt that one difficulty may have been the presence of several local minimum solutions in close proximity which precluded the selection of the proper parameter set by the Powell optimization scheme. Additional studies in this area will continue.

In order to gain further insight into the physical interactions involved in gun operation and to provide experimental support for the analytical studies, a small-scale compressed-air driven light gas gun was designed and constructed. The gun is instrumented to permit measurement of piston and projectile velocities and system pressure distribution. This gun has been test fired to 8000 feet per second and is now ready to provide experimental support for the continuing analytical studies.

# LIGHT-GAS GUN FIRING CYCLE OPTIMIZATION FOR HIGH VELOCITY AND MODERATE PROJECTILE ACCELERATIONS

Robert W. Courter

## INTRODUCTION

A light-gas gun is the current facility of choice for launching projectiles at high speed for free-flight aerodynamic studies in a ballistic range. The so-called "isentropic" firing cycle is most commonly used in this research because it produces high velocities while maintaining manageable system pressures and projectile accelerations. However, the Air Force has a continuing need to test a variety of configurations, some of which are too fragile to withstand the loads which are incurred with present launcher cycles. Thus, it is advantageous to investigate other firing cycle designs in an attempt to develop a cycle which will still produce high launch velocity while incurring much lower accelerations than are currently possible.

A gun firing cycle design depends on the selection of certain physical and geometrical parameters. Because there are a large number of such parameters, the selection of a particular set of these parameters to achieve maximum launch velocity within system pressure and projectile acceleration constraints is a very difficult, if not impossible, task. Furthermore, present gun cycle simulation methods can provide comparative performance estimates, but because of uncertainties in friction and the transfer predictions, they cannot provide absolute results. Therefore, it is advantageous to develop a test facility in which real system performance can be measured and which will provide data to properly quantify simulation results. The following sections describe the work which has been accomplished under the present Migrant in these two areas, namely (1) analytical gun cycle optimization and (2) light gas gun test facility design and construction.

## 1. ANALYTICAL GUN CYCLE OPTIMIZATION

Methodology - A typical light-gas gun configuration is shown in Figure 1. The gun firing cycle is defined as the sequence of events which leads to ejection of the projectile from the barrel at a certain muzzle velocity. Gun firing cycle design is important in free flight aerodynamic testing because the cycle determines the projectile launching loads and free flight initial conditions. For a light gas gun the so-called isentropic cycle involving a heavy slow moving piston is the standard because high velocities can be reached with relatively

low launching loads. Recently, a multiple shock compression cycle was proposed which showed promise of achieving better performance (Reference 4). The technique relies on shock interactions to produce high velocities with incurring large sustained accelerations. These gun performance characteristics are determined by a set of geometric parameters which define the gun and by a set of physical parameters, called the "shot" parameters, which define the characteristics of the projectile, the driving propellant and the gun charging conditions. These two sets of parameters can be listed as follows:

Geometric parameters -	Powder chamber volume
	Pump tube bore diameter
	Pump tube length
	Launch tube bore diameter
	Launch tube length
	Transition section length
"Shot" parameters -	Piston length
	Piston weight
	Projectile length
	Projectile weight
	Pump tube initial pressure
	Launch tube initial pressure
	Diaphragm rupture pressure
	Propellant type
	Propellant weight

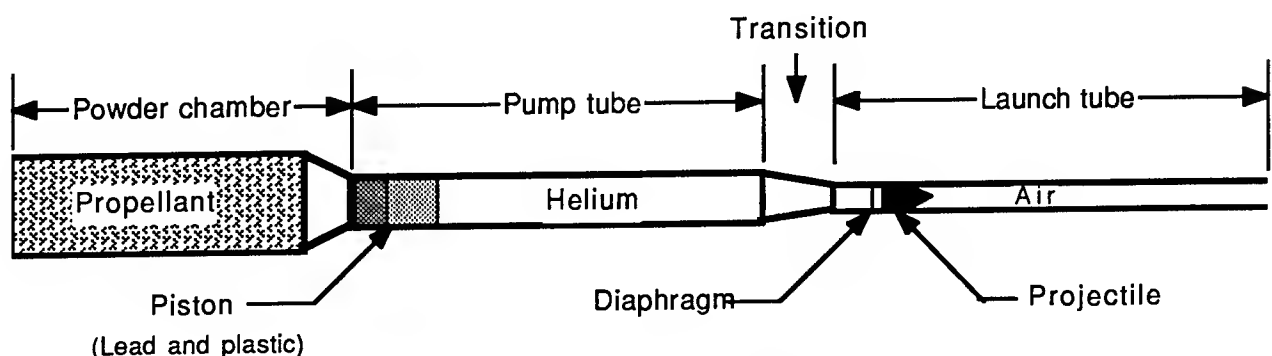


Figure 1. Light-Gas Gun Geometry



In the present case, it is desired to determine the optimal parameter set for an existing gun facility. In this case the gun geometry is fixed upstream of the piston and downstream of the diaphragm. In addition, to test the analysis methodology it is convenient to fix the projectile geometry and the propellant type and weight. Furthermore, the launch tube gas is assumed to be at atmospheric pressure. Under these conditions, a working set of geometric parameters becomes:

Pump tube length  
Piston length (lead)  
Piston length (plastic)  
Transition section length  
Transition to diaphragm length

The general method employed to optimize the gun cycle first requires a method for simulating the interior ballistics of the gun. There are a number of "gun codes" available around the country, but the code most commonly cited in the literature is the so-called "AEDC Code" which is currently being utilized by the CALSPAN Corporation in gun performance studies at the Arnold Engineering Development Center, Tullahoma, Tennessee. This code is an updated version of an original procedure described in Reference 1. It utilizes a lagrangean scheme with the original "q"-parameter artificial viscosity method of von Neumann and Richtmeyer (Reference 2) to solve the equations of conservation for mass, momentum and energy for a sequence of computation zones in the region between the piston face and the projectile base. These equations are:

Conservation of mass

$$M = \int_0^x \rho(x) A(x) dx$$

Conservation of momentum

$$\frac{\partial u}{\partial t} = - \frac{\partial (p + q)}{\partial M} A(x)$$

where

$$q = \frac{c_0^2}{v} \left( \frac{\partial u}{\partial x} \right)_j^2, \quad \text{if } \left( \frac{\partial u}{\partial x} \right)_j < 0$$

$$q = 0, \quad \text{if } \left( \frac{\partial u}{\partial x} \right)_j \geq 0$$

Conservation of energy

$$\frac{\partial e}{\partial t} = - (p + q) \frac{\partial v}{\partial t}$$

Equation of state

$$p = p(e, v)$$

In the above equations,  $u$  is the fluid velocity,  $v$  is the specific volume,  $e$  is the specific internal energy,  $M$  is the mass,  $A$  is the cross-sectional area of the tube and  $q$  is the artificial viscosity. The propellant combustion dynamics are represented by the familiar burning rate equation

$$r = \alpha p^\beta$$

where  $\alpha$  and  $\beta$  are experimentally determined. The combustion chamber pressure is formulated in terms of the burning rate and piston kinematics, and the piston and projectile kinetics are treated in the conventional manner, including frictional as well as pressure forces. Frictional effects in the gas are estimated by the methods of boundary layer theory, and the Reynolds analogy is used to determine the heat transfer coefficient. The resulting simulation not only provides piston and projectile kinematic information, but it also yields the thermodynamic and kinematic property distributions of the propelling gas in the region bounded by the piston face and the projectile base.

The optimization algorithm selected for this project is that reported by Powell in Reference 3. This unconstrained optimization method is advantageous because it does not require the use of derivatives, thus eliminating tedious analytical calculations and possible numerical errors incurred by numerical evaluation of derivatives. Furthermore, the method is unlikely to attain convergence before a minimum is actually reached, it chooses conjugate search paths which are adapted after each iteration and the total number of least-squares evaluations required is roughly equal to the number of variables involved. The method does have one drawback that is worth noting: it has no provision for differentiating between a local and a global minimum. Also, the method is an unconstrained optimization method. This means that any limitations on the solution must be imposed by artificial

means. This feature of the present method involves the creation of a penalty function which can be imposed on the optimization algorithm. The details of the method used in the present case will be explained later.

The essential features of the optimization method are illustrated in Figure 2 for the case of two optimization parameter vectors, **A** and **B**. A cost function is defined which expresses the goals of the optimization procedure (for example, launch velocity is to be maximized within the constraints that system pressure and projectile acceleration are below certain maximum values. Using initial values for the system parameters, an initial search along **B** is mounted. The values in the solution vector are then adjusted until a local minimum is found (at point  $P_1$  in this case). Then a similar search is begun along **A** until a local minimum is found at point  $P_2$ . Another search along **B** leads to point  $P_3$ . At this point the base of direction vectors is adjusted such that the next search direction is along **C**, which is parallel to the line ( $P_1P_3$ ). This procedure continues until the minimum of the two-parameter set is reached at point  $P_7$ . The values of the parameters which yield this solution now form the set which minimizes the cost function, which in the present case, is simply the inverse of the muzzle velocity. As was mentioned earlier, the technique is an unconstrained optimization method. The required system pressure and projectile

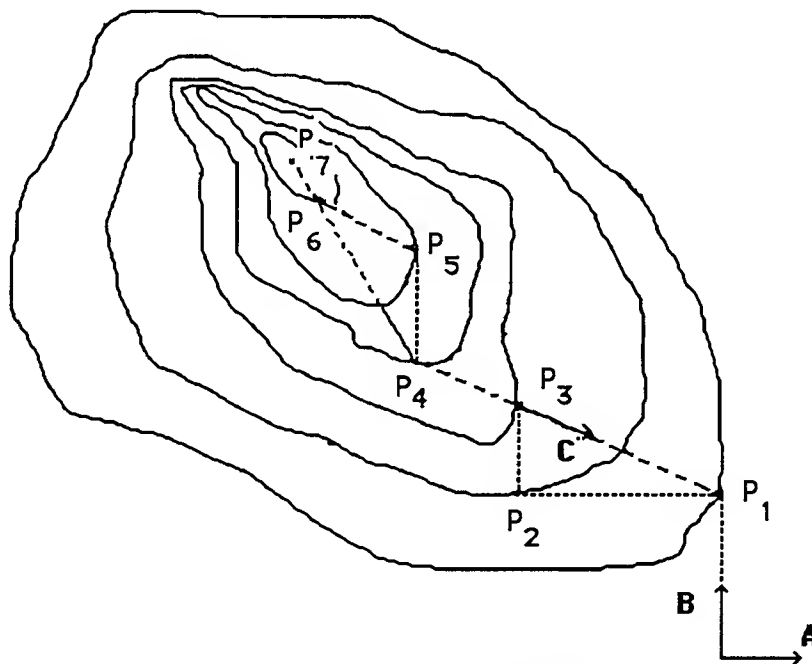


Figure 2. Optimization scheme

acceleration constraints are provided artificially through the specification of a penalty function. The penalty function is designed such that it will be larger than the cost function when the constraining values of the pressure and acceleration are exceeded. A quadratic form is used to preclude introduction of a numerical instability caused by an abrupt change in the cost function.

Implementation - The calculations necessary to perform the cycle optimization are contained in a computer program which manages the interaction of the gun cycle simulation driver (SUBAEDC) and the Powell optimization algorithm (MNWD4B). A flow chart of the main program is shown in Figure 3. Initially, SUBAEDC is called to initialize parameters and set up the shot conditions and other data that are required for the simulation. In the terminology of the program, the parameters in the optimization routine are:

PARAM1 = lead piston length  
PARAM2 = plastic piston length  
PARAM3 = transition to diaphragm length  
PARAM4 = pump tube length  
PARAM5 = transition section length

Note that these calculations investigate only the geometric aspects of the optimization. Later work will address the issue of shot parameter selection. After initialization, the optimization algorithm (MNWD4B) is called, and it, in turn, calls SUBAEDC (see the flow chart of Figure 4) to compute the cost function. An iteration ensues in which the optimization routine systematically establishes a set of parameter values which maximize muzzle velocity by following the algorithm sketched in Figure 2.

Results: It was mentioned previously that in the present phase of the study the effect of variation of geometric parameters would be investigated. Before specific results are presented and discussed, it is worthwhile to comment on the effect that each, acting independently, would have on the gun cycle.

PARAM1 (length of lead portion of the piston) - This parameter primarily affects the piston weight since the density of lead is over five times that of plastic. A heavy piston (large value of PARAM1) will provide a tendency toward an isentropic cycle while a light piston will produce a shock-compression cycle.

PARAM2 (length of the plastic portion of the piston) - This parameter primarily

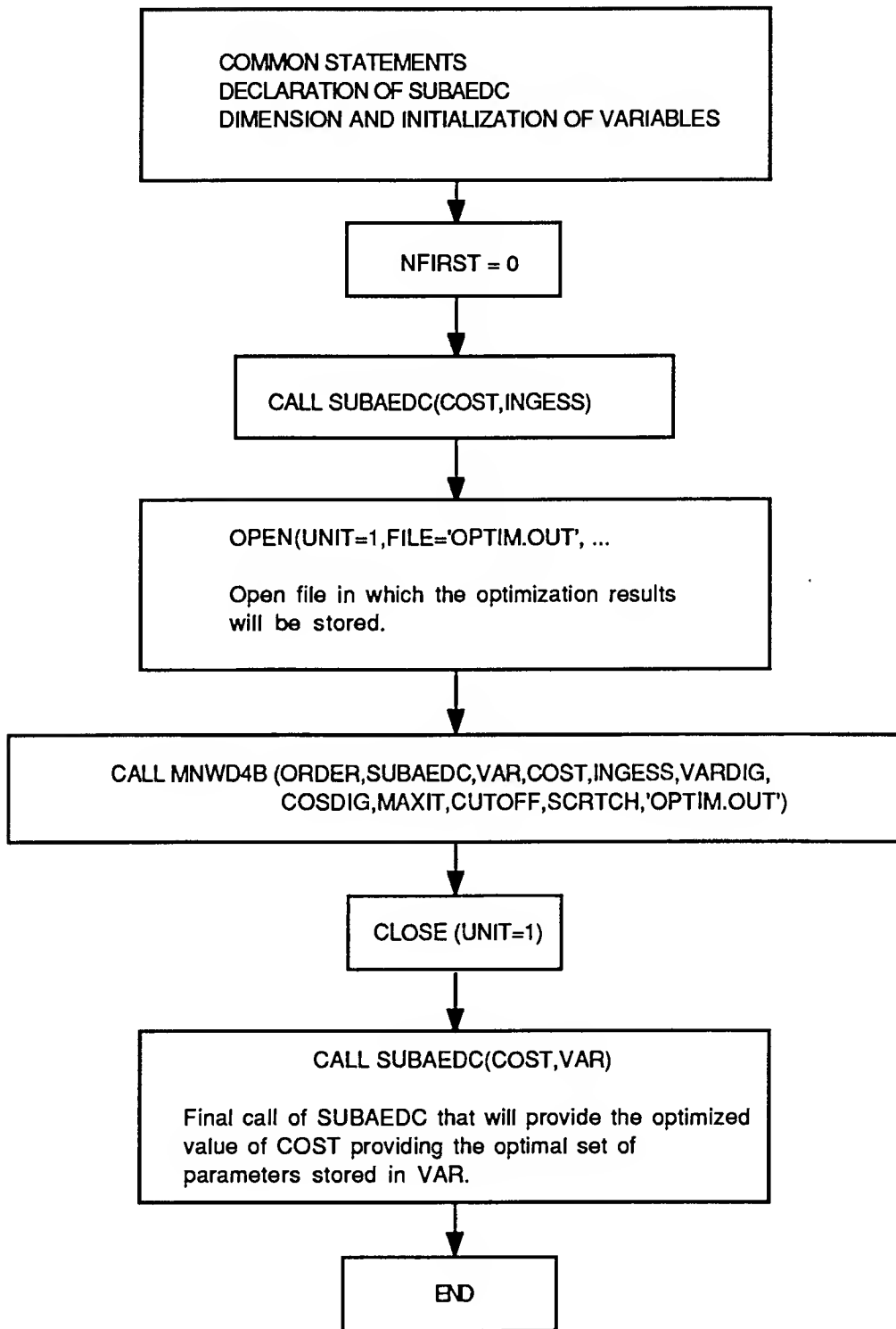


Figure 3. Flow Chart for Main Program

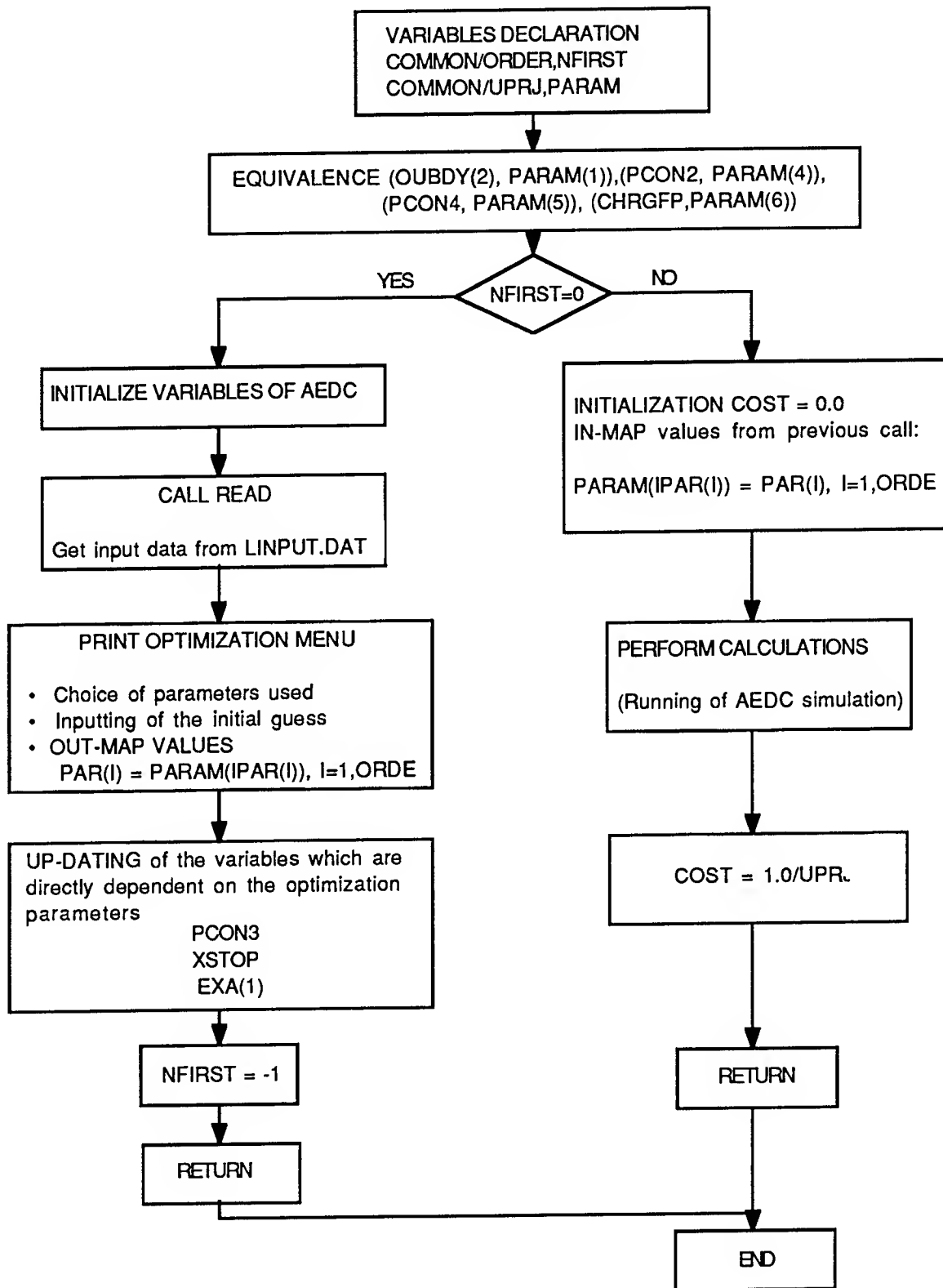


Figure 4. Simulation Routine Flow Chart

affects the length of the piston. It is difficult to predict the effect it may have because it influences the distance between the piston face and the projectile base and, hence, the shock interaction characteristics of the cycle. The interaction is obviously also affected by piston speed, projectile speed and the characteristics of the gas in the pump tube. It is interesting to note that while the piston length and the pump tube length are independent physically, they actually have an interactive effect during the gun cycle because their values influence the actual distance between the piston face and the projectile base. This relationship leads to some difficulty in the optimization process which will be discussed later.

PARAM3 (transition to diaphragm length) - This parameter influences the timing of diaphragm rupture because it affects the length of the light-gas chamber. Comparisons of simulations for conventional light-gas gun geometries indicate that this parameter has a weak effect on the cycle, but it was included because a particular geometric relationship among gun components was not assumed for this study.

PARAM4 (pump tube length) - This parameter is a primary factor in determining a gun cycle. There appear to be two important contributions, namely: (1) the volume of light gas which is compressed during the cycle and which forms the driver for the projectile is directly proportional to pump tube length, and (2) the distance between piston face and projectile base which determines the shock reflection timing is directly proportional to the pump tube length. Both of these factors have a strong influence on both the projectile acceleration and the muzzle velocity.

PARAM5 (transition section length) - The effect of this parameter is difficult to gauge, but it is felt that the area-reduction gradient may influence the shock reflection timing and strength to a sufficient degree that it would influence both the piston speed and, ultimately, the projectile loads and velocity. However, simulations that were performed on conventional configurations indicated that it had a very weak influence.

The results of a representative sample of 19 computations are shown in Tables 1, 2 and 3. The simulation titles can be identified as follows:

ISEN1 and ISEN2 - simulations of existing gun geometry showing the effect of small changes in piston weight.

SIM1 and SIM2 - simulations showing the effect of pump tube length.

SIM3 and SIM4 - simulations showing the effect of using a very light piston.

S1 - optimization with both piston length and pump tube length as parameters.

SP1, SP2, SP3 and SP4 - optimizations on pump tube length for a moderate piston.

OPT1, OPT2 and OPT3 - single parameter optimizations on heavy piston.

OPT4, OPT5 and OPT6 - single parameter optimizations on light piston.

MULT1 - six parameter optimization on all geometric parameters and the powder load.

Table 1: Initial values of parameters (\* indicates parameter used in optimization.)

Simulation	Lead piston length (cm)	Plastic piston length (cm)	Transition to diaphragm length (cm)	Pump tube length (cm)	Transition section length (cm)
ISEN1	119.60	163.7902	745.3272	712.43	729.4705
ISEN2	118.88	163.7902	745.3272	712.43	729.4705
SIM1	119.6	163.7902	745.3272	576.1661	729.4705
SIM2	119.0	120.00	745.3272	576.1661	729.4705
SIM3	119.0	120.00	609.0951	576.2661	593.2024
SIM4	119.7902	122.7803	611.7477	578.9047	595.8910
S1	119.00	*140.0	609.0591	*576.2024	593.2024
SP1	119.00	126.7902	208.00	*175.00	192.00
SP2	119.00	126.7902	208.00	*175.00	192.00
SP3	119.00	126.7902	213.00	*175.00	197.00
SP4	119.00	126.7902	308.00	*180.00	292.00
OPT1	119.60	163.7902	745.3272	*712.43	729.4705
OPT2	119.60	163.7902	745.3272	400.00	729.4705
OPT3	119.60	163.7902	745.3272	300.00	729.4705
OPT4	119.00	120.00	609.0551	*576.2661	593.2024
OPT5	*119.00	120.00	609.0551	576.2661	593.2024
OPT6	119.0478	*120.00	609.0551	576.2661	593.2024
MULT1	*119.00	*163.7902	*745.3272	*712.4842	*729.4705

Several interesting features of the gun cycle are noted. Comparison of ISEN1 and ISEN2 indicates that small changes in the weight of a heavy piston can lead to significant velocity reductions with very little relief from launching loads. On the other hand, changing the pump tube length, even with a heavy piston, can alter the gasdynamics enough to effect a 20% reduction in launch loads while producing a 7% velocity increase. The use of a very light piston in a gun with conventional geometry can produce dramatic reductions in projectile acceleration. This is demonstrated by a comparison of ISEN1 with SIM3. All of these features point to the use of formal optimization techniques to seek the "best" solution.



Table 2. The optimized parameter vector

Simulation	Lead piston length (cm)	Plastic piston length (cm)	Transition to diaphragm length (cm)	Pump tube length (cm)	Transition section length (cm)
ISEN1	----	----	----	----	----
ISEN2	----	----	----	----	----
SIM1	----	----	----	----	----
SIM2	----	----	----	----	----
SIM3	----	----	----	----	----
SIM4	----	----	----	----	----
S1	----	----	----	339.7084	----
SP1	----	----	----	174.24	----
SP2	----	----	----	173.58	----
SP3	----	----	----	178.53	----
SP4	----	----	----	269.34	----
OPT1	----	----	----	713.93	----
OPT2	----	----	----	577.96	----
OPT3	----	----	----	576.2161	----
OPT4	----	----	----	583.58	----
OPT5	119.0478	----	----	----	----
OPT6	----	120.0944	----	----	----
MULT1	149.98	150.10	748.65	717.81	718.83

Table 3. Final Results

Simulation	Cycle Time (ms)	Piston Weight (lbs)	Max. Piston Velocity (ft./sec)	Max. Projectile Accel. (g's)	Max. Pressure (psi)	Muzzle Velocity (ft/sec.)
ISEN1	19.96	2.2	1469.2	91652.1	10967.0	3606.06
ISEN2	19.56	1.9	1471.8	91008.2	10142.0	3418.70
SIM1	15.74	2.2	1654.2	74101.9	14266.0	3851.24
SIM2	25.67	1.9	2186.3	42642.3	8663.6	2995.40
SIM3	23.73	0.2	1836.4	38471.6	9073.0	2879.10
SIM4	23.94	0.2	1780.8	37906.6	9168.4	2855.62
S1	13.36	1.3	1316.5	74272.4	14900.0	3471.12
SP1	7.49	0.8	879.1	115669.0	13108.0	2659.64
SP2	7.47	0.7	909.4	116944.0	13254.0	2566.80
SP3	7.56	0.7	945.1	122002.0	13266.0	2593.67
SP4	8.32	0.7	1428.1	91770.9	14000.0	2878.90
OPT1	19.98	2.2	1469.7	92425.8	11287.0	3601.65
OPT2	17.09	2.2	1410.5	51885.6	13003.0	3101.10
OPT3	17.12	2.2	1413.6	51816.8	13013.0	3102.97
OPT4	23.85	0.2	1829.6	38768.1	9621.2	2875.90
OPT5	23.85	0.2	1809.9	38526.0	9988.3	2962.70
OPT6	23.88	0.2	1802.1	38515.0	10122.0	2971.57
MULT1	21.94	0.2	1673.2	346441.0	339800.0	8994.80

Optimization using all fifteen of the parameters previously enumerated is not feasible. However, it was felt that optimization over the five parameters listed in the tables would be possible. In fact, initially the propellant weight was included as a sixth parameter. The simulation MULT1 represents an attempt at this type of optimization. The optimization required an enormous expenditure of computer time, and it is obvious that the inclusion of the propellant weight as a parameter drove the solution toward a strong isentropic solution which produces very high velocity at the cost of catastrophic projectile loads. This result was certainly not acceptable because the result was useless and the cost was exorbitant. Other attempts using several parameters proved very costly and produced questionable results. The simulation S1 is representative of these efforts. In this case the piston length and the pump tube length were selected as parameters for the optimization. This calculation resulted in a modest reduction in projectile acceleration with a correspondingly small drop in muzzle velocity. It was concluded that the close proximity of several local minimal solutions led to results which were valid over a very narrow range of shot conditions. Nevertheless, a final attempt was made to show the probability of achieving results which would be useful in practice. In this case, the pump tube length was first optimized in a single parameter calculation. Simulations SP1, SP2, SP3 and SP4 are typical examples for various light piston weights. Then the piston characteristics (length and weight) were optimized (e.g., in simulations OPT5 and OPT6). The final result is best illustrated in the gasdynamic details of OPT6. In this case which, compared with an isentropic solution, produced an acceleration reduction of 58% for a velocity reduction of 17%, multiple shock reflections produced oscillations of the piston and a series of small acceleration boosts. Ultimately, the piston velocity was near zero when the projectile left the launch tube. In this case, then the gun structural loads were low because the piston did not slam into the transition section at high speed.

Conclusion - The results achieved with this approach to firing cycle design were disappointing. First, it is obvious that the solutions reached are not global optimizations. In fact, apparently local minima are in relatively close proximity in the solution space, and the solutions achieved do not offer a solid basis for decisions regarding changes in gun geometry or selection of shot parameters. However, the study has indicated that some gains toward the "soft", high velocity launch can be made. The author will continue his work in seeking better launch cycles through funding provided by the Louisiana State University.

## 2. LIGHT-GAS GUN DESIGN AND CONSTRUCTION

Introduction - During the course of the analytical phase of this project it was recognized that an experimental facility would be useful for providing validation of numerical predictions and for investigating particular physical phenomena. The project monitor at Eglin AFB agreed to divert some of the original funding from numerical studies to aid in design and construction of such a facility. The project also had an educational goal: to serve as a capstone senior design project for mechanical engineering students at the Louisiana State University. Three students performed the design and construction of the gun in about ten months.

Gun Operation - An overview of the gun design is given in Figure 5. The firing sequence for the gun is as follows: The firing button is depressed, sending an electrical pulse to the solenoid-activated dump valve. The pressure reservoir contains a valve plunger that initially seals the pump tube via the pressurized air in the reservoir. Activation of the dump valve releases pressure on this plunger, causing it to unseal the pump tube chamber and permit high pressure air to flow rapidly into the pump tube. A piston in the pump tube seals the helium gas in the tube from the high pressure air in the reservoir. The piston is then driven by this high pressure air into the helium, causing a compression process which produces high pressure and temperature in the helium. Ultimately, the pressure in the pump tube reaches a level which causes the diaphragm to burst, forcing the projectile down and out of the launch tube.

Design Features - The gun has certain design features which make it appealing both as a research facility and as an addition to a teaching laboratory. These can be summarized as follows:

- (1). The gun uses no explosive charge. This is a convenient safety feature, but it also facilitates rapid shot turnaround and it minimizes cleanup and maintenance after a shot.
- (2). The couplings at the central breech and the launch tube are both designed so that they can be tightened and loosened by hand using built-in turning handles.
- (3). Placement of the projectile, diaphragm and piston can all be accomplished without special tools.
- (4). The charging system contains a manual release valve so that the gun can be deactivated prior to firing in the event of an emergency.
- (5). Instrumentation provides charging pressures prior to launch and piston velocity, pump tube pressure and projectile velocity during launch.

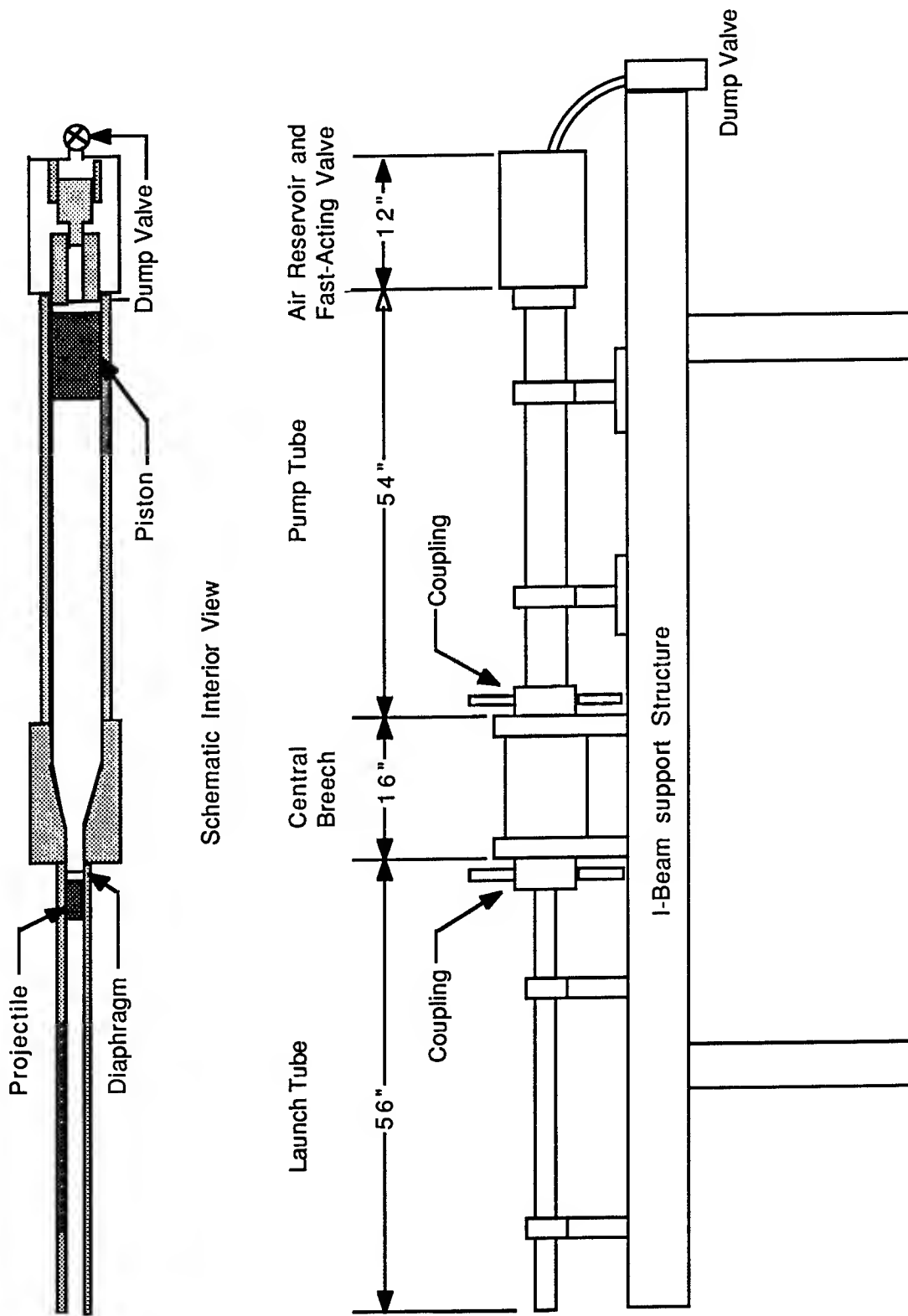


Figure 5. Light-gas Gun Layout

The specific characteristics of each part of the gun are provided in the following paragraphs.

**DUMP VALVE** - This small-capacity solenoid valve, manufactured by the Secodyne Corporation, acts as a dump valve from the air pressure chamber. When it is activated by an electrical pulse, it releases pressure behind the air valve and begins the firing process.

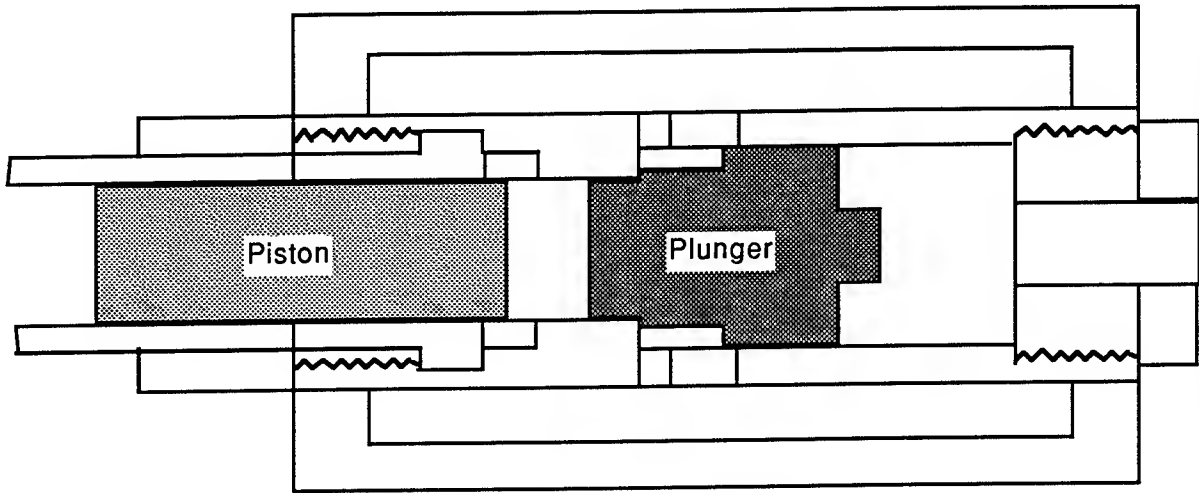
**PRESSURE RESERVOIR AND FAST-ACTING AIR VALVE** - The reservoir component was manufactured by welding 3/4-inch steel plates to the ends of a piece of 8-inch heavy wall pipe. The valve assembly was then fitted through the reservoir and sealed with O-rings. The installation of the pump tube on the reservoir side opposite the valve assembly completes the installation. This is shown in Figure 6.

**PUMP TUBE AND COUPLINGS** - The pump tube is manufactured from heavy-wall pipe which is honed inside and threaded at each end to accommodate a coupling with which it can be joined to the fast-acting air valve at one end and the central breech at the other end. The pump tube and its assembly to the pressure reservoir and the central breech are shown in Figure 7.

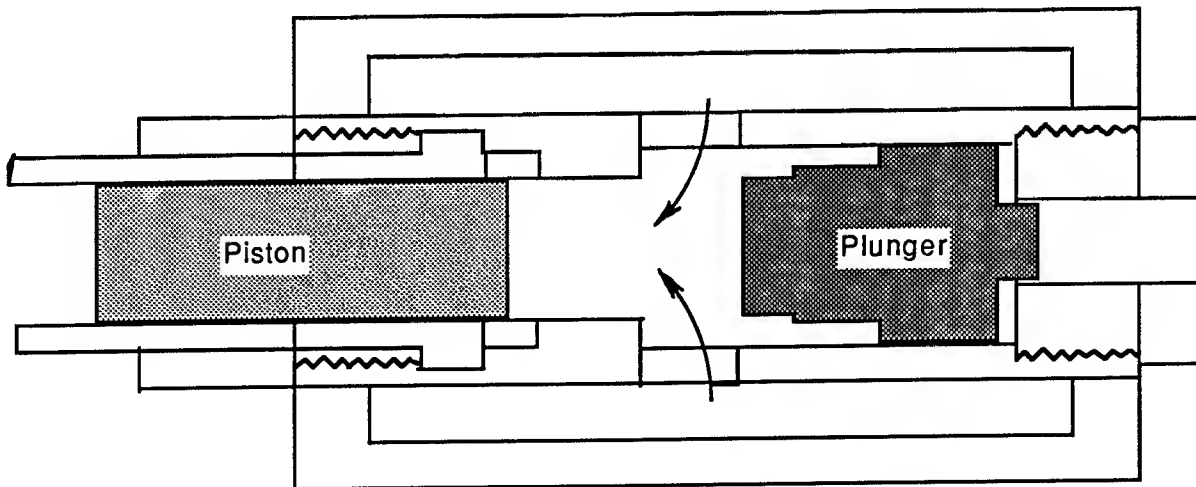
**CENTRAL BREECH** - This component is often called the high pressure section because the maximum pressure and impact loads on the entire gun assembly are felt here. The central breech is constructed of a single piece of high-strength steel which is machined to form a transition between the large diameter pump tube and the smaller diameter launch tube. Ports are also provided in the central breech for instrumentation and for helium charging. This component is shown in Figure 8.

**LAUNCH TUBE AND DIAPHRAGM ASSEMBLY** - The launch tube, or barrel, of the gun is fabricated from heavy-wall pipe in a manner similar to that used for the pump tube. It is threaded at each end. One end accommodates an end cap which holds a plastic diaphragm and steel diaphragm cutter in place. This diaphragm assembly is fitted with O-rings so that it forms a seal when it is mounted to the downstream end of the central breech via a hand-tightened coupling. The other end is threaded to facilitate the installation of a choke, a silencer or muzzle-velocity instrumentation. These components are shown in Figure 9.

**GUN MOUNTS AND CONTROL PANEL** - The entire gun assembly is mounted on a frame constructed of heavy steel I-beam. The central breech is leveled, rigidly mounted to the frame and fitted with a blast shield fabricated from heavy-wall steel pipe. Then the high pressure reservoir and valve, the pump tube and the launch tube are aligned



Valve in Closed Position



Valve in Open Position

Figure 6. Fast Acting Valve

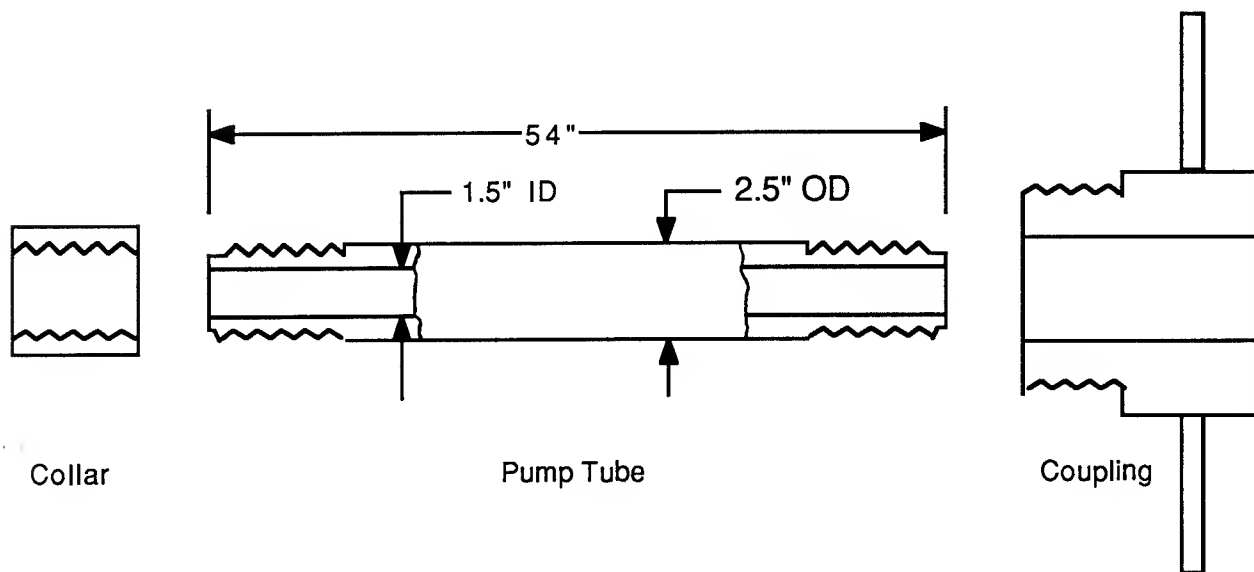


Figure 7. Pump Tube Assembly

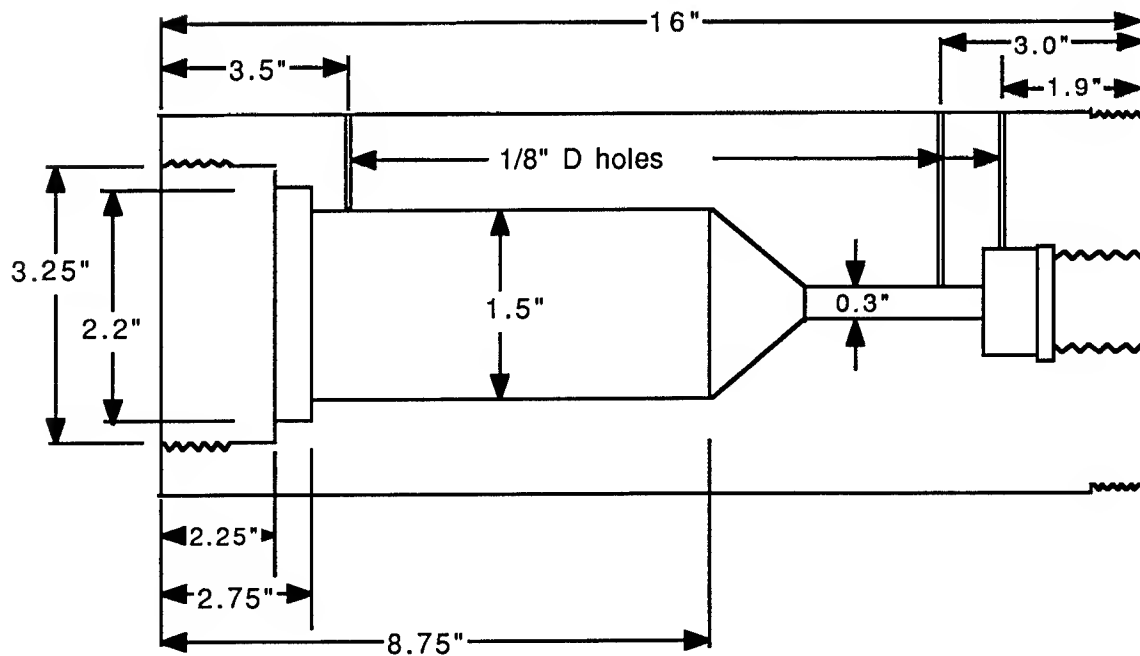


Figure 8. Central Breech

with the central breech and fixed to the frame with adjustable supports. Finally, a control panel is mounted on the frame. This control panel contains all charging valve controls and gauges in addition to lights that indicate the degree of readiness of the

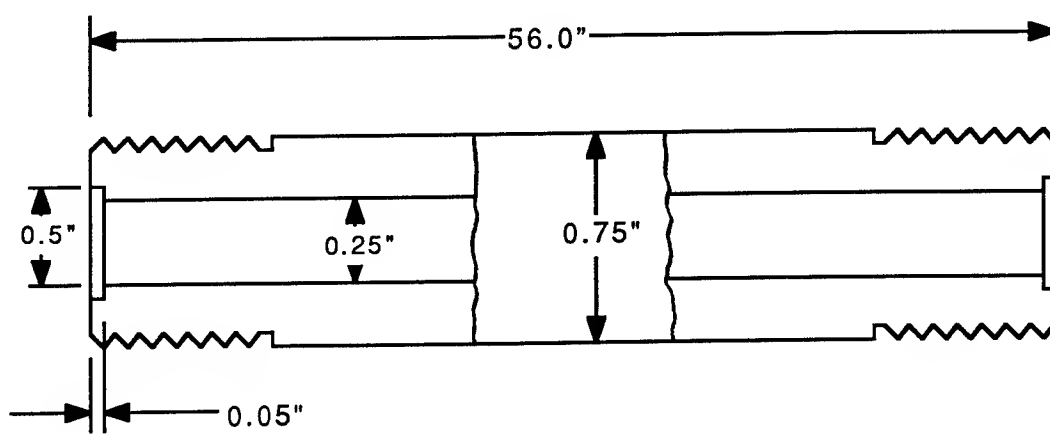


Figure 9. Launch tube

gun. The gun is ultimately fired with a remote switch located outside the gun room. This arrangement is shown in Figure 5.

Instrumentation and performance - Provisions are made for the installation of three pressure transducers which will indicate the transient pressure during a shot. One transducer mount is located on the pump tube, one is located in the central breech just upstream of the area reduction section and one is located in the central breech near the diaphragm. It is intended that these transducers will provide, respectively, the piston speed, the peak pressure and the diaphragm rupture pressure. Currently, only the pump tube transducer is installed, though the other two will be installed when funding becomes available.

A magnetic sensing device for determining muzzle velocity was fabricated and is currently installed at the end of the launch tube. This is suitable for measuring the velocity of low performance shots with steel projectiles, but it is not useful for non-magnetic projectiles, and launch tube vibrations during high performance shots cause premature triggering of the oscilloscope. Isolating the device from the gun will eliminate the latter problem. However, to add versatility to the facility a student design



team is currently working on an optical system for velocity determination which will also include two photographic stations. This latter facility will not be operational until November.

The gun has been fired many times to check out various aspects of the design. To date the shots have been made with a low pressure diaphragm and with the helium in the pump tube initially at atmospheric pressure. A summary of performance with shots for which all of the instrumentation provided useful results is shown in Figure 10. The high pressure reservoir has a design pressure of 650 psi with a factor of safety of 4.5, whereas the data indicated in the figure show a maximum charge pressure of only 500 psi. However, one shot was made at a charge pressure of 800 psi. A muzzle velocity was not measured for that shot, but based on the characteristics of the impact, it is estimated that the muzzle velocity exceeded 8000 feet per second. In the months ahead a comprehensive testing program will be carried out to determine the limits of gun performance.

Conclusion - A light gas gun facility has been designed, constructed and tested. When fully instrumented, this gun is capable of providing sufficient experimental data to validate numerical performance estimates and to provide valuable insight into the interior ballistics of the gun. In particular, it should provide sufficient data to monitor the shock interaction process which is believed to be the key to producing high velocity shots with low projectile loading.

#### Acknowledgements

The author acknowledges the considerable contributions of Mr. Jean-Yves Lorin to the analytical optimization study and the dedicated efforts of Messrs. Brian Breaux, Tim Poirrier, Thomas Tamplain in the design and construction of the light-gas gun. He also thanks Mr. Gerald Winchenbach for serving as project monitor for the Air Force. The support of the Research Development Laboratory and the Air Force Office Of Scientific Research are also appreciated.

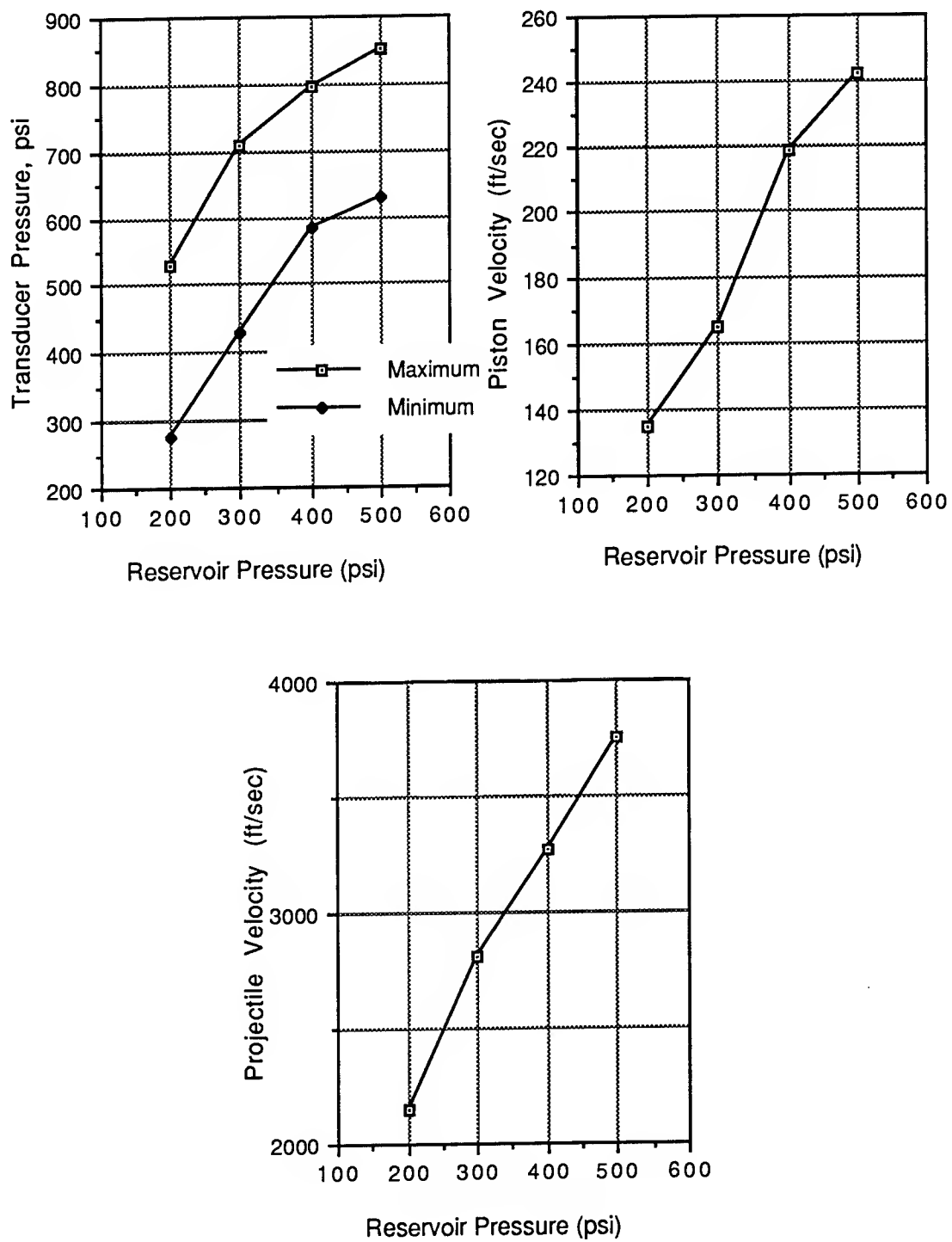


Figure 10. Light-gas Gun Performance

### References

1. Piacesi, R., D. F. Gates and A. E. Seigel, "Computer Analysis of Two-Stage Hypervelocity Launchers," Naval Ordnance Laboratory Report NOLTR 62-87, White Oak, Maryland, August, 1963.
2. von Neumann, J. and R. D. Richtmeyer, "A Method for the Numerical Calculation of Hydrodynamic Shocks," Journal of Applied Physics, v. 21, March, 1950.
3. Powell, M. J. D., "A Method for Minimizing a Sum of Squares of Non-Linear Functions without Calculating Derivatives," The Computer Journal, v. 7, no. 4, January, 1965.
4. Dahm, T. J. and D. S. Randall, "The Wave Gun Concept for a Hypervelocity Rapid-Fire Weapon," Astron Research and Engineering, Mountain View, CA, January, 1984.



**A STUDY OF DECENTRALIZED CONTROL OF A FLEXIBLE  
STRUCTURE WITH UNCERTAIN INTERCONNECTIONS**

**George T. Flowers  
Assistant Professor  
Department of Mechanical Engineering**

**Auburn University  
201 Ross Hall  
Auburn University, AL 36849-5341**

**Final Report for:  
Research Initiation Program  
Wright Laboratory**

**Sponsored by:  
Air Force Office of Scientific Research  
Bolling Air Force Base, Washington, D.C.**

**and**

**Auburn University**

**December 1992**

# **A STUDY OF DECENTRALIZED CONTROL OF A FLEXIBLE STRUCTURE WITH UNCERTAIN INTERCONNECTIONS**

**George T. Flowers  
Assistant Professor  
Department of Mechanical Engineering  
Auburn University**

## **Abstract**

An area of current interest in the decentralized control of large flexible structures is the development of adaptive strategies that will allow for acceptable vibration suppression and tracking in the presence of uncertainties. One such strategy is the Gavel-Siljak approach, which is based upon direct control using adaptive gains. The approach treats the interconnections effects between subsystems as uncertain quantities. The current study is aimed at examining the appropriateness of such an algorithm for the control of multibody flexible structures. A two body simulation model is developed. The application of the adaptive control algorithm to this structure is discussed in the context of the simulation model. Results using this model are presented and discussed.

# **A STUDY OF DECENTRALIZED CONTROL OF A FLEXIBLE STRUCTURE WITH UNCERTAIN INTERCONNECTIONS**

**George T. Flowers**

## **Introduction**

The field of decentralized control is one that is of great interest in the development of control strategies for complex structural systems. Decentralized techniques allow the structural model to be divided into a set of subsystems, each of which is controlled independently of the others. For such an approach, it is natural to arrange the structural decomposition so that the dynamics of the subsystem models are known and any uncertainties are attributed to the interconnection forces linking the subsystems. Thus, it is of interest to consider strategies for controlling subsystems with uncertain (possibly time-varying and nonlinear) interconnections. The most promising techniques for such systems appear to be based upon adaptive control methods. In this regard, adaptive strategies are a relatively new field and one that is wide open for further research.

The current work is a study aimed at examining the application of the direct adaptive decentralized control scheme formulated by Gavel and Siljak (1989) to flexible multibody structures. A mathematical model is developed for a two body truss structure. The implementation of this control algorithm is discussed in the context of the model. A simulation study is performed and the results presented.

## **Previous Work**

Adaptive control schemes offer several valuable advantages to the control system designer. Such approaches are typically more tolerant of modelling errors and uncertainties. Under appropriate conditions, certain stability characteristics can be assured even though there may be great deal of modelling uncertainty. In addition, adaptive strategies usually

produce lower closed loop feedback gains and, thus, significantly improved noise rejection characteristics as compared to fixed-gain methods. The application of adaptive techniques to decentralized control is a topic of current interest and one that promises to produce important advances.

A number of investigators have made important contributions to the field of adaptive decentralized control. Among them are Hmamed and Radouane (1983), Ioannou and Kokotović (1983), Ioannou and Reed (1988), and Siljak (1991). Much of this work has been directed toward using model reference adaptive controllers (MRAC) for the decentralized control of unknown subsystems as if they were disconnected from each other.

An important category of this work consists of direct control strategies for which the interconnection effects are directly reachable by the control actuators. One such approach has been developed by Gavel and Siljak (1989). They describe an adaptive method for designing a decentralized control strategy for a system with known subsystems that will be stable regardless of the magnitude of the interconnection forces. Their development starts with the following mathematical description for a system consisting of a set of interconnected subsystems.

$$\dot{\bar{x}}_i = A_i \bar{x}_i + B_i \bar{u}_i + P_i \bar{v}_i \quad (1)$$

$$\bar{y}_i = C_i \bar{x}_i$$

$$\bar{w}_i = Q_i \bar{x}_i$$

Each pair  $(A_i, B_i)$  and  $(A_i, C_i)$  are respectively controllable and observable.

The assumption is made that the interconnection inputs and outputs  $\bar{v}_i$  and  $\bar{w}_i$  are related as



$$\bar{v}_i = \bar{d}_i(t, w) \quad (2)$$

The boundedness condition for the interconnection forces

$$\| \bar{d}_i(t, w) \| \leq \sum_{j=1}^N \xi_{ij} \| \bar{w}_j \| \quad (3)$$

is also assumed

For direct control, it is necessary to impose the requirement that the interconnection matrices  $P_i$  can be factored as

$$P_i = B_i P'_i \quad (4)$$

This requirement assures that the actuator forces can directly reach the interconnection forces. Note that it is not necessary that the scalar quantities  $\xi_{ij}$  or the matrices  $P'_i$  be known, but it is required that they be constant.

The control objective is for each of the closed loop subsystems to track stable isolated reference models. A typical approach for selecting appropriate reference models consists of first selecting local feedback gain matrices  $J_i$  to stabilize the disconnected subsystems. This results in state matrices for the closed loops subsystems of the form:

$$A_{m,i} = A_i - B_i J_i \quad (5)$$

The resulting reference models are governed by the relations:

$$\begin{aligned} \dot{\bar{x}}_{mi} &= A_{mi} \bar{x}_{mi} + B_i \bar{r}_i \\ \bar{y}_{mi} &= C_i \bar{x}_{mi} \end{aligned} \quad (6)$$

It is required that  $\bar{r}_i$  be bounded, piecewise continuous vector functions of time.

An adaptive local control law is formulated in the following manner. First, define

$$Z_i = R_i^{-1} B_i^T H_i \quad (7)$$

where  $H_i$  is the symmetric positive definite solution to the matrix Lyapunov equation

$$A_{mi}^T H_i + H_i A_{mi} = -G_i \quad (8)$$

$G_i$  is any symmetric, positive definite  $n_i \times n_i$  matrix. A solution to (8) is guaranteed to exist since  $A_{mi}$  is stable.

The resulting feedback control law is then

$$\bar{u}_i = -J_i \bar{x}_i - \alpha_i(t) Z_i \bar{e}_i + \bar{r}_i \quad (9)$$

where  $\alpha_i(t)$  is a time variable scalar adaptation gain and  $\bar{e}_i(t) = \bar{x}_i(t) - \bar{x}_{mi}(t)$ . The adaptation law for  $\alpha_i(t)$  is chosen as:

$$\dot{\alpha}_i = \gamma_i \bar{e}_i^T Z_i^T R_i Z_i \bar{e}_i - \sigma_i \alpha_i, \quad \alpha_i(t_0) > 0 \quad (10)$$

where  $\gamma_i$  and  $\sigma_i$  are given positive scalars.

Further details of the development and proof of the stability characteristics of this approach can be found in Gavel and Siljak (1989).

### **Current Work**

Of concern in the present study, is the application of the controller strategy described in the preceding section to the vibration suppression of a large flexible space structure. To examine the issues relevant to the implementation of this strategy and the performance of

the resulting controller, a simulation study was performed. The model used in the study and the results obtained are described below.

### Simulation Model

The simulation model consists of a two body flexible truss structure as shown in Figure 1. The structure is comprised of a boom truss and an antenna. The node coordinates for each structure are shown in Tables 1 and 2. The coordinates are taken with respect to the location of node 1 for the corresponding substructure. The node locations are shown in Figure 2. The material for each structure is steel. The area of each spar is 1.0 in<sup>2</sup>.

Antenna Model		
Node	'X' Coord.	'Y' Coord.
1	0	0
2	48	24
3	48	-24
4	96	24
5	96	-24
6	72	48
7	72	-48
8	96	96
9	96	-96

**Table 2:** Node Coordinates for Antenna Model

The equations of motion for this model were developed using the Gibbs–Appell formulation [Ginsberg (1988)]. The development proceeds in the following manner. It is assumed that each body can be modelled as a collection of discrete masses connected in a linearly elastic fashion. Based upon this assumption, acceleration relations for each point on a body can be developed. For the supporting boom truss, the relation is:

$$\vec{a}_{1,k} = (W_{1,k}^X + g_k^X)\hat{i}_1 + (W_{1,k}^Y + g_k^Y)\hat{j}_1 \quad (11.a)$$

Boom Truss Model		
Node	'X' Coord.	'Y' Coord.
1	0	0
2	-12	24
3	12	24
4	-12	48
5	12	48
6	-12	72
7	12	72
8	-12	96
9	12	96
10	-12	120
11	12	120
12	-12	144
13	12	144
14	-12	168
15	12	168
16	-12	192
17	12	192
18	-12	216
19	12	216
20	-12	240
21	12	240
22	-12	264
23	12	264

**Table 1:** Node Locations for Boom Truss Model

where

$$W_{1,k}^X = \ddot{u}_{1,k} - \ddot{\theta}_1(Y_{1,k} + v_{1,k}) \quad (11.b)$$

$$W_{1,k}^Y = \ddot{v}_{1,k} + \ddot{\theta}_1(X_{1,k} + u_{1,k}) \quad (11.c)$$

$$g_k^X = -2\dot{\theta}_1\dot{v}_{1,k} - (\dot{\theta}_1)^2(X_{1,k} + u_{1,k}) \quad (11.d)$$

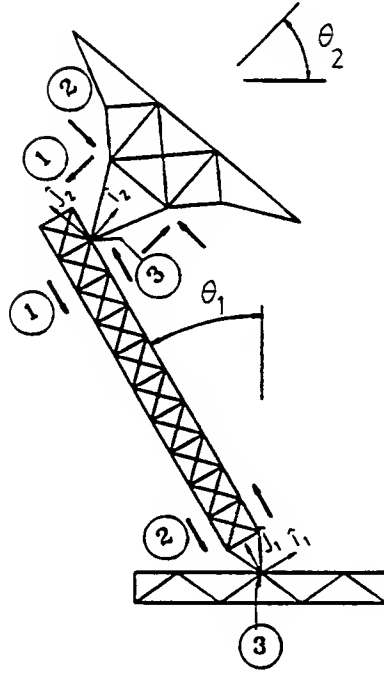


**Figure 1: Two body truss structure**

$$g_k^Y = 2\dot{\theta}_1 \dot{u}_{1,k} - (\dot{\theta}_1)^2 (Y_{1,k} + v_{1,k}) \quad (11.e)$$

For the antenna truss, the relation is:

$$\tilde{a}_{2,l} = \tilde{a}_{1,o} + (W_{2,l}^X + h_l^X)\hat{i}_2 + (W_{2,l}^Y + h_l^Y)\hat{j}_2 \quad (12.a)$$

where

$$W_{2,l}^X = \ddot{u}_{2,l} - \ddot{\theta}_2 (Y_{2,l} + v_{2,l}) \quad (12.b)$$

$$W_{2,l}^Y = \ddot{v}_{2,l} + \ddot{\theta}_2 (X_{2,l} + u_{2,l}) \quad (12.c)$$

$$h_l^X = -2\dot{\theta}_2 \dot{v}_{2,l} - (\dot{\theta}_2)^2 (X_{2,l} + u_{2,l}) \quad (12.d)$$

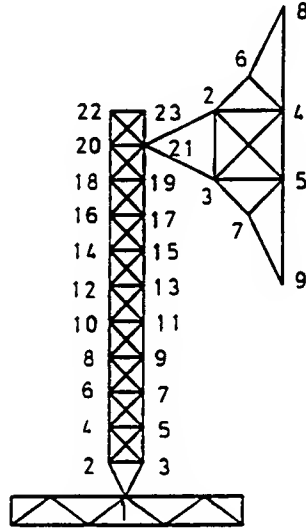


**Figure 2:** Node locations for two body truss structure

$$h_l^Y = 2\dot{\theta}_2 \dot{u}_{2,l} - (\dot{\theta}_2)^2 (Y_{2,l} + v_{2,l}) \quad (12.e)$$

$$\hat{i}_1 = \cos(\theta_2 - \theta_1) \hat{i}_2 - \sin(\theta_2 - \theta_1) \hat{j}_2 \quad (13.a)$$

$$\hat{j}_1 = \cos(\theta_2 - \theta_1) \hat{j}_2 + \sin(\theta_2 - \theta_1) \hat{i}_2 \quad (13.b)$$

Mode shapes obtained from finite element analyses are used to express the elastic deflections associated with each node point as:

$$\ddot{u}_{1,k} = \sum_{k=1}^{I_1} Q_{k,i}^X q_{1,i}$$

$$\ddot{v}_{1,k} = \sum_{k=1}^{I_1} Q_{k,i}^Y q_{1,i}$$

$$\ddot{u}_{2,l} = \sum_{l=1}^{I_2} R_{l,i}^X q_{2,i}$$

$$\ddot{v}_{2,l} = \sum_{l=1}^{I_2} R_{l,i}^Y q_{2,i}$$

For the purposes of this study, the first two elastic modes for each of the bodies will be considered. Thus,  $I_1 = 2$  and  $I_2 = 2$ . The effects of the higher elastic modes on the dynamics of the reduced order system can be considered to be included in the (uncertain) interconnection forces. The modes selected are the lowest frequency modes for that particular substructure. For the boom truss, the two modes are (1) the first bending mode and (2) a longitudinal stretching mode. For the antenna, the first two modes are (1) a symmetric bending mode and (2) an anti-symmetric bending mode.

The Gibbs-Appell function can be formed as:

$$S = \frac{1}{2} \sum_k^{L_1} (m_{1,k} \vec{a}_{1,k} \cdot \vec{a}_{1,k}) + \frac{1}{2} \sum_l^{L_2} (m_{2,l} \vec{a}_{2,l} \cdot \vec{a}_{2,l}) \quad (14)$$

The equations of motion that result are as follows:

$$\begin{aligned} M_1 \{\ddot{\bar{z}}_1\} + [(N_1)(N_2)] \{(\ddot{\bar{z}}_1)^T (\ddot{\bar{z}}_2)^T\}^T + K_1 \{\bar{z}_1\} \\ + \Delta_1 \{\bar{f}_1\} = E_{11} \{\bar{u}_1\} + E_{12} \{\bar{u}_2\} \end{aligned} \quad (15)$$

$$\{\bar{z}_1\} \equiv \begin{pmatrix} q_{1,1} \\ q_{1,2} \\ \theta_1 \end{pmatrix}$$

Where

$$K_1 = \begin{pmatrix} \omega_{1,1}^2 & 0 & 0 \\ 0 & \omega_{1,2}^2 & 0 \\ 0 & 0 & 0 \end{pmatrix}$$

$$\begin{aligned} M_2\{\ddot{\bar{z}}_2\} + N_2^T\{\ddot{\bar{z}}_1\} + K_2\{\bar{z}_2\} \\ + \Delta_2\{\bar{f}_2\} = E_{22}\{\bar{u}_2\} \end{aligned} \quad (16)$$

$$\{\bar{z}_2\} \equiv \begin{pmatrix} q_{2,1} \\ q_{2,2} \\ \theta_2 \end{pmatrix}$$

$$K_2 = \begin{pmatrix} \omega_{2,1}^2 & 0 & 0 \\ 0 & \omega_{2,2}^2 & 0 \\ 0 & 0 & 0 \end{pmatrix}$$

The elements of the matrices  $M_1$ ,  $M_2$ ,  $N_1$ , and  $N_2$  and of the vectors  $\bar{f}_1$  and  $\bar{f}_2$  are listed in Appendix B.

The state equations that result are of the form:

$$\begin{aligned} \begin{pmatrix} \ddot{\bar{z}}_1 \\ \dot{\bar{z}}_1 \end{pmatrix} &= \begin{pmatrix} 0 & -M_1^{-1}K_1 \\ I & 0 \end{pmatrix} \begin{pmatrix} \dot{\bar{z}}_1 \\ \bar{z}_1 \end{pmatrix} \\ &+ \begin{pmatrix} -M_1^{-1}[(N_1)(N_2)] \\ 0 \end{pmatrix} \begin{pmatrix} \ddot{\bar{z}}_1 \\ \ddot{\bar{z}}_2 \end{pmatrix} \\ &+ \begin{pmatrix} -M_1^{-1}\Delta_1 \\ 0 \end{pmatrix} \begin{pmatrix} \bar{f}_1 \\ 0 \end{pmatrix} + \begin{pmatrix} M_1^{-1}E_{11} \\ 0 \end{pmatrix} \begin{pmatrix} \bar{u}_1 \\ 0 \end{pmatrix} \\ &+ \begin{pmatrix} M_1^{-1}E_{12} \\ 0 \end{pmatrix} \begin{pmatrix} \bar{u}_2 \\ 0 \end{pmatrix} \end{aligned} \quad (17)$$

$$\begin{aligned} \begin{pmatrix} \ddot{\bar{z}}_2 \\ \dot{\bar{z}}_2 \end{pmatrix} &= \begin{pmatrix} 0 & -M_2^{-1}K_2 \\ I & 0 \end{pmatrix} \begin{pmatrix} \dot{\bar{z}}_2 \\ \bar{z}_2 \end{pmatrix} + \begin{pmatrix} -M_2^{-1}N_2^T \\ 0 \end{pmatrix} \begin{pmatrix} \ddot{\bar{z}}_1 \\ \ddot{\bar{z}}_2 \end{pmatrix} \\ &+ \begin{pmatrix} -M_2^{-1}\Delta_2 \\ 0 \end{pmatrix} \begin{pmatrix} \bar{f}_2 \\ 0 \end{pmatrix} + \begin{pmatrix} M_2^{-1}E_{22} \\ 0 \end{pmatrix} \begin{pmatrix} \bar{u}_2 \\ 0 \end{pmatrix} \end{aligned} \quad (18)$$



Examination of (17) and (18) and comparison with (1) indicates that, for the current structural system, the  $B_i$  matrices are of the form

$$B_1 = (\hat{B}_1^T[0])^T \quad (19.a)$$

$$B_2 = (\hat{B}_2^T[0])^T \quad (19.b)$$

where

$$\hat{B}_1 = M_1^{-1} E_{11}$$

$$\hat{B}_2 = M_2^{-1} E_{22}$$

Examination of the equations of motion indicate that the matrices  $M_1$  and  $M_2$  consist of constant terms and linear terms in the elastic generalized coordinates. The matrices  $N_1$  and  $N_2$  consist of constant terms and trigonometric functions of the angular coordinates, and products of these trigonometric functions and the elastic generalized coordinates. The vectors  $\bar{f}_1$  and  $\bar{f}_2$  consist of nonlinear expressions containing trigonometric terms and the elastic generalized coordinates. Such nonlinear effects are accounted for in the development of the control algorithm and should present no problem to the performance of the controller. However, an examination of (17) and (18) and comparison with the form of (1) shows that the interconnection forces,  $\bar{v}_i$  may be functions of the actuator forces. Such effects are not accounted for in the algorithm development and stability proof. This issue may have serious consequences for the performance of this controller as applied to structural systems and needs to be examined further.

## Simulation Results

For the purposes of this study, actuators are placed as shown in Figure 1. The actuator forces are applied (as couples) at the nodes shown with bold arrows. The numbers associated with each pair of arrows indicates the corresponding row of the control input vector. The directions of the actuator forces are indicated by the directions of the arrows in relation to the associated substructure. This particular arrangement is selected so that  $E_{12} = [0]$ . The controller parameters used in this study are listed in Appendix C.

Figures 3 and 4 present the time responses for the flexible and rigid body motion of the boom truss and the antenna with the adaptive controller parameters,  $\gamma_i$  and  $\sigma_i$ , set to zero. The oscillations are clearly unstable. The system responses diverge very rapidly from those of the reference model. Note that each isolated substructure is stable. However, an eigenanalysis of a linearized model of the complete system with just the linear controller indicates that it is unstable. This effect is due to the impact of the interconnections on the system behavior. The dynamics of the antenna acting through the interconnection (at boom truss node 21) on the dynamics of the boom truss and vice-versa serve to cause unstable oscillations.

Figures 5 and 6 present the time responses for the flexible and rigid body angular motion of the boom truss and the antenna for the indicated parameters. For this case, the ability of the actual system to track the desired behavior is acceptable for both the rigid body motion and for both modes of the flexible vibration. In fact, the model tracking for the boom truss is almost exact from the starting time. The responses of the antenna are also quite good. So it can be seen that the current algorithm can produce a controller that gives excellent reference model tracking.

## Conclusion

A discussion of an adaptive, decentralized control algorithm has been presented in the

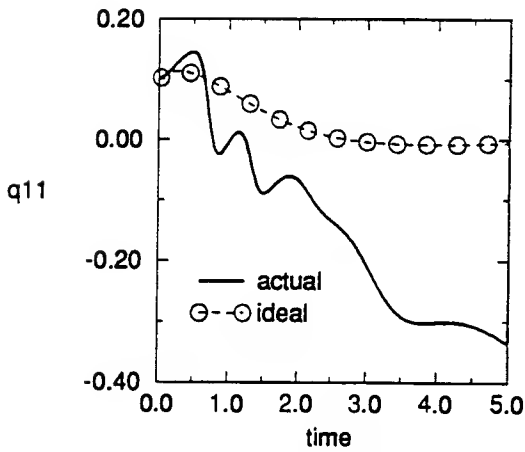


Figure 3.a Time response for boom truss.

( $\gamma_1 = 0, \gamma_2 = 0, \sigma_1 = 0, \sigma_2 = 0$ )

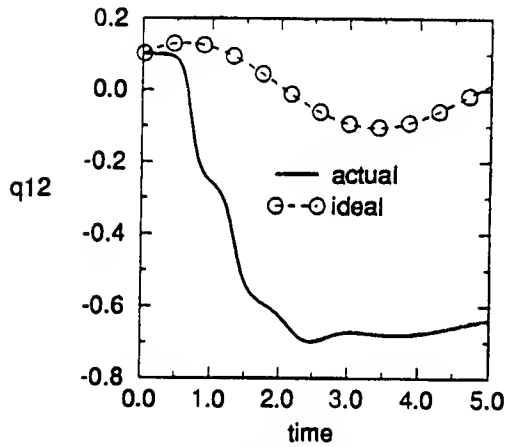


Figure 3.b Time response for boom truss.

( $\gamma_1 = 0, \gamma_2 = 0, \sigma_1 = 0, \sigma_2 = 0$ )

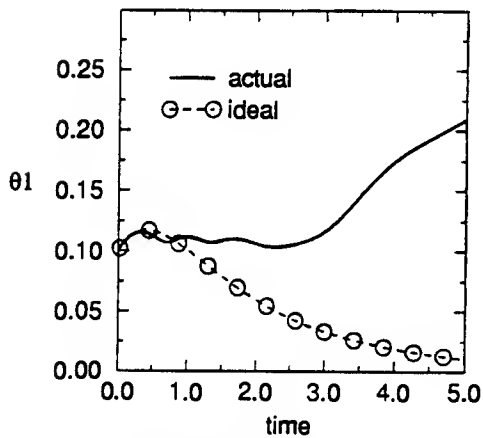


Figure 3.c Time response for boom truss.

( $\gamma_1 = 0, \gamma_2 = 0, \sigma_1 = 0, \sigma_2 = 0$ )

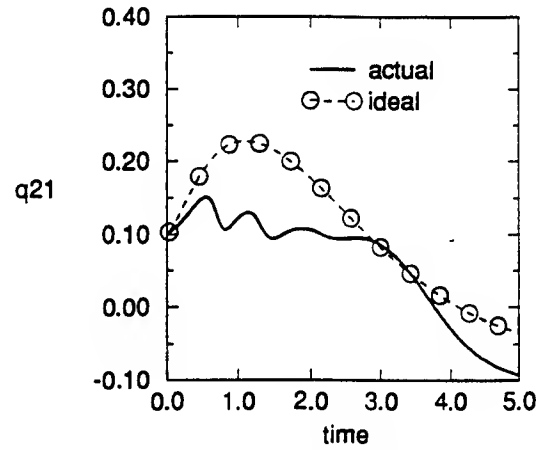


Figure 4.a Time response for antenna.

( $\gamma_1 = 0, \gamma_2 = 0, \sigma_1 = 0, \sigma_2 = 0$ )

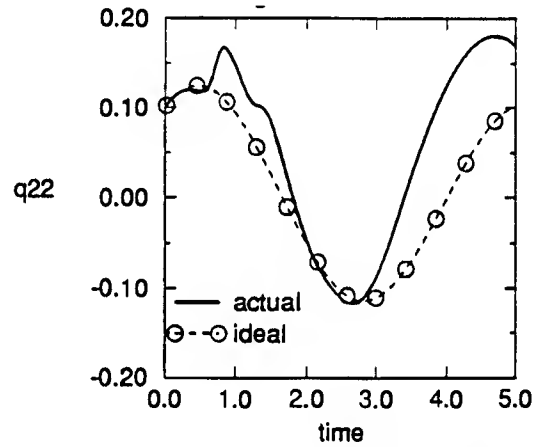


Figure 4.b Time response for antenna.

( $\gamma_1 = 0, \gamma_2 = 0, \sigma_1 = 0, \sigma_2 = 0$ )

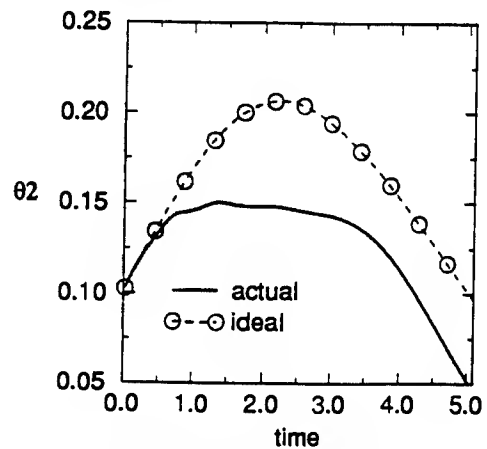


Figure 4.c Time response for antenna.

( $\gamma_1 = 0, \gamma_2 = 0, \sigma_1 = 0, \sigma_2 = 0$ )

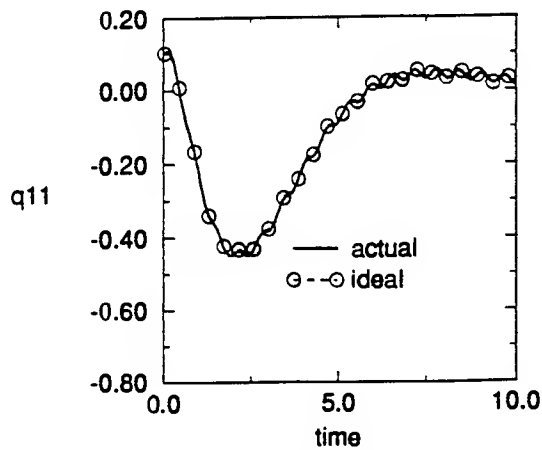


Figure 5.a Time response for boom truss  
( $\gamma_1 = 10, \gamma_2 = 10, \sigma_1 = 0.1, \sigma_2 = 0.1$ )

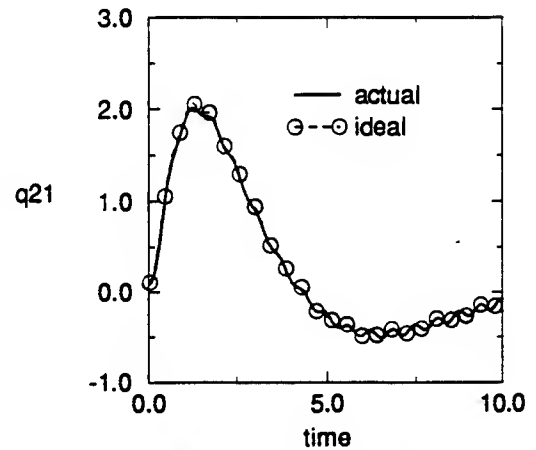


Figure 6.a Time response for antenna  
( $\gamma_1 = 10, \gamma_2 = 10, \sigma_1 = 0.1, \sigma_2 = 0.1$ )

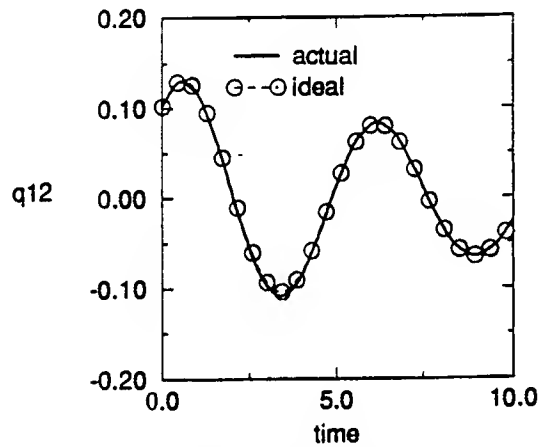


Figure 5.b Time response for boom truss  
( $\gamma_1 = 10, \gamma_2 = 10, \sigma_1 = 0.1, \sigma_2 = 0.1$ )

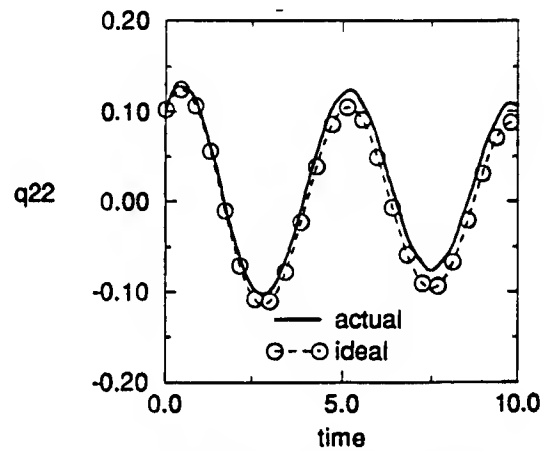


Figure 6.b Time response for antenna  
( $\gamma_1 = 10, \gamma_2 = 10, \sigma_1 = 0.1, \sigma_2 = 0.1$ )

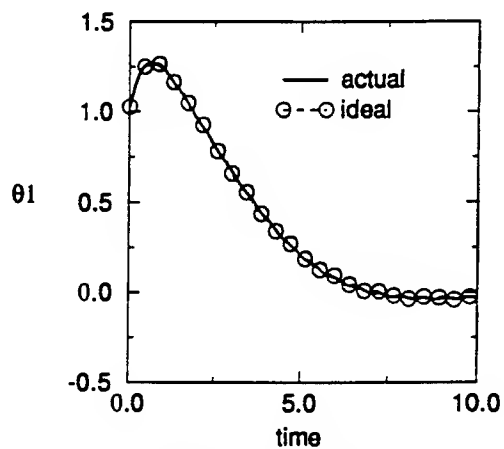


Figure 5.c Time response for boom truss  
( $\gamma_1 = 10, \gamma_2 = 10, \sigma_1 = 0.1, \sigma_2 = 0.1$ )

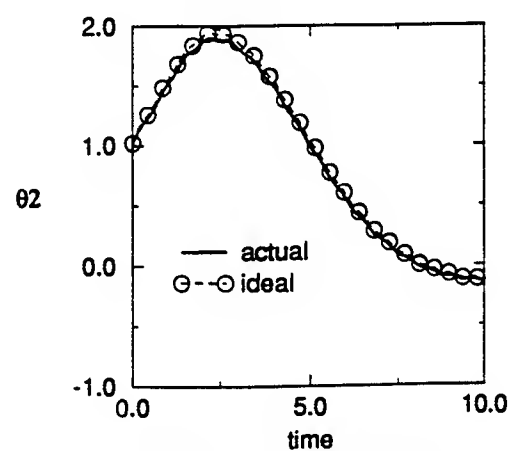


Figure 6.c Time response for antenna  
( $\gamma_1 = 10, \gamma_2 = 10, \sigma_1 = 0.1, \sigma_2 = 0.1$ )

context of a two body, flexible truss structure. The model development has been presented and discussed. Some observations concerning the implementation of this control technique have been noted. A simulation study was performed to illustrate the performance and implementation of the algorithm for a structural system.

## **References**

- Craig, J.J., *Adaptive Control of Mechanical Manipulators* Addison-Wesley Publishing Company, Reading, MA, 1988.
- Gavel, D.T., and Siljak, D.D., *Decentralized Adaptive Control: Structural Conditions for Stability*, IEEE Transactions on Automatic Control, Vol. 34, No. 4, April 1989, pp 413-426.
- Ginsberg, J. H., *Advanced Engineering Dynamics*, Harper and Row, New York, 1988.
- Hmamed, A., and L. Radouane, *Decentralized Nonlinear adaptive feedback stabilization of Large-scale interconnected systems*, IEE Proceedings, Vol. 130-D, 1983 PP. 57-62.
- Ioannou, P.A., and P.V. Kokotović, *Adaptive System with Reduced Models*, Springer, New York, 1983.
- Ioannou, P.A., and P.V. Kokotović, *Robust Design of Adaptive Control*, IEEE Transactions on Automatic Control, Vol. AC-29, 1984, pp. 202-211.
- Ioannou, P.S., *Decentralized Adaptive Control of Interconnected Systems*, IEEE Transactions on Automatic Control, Vol. AC-31, No. 4, April, 1986, pp. 291-298.
- Ioannou, P.A., and J.S. Reed, *Discrete-time Decentralized Control*, Automatica, Vol. 24, 1988, pp. 419-421.
- Mao, Cheng-Jyl, and Lin, Wei-Song, *On-Line Decentralized Control of Interconnected Systems With Unmodelled Nonlinearity and Interaction*, Proceedings of the 1989 Automatic Controls Conference, Vol. 1, pp. 248-252.
- Rao, S.S., Pan, T.S., and Venkayya, V.B., *Modeling, control, and design of flexible structures: A survey*, Applied Mechanics Review, vol. 43, no. 5, part 1, may 1990, pp. 99-117.
- Sandell, N.R., Varaiya, P., Athans, and Safonov, M.G., *Survey of Decentralized Control Methods for Large Scale Systems*, IEEE Transactions of Automatic Control, Vol. AC-23, No. 2, April 1978, pp. 108-128.
- Siljak, D.D., *Parameter Space Methods for Robust Control Design: A Guided Tour*, IEEE Transactions on Automatic Control, Vol. 34, NO. 7, July 1988, pp. 674-688.
- Siljak, D.D., *Decentralized Control of Complex Systems*, Academic Press, Inc., 1991.
- Singh, M.D., *Decentralised Control*, North-Holland Publishing Company, Amsterdam, 1981.

## Appendix A – Nomenclature

- $A_i$  = disconnected linear state matrix  
for  $i^{\text{th}}$  subsystem  
 $A_{mi}$  = decentrally stabilized linear state matrix  
for  $i^{\text{th}}$  subsystem  
 $B_i$  = input matrix for  $i^{\text{th}}$  subsystem  
 $C_i$  = output matrix for  $i^{\text{th}}$  subsystem  
 $E_{11}, E_{12}, E_{22}$  = actuator matrices  
 $\bar{e}_i$  = error vector for  $i^{\text{th}}$  subsystem ( $\bar{x}_i - \bar{x}_{mi}$ )  
 $\bar{d}_i$  = interconnection function for  $i^{\text{th}}$  subsystem  
 $\bar{f}_1, \bar{f}_2$  = interconnection forces  
 $G_i$  = positive definite  $n_i \times n_i$  matrix  
 $H_i$  = solution matrix for Lyapunov equation  
 $i$  = subsystem index  
 $I_1$  = number of elastic modes for boom truss  
 $I_2$  = number of elastic modes for antenna  
 $J_i$  = linear local feedback control law  
for  $i^{\text{th}}$  subsystem  
 $K_i$  = structural stiffness matrix  
for  $i^{\text{th}}$  subsystem  
 $k$  = node index for boom truss  
 $L_1$  = number of nodes for boom truss  
 $L_2$  = number of nodes for antenna  
 $l_i$  = number of outputs for subsystem  $i$   
 $l$  = node index for antenna  
 $M_{1,k}$  = mass associated with  $k^{\text{th}}$   
node point on boom truss  
 $M_{2,l}$  = mass associated with  $l^{\text{th}}$   
node point on antenna  
 $M_2^T$  = total mass of antenna  
 $o$  = interconnection node point  
 $m_i$  = number of interconnection forces  $i$   
 $n_i$  = number of states for subsystem  $i$   
 $N$  = number of subsystems  
 $P_i$  = interconnection matrix for subsystem  $i$   
 $p_i$  = number of control inputs for subsystem  $i$   
 $Q_i$  = output matrix  
 $Q_{k,i}^X, Q_{k,i}^Y$  = linear mode shapes  
for boom truss  
 $q_{ij}$  =  $j^{\text{th}}$  generalized coordinate for flexible  
vibration of subsystem  $i$   
 $R_i$  = positive definite  $p_i \times p_i$  matrix

$R_{l,i}^X, R_{l,i}^Y$  = linear mode shapes  
for antenna  
 $\bar{u}_i$  = local control input acting  
on subsystem i  
 $u_{1,k}, v_{1,k}$  = elastic deflections associated with  
 $k^{\text{th}}$  node of boom truss  
 $u_{2,l}, v_{2,l}$  = elastic deflections associated with  
 $l^{\text{th}}$  node of antenna  
 $\bar{v}_i$  = interconnection vector for subsystem i  
 $X_{1,k}, Y_{1,k}$  = coordinates for  $k^{\text{th}}$   
node of boom truss  
 $X_{2,l}, Y_{2,l}$  = coordinates for  $l^{\text{th}}$   
node of antenna  
 $\bar{x}_i$  = state vector for  $i^{\text{th}}$  subsystem  
 $\bar{x}_{mi}$  = desired state vector for  $i^{\text{th}}$  subsystem  
 $\bar{y}_i$  = output vector for  $i^{\text{th}}$  subsystem  
 $Z_i$  = adaptive feedback control law  
for  $i^{\text{th}}$  subsystem  
 $\alpha_i$  = adaptive gain for  $i^{\text{th}}$  subsystem  
 $\Delta_1, \Delta_2$  = interconnection matrix  
 $\theta_1, \theta_2$  = angular position of  
trusses 1 and 2 respectively  
 $\gamma_i, \sigma_i$  = scalar parameters for adaptive  
controller for  $i^{\text{th}}$  subsystem  
 $\omega_{1,i}$  = natural frequency for  $i^{\text{th}}$   
mode of boom truss  
 $\omega_{2,i}$  = natural frequency for  $i^{\text{th}}$   
mode of antenna  
 $\dot{(\ )}$  = differentiation with respect  
to time  
 $[ \ ]$  = matrix quantity  
 $( \ )$  = indicates a vector quantity

## Appendix B

The matrices  $N_1$ ,  $M_1$ , and  $M_2$  are symmetric.

$$M_1(1, 1) = \sum_{k=1}^{L_1} Q_{k,1}^X Q_{k,1}^X m_{1,k} + \sum_{k=1}^{L_1} Q_{k,1}^Y Q_{k,1}^Y m_{1,k}$$

$$M_1(1, 2) = \sum_{k=1}^{L_1} Q_{k,1}^X Q_{k,2}^X m_{1,k} + \sum_{k=1}^{L_1} Q_{k,1}^Y Q_{k,2}^Y m_{1,k}$$

$$\begin{aligned} M_1(1, 3) = & - \sum_{k=1}^{L_1} (Y_{1,k} + v_{1,k}) Q_{k,1}^X m_{1,k} \\ & + \sum_{k=1}^{L_1} (X_{1,k} + u_{1,k}) Q_{k,1}^Y m_{1,k} \end{aligned}$$

$$M_1(2, 2) = \sum_{k=1}^{L_1} Q_{k,2}^X Q_{k,2}^X m_{1,k} + \sum_{k=1}^{L_1} Q_{k,2}^Y Q_{k,2}^Y m_{1,k}$$

$$\begin{aligned} M_1(2, 3) = & - \sum_{k=1}^{L_1} (Y_{1,k} + v_{1,k}) Q_{k,2}^X m_{1,k} \\ & + \sum_{k=1}^{L_1} (X_{1,k} + u_{1,k}) Q_{k,2}^Y m_{1,k} \end{aligned}$$

$$\begin{aligned} M_1(3, 3) = & \sum_{k=1}^{L_1} (Y_{1,k} + v_{1,k})^2 m_{1,k} \\ & + \sum_{k=1}^{L_1} (X_{1,k} + u_{1,k})^2 m_{1,k} \end{aligned}$$

$$N_1(1, 1) = Q_{o,1}^X Q_{o,1}^X m_2^T + Q_{o,1}^Y Q_{o,1}^Y m_2^T$$

$$N_1(1, 2) = Q_{o,1}^X Q_{o,2}^X m_2^T + Q_{o,1}^Y Q_{o,2}^Y m_2^T$$

$$\begin{aligned} N_1(1, 3) = & - (Y_{1,o} + v_{1,o}) Q_{o,1}^X m_2^T \\ & + (X_{1,o} + u_{1,o}) Q_{o,1}^Y m_2^T \end{aligned}$$

$$N_1(2, 2) = Q_{o,2}^X Q_{o,2}^X m_2^T + Q_{o,2}^Y Q_{o,2}^Y m_2^T$$



$$N_1(2,3) = -(Y_{1,o} + v_{1,o})Q_{o,2}^X m_2^T \\ + (X_{1,o} + u_{1,o})Q_{o,2}^Y m_2^T$$

$$N_1(3,3) = (Y_{1,o} + v_{1,o})^2 m_2^T + (X_{1,o} + u_{1,o})^2 m_2^T$$

$$N_2(1,1) = \cos(\theta_2 - \theta_1)Q_{o,1}^X \sum_{l=1}^{L_2} R_{l,1}^X m_{2,l} \\ - \sin(\theta_2 - \theta_1)Q_{o,1}^X \sum_{l=1}^{L_2} R_{l,1}^Y m_{2,l} \\ + \sin(\theta_2 - \theta_1)Q_{o,1}^Y \sum_{l=1}^{L_2} R_{l,1}^X m_{2,l} \\ + \cos(\theta_2 - \theta_1)Q_{o,1}^Y \sum_{l=1}^{L_2} R_{l,1}^Y m_{2,l}$$

$$N_2(1,2) = \cos(\theta_2 - \theta_1)Q_{o,1}^X \sum_{l=1}^{L_2} R_{l,2}^X m_{2,l} \\ - \sin(\theta_2 - \theta_1)Q_{o,1}^X \sum_{l=1}^{L_2} R_{l,2}^Y m_{2,l} \\ + \sin(\theta_2 - \theta_1)Q_{o,1}^Y \sum_{l=1}^{L_2} R_{l,2}^X m_{2,l} \\ + \cos(\theta_2 - \theta_1)Q_{o,1}^Y \sum_{l=1}^{L_2} R_{l,2}^Y m_{2,l}$$

$$N_2(1,3) = -\cos(\theta_2 - \theta_1)Q_{o,1}^X \sum_{l=1}^{L_2} (Y_{2,l} + v_{2,l})m_{2,l} \\ - \sin(\theta_2 - \theta_1)Q_{o,1}^X \sum_{l=1}^{L_2} (X_{2,l} + u_{2,l})m_{2,l} \\ - \sin(\theta_2 - \theta_1)Q_{o,1}^Y \sum_{l=1}^{L_2} (Y_{2,l} + v_{2,l})m_{2,l} \\ + \cos(\theta_2 - \theta_1)Q_{o,1}^Y \sum_{l=1}^{L_2} (X_{2,l} + u_{2,l})m_{2,l}$$

$$\begin{aligned}
N_2(2, 1) = & \cos(\theta_2 - \theta_1) Q_{o,2}^X \sum_{l=1}^{L_2} R_{l,1}^X m_{2,l} \\
& - \sin(\theta_2 - \theta_1) Q_{o,2}^X \sum_{l=1}^{L_2} R_{l,1}^Y m_{2,l} \\
& + \sin(\theta_2 - \theta_1) Q_{o,2}^Y \sum_{l=1}^{L_2} R_{l,1}^X m_{2,l} \\
& + \cos(\theta_2 - \theta_1) Q_{o,2}^Y \sum_{l=1}^{L_2} R_{l,1}^Y m_{2,l}
\end{aligned}$$

$$\begin{aligned}
N_2(2, 2) = & \cos(\theta_2 - \theta_1) Q_{o,2}^X \sum_{l=1}^{L_2} R_{l,2}^X m_{2,l} \\
& - \sin(\theta_2 - \theta_1) Q_{o,2}^X \sum_{l=1}^{L_2} R_{l,2}^Y m_{2,l} \\
& + \sin(\theta_2 - \theta_1) Q_{o,2}^Y \sum_{l=1}^{L_2} R_{l,2}^X m_{2,l} \\
& + \cos(\theta_2 - \theta_1) Q_{o,2}^Y \sum_{l=1}^{L_2} R_{l,2}^Y m_{2,l}
\end{aligned}$$

$$\begin{aligned}
N_2(2, 3) = & -\cos(\theta_2 - \theta_1) Q_{o,2}^X \sum_{l=1}^{L_2} (Y_{2,l} + v_{2,l}) m_{2,l} \\
& - \sin(\theta_2 - \theta_1) Q_{o,2}^X \sum_{l=1}^{L_2} (X_{2,l} + u_{2,l}) m_{2,l} \\
& - \sin(\theta_2 - \theta_1) Q_{o,2}^Y \sum_{l=1}^{L_2} (Y_{2,l} + v_{2,l}) m_{2,l} \\
& + \cos(\theta_2 - \theta_1) Q_{o,2}^Y \sum_{l=1}^{L_2} (X_{2,l} + u_{2,l}) m_{2,l}
\end{aligned}$$

$$N_2(3, 1) = -\cos(\theta_2 - \theta_1) (Y_{1,o} + v_{1,o}) \sum_{l=1}^{L_2} R_{l,1}^X m_{2,l}$$

$$\begin{aligned}
& + \sin(\theta_2 - \theta_1)(Y_{1,o} + v_{1,o}) \sum_{l=1}^{L_2} R_{l,1}^Y m_{2,l} \\
& + \sin(\theta_2 - \theta_1)(X_{1,o} + u_{1,o}) \sum_{l=1}^{L_2} R_{l,1}^X m_{2,l} \\
& + \cos(\theta_2 - \theta_1)(X_{1,o} + u_{1,o}) \sum_{l=1}^{L_2} R_{l,1}^Y m_{2,l}
\end{aligned}$$

$$\begin{aligned}
N_2(3, 2) = & -\cos(\theta_2 - \theta_1)(Y_{1,o} + v_{1,o}) \sum_{l=1}^{L_2} R_{l,2}^X m_{2,l} \\
& + \sin(\theta_2 - \theta_1)(Y_{1,o} + v_{1,o}) \sum_{l=1}^{L_2} R_{l,2}^Y m_{2,l} \\
& + \sin(\theta_2 - \theta_1)(X_{1,o} + u_{1,o}) \sum_{l=1}^{L_2} R_{l,2}^X m_{2,l} \\
& + \cos(\theta_2 - \theta_1)(X_{1,o} + u_{1,o}) \sum_{l=1}^{L_2} R_{l,2}^Y m_{2,l}
\end{aligned}$$

$$\begin{aligned}
N_2(3, 3) = & \cos(\theta_2 - \theta_1)(Y_{1,o} + v_{1,o}) \sum_{l=1}^{L_2} (Y_{2,l} + v_{2,l}) m_{2,l} \\
& + \sin(\theta_2 - \theta_1)(Y_{1,o} + v_{1,o}) \sum_{l=1}^{L_2} (X_{2,l} + u_{2,l}) m_{2,l} \\
& - \sin(\theta_2 - \theta_1)(X_{1,o} + u_{1,o}) \sum_{l=1}^{L_2} (Y_{2,l} + v_{2,l}) m_{2,l} \\
& + \cos(\theta_2 - \theta_1)(X_{1,o} + u_{1,o}) \sum_{l=1}^{L_2} (X_{2,l} + u_{2,l}) m_{2,l}
\end{aligned}$$

$$\begin{aligned}
f_1(1) = & g_o^X Q_{o,1}^X m_2^T + g_o^Y Q_{o,1}^Y m_2^T \\
& + \sum_{k=1}^{L_1} g_k^X Q_{k,1}^X m_{1,k} + \sum_{k=1}^{L_1} g_k^Y Q_{k,1}^Y m_{1,k} \\
& + \cos(\theta_2 - \theta_1) Q_{o,1}^X \sum_{l=1}^{L_2} h_l^X m_{2,l}
\end{aligned}$$

$$\begin{aligned}
& -\sin(\theta_2 - \theta_1)Q_{o,1}^X \sum_{l=1}^{L_2} h_l^Y m_{2,l} \\
& + \sin(\theta_2 - \theta_1)Q_{o,1}^Y \sum_{l=1}^{L_2} h_l^X m_{2,l} \\
& + \cos(\theta_2 - \theta_1)Q_{o,1}^Y \sum_{l=1}^{L_2} h_l^Y m_{2,l}
\end{aligned}$$

$$\begin{aligned}
f_1(2) = & g_o^X Q_{o,2}^X m_2^T + g_o^Y Q_{o,2}^Y m_2^T \\
& + \sum_{k=1}^{L_1} g_k^X Q_{i,2}^X m_{1,k} + \sum_{k=1}^{L_1} g_k^Y Q_{i,2}^Y m_{1,k} \\
& + \cos(\theta_2 - \theta_1)Q_{o,2}^X \sum_{l=1}^{L_2} h_l^X m_{2,l} \\
& - \sin(\theta_2 - \theta_1)Q_{o,2}^X \sum_{l=1}^{L_2} h_l^Y m_{2,l} \\
& + \sin(\theta_2 - \theta_1)Q_{o,2}^Y \sum_{l=1}^{L_2} h_l^X m_{2,l} \\
& + \cos(\theta_2 - \theta_1)Q_{o,2}^Y \sum_{l=1}^{L_2} h_l^Y m_{2,l}
\end{aligned}$$

$$\begin{aligned}
f_1(3) = & -g_o^X (Y_{1,o} + v_{1,o}) m_2^T + g_o^Y (X_{1,o} + u_{1,o}) m_2^T \\
& - \sum_{k=1}^{L_1} g_k^X (Y_{1,k} + v_{1,k}) m_{1,k} \\
& + \sum_{k=1}^{L_1} g_i^Y (X_{1,k} + u_{1,k}) m_{1,k} \\
& - \cos(\theta_2 - \theta_1)(Y_{1,o} + v_{1,o}) \sum_{l=1}^{L_2} h_l^X m_{2,l} \\
& + \sin(\theta_2 - \theta_1)(Y_{1,o} + v_{1,o}) \sum_{l=1}^{L_2} h_l^Y m_{2,l} \\
& + \sin(\theta_2 - \theta_1)(X_{1,o} + u_{1,o}) \sum_{l=1}^{L_2} h_l^X m_{2,l}
\end{aligned}$$

$$+ \cos(\theta_2 - \theta_1)(X_{1,o} + u_{1,o}) \sum_{l=1}^{L_2} h_l^Y m_{2,l}$$

$$M_2(1, 1) = \sum_{l=1}^{L_2} R_{l,1}^X R_{l,1}^X m_{2,l} + \sum_{l=1}^{L_2} R_{l,1}^Y R_{l,1}^Y m_{2,l}$$

$$M_2(1, 2) = \sum_{l=1}^{L_2} R_{l,1}^X R_{l,2}^X m_{2,l} + \sum_{l=1}^{L_2} R_{l,1}^Y R_{l,2}^Y m_{2,l}$$

$$\begin{aligned} M_2(1, 3) = & - \sum_{l=1}^{L_2} (Y_{2,l} + v_{2,l}) R_{l,1}^X m_{2,l} \\ & + \sum_{l=1}^{L_2} (X_{2,l} + u_{2,l}) R_{l,1}^Y m_{2,l} \end{aligned}$$

$$M_2(2, 2) = \sum_{l=1}^{L_2} R_{l,2}^X R_{l,2}^X m_{2,l} + \sum_{l=1}^{L_2} R_{l,2}^Y R_{l,2}^Y m_{2,l}$$

$$\begin{aligned} M_2(3, 3) = & \sum_{l=1}^{L_2} (Y_{2,l} + v_{2,l})^2 m_{2,l} \\ & + \sum_{l=1}^{L_2} (X_{2,l} + u_{2,l})^2 m_{2,l} \end{aligned}$$

$$\begin{aligned} f_2(1) = & \sum_{l=1}^{L_2} h_i^X R_{l,1}^X m_{2,l} + \sum_{l=1}^{L_2} h_i^Y R_{l,1}^Y m_{2,l} \\ & + \cos(\theta_2 - \theta_1) g_o^X \sum_{l=1}^{L_2} R_{1,l}^X m_{2,l} \\ & + \sin(\theta_2 - \theta_1) g_o^Y \sum_{l=1}^{L_2} R_{1,l}^X m_{2,l} \\ & + \cos(\theta_2 - \theta_1) g_o^Y \sum_{l=1}^{L_2} R_{1,l}^Y m_{2,l} \\ & - \sin(\theta_2 - \theta_1) g_o^X \sum_{l=1}^{L_2} R_{1,l}^Y m_{2,l} \end{aligned}$$

$$\begin{aligned}
f_2(2) = & \sum_{l=1}^{L_2} h_i^X R_{l,1}^X m_{2,l} + \sum_{l=1}^{L_2} h_i^Y R_{l,1}^Y m_{2,l} \\
& + \cos(\theta_2 - \theta_1) g_o^X \sum_{l=1}^{L_2} R_{2,l}^X m_{2,l} \\
& + \sin(\theta_2 - \theta_1) g_o^Y \sum_{l=1}^{L_2} R_{2,l}^X m_{2,l} \\
& + \cos(\theta_2 - \theta_1) g_o^Y \sum_{l=1}^{L_2} R_{2,l}^Y m_{2,l} \\
& - \sin(\theta_2 - \theta_1) g_o^X \sum_{l=1}^{L_2} R_{2,l}^Y m_{2,l} \\
f_2(3) = & - \sum_{l=1}^{L_2} h_l^X (Y_{2,l} + v_{2,l}) m_{2,l} \\
& + \sum_{l=1}^{L_2} h_l^Y (X_{2,l} + u_{2,l}) m_{2,l} \\
& - \cos(\theta_2 - \theta_1) g_o^X \sum_{l=1}^{L_2} (Y_{2,l} + v_{2,l}) m_{2,l} \\
& - \sin(\theta_2 - \theta_1) g_o^Y \sum_{l=1}^{L_2} (Y_{2,l} + v_{2,l}) m_{2,l} \\
& + \cos(\theta_2 - \theta_1) g_o^Y \sum_{l=1}^{L_2} (X_{2,l} + u_{2,l}) m_{2,l} \\
& - \sin(\theta_2 - \theta_1) g_o^X \sum_{l=1}^{L_2} (X_{2,l} + u_{2,l}) m_{2,l}
\end{aligned}$$

### Appendix C

$$\begin{aligned}
(\hat{B}_1)_{\text{nom}} &= \begin{pmatrix} -0.596 & 0.0 & 1.21 \\ 0.0 & -0.125 & 0.0 \\ 0.0009 & 0.0 & 1.00 \end{pmatrix} \\
(\hat{B}_2)_{\text{nom}} &= \begin{pmatrix} 0.131 & 0.0 & -5.11 \\ 0.0 & -0.0584 & 0.0 \\ 0.0097 & 0.0 & 1.00 \end{pmatrix}
\end{aligned}$$

### Linear Controller Design

$$J_1 =$$

$$\begin{pmatrix} -1.55 & 0.0 & 1.53 & -0.521 & 0.0 & 0.562 \\ 0.0 & -1.33 & 0.0 & 0.0 & -0.049 & 0.0 \\ 0.594 & 0.0 & 1.61 & 0.596 & 0.0 & 0.827 \end{pmatrix}$$

$$J_2 =$$

$$\begin{pmatrix} 0.108 & 0.0 & 0.503 & -0.0678 & 0.0 & 0.166 \\ 0.0 & -1.25 & 0.0 & 0.0 & -0.162 & 0.0 \\ -0.621 & 0.0 & 3.39 & 1.40 & 0.0 & 0.986 \end{pmatrix}$$

### Adaptive Controller Design

$$R_1 = R_2 = \begin{pmatrix} 1 \times 10^{-3} & 0 & 0 \\ 0 & 1 \times 10^{-4} & 0 \\ 0 & 0 & 1 \end{pmatrix}$$

$$G_1 = G_2 = \begin{pmatrix} 5 & 0 & 0 & 0 & 0 & 0 \\ 0 & 5 & 0 & 0 & 0 & 0 \\ 0 & 0 & 1 & 0 & 0 & 0 \\ 0 & 0 & 0 & 1 & 0 & 0 \\ 0 & 0 & 0 & 0 & 1 & 0 \\ 0 & 0 & 0 & 0 & 0 & 1 \end{pmatrix}$$

The matrices that result are:

$$H_1 =$$

$$\begin{pmatrix} 2.26 & 0.0 & -1.34 & 0.425 & 0.0 & -0.785 \\ 0.0 & 17.3 & 0.0 & 0.0 & 0.390 & 0.0 \\ -1.34 & 0.0 & 1.95 & -0.0521 & 0.0 & 1.24 \\ 0.425 & 0.0 & -0.0521 & 2.70 & 0.0 & -0.15 \\ 0.0 & 0.390 & 0.0 & 0.0 & 22.3 & 0.0 \\ -0.785 & 0.0 & 1.24 & -0.15 & 0.0 & 1.89 \end{pmatrix}$$

$$H_2 =$$

$$\begin{pmatrix} 1.37 & 0.0 & 5.24 & -1.39 & 0.0 & 1.63 \\ 0.0 & 38.1 & 0.0 & 0.0 & 0.278 & 0.0 \\ 5.24 & 0.0 & 29.2 & -8.95 & 0.0 & 8.71 \\ -1.39 & 0.0 & -8.95 & 5.82 & 0.0 & -1.94 \\ 0.0 & 0.278 & 0.0 & 0.0 & 68.6 & 0.0 \\ 1.63 & 0.0 & 8.71 & -1.94 & 0.0 & 4.40 \end{pmatrix}$$

DIRECT MEASUREMENTS OF TURBULENT DISSIPATION RATE  
USING DUAL LASER DOPPLER VELOCIMETERS

Dr. Richard D. Gould  
Assistant Professor

Mechanical and Aerospace Engineering  
North Carolina State University  
Raleigh, NC 27695

Final Report for:  
Research Initiation Program  
Wright Laboratory

Sponsored by:  
Air Force Office of Scientific Research  
Bolling Air Force Base, Washington, D.C.

and

North Carolina State University

December 1992



# DIRECT MEASUREMENTS OF TURBULENT DISSIPATION RATE USING DUAL LASER DOPPLER VELOCIMETERS

Dr. Richard D. Gould  
Mechanical and Aerospace Engineering  
North Carolina State University  
Raleigh, NC 27695

## ABSTRACT

An analysis of two-point velocity correlation measurements, made in the anisotropic flow field of an axisymmetric sudden expansion using two single component LDV systems, has been performed. Estimations of the Taylor microscale were made and the one-dimensional energy spectrum was determined using the spatial and autocorrelation functions from these measurements. Difficulties in estimating the Taylor microscale from spatial and autocorrelations are discussed and methods to overcome these difficulties are suggested. Calculation of the one-dimensional energy spectrum from curve fits to the correlation functions is explored and some hazards of the process are highlighted. In addition, a dual LDV system which can be used to make turbulence length scale and turbulent dissipation rate estimations has been fabricated and is located at the Applied Energy Research Laboratory at North Carolina State University.

# DIRECT MEASUREMENTS OF TURBULENT DISSIPATION RATE USING DUAL LASER DOPPLER VELOCIMETERS

Dr. Richard D. Gould

## INTRODUCTION

The research program had two major thrusts, both of which have been completed. The first was to perform a detailed analysis of two-point and single point velocity measurements, obtained using laser Doppler velocimetry (LDV), in an effort to give accurate turbulent length scales and the turbulent dissipation rate. Four publications reporting our findings regarding the calculation of turbulence scales from LDV measurements have resulted from the support provided by this grant. They are :

1. Benedict, L. H. and Gould, R. D. (1993) "Calculation of One-Dimensional Energy Spectra from Spatial Correlation Measurements using LDV," Accepted ASME 1993 Forum on Turbulent Flows, Washington, DC, June 20-24.
2. Gould, R. D., Nejad, A. S. and Ahmed, S. A., (1992a), "Turbulent Length Scale Measurements in an Axisymmetric Sudden Expansion Using LDV, The Fourth International Conference for Fluid Mechanics, Alexandria, Egypt, April 28-30.
3. Gould, R. D., Benedict, L. H., Nejad, A.S., and Ahmed, S.A., (1992b), "Two-Point Velocity Correlation Measurements in an Axisymmetric Sudden Expansion Using LDV," Proc of 6th Intl Sym on Appl of Laser Anemometry to Fluid Mech., Lisbon, Port.
4. Gould, R. D., Benedict, L. H., (1992c) "A Comparison of Spatial Correlation and Autocorrelation Measurements in an Axisymmetric Sudden Expansion Using LDV," 13th Symposium on Turbulence, Univ. of Rolla-Missouri, Rolla, Mo., Sept. 21-23.

A summary of the important findings from this analysis is given below. The second task involved fabricating a dual LDV capable of making two-point and single point velocity correlation measurements at the Applied Energy Research Laboratory (AERL) at North Carolina State University (NCSSU). Details of this system are also given below.

## EXPERIMENTAL APPARATUS

Two-point velocity correlation measurements using two single component LDV's and single-point velocity correlation measurements using one single component LDV were made in an axisymmetric sudden expansion air flow (Gould and Benedict, 1992). The geometry was produced by joining a 101.6 mm (4 in.) inside diameter entry pipe to a 152.4 mm (6 in.) inside diameter clear acrylic test section. The entry pipe was 3.5 m long so that a fully developed pipe flow velocity profile existed at the entrance to the sudden expansion. The

step height for this geometry was 25.4 mm (1 in.). Flat quartz windows 50 mm  $\times$  152 mm  $\times$  3.2 mm (2  $\times$  6  $\times$  .125 in) were mounted in flanges on both sides of the 152.4 mm diameter test section such that the inner flat surfaces were flush with the inside diameter of the test section.

Flow velocities for the spatial correlations were measured using two TSI single component dual-beam LDV systems, both operating in backscatter mode. Both systems were oriented to measure the axial velocity component on the diameter of the test section as shown in Figure 1. One LDV system was adjusted so that the probe volume was located at the required axial,  $x$ , and radial,  $r$ , measurement location. Once this position was found, the LDV system was locked in place. The 514.5  $\mu\text{m}$  laser line from a Model 2025 Spectra Physics argon ion laser was used in this system. A Bragg cell shifted the frequency of one beam by 40 MHz causing the fringes to move in the downstream direction. A second LDV system (TSI Model 9277 190 mm fiber optic probe), mounted on a precision  $xyz$  positioning table with resolution of  $\pm 2.5 \mu\text{m}$  in each axis, was located on the opposite side of the test section (see Figure 1). The 488  $\mu\text{m}$  laser line from a Model 165 Spectra Physics argon ion laser was used in this system. A frequency shift of 40 MHz was used causing the fringes of this system to move in the upstream direction. Both LDV systems employed  $3.75\times$  beam expansion optics and gave probe volumes approximately 60  $\mu\text{m}$  in diameter and 450  $\mu\text{m}$  in length.

A 20  $\mu\text{m}$  diameter pinhole mounted on a fixture supported on a spare test section window was used to find the position where both laser beam probe volumes overlapped. This fixture was used prior to each test sequence, thus ensuring that both probe volumes overlapped at the zero separation distance point. Specially designed beam blocks were fabricated to block reflections from the LDV focusing lens (they faced one another) and from test section windows. Narrow bandpass filters were placed in front of each photomultiplier tube to eliminate cross-talk between the two channels.

Two TSI Model 1990C counter processors interfaced to a custom built coincidence timing unit were used in the data collection and processing system. High and low pass filters were set to 10 MHz and 50 MHz, respectively, for the stationary LDV system, and 20 MHz and 100 MHz, respectively, for the fiber optic LDV system. Both processors were set to sample continuously (multiple measurements per burst possible), count 16 fringes and use a 1 % comparator. A hardware coincident window was set at 20  $\mu\text{s}$  for all of the tests. Data (two velocities and the running time for each realization) were transferred through two DMA ports to a MicroVax minicomputer and later uploaded to a VAX 8650 for analysis.

The flow field was seeded using titanium dioxide ( $\text{TiO}_2$ ) particles generated by reacting dry titanium tetra-chloride ( $\text{TiCl}_4$ ) with the moist shop air. Craig et al. (1984) measured the particle sizes generated by this device and found that they were fairly uniform and in the 0.2 – 1  $\mu\text{m}$  diameter range. Data validation rates varied between 5000 and 500 per second on each counter processor and depended mainly on how well the chemical reaction proceeded. This seemed to be very sensitive to shop air temperature and relative humidity. Coincident data validation rates ranged from 1000 to 50 measurements per second.

## EXPERIMENTAL PROCEDURE

All flow conditions were maintained at near constant values throughout the testing procedure. The inlet centerline velocity,  $U_{cl}$ , was maintained at  $18.0 \text{ m/s} \pm 0.1 \text{ m/s}$  ( $59 \text{ ft/s} \pm 0.3 \text{ ft/s}$ ) giving  $Re_D = 114,000$  based on centerline velocity and inlet diameter. Spatial correlation statistics and histograms were formed by using 5000 individual realizations for each velocity channel at each measurement point. Autocorrelations were formed by using 50,000 individual realizations from the stationary LDV system with data validation rates between 25,000 and 1000 per second. In computing statistical parameters, a two step process suggested by Meyers (1988) was used to eliminate noise from the data. All velocity measurements deviating more than 3 standard deviations from the mean are thus eliminated. For a properly operating LDV system less than 1 % of the data should be discarded. In addition, Srikantaiah and Coleman (1985) have found that as long as the total number of removed points is within 1 % of the total sample size, the effect of the removal of noise on the autocorrelation function is negligible.

## EXPERIMENTAL RESULTS

### Autocorrelations and Microscales

Two-point (spatial) velocity correlation measurements and single point (auto) velocity correlation measurements were made at three locations in the axisymmetric sudden expansion flow field. These results, including the calculation of integral length scales and Taylor microscales, were presented by Gould and Benedict (1992). In this earlier paper mention was made of the difficulty in accurately determining the Taylor microscale from either the discrete spatial or autocorrelation functions. This difficulty is addressed in more detail here. Additionally, the problem of calculating one-dimensional energy spectra from spatial and autocorrelation functions is discussed.

In Figure 2, typical autocorrelation functions measured at 6 step heights downstream ( $x/H = 6$ ) and 2 step heights ( $r/H = 2$ ) from the axis are presented. The autocorrelation can be transformed to the spatial domain by use of Taylor's hypothesis (*i.e.*  $x = \bar{U}t$ ) which was shown to be an accurate transformation for this flow field (Gould and Benedict, 1992). Discrete autocorrelation measurements were made using the slotting technique described by Jones (1972) and Mayo, et al. (1974). The time lag axis was divided into bins of equal width and the exact lag products of all points up to a specified maximum lag time were accumulated in appropriate bins. The average of all the auto-products falling in each bin was assumed to be the value of the discrete autocorrelation function, *i.e.*

$$R_E(\tau) = \frac{\overline{u'(t)u'(t+\tau)}}{\overline{u'^2(t)}} \quad (1)$$

at the midpoint of the bin. The data was filtered first using the previously described method to eliminate velocity measurements more than three standard deviations from the mean. The zero-lag products were not included to avoid the spiking effect at the origin ( $\tau = 0$ )

due to squaring of uncorrelated noise (Absil, 1988). The discrete autocorrelations, shown in Figure 2, were obtained using a slot width of  $50 \mu\text{s}$  with a maximum lag time of 3 ms. Note that there is still some scatter in the data even though 50,000 samples were used to build the autocorrelation functions. A mean data validation rate of approximately 12,000 per second was used here. This scatter is statistical in nature and is due to too few lag products in each slot which causes some variance in the data (each bin contained approximately 30,000 lag products). The error bars shown in this figure indicate the variances of the calculated mean values of the autocorrelation function. These statistical uncertainties in the mean of the quantity  $\overline{u'u'}$  are estimated using the sample size and standard deviation of the sample in each slot (Yanta, 1973). Interestingly, although zero-lag products were not included in the first slot of the discrete autocorrelation function, a severe spike results at the origin (bottom curve). This spike is an unnatural characteristic of the autocorrelation function and prohibits the estimation of the Taylor microscale (dissipation scale).

One popular, but perhaps questionable, way around this problem is simply to ignore the first slot value and normalize the autocorrelation with respect to the second slot. Another approach was considered, however, based on the belief that the spiking effect was caused by the continuous sampling of the LDV system. Continuous sampling allows for multiple measurements to be made on a single Doppler burst. In such a situation, a slow moving particle can be sampled more than once as it passes through the probe volume. Such measurements are inherently highly correlated with one another as they come from the same particle at close proximity in time. A simple computer algorithm was employed to remove multiply sampled velocity measurements from the data set. Basically, the data set was searched for successive measurements which had velocity-time between data products less than the probe volume diameter. If this occurred, these measurements were assumed to have come from the same particle. After eliminating these redundant measurements, a new autocorrelation function was calculated and is also shown in Figure 2 (top curve). One may observe that this new autocorrelation function displays the expected parabolic behavior near the origin without any spiking.

From such an autocorrelation function the Taylor microscale may be easily estimated by fitting an osculating parabola to the spatial correlation function between the first measured two points. The discrete spatial correlation function is obtained by transforming the discrete autocorrelation function via Taylor's hypothesis (*i.e.*  $\lambda_f = \bar{U}\tau_E$ ). Thus the longitudinal microscale is obtained from,

$$R(x) \approx 1 - \frac{x^2}{\lambda_f^2} \quad (2)$$

where  $x$  represents the separation distance between the first two measurements. For the autocorrelation function shown as the top curve in Figure 2, where  $\bar{U} = 8.5 \text{ m/s}$ ,  $\lambda_f$  was found to equal 3.3 mm. In previous work (Gould and Benedict, 1992), this estimate had been considered to be on the order of 6 mm, however, an earlier experimental investigation (Gould et al., 1990) estimated the dissipation at this location in the flow field to be approximately  $1340 \text{ m}^2/\text{s}^3$  by using a turbulent kinetic energy balance. Using an isotropic turbulence

assumption, the microscale can be estimated from:

$$\epsilon = 30\nu \frac{\overline{u'^2}}{\lambda_f^2} \quad (3)$$

The microscale estimate based on a turbulent kinetic energy balance and the assumption of isotropy is then calculated as approximately 2.3 mm. As the dissipation rates obtained from the turbulent kinetic energy balance are believed to be more correct than the first microscale estimates from the autocorrelation functions presented by Gould and Benedict (1992), the newer estimate of the microscale from these functions is considered to be an improvement over the old.

As will be shown later, two-point spatial correlations seem to suffer from probe volume integration effects such that near the origin ( $\Delta x = 0$ ) no parabolic region can be found and any estimation of the microscale must be considered a crude approximation. Until these probe volume integration effects can be reduced, the transformed autocorrelation function (using Taylor's hypothesis) should be considered as the method of choice for estimating the microscale from LDV measurements.

Some guidelines are thus in order as to how to best pursue this goal. Firstly, one should always be aware that Taylor's hypothesis is limited by turbulence intensity. It should not be applied in flows with turbulence intensities greater than about 20%. Work by Gould and Benedict (1992) and Cenedese (1991) suggests, however, that oftentimes Taylor's hypothesis is approximately valid for much higher turbulence intensities. Another point to make is that a very high mean data validation rate is often necessary to resolve the small scales. Previous work such as that of Cenedese (1991), Morton and Clark (1971), Absil (1988), and Fraser et al. (1986) make use of relatively low Reynolds number flows to simplify the measuring process. In the current work, a Reynolds number based on inlet diameter of approximately 114,000 was achieved in the axisymmetric sudden expansion flow. For this flow condition additional studies, not reported here, suggest that approximately 100,000 samples need to be recorded at data rates approaching 20,000 Hz in order to accurately resolve the small scales. Oftentimes, however, such high data rates are not achievable. Additionally, single measurement per burst mode is preferred over continuous sampling in order to prevent biasing of the autocorrelation function as described above. As was done in this work, zero-lag products should not be included in the first slot of the discrete autocorrelation function.

### Spatial Correlations and 1-D Energy Spectra

As mentioned above, spatial correlations suffer from a probe volume integration effect at small separation distance. This effect tends to obscure correlation information pertaining to the microscale as even when the two probe volumes overlap (*i.e.*  $\Delta x = 0$ ), their lengths allow for a finite separation distance (Benedict and Gould, 1992). If the probe volume length is of the same size as the parabolic region of the correlation function, then this parabolic section can quite possibly be obscured. As flow Reynolds number increases, such a situation is more likely to happen, and thus the determination of a microscale through a two-point spatial correlation function becomes an approximate analysis.

Figure 3 shows the longitudinal spatial correlation coefficients at  $x/H = 10$  and  $r/H = 2$  in the axisymmetric sudden expansion flow obtained using two-point correlation measurements and also shows an exponential fit to the data. The lack of a parabolic region in the data near zero spatial separation should be pointed out. Also, it can be seen that the spatial correlation function does not reach unity at zero spatial separation. Both of these characteristics may be attributed to the probe volume integration effect mentioned above. Obviously, there is little basis for fitting a parabola to such a correlation function near zero separation, which, in turn, increases the difficulty in making an estimation of the microscale.

It is also possible to make an estimation of the microscale from the one-dimensional energy spectrum defined as the Fourier transform of the spatial correlation function,

$$E_1(k) = \frac{4\overline{u_1'^2}}{\overline{U}} \int_0^\infty dx_1 R_{11}(x_1) \cos(kx_1) \quad (4)$$

where  $\overline{u'^2}$  is the variance of the velocity,  $\overline{U}$  is the mean velocity,  $x$  is the separation distance and  $k$  is the wavenumber. The subscript "1" denotes that quantities are measured in the axial direction only. The microscale can be obtained by integration of the one-dimensional energy spectrum,

$$\frac{1}{\lambda_f^2} = \int_0^\infty \frac{k^2}{2\overline{U}} \Lambda_f E_1(k) dk \quad (5)$$

where  $\Lambda_f$  denotes the integral length scale in the axial direction.

From the correlation function shown in Figure 3, the 1-D energy spectrum may be arrived at by a discrete numerical integration process involving the cosine transform of the correlation function as stated mathematically above. This process may be carried out on the discrete correlation data points themselves if care is exercised. If the discrete cosine transform is applied to the discrete correlation data shown in Figure 3, an unrealistic energy spectrum as shown in Figure 4 results. The solid line in Figure 4 shows the theoretical energy spectrum corresponding to the exponential fit to the spatial correlation data.

This misrepresentation of the 1-D energy spectrum can be traced to two problem: (1) a non-zero value for the correlation coefficient at maximum separation distance (*i.e.* the correlation function does not approach zero closely enough) and, (2) insufficient spatial resolution of the cosine function within the transform at high wave numbers (*i.e.* discrete correlation coefficients not spaced closely enough). The first problem is usually solved by applying a window function to the correlation coefficient such that the correlation coefficient is forced to zero when  $\Delta x$  becomes larger than a prescribed value.

To study the problem of non-zero correlation coefficient at maximum separation distance, the exponential fit to the data was integrated analytically using various maximum separation distances. Analytic integration allowed the truncation problem to be isolated from the spatial resolution inaccuracies. Figure 5 shows the effect produced by integration over a distance equivalent to the maximum separation present in the data set shown in Figure 3 (*i.e.*  $\Delta x_{max} = 88$  mm). Since the correlation function did not reach zero at this

maximum separation distance (the LDVs could not be separated further), a truncation effect in the Fourier transform produced the oscillatory behavior in the energy spectrum as seen in Figure 5. This problem can be eliminated through the use of a smoothing window which effectively drives the correlation coefficient to zero at maximum separation.

To study the resolution problem, the correlation function was modeled with an exponential fit with various discrete separation distances in the data. The Hanning window was used to eliminate the problem of truncation of the correlation curve. Figure 6 shows the discrete cosine transform results for an exponential correlation coefficient when 35 evenly spaced points, out to a separation distance of 88 mm, were used. Notice the large spike in the one-dimensional energy spectrum at high wavenumber. This corresponds to the wavenumber at which the cosine function in the Fourier transform is no longer properly resolved. Proper resolution of the cosine function requires the spacing of the correlation data,  $\Delta x$ , to be less than  $\pi/2k$ .

The above examples indicate that fairly simple operations, such as the Fourier transform of a correlation function, can give highly erratic results if used improperly. In order to properly represent the one-dimensional energy spectrum from spatial correlation functions, the correlation function must be driven to zero by a window function if it does not go to zero naturally at the maximum separation distance. Note that there will always be a practical maximum separation distance limited by the experimental equipment. Moreover, the spacing of the discrete data points must be less than  $\pi/2k$ , where  $k$  is the maximum wavenumber of interest.

The maximum wavenumber for which the energy spectrum may be calculated can be increased by curve fitting experimental data and interpolating intermediate values of the correlation coefficient - while remaining conscious of the  $\pi/2k$  guideline. It is well known that the exponential fit shown in Figure 3 has a Fourier cosine transform which may be integrated analytically (Hinze, 1975). This transform is represented as either a solid or dashed curve in Figures 4-6. It should be noted that the exponential representation of the spatial correlation function produces a 1-D energy spectrum with a slope of -2 on a log-log axis plot. Such a function has a non-finite integral. The Taylor microscale, therefore, cannot be estimated by integration of the 1-D energy spectrum which is calculated using a pure exponential representation of the spatial correlation function.

In order to more properly represent the 1-D energy spectrum a multi-piece fit to either the spatial or autocorrelation function is necessary. Since the high frequency portion of the spectrum is dominated by behavior near zero separation in the correlation functions and typical correlation functions possess a parabolic region near zero separation (not characterized by the exponential fit shown in Figure 3), an attempt was made to mate a parabolic curve near zero separation to an exponential curve (which represents the measurements well at large separation distances). Some results appear in Figure 7, which shows the effects on the 1-D energy spectrum of mating parabolic regions representing differing microscales to the exponential curve. As expected, the parabolic region is responsible for driving the energy spectrum to zero at high frequency and that the larger the microscale, the lower the wavenumber where this happens. This makes sense from the standpoint that a larger mi-



crosscale implies more correlation which in turn implies less turbulence intensity (in the limit laminar flows are perfectly correlated) and hence less energy. Interestingly, the steep descent of the 1-D energy spectrum at high frequency mimics the -7 slope predicted by Kolmogoroff for homogeneous turbulence.

These energy spectra, which result when representing the spatial correlation coefficient with two-piece fits, may indeed be integrated using Eq. (5). The microscales returned by the integration process, however, are 30 to 40 percent higher than the original values assumed to determine the exact shape of the parabolic fit. Obviously, an actual correlation function can not usually be represented exactly by mating a parabolic and an exponential curve; so one would not expect such a fit to return the exact value of the microscale when determined by numerical integration of the 1-D energy spectrum. Microscales calculated by numerical integration of the 1-D energy spectrum would be reasonably close, however, to the actual values and would provide valuable insight into turbulent structure.

Figure 9 is a similar plot of the 1-D energy spectrum. In this case, the 1-D energy spectrum using the parabolic fit near zero-separation is compared to that using a third order polynomial fit. In both cases, these curves are mated to the same exponential curve. Note that the third order fit drives the 1-D energy spectrum to zero at a lower wavenumber when compared to a parabolic fit. Both fits were derived from an assumed microscale of 10 mm. Numerical integration of the 1-D energy spectrum (using Eq. (5)), returned a microscale value of 12.6 mm for the third order fit as opposed to 14.2 mm for the parabolic fit. Once again this trend makes sense as the third order fit rolls off more slowly than a parabolic fit giving higher correlation values near zero separation and thereby less turbulent intensity and less energy. Evidently a fourth or fifth order fit would return through numerical integration of the 1-D energy spectrum almost the exact value of the microscale that had been used to create the fit. It is recommended then that when using LDV, microscales be determined by the following procedure: (1) measure the autocorrelation function, (2) fit this function with a higher order polynomial near zero- separation and an exponential function at larger separation distances, (3) calculate the 1-D energy spectrum from the curve fit to the correlation function and (4) numerically integrate the resulting 1-D energy spectrum to determine the microscale. When making the curve fit to the experimental data and interpolating between data points, spacing requirements and window function requirements should be observed as mentioned above.

One last point to mention concerning the curve fitting of correlation functions is that when merging two different curve fits, continuity of slope is of utmost importance. Any discontinuity in slope will produce ringing at high wavenumber in the calculated 1-D energy spectrum. This is because the Fourier cosine transform of the correlation function is the integral of the correlation function multiplied by a cosine function which in effect is a weakly damped cosine function. As wavenumber increases, such a function has an integral which rapidly approaches zero – something which is profoundly obvious when the energy spectrum is plotted on normal (not log) axes. A small discontinuity in the slope of the correlation function thus changes the way the integral approaches zero. But for each new wavenumber this happens in a different way since the discontinuity occurs each time at a different location on the damped cosine function. Ringing in the 1-D energy spectrum is a direct and inevitable

consequence of slope discontinuity.

## DEVELOPMENT OF DUAL LDV AT NCSU

Optical components including, fiber optic input and output couplers, polarization preserving optical fiber, bandpass laser line filters, and an acoustic optic modulator (Bragg cell) were purchased to modify an existing LDV system so that two-point velocity correlation measurements can be made at NCSU. A schematic diagram of the completed dual LDV system is shown in Figures 9 and 10. The LDV system shown in Figure 9 is a two-color, two-component. It has been modified, by adding beam splitting prisms and fiber optic input couplers, to provide laser light for the second LDV system which is required to make two-point velocity measurements. This second system is a single-color single-component LDV system. Note that two fiber optic input couplers have been added to the two-color system. This allows the flexibility to choose either color (blue or green) for the single component system. Both systems are mounted on 3-axis tables so that the probe volumes can be placed at user selectable locations. Presently, both systems operate in forward scatter collection mode, however, modifications are being made to the systems so that either forward scatter or 90 degree collection angle can be used. In addition, to the optical components, the LDV data acquisition interface has been upgraded so that up to three-channels of velocity data can be acquired simultaneously. It is envisioned that this apparatus will be used to make many state of the art turbulence measurements in the future. Measurements in combustion environments are of particular interest.

## SUMMARY

It has been shown that spiking in autocorrelation measurements obtained using LDV is a prevalent phenomena that may be caused by biases induced by continuous sampling. This spiking should be distinguished from that attributed to inclusion of zero-lag terms in the slotting technique. The spiking caused by a continuous sampling bias may be overcome by filtering the data to remove the multiply sampled particle measurements. Spatial correlation measurements have been shown on the other hand to suffer from probe volume integration effects which cannot be remedied once the measurements have been made. These probe volume integration effects may obscure the classic parabolic region near zero-separation in spatial correlation functions, which degrade microscale estimations.

Calculation of 1-D energy spectra from correlation functions for purposes of calculating the Taylor microscale is a viable alternative to fitting a parabola to either spatial or autocorrelation functions. It has been shown, however, that even a fairly simple operation such as the Fourier transform of a correlation function can give highly erratic results if used improperly. In order to properly represent energy spectra from correlation measurements or curve fits to those measurements, the correlation function must be driven to zero by a window function and the spacing of the discrete data points must be less than  $\pi/2k$ , where  $k$  is the maximum wavenumber of interest. For piecewise curve fits, continuity of slope must

be maintained when merging the different pieces of a given curve fit. Lastly, an in-house dual LDV system capable of making general two-point velocity measurements has been fabricated and will be used to further our understanding of turbulence and the combustion process.

## REFERENCES

Absil, L. H. J., (1988), "Laser Doppler Measurements of Mean Turbulence Quantities, Time and Spatial-Correlation Coefficients in the Wake of a Circular Cylinder," *Proc. of the 4th Int'l Sym. on Appl. of Laser Anem. to Fluid Mech.*, Lisbon, Port., p. 1.1.

Cenedese, A., Romano, G. P. and Di Felice, F., (1991), "Experimental Testing of Taylor's Hypothesis by LDA in Highly Turbulent Flow," *Experiments in Fluids*, **11**, pp. 351-358.

Craig, R. R., Nejad, A. S., Hahn, E. Y. and Schwartzkopf, K. G., (1984) "A General Approach for Obtaining Unbiased LDV Data in Highly Turbulent Non-Reacting and Reacting Flows," AIAA Paper. No. 84-0366.

Fraser, R., Pack, C. J. and Santavicca, D. A., (1986), "An LDV System for Turbulence Length Scale Measurements," *Experiments in Fluids*, **4**, pp. 150-152.

Gould, R. D., and Benedict, L. H., (1992), "A Comparison of Spatial Correlation and Autocorrelation Measurements in an Axisymmetric Sudden Expansion Flow Using LDV," *The Thirteenth Symposium on Turbulence*, Rolla, Missouri, September 21-23. on Appl. of Laser Tech. to Fluid Mech., Lisbon, Port., July 20-23.

Gould, R. D., Stevenson, W. H. and Thompson, H. D., (1990), "Investigation of Turbulent Transport in an Axisymmetric Sudden Expansion," *AIAA Journal*, **28**, pp. 276-283.

Hinze, J. O., (1975), *Turbulence*, McGraw-Hill.

Jones, R. H., (1972). "Aliasing with Unequally Spaced Observations," *J. Appl. Meteorology*, **11**, pp. 245-254.

Mayo, W. T., Shay, M. T. and Ritter, S., (1974), "Development of New Digital Data Processing Techniques for Turbulence Measurements with LV," AEDC-TR-74-53.

Meyers, J. F., (1988), "LDV Data Acquisition and Real Time Processing using a Micro-computer," *Proc. 4th Int'l Sym. on Appl. Laser Anem. to Fluid Mech.*, Lisbon, Port., p. 7.20.

Morton, J. B. and Clark, W. H., (1971), "Measurements of Two Point Velocity Correlations in a Pipe Flow using Laser Anemometers," *J. Phys. E: Scient. Instrum.*, **4**, pp. 809-814.

Srikantaiah, D. V. and Coleman, H. W., (1985), "Turbulence Spectra from Individual Realization Laser Velocimetry Data," *Experiments in Fluids*, **3**, pp. 35-44.

Yanta, W. J. and Smith, R. A., (1973), "Measurements of Turbulence Transport Properties with a Laser Doppler Velocimeter," AIAA Paper 73-169.

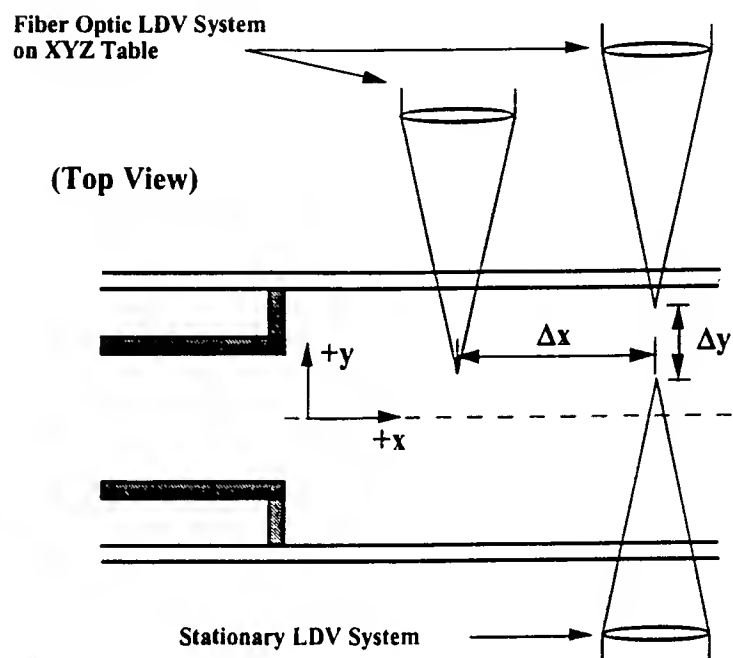


Figure 1. Dual LDV's in an axisymmetric sudden expansion.

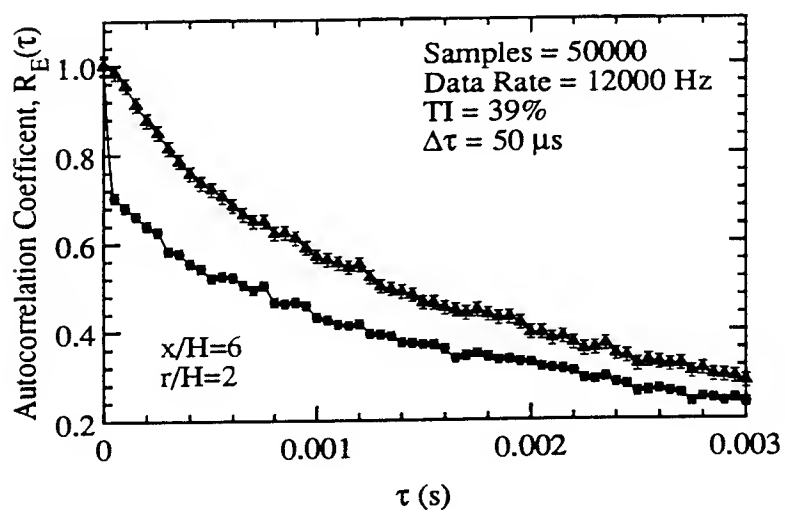


Figure 2. Autocorrelation measurements.

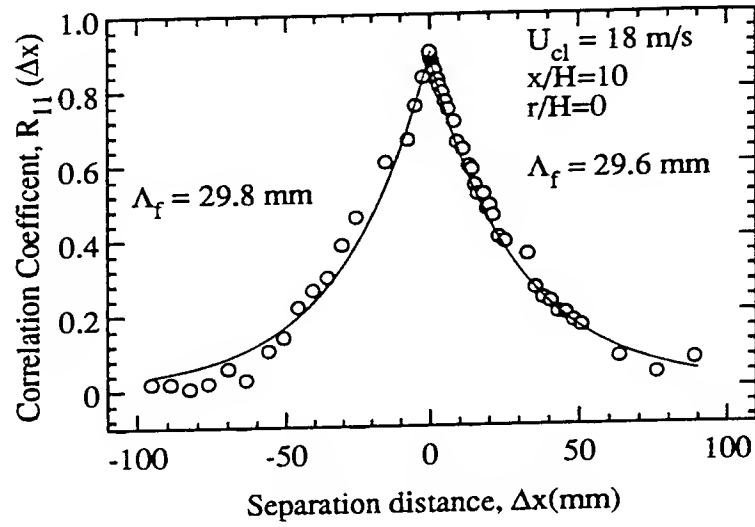


Figure 3. Longitudinal spatial correlation measurements.

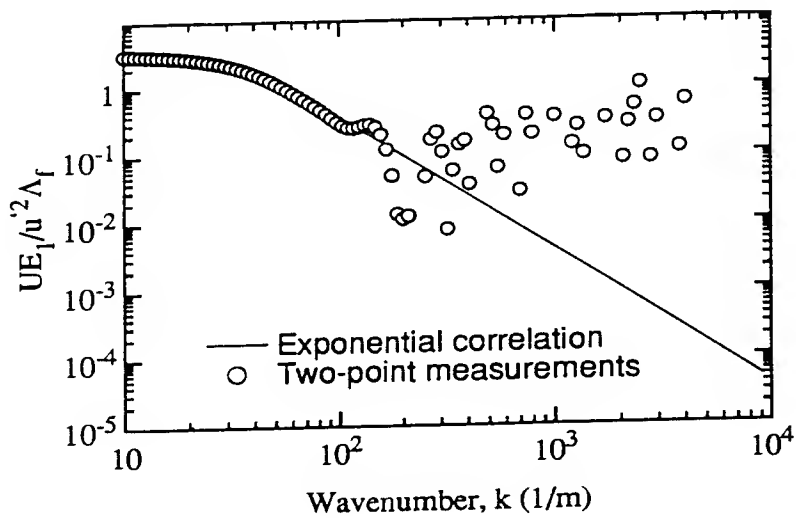


Figure 4. 1-D energy spectrum.

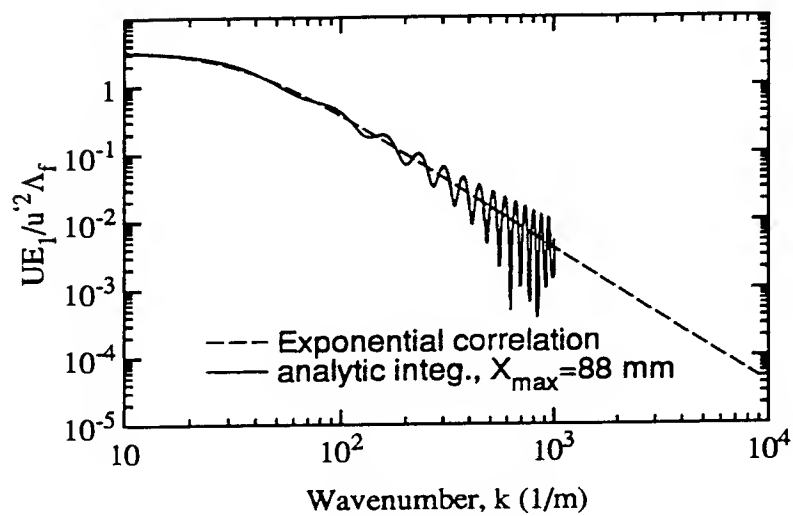


Figure 5. 1-D energy spectrum.

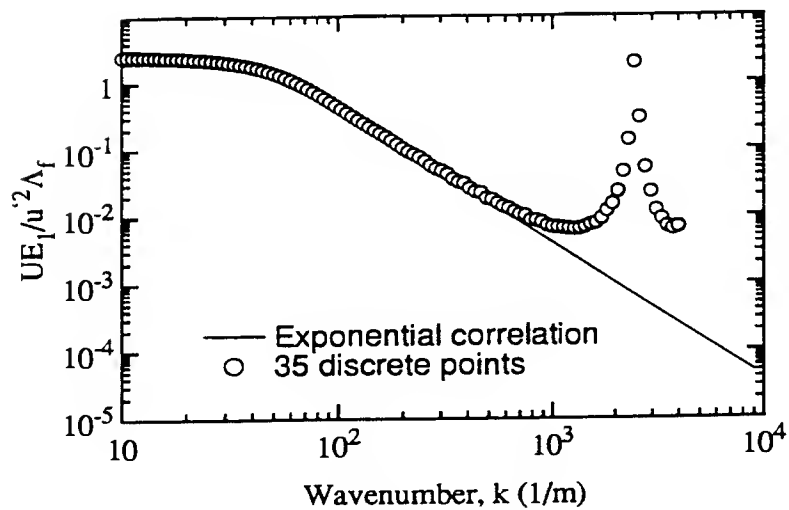


Figure 6. Lateral spatial correlation measurements.

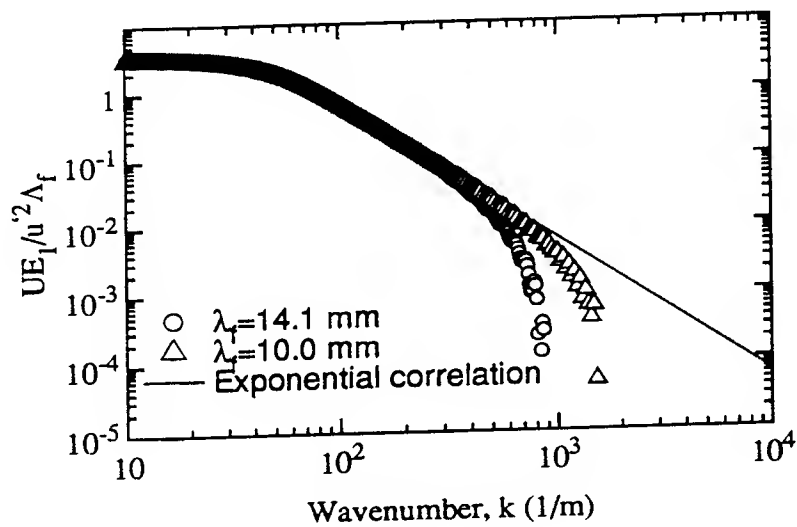


Figure 7. 1-D energy spectrum(fits to correlation function).

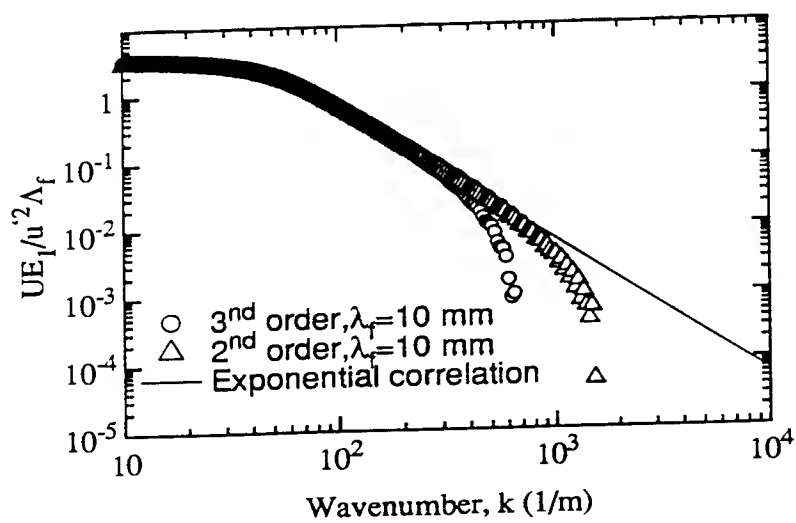


Figure 8. 1-D energy spectrum(fits to correlation function).

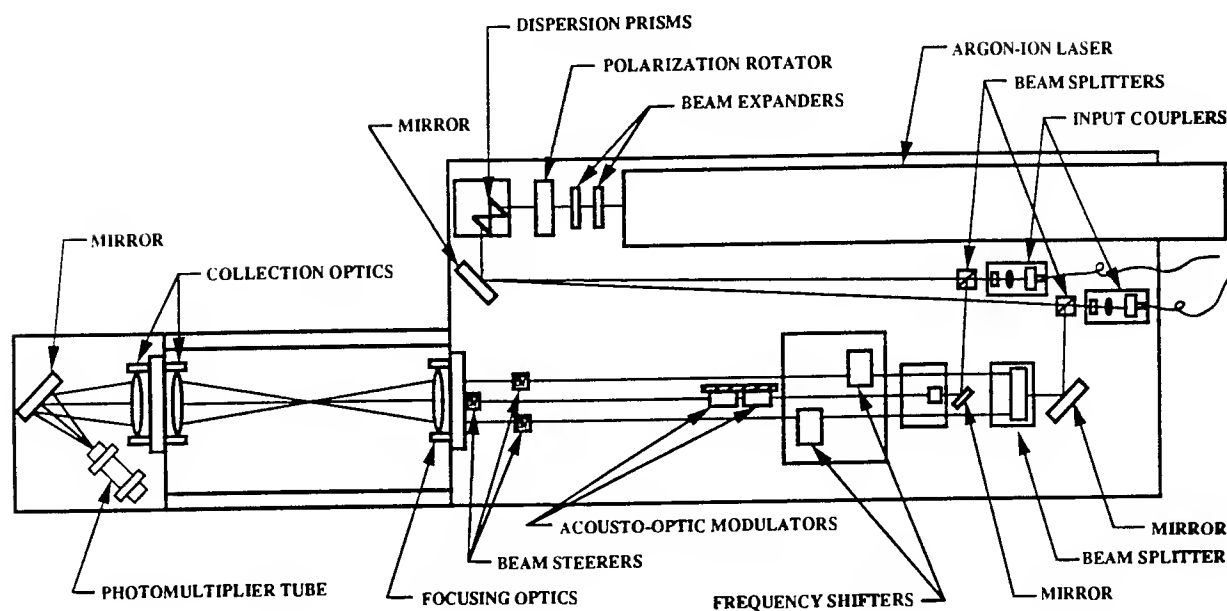


Figure 9. Two-color, two-component LDV system.

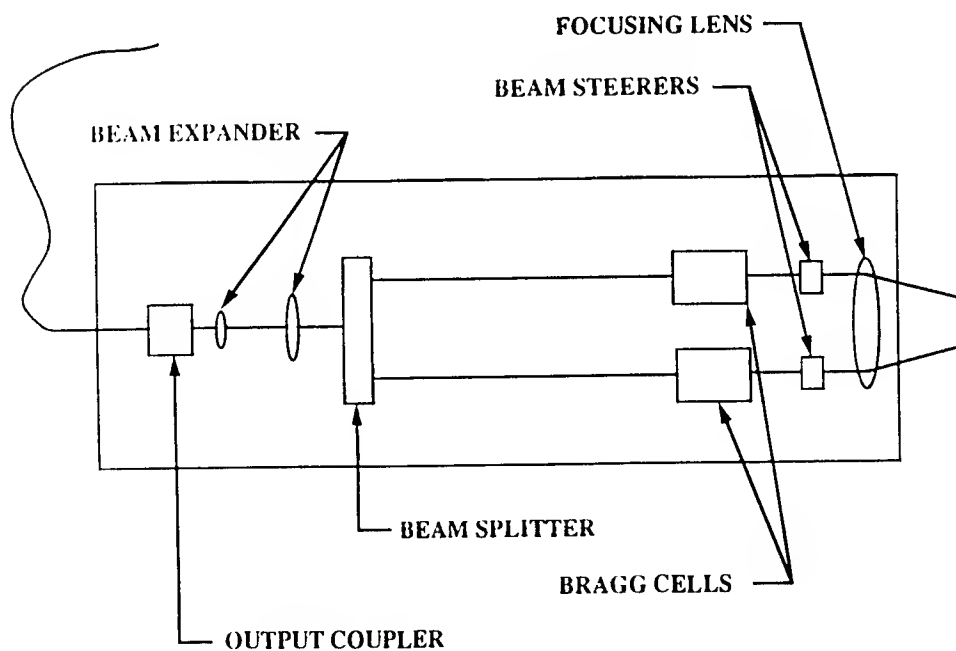


Figure 10. Single-component fiber optically coupled LDV system.



POLARIZATION SPECTRA FOR  
INFRARED MATERIALS AND ELEMENTS

Russell A. Chipman  
Associate Professor  
Department of Physics  
University of Alabama in Huntsville  
Huntsville, AL 35899

Randy Gove  
Shih-Yau Lu  
Research Assistant

Final Report for:  
Research Initiation Program  
Research & Development Laboratories

Sponsored by:  
Air Force Office of Scientific Research

December 1992

POLARIZATION SPECTRA FOR  
INFRARED MATERIALS AND ELEMENTS

Russell A. Chipman  
Associate Professor  
Department of Physics  
University of Alabama in Huntsville  
Huntsville, AL 35899

**Abstract**

The polarization properties of optical devices in the infrared spectrum have been investigated. A Fourier transform infrared spectrometer outfitted with polarimeter has been used to measure polarization properties from 3 to 14 microns. Liquid crystals, the CdTe modulator, an infrared retarder, and infrared polarizer have been measured. Diattenuation and retardance spectra and full Mueller matrices have been obtained for those samples. Research into the theoretical interpretation of the Mueller matrix data provides insight into the physical properties contained in the data.

# POLARIZATION SPECTRA FOR INFRARED MATERIALS AND ELEMENTS

Russell A. Chipman

## Introduction

The polarization properties of materials and devices in the infrared spectrum are difficult to measure. Polarization elements which perform well over a broad wavelength band are rare in the IR, and their properties are poorly characterized in the technical literature. However, polarization characterization is important for several reasons. First, the performance of many existing optical systems, including optical computers, correlators, spatial light modulators, remote sensing systems, and laser radars, can be compromised by polarization aberrations. Accurate measurement of the polarization of their components is critical in order to properly design and characterize such systems. Second, polarimetric measurement, or polarimetry, is a useful tool in materials research. Polarimetric measurements indicate promising infrared materials for use in modulators and other opto-electronic devices. Third, polarization measurements lead to a better understanding of the physical properties of the light-matter interaction.

The instrument used in this research is a Fourier transform infrared (FTIR) spectropolarimeter which is a novel combination of two advanced techniques: FTIR spectroscopy and polarimeter. This spectropolarimeter, described detailedly below, measures the 4 by 4 Mueller matrix in the 3 to 14 micron wavelength range. This enables us to probe the polarization properties of samples in the infrared. With this instrument we have measured polarization properties of several interesting samples.

The 4 by 4 Mueller matrix can be difficult to interpret. We have investigated the relationships between the Mueller matrix elements and more readily accessible quantities, such as diattenuation and retardance. This allows to draw the most meaningful physical understanding from the raw data.

## Spectropolarimetry

The UAH Fourier transform infrared (FTIR) spectropolarimeter [1],[2] is a unique instrument that is capable of measuring the polarization properties of a sample, liquid or solid, as a continuous function of wavelength. This spectropolarimeter is able to measure linear diattenuation and retardance spectra from 2.5 - 24  $\mu\text{m}$ . Besides, it is also capable of measuring complete Mueller matrix spectra in the wavelength range 3 - 14  $\mu\text{m}$ . This instrument can be used to measure the polarization response and properties of materials of current technological interest in the infrared, for example liquid crystals and cadmium telluride, etc. These electrooptical materials have application in devices currently under development, such as pattern recognition systems, programmable masks, and optical isolators.

This spectropolarimeter, developed by Russell Chipman and David Chenault of UAH and Dennis Goldstein of Elgin Air Force Base, is an FTIR spectrometer with a polarimeter in the sample compartment.

In normal operation, the instrument illuminates the sample with a sequence of polarization states, acquires a series of spectra, and calculates the Mueller matrix spectrum of the sample. The Mueller matrix is a full description of the polarization properties of the sample, describing the transformations undergone by arbitrary polarization states incident on the sample. From the Mueller matrix spectrum, the diattenuation and retardance spectra as well as depolarization spectra can be determined.

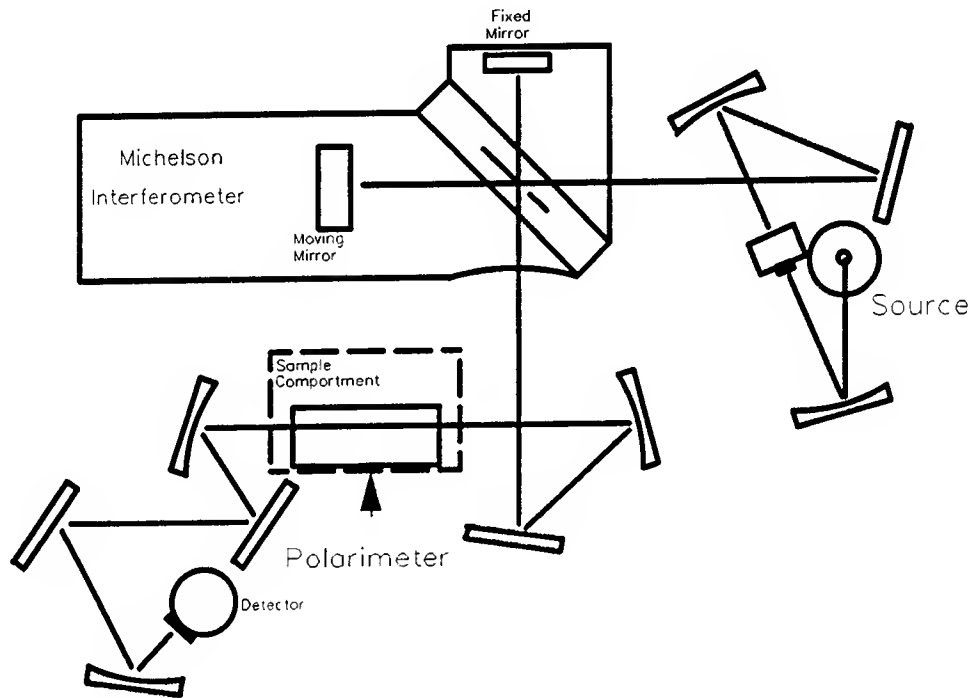


Figure 1: The Fourier transform infrared spectropolarimeter.

Two different polarimeter configurations are used in this research, and they are dual rotating retarder polarimeter and rotating sample polarimeter. They are described below [2].

#### 1. The dual rotating retarder Mueller matrix polarimeter

The dual rotating retarder polarimeter proposed by Azzam [3],[4] yields a complete Mueller matrix through the Fourier analysis of a single detected signal. The data reduction algorithm for this polarimeter as originally presented assumes ideal polarization elements and no orientational errors. The data reduction algorithms may be generalized to remove systematic errors which result when these requirements on the polarization elements and their orientation are relaxed [2],[5],[6]. We also developed a technique to determine and remove systematic errors generated by large orientation errors of the polarization elements and large retardance errors in the quarter-wave retarders [2],[5].

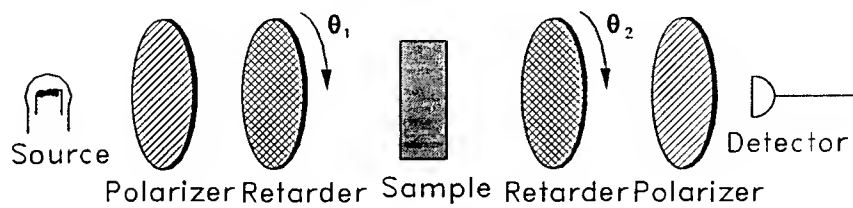


Figure 2: The dual rotating retarder polarimeter configuration.

Figure 2 shows the configuration of a dual rotating retarder polarimeter. It consists of a sample between a polarization state generator and polarization state analyzer each comprised of a stationary linear polarizer and rotating quarter-wave linear retarder. When the retarders are rotated in a five to one ratio, all sixteen elements of the sample Mueller matrix are encoded onto twelve harmonics of the detected intensity signal, which can then be Fourier analyzed to recover the Mueller matrix elements. If the polarization elements are misaligned, or the retarders do not have exactly one-quarter wave of retardance, the Fourier amplitudes and phases change resulting in errors in the sample Mueller matrix. Even small orientational and retardance errors ( $< 1^\circ$ ) can lead to large errors in the measured Mueller matrix ( $> 10\%$  in some matrix elements). These errors become especially important when the retardance and alignment vary significantly from their nominal values such as in multi-wavelength or spectral instruments. Here we expand on previous work incorporating correction terms for large orientation and retardance errors into the dual rotating retarder data reduction algorithm. This procedure is useful for spectral and multi-wavelength systems where changing the retardances of the retardation elements or exchanging the retardation elements is impractical or impossible.

Goldstein and Chipman [5] developed data reduction equations to remove systematic errors in the measured Mueller matrix due to small errors in the initial orientations of the polarization elements ( $< 0.3^\circ$ ) and small retardance errors ( $< 2^\circ$ ). Hauge presented a similar analysis with imperfect retarders [6]. Hauge includes the diattenuation of the retarders but does not include orientational error of the second polarizer. In our application the former is less important than the latter [5]. We have extended the research by Goldstein to include large orientation errors of the retarders and the second polarizer and large retardance errors in the retarders. The data reduction equations we have developed correct for orientational errors up to  $22.5^\circ$  and retardance errors up to  $\lambda/8$ . The motivation was to establish data reduction equations for Mueller matrix measurements over a large spectral band ( $3\ \mu m$  to  $14\ \mu m$ ) in which the achromatic retarders in our infrared spectropolarimeter display relatively large deviations ( $\pm 15^\circ$ ) from one quarter wave of retardance.

A set of  $N$  intensity measurements is required to determine the sample Mueller matrix. The  $n$ Th measurement is described by the following Mueller matrix equation for the polarimeter,

$$\begin{aligned}\vec{S}_{out}(n) &= M_{sys} \vec{S}_{in} \\ &= M_{LP2} M_{LR2}(n) M_{sample} M_{LRI}(n) M_{LPI} \vec{S}_{in}\end{aligned}\quad (1)$$

where  $M_{LPI}$  and  $M_{LP2}$  are the Mueller matrices of ideal polarizers with their transmission axes oriented along the horizontal  $\hat{x}$  direction,

$$M_{LPI} = M_{LP2} = \frac{1}{2} \begin{pmatrix} 1 & 1 & 0 & 0 \\ 1 & 1 & 0 & 0 \\ 0 & 0 & 0 & 0 \\ 0 & 0 & 0 & 0 \end{pmatrix}. \quad (2)$$

$M_{LRI}(n)$  and  $M_{LR2}(n)$  are the Mueller matrices of the quarter wave linear retarders in the polarization state generator and the polarization state analyzer,

$$M_{LRI} = \begin{pmatrix} 1 & 0 & 0 & 0 \\ 0 & \cos^2 2n\Delta\theta & \sin 2n\Delta\theta \cos 2n\Delta\theta & -\sin 2n\Delta\theta \\ 0 & \cos 2n\Delta\theta \sin 2n\Delta\theta & \sin^2 2n\Delta\theta & \cos 2n\Delta\theta \\ 0 & \sin 2n\Delta\theta & -\cos 2n\Delta\theta & 0 \end{pmatrix} \quad (3)$$

and

$$M_{LR2} = \begin{pmatrix} 1 & 0 & 0 & 0 \\ 0 & \cos^2 10n\Delta\theta & \sin 10n\Delta\theta \cos 10n\Delta\theta & -\sin 10n\Delta\theta \\ 0 & \cos 10n\Delta\theta \sin 10n\Delta\theta & \sin^2 10n\Delta\theta & \cos 10n\Delta\theta \\ 0 & \sin 10n\Delta\theta & -\cos 10n\Delta\theta & 0 \end{pmatrix}, \quad (4)$$

where  $\theta_n = n\Delta\theta$ .  $\Delta\theta$  is given by  $\Delta\theta = T/N$  where  $T$  is the total rotation of the first retarder in the measurement cycle (typically  $\pi$  or  $2\pi$ ) and  $N$  is the total number of measurements within one measurement cycle. For example if  $T = \pi$  and  $N = 30$ , the first measurement is made with the first retarder oriented at  $0^\circ$  and the second retarder at  $0^\circ$ , the second measurement is made with the first retarder oriented at  $\Delta\theta = 6^\circ$  and the second retarder at  $5\Delta\theta = 30^\circ$ , and the  $n$  Th measurement is made with the first retarder oriented at  $n\Delta\theta$  and the second retarder at  $5n\Delta\theta$ . Finally,  $M_{sample}$  in Eq. 1 is the Mueller matrix of the sample under test,

$$M_{sample} = \begin{pmatrix} m_{11} & m_{12} & m_{13} & m_{14} \\ m_{21} & m_{22} & m_{23} & m_{24} \\ m_{31} & m_{32} & m_{33} & m_{34} \\ m_{41} & m_{42} & m_{43} & m_{44} \end{pmatrix}. \quad (5)$$

The output intensity is given by the first element of the output Stokes vector,  $S_{0,out}(n)$ . The expression for the measured intensity  $I_n$  is expanded and rewritten to produce terms that correspond to the Fourier series expansion

$$I_n = \frac{\alpha_0}{2} \sum_{k=1}^{12} (\alpha_k \cos 2k\theta_n + b_k \sin 2k\theta_n). \quad (6)$$

The Fourier coefficients  $a_k$  and  $b_k$  are functions of the sixteen elements of the sample Mueller matrix. These expressions are inverted to give the Mueller matrix elements in terms of the Fourier series coefficients. These relations for the Mueller matrix elements are given in Table 1.

Table 1: Sample Mueller matrix elements in terms of Fourier coefficients when no errors are assumed in the polarimeter.

$$\begin{aligned}
 m_{11} &= 4a_0 - 4a_2 + 4a_8 - 4a_{10} + 4a_{12} \\
 m_{12} &= 8a_2 - 8a_8 - 8a_{12} \\
 m_{13} &= 8b_2 + 8b_8 - 8b_{12} \\
 m_{14} &= 4b_1 + 4b_9 - 4b_{11} \\
 m_{21} &= -8a_8 + 8a_{10} - 8a_{12} \\
 m_{22} &= 16a_8 + 16a_{12} \\
 m_{23} &= 16b_8 + 16b_{12} \\
 m_{24} &= -8b_9 + 8b_{11} \\
 m_{31} &= -8b_8 + 8b_{10} - 8b_{12} \\
 m_{32} &= 16b_8 + 16b_{12} \\
 m_{33} &= 16a_8 - 16a_{12} \\
 m_{34} &= 8a_9 - 8a_{11} \\
 m_{41} &= 4b_3 - 4b_5 + 4b_7 \\
 m_{42} &= -8a_3 - 8b_7 \\
 m_{43} &= -8a_3 + 8a_7 \\
 m_{44} &= 4a_6 - 4a_4
 \end{aligned}$$

The dual rotating retarder configuration has a number of advantages. First, the effect of any instrumental polarization preceding the polarizing optics or following the polarimeter is negated by the fixed position of the polarizers. Second, the Fourier transform on the data automatically performs a least squares fit to the overdetermined data set. Third, this configuration is largely immune to beam wander if measurements are made over a  $2\pi$  cycle. In this case, modulation from beam wander produced by wedges in the rotating retarders is encoded principally on the first and fifth Fourier amplitudes. Since the polarimeter does not modulate these frequencies, the beam wander signal does not affect the accuracy of the measured Mueller matrix.

## 2. The rotating sample polarimeter

A rotating sample is placed between two linear polarizers whose transmission axes are parallel, as shown in Figure 3. This configuration is useful in measuring linear diattenuation and retardance.

A sample with principal intensity transmittances  $k_1$  and  $k_2$  and retardance  $\delta = |\delta_1 - \delta_2|$  and whose axes of diattenuation and retardance are coincident and aligned with the  $x$  and  $y$  axes is represented by the Mueller matrix  $M_s$

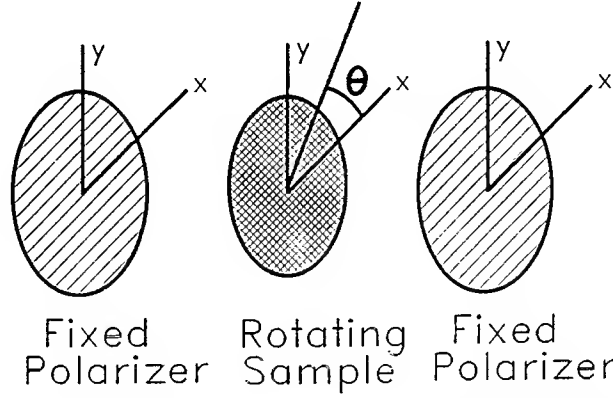


Figure 3: The rotating sample polarimeter configuration. The sample is rotated between two fixed linear polarizers.

$$\begin{aligned}
 \mathbf{M}_s &= \frac{1}{2} \begin{pmatrix} k_1 + k_2 & k_1 - k_2 & 0 & 0 \\ k_1 - k_2 & k_1 + k_2 & 0 & 0 \\ 0 & 0 & 2\sqrt{k_1 k_2} \cos \delta & 2\sqrt{k_1 k_2} \sin \delta \\ 0 & 0 & -2\sqrt{k_1 k_2} \sin \delta & 2\sqrt{k_1 k_2} \cos \delta \end{pmatrix} \\
 &= \tau_s \begin{pmatrix} 1 & \mathcal{D} & 0 & 0 \\ \mathcal{D} & 1 & 0 & 0 \\ 0 & 0 & \sqrt{1 - \mathcal{D}^2} \cos \delta & \sqrt{1 - \mathcal{D}^2} \sin \delta \\ 0 & 0 & -\sqrt{1 - \mathcal{D}^2} \sin \delta & \sqrt{1 - \mathcal{D}^2} \cos \delta \end{pmatrix},
 \end{aligned} \tag{7}$$

where

$$\mathcal{D} = \frac{k_1 - k_2}{k_1 + k_2} \quad \text{and} \quad \tau_s = \frac{1}{2}(k_1 + k_2). \tag{8}$$

are the linear diattenuation and the average transmission, and the axis of the principal transmittance  $k_1$  is aligned with the  $x$ -axis [7].

For precision measurements, the polarizers cannot necessarily be assumed ideal. The linear polarizers are assumed to have diattenuation  $\mathcal{D}_p$  and the systematic error introduced by the non-ideal diattenuation is corrected in the data reduction procedure. The system Mueller matrix  $\mathbf{M}_{sys}$  for the polarimeter with the sample at an angle  $\theta$  between parallel polarizers is



$$\begin{aligned}
M_{sys} &= M_{p2}(\mathcal{D}_2)R(-\theta)M_S R(\theta)M_{p1}(\mathcal{D}_1) \\
&= \tau_2 \begin{pmatrix} 1 & \mathcal{D}_2 & 0 & 0 \\ \mathcal{D}_2 & 1 & 0 & 0 \\ 0 & 0 & \sqrt{1-\mathcal{D}_2^2} & 0 \\ 0 & 0 & 0 & \sqrt{1-\mathcal{D}_2^2} \end{pmatrix} \begin{pmatrix} 1 & 0 & 0 & 0 \\ 0 & \cos 2\theta & -\sin 2\theta & 0 \\ 0 & \sin 2\theta & \cos 2\theta & 0 \\ 0 & 0 & 0 & 1 \end{pmatrix} \\
&\quad \times \tau_s \begin{pmatrix} 1 & \mathcal{D} & 0 & 0 \\ \mathcal{D} & 1 & 0 & 0 \\ 0 & 0 & \sqrt{1-\mathcal{D}^2} \cos \delta & \sqrt{1-\mathcal{D}^2} \sin \delta \\ 0 & 0 & -\sqrt{1-\mathcal{D}^2} \sin \delta & \sqrt{1-\mathcal{D}^2} \cos \delta \end{pmatrix} \\
&\quad \times \begin{pmatrix} 1 & 0 & 0 & 0 \\ 0 & \cos 2\theta & \sin 2\theta & 0 \\ 0 & -\sin 2\theta & \cos 2\theta & 0 \\ 0 & 0 & 0 & 1 \end{pmatrix} \tau_1 \begin{pmatrix} 1 & \mathcal{D}_1 & 0 & 0 \\ \mathcal{D}_1 & 1 & 0 & 0 \\ 0 & 0 & \sqrt{1-\mathcal{D}_1^2} & 0 \\ 0 & 0 & 0 & \sqrt{1-\mathcal{D}_1^2} \end{pmatrix},
\end{aligned} \tag{9}$$

where  $R(\theta)$  is the matrix for a rotational change of basis in the Mueller calculus.  $M_{pi}(\mathcal{D}_i)$  represents the  $i$ th horizontal linear polarizer with diattenuation  $\mathcal{D}_i$  and average transmission  $\tau_i = \frac{1}{2}(k_{i,1} + k_{i,2})$ .

The Stokes vector  $\bar{S}'$  of the light transmitted by the polarimeter and incident on the detector is given by

$$\bar{S}' = M_{sys} \bar{S}_{inc}. \tag{10}$$

The transmitted intensity is given by the first element of the transmitted Stokes vector. At each wavelength the intensity transmittance  $I$  as a function of sample orientation  $\theta$  has the form

$$\begin{aligned}
I(\theta) &= \tau \left[ 1 + \frac{1}{2} \mathcal{D}_1 \mathcal{D}_2 (1 + \sqrt{1-\mathcal{D}^2} \cos \delta) \right. \\
&\quad \left. + \mathcal{D}(\mathcal{D}_1 + \mathcal{D}_2) \cos 2\theta \right. \\
&\quad \left. + \frac{1}{2} \mathcal{D}_1 \mathcal{D}_2 (1 - \sqrt{1-\mathcal{D}^2} \cos \delta) \cos 4\theta \right] \\
&\approx \tau (\alpha_0 + \alpha_2 \cos 2\theta + \alpha_4 \cos 4\theta).
\end{aligned} \tag{11}$$

where  $\tau$  is a normalization factor including the radiance of the source, the responsivity of the detector, and the average transmission of the polarimeter. Equation 5 is a Fourier series in  $\theta$  with coefficients  $\alpha_0$ ,  $\alpha_2$ , and  $\alpha_4$ . The diattenuation  $\mathcal{D}$  and retardance  $\delta$  of the sample expressed in terms of the Fourier coefficients are

$$\mathcal{D} = \frac{\alpha_2}{\alpha_0 + \alpha_4} \left( \frac{1 + \mathcal{D}_1 \mathcal{D}_2}{\mathcal{D}_1 + \mathcal{D}_2} \right). \tag{12}$$

$$\delta = \cos^{-1} \left( \frac{\alpha_0 - \alpha_4 \left( 1 + \frac{2}{D_1 D_2} \right)}{\left[ (\alpha_0 + \alpha_4)^2 - \alpha_2^2 \left( \frac{1 + D_1 D_2}{D_1 + D_2} \right)^2 \right]^{\frac{1}{2}}} \right). \quad (13)$$

For nearly ideal linear polarizers,  $\mathcal{D}_1, \mathcal{D}_2 > 99\%$ , the correction for nonideal polarizers is negligible and ideal diattenuations  $\mathcal{D}_1 = \mathcal{D}_2 = 1$  can be assumed.

The quantities  $\alpha_0$ ,  $\alpha_2$ , and  $\alpha_4$  are determined experimentally by rotating the sample in increments of  $\Delta\theta$  to a set of  $N$  angles  $\theta_n = n \Delta\theta$ , where  $n = 0, 1, 2, \dots, N-1$ . The number of measurements  $N$  and the increment  $\Delta\theta$  must satisfy  $N \Delta\theta = 360^\circ$ , where  $N > 8$ . An intensity measurement is made at each  $\theta_n$ . At a particular wavelength, each set of  $N$  intensity measurements  $I(\theta_n)$  may be expressed as a Fourier series

$$\begin{aligned} I(\theta_n) &= \frac{b_0}{2} + \sum_{k=1}^K (b_k \cos k\theta_n + c_k \sin k\theta_n) \\ &= \frac{\alpha_0}{2} + \sum_{k=1}^K \alpha_k \cos(k\theta_n - k\phi_k) \end{aligned} \quad (14)$$

where  $\alpha_k^2 = b_k^2 + c_k^2$ ,  $K \geq 4$ , and  $N \geq 2K$ . The Fourier coefficients  $b_k$  and  $c_k$  are calculated from the set of measured intensities  $I(\theta_n)$  by a discrete Fourier transform.

The phase of the Fourier frequencies  $\phi_k$  is

$$\phi_k = \frac{1}{k} \arctan \left( \frac{c_k}{b_k} \right). \quad (15)$$

The phase of the second harmonic  $\phi_2$  gives the orientation of the sample's principal transmittance  $k_1$  with respect to the  $x$ -axis. The phase of the fourth harmonic  $\phi_4$  gives the orientation of the phase delay  $\delta_1$  with respect to the  $x$ -axis within an integer multiple of  $\pi/2$ . The fast and slow axes of a device are not determined by this technique.

Only the Fourier coefficients  $\alpha_0$ ,  $\alpha_2$ , and  $\alpha_4$  are used to determine the diattenuation and retardance spectra. The other Fourier coefficients,  $\alpha_1$ ,  $\alpha_3$ ,  $\alpha_5$ ,  $\alpha_6$ ,  $\alpha_7 \dots$ , which should be zero in the absence of noise and systematic errors, provide valuable information on the operation of the polarimeter. For example, beam wander arising from the rotation of a sample with non-plane parallel surfaces couples strongly into the first harmonic  $\alpha_1$  and decreasingly into the higher harmonics. A nonzero value for  $\alpha_1$  suggests the presence of beam wander. Since significant beam wander also couples into  $\alpha_2$  and  $\alpha_4$ , measurements on samples with non plane-parallel surfaces have reduced accuracy.

The following three points summarize the conclusions of our analysis: the rotating sample polarimeter (1) is immune to instrumental polarization, (2) is immune to circular diattenuation and circular retardance, and (3) has increased accuracy relative to other more complete polarimeters. First, substantial instrumental polarization in spectrometers is caused by large angles of incidence on fold mirrors and

polarization of the beamsplitter or grating [8]. It is necessary to either neutralize this instrumental polarization or perform complex data reduction to remove systematic errors introduced by the instrumental polarization. Fixing the orientation of the polarizers ensures that only one polarization state is transmitted to the sample and to the optics following the polarimeter [3]. The detected signal thus depends only on the linear diattenuation and retardance in the sample and not on the orientation of the polarizers in the instrument.

## **Polarimetric Data**

### **1. The Wire Grid Polarizer**

Figure 4 shows the diattenuation and retardance spectra of the wire grid polarizer. The diattenuation falls off at short wavelengths as would be expected for a wavelength close to the size of the wire grid spacings. The spectrum of retardance does not show the retardance for wavelengths longer than  $4\ \mu m$  since at those wavelengths the diattenuation is very close one and almost no light is transmitted in the orthogonal polarization.

### **2. Liquid Crystals [9]**

The interest in ferroelectric liquid crystals as spatial light modulators for the visible and near infrared has grown recently due to their high switching speed, substantial birefringence, and low power requirements. The three liquid crystals investigated in this study were the British Drug House mixtures 764E, SCE4, and SCE9. The 764E mixture is an electroclinic mixture at elevated temperatures <sup>1</sup> while the latter two are broad temperature smectic C\* ferroelectric liquid crystals. All three samples were in the SMC\* phase at the measurement temperature 25°C. The samples were mounted between two uncoated CaF<sub>2</sub> windows with 50  $\mu m$  spacing. Their linear birefringence and linear diattenuation spectra from 2.5 to 12  $\mu m$  for the BDH 764E smectic A\* electroclinic and BDH SCE4 and SCE9 smectic C\* ferroelectric liquid crystals <sup>2</sup> are presented (Figures 5, 6 and 7). The liquid crystal samples were prepared at the University of Colorado in Boulder.

Gaps have been introduced in the diattenuation and birefringence spectra where the transmission is less than 2%. In these regions, the spectropolarimeter cannot determine accurate values of the diattenuation and retardance because there is not enough light. In the absorption bands, the magnitudes of the Fourier components of the polarimetric signal become small and noisy and the resulting quantities are consequently less accurate.

The results presented here indicate that the large birefringence ( $\Delta n > 0.1$ ) and the small linear diattenuation ( $\mathcal{D} < 2\%$  in non-absorbing regions) warrant investigation of these liquid crystalline materials for use as spatial light modulators in the mid-infrared.

### **3. The Cadmium Telluride Modulator**

---

<sup>1</sup> G. Anderson, I. Pahl, and P. Kells, "Submicrosecond electro-optic switching in the liquid crystal smectic A phase," Appl. Phys. Lett. 51, 640-642 (1987).

<sup>2</sup> British Drug House FLC mixtures available from EM Industries, Inc., 5 Skyline Drive, Hawthorne, NY 10532.

Mueller matrix spectra were acquired for various applied voltage ranging from zero to 2700 volts (Figures 8-14). Those figures indicate that this modulator has low diattenuation in 3 - 14  $\mu\text{m}$ . Retardance spectra were calculated from the Mueller matrix spectra for each of the applied voltages. Figure 15 shows the resulting retardance spectra. The plots range from applied voltages of 300 volts on the bottom to 2700 volts on top. A linear regression was performed on the retardance as a function of voltage at each wavelength over the spectrum shown. An example of the linear regression for a wavelength of 10.6  $\mu\text{m}$  is shown in Figure 16.

The value of  $n^3 r_{41}$  at 10.6  $\mu\text{m}$  is  $1.09 \times 10^{-10}$  m/V. This value agrees well with values previously published. The value of  $r_{41}$  at 3.39  $\mu\text{m}$  is  $5.5 \times 10^{-12}$  m/V if an index of 2.696 is assumed. This value differs from the value given by Yariv [10] by almost 20%. However, due to the large discrepancy in previously reported refractive indices, the quantity  $n^3 r_{41}$  is believed to be more accurate than  $r_{41}$  and is emphasized here. The  $n^3 r_{41}$  spectrum is shown in Figure 17.

#### 4. The Achromatic retarder

The IR achromatic retarder was also measured. The Mueller matrix spectrum is shown in Figure 19. Since elements of the first row of the Mueller matrix is very small, this element does not have significant diattenuation. Also, from the 34 and 43 elements, we see that the fast axis of this retarder is oriented at  $0^\circ$ . The retardance spectrum is shown in Figure 19.

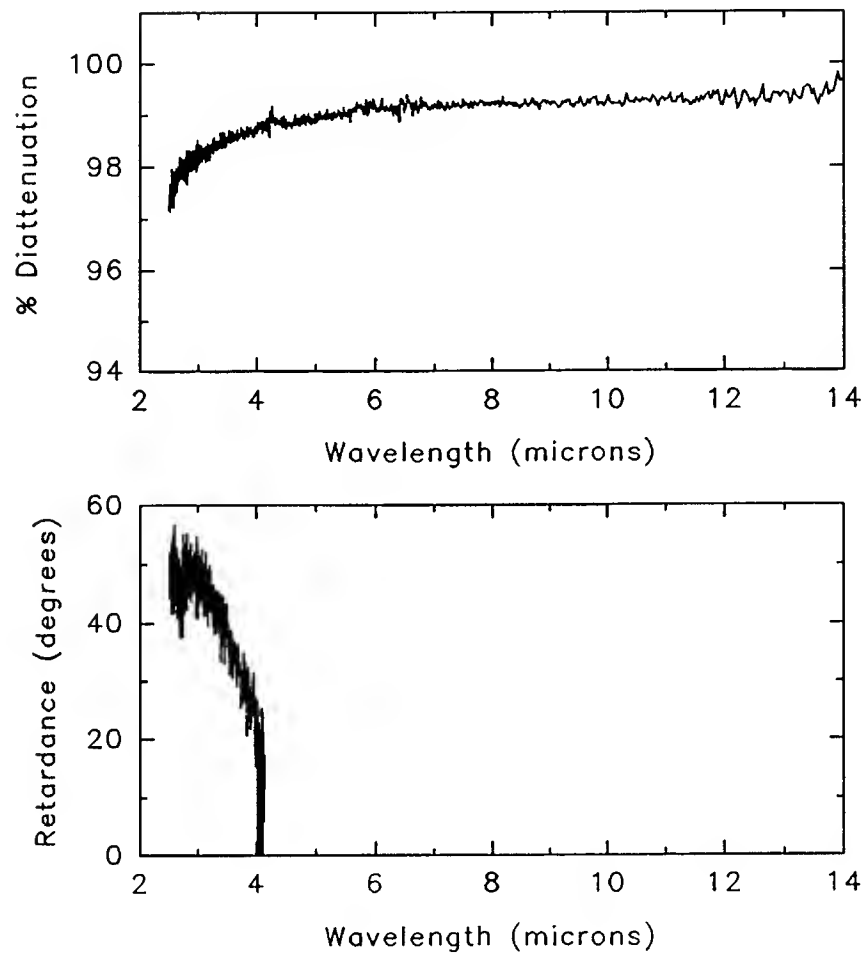


Figure 4: Linear diattenuation and retardance spectra of the wire grid polarizer.

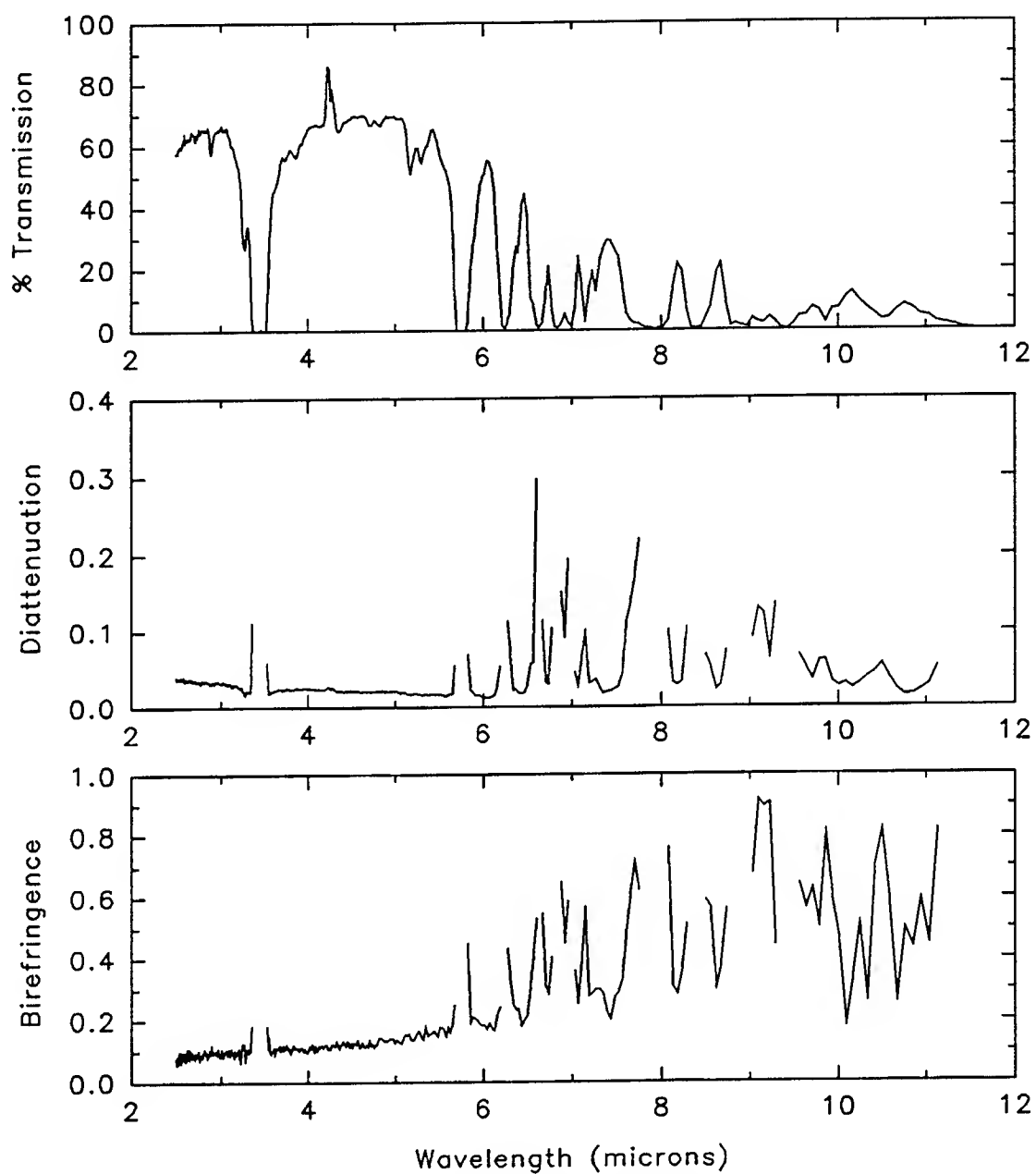


Figure 5: The transmission, linear diattenuation, and linear birefringence of the BDH 764E liquid crystal.

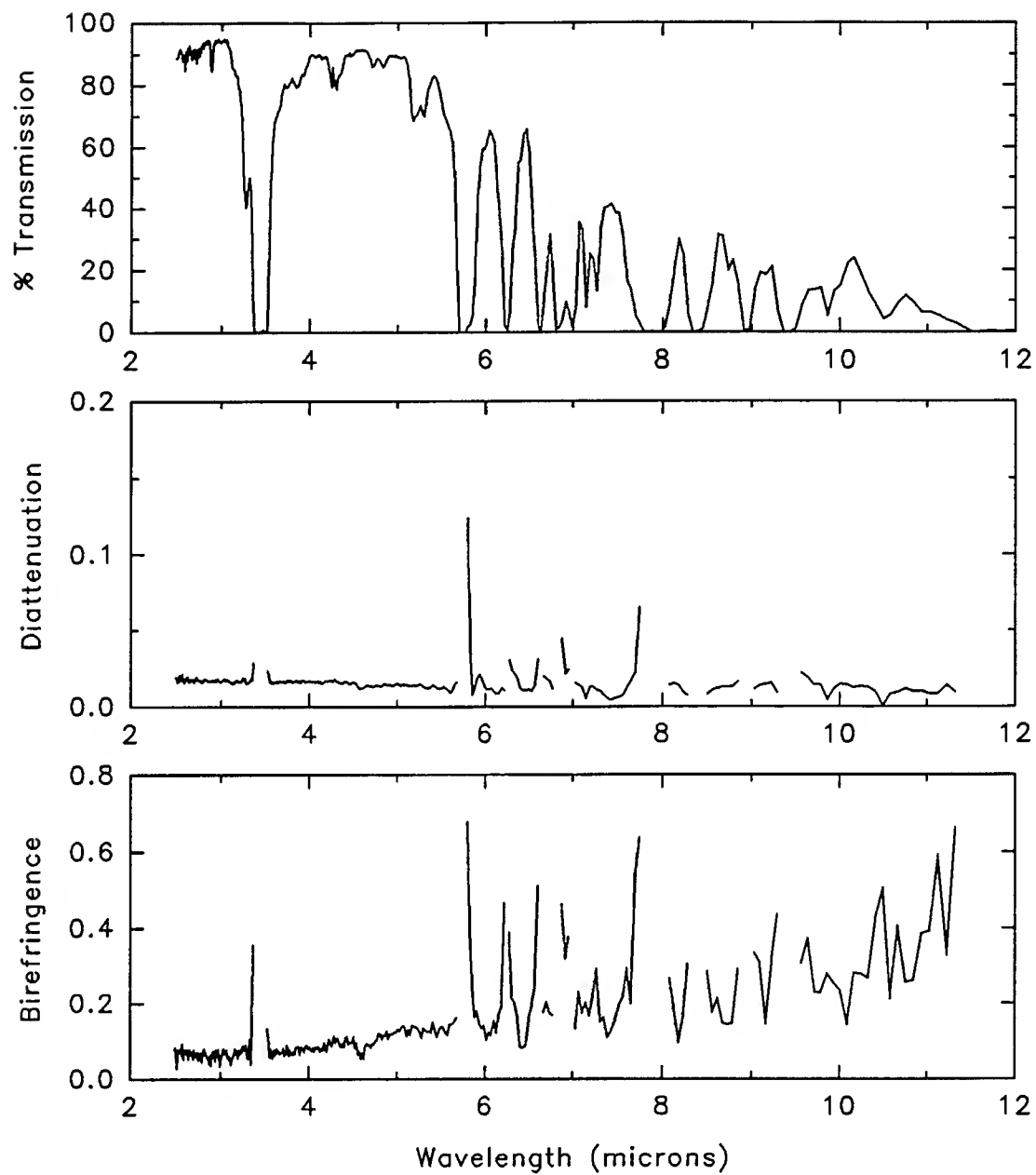


Figure 6: The transmission, linear diattenuation, and linear birefringence of the BDH SCE4 liquid crystal.

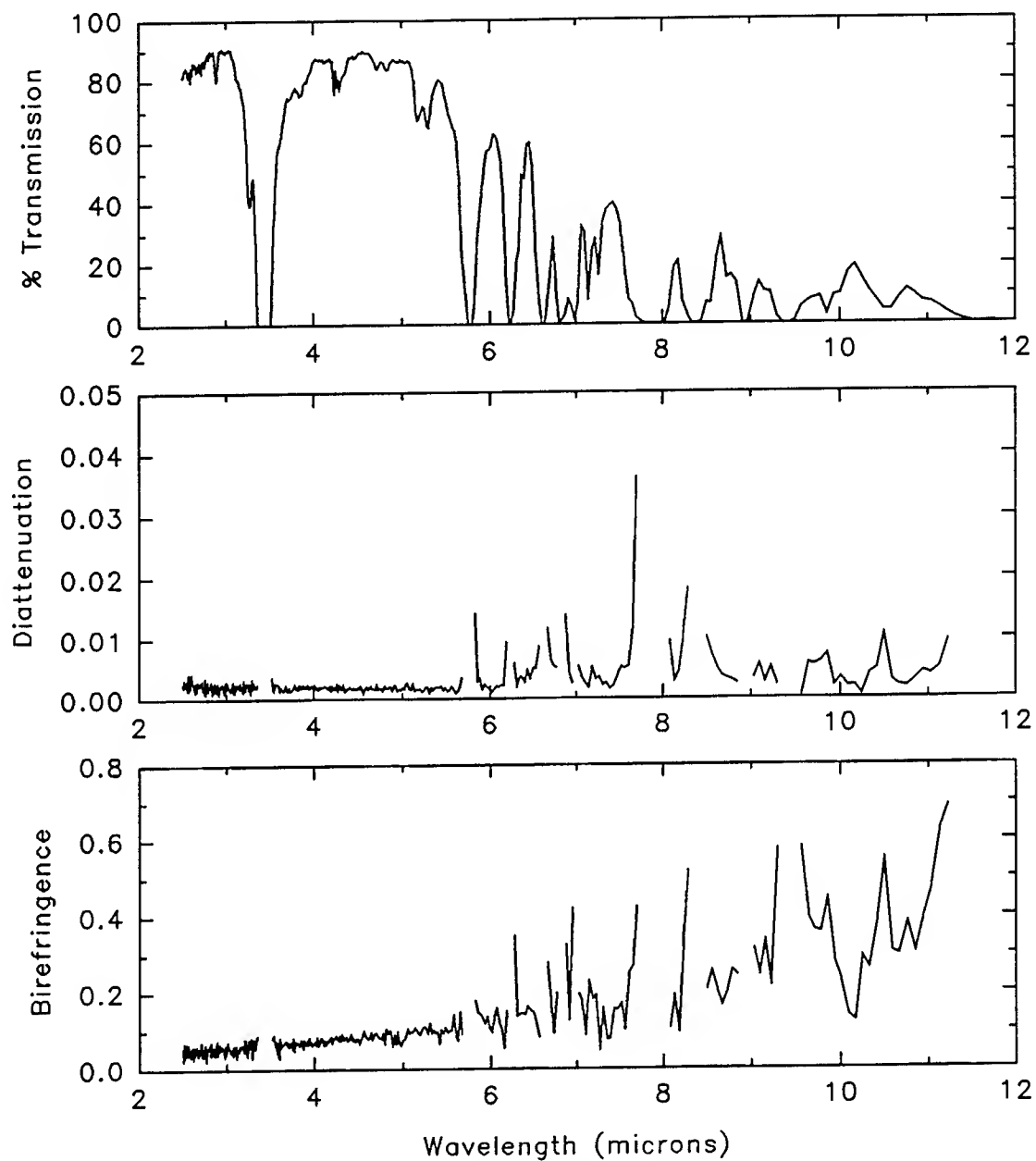


Figure 7: The transmission, linear diattenuation, and linear birefringence of the BDH SCE9 liquid crystal.



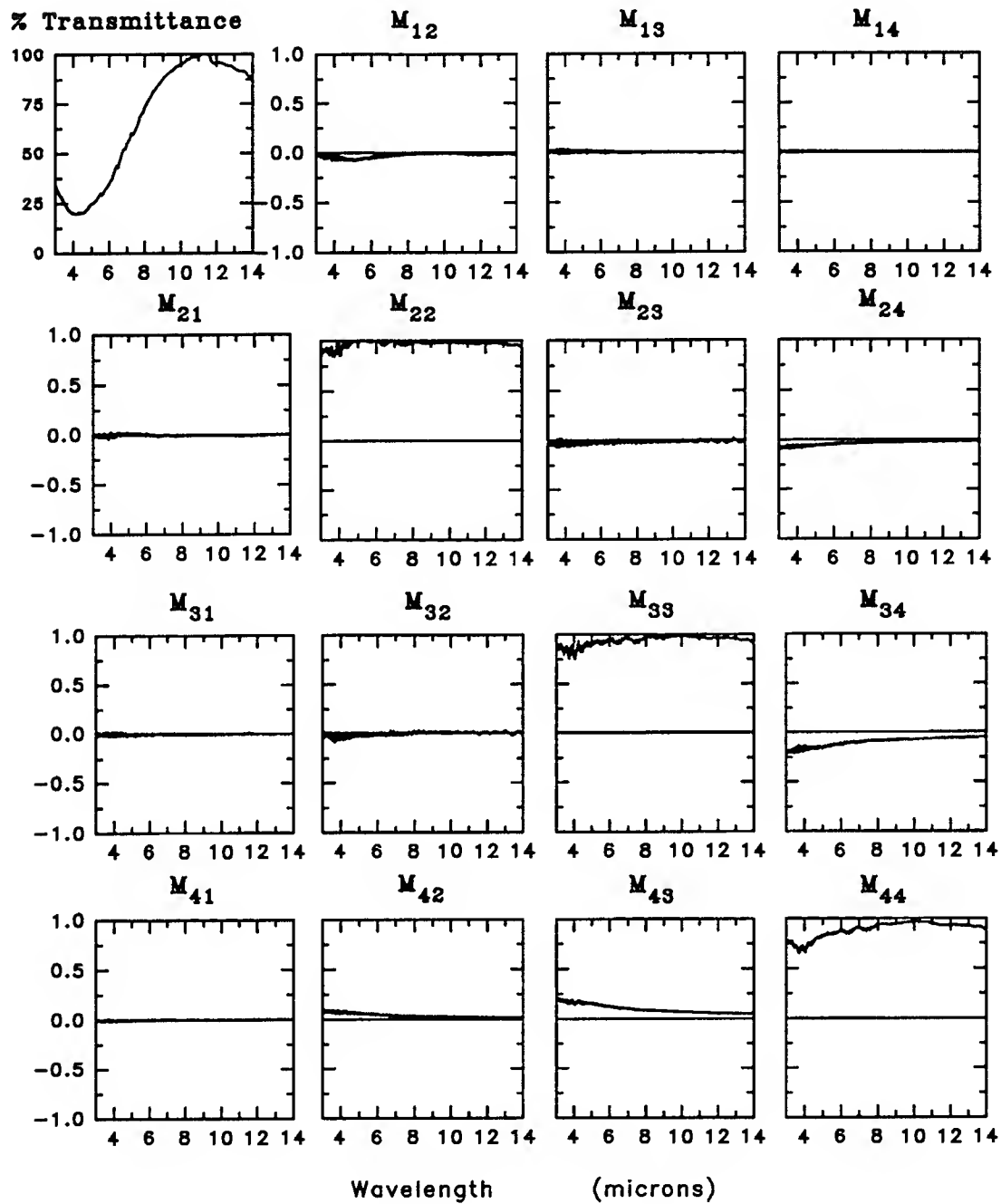


Figure 8 Mueller matrix of CdTe modulator with no applied voltage.

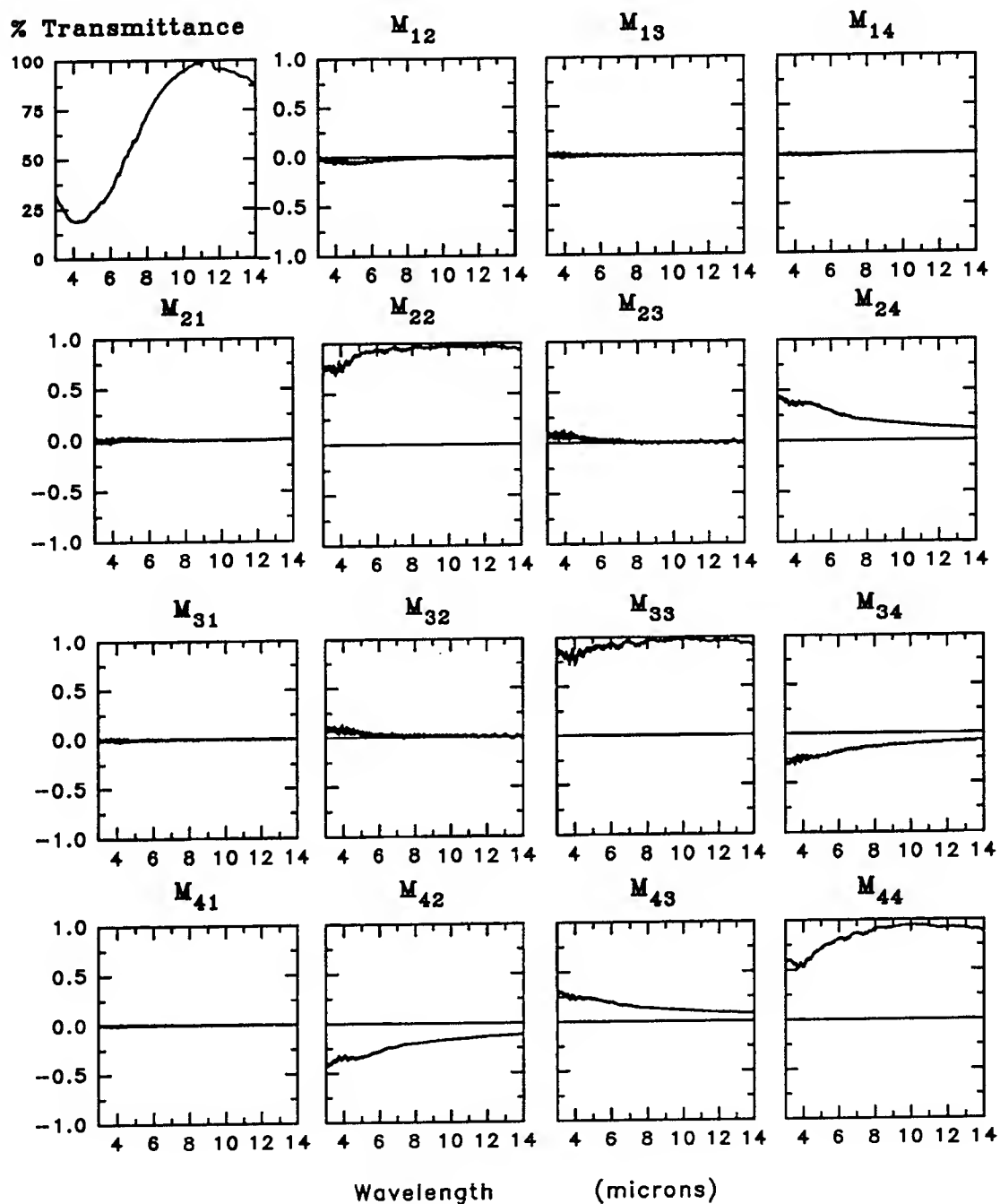


Figure 9 Mueller matrix of CdTe modulator with an applied voltage of 300 volts.

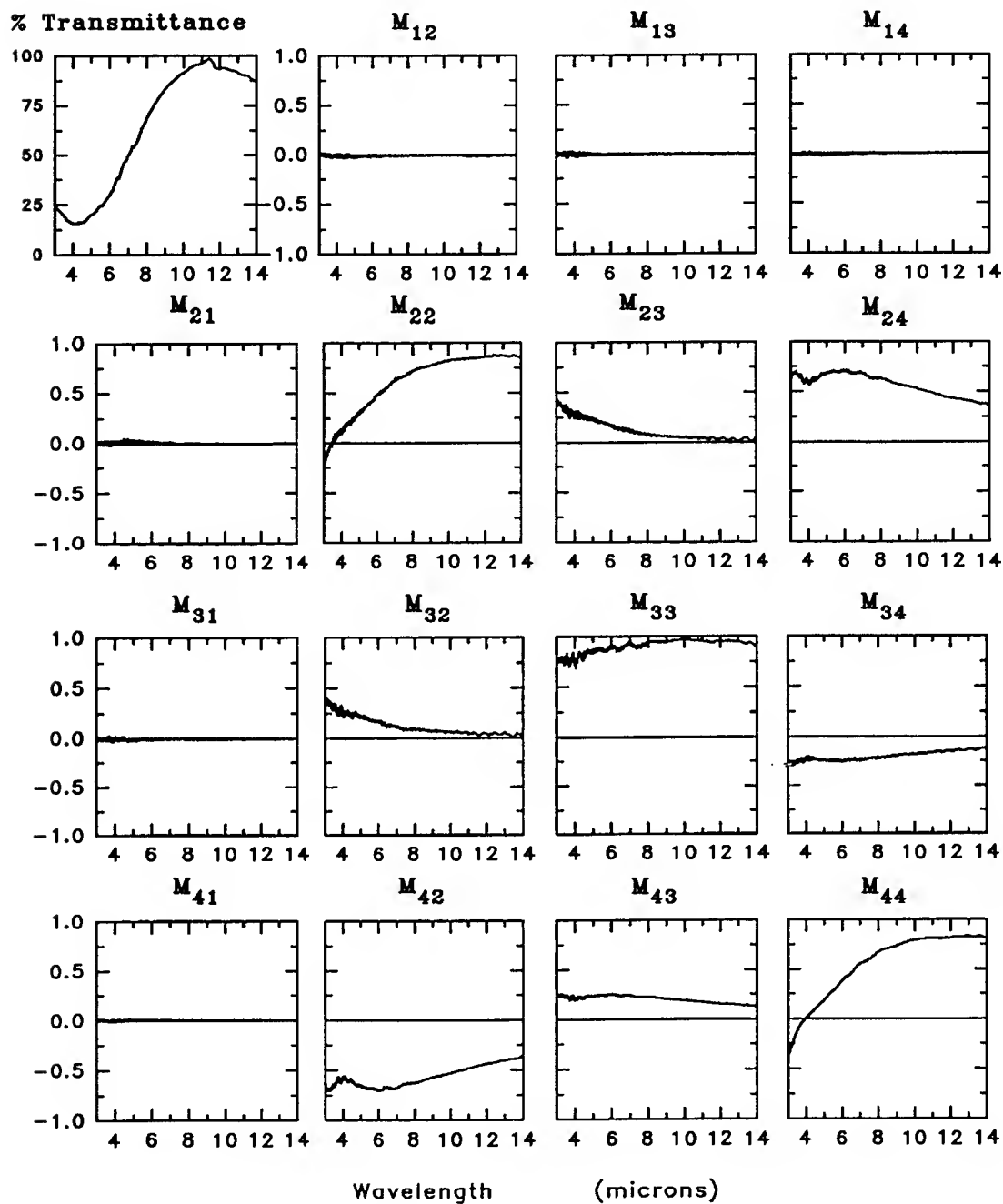


Figure 10 Mueller matrix of CdTe modulator with an applied voltage of 900 volts.

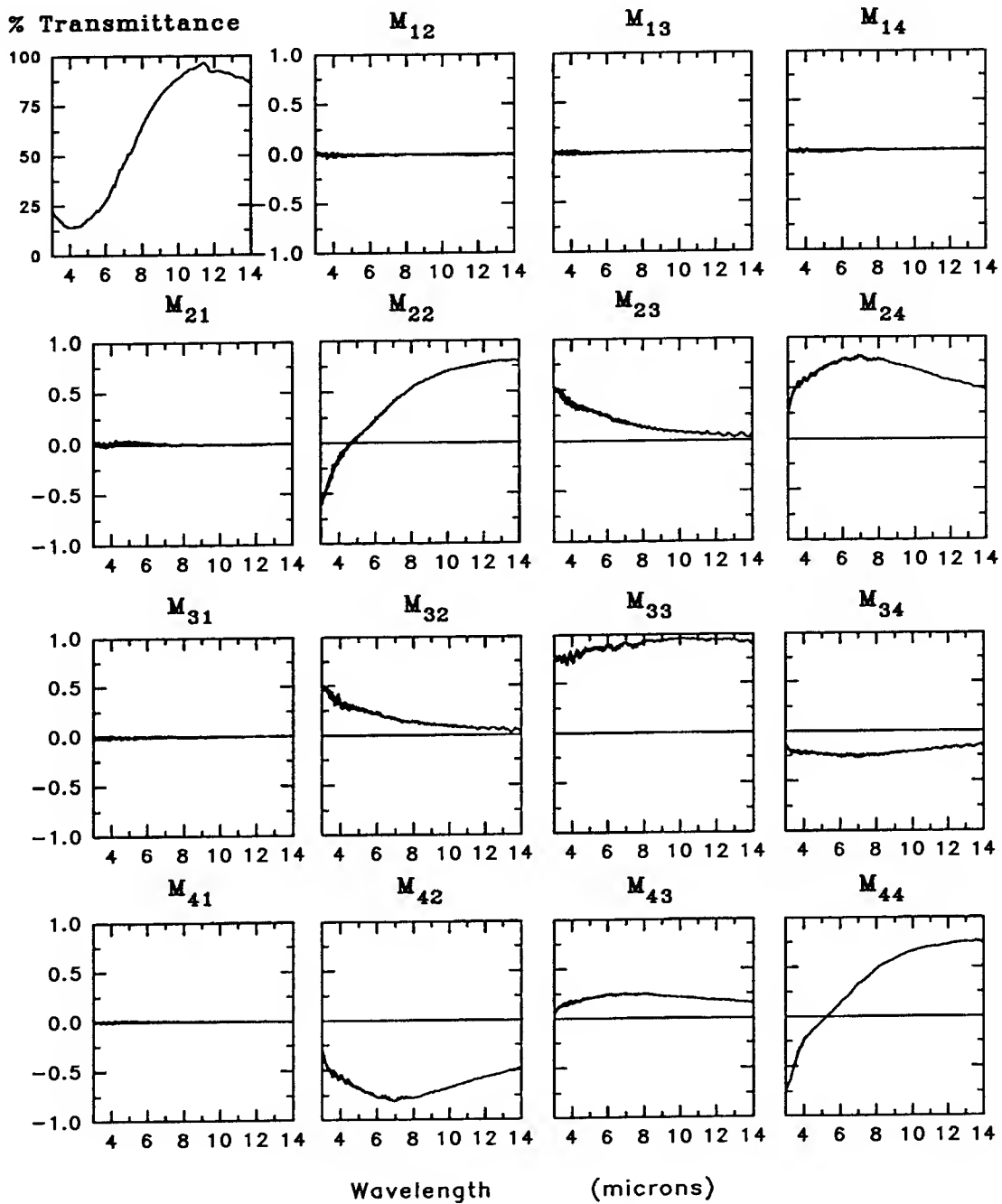


Figure 11 Mueller matrix of CdTe modulator with an applied voltage of 1200 volts.

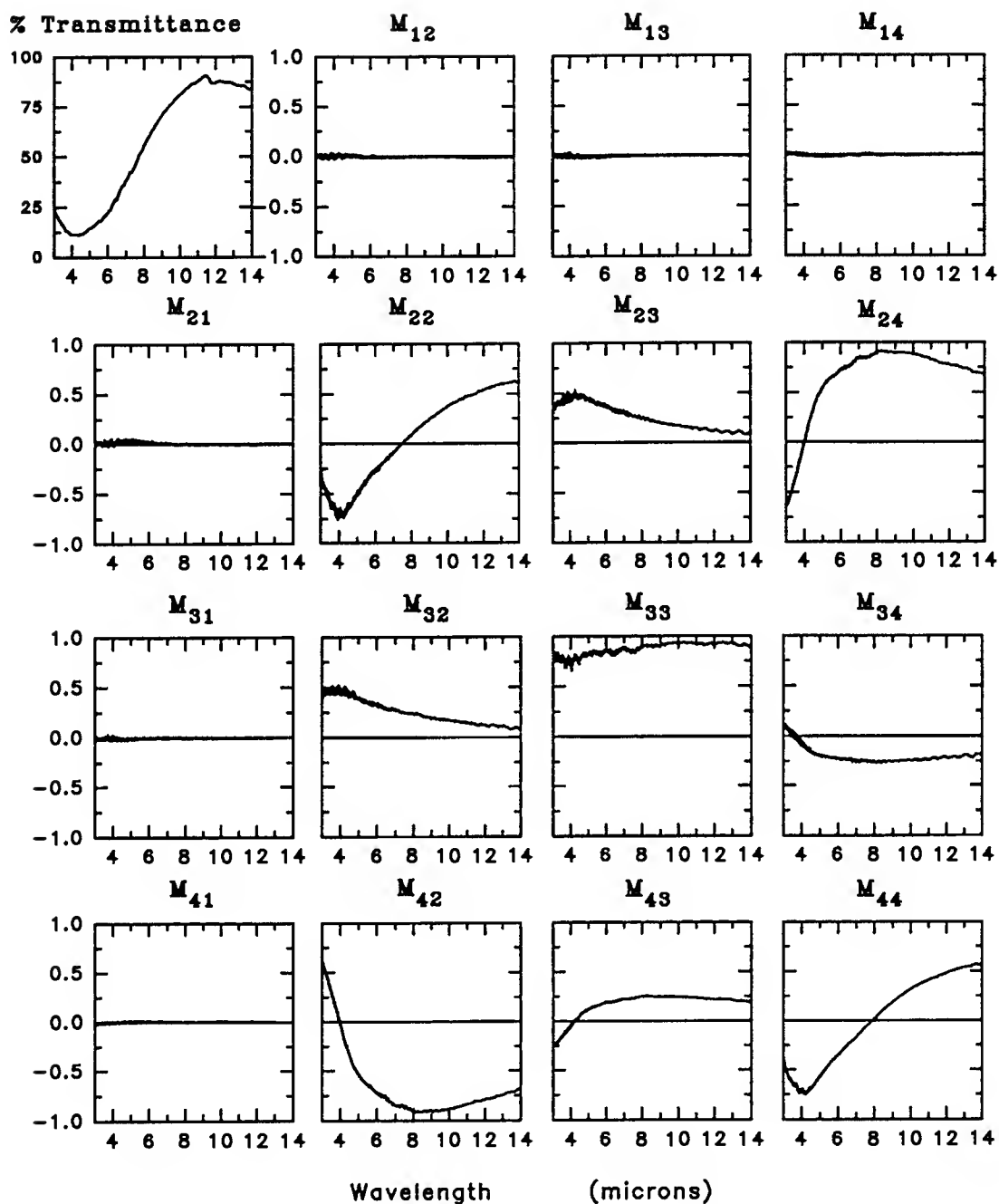


Figure 12 Mueller matrix of CdTe modulator with an applied voltage of 1800 volts.

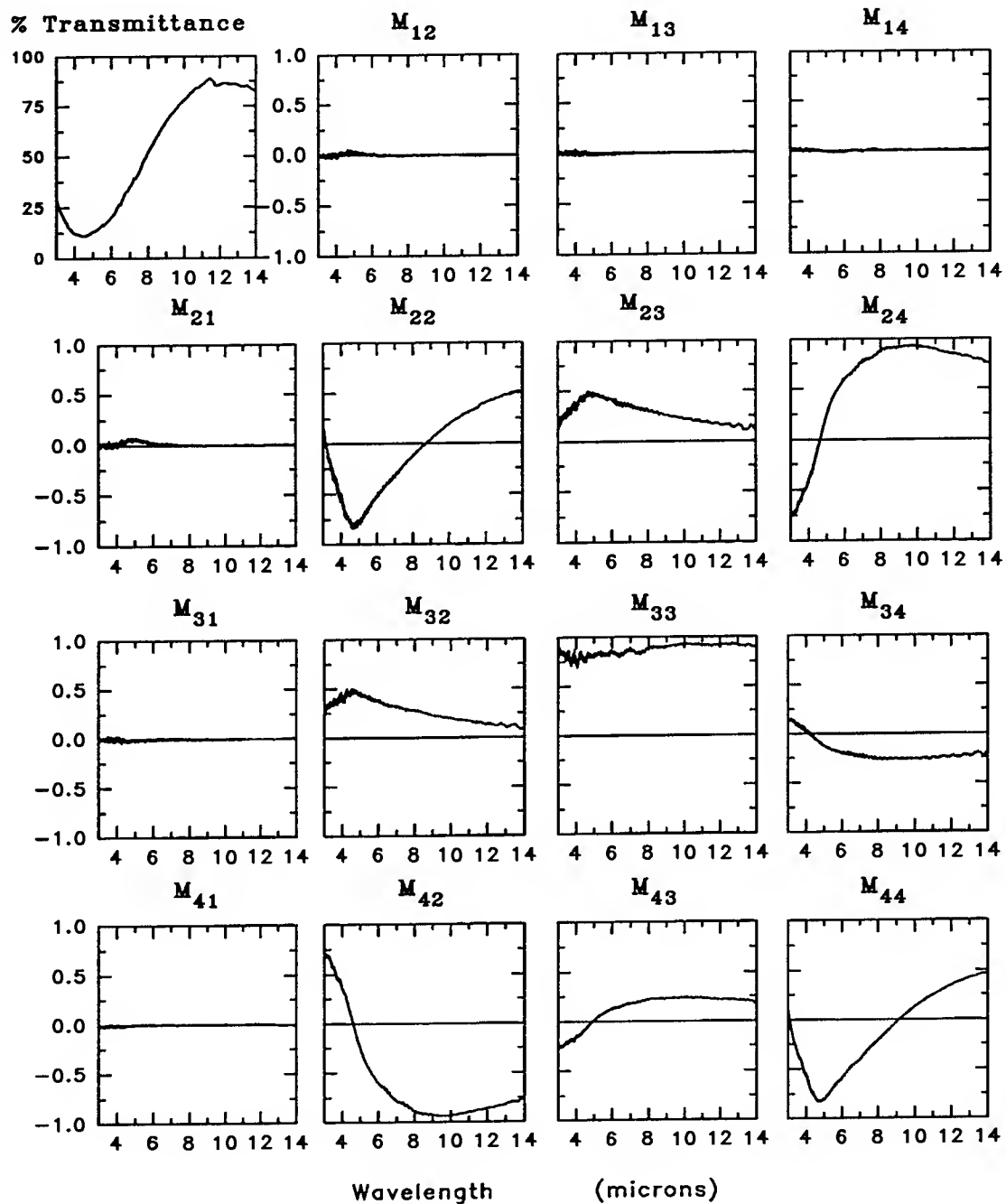


Figure 13 Mueller matrix of CdTe modulator with an applied voltage of 2100 volts.

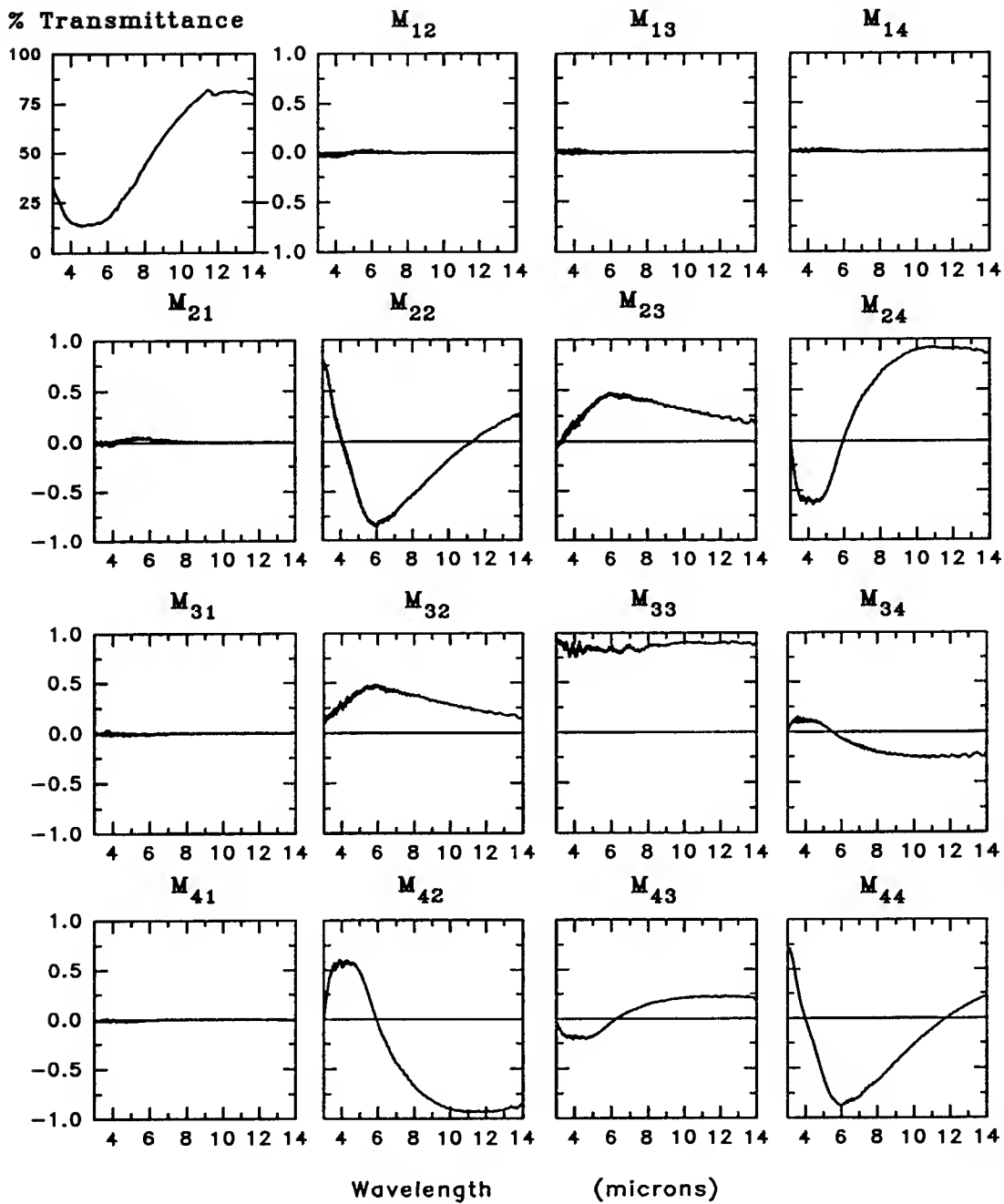


Figure 14 Mueller matrix of CdTe modulator with an applied voltage of 2700 volts.

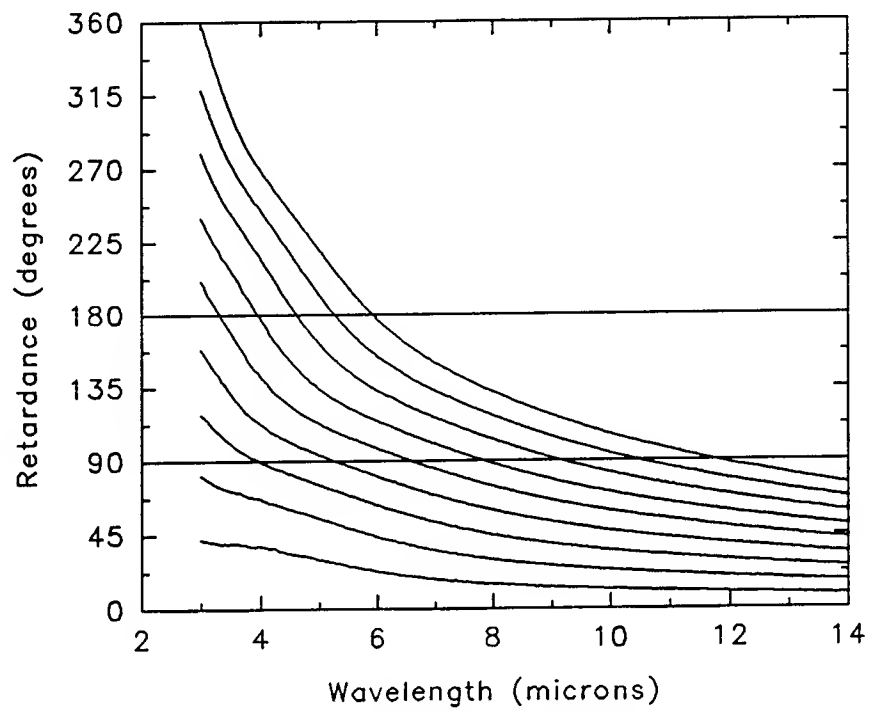


Figure 15 Retardance as a function of wavelength and voltage.

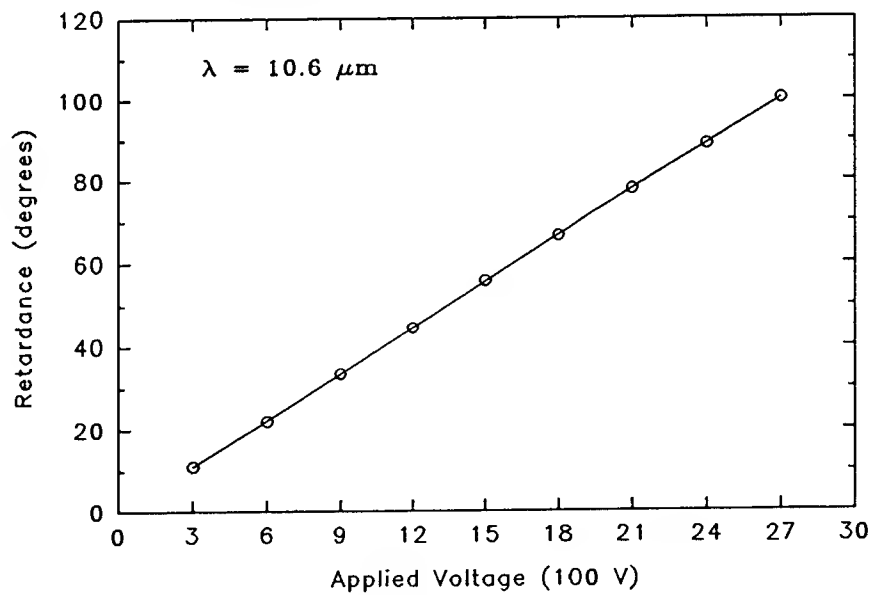


Figure 16 Linear regression of retardance as a function of voltage at  $10.6 \mu\text{m}$ .



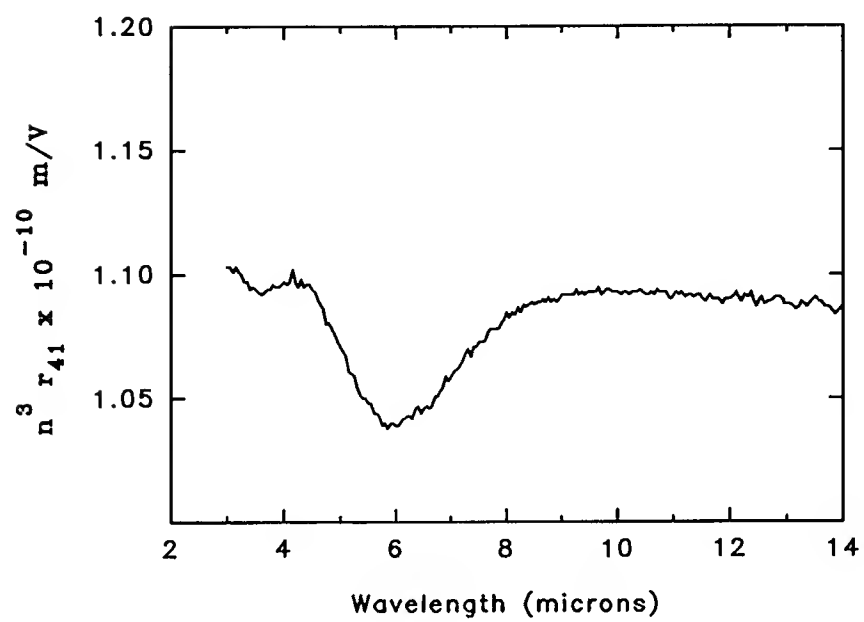


Figure 17 Spectrum of  $n^3 r_{41}$  calculated from retardance.

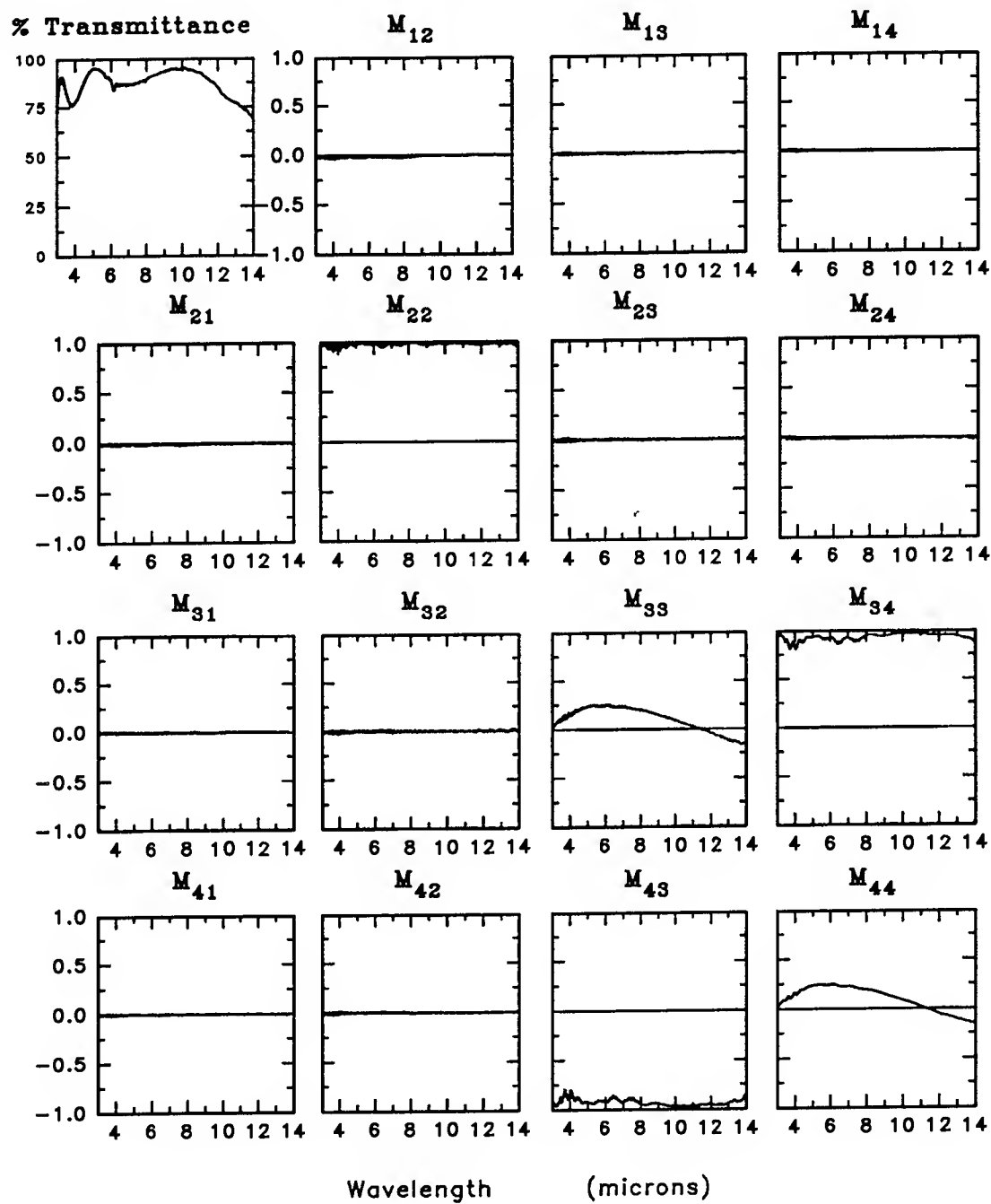


Fig 18 Mueller matrix of an IR achromatic retarder

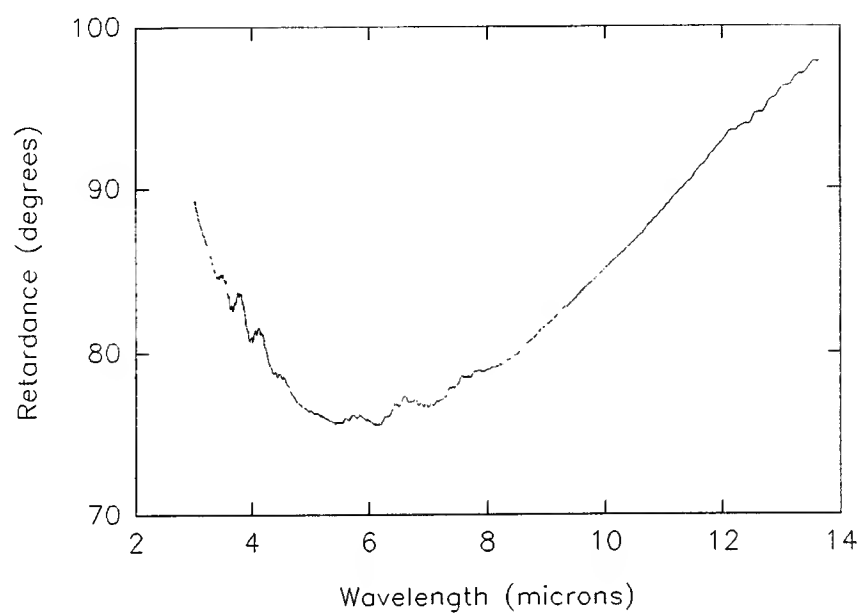


Figure 19 The retardance spectrum of the achromatic retarder

### Interpretation of Mueller Matrices

It is well known that the polarization properties of a polarization element can be completely described by the 4 by 4 Mueller matrix. However, the interpretation of Mueller matrices is not yet clear. Nevertheless, two useful quantities- diattenuation and retardance [8], have been introduced for this purpose. In this section the interpretation of Mueller matrices is discussed.

Consider a nondepolarizing element described by the Mueller matrix  $M$ ,

$$M = \begin{bmatrix} m_{11} & m_{12} & m_{13} & m_{14} \\ m_{21} & m_{22} & m_{23} & m_{24} \\ m_{31} & m_{32} & m_{33} & m_{34} \\ m_{41} & m_{42} & m_{43} & m_{44} \end{bmatrix} \quad (16)$$

For incident light with the Stokes vector of unit intensity

$$S = \begin{bmatrix} 1 \\ s_2 \\ s_3 \\ s_4 \end{bmatrix} \quad (17)$$

the transmittance of this polarization element is given by

$$T(S) = m_{11} + m_{12}s_2 + m_{13}s_3 + m_{14}s_4 \quad (18)$$

which is determined by the first row of the Mueller matrix. It is not difficult to show that the maximum and minimum transmittances are given by [11]

$$T_{\max} = m_{11} + \sqrt{m_{12}^2 + m_{13}^2 + m_{14}^2} \quad (19)$$

$$T_{\min} = m_{11} - \sqrt{m_{12}^2 + m_{13}^2 + m_{14}^2} \quad (20)$$

We, thus, define the diattenuation  $\mathcal{D}$  of a polarization element as [12]

$$\mathcal{D} = \frac{T_{\max} - T_{\min}}{T_{\max} + T_{\min}} = \frac{\sqrt{m_{12}^2 + m_{13}^2 + m_{14}^2}}{m_{11}} \quad (21)$$

which clearly describes the polarization sensitivity of this element.

Furthermore, the transmittance for horizontally and vertically polarized light are, respectively,

$$T_H = m_{11} + m_{12} \quad , \quad T_V = m_{11} - m_{12} \quad (22)$$

Thus, we define the linear diattenuation  $\mathcal{D}_H$  as [13]

$$\mathcal{D}_H = \frac{T_H - T_V}{T_H + T_V} = \frac{m_{12}}{m_{11}} \quad (23)$$

Similarly, we can define the linear diattenuation at  $45^\circ$   $\mathcal{D}_{45}$  and the circular diattenuation  $\mathcal{D}_R$  respectively as [13]

$$\mathcal{D}_{45} = \frac{T_{45} - T_{135}}{T_{45} + T_{135}} = \frac{m_{13}}{m_{11}} \quad (24)$$

and

$$\mathcal{D}_R = \frac{T_R - T_L}{T_R + T_L} = \frac{m_{14}}{m_{11}} \quad (25)$$

It should be noted that

$$\mathcal{D} = \sqrt{\mathcal{D}_H^2 + \mathcal{D}_{45}^2 + \mathcal{D}_R^2} \quad (26)$$

According to the polar decomposition theorem [12],[14], any nondepolarizing element can be decomposed as a cascade of a diattenuator followed by a retarder, or in reversed order with a different diattenuator. Thus, this nondepolarizing Mueller matrix can be expressed as

$$M = M_R M_D \quad (27)$$

where  $M_R$  and  $M_D$  denote a pure retarder and diattenuator, respectively. From the first row of the Mueller matrix, we can easily find the  $M_D$ . The retarding part is, then, given by

$$M_R = M M_D^{-1} \quad (28)$$

Moreover, the retardance of  $M_R$  is defined to be the retardance of this element which is given by

$$\mathcal{R} = \cos^{-1} \left( \frac{1}{2} \text{Tr} M_R - 1 \right) \quad (29)$$

## Conclusions

The spectropolarimeter has been proven to be a powerful instrument in investigating the polarization properties of materials in IR region. The interpretation of Mueller matrices are also presented, and it allows us to relate the measured Mueller matrix elements to the diattenuation and retardance of the sample.

## References

1. D. H. Goldstein, R. A. Chipman, and D. B. Chenault, "Infrared spectropolarimetry," Opt. Eng. 28(2), 120-125 (1989).
2. D. B. Chenault, "Infrared Spectropolarimetry," Ph.D. Dissertation, University of Alabama in Huntsville, 1992.
3. R. M. A. Azzam, "Photopolarimetric measurement of the Mueller matrix by Fourier analysis of a single detected signal," Opt. Lett. 2(6), 148-150 (1978).
4. D. H. Goldstein, "Polarization modulation in infrared electro-optic materials," Ph.D. Dissertation, University of Alabama in Huntsville (1990).
5. D. H. Goldstein and R. A. Chipman, "Error analysis of Mueller matrix polarimeter," JOSA A7(4) 693-700 (1990).
6. P. S. Hauge, "Mueller matrix ellipsometry with imperfection compensator," JOSA 68(11) 1519-1528 (1978).
7. D. S. Kliger, J. S. Lewis, and C. E. Randall, Polarized Light in Optics and Spectroscopy, Academic Press, New York (1990).
8. R. A. Chipman, "Polarization analysis of optical system," Opt. Eng. 28(2), 90-99 (1989).
9. D. B. Chenault, R. A. Chipman, K. M. Johnson, and D. Doroski, "Infrared linear diattenuation and birefringence spectra of ferroelectric liquid crystals," Opt. Lett. 17(6), 447-449 (1992).
10. A. Yariv and P. Yeh, Optical Waves in Crystals, Wiley and Sons, New York (1985).
11. R. Barakat, "Conditions for physical realizability of polarization matrices characterizing passive systems," J. Mod. Opt. 34, 1535-1544 (1987).
12. S. Y. Lu and R. A. Chipman, "Generalized diattenuation and retardance for inhomogeneous polarization

elements," in Polarization Analysis and Measurement, D. H. Goldstein and R. A. Chipman eds., Proc. SPIE 1746, in press (1992).

13. A. B. Wedding, A. G. Mikosza, and J. F. Williams, "Polarimetry in electron-photon coincidence studies", J. Opt. Soc. Amer. **A8**, 1729-1738 (1991).

14. P. Lancaster and M. Tismenetsky, The Theory of Matrices, 2nd ed., Academic Press, New York (1985).

COMPUTATIONAL STUDY OF FACTORS CONTRIBUTING TO TIRE WEAR

By

Manjriker Gunaratne, Ph.D., P.E.

Assistant Professor

Department of Civil Engineering and Mechanics

University of South Florida

Tampa, FL. 33620

A report submitted to the  
RESEARCH AND DEVELOPMENT LABORATORIES  
Culver City, CA.

And

LANDING GEAR SYSTEMS GROUP  
WRIGHT-PATTERSON AIRFORCE BASE  
Dayton, OH.

December 1992

### Acknowledgments

The Principal Investigator is thankful to the University of South Florida Graduate Assistant Sashi Bushan Tadepallai for his contribution towards the completion of this project. He is also indebted to Mr. John Medzorian, Mr. Paul Ulrich, Dr. M. Chowla, Ms. Dot Homa and Mr. Paul Wagner of the Landing Gear Systems Group (Wright-Patterson Airforce Base) as well as Mr. Gary Moore of Research and Development Laboratories (RDL) for their cooperation during this work. Finally, the RDL/Airforce Office of Scientific Research (AFOSR) initiation grant is gratefully acknowledged.



## TABLE OF CONTENTS

	Page
Acknowledgments	i
LIST OF FIGURES	iii
CHAPTER 1. INTRODUCTION	1
CHAPTER 2. FREE ROLLING KINEMATICS OF F-16 TIRE	4
CHAPTER 3. BRAKING AND CORNERING KINEMATICS OF F-16 TIRE	26
CHAPTER 4. PREDICTION OF WEAR SLIP ENERGY	36
CHAPTER 5. MANUAL FOR MODELING AIRCRAFT TIRES ON WPAFB COMPUTER SYSTEM	47
CHAPTER 6. EFFECT OF PAVEMENT TEXTURE ON RUNWAY FRICTION	55
REFERENCES	66
APPENDIX A. F-16 Data file for free rolling and braking	69
APPENDIX B. Computer program for obtaining sample output from TIRE3D	80
APPENDIX C. Computer program for predicting wear slip energy	85

## LIST OF FIGURES

## Page

2.1	F-16 finite element mesh showing "J" and "K" variation.	5
2.2	F-16 finite element mesh showing "I" variation.	6
2.3	Finite element configuration under 83% of maximum load.	7
2.4	3-D distribution of normal pressure on the contact patch.	8
2.5	Pressure isobars on the contact patch.	9
2.6	Comparison of TIRE3D and experimental load Vs. deflection data for F-16 tire.	10
2.7	Contact patch configuration.	12
2.8	3-D distribution of normal pressure at 50% of maximum load.	13
2.9	Pressure isobars under 50% of maximum load.	14
2.10	Pressure isobars under rolling.	15
2.11	Free body of a free rolling wheel.	17
2.12	Deformation of a pneumatic tire.	20
2.13	Configuration of meridians and parallels.	22
3.1	3-D distribution of normal pressure under braking.	27
3.2	Pressure isobars under braking.	28
3.3	Free body of a braked tire.	29
3.4	Typical brake force ratio Vs. brake slip ratio curve .	31

3.5	Configuration of slip angle and path of cornering tire.	34
3.6	Lateral slip of a cornering tire.	35
4.1	Dynamics of longitudinal sliding.	39
4.2	Slip velocities on the contact patch on rolling.	41
4.3	Slip velocities on the contact patch on braking.	42
4.4	Shear stresses on the contact patch on rolling.	43
4.5	Shear stresses on the contact patch on braking.	44
6.1	Phenomenon of hysteresis.	60
6.2	Variation of $E$ , $E'$ and $E^*$ with frequency.	63
6.3	Variation of frictional components with frequency.	64

## CHAPTER 1

### INTRODUCTION

Accurate prediction of tire wear is essential to improved tire designs. Hence, the Landing Gear Systems Group of the Wright-Patterson Airforce Base currently directs its research emphasis in methods predicting tire wear. Consequent to the Principal Investigator's summer work with the above Group, it was found that the 3-dimensional finite element program TIRE3D has the potential of modeling dynamic behavior of aircraft tires. Hence, it was envisaged that this program provides a way to study the wear potential of aircraft tires with various construction under different maneuvers. Thus, one task of this follow-up study was to lay the foundation for establishing the above capability of TIRE3D.

During initial studies, the investigator also became aware of some theoretical models predicting tire behavior which have emerged in the recent years. Although these have the ability to predict the wear potential of tires using deterministic expressions, they certainly incorporate simplistic assumptions regarding the tire construction. Moreover, since it is quite complicated to form one general solution for every possible tire maneuver, these solutions are usually maneuver specific and so far have only modeled the simplest tire maneuvers. Therefore, the computational methods will continue to have the advantage of producing approximate solutions to any tire construction, properly modeled using finite elements. The capability of such methods is enhanced if they can handle

complicated tire dynamics. Hence, a computer program in the caliber of TIRE3D has an edge over deterministic solutions. As another task of the extended research, the investigator scrutinized some closed form solutions and compared the results with those of the TIRE3D, whenever possible.

The preliminary work done using the program TIRE3D in the summer of 1991 basically covered the following tasks.

1. Compilation and conversion of TIRE3D to an executable form.
2. Finite Element Modeling of a KC-135 aircraft tire.
3. Study of inflation and static loading of the above tire.
4. Formulation of a theoretical procedure to estimate contact patch slip velocities.

In the present study covered by the mini grant, this work has been extended to cover the following tasks:

1. Rescrutinity and computerization of the slip velocity determination using a PC-based program written in C language.
2. Finite element modeling of an F-16 tire (Chapter 2)

3. Study of inflation, static loading, free rolling and braked rolling of the above tire (Chapters 2 and 3).
4. Prediction of slip velocities as well as wear slip energy associated with the above maneuvers (Chapter 4).
5. Preparation of a secondary manual to aid in finite element modeling of an aircraft tire using TIRE3D on the WPAFB computer system and predicting the wear slip energy associated with different maneuvers (Chapter 5).
6. Theoretical studies leading to a better understanding of the runway friction (Chapter 6).

## CHAPTER 2

### FREE ROLLING KINEMATICS OF F-16 TIRE

#### 2.1 Simulation of loading

An F-16 tire was modeled as described in Chapter 5 and loaded upto 83% of its maximum rated load (Figs. 2.1 and 2.2). TIRE3D program was used to obtain the following results shown in Figs. (2.3)-(2.5) respectively:

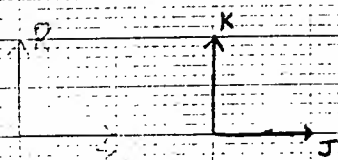
- i. Finite element configuration under maximum deformation.
- ii. Distribution of normal pressure on the contact patch.
- iii. Pressure isobars on the contact patch.

A comparison of the TIRE3D predicted load Vs. deflection data for this tire with the experimental curves are shown in Fig. 2.6.

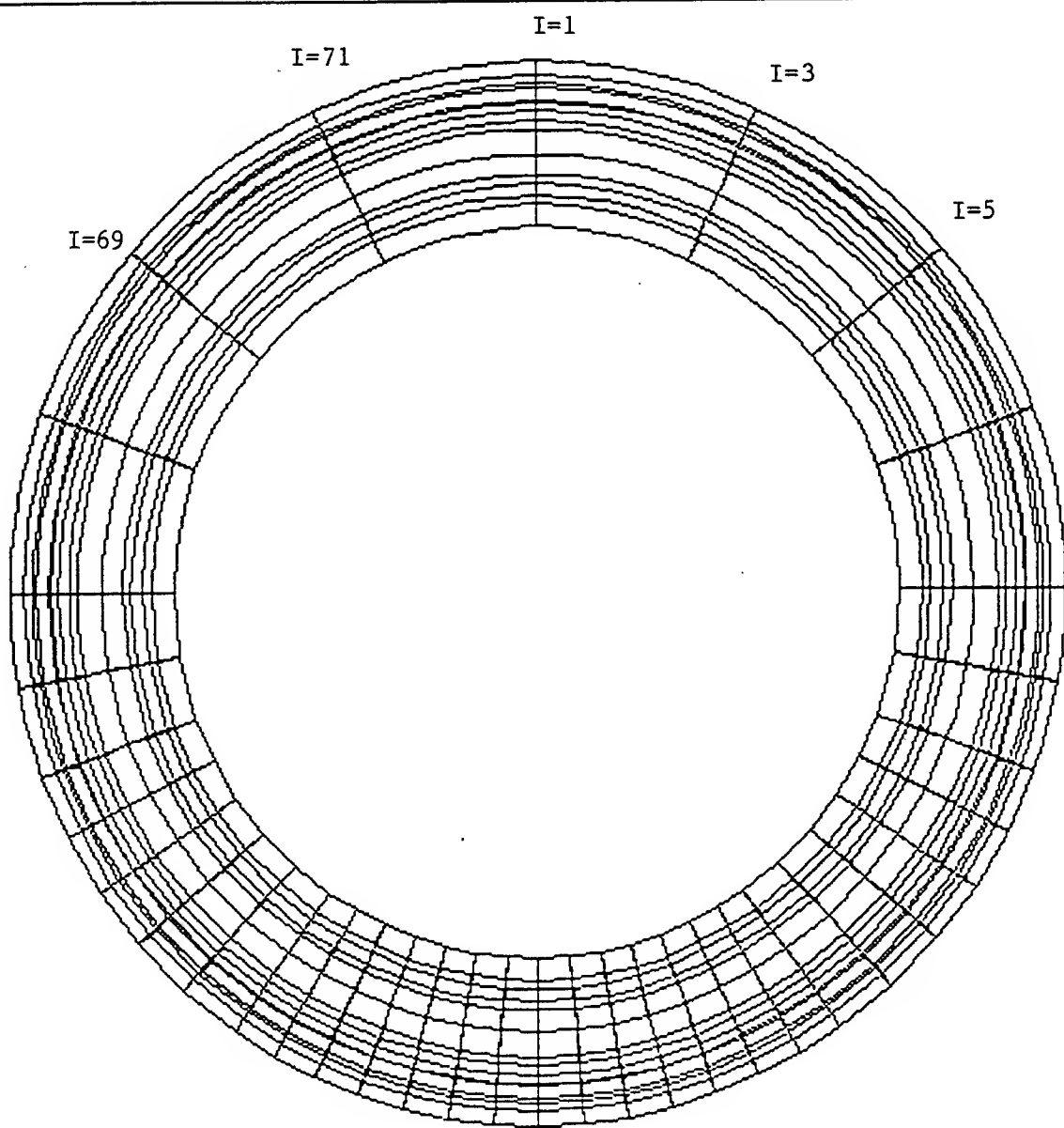
#### 2.2 Modeling of straight free rolling

Rolling is defined as a relative angular motion between two bodies in contact about an axis parallel to their common tangent plane. Consider a rigid wheel  $B_1$  which is rolling on a stationary ground  $B_2$ . Then the phenomenon of perfect rolling is said to occur when a continuous sequence of points on the surface of  $B_1$  comes one to one contact with a sequence of points on the surface of  $B_2$ .

If these two bodies or any one of them are not perfectly rigid, there will be an elastic deformation at the place where these two bodies meet. In such cases, some contacting points at the interface may 'slip' while others may 'stick'. This phenomenon will occur if



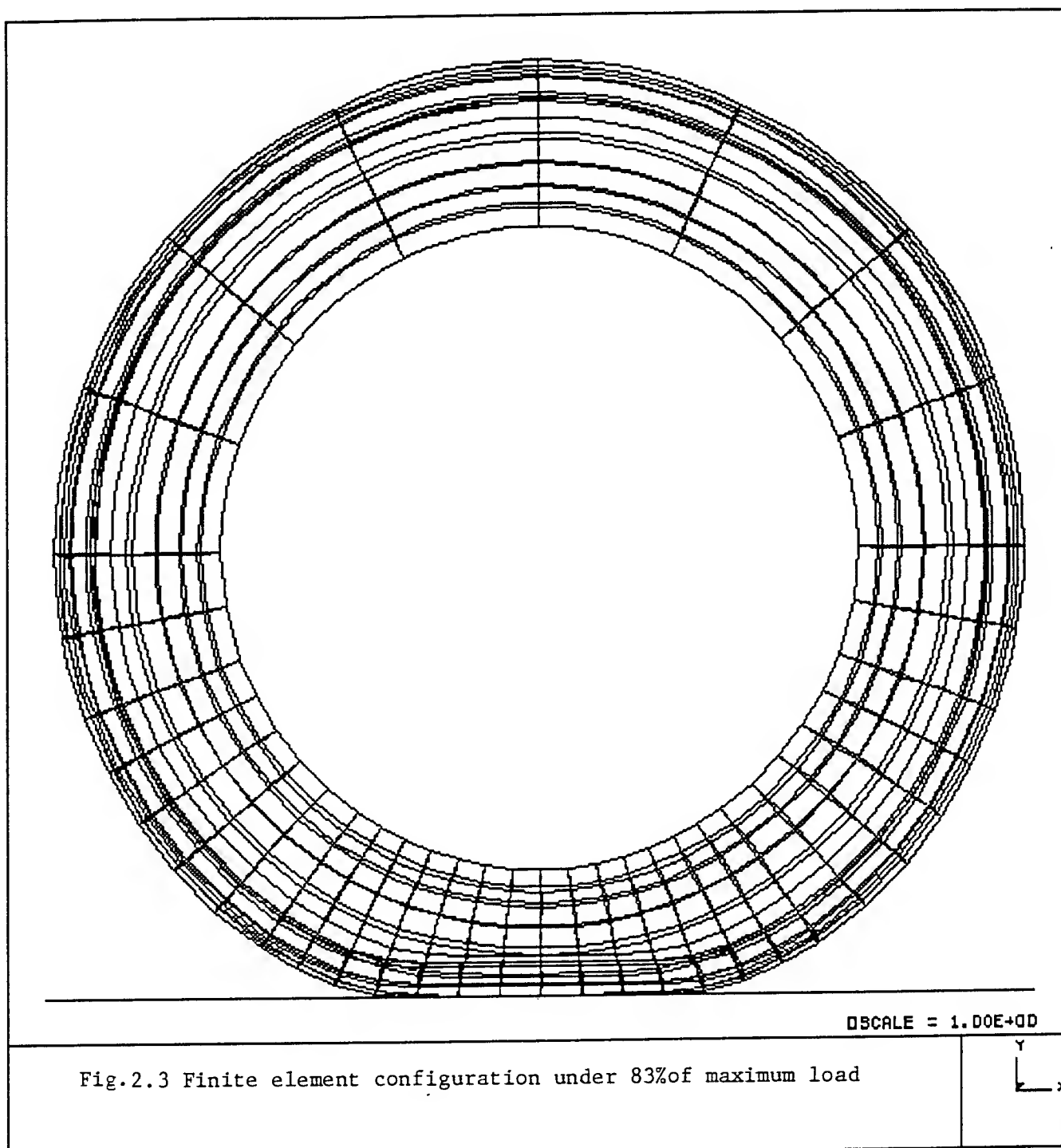




DSCALE = 1.00E+00

Fig. 2.2 F-16 finite element mesh showing "I" variation





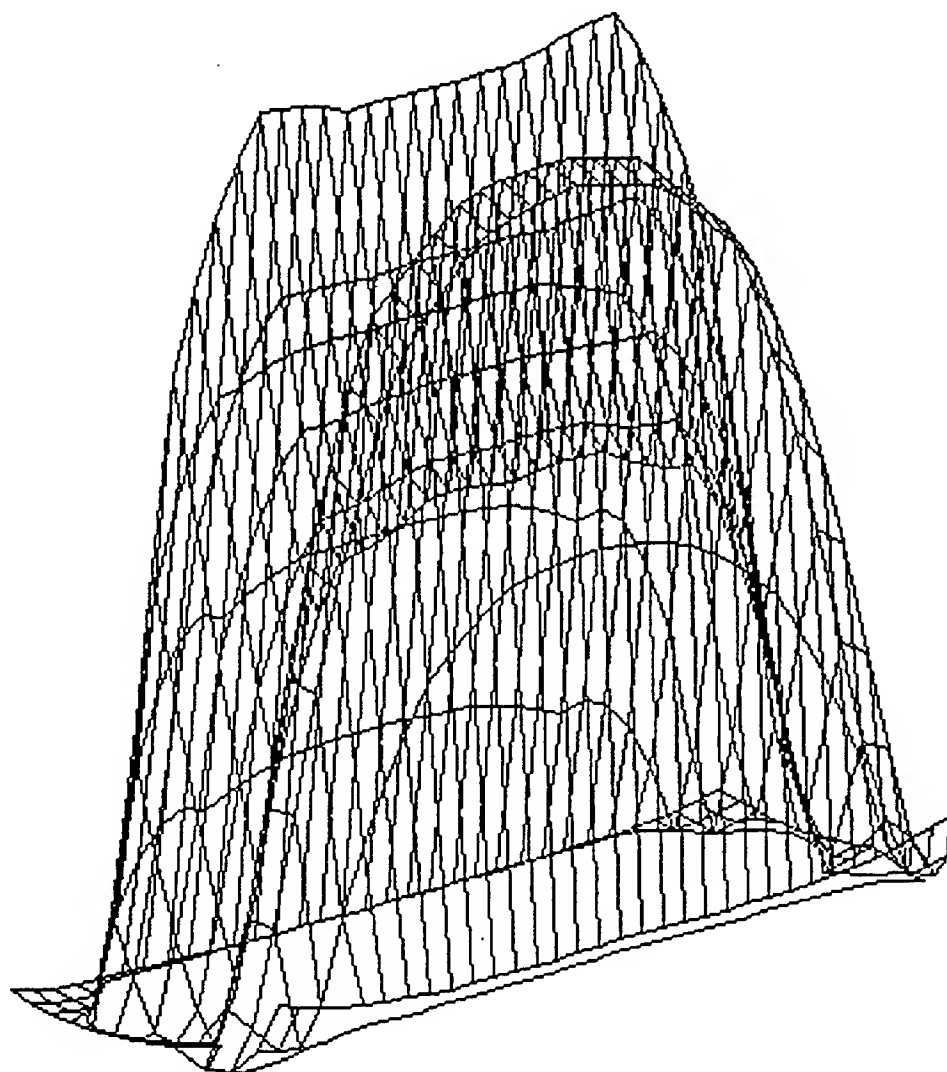
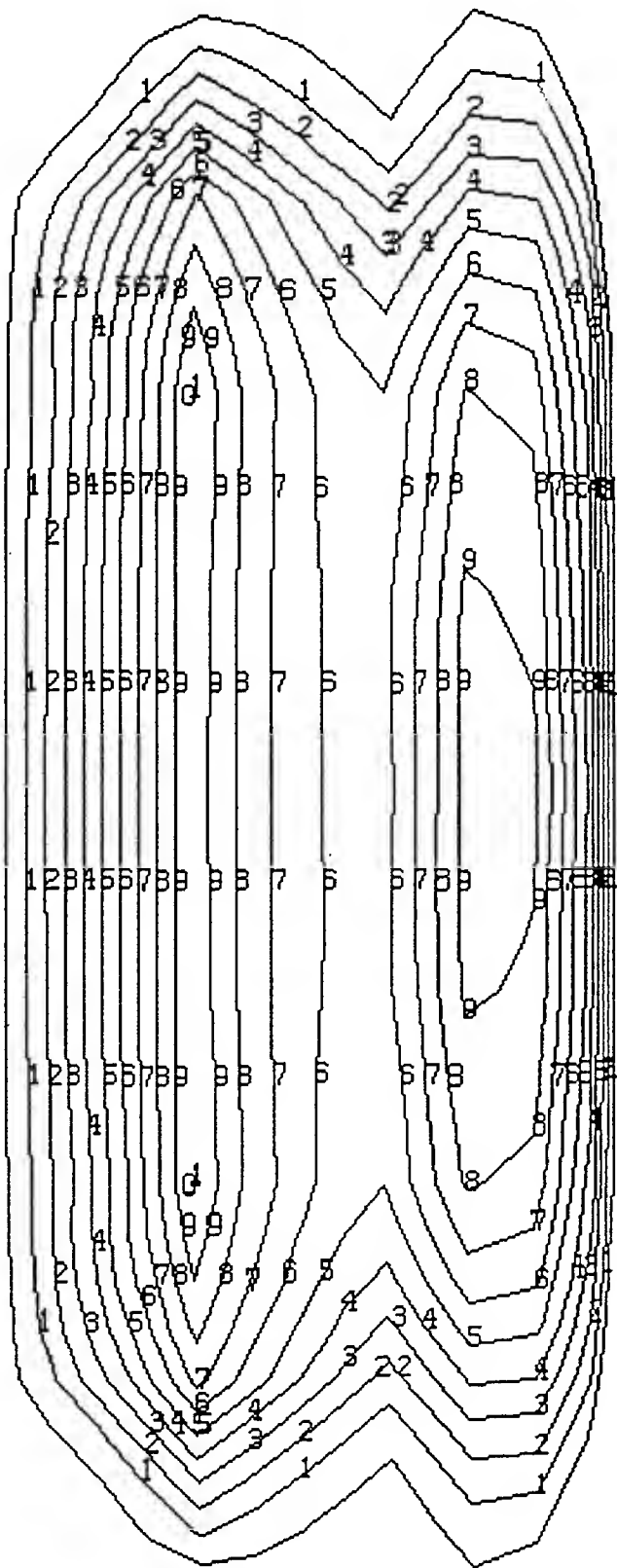


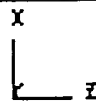
Fig.2.4 3-Ddistribution of normal pressure on the contact patch





PRESSURE CONTOURS MAX(10) = 955.0 MIN(1) = 50.5 (INTERVL = 95.3)

Fig.2.5 Pressure isobars on the  
contact patch





the interface is influenced by tangential tractions (shear stresses). Then a difference between the tangential strains produced between these two bodies  $B_1$  and  $B_2$  in the contact area leads to small apparent slip.

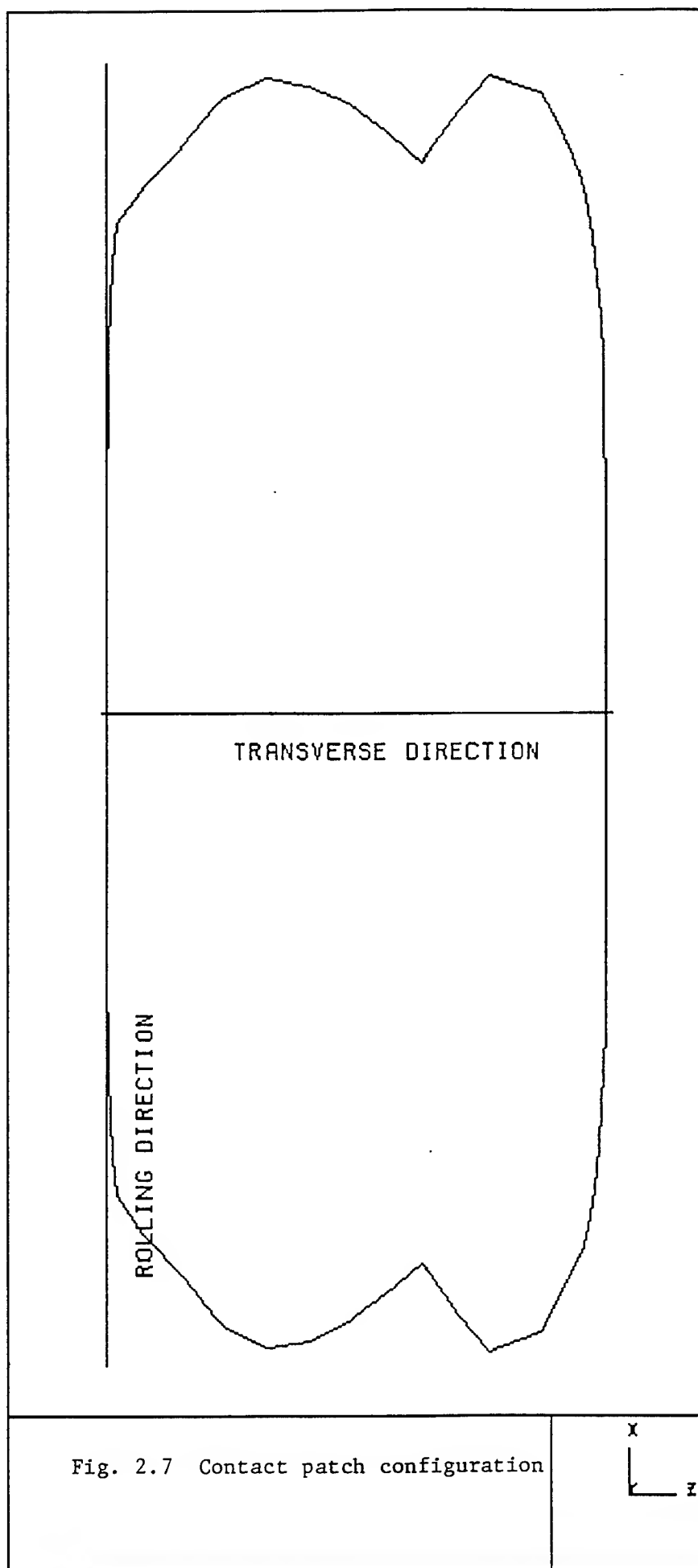
If the body  $B_1$  slips fully on  $B_2$  without rotating about its own axis, then  $B_1$  is said to slide on  $B_2$  which is also called locked-wheel skidding. It usually occurs at high speeds on dry surfaces when brakes are applied. This produces a noticeable wear of the tread along the portion of the circumference. Sliding also occurs on wet surfaces at high speeds when a tire is separated from the pavement by a film of water. This phenomenon is called hydroplaning.

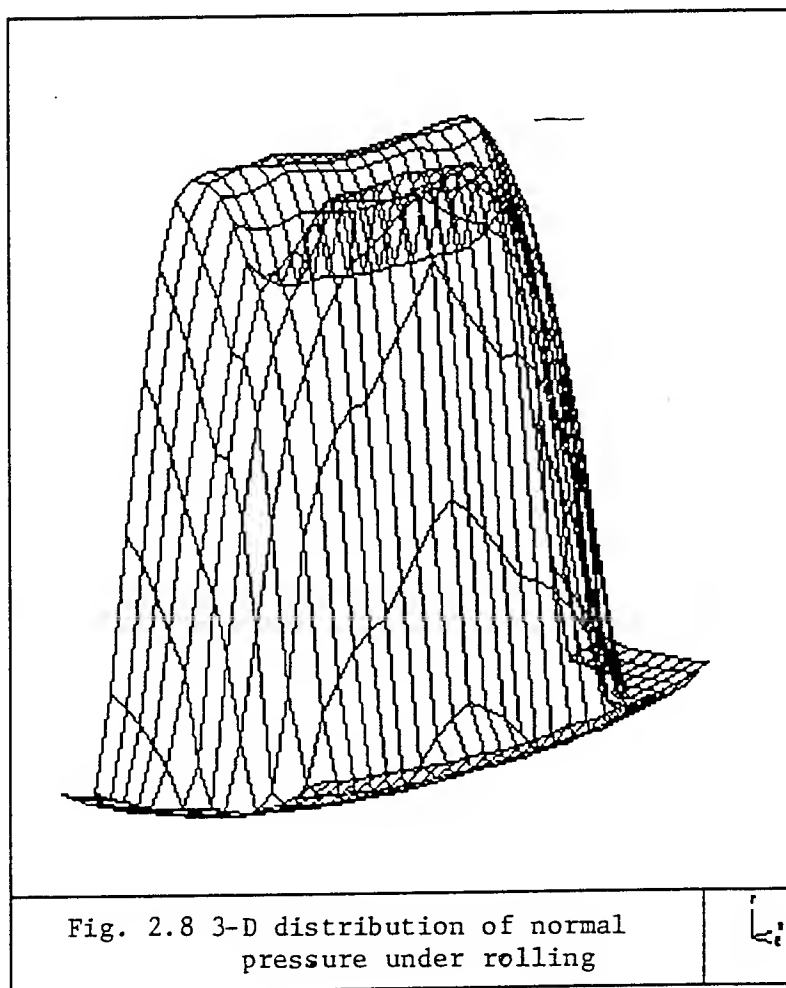
In order to model free rolling of the F-16 tire, the following parameters were chosen, at an inflation pressure of 310 psi:

Load	= 8100 lbs. (50% of the rated load)
Translational velocity	= 12 mph
Coefficient of friction	= 0.1

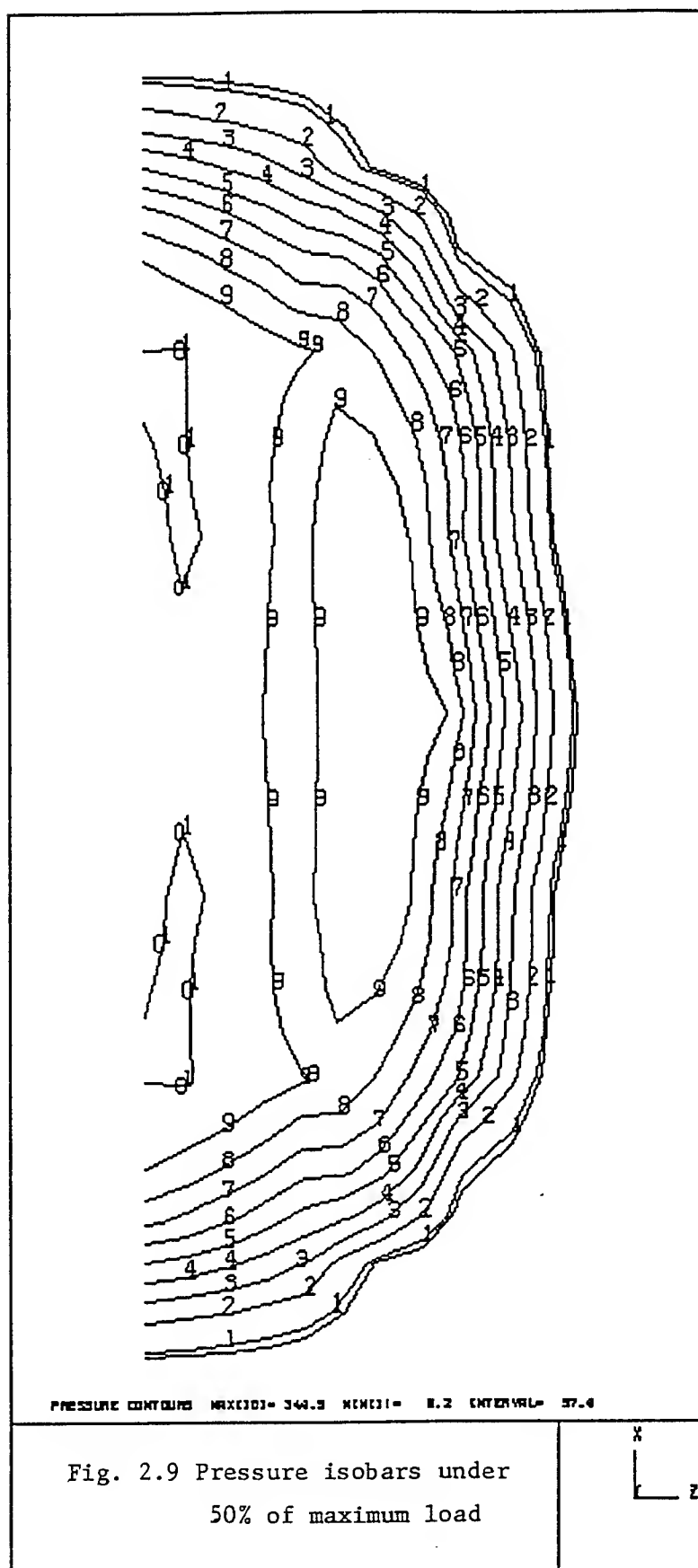
TIRE3D was then used to obtain graphic plots of:

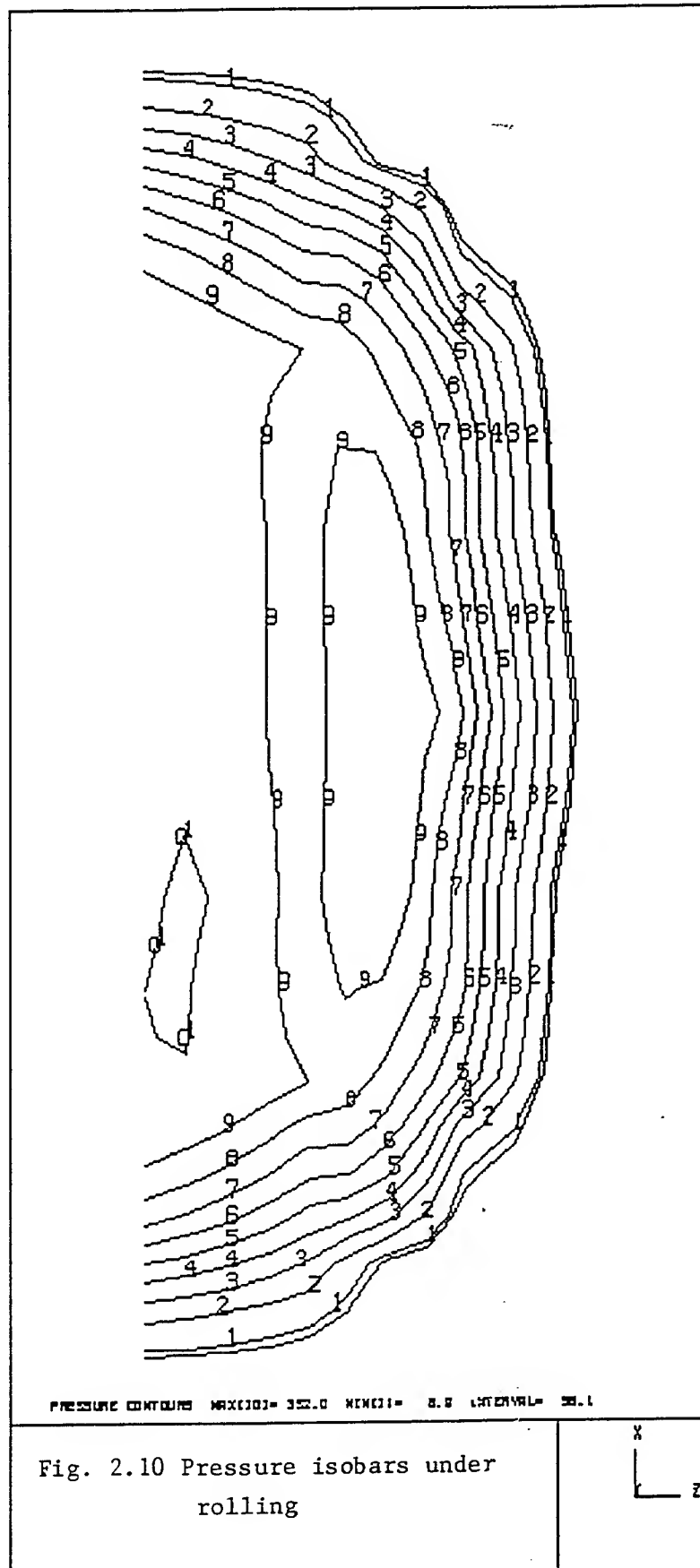
- i. Contact patch configuration (Fig. 2.7)
- ii. Pressure distribution under loading (Fig. 2.8)
- iii. Pressure isobars under loading (Fig. 2.9)
- v. Pressure isobars under rolling (Fig. 2.10)











## 2.3 Mechanics of free rolling

### 2.3.1 Rolling resistance

Experimental results have shown that within the front half of the contact patch forward shear force is developed whereas within the rear half of the contact patch larger rearward shear force is created. The difference between these horizontal forces ( $F_x$ ) gives the net longitudinal force,  $F_r$ , which acts in the direction opposite to the travel.

For a free rolling tire the force,  $F_r$  is mainly due to friction and the coefficient of rolling resistance is given as:

$$f = F_r/W \quad (2.1)$$

where  $W$  is the load reaction.

Due to the unsymmetric pressure distribution in the contact patch the load reaction,  $W$  does not coincide with the vertical line passing through wheel centre of the contact patch but it occurs at an offset distance ' $a$ ', ahead of the centre of the contact. The resultant of the two forces ( $F_r$  and  $W$ ) is given as  $\sqrt{W^2 + F_r^2}$ , which passes through wheel centre ' $O$ ', so that no net torque acts on the tire (Fig. 2.11). Taking balance of moments for a steady state free rolling condition:

$$F_r.H = W.a$$

Hence, the coefficient of rolling friction for free rolling can also be expressed as  $a/H$ ,

$$f = F_r/W = a/H \quad (2.2)$$

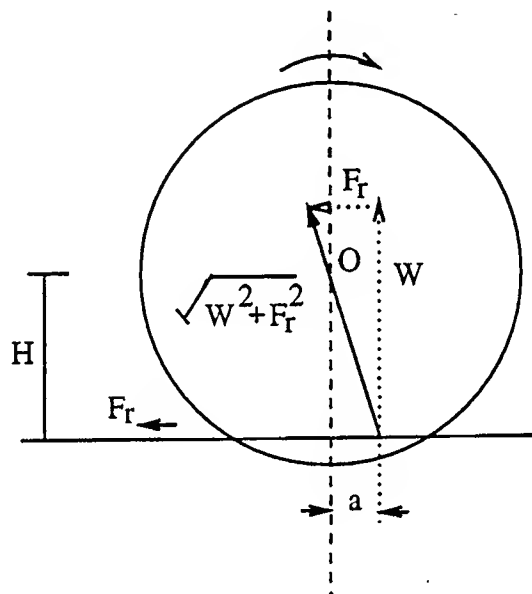


Fig. 2.11 Free body of a free rolling wheel

where,

H = axle-to-ground height and

a = offset distance.

For the F-16 tire rolling under the above mentioned conditions,

$$a = 0.0089 \text{ in.}$$

$$f = 0.00071$$

This rolling resistance coefficient was found to vary with the speed and the load. The TIRE3D program is endowed with the property of calculating the components of this rolling resistance at every load step once the coefficient of friction is declared. The program calculates the frictional force at every point using local normal pressure and area surrounding that point. Finally these forces are added to get an overall frictional force, the components of which are printed as frictional force components at every load step in the output.

### 2.3.2. Effective rolling radius

When a rigid wheel of radius R rolls freely the relation between travel velocity 'V' and angular velocity 'W' is given as:

$$V = \omega * R \quad (2.3)$$

When a non-rigid loaded pneumatic tire rolls on stationary ground, flattening of tire occurs in the contact patch. This means the radius of any point on the tire circumference changes whenever it enters and leaves the contact patch. This continuous change in the radius produces slip in the contact patch because of which

tangential forces are developed in the longitudinal direction between tire and the road.

When this tire rolls freely through one revolution, it travels a distance less than that given by  $2\pi$  times the undeflected radius,  $R$ . This is equivalent to stating that the effective rolling radius,  $R_e$  is less than undeflected or undistorted radius,  $R$ .

Hence the forward velocity of a free rolling tire is given as:

$$V = \omega * R_e \quad (2.4)$$

Also  $R_e > H$

where,  $H$  is axle to the ground height (Fig. 2.12)

Hence  $R > R_e > H$

### 2.3.3 Determination of effective rolling radius

The effective rolling radius ' $R_e$ ' can be determined by performing various laboratory tests like Drumtests or by movable platform (Hadekal, 1952). The relation between effective radius  $R_e$  and free (undeflected) radius  $R$  can be analytically found as follows.

The term "equator" is used to denote the line of highest points on the tire or the line of points passing through wheel central plane. A parallel is a circle on the tire surface in a plane parallel to that of the equator. The term meridian line is used to denote a line normal to the equator and its parallels.

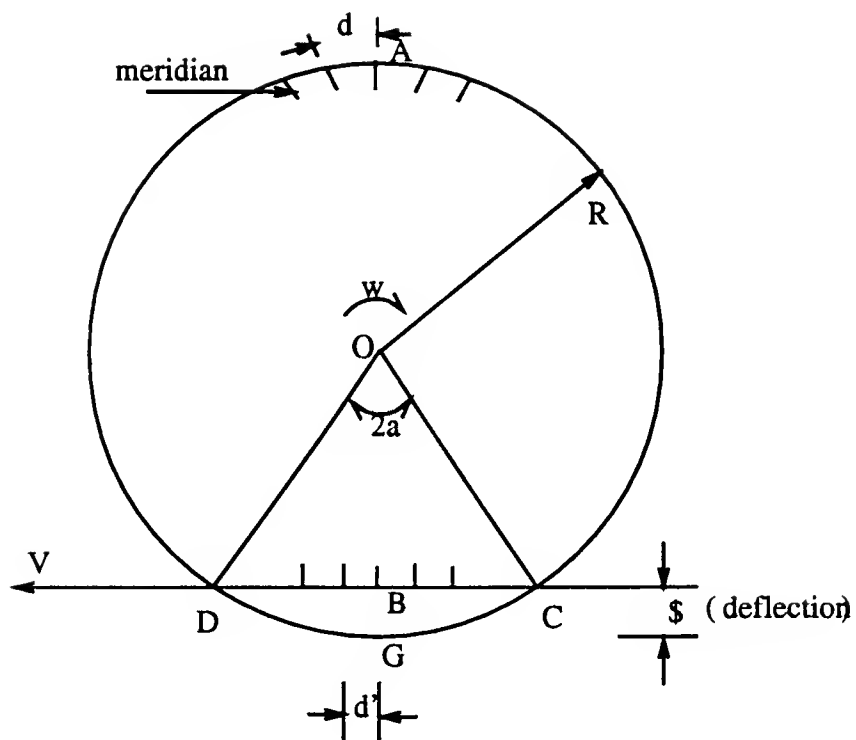


Fig. 2.12 Deformation of a pneumatic tire

Assume that a number of equi-distant meridian lines are drawn on the tire surface (Fig. 2.13).

Fig. 2.13 shows the deformation of the tire at the road surface. Let 'A' be the top most point on the undeflected tire surface, 'B' the bottom most point in the contact patch,  $2\alpha$  the angle subtended by the contact patch with the tire centre 'O', 'd' the distance between two adjoining meridians near A measured circumferentially, and 'd'' the distance between two adjoining meridians near B.

The number of meridians passing through point A in any given time is same as that passing through point B. The velocity of any point 'F' on the undeflected surface is  $\omega R$ .

Then,

$$\omega R/d = V/d' \quad (2.5)$$

i.e.  $R \cdot d'/d = V/\omega$

Since  $V/\omega = R_e$  (2.6)

$$R_e = R(d'/d) \quad (2.7)$$

The tire is subjected to a strain 'e' in the contact patch as it experiences deformation in this area. Hence the strain 'e' is given as :

$$e = (d-d')/d$$

$$d' = d - d(e)$$

$$d' = d(1 - e)$$



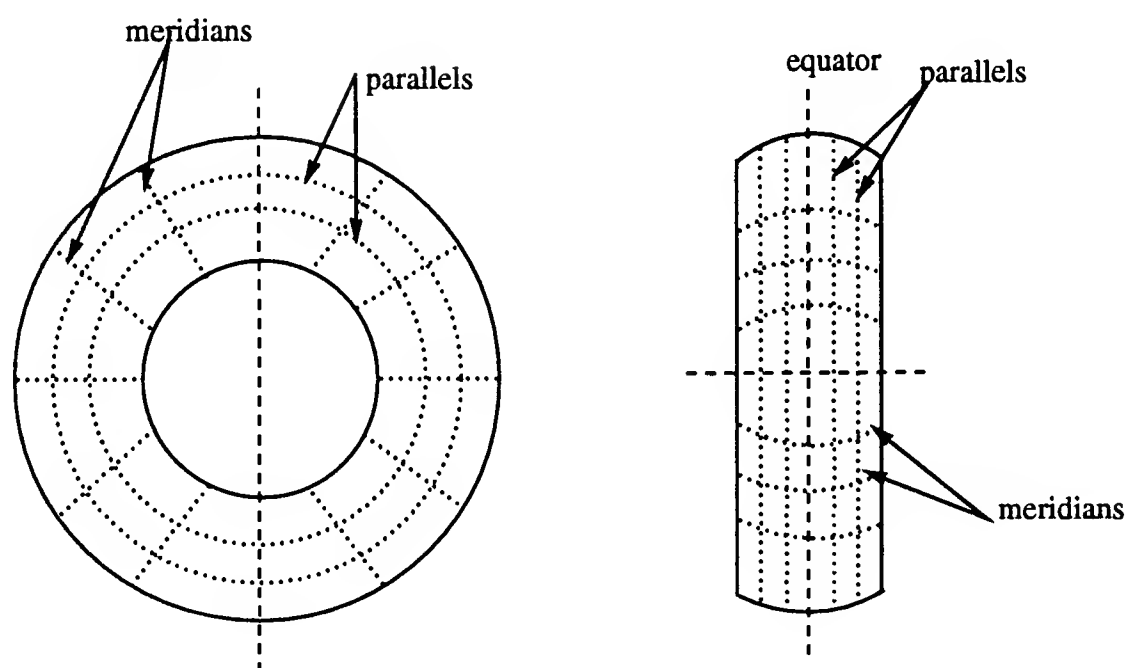


Figure 2.13 Configuration of meridians and parallels

Substituting this relation in (2.7),

$$\begin{aligned} R_e &= R\{d(1 - e)\}/d \\ R_e &= R(1 - e) \end{aligned} \quad (2.8)$$

The strain 'e' in the contact patch can also be defined as:

$$\begin{aligned} e &= ( \text{arc CGD} - \text{chord CBD} ) / \text{arc CGD} \\ 1 - e &= \text{chord CBD} / \text{arc CGD} \end{aligned}$$

for small angles of  $\alpha$ ,

$$\text{chord CBD} / \text{arc CGD} = \sin \alpha / \alpha$$

expanding sine function and dividing by  $\alpha$ , we get,

$$\text{chord CBD} / \text{arc CGD} = 1 - (\alpha^2/6) \quad (2.9)$$

Also the deflection,  $\delta = R - R \cos(\alpha)$

$$\delta = R(1 - \cos \alpha)$$

expanding cosine function,

$$\delta = R (\alpha^2/2)$$

$$\text{i.e.} \quad \delta/R = \alpha^2/2$$

substituting the above relation in the Eqn. (2.9) we get,

$$\text{chord CBD} / \text{arc CGD} = 1 - (\delta/R)/3$$

$$\text{i.e.} \quad 1 - e = 1 - \delta/3R \quad (2.10)$$

substituting the above relation in the Eqn. (2.8) we get,

$$R_e = R\{ 1 - \delta/(3R) \}$$

Hence

$$R_e = R - \delta/3 \quad (2.11)$$

However, experimental results have shown that the above expression is fair for only low speeds (less than 30mph) and an increase in  $R_e$  is detected for high speeds.

#### 2.3.4 Effect of speed on rolling radius

Experimental data have shown that there is a definite increase in rolling radius with increase in speed of order 4% from 0 to 85mph. The effect is more marked at lower pressures i.e. for high deflections (Hadekal, 1952).

The Dunlop rubber Co. proposed an equation for the modification of  $R_e$  at any velocity  $V$  (Hadekal, 1952) which is given as:

$$R_e'/R_e = ((V^2 - 900)/2000) + 1 \quad (2.12)$$

But this expression is applicable only over a limited range of  $V$  since the rate of increase of radius diminish at very high speeds. The main factors involved in the change of effective rolling radius with speed are:

- 1) pressure rise (and hence decrease in deflection) due to heating of tire.
- 2) centrifugal growth.

Whenever a body rolls, the centrifugal force will act radially

away from the centre. With the increase in the speed, this force increases and tries to pull the body thereby increasing the rolling radius. If we assume that the centrifugal growth is proportional to speed, it is true that after a particular speed the centrifugal growth is more than  $\delta/3$ . Then effective rolling radius  $R_e$  is greater than the free rolling radius  $R$ .

Experiment results have shown that the value  $\delta/3$  in the relation  $R_e = R - \delta/3$  is of magnitude  $0.05R$  at the static deflection for a typical aircraft tire. For aircrafts which have a take off speeds between 350mph to 450mph and landing speeds of 70% of the above speeds respectively, the value  $\delta/3$  is negligible and the expression  $R_e = R - \delta/3$  is inapplicable at these high speeds. Hence taking effective rolling radius  $R_e$  equal to free radius  $R$  is more viable for aircrafts moving at high speeds.

## CHAPTER 3

## BRAKING AND CORNERING KINEMATICS OF F-16 TIRE

## 3.1 Modeling of braking

In order to model braking of the F-16 tire, the following parameters were chosen, at an inflation pressure of 310 psi:

Load	= 8100 lbs. (50% of the rated load)
Translational velocity	= 12 mph
Coefficient of friction	= 0.1
Brake torque	= 700 lb.in.

TIRE3D was then used to obtain graphic plots of:

- i. Pressure distribution under braking (Fig. 3.1)
- ii. Pressure isobars under braking (Fig. 3.2)

## 3.2 Mechanics of braking

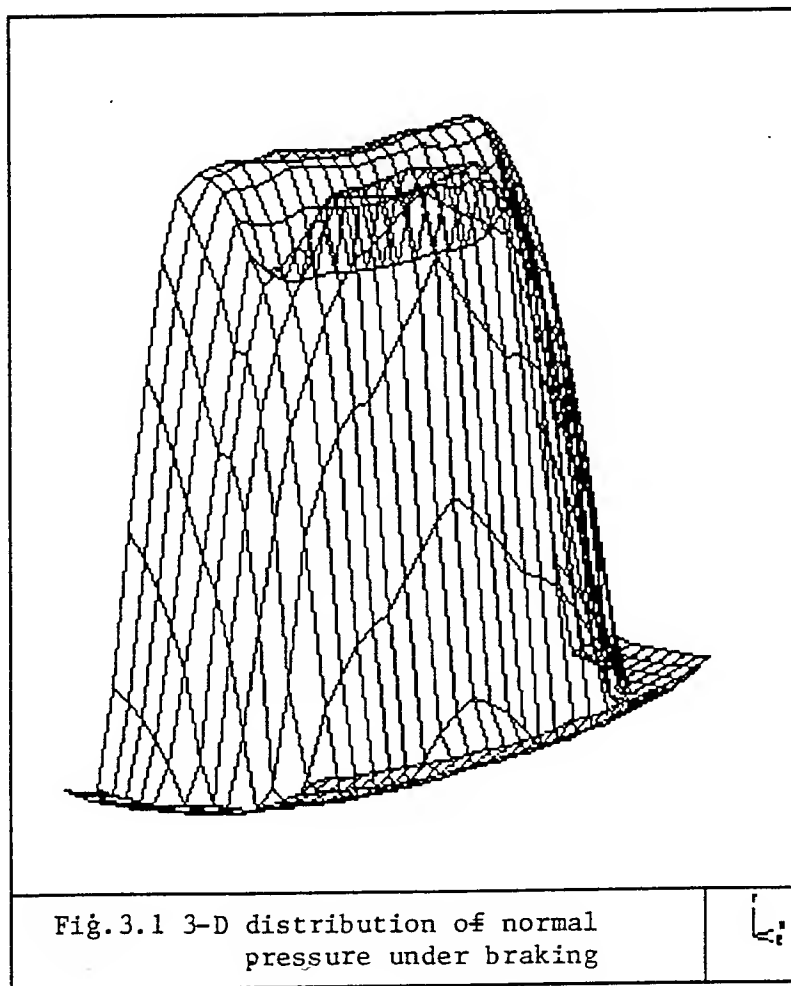
If a braking torque is applied to a wheel moving at a constant velocity, the velocity of the tire decreases and there is an increase of rolling resistance,  $F_r$ , to a greater braking force,  $F_b$ . Because of this, the deformation of the tread and sidewalls is much severe and greater distortion is produced in the tire carcass.

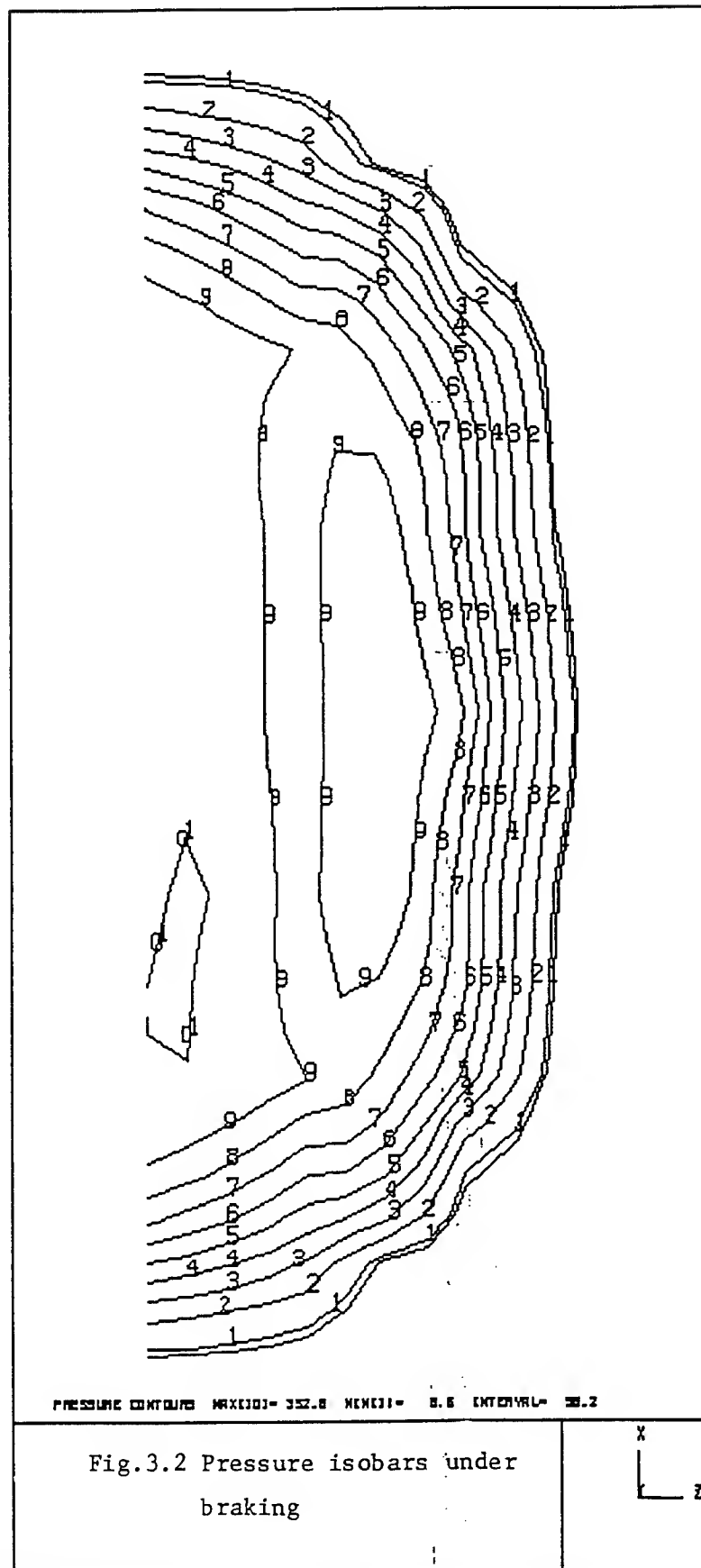
For the above mentioned F-16 tire parameters;

$$F^r = 2.884 \text{ lbs.}$$

$$F^b = 55.989 \text{ lbs.}$$

In the free-body diagram shown in Fig. 3.3, taking moments





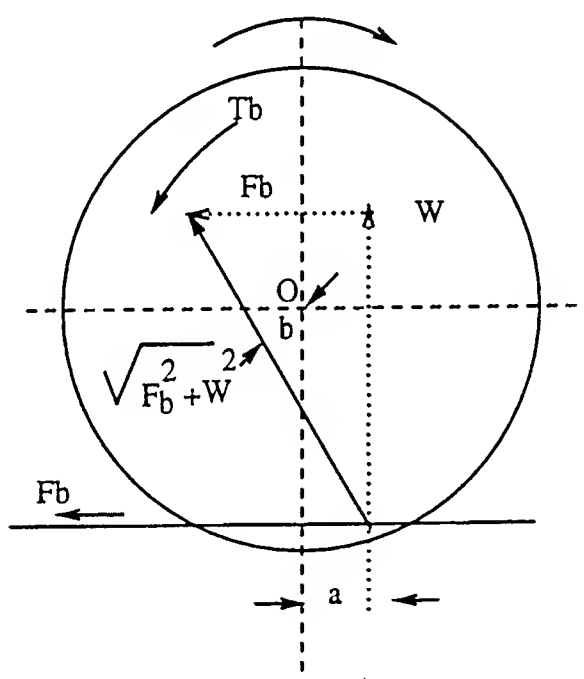


Fig.3.3 Free body of a braked tire



about tire centre 'O',

$$T_b + W * a = F_b * h \quad (3.1)$$

For the F-16 tire at the above mentioned conditions, the offset distance  $a$  was equal to 0.0008 in.

### 3.2.1 Brake slip ratio

The severity of braking is generally measured by brake slip ratio  $S_b$  which is expressed as follows:

$$S_b = (\omega_{fr} - \omega_{br}) / \omega_{fr} \quad (3.2)$$

where  $\omega_{fr}$  = angular velocity in the free rolling

$\omega_{br}$  = angular velocity in the braked rolling

both these values are measured at constant forward velocity.

for free rolling	$\omega_{br} = \omega_{fr}$	thus $S_b = 0$
for locked wheel braking	$\omega_{br} = 0$	thus $S_b = 1$

The ratio of  $F_b$  and load reaction  $W$  is called braking force coefficient ( $f_b$ ). The relationship between braking force coefficient and Brake slip ratio is given in Fig. 3.4.

For the F-16 tire with the above parameters  $S_b=0.7\%$  and  $f_b = 0.0138$ .

The following observations are made from Fig. 3.4:

1. The maximum braking force coefficient,  $f_{bmax}$  is obtained for the value of  $S_b$  in the range of 0.10 to 0.30.

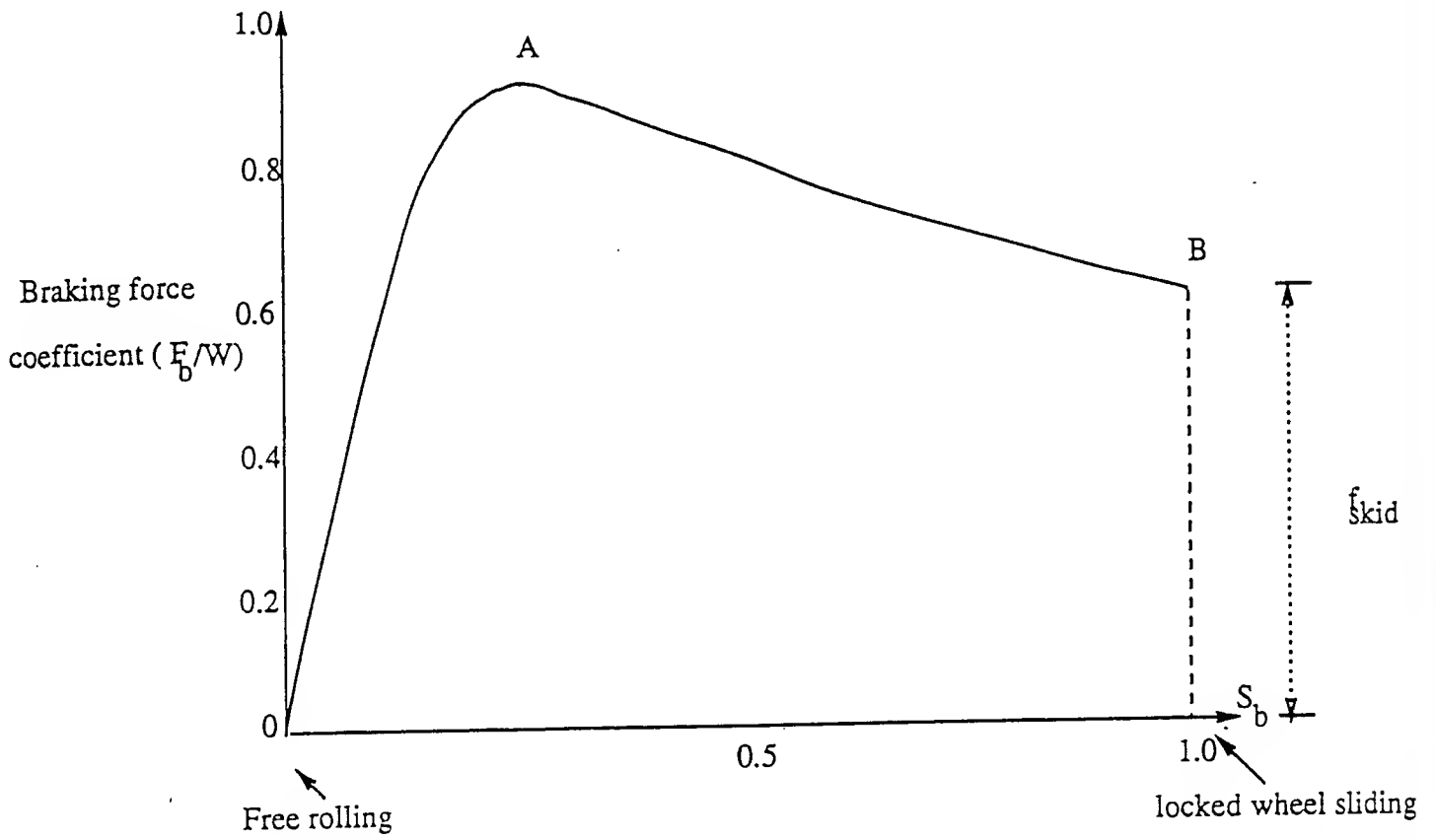


Figure 3.4 Typical brake force Vs. brake slip ratio curve

2. The braking force coefficient at  $S_b = 1.0$  can be represented as  $f_{skid}$ . At  $S_b = 1.0$ , the tire slides as a rigid body with no rotation and hence  $f_{skid} = \mu$ . Using TIRE3D this condition can be directly simulated by not specifying the torque in rolling. Under these conditions  $f_b$  was found to be equal to  $\mu$ .

3) The speed of travel and texture of road surface effects the shape of the curve.

The brake slip ratio can also be expressed in terms of effective rolling radius as follows:

The effective rolling radius  $R_e = V/\omega$

Hence,

$$\omega_{fr} = V / R_{e(fr)}$$

$$\omega_{br} = V / R_{e(br)}$$

Substituting the values in Eqn. (3.2), one obtains

$$S_b = (R_{e(br)} - R_{e(fr)}) / R_{e(br)} \quad (3.3)$$

where

$R_{e(fr)}$  = effective rolling radius in free rolling

$R_{e(br)}$  = effective rolling radius in braked rolling

Since the angular velocity in braking is less than that in free rolling, it is imperative that effective rolling radius in braked rolling is greater than that in free rolling. This is true because the tread elements of a braked wheel are subjected to elongation when ever they enter the contact patch, Thus the effective rolling radius is increased, accounting for slip.

### 3.3 Mechanics of cornering

The Principal Investigator studied Livingston's (1991) solutions for a cornering tire as follows:

The force developed is given by;

$$f = 0.5nwk l^2 \tan \alpha \quad (3.4)$$

where       $w$       =      width of the tire  
               $n$       =      net fraction of the tread on the footprint  
               $\alpha$       =      slip angle (Fig. 3.5)  
               $k$       =      lateral stiffness (Fig. 3.6)  
 and         $l$       =      length of footprint

The wear slip energy was expressed by;

(3.5)

$$W = r \gamma F s \sin \alpha$$

When cornering of tires is to be modeled, obviously the symmetry of the tire cross-section cannot be exploited. In such cases, since the entire cross-section of the tire had to be modeled by finite elements vastly increasing the processing time. Thus, this task could not be accomplished within the computer time allocation.

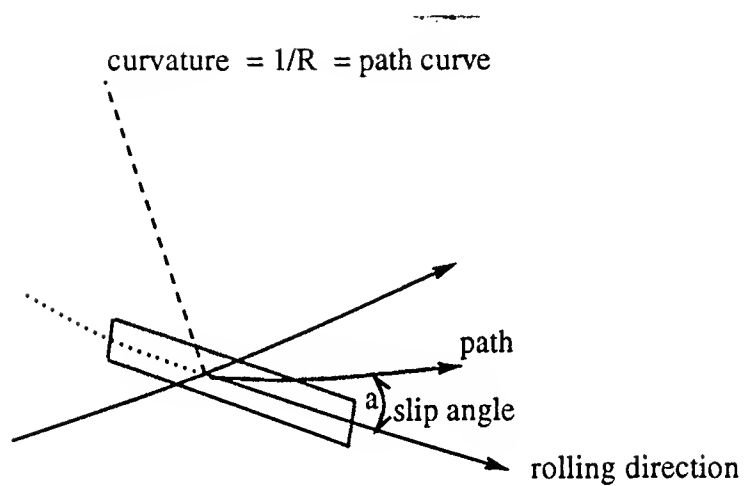


Fig. 3.5 Configuration of slip angle and path of cornering tire

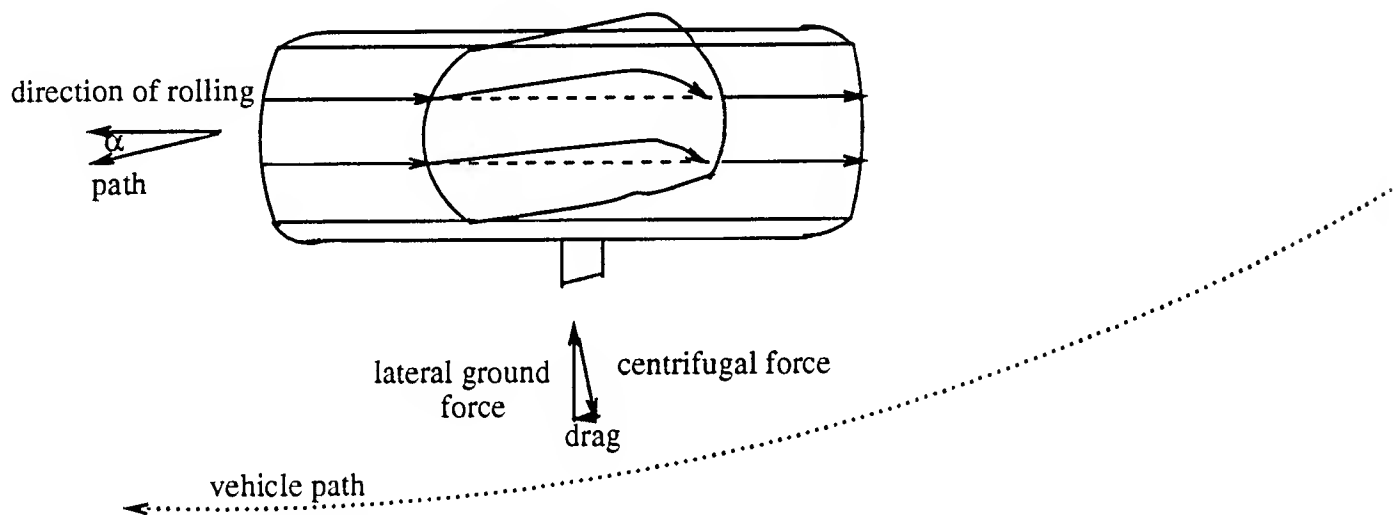


Fig 3.6 Lateral slip of a cornering tire

## CHAPTER 4

## PREDICTION OF WEAR SLIP ENERGY

Recent research has shown that maneuvers contributing mostly to aircraft tire wear are 1) braked rolling, 2) cornering and 3) spinup associated with aircraft landing. It has been revealed from NASA wear tests that footprint energy is a good indicator of wear. This is supported by the widely observed fact that energy dissipation and wear are considerably higher for a braking torque compared to a driving torque of equal magnitude. For cornering on the otherhand, it is the lateral forces that produce the frictional work.

## 4.1 Numerical prediction of slip velocities

During his summer research, the Principal Investigator used the following formulation due to Faria et. al (1989) to determine the particle slip velocity  $V$  on the contact patch. According to this, the motion of a particle is separated into three components, which are

- 1) translational component equal to the tire center velocity ( $V_{oi}$ ),  
It should noted that in the TIRE3D program, this is input as a reversed foundation velocity.
- 2) rigid body rotations introduced by spinning angular velocity ( $\omega$ ) and cornering angular velocity ( $\Omega$ ).
- 3) deformation  $u$  due to the contact constraint.

Since the theoretical procedure is elaborated in the summer research report (Gunaratne, 1991), only the final expressions for the three particle velocity components are reproduced below.

$$V_1 = v_{o1} + (\partial u_1 / \partial Y_1 + 1) \cdot [\Omega Y_3 \cos \gamma - (\omega + \Omega \sin \gamma) Y_2] \\ + \partial u_1 / \partial Y_2 \cdot (\omega + \Omega \sin \gamma) Y_1 - \partial u_1 / \partial Y_3 \cdot \Omega Y_1 \cos \gamma + V_{o1} \quad (4.1)$$

$$V_2 = v_{o2} + \partial u_2 / \partial Y_1 \cdot [\Omega Y_3 \cos \gamma - (\omega + \Omega \sin \gamma) Y_2] \\ + (\partial u_2 / \partial Y_2 + 1) \cdot (\omega + \Omega \sin \gamma) Y_1 - \partial u_2 / \partial Y_3 \cdot \Omega Y_1 \cos \gamma + V_{o2} \quad (4.2)$$

$$V_3 = v_{o3} + \partial u_3 / \partial Y_1 \cdot [\Omega Y_3 \cos \gamma - (\omega + \Omega \sin \gamma) Y_2] \\ + \partial u_3 / \partial Y_2 \cdot (\omega + \Omega \sin \gamma) Y_1 - (\partial u_3 / \partial Y_3 + 1) \cdot \Omega Y_1 \cos \gamma + V_{o3} \quad (4.3)$$

where  $\gamma$  is the camber

It is neccessary to determine the nodal displacement gradients to estimate nodal velocities from Eqns. (4.1) to (4.3). However, most finite element programs such as TIRE3D provide only the displacements at the element nodes. Hence, the principal investigator employed the following numerical approximations to compute the nodal displacement gradients.

Determination of  $\partial u_i / \partial Y_1$



For the lagging area,

$$\partial u_i / \partial y_1(I) = [-3 u(I) + 4u(I+1) - u(I+2)] / 2h \quad (4.4)$$

For the leading area,

$$\partial u_i / \partial y_1(I+2) = [u(I) - 4u(I+1) + 3 u(I+2)] / 2h \quad (4.5)$$

For inner nodes,

$$\partial u_i / \partial y_1(I) = [u(I-2) - 4u(I-1) + 4u(I+1) - u(I+2)] / 2h \quad (4.6)$$

where I is the loop direction coordinate used in the TIRE3D and h is the distance interval in the direction 1 (Fig. 4.1).

Determination of  $\partial u_i / \partial y_2$

For the entire region,

$$\partial u_i / \partial y_2(K) = [-3 u(K) + 4u(K-2) - u(K-3)] / 2k \quad (4.7)$$

where K is the radial direction coordinate used in the TIRE3D and k is the distance interval in the direction 2 (Fig. 4.1).

When a tire rolls on a foundation that has a velocity of its own of  $V_{fi}$ , the slip velocity  $V_{si}$  at a point on the tire contact patch is given by,

$$V_{si} = V_i - V_{fi} \quad (4.8)$$

In the TIRE3D program, the translational velocity is introduced only by a reverse foundation velocity, although  $V_{oi}$  of

DATA

12.56  
5  
0.35  
1.092  
14.4  
37 1 4  
36 1 4  
35 1 4  
34 1 4  
33 1 4  
32 1 4  
31 1 4  
30 1 4  
29 1 4  
28 5 4  
27 5 4  
26 5 4  
25 5 4  
24 5 4  
23 5 4  
22 5 4  
21 5 4  
20 5 4  
19 5 4  
18 5 4  
17 5 4  
16 5 4  
15 5 4  
14 5 4  
13 5 4  
12 5 4  
11 5 4  
10 5 4  
9 5 4  
8 5 4  
7 5 4  
6 5 4  
5 5 4  
4 5 4  
3 5 4  
2 5 4  
1 5 4

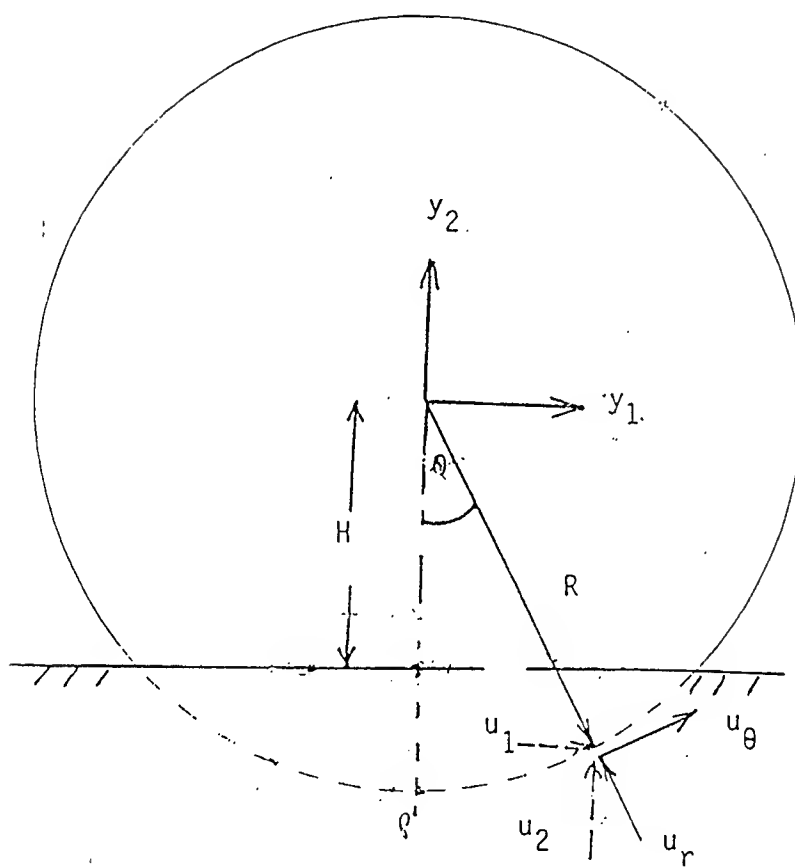


Fig. 4.1 Dynamics of longitudinal sliding

Eqns. (4.1) -(4.3) are set zero,  $V_{fi}$  term in Eqn. (4.8) is set to  $-V_{oi}$ . Then, one realizes that the slip velocities  $V_{si}$  are given by the same Eqns. (4.1)-(4.3). Thus, Eqns. (4.1)-(4.7) are utilized in the program SLIP in Appendix C.

#### 4.2 Results of SLIP program

The field of slip velocities on the contact patch during rolling and braking are given respectively by Figs. 4.2 and 4.3. Figs. 4.4 and 4.5 show the shear stress distribution on the contact patch which is used to compute the wear slip energy.

From the above results,

Wear slip energy during rolling at 12 mph = 2765.2 lb.in./s.

Wear slip energy during braking at 12 mph = 2853.0 lb.in./s.

#### 4.3 Role of abrasability

The following basic relationship for wear (W) has been theoretically demonstrated by Schallamach (1960) by assuming a uniform contact pressure distribution.

$$W = r \gamma (F.s) \quad (4.9)$$

where  $\gamma$  is the abrasability and  $r$  is the resilience or fraction of energy available after hysteretic dissipation.  $F$  and  $s$  denote the force (braking, accelerating or cornering) and the wheel slip respectively. The frictional work ( $F.s$ ) however depends on the vehicle characteristics, tire construction and the aircraft maneuvers.

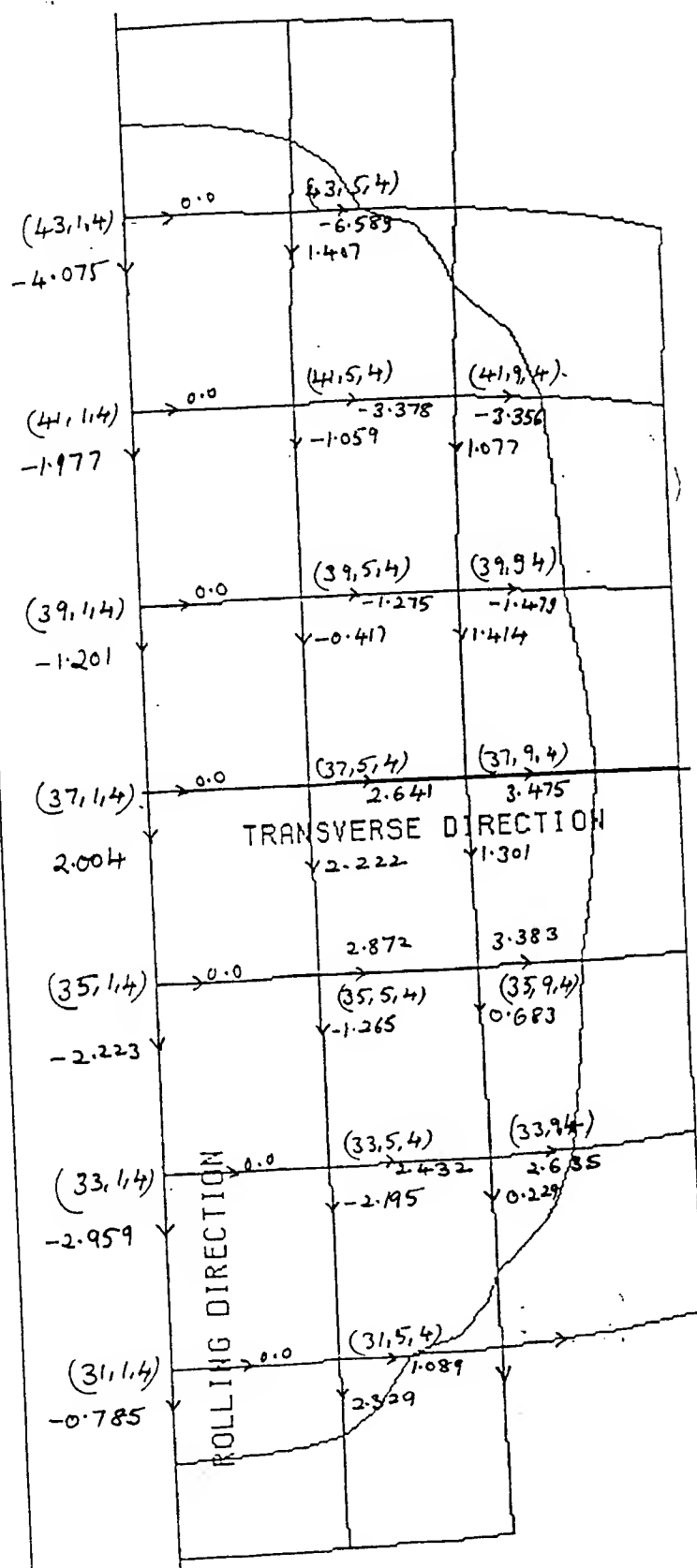


Fig. 4.2 Slip velocities on the contact patch on rolling

X  
Y

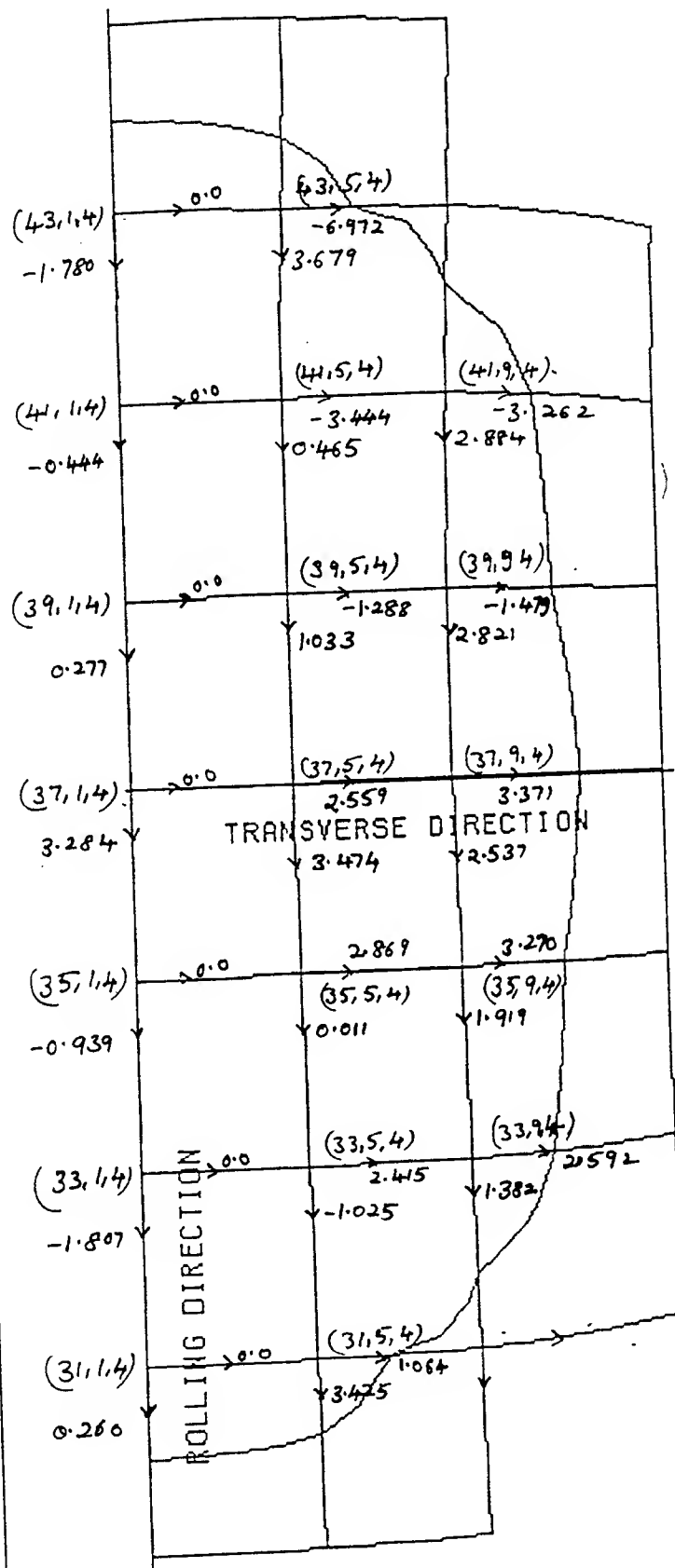


Fig. 4.3 Slip velocities on the contact  
Contact patch on braking

X  
Z



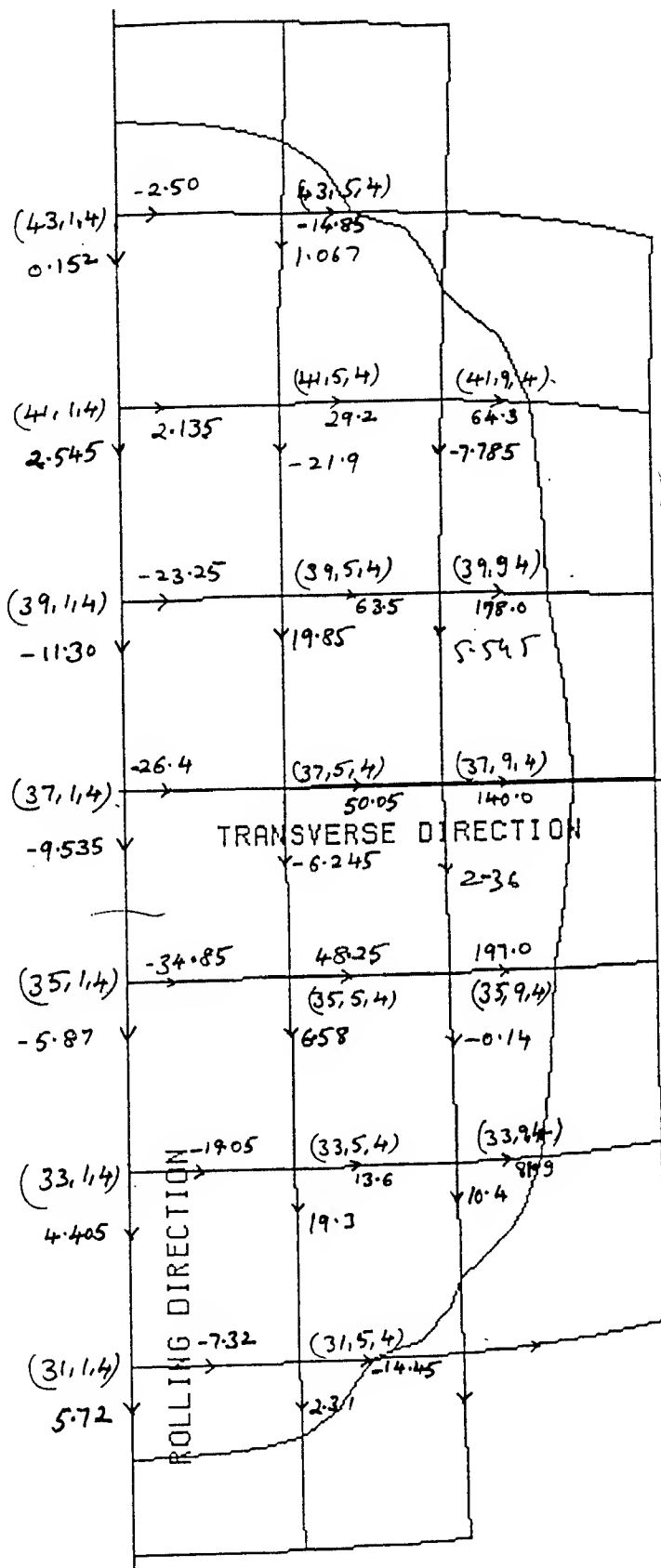
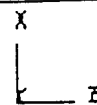


Fig. 4.5 Shear stresses on the contact patch on braking





Eqn. (4.9) shows that abrasability ( $\gamma$ ) is the wear per unit frictional work. Since the wear slip energy estimated in the present work obviously is indicative of the frictional work, one can see the use of Eqn. (4.9) in the prediction of wear from wear slip energy. Veith (1982) demonstrates that the relative tread wear resistances of natural rubber (NR) and synthetic rubbers (SBR, BR) depend upon the tire temperatures, seasonal changes and the pavement texture. All of the above observations demonstrate the dependence of  $\gamma$  on the tread composition, tread temperature and pavement texture.

Literature (Nevada Automotive Center, 1975) indicates that most wear research done in the recent past has been directed either at quantifying  $\gamma$  or determining the wear slip energy (F.s) even though most researchers have failed to clearly define any of them. In the above work, they linearly correlated the wear slip energy to measured volumetric wear.

Recently, Livingston (1991) mathematically simulated tire wear based on the work of Schallamach and Gough. Although he obtained closed-form solutions for the slip energy (F.s) by using a simplistic block-spring model of the tire (Eqn. 3.5), a finite element solution is advocated in his work for better accuracy. As for the determination of  $\gamma$ , Livingston (1991) attempts an experimental regression procedure. The results are obtained for wear of different tread compounds on a standard test course thereby

averting the application of  $\gamma$  values to other pavement conditions.

Unlike in other hard, brittle or ductile material, even the contact mechanics and the wear of rubber is governed by the visco-elastic behavior of rubber. Four major types of tire wear have been distinguished (Moore, 1975): 1) fatigue, hysteresis or "normal" wear (observed in automobile tires over a prolonged period of usage), 2) ablative or "catastrophic" wear (observed in aircraft tires rendering a tire useless within a limited number of flights), and less importantly, 3) cohesive tearing, and 4) tread reversion and blistering.

Of these, ablative wear of polymers has been very inadequately studied. Researchers have had no general consistent concepts of the nature of ablative wear. Only applied studies have been conducted by various methods under different conditions (Bartenev and Lavrentev, 1981). Ablative wear produces severe degradation of the rubber surface consequent to the release of excessive slip energy. Maneuvers involving high tractions and slip velocities, macro-roughness in the pavement or elevated temperatures may all contribute to ablative wear. Majority of past tests have been done at lower tire pressures and speeds and thus the results are insufficient to make any predictions regarding most new aircraft such as NASP, RASV etc.. As a result of this, at present, there is no theory of abrasive wear of polymers. Hence, there is an urgent need for analytical models to predict ablative wear.

## CHAPTER 5

## MANUAL FOR MODELING AIRCRAFT TIRES ON WPAFB COMPUTER SYSTEM

## 5.1 Modeling tire mechanics using TIRE-3D

The following sequence of steps can be followed by any beginner wishing to model an aircraft tire.

1. A finite element grid is prepared for the cross-section of the tire about its radial axis ( $r$ ). For straight rolling and braking, only half of the section is modeled because the tire is symmetric about its radial axis (Figure 2.1).

2. For each element, the co-ordinates in meridional direction ( $J$ ) and radial or thickness direction ( $K$ ) are defined. In the present case, the liner elements which are modeled as 16-node shell elements have co-ordinate " $K$ " between 1 and 2 and the tread elements which are modeled as 20-node brick elements have co-ordinates between 2 and 4 respectively.

3. The hoop direction  $I$  is fixed at 1 for all the elements in the cross-section which is to be rotated to generate the entire tire (Fig.2.2).

4. The command CSFACE is used to define the tire cross-section. For F-16, tire a quadratic interpolation function is assumed between key points (these are corner points whose co-ordinates are

defined). Hence, co-ordinates for two additional points, 5 and 7 are defined apart from four key points for every element. For the format of this command see section 5.2.3 of USER'S manual.

5. The command HOOP is used to rotate the cross-section in the hoop direction (I). With this command the number of elements in hoop direction and the angle subtended by each element is declared. For F-16 tire a total of 36 elements are defined in the hoop direction to model a full tire and hence the sum of all angles is  $360^\circ$  (Figure 2.2).

6. As the cord angle changes along the cross section of the tire, the entire cross section is divided into small sections and cord angle for each section is determined using the following relation.

$$r/r_0 = \cos\theta/\cos\theta_0 \quad (5.1)$$

where

$r_0$  = radial distance from axis of revolution to crown

$r$  = vertical distance between tire centre and midpoint of the given part.

$\theta_0$  = cord angle at the crown or crown angle

$\theta$  = cord angle in the given part.

For F-16 tire, the entire cross-section is divided into 7 sections and cord angle for each section is found using the above equation.

7. The plies in each section are modeled as orthotropic materials.

Every section of the liner is assumed to be made of 4 plies arranged in 'ABBA' fashion (Gunaratne,1991). The thickness of each ply was found to be 0.125 inches. For further details see section 5.12 of USER'S manual.

8. The tread elements are modeled as 20 node brick elements and liner elements are modeled as 16 node shell elements. While tread elements are considered to be exhibiting Mooney-Rivlin elasticity, the liner has to be modeled as isotropic elastic material. This is a deficiency of the current TIRE-3D version.

9. Once the properties of plies and co-ordinates of various elements in the cross-section and number of elements in hoop direction are defined, the command FUNCTION is used to define loading function. See section 6 of USER'S manual for further details.

10. The command BC is used to read the applied boundary conditions. The commands defining boundary displacements, symmetry conditions, inflation pressure, normal load and applied torque are defined with corresponding functions. For example:

For free rolling

ROLLING,VELTRAVL=-210,LOAD3

FRICTION,MU=0.1,REGPAR=10.0,,TORQUE=0.0

Braked rolling

ROLLING,VELTRAVL=-210,LOAD3

FRICTION,MU=0.1,REGPAR=10.0,,TORQUE=-2000,LOAD3

In case of driving, applied torque should be a positive value. For further details see section 7.0 of USER'S manual.

11. SOLVE command is used to initiate the solution process and POST command to process the data and to store the output suitable for graphics. See Section 8 and Section 9 of USER'S manual for further details. A typical data file prepared for F-16 tire is given in Appendix A.

#### 5.1.1 Execution of the program

1. If a data file (ex: A.dat) is submitted to tire-3D program. Four additional files called A.out, A.cpr, A.plot and A.tapel2 are created.

(i) A.out gives the summary output for inflation pressure, normal force, vertical height of the tire centre above the ground, components of twisting moments and frictional force, spinning velocity and components of traveling and cornering velocities at every step.

(ii) A.cpr is a backup file which gives processing details of data

file. This file also includes description of any errors.

(iii) A.plot stores raw data to generate plots using a separate graphics program. Such a program is given in Appendix B

(iv A.tape12 is a binary file which contains input and solution data

2. In order to restart a file the ".tape12" file of the main data file should be copied to the ".tape12" file of restart file. This is necessary because the ".tape12" file of the main data file contains the entire processing details upto that point of the solution process. For example, if Ares.dat is a restart data file to be submitted for the continuation of the solution process, then A.tape12 should be copied to Ares.tape12 before restarting is done.

3. As tire-3D program is not accessible to all users, an executable file (ex: 'testjob') is used to run a data file. Then the command 'qsub testjob' should be used to submit a data file to tire-3d program. Before this command is executed, the name of the data file to be processed, its ".cpr" file and time allotted to process the job should be declared in the executable file. A typical executable file is enclosed in Appendix A for reference

4. A restart file can also be executed in the same manner but necessary changes described in the previous step should be made in

the executable file before the command 'qsub testjob' is executed.

5. To check the status of the job, the command 'qstat -a' is used. Letter 'Q' indicates the job is still in queue whereas 'R' indicates the job is being executed.

6. To delete a job in queue, the command 'qdel' followed by the PID number should be given.

7. To delete a job having a status 'R', the command 'qdel -k' followed by the corresponding PID number should be used.

## 5.2 Prediction of slip velocity and wear slip energy

The slip velocity ( $V_1$ ) in the rolling direction and in the transverse direction ( $V_3$ ) can be predicted from Eqns. (4.1) and (4.2). A "C" computer program to compute  $V_1$  and  $V_3$  at various nodes in the tire contact patch is enclosed in Appendix C. Figures 4.2 and 4.3 shows the slip velocities at different nodes for free rolling and braking respectively. Once the slip velocities of different nodes are obtained, the rate of production of wear slip energy can be obtained as follows:

$$W = \sum_{1}^n (V_1 * \tau^{xy} + V_3 * \tau^{yz}) * A' \quad (5.2)$$

where

n=total number of nodes in the contact patch

A'= influence area of each node.



For example, consider Element No.200 of F-16 tire whose corner nodes [(37,1,4),( 39,1,4),(37,5,4),(39,5,4)] are in the contact patch (Fig.4.2).

### 5.2.1 Contact area of the element

$$\begin{aligned}\text{Element length} &= (\text{angle interval in hoop direction}/360) * 2\pi R \\ &= (5/360) * 2\pi * 12.75 = 1.11 \text{ inches.}\end{aligned}$$

$$\text{Element width} = 1.0 \text{ inches ( from Fig. 2.1)}$$

$$\text{Thus, Area, of element} = 1.11 * 1.0 = 1.11 \text{ sq. inches.}$$

The shear stresses in Eqn. (5.2) are obtained from the output of the tire-3D by specifying the following option in the POST command.

" WRITE, STRESS, POINT=4, OPTION=4, JPLANE=1"

### 5.2.2 Execution of the slip program

The following data files should be opened.

a) DISP1 - contains nodal displacements after inflation for various nodes in the contact patch

b) DISP2 - contains nodal displacements after rolling or driving or braking (i.e. at the load step where slip velocities to be found) for various nodes in the contact patch.

c) DATA - The following things should be given one below the other.

- i) vertical ht. of tire centre above the ground (H)
- ii) angle interval in the hoop direction ( $\theta$ )
- iii) thickness of the tread
- iv) angular velocity ( $\omega$ )
- v) travel velocity ( $V_{o1}$ )
- vi) Nodal points whose slip velocities to be calculated.

Note: The first point should be an innernode on the centre line of the tire.

The file 'DATA' is also enclosed along with the program in the Appendix C.

## CHAPTER 6

## EFFECT OF PAVEMENT TEXTURE ON TIRE-PAVEMENT FRICTION

## 6.1 Need for study of texture

Pavement texture should be sufficient to provide adequate skid-resistance and yet not too excessive in order not to cause mechanical and thermal tire degradation. On one hand, surface asperities cause friction producing slip energy which transforms into wear thermal energy. On the otherhand, it cause mechanical machining of tread rubber. Therefore, texture has to be well regulated on runways between these extremes for optimum performance.

Availability of skid resistance on highway pavements is assured by utilizing the ASTM E 274 Locked-Wheel-Trailer by various highway agencies in the U.S.. (TRB, 1986). Using this, the pavement Skid Number (SN) representing the frictional coefficient, is measured under wet conditions at a speed of 40 mph. Since wet friction on pavements is strongly speed dependent, a SN-speed ( $V$ ) gradient is used to adjust the skid levels ( $SN_v$ ) to any traffic speed.

On the otherhand, there is currently no established way of using measured pavement friction to predict tire wear and thus facilitate wear resistant tire designs. Most theoretical and numerical approaches modeling tire wear merely assume a "suitable"

frictional coefficient. In the literature, the investigator found one reference (Padovan and Kazempour, 1991) where a theoretical asperity volume and asperity root temperature has been used to model the machining effect due to the pavement. Veith, (1986) also indicates one regression equation expressing the dependence of macrotexture and microtexture on wear.

$$W = -9.2 + 90(s_{50}) + 18T \quad (6.1)$$

where  $s_{50}$  is the wet cornering traction coefficient at 50 km/h for a smooth no tread pattern tire and  $T$  is the normalized macrotexture depth. Apart from the above, in most other wear work, pavements are classified as either "blunt" pavements or "harsh" pavements from the tread rubber perspective.

When proposing the present work, the Principal Investigator envisaged a future development where measured pavement roughness can serve as an input to estimating an appropriate frictional coefficient to be used in tire dynamic models. Needless to say that it will also provide more applicable parameters to models that incorporate the machining effect as well. Further, if runway pavement maintenance engineers can continuously identify all of the hazardous sections based on routine measurements, those with the greatest risk can be improved at time. Hence, the present work was expanded to cover this aspect.

Tire construction, pavement texture and moisture condition are the vital factors that define the magnitude of the runway pavement friction. The pavement moisture condition itself is governed to some extent by its texture. Fig. shows how the brake force coefficient varies with the type of pavements. Hence, it should be possible to define the frictional coefficient using the texture parameters!

Pavement texture is due to two distinct sources; (1) micro deviations from the planar surface smaller than 0.5 mm. that originate from the roughness of the aggregate, and (2) larger macro deviations resulting from the asperities of the aggregate/binder mix. While, the Sand-Patch method (FHWA, 1978) is the most widely used macrotexture (MD) measuring technique, the British Portable Skid-Tester (BPN) is believed to gauge the microtexture. A combination of both the above measurements in determining skid levels at any vehicle speed was amply demonstrated by Leu and Henry (1978) in Eqn. (6.2). This kind of an expression can be utilized in predicting the current state of a pavement under any speed.

Yet, it is impractical to measure the BPN and MD for all runway sections of a highway network! However, recent studies (FHWA, 1981) have evolved continuous and rapid techniques to measure the pavement texture. Since the final objective is to use

$$SN_v = (-31.0 + 1.38BPN) e^{-0.23 \cdot V(MD)^{-0.47}} \quad (6.2)$$

such advanced texture measuring techniques to predict the friction variation, theoretical investigation of the correlation of MD and BPN with pavement texture parameters is essential.

The majority of studies attempting to establish the dependence of skid measurements on pavement texture and moisture have been statistical correlations. FHWA (1981) mentions an attractive study where BPN was correlated to three average roughness parameters (1) asperity height (2) asperity density and (3) asperity shape factor measured using optical image analysis. The above research concludes that there is a significant correlation between BPN and the shape factor. The investigators believe that a tribological analysis of the mechanism of the British Portable Skid-Tester would shed more light into a combination of the above three parameters possibly along with other roughness parameters such as micro-roughness at asperity peaks and height distribution to yield a stronger correlation. If successfully established, this will enable one to use the fast and accurate roughness measuring techniques such as Optical image analysis (FHWA-107, 1981), Light depolarization (FHWA-108, 1981) to predict an equivalent BPN.

## 6.2 Tribological approach

When an elastomer like rubber moves in contact with a rough pavement, two elementary friction mechanisms both recognized to be viscoelastic phenomena are invoked as noted by Eqn. (6.3):

$$F = F_{\text{adhesion}} + F_{\text{hysteresis}} \quad (6.3)$$

Of these, the adhesion component of friction is due to the molecular bonding of exposed surface atoms in the pavement as well as the rubber followed by a stretch, break and relaxation cycle of events. Essentially the rubber molecules jump a molecular distance to their new equilibrium position during the above cycle. It is realized that adhesion diminishes with increasing pavement macrostructure. The existence of a lubricant like water also reduces the adhesion. Therefore, adhesion component of friction predominates under smooth and dry pavement conditions. The very same macrotexture that decreases adhesion facilitates surface drainage thereby increasing it under wet conditions ! Hence, one realizes that the issue of an optimum macrotexture arises for adhesion!

The hysteresis component on the otherhand is due to continuous draping of rubber over the pavement aggregate asperities. The pressure distribution about the asperity is seen in Fig. 6.1 under two conditions; 1) when no relative motion exists at the interface 2) in the presence of relative sliding. When there is no relative motion, the draping and hence the pressure distribution is symmetrical about the asperity giving rise to no net horizontal frictional force. As the sliding begins, rubber accumulates in the leading edge of the asperity as shown in Fig. 6.1 creating an asymmetrical pressure distribution producing a net friction force

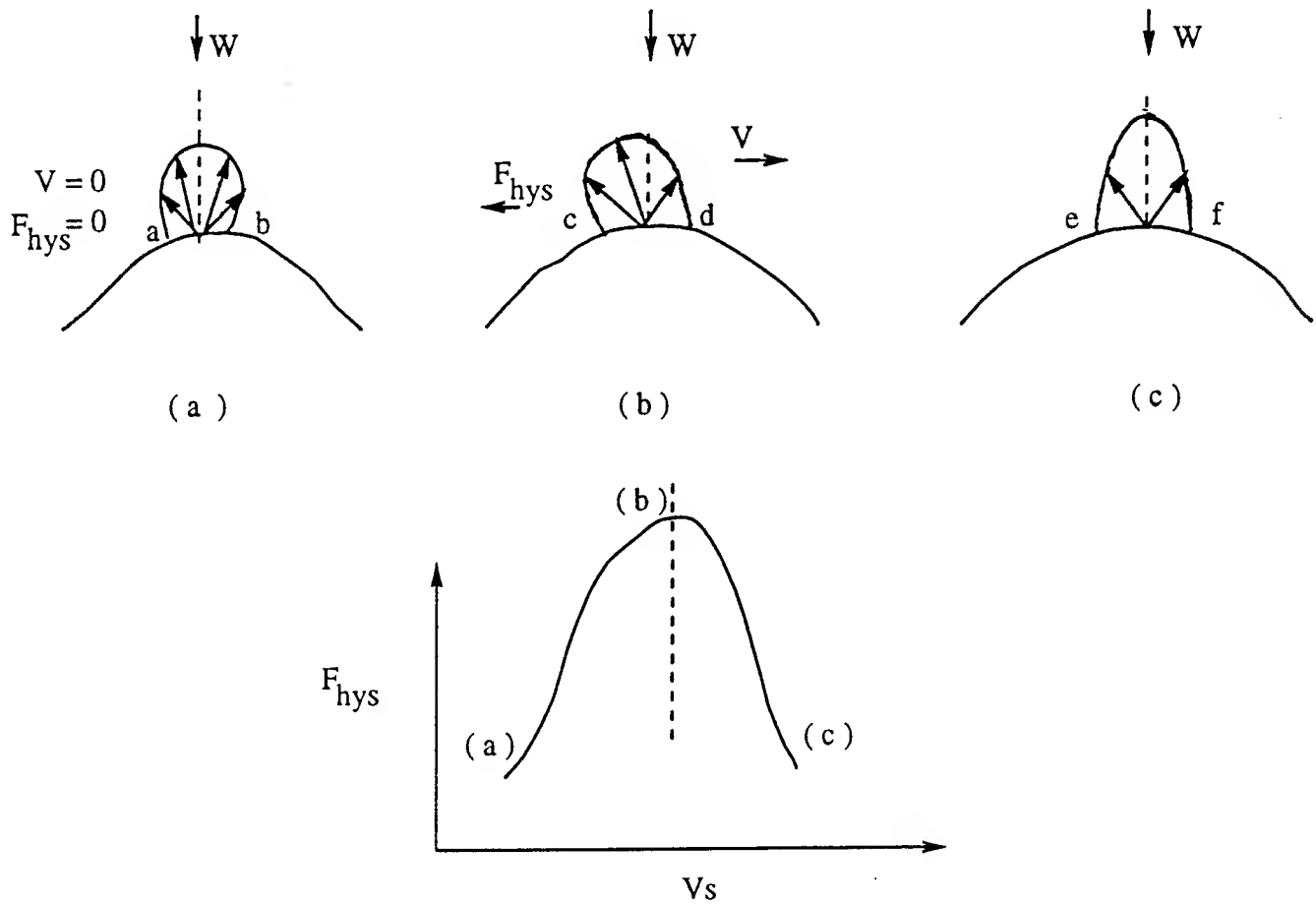


Fig. 6.1 Phenomenon of hysteresis



opposing the motion. At higher sliding speeds, the contact arc decreases and approaches symmetrical conditions, thereby reducing hysteresis under very high speeds of sliding. Hysteresis provides the bulk of friction in wet and rough pavements.

Microtexture  $\epsilon_{MR}$  on the otherhand penetrates water films to make the tire/pavement intimate contact needed for adhesion thus inceasing skid-resistance and eliminating the hydroplaning. An appropriate combination of both macro and micro texture is essential to pavement design. Thus, it can be concluded that the optimum pavement surface must have low tire wear and high wet friction.

The above variations in frictional characteristics due to pavement texture and moisture are generally overlooked for simplicity. This practice clearly precludes the incorporation of frictional changes due to pavement texture, moisture and even slipping. It is seen that the treatment of hydrodynamic and viscoelastic effects is imperative for an understanding of the actual friction-texture relationship.

Adhesion  $f_a$  and hysteresis  $f_h$  are expressed by the following expressions (Moore, 1975):

$$f_a = K_1 s [E \cdot p^{-r}] \tan \theta \quad (6.4)$$

$$f_h = K_2 \left[ \frac{p}{E} \right]^n \tan \theta \quad (6.5)$$

where  $s$  = shear strength of the sliding surface.  
 $p$  = normal pressure.  
 $E$  = modulus for the strain component in phase with the stress (represents energy stored).  
 $r$  = exponent value equal to 0.2  
 $n$  = index greater than 1.0  
 $\tan \theta$  = energy dissipated to the energy stored per cycle.

The extensively used viscoelastic stress-strain moduli relationship can be used to express  $\tan \theta$  as follows:

$$E^* = E + iE' \quad (6.6)$$

$$\tan \theta = \frac{E'}{E} \quad (6.7)$$

where  $E^*$  = Complex modulus  
 $E'$  = modulus for the strain component out-of-phase with the stress (represents energy dissipation).

Due to the variations of  $E$  and  $E'$  (and hence  $\tan \theta$ ) with the frequency ( $n$ ) of indentation shown in Fig. 6.2, the adhesive friction, hysteresis friction and the total friction varies as shown in Fig. 6.3 with the frequency,  $n$ .

Finally, when one recalls the following relationship between the sliding speed  $V$ , macrotexture usually indicated by the

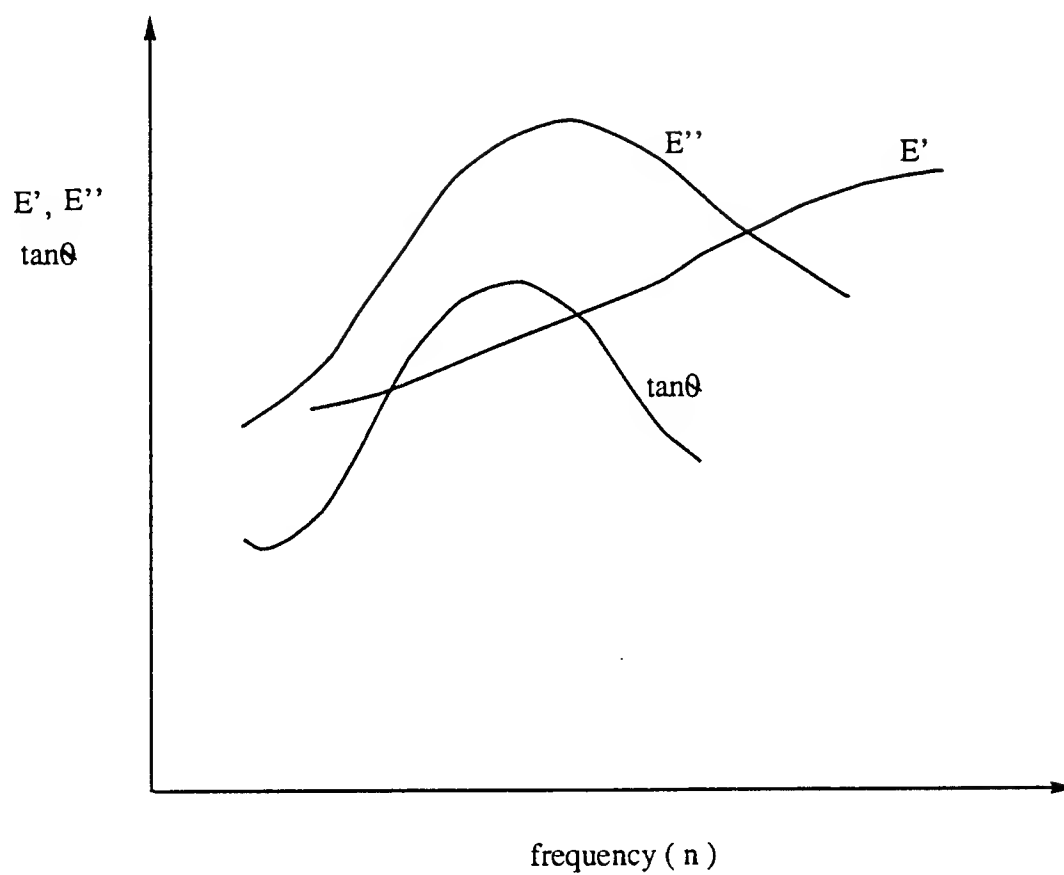


Fig.6.2 Variation of  $E'$  and  $E''$  with frequency

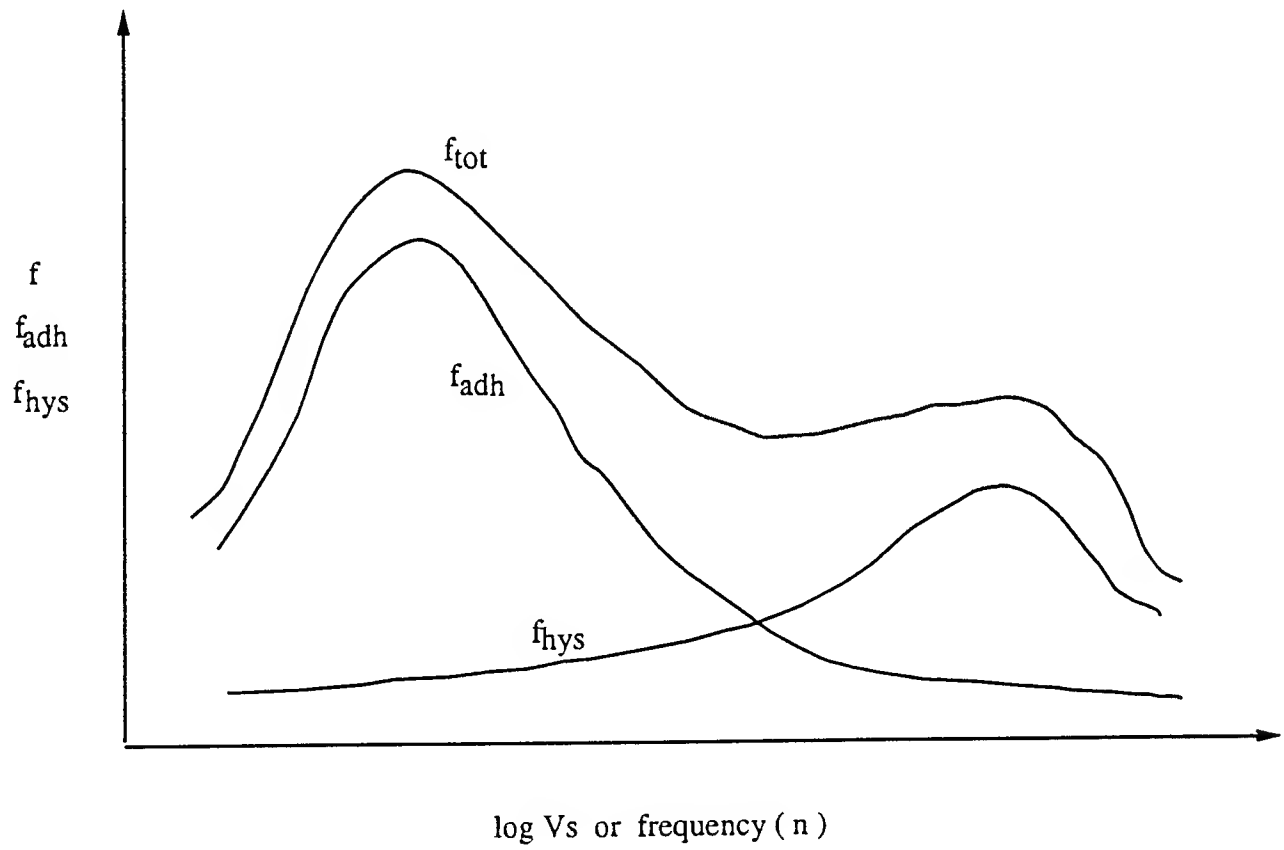


Fig. 6.3 Variation of frictional components with frequency

roughness profile wavelength  $\lambda$  and  $n$ ,

$$n = \frac{V}{\lambda} \quad (6.8)$$

one realizes how strongly the total pavement friction is related to the sliding velocity and the texture! Further, the hysteresis component of friction is augmented in the vicinity of a natural frequency of indentation  $\omega$  given by  $V/\lambda$ .

### 6.3 Future directions

The most recent thinking on texture parameter indicates that at least five distinct parameters are necessary to represent significant features of texture. They are 1) size 2) spacing 3) shape and 4) height distribution of macro-roughness as well as 5) micro-roughness. A tribological study should reveal the relationship between pavement friction and the texture well represented by the above parameters and the sliding velocity. Further, this kind of a study should shed light into ways of representing pavement friction in terms of regularly collected maintenance data.

## REFERENCES

Bartenev, G.M., and Lavrentev, V.V., "Friction and Wear of Polymers", Tribology Series, 6, Elsevier Scientific Publishing Company, New York, 1981.

Clark, S.K., " Mechanics of Pneumatic tires " US Dept of Transportation, National Highway Traffic Safety Administration, Washington D.C.

Faria, L.O., Bass, J.M., Oden, J.T., and Becker, E.B., "A three-dimensional rolling contact model for a reinforced rubber tire", Tire Science and Technology, Vol. 17, No. 3, July-Sep. 1989, pp. 217-233.

Gough, V.E., "Tire-to-ground contact stresses", Presentation to the Stress Analysis Group Conference on Contact Stresses, London, May, 1958.

Gunaratne, M., "Computational prediction of static and rolling response of an aircraft tire on a rigid surface as a prelude to wear studies", Research report submitted to Landing Gear System, Wright-Patterson AFB, Ohio, and Research and Development Laboratories, Culver City, California.

Hadekel, R. " The Mechanical prediction of pneumatic tires"

Technical Information Bureau for Chief Scientist, British Ministry of Supply, 1952.

Howell, W.E., Perez, S. E., and Vogler, W.A., "Aircraft tire footprint forces", the Tire Pavement Interface, ASTM STP 929, M.G. Potinger and T.J. Yager, Eds, Philadelphia, 1986, pp. 110-124.

Livingstone, D.I., "Concepts of tire wear", Clemson Tire Industry Presentation, Clemson, Oct. 1991.

Mooney, M., "A theory of large deformations", Journal of Applied Physics, Vol. 11, Sept. 1940.

Moore, D.F., "The friction of pneumatic tires", Elsevier Scientific Publishing Company, New York, 1975.

Nevada Automotive Test Center, "Tire treadwear validation", Executive Summary Report, Prepared for U.S. Dept. of Transportation, National Highway safety Administration, June 1974 - November 1975.

Padovan, J., Padovan, P., and Kazempour, A., "Spinup wear in aircraft tires", Research report F33615-90-C-3416, Submitted to the WPAFB, 1991.

Schallamach, A., and Turner, D.M., Wear 3, page 1, 1960.

Tielking, J.T., "A finite element tire model", Tire Science and Technology, Vol. 11, Nos. 1-4, Jan. - Dec. 1984, pp. 50-63.

Veith, A.G., "The wear of pneumatic tires, a review", Department of Mechanical Engineering, University of Akron, August 1982.

Veith, A.G., "The most complex tire-pavement interaction: tire wear", The Tire Pavement Interface, ASTM STP 929, M.G. Pottinger and T.J. Yager, Eds, Philadelphia, 1986, pp. 125-157.

Wagner, P.M., "Improved tire life", Proceedings of the Kick Off meeting, WPAFB, June 1991.



## APPENDIX A

```

$
$ F-16 aircraft tire cross section data - rolling tire
$
GEOMETRY
$
$Material properties
$
MOONEY,TREAD,32, 51, BULK=13433.0, RHO=0.0001
$
MOONEY,LINER,41, 26, BULK=6556.00, RHO=0.0001
$
$Volumetric ratio changes within the tire are neglected
$
O-ENGR,PLY11,112000,1430,1430,0.69,0.69,0.69,365.0,365.0,368.0 /
LOCAL,VECTORS=0.857,0.515,0.0,-0.515,0.857,0.0,RHO=0.0001
$
O-ENGR,PLY12,112000,1430,1430,0.69,0.69,0.69,365.0,365.0,368.0 /
LOCAL,VECTORS=0.857,0.515,0.0,0.515,0.857,0.0,RHO=0.0001
$
$
O-ENGR,PLY21,112000,1430,1430,0.69,0.69,0.69,365.0,365.0,368.0 /
LOCAL,VECTORS=0.815,0.580,0.0,-0.580,0.815,0.0,RHO=0.0001
$
O-ENGR,PLY22,112000,1430,1430,0.69,0.69,0.69,365.0,365.0,368.0 /
LOCAL,VECTORS=0.815,0.580,0.0,0.580,0.815,0.0,RHO=0.0001
$
$
O-ENGR,PLY31,112000,1430,1430,0.69,0.69,0.69,365.0,365.0,368.0 /
LOCAL,VECTORS=0.765,0.643,0.0,-0.643,0.765,0.0,RHO=0.0001
$
O-ENGR,PLY32,112000,1430,1430,0.69,0.69,0.69,365.0,365.0,368.0 /
LOCAL,VECTORS=0.765,0.643,0.0,0.643,0.765,0.0,RHO=0.0001
$
$
O-ENGR,PLY41,112000,1430,1430,0.69,0.69,0.69,365.0,365.0,368.0 /
LOCAL,VECTORS=0.717,0.695,0.0,-0.695,0.717,0.0,RHO=0.0001
$
O-ENGR,PLY42,112000,1430,1430,0.69,0.69,0.69,365.0,365.0,368.0 /
LOCAL,VECTORS=0.717,0.695,0.0,0.695,0.717,0.0,RHO=0.0001
$
$
O-ENGR,PLY51,112000,1430,1430,0.69,0.69,0.69,365.0,365.0,368.0 /
LOCAL,VECTORS=0.681,0.733,0.0,-0.733,0.681,0.0,RHO=0.0001
$
O-ENGR,PLY52,112000,1430,1430,0.69,0.69,0.69,365.0,365.0,368.0 /
LOCAL,VECTORS=0.681,0.733,0.0,0.733,0.681,0.0,RHO=0.0001
$
$
O-ENGR,PLY61,112000,1430,1430,0.69,0.69,0.69,365.0,365.0,368.0 /
LOCAL,VECTORS=0.642,0.767,0.0,-0.767,0.642,0.0,RHO=0.0001
$
O-ENGR,PLY62,112000,1430,1430,0.69,0.69,0.69,365.0,365.0,368.0 /
LOCAL,VECTORS=0.642,0.767,0.0,0.767,0.642,0.0,RHO=0.0001
$
$
END,MATERIALS
$
$
$

```

```

$
$Define the cross-section
$
CSFACE-0,1,1,5,2
11,75,0,0,11,8,1,0,12,4,1,0,12,4,0,0
5,11,80,0,0,7,12,4,0,5
$
CSFACE-0,5,1,7,2
11,8,1,0,11,75,2,0,12,4,2,0,12,4,1,0
5,11,8,1,5,7,12,4,1,5
$
CSFACE-0,9,1,13,2
11,75,2,0,11,55,2,0,12,1,1,0,12,4,2,0
5,11,6,2,5,7,12,35,2,5
$
CSFACE-0,15,1,17,2
11,55,2,0,11,10,3,10,11,3,0,1,80,12,1,3,2
5,11,30,2,75,7,11,5,3,5
$
CSFACE-0,17,1,21,2
11,10,3,10,10,5,3,15,10,5,0,5,11,2,3,8
5,10,8,3,15,7,10,7,3,7
$
CSFACE-0,21,1,25,2
10,5,3,15,10,0,2,75,9,8,3,0,10,5,3,95
5,10,25,3,0,7,10,2,2,95
$
CSFACE-0,23,1,29,2
10,0,2,75,7,5,2,1,7,3,3,55,7,80,3,50
5,9,6,2,55,7,7,5,3,7
$
CSFACE-0,25,1,33,2
9,5,2,1,2,75,1,35,3,75,3,0,1,3,2,15
5,9,15,1,7,7,4,3,20
$
$Define the tread cross-section
$
CSFACE-0,1,2,5,4
12,4,0,0,12,4,1,0,12,75,1,0,12,75,2,0
5,12,4,0,1,0,12,75,0,5
$
CSFACE-0,5,2,7,4
12,4,1,0,12,4,2,0,12,75,2,0,12,75,1,0
5,12,4,1,5,7,12,75,1,5
$
CSFACE-0,9,2,13,4
12,4,2,0,12,1,3,2,12,2,3,3,1,75,2,0
5,12,35,2,5,7,12,65,2,5
$
HOOP
ELEMENTS=2, ANGLE=50, 00
ELEMENTS=2, ANGLE=40, 00
ELEMENTS=2, ANGLE=20, 00
ELEMENTS=5, ANGLE=35, 00
ELEMENTS=14, ANGLE=70, 0
ELEMENTS=5, ANGLE=35, 00
ELEMENTS=2, ANGLE=20, 00
ELEMENTS=2, ANGLE=40, 00
ELEMENTS=2, ANGLE=50, 00
END, HOOP
$
END, GRID
$
$Element assignment

```



```

$
PART=TIRE
$
KLOOP, 2, 1
    DISP-R, 33, 1, 0
    DISP-Z, 33, 1, 0
KEND
$
SYM-XY
$
INFLPRES, 310, 0, LOAD1
$
CONTACT, NGRMLoad=4050, 0, LOAD1
$
ROLLING, VELTRAVL=-210, 0, LOAD1
$
FRICTION, MU=0.1, RECPAR=10., TORQUE=0.0,
$
END, BC
$
$
SOLVE
    STATIC, 4, 1, 0, LINEAR, 3, 2, 0, ITMAX=25
END, SOLVE
$
$POST, TIRE, LAST
$FOOTPRNT, CONTOUR, PRESSURE
$END, POST
$
STOP

```

```

$
$ F-16 aircraft tire cross section data
$
GEOMETRY
$
$ Material properties
$
MOONEY,TREAD,82, 51, BULK=13333.0, RHO=0.0001
$
MOONEY,LINER,41, 26, BULK=6666.00, RHO=0.0001
$
$ Volumetric ratio changes within the tire are neglected
$
LINER,PLY11,112000,1430,1430,0.69,0.69,0.69,365.0,365.0,368.0 /
    LOCAL,VECTORS=0.8570,0.515,0.0,-0.515,0.857,0.0,RHO=0.0001
$
LINER,PLY12,112000,1430,1430,0.69,0.69,0.69,365.0,365.0,368.0 /
    LOCAL,VECTORS=0.857,-0.515,0.0,0.515,0.857,0.0,RHO=0.0001
$
LINER,PLY21,112000,1430,1430,0.69,0.69,0.69,365.0,365.0,368.0 /
    LOCAL,VECTORS=0.815,0.580,0.0,-0.580,0.815,0.0,RHO=0.0001
$
LINER,PLY22,112000,1430,1430,0.69,0.69,0.69,365.0,365.0,368.0 /
    LOCAL,VECTORS=0.815,-0.580,0.0,0.580,0.815,0.0,RHO=0.0001
$
LINER,PLY31,112000,1430,1430,0.69,0.69,0.69,365.0,365.0,368.0 /
    LOCAL,VECTORS=0.765,0.643,0.0,-0.643,0.765,0.0,RHO=0.0001
$
LINER,PLY32,112000,1430,1430,0.69,0.69,0.69,365.0,365.0,368.0 /
    LOCAL,VECTORS=0.765,-0.643,0.0,0.643,0.765,0.0,RHO=0.0001
$
LINER,PLY41,112000,1430,1430,0.69,0.69,0.69,365.0,365.0,368.0 /
    LOCAL,VECTORS=0.719,0.695,0.0,-0.695,0.719,0.0,RHO=0.0001
$
LINER,PLY42,112000,1430,1430,0.69,0.69,0.69,365.0,365.0,368.0 /
    LOCAL,VECTORS=0.719,-0.695,0.0,0.695,0.719,0.0,RHO=0.0001
$
LINER,PLY51,112000,1430,1430,0.69,0.69,0.69,365.0,365.0,368.0 /
    LOCAL,VECTORS=0.681,0.733,0.0,-0.733,0.681,0.0,RHO=0.0001
$
LINER,PLY52,112000,1430,1430,0.69,0.69,0.69,365.0,365.0,368.0 /
    LOCAL,VECTORS=0.681,-0.733,0.0,0.733,0.681,0.0,RHO=0.0001
$
LINER,PLY61,112000,1430,1430,0.69,0.69,0.69,365.0,365.0,368.0 /
    LOCAL,VECTORS=0.642,0.767,0.0,-0.767,0.642,0.0,RHO=0.0001
$
LINER,PLY62,112000,1430,1430,0.69,0.69,0.69,365.0,365.0,368.0 /
    LOCAL,VECTORS=0.642,-0.767,0.0,0.767,0.642,0.0,RHO=0.0001

```

MATERIALS

1. generation

WIRE, 73, 33, 4, 1

line the cross-section

W-2, 1, 1, 5, 2

1.0, 11.8, 1.0, 12.4, 1.0, 12.4, 0.0

1.0, 0.5, 7, 12.4, 0.5

W-2, 5, 1, 9, 2

1.0, 11.75, 2.0, 12.4, 2.0, 12.4, 1.0

1.0, 1.5, 7, 12.4, 1.5

W-2, 9, 1, 13, 2

1.0, 11.55, 2.65, 12.1, 3.2, 12.4, 2.0

1.0, 2.5, 7, 12.35, 2.5

W-2, 13, 1, 17, 2

1.0, 11.65, 11.10, 3.10, 11.30, 3.80, 12.1, 3.2

1.0, 2.95, 7, 11.85, 3.5

W-2, 17, 1, 21, 2

1.0, 11.10, 10.5, 3.15, 10.5, 3.95, 11.3, 3.8

1.0, 3.15, 7, 10.9, 3.9

W-2, 21, 1, 25, 2

1.0, 11.15, 10.0, 2.75, 9.8, 3.80, 10.5, 3.95

1.0, 3.0, 7, 10.2, 3.95

W-2, 25, 1, 29, 2

1.0, 11.2, 9.5, 2.1, 9.3, 3.55, 9.80, 3.80

1.0, 3.15, 7, 9.5, 3.7

W-2, 29, 1, 33, 2

1.0, 11.25, 1.35, 8.75, 3.05, 9.3, 3.55

1.0, 3.2, 7, 9, 3.25

line the tread cross-section

W-2, 1, 2, 5, 4

1.0, 12.4, 1.0, 12.75, 1.0, 12.75, 0.0

1.0, 1.5, 7, 12.75, 0.5

W-2, 5, 2, 9, 4

1.0, 12.4, 2.0, 12.75, 2.0, 12.75, 1.0

1.0, 1.5, 7, 12.75, 1.5

W-2, 9, 2, 13, 4

1.0, 12.1, 3.2, 12.2, 3.3, 12.75, 2.0

1.0, 2.5, 7, 12.65, 2.5

W-2, ANGLE=50.00

W-2, ANGLE=40.00

W-2, ANGLE=20.00

W-5, ANGLE=35.00

```

... LAMPTS=14,ANGLE=70.0
... LAMPTS=5,ANGLE=35.00
... LAMPTS=2,ANGLE=20.00
... LAMPTS=2,ANGLE=40.00
... LAMPTS=2,ANGLE=50.00

```

15 assignment

```

16
  JLOOP,3,4
    SHELL-16,LINER,THICK=0.060,PLY11,THICK=0.125 /
    PLY12,THICK=0.250,PLY11,THICK=0.125 /
    LINER,THICK=REMAIN,1,1,1
  JEND

```

```

  JLOOP,3,4
    BRICK-20,TREAD,1,1,2
  JEND

```

17 element assignment

```

  JLOOP,1,4
    SHELL-16,LINER,THICK=0.060,PLY21,THICK=0.125 /
    PLY22,THICK=0.250,PLY21,THICK=0.125 /
    LINER,THICK=REMAIN,1,13,1
  JEND

```

```

  JLOOP,1,4
    SHELL-16,LINER,THICK=0.060,PLY31,THICK=0.125 /
    PLY32,THICK=0.250,PLY31,THICK=0.125 /
    LINER,THICK=REMAIN,1,17,1
  JEND

```

```

  JLOOP,1,4
    SHELL-16,LINER,THICK=0.100,PLY41,THICK=0.125 /
    PLY42,THICK=0.250,PLY41,THICK=0.125 /
    LINER,THICK=REMAIN,1,21,1
  JEND

```

```

  JLOOP,1,4
    SHELL-16,LINER,THICK=0.100,PLY51,THICK=0.125 /
    PLY52,THICK=0.250,PLY51,THICK=0.125 /
    LINER,THICK=REMAIN,1,25,1
  JEND

```

```

  JLOOP,1,4
    SHELL-16,LINER,THICK=0.100,PLY61,THICK=0.225 /
    PLY62,THICK=0.450,PLY61,THICK=0.225 /
    LINER,THICK=REMAIN,1,29,1
  JEND

```



END

## 10. ELEMENTS

### SYMMETRY

### LOADS

LOAD1, 0.0,0.0,1.0,1.0,15.0,1.0,25.0,1.0  
LOAD2, 0.0,0.0,1.0,0.0,2.0,1.0,25.0,1.0  
LOAD3, 0.0,0.0,2.0,0.0,3.0,1.0,25.0,1.0  
LOAD0, 0.0,0.0,3.0,0.0,4.0,1.0,25.0,1.0

### BOUNDARY

### BOUND

DEP-R,33,1,0  
DEP-Z,33,1,0

,210.0,LOAD1

,NORMLOAD=4050.0,LOAD2

,TANGRAVL=-210.0,LOAD3

,H,NS=0.1,REGPAR=10.,,TORQUE=-2100.0,LOAD3

,,IC,4,1.0,LINESEAR,8,2.0,ITMAX=25

,,LAST

,,CONTOUR,PRESSURE

# RESTART FILE

```
TITLE
Test run restart
$
$
RESTART
$
SOLVE
STATIC,10,2.0,STEP=4,ITMAX=25
END,SOLVE
$
POST,ALL, LAST
PRINT,STRESS,POINT=3,OPTION=4
DEFORMED,ANGLES,0,90,0
$
PRINT,STRESS,POINT=4,OPTION=4,JPLANE=1
END,POST
$
```

EXECUTABLE FILE

```
SUB -s /bin/sh
SUB -lt 1900
SUB -lT 1900
SUB -lM 8Mw
SUB -lm 8Mw
SUB -eo
SUB -me
SUB -o /usr/local/tire3d/job/A.cpr
  /usr/local/tire3d/job
t -vxS

ap 'ja -stc' 0
r/local/tire3d/obj/tire3d_old A.dat
```

## APPENDIX B

```

/*****
GRAPHICS PROGRAM TO GENERATE PLOTS
*****/
#include <stdio.h>
#include "pixrect.h"
struct pixrect screen;

/*****
plot
*****/
plot(x,y)
int x,y;
{
    pr_put(screen,x,y,255);
}

/*****
blin:

data file : plotfile
output file: outfile
Note: Convert raw outfile to .ps file and then to ps file

compiling the program

cc <filename> c -o <filename> -lpixrect

*****/
void bline(xa,ya,xb,yb)
int xa,xb,ya,yb;
{
    int dx,dy,adx,ady,final,incr,inc2,g;
    register col,row;
    register posslope;

    dx=xb-xa;
    dy=yb-ya;
    if (dx>0) posslope=1;
    else posslope= (-1);
    if (dy<0)
        posslope= (-posslope);
    adx=abs(dx);
    ady=abs(dy);

    if (adx>ady)
    {
        if (dx>0)
            { col=xa; row=ya; final=xb; }
        else { col=xb; row=yb; final=xa; }
        incr= ady<<1;
        inc2= (ady - adx)<<1;
        g = incr - inc2;
        while (col<final)
        {
            plot(col,row);

```

```

        col+=1;
        if (g>=0)
        { row+=posslope; g=inc2;
          else g += inc1;
        }
    }
else
{
    if (dy>0)
    { row=ya; col=xb; final=yb;
      else { row=yb; col=xb; final=xb; }
      inc1= adx<<1;
      inc2= (adx + ady)<<1;
      g = inc1 - ady;
      while (row<=final)
      {
          plot(col,row);
          row+=1;
          if (g>=0)
          { col+=posslope; g=inc2;
            else g += inc1;
          }
      }
    }
}
}

```

```

main()
{
    int x,y;
    int a,x1,y1;
    int i,j;
    int ch;
    float x2,y2;
    FILE *fp,*fpout;

```

```

    fp=fopen("plotfile","r");
    fpout=fopen("outfile","w");

```

```

/*      Initializes the screen and graphics buffer */

```

```

/*system("clear");*/                                /* clear screen */
init_screen();                                       /* initilaizes the graphics buffer*/
clear(400,200,600,300);

```

```

x1=0; y1=0;
while(a!=999)
{
    fscanf(fp,"%d %f %f\n",&a,&x2,&y2);

```

```

    x=(x2*(-1))*70000;
    y=y2*70000;
    x=(850*x)/900000;
    y=(850*y)/900000;
    x=850-x;
    y=850-y;
    if((a==2))
    /*fprintf(fp,"%d %d\n",x,y);*/

```

```

bline(x1,y1,x,y);
x1=x;
y1=y;
}
for (i=0; i<800; i++)
{
for (j=0; j<800; j++)
{
ch= (int) pr_get(screen,1200-i,j,200+j);
if(ch) putc(0,fpout); else putc(255,fpout);
}
}
pr_close(screen);
fclose(fp);
fclose(fpout);
}

```

```

/*****
/* Function init_screen will open the graphics frame buffer and set the
/* color map up to give a 256 gray level output : 0 - black, 255 - white.
*****/

```

```

init_screen ()
{
unsigned char    red[256],
                 green[256],
                 blue[256];          /* color map arrays */
int              j;                 /* loop counter */

screen = pr_open("/dev/fb");        /* open graphics frame buffer */

for (i = 1; i < 255; i++)           /* initialize color map arrays */
    red[i] = green[i] = blue[i] = i; /* 1 - 254, black to white */

red[0]   = green[0]   = blue[0]   = 255; /* set background to white */
red[255] = green[255] = blue[255] = 0;   /* set foreground to black */

/* call routine to set colormap */
pr_putcolormap(screen,0,255,red,green,blue);
}

```

```

/*****
/* Function clear will reset the screen to the background color over
/* a user specified area. The upper left corner and the maximum x and y
/* dimensions of the area must be specified.
*****/

```

```

clear (xoffset,yoffset,maxx,maxy)

```

```

int xoffset,yoffset;          /* (x,y) offset for corner */
int maxx,maxy;              /* dimensions of clear area */

```

```

{
    int i, j;                                /* loop counters */

    for (j = 0; j < maxy; j++)               /* loop thru entire area */
        for (i = 0; i < maxx; i++)           /* print background color */
            pr_put(screen, i + xoffset, maxy-j-j+yoffset, 0); /* for each pixel in it */
}

/*****+*****/

```



## APPENDIX C



```

{
    if(i<refi)
        m=3;
    else
        if(i>refi)
            m=2;
        else
            m=1;
}

if(m==1)
    printf(" (inner node)\n\n");
else
    if(m==2)
        printf(" (lagging area)\n\n");
    else
        if(m==3)
            printf(" (leading area)\n\n");

x0=x1=x2=x3=x4=x5=x6=0;
flag=0;
for (y=1;y<=x;y++)
{
    if((a[y][2]==j)&&(a[y][3]==k))
    {
        flag=1;
    }
    if(flag==1)
    {
        p=a[y][1];
        if(p==i) x0=y;
        else if(p==(i+1)) x1=y;
        else if(p==(i+2)) x2=y;
        else if(p==(i-1)) x3=y;
        else if(p==(i-2)) x4=y;
    }
}
flag=0;
}
flag2=0;
if((m==1)&&((x1==0)|| (x2==0)|| (x3==0)|| (x4==0)))
{
    printf("insufficient data\n");
    if(x1==0)
        printf("the coordinate needed is (%d %d %d)\n",i+1,j,k);
    if(x2==0)
        printf("the coordinate needed is (%d %d %d)\n",i+2,j,k);
    if(x3==0)
        printf("the coordinate needed is (%d %d %d)\n",i-1,j,k);
    if(x4==0)
        printf("the coordinate needed is (%d %d %d)\n",i-2,j,k);
    flag2=1;
}
else if((m==2)&&((x0==0)|| (x3==0)|| (x4==0)))
{
    printf("insufficient data\n");
    if(x0==0)
        printf("the coordinate needed is (%d %d %d)\n",i,j,k);
    if(x3==0)
        printf("the coordinate needed is (%d %d %d)\n",i-1,j,k);
}

```

```

        if(x4==0)
        printf("the coordinate needed is (%d %d %d)\n",i-2,j,k);
        flag2=1;
    }
    else if((m==3)&&((x0==0)|| (x1==0)|| (x2==0)))
    {
        printf("insufficient data\n");
        if(x0==0)
        printf("the coordinate needed is (%d %d %d)\n",i,j,k);
        if(x1==0)
        printf("the coordinate needed is (%d %d %d)\n",i+1,j,k);
        if(x2==0)
        printf("the coordinate needed is (%d %d %d)\n",i+2,j,k);
        flag2=1;
    }
    flag=0;
    for (y=1;y<=x;y++)
    {
        if((a[y][1]==i)&&(a[y][2]==j))
            flag=1;
        if(flag==1)
        {
            p=a[y][3];
            if(p==(k-2))
                x5=y;
            else if (p==(k-3))
                x6=y;
        }
        flag=0;
    }
    flag3=0;
    if((x0==0)|| (x5==0)|| (x6==0))
    {
        if(flag2!=1)
        printf("insufficient data\n");
        if(x0==0)
        printf("the coordinate needed is (%d %d %d)\n",i,j,k);
        if(x5==0)
        printf("the coordinate needed is (%d %d %d)\n",i,j,k-2);
        if(x6==0)
        printf("the coordinate needed is (%d %d %d)\n",i,j,k-3);
        flag3=1;
    }
    y1=-(b[x0][1]);
    y2=-(H+b[x0][2]);
    switch(m)
    {
    case 1:
        {
            z=(b[x4][1]-4*b[x3][1]+4*b[x1][1]-b[x2][1])/(2*h);
            z3=(b[x4][3]-4*b[x3][3]+4*b[x1][3]-b[x2][3])/(2*h);
            break;
        }
    case 2:
        {
            z=(b[x4][1]-4*b[x3][1]+3*b[x0][1])/(2*h);
            z3=(b[x4][3]-4*b[x3][3]+3*b[x0][3])/(2*h);
            break;
        }
    }

```

```

case 3:
{
z=(-3*b[x0][1]+4*b[x1][1]-b[x2][1])/(2*h);
z3=(-3*b[x0][3]+4*b[x1][3]-b[x2][3])/(2*h);
break;
}
}
if((flag2!=1)&&(flag3!=1))
{
z1=(-3*b[x0][1]+4*b[x5][1]-b[x6][1])/(2*thktrd);
z13=(-3*b[x0][3]+4*b[x5][3]-b[x6][3])/(2*thktrd);
V1=(z+1)*angvel*y2 - z1*angvel*y1 + vel;
if(refj==j)
V3=0;
else
V3=(z3)*angvel*y2 - z13*angvel*y1;
printf ("The absolute particle velocity component (V1)
at (%d %d %d) is %f inches/sec\n\n", i,j,k,V1);
printf ("The absolute particle velocity component (V3)
at (%d %d %d) is %f inches/sec\n\n", i,j,k,V3);
}
}
fclose(fp);

```

THE EFFECT OF ELECTRIC FIELDS  
ON PROPANE/AIR FLAMES

Harold H. Harris  
Associate Professor

Department of Chemistry  
University of Missouri-St. Louis  
8001 Natural Bridge Road  
St. Louis, MO 63121

Final Report for:  
Research Initiation Program  
Wright-Patterson Laboratory

Sponsored by:  
Air Force Office of Scientific Research  
Bolling Air Force Base, Washington, D.C.  
and  
University of Missouri-St. Louis,  
National Science Foundation Research Experience for Undergraduates,  
and  
St. Louis Science-Math Education Center STARS Program

December 1992

## THE EFFECT OF ELECTRIC FIELDS ON PROPANE/AIR FLAMES

Harold H. Harris  
Associate Professor  
Department of Chemistry  
University of Missouri-St. Louis

### Abstract

Studies have been initiated of the effects of modest electric fields on premixed propane/air flames at atmospheric pressure. A surplus commercial flame atomic absorption spectrometer has been modified so as to provide the foundation for a study of both the temporal and the spatial variation of flames as they are perturbed by an axially symmetric positive DC electrical potential up to twenty-four hundred volts. Two separate electrooptical systems interfaced to a computer were constructed for the quantification of temporal and spatial changes in flames. The polarity of the field is key to the production of any effect; potentials negative with respect to the burner cause no perceptible or measurable change in the flame. Reported here for the first time is the dramatic effect that modest electric fields have on the structure of cellular flames. The number of cells is increased and their size diminished as the electric field increases. Quantification of these effects is continuing.

## THE EFFECT OF ELECTRIC FIELDS ON PROPANE/AIR FLAMES

Harold H. Harris

### Introduction

The first indication of charged species in flames dates from 1600, when W. Gilbert, physician to Queen Elizabeth I, showed that flames were capable of discharging an electroscope. Through the years, the role of ions and electrons in flames has been the subject of numerous studies. Those before 1966 were summarized and reviewed in the classic monograph by Lawton and Weinberg<sup>1</sup>. The phenomenon originally called "polyhedral flame structure" was first reported 100 years ago, by Smithells and Ingle<sup>2</sup>, who discovered that rich mixtures of air and benzene, pentane, or heptane, "The inner cone is divided by dark lines into several petal-like segments, which often revolve with rapidity around a vertical axis." Systematic reinvestigation of the phenomenon was reported 36 years later by Smith and Pickering<sup>3</sup>, who noted that the length of the side at the base of the polyhedral flame seemed to be a characteristic of the gas mixture, and that the rate of rotation of the segments could be influenced greatly by slight changes in the composition of the mixture and the flow velocity. Later investigations showed that this polyhedral structure was only a special case of a more general phenomenon known now as "cellular flame structure", and the range of combustion mixtures that produce them has been greatly broadened to include hydrogen/air<sup>4,5</sup>,  $H_2/Br_2$ <sup>6</sup>, and  $CO/O_2/N_2$ . The comprehensive review of cellular flame phenomena up to 1964 is found in a chapter by G. H. Markstein published that year<sup>7</sup>. Markstein proposed that the cellular structure is due to the interaction of selective diffusion with hydrodynamic flow<sup>8</sup>. This conclusion was challenged by Sivashinsky, whose quantitative analysis indicated that the "real reason for cell formation is purely diffusional-thermal, and is not connected with the hydrodynamics of the perturbed flow".

Neither of these analyses, it seems to us, adequately rationalize the electrical perturbations of cellular flames that we observe. Neither of them include charged species in the flame model, and therefore cannot take into account any but effects that modify diffusion, hydrodynamics, or heat transfer in an indirect way. A continuation of the experimental studies of the dynamics of premixed flames, including their cellular structure, has been undertaken by Michael Gorman and coworkers<sup>9</sup>, who have



employed video techniques to quantify flame dynamics on flat-flame burners. Their approach generally has been to classify cellular modes by symmetry and to analyze the dynamics by nonlinear mechanics of transient waves, rather than to use the principles of detailed chemistry and thermodynamical methods. Their work does not include electrical perturbation of cellular flame systems.

### Gas Handling and Burner Design

An obsolete and surplus Jarrell Ash Model 850 Atomic Absorption spectrometer owned by the UMSL Department of Chemistry was used for its optical bench, monochromator, photomultiplier detector, and a portion of its gas-handling capabilities. The burner base of the instrument, which holds the burner head, was loosely packed with glass wool in order to help insure thorough premixing of the reactant gases. The original acetylene/oxygen slot burner, which had been designed to produce a long absorption path for the atomic absorption instrument, was removed and replaced with a new burner head, designed using MathCAD software. Figures 1 and 2 illustrate the new burner, which was intended to produce as stable a flame as possible.

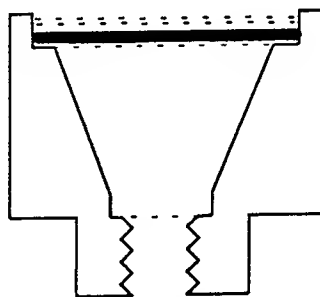


**Figure 1.** Cross section of modified burner head. Dotted lines indicate Microscreen layers. The heavy solid line represents the brass diffuser. The head shown screws onto an adaptor to the original burner holder. An additional ring (not shown) holds the upper screens and diffuser in place. The top screen of this assembly is visible in Figure 3.

The outside diameter of the burner head is 57 mm, and the active flame diameter is approximately 41 mm. Propane gas and compressed air were obtained from Acetylene Gas Company, and used without further purification. Propane flow was measured with a Matheson Gas Company FM-1050 flowmeter and air flow was measured with an Omega FL-114. Both were calibrated by us for use with the appropriate gases. Under certain ambient conditions and with relatively high flow rates, we sometimes observed sizable fluctuations in propane flow rates. These fluctuations were determined to be a result of liquid propane in

the supply cylinder boiling as the pressure above the liquid decreased. We eliminated this source of fluctuation by installing a second, ballast propane tank along the supply line to the burner, after the pressure regulator.<sup>10</sup>

Attempts were made to obtain a gas distribution across the burner top that could produce a steady state turbulent, unperturbed flame. The hole pattern used for the brass diffuser was designed to produce a logarithmic distribution from the center to the outer edge of the burner, using the MathCAD program and its graphical output shown in Figure 2. This design was not completely successful in producing a steady-state flame, probably because of unavoidably large shear forces at the sides of a burner of this size. Among other things, a separate supply of inert gases flowing around the burner would have been required in order to obtain a flat flame.

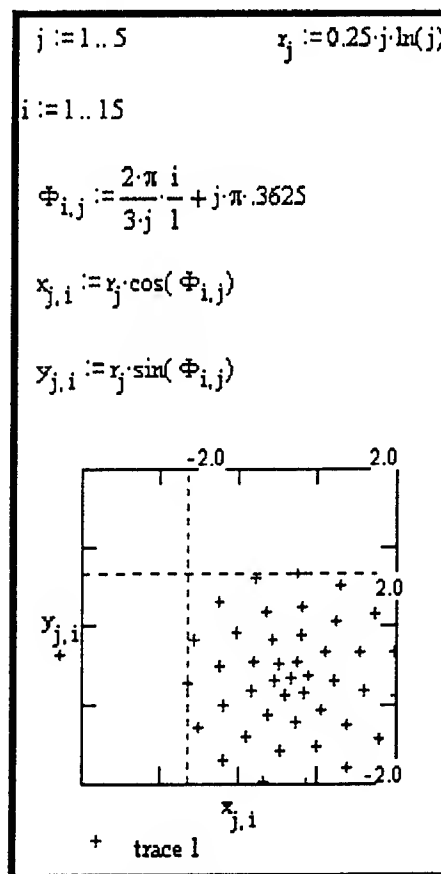


**Figure 2.** The MathCAD program and its graphic output used to produce the hole pattern in the brass diffuser plate. At each indicated +, a 0.032 inch hole was drilled.

A top view of the apparatus obtained using the video system we will describe later is presented as Figure 3. The ring-shaped electrode used to perturb the flame is made of stainless steel and located 31 mm directly above the burner. The inside diameter is 47 mm and its outside diameter is 50 mm. The white object in the upper right quadrant of the figure is a ceramic insulator that supports the perturbing electrode. Looking through the electrode, one can see topmost of the screens through which the premixed gases are supplied to the burner. The apparatus is illuminated in this figure by the fluorescent lights of the laboratory, but when images of flame structure are being obtained, these lights are extinguished, and the camera sees only the light emitted by the flame. For this reason, video images presented later show only the flame, circumscribed by the screen and slightly distorted by the heat of the combustion, as it changes the index of refraction of the air between the burner and the camera.

The maximum potential used in the present studies was 2400 volts, but the current drawn by the flame is relatively small. While the current depends on the equivalence ratio as well as the total flow rate, the largest values we measured were approximately 300  $\mu\text{A}$ , so the energy provided by the power supply is only on the order of 0.68 watt. When this is compared to the approximate 1.5 kilowatt power produced by the flame, it is clear that the present experiments are not on "augmented" flames, where electrical power substantially increases flame temperature and power, but on natural flames burning under conditions representative of the most common applications of hydrocarbon combustion, and the electrical perturbation represents a very small fraction of the system energy.

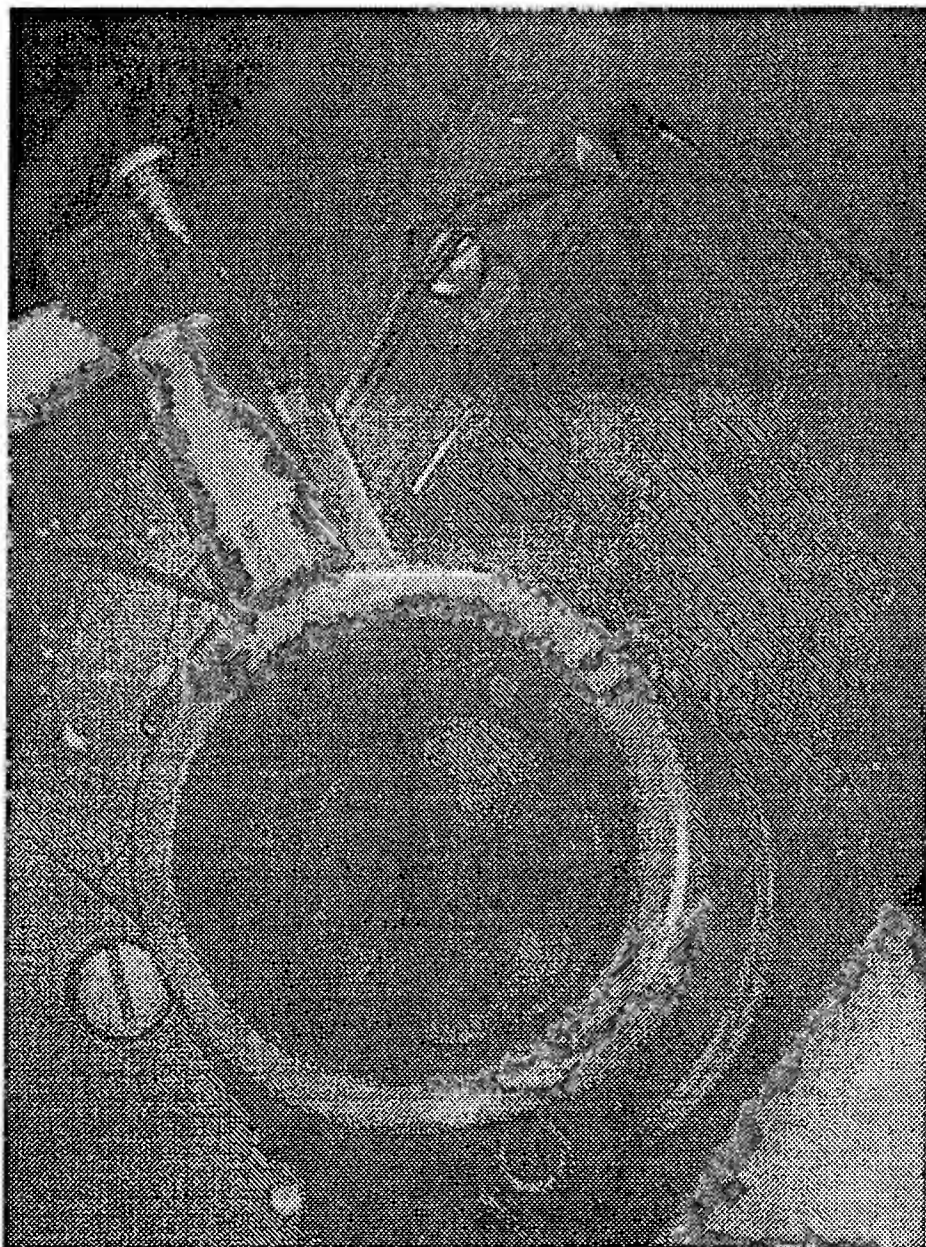


Figure 3. A view of the burner and perturbing electrode, taken by the video camera through a front-surface mirror mounted almost directly above the apparatus. Visible is the circular top screen of the burner assembly. It is viewed through the stainless steel ring electrode. In the upper right is a ceramic insulator for the electrode attached to a vertical post. Images shown later (Figure 10) include only the region around the burner top; and were obtained with laboratory lights extinguished, so only the flame emission is visible.

### Temporal variation in emission intensity

The monochromator and detector systems of the original atomic absorption instrument were modified for emission fluctuation measurements. The deuterium lamp, chopper, and all but one mirror of the original optical system were removed from the optical bench. The remaining concave mirror focuses a portion (approximately  $1 \text{ mm}^2$ ) of the flame emission onto the entrance slit of the .25 meter grating monochromator of the spectrophotometer. The imaged region can be changed by moving the burner head vertically or laterally. This optical arrangement as seen from above is shown in Figure 4.

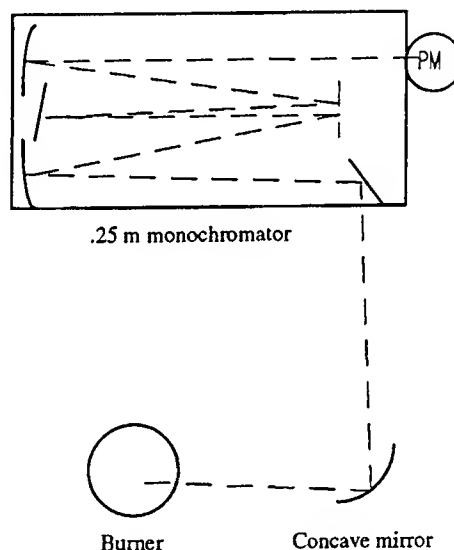
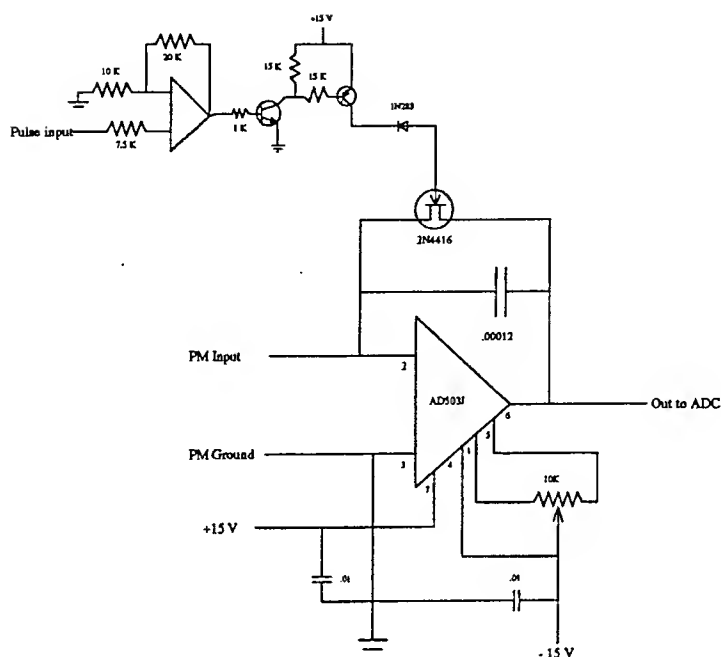


Figure 4. Optical arrangement for measurement of flame fluctuations.

The original photomultiplier, a Hamamatsu R456 HA, is powered by the 1000 volt supply of the original instrument. However, since the original system was designed to measure photocurrent synchronously with a chopper, much of the electronic amplification system required modification. We use the original photomultiplier preamplifier, providing the required timing pulses from our computer. The modified preamplifier circuit is shown in Figure 5. The heart of the integrating amplifier is the differential operational amplifier AD503J, which accumulates charge on the .00012 mfd capacitor across its input and output.



**Figure 5.** The circuit for the integrator/amplifier used in measurement of flame fluctuations.

A negative 10V pulse from an external circuit, after amplification, causes the N-channel FET (Motorola 2N4416) to conduct, discharging this capacitor, and the output voltage momentarily falls to zero. The photocurrent multiplied by the PM tube charges this capacitor at a rate proportional to the current, and the maximum voltage is determined by the photocurrent and the integration time. The maximum voltage accumulated may not exceed the supply potential (15 V), but is limited practically by the potential at which the analog to digital converter saturates (approximately 10 volts).

In modifying this circuit for use in a system without a chopper, replacement for the pulse signal that initiates and terminates the accumulation of charge was necessary. We chose a computer interface board (PC-LPM-16 from National Instruments) which included an analog to digital converter and several digital outputs. Since output signals only as large as 5 volts are available from this computer I/O board, we built a pulse amplifier depicted at the upper left of the diagram to produce 13 volt pulses to discharge the capacitor. The timing sequence for data acquisition is as shown in Figure 6, below:

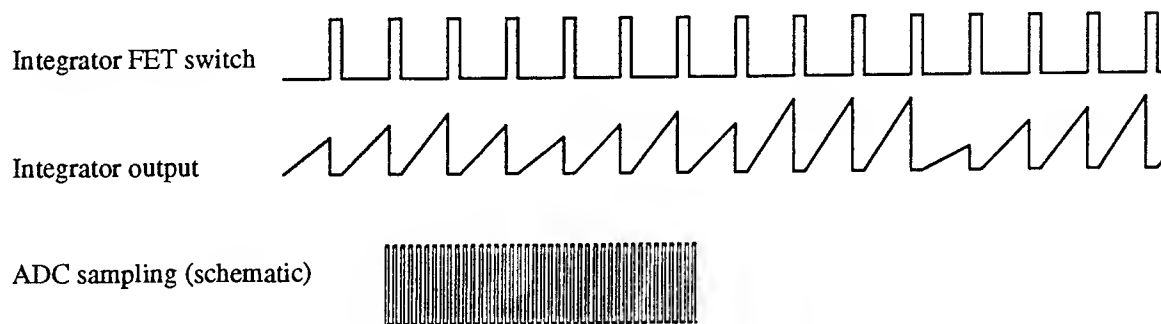


**Figure 6.** Data acquisition timing sequences. Timing intervals are variable in software.

Data acquisition is controlled by a program written in compiled QuickBASIC 4.5 using Lab Windows, a software product of National Instruments. The ADC has resolution of 12 bits across 10 volts, or 2.44 mV. The time between pulses is varied in software depending on the signal intensity, so as to obtain maximum ADC samples as near as possible to 10 volts, without saturating the ADC. For this reason, the temporal resolution of the instrument is inversely proportional to the photocurrent.

An example of temporal variations in the emission intensity in the 515 nm (0-0)  $C_2$  Swan band ( $A^3\Pi_g \rightarrow X^3\Pi_u$ ) of a flame is shown in Figure 7. Here are graphed 1024 samples obtained in slightly more than 4 seconds, using the photomultiplier and amplifier/integrator described. Data acquired were written to a computer file, then imported to SigmaPlot 5.0 for graphing. Studies of such fluctuations in the frequency domain have been attempted, but satisfactory results have not yet been achieved, for reasons described below. The computation of Fourier transforms of the temporal data are done by reading the data file into MathCAD, and performing the transformation and graphing in that environment.

This integrator/amplifier arrangement apparently is not quite fast enough to reliably obtain the power spectrum of fluctuations in our flames, and will require some modification before it can be used for that purpose. In order to avoid aliasing errors, the sampling rate should be several times the frequency of the fastest transients to be measured, and tests with a signal generator and oscilloscope have shown that this criterion is not being met by this combination of detector and electronics. We are considering the substitution of the monochromator by a narrow bandpass optical filter such as that used in the video

system, so as to obtain larger photocurrents. Then the speed limitation likely will be the rate at which start/stop pulses can be obtained from the computer, since the 50 kHz ADC acquisition rate should comfortably exceed fluctuation rates. If that stratagem does not succeed, we intend to investigate a more modern, higher-speed solid state detector in place of the photomultiplier.

File Test6 Aug. 3, 1992

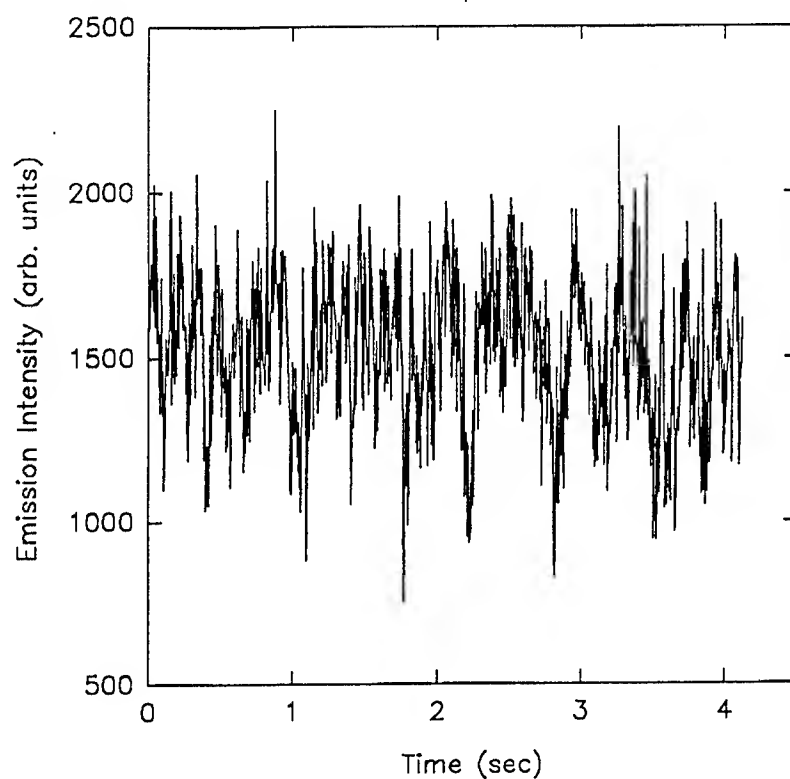


**Figure 7.** Temporal variation in a flame that displays no quasiperiodicity. 1024 points were acquired in just over four seconds.



### Video System

At the suggestion of Bish Ganguly of the Wright Laboratory, we decided to characterize the flame spatially as well as temporally using a digital video system. Because we used several salvaged components in other parts of the experiment, it was possible to create such a capability within the available budget. The electronic arrangement of the video system is displayed in Figure 8.

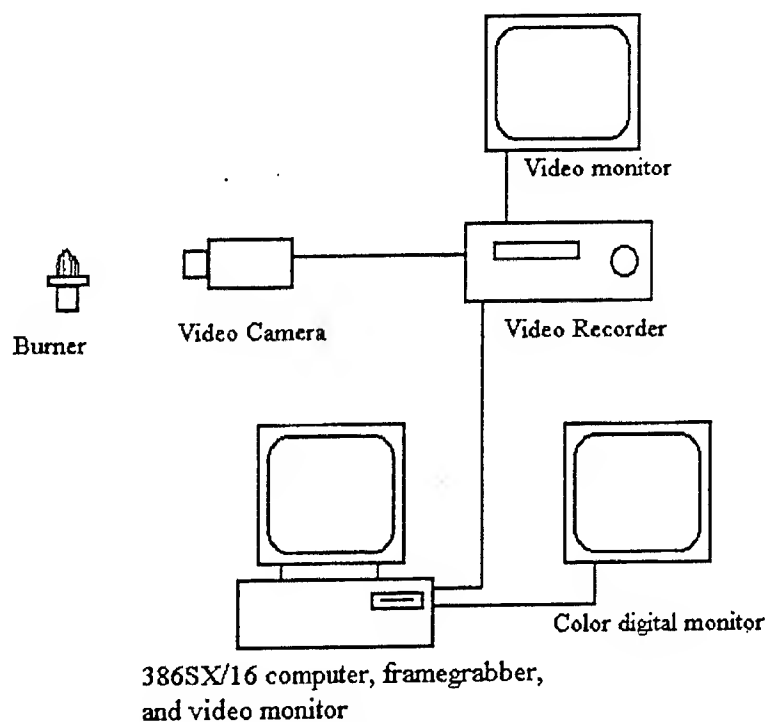


**Figure 8.** The video system components. The framegrabber is installed as an internal board in the computer.

The flame image is acquired using a Sony SSC-M350 monochrome CCD-Iris video camera. The camera is fitted with a 50 mm, f 1.8 lens, which magnifies the image about sixfold on the 13 inch video monitor. Data are normally obtained in a darkened laboratory, so that emission from the flame itself is the only light seen by the camera. Nearly all the data are obtained with a Corion P10-515 bandpass filter installed inside the camera housing, between the charge-coupled detector and the lens, so as to obtain only the emission from the  $C_2^*$  radical species that is characteristic of the reaction zone. This has the desirable secondary effect of eliminating the image of hot electrode, whose blackbody radiation is quite strongly

detected when the filter is absent. Since the image is quite small at that point, a filter only 12.5 mm in diameter is sufficient. The bandpass filter serves to emphasize the reaction zone, and to better define the boundaries between cells in cellular flames. Comparison of the bandpass of this filter to the previously-measured (0-0) Swan band head structure is shown in Figure 9.

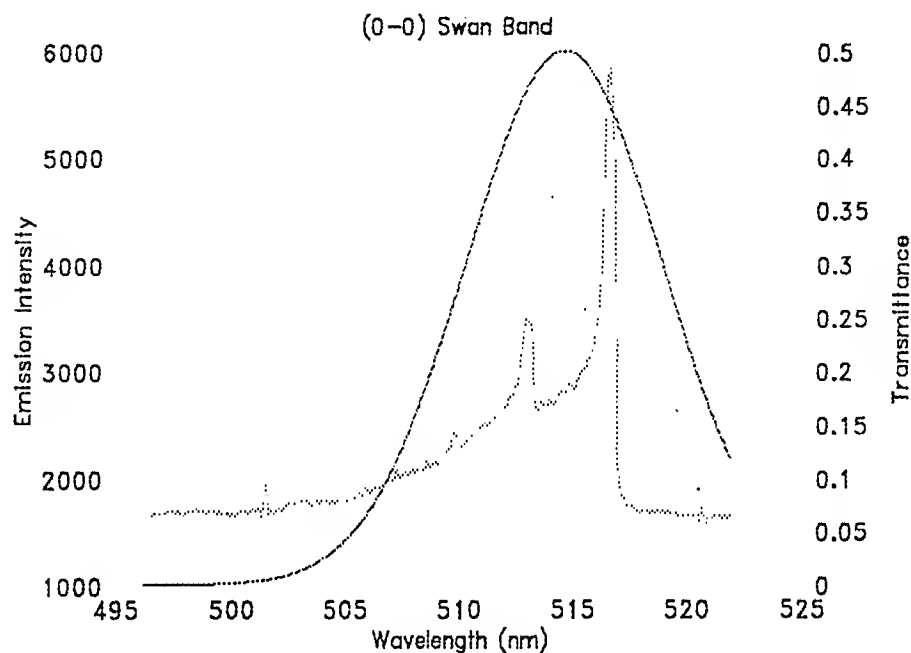


**Figure 9.** The (0-0) component of the  $C_2$  Swan band emission (as measured during summer, 1991 investigations) juxtaposed with the transmittance of the narrow bandpass optical filter installed in the video camera.

The camera is located just above the level of the burner top when side views of the flame are needed, but angled up to a front-surface mirror mounted approximately 30 cm above the flame when top views are more informative. This proves particularly useful in displaying the structure of cellular flames. Figure 10 was obtained with this geometry.

Flame images are recorded using a Sony SLV-393 video recorder that, like most consumer video equipment, obtains a new image each 33 ms. Freeze-frame capabilities and shuttle control facilitate the digital analysis of individual images. The live or recorded video image is displayed on a 13 inch Sony Video monitor. An 80386SX-based computer with 80387 coprocessor is the basis for a modest image analysis system, the most important component of which was an image processing board ("frame

grabber"), Data Translation Corporation model DT2855. This is a monochrome frame grabber board that digitizes 640 x 480 square pixels at 256 gray levels in real time, stores one frame onboard, and saves processed images in compressed TIFF, PCX, or DT-IRIS (a proprietary designation) formats. With this "low-end" processing board, some functions that are performed more quickly in hardware on more powerful systems are achieved in software here. These include picture averaging, geometric processing, arithmetic processing, filtering, histograms, and FFT processing. Other advanced functions such as adjustable offset, reference, and gain, zooming and panning are beyond the capabilities of the system. Processed images are displayed on a separate, RGB multimode digital monitor.

Interpretation of images is greatly expedited by the use of a powerful software package, Global Lab Image, purchased from Data Translation Corporation with the image processing board. This package runs under Windows 3.1 on our computer. With this software, one can automate some of the analytical procedures used to enhance video images. For example, pixel intensities can be altered as they are mapped to the digital monitor so as to change their distribution almost arbitrarily. This capability is most often used to expand the most informative range of pixel values by post-processing the equivalent of "brightness" or "contrast", but it may also be used to create false-color images on the (color) digital monitor so as to highlight pixel ranges of interest.

After calibration, the software can be used to simplify the measurement of sizes of flame features such as height or cell dimensions. After acquiring a frame, one may draw a line through the feature of interest, and the pixel coordinates are converted to measurements in millimeters. This method provides a completely non invasive measurement of flame height, and can be applied to time-averaged flame images. Another tool provides the intensity distribution along any drawn straight line on the image. Image analysis can also be expedited by the use of enhancement filters (for edge sharpening and detection, smoothing, and removal of noise) and morphology filters (for smoothing boundaries, amongst others). Arithmetic tools allow one to perform pixel-by-pixel arithmetic operations on one or two images. Summing two images (with 0.5 gain) will average the two pictures, while the subtraction of two images can be used to remove background noise or to locate an object (flame) while neglecting a background

(burner). The difference between two images can be obtained in this way, as a diagnostic of motion. Logical AND and OR operations are intended for masking uninteresting portions of the image, but we achieved the same effect, when necessary, by using defined "regions of interest" (ROI). Logical XOR was used for comparing similar images. The differences between two similar images are displayed in the result when this tool is employed.

Two-dimensional Fast Fourier Transform (FFT) can be used to convert the spatial variations of an image to the frequency domain. If desired, the transformed image can be modified so as to remove undesirable components (usually high-frequency noise), and then the image transformed back to the spatial mode. We found this feature unnecessary for the images obtained so far, but it may be useful in future work. One of the disadvantages of this process is the considerable time required for the transformations when the region of interest is relatively large.

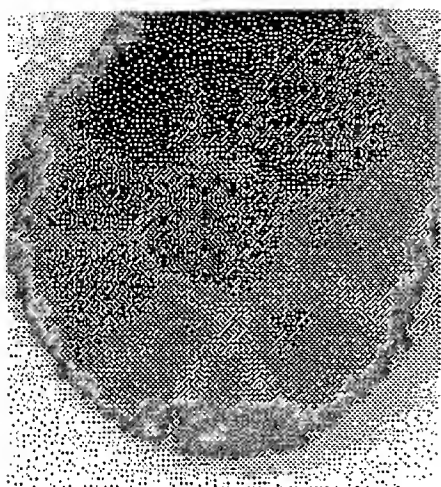
The so-called "particle tool", is designed to automatically find, count, and measure defined objects. The "particle" name comes from the fact that this software is often used in video microscopy, so that small particles appear macroscopic in the image. In our case, we define the objects to be cells within a structured flame. The boundaries between such cells are clearly distinguishable to the human eye, as is illustrated in Figure 10. These images were captured as described above, using the Framegrabber board. The intensities were inverted, and the images saved to a file in compressed TIFF format, using Global Lab Image software. (For the purpose of illustration in this report, no enhancement by digital filters was employed, although such preprocessing is essential to automated analysis.) The TIFF files were read and converted to PCX format by Image Alchemy software, then cropped to the region around the burner head, and dithered to 16 intensity values by WinGIF software so as to be reproducible with Windows drivers. For the purpose of writing reports, images can be imported to Word for Windows, which was used to prepare this document. The image quality available before dithering is substantially better than that reproduced in the figure. A better idea of the quality of the undithered image is obtained by holding the figure at arm's length! Nevertheless, these data clearly show how flame structure is affected by an applied electrical potential.

These images are of a flame having an air/propane ratio of 22/1, therefore an equivalence ratio of 0.88 (ignoring, as usual, the participation of ambient air). The images displayed represent subjective choices of "representative" cell structure at a given potential, and have been neither averaged nor randomly selected. We do not report the mean electric field in which these flames are produced because preliminary measurements reported after the summer, 1991 showed peculiar and decidedly nonlinear fields in flames perturbed as these are. Those earlier measurements showed that the upper regions of the flame acquire a potential very near that applied to the electrode. Because the flame above the reaction zone is quite conductive, the effective "electric field" is that across the non ionized bottom of the flame. These fields could be tens or hundreds of times larger than that (mis)calculated by dividing the applied potential by the gap between the electrode and the grounded burner.

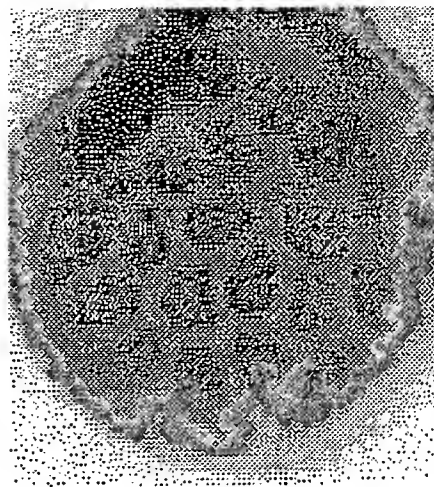
We do not claim that the images reproduced in Figure 10 quantitatively represent the magnitude of the perturbation effect. A statement of that nature will be made only after careful analysis of a larger number of images from videotapes. However, Table 1 below shows approximate numbers of cells in a larger survey of images at each potential. The power supply used to provide the electrode voltage current-limits at 300  $\mu$ A, and the perturbation at higher potentials could be larger than we have observed so far if larger currents were available. This possibility is will be resolved by the use of a higher-current supply, which is under construction.

Table 1

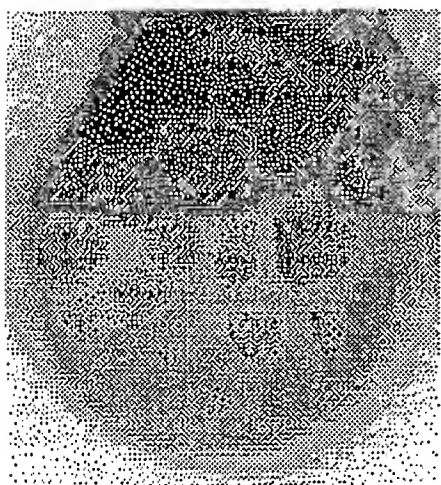
Applied Voltage	Number of cells
0	11
400	13
800	18
1200	20
1600	22
2000	26



0 volts



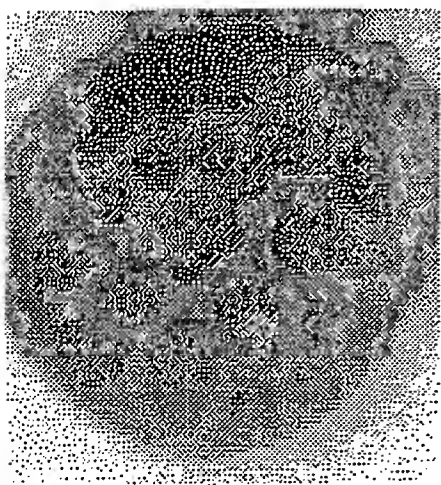
1200 volts



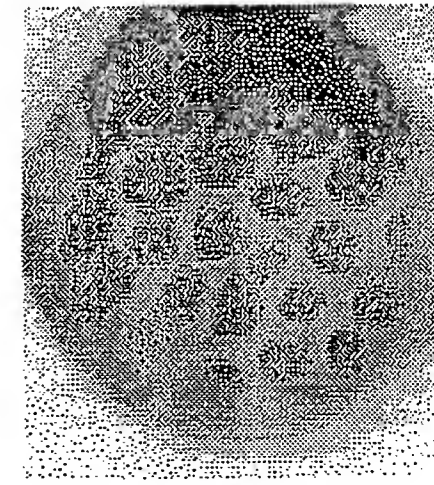
400 volts



1600 volts



800 volts



2000 volts

Figure 10. Images of perturbed cellular flames. View is from the top, and image intensities have been inverted, so that least-emitting regions appear lightest. It is clear that the size and number of such cells are strongly affected by the applied field.

## Conclusions

The data obtained to this point support the following conclusions.

1. Some premixed propane/air flames are susceptible to sizable perturbations by electric fields.
2. The polarity of the field is critical. An electrode negative with respect to the burner top (ground) causes no perturbation.
3. The equivalence ratio (the molar ratio of oxidant/fuel, relative to the stoichiometric amount) strongly affects the magnitude of the effect. Earlier (summer, 1991), it had been concluded that slightly rich flames were susceptible and that slightly lean flames were not. Since then, we have confirmed that propane/air flame susceptibility extends all the way to diffusion flames (where no air is premixed, and combustion proceeds on ambient air alone). This had been reported earlier for ethylene diffusion flames<sup>11</sup>
4. Not only the size of the flame, but the structure of cellular flames is altered by applied fields. This is the first report of this phenomenon.
5. The size and structure of flames can be captured and analyzed effectively using relatively conventional video equipment combined with computer software currently available.
6. The characteristic frequencies of fluctuations in flames also are altered by applied fields. Although we have not made as much progress on this aspect of the problem as on the spatial distribution, there is every reason to believe that a slightly modified, higher-speed version of our photon detection system will be successful in quantifying this effect.

## Continuing Analysis

These studies continue in our laboratory, beyond this official "final" reporting period. We will continue over the next few weeks and months to survey the large parameter space of these phenomena, which includes the equivalence ratio, absolute flow rates, and the applied potential. We will modify or replace the detection system needed for measurements of temporal variations, and will test a more powerful power supply to make certain that current limitations in the supply have not been determining

the magnitude of the measured perturbations. It is anticipated that these measurements will be reported in the refereed literature.

Preliminary reports of the investigations completed during summers, 1991 and 1992 have been made. These presentations were:

"Electrical Perturbation of Hydrocarbon Flames", Christine L. Maupin and Harold H. Harris, presented at the Third Annual Argonne Symposium for Undergraduates in Science, Engineering, and Mathematics, Argonne National Laboratory, Argonne, Illinois, November 6 and 7, 1992.

"Electric Field Effects on Propane/Air Flames", Harold H. Harris and B. Ganguly, presented at the 27th Midwest Regional Meeting of the American Chemical Society, Lawrence, Kansas, November 4-6, 1992. (This report was of work completed during summer, 1991).

#### Personnel

In addition to the Principal Investigator, these investigations have been accomplished by undergraduate UM-St. Louis chemistry student Christine Maupin, undergraduate UM-Rolla chemical engineering student Don Brown, and John Burroughs School physics teacher Jerome Taylor. All three of them worked during the summer of 1992. Ms. Maupin also earned one credit each semester for research accomplished during Winter and Fall semesters, 1992.

---

#### References

<sup>1</sup>James Lawton and Felix J. Weinberg, *Electrical Aspects of Combustion*, Clarendon Press, Oxford (1969).

<sup>2</sup>A. Smithells and H. Ingle, *J. Chem. Soc.*, **61**, 204 (1892).

<sup>3</sup>F. A. Smith and S. F. Pickering, *J. Res. Nat. Bur. Stand.*, **3**, 65, (1929); *Ind. Eng. Chem.*, **20**, 1012 (1928)

<sup>4</sup>V. P. Karpov, *J. Combustion Explosion and Shock Waves*, **3**, 1 (1965).

<sup>5</sup>T. Mitani and F. A. Williams, *Combustion and Flame*, **39**, 169 (1980).

<sup>6</sup>V. I. Kokochashvili, *Zurn. Fiz. Chim.*, **25**, 445 (1951) [in Russian].



---

<sup>7</sup>G. H. Markstein, "Experimental Studies of Flame-Front Instability", chapter D in *Nonsteady Flame Propagation*, G. H. Markstein, ed., Macmillan Co., New York (1964).

<sup>8</sup>G. H. Markstein, *J. Aeronaut. Sci.*, **3**, 18 (1951); "Instability pheonmena in combustion waves", *Fourth Symposium on Combustion*, Baltimore, pp. 43-59 (1953).

<sup>9</sup>M. A. Gorman, M. El-Hamdi, and K. A. Robbins, "Dynamics of Premixed Flames", in *Nonlinear Structures in Physical Systems*, Liu Lam and Hedley C. Morris, eds., Springer-Verlag, New York (1990); M. El-Hamdi, M. Gorman, K. A. Robbins, "Deterministic Chaos in Laminar Premixed Flames I: Experimental Identification", to appear in *Comb. Sci. Tech.* (private communication).

<sup>10</sup>Weinberg, F. J. "Flame Processes.". *Enciclopedia del petrolio e dei gas naturali*. Ente Nazionale Idrocarburi (1960).

<sup>11</sup>K. G. Payne and F. J. Weinberg, *Proc. Royal Soc.* **A279**, 316 (1959).

ANISOTROPIC PLASTIC DEFORMATION OF METALS

Steven L. Hatfield  
Research Assistant  
Department of Materials Science and Engineering

University of Kentucky  
Lexington, KY 40506-0046

Final Report for:  
Research Initiation Program  
Wright Laboratory

Sponsored by:  
Air Force Office of Scientific Research  
Eglin Air Force Base, Florida

and

University of Kentucky

December 1992

## ANISOTROPIC PLASTIC DEFORMATION OF METALS

Steven L. Hatfield  
Research Assistant  
Department of Materials Science and Engineering  
University of Kentucky

### Abstract

This research project is in the broad general field of the theoretical understanding of plastic deformation in anisotropic metals. Two methods were implemented to determine grain orientation distributions for a specific metal. Pole figures were measured experimentally using an x-ray diffractometer and pole figures were calculated theoretically using a simulation program. Appropriate methodology is described with the intention of providing a basis for subsequent calculations (performed elsewhere) of anisotropic yield criteria and flow rules.

This project was carried out in cooperation with "Textural Characterization of Deformed Metals", RIP number 19. The research was developed simultaneously under the direction of the same research supervisor and, therefore, the information contained within each report is applicable to both. For this reason, the background and general research plan are identical in the two reports which differ only in emphasis on experimental data in this paper versus theoretical modeling in the other report.

## ANISOTROPIC PLASTIC DEFORMATION OF METALS

Steven L. Hatfield

### INTRODUCTION

It is frequently found that the mechanical properties of wrought metal products are not the same in all directions. The dependence of properties on orientation is called anisotropy [1]. Independence of properties on orientation is referred to as isotropy or the material is called isotropic. Very often anisotropy is troublesome, as in the formation of "ears" or non-uniform deformation in deep-drawn cups. However, it can also be beneficial, as when different strengths are required in different directions; for example, in a cylindrical pressure vessel. It is up to the ingenuity of engineers and materials scientists to control the deformation process of wrought metal products in order to derive the greatest benefit from the attendant structural alterations.

In striving to achieve this goal, the main emphasis of past development has been aimed toward isotropic materials. Deformation processing is frequently carried out at elevated temperatures (for example, hot rolling). Grain growth and recrystallization are enhanced at these temperatures, tending to keep the grain structure equiaxed and the material, therefore, relatively isotropic.

Two factors have promoted this past development. One has already been stated: very often anisotropy is troublesome. The other reason is the paucity of mathematical models available to the analyst attempting to understand and predict anisotropic plastic deformation.

In the early sixties, analyses such as those of Paul [2] and Greszczuk [3] opened the door to application of the work of Lekhnitskii [4] on anisotropic elasticity and interpretations such as the Primer [5]. Since that time, research interest in the necessarily anisotropic, composite materials has relied on these early elastic theories, even in the investigation of fracture. On the other hand, theories of plasticity have mainly assumed isotropic deformation.

The principal exceptions have been theories proposed by Hill [6-8] and by Hosford [9]. Of these, only the 1948 theory of Hill is fully three-dimensional. The other three are attempts to improve this early theory in the relatively simple case of plane stress. Plane stress is an approximation often applied to sheet metal deformation. The first theory of Hill, applied to plane stress deformation, leads to results that are inconsistent with experiments when simple tension is compared with balanced biaxial stretching. This discrepancy motivated the later theories, all of which are formulated to apply only to plane stress.

The second theory proposed by Hill is restricted to sheet materials that are anisotropic only with respect to the thickness direction; within the plane of the sheet, the material is assumed to be isotropic in its

mechanical properties. This is an extremely restrictive idealization that severely limits applicability of this theory even though it incorporates a totally arbitrary "Hill Index" as an adjustable parameter that can be used to improve agreement between calculated and experimental results.

Both the theory proposed by Hosford and the most recent theory proposed by Hill accommodate planar anisotropy. Each also features a totally arbitrary, adjustable parameter. Consequently, it can be expected that reasonably good agreement can be obtained between theory and experiment using either of them. In fact, Hosford and co-workers [11-13] have shown some very favorable comparisons. At present, no one has yet published any calculations based on the recent Hill theory.

A substantially different approach to anisotropic plasticity theory is based on the seminal work of G.I. Taylor [13]. The so-called Taylor factor is a theoretical ratio of polycrystal to monocrystal yield strengths. This calculation, subsequently modified by Bishop and Hill [14] and Chin and Mammel [15], requires that the distribution of grain orientations in the polycrystal be specified. Taylor assumed a random distribution. He also assumed a polycrystalline deformation corresponding to homogeneous axial tension of an isotropic material. Material anisotropy can readily be introduced into such a calculation by prescribing a non-random distribution of grain orientations. Three-dimensionality can be dealt with through consideration of different deformation paths.

Current research into such anisotropic plasticity theories has been conducted by Kochs [16] and others at Los Alamos National Laboratory. Codes developed there are capable of predicting the fully three-dimensional yield surface, and corresponding plastic flow rule, for anisotropic, polycrystalline metals. The input required for such codes comprise uniaxial yield strengths and the grain orientation distribution function. With additional information concerning hardening, these codes can also predict subsequent flow surfaces and subsequent flow rules.

#### RESEARCH PLAN

Grain orientation distributions for a particular material of interest can be created in two ways: experimental measurement by an x-ray diffractometer and by theoretical calculations (codes). These codes can be further utilized to produce five-dimensional yield surfaces- an ultimate goal of mechanical analysis.

Some of the criteria for choosing a material for this type of research includes: workability, to attain several distinct levels of deformation; known anisotropy, so that the experimental grain orientation distributions are not always random; and other factors such as the ease of preparation of experimental specimens and availability of material. After consulting with the focal lab, it was determined that a suitable material for establishing the desired methodology, which would simultaneously possess appropriate material properties for beneficial results in itself, would be OFE copper.

In order to facilitate determination of the experimental pole figures, modifications were necessary to the existing equipment. The University of Kentucky Department of Materials Science and Engineering has a Rigaku x-ray diffractometer outfitted with a  $\Theta$ - $2\Theta$  goniometer. Because of recent "upgrades" to the x-ray capabilities of the equipment and software, the limited pole figure capabilities of the system were temporarily eliminated. In order to replace these options on the existing equipment with modern, convenient, PC-ready capabilities, it was necessary to send the unit to Japan for installation of new stepping motors and gears. In addition, the University acquired Rikagu's "Attachment Control" board and "Texture" software. One accomplishment of this research project was to leverage approximately \$8000 of project funds into a \$35,000 purchase of this new equipment, which is of central importance in follow-on research in this area.

On the computational side, Dr. Anthony Rollett has developed a very useful computer code [21] at Los Alamos National Laboratory for calculating theoretical pole figures. It is based upon postulated polycrystalline grain orientation distributions. A related code, developed there, can then take the postulated polycrystalline grain orientation distribution as the basis for computation of a texture-dependent polycrystalline yield surface. The University of Kentucky has obtained from Los Alamos copies of both popLA (preferred orientation package-Los Alamos) and LApp (Los Alamos polycrystal plasticity code). The basic research plan was to acquire the necessary x-ray equipment, determine pole figures for the selected material, and to apply these Los Alamos codes to the data generated.



## METHODOLOGY

Having selected OFE copper as the project material, an initial stock of 8 mm (5/16 in.) diameter rod was obtained and fully characterized. Initially, tests were conducted to obtain yield strengths and other mechanical properties for specimens deformed at low strain rates (Standard Tensile Test). Because of the obvious applicability to technology, high strain rate deformation behavior data was also desired. To characterize this, both Taylor-Anvil Tests [23] and the Rod-on-Rod (ROR) Impact Tests [24] were performed using cylindrical projectiles.

In the Taylor Impact test, a cylindrical copper rod of 7.62 mm (0.3 inch) diameter is fired at high velocity into a large steel anvil, Figure 1a. In the Rod-on-Rod (ROR) Test, a similar impacting rod as that used in the Taylor test, 25 mm (1 inch) long, is impacted against a longer, 152 mm (6 inch), rod of the same material and cross-section, Figure 1b.

Special emphasis was placed on the ROR tests. By comparison to the anvil tests this test method eliminates rod-anvil compliance mismatch and frictional effects during impact. It also has the advantage of one continuous deformation medium throughout the impact sequence (especially beneficial for continuum code evaluations). For these reasons, ROR testing became the principal technique in the study of high strain rate behavior.

After the ROR specimens were impacted and recovered, they were sectioned axially, mounted, polished and etched for evaluation of their microstructural characteristics. A striking aspect of their microstructures

was the occurrence of voids near the specimen axis near the impact edge. The severity of void formation depended upon the impact velocity and on the initial grain size. Investigation of this aspect of high strain rate material deformation behavior became a primary concern in the microstructural characteristic documentation of these specimens. This investigation resulted in a publication entitled "Void Formation in OFE Copper" that was presented at the 1992 Hypervelocity Impact Symposium and accepted for publication in the Journal of Impact Engineering [25].

The aforementioned microstructural characterization comprised a superficial analysis of the deformation. This is important in relation to damage models of material constitutive behavior for use in finite element, continuum codes. These voids dramatically indicate the occurrence of severe hydrostatic tension during what is commonly considered a compression test. This is a subject that certainly requires further study and must be taken into consideration in constitutive modeling.

However, the physical structure of the material on a much finer scale is what determines mechanical anisotropy and is the principal object of this project. Materials that show a preferred crystallographic orientation or texture exhibit a certain amount of mechanical anisotropy. Even cubic crystals such as copper, which have a high degree of symmetry become textured as a result of plastic deformation. The subsequent degree of anisotropy in a polycrystalline material is directly dependent on the properties of the individual crystals and the fraction oriented in a particular direction [26].

Texture can be quantitatively described by pole figure data. Once this data is obtained (and stored in ASCII format) it can be processed by appropriate software (popLA) to produce a corresponding grain orientation distribution, i.e., a three-dimensional Orientation Distribution Function (ODF). The ODF can subsequently be incorporated into a theoretical model of polycrystal plasticity (LApp) that will create a three-dimensional, anisotropic yield surface.

The experimental pole figures themselves are the backbone of the comparative analysis. They provide the baseline for development and fine-tuning of the data that comprises the eventual yield surface.

The test samples that were used in the Rigaku x-ray unit to produce pole figures were prepared as follows. An impact specimen was sliced perpendicular to its axis using a wafering saw with a thickness of 2.5 mm (0.10 inch). The resulting wafers were approximately 5 mm (0.2 inch) thick. They were ultrasonically cleaned to remove any materials introduced by the sectioning process. The wafers were then mechanically polished using 1  $\mu$ m and 0.3  $\mu$ m alumina powder to remove the deformation layer created by wafering. The specimen was ultrasonically cleaned after each polishing step to prevent cross-contamination between alumina particle sizes. After the polishing was complete the specimens were then chemically etched to remove the fine layer of deformation created by polishing. Careful attention must be paid to avoid overheating or plastic deformation during the polishing process. During chemical etching material must be removed

uniformly and without pitting. The finished specimen may have a "matte" appearance, but surfaces must be flat and parallel [18].

Each prepared sample was secured in the mounting ring of the pole figure device using ordinary, clear pressure-sensitive tape. Note that the surface of the sample was not covered with tape. The tape was placed around the perimeter of the sample so that sufficient area is left uncovered for testing. Care must be taken so that the sample surface is in the same plane as the mounting ring of the pole figure device. Because of rotations and the lack of a reference "rolling direction" in rod-stock copper, it is important to initially identify a reference direction in the rod so that subsequent experimental figures are the same relative to each other.

#### GENERAL ANALYSIS OF POLE FIGURES

A pole figure is a stereographic projection, with a specified orientation relative to the specimen, that shows the variation of pole density with pole orientation for a selected set of crystal planes [27]. The basic method to display preferred orientation is to represent the orientation of a particular crystal direction  $[uvw]$  or the normal to a lattice plane  $(hkl)$  in a specimen coordinate system. The crystal direction is first projected onto a sphere of unit radius surrounding the crystal and the point on the sphere is defined by two angles, a co-latitude  $\alpha$ , measured from the pole N, and an azimuth  $\beta$ , measured from an equatorial point E counterclockwise, Figure 2 [26]. This sphere is usually

represented by its projection onto a plane. The pole figure shows where and to what extent (quantitatively) various orientations of crystals occur with respect to fixed directions within the specimen, for example, the rolling, transverse, and normal directions. Generally, a pole figure is derived from a spherical projection and lines are extended parallel to various crystallographic directions, or perpendicular to various crystallographic planes, in the crystal, from the center until they meet the surface of the sphere. These intersections of the various directions with the sphere are called poles and the reference points P and E in Figure 2 are usually selected as principal crystallographic axes. Every other pole can then be located by the two angles  $\alpha$  and  $\beta$  as described above.

In order to transfer this three-dimensional sphere onto a two-dimensional sheet of paper, the sphere is projected onto a plane. Common ways of projecting spheres onto planes include cylindrical, conical, polyconic and circular projections [27]. There are two kinds of circular projections: stereographic and equal area. A stereographic net is constructed on a plane that slices through the center of the sphere perpendicular to the north-pole and south-pole axis.

Because of variations in intensities due to the way a crystal may be facing, its orientation can be found by measuring the intensities at different angles by x-ray diffraction and plotting their angular coordinates onto a net. Then, by laying a standard projection on top of the net, which has all the intensity points plotted onto it, one can tell which of the poles are appearing and relate that to the sample

orientation [27]. To further simplify the pole map, equal intensity contours are drawn for various intensities from the lowest to the highest, so that the end result is something like a topographical map. The map is circular in outline corresponding to the stereographic plane within the sphere. The locations of peaks or mountains then correspond to the locations of certain crystallographic poles on the plane. The higher the peak, the greater number of such planes in the crystal. But, a crystal has only a specified number of each sort of plane. However, if the center sample is a polycrystal, an intensity peak indicates preferential alignment of certain planes with respect to poles N and E. Now, though, these reference points must relate to specimen orientation.

There are two methods generally used to make measurements for pole figures; one is transmission and the other is reflection. The central region of the pole figure is inaccessible to any transmission method and can be explored only by a reflection technique [27]. The most popular technique is the Schulz reflection method [27] because of the ease of sample preparation and accessibility to the central region of the pole figure. In this report, all pole figures and their analyses are based on the Schulz reflection method. The specimen must be of effectively infinite thickness (relative to the depth of penetration of the x-ray beam), or some rays will actually transmit through the sample, requiring extra data correction.

## RESULTS AND DISCUSSION

The first step in producing a pole figure is to obtain a powder standard of the material of interest. A powder sample is meant to ensure a completely random distribution of grain orientations. A powder standard was prepared by filing the undeformed specimen material. A  $2\theta$  scan of the standard (Figure 3) was obtained by using x-ray diffraction techniques. This shows the relative peak intensities for different crystal planes in the material. Because copper has an FCC crystal structure the (111), (200), and (220) planes are expected to be between 38 and 78 degrees on the  $2\theta$  scan. Figure 3 shows the (111) plane at 43.4 degrees, the (200) plane at 50.6 degrees, and the (220) plane at 74.2 degrees. These angles are important because these planes are the poles subsequently used when creating pole figures.

After the diffraction work is completed on the powder standard, the pole figure device and pole figure program are used to collect data from a deformed wafer to construct a pole figure. Check the operation procedure manual of the x-ray unit to see how pole figures are compiled on the particular unit being used. To construct an  $(hkl)$  pole figure the program will ask for the  $2\theta$  angle at which the  $(hkl)$  plane is located. For example, for copper the (111) reflection is at  $2\theta = 43.4$  degrees. Once the  $2\theta$  angle is entered, the x-ray unit proceeds to that angle to start intensity measurements to construct a pole figure. After data collection is complete the data is stored in a data file with the filename followed by the extension RAW. At this point the pole figure can be plotted on a graphics plotter to produce a hard copy for future examination. When the

(111) pole figure of the material is completed then we proceed to repeat the process to produce the (200) and (220) pole figures of the material.

Before beginning on deformed wafers, pole figure data was obtained from the powder sample. Because it was assumed to be random, lines of equal x-ray intensity should plot as circles on the pole figure. As shown in Figures 4, 5 and 6. These pole figures can be seen in Figures 3 (111), 5 (200) and 6 (220) planes. These poles generally show the random orientation (lack of texture) to be expected from a powder sample.

Having completed analysis of the powder standard we proceed to run a pole figure analysis on the prepared specimen of interest, in this case a wafer from an as received OFE copper rod. Before the wafering process a line was drawn along the axis of the rod to establish reference point E so that all samples could be oriented the same in the pole figure device. First we do a  $2\theta$  scan of the specimen using the same scan conditions that were used on the powder standard, in this case: start 30.0 degrees, stop 80.0 degrees, scan speed was set at 5.0, and sampling interval was set at 0.050. We then set the pole figure scan conditions to those used on the standard, in this case: tilt start 15.0 degrees, tilt stop 78 degrees, tilt step 5.0 degrees and azimuth step 8.0 degrees. After the (111), (200), and (220) pole figure data of the textured sample are collected and saved, the pole figures are plotted. These are shown in Figures 7, 8 and 9. The ASCII data files must subsequently be converted, using a program to be provided by Rigaku, so that theoretical modeling of the data can be performed.



Figures 7, 8 and 9 show preferred orientations for each respective pole, i.e., texture. The sample symmetry contains a rotation axis of infinite order which coincides with the rod axis. The orientation distribution is then independent of a rotation about this axis and, as expected, the pole figures are axially symmetric. Textures of this type are called axially symmetric or fiber textures. They frequently occur in materials fabricated by axially symmetric deformation such as fibers or wires. These pole figures graphically illustrate the anisotropy of the material and from them grain orientation distributions can be obtained.

The industrial importance of preferred orientation lies in the effect, often very marked, which it has on the overall, macroscopic properties of materials. Given the fact that all single crystals are anisotropic, i.e., have different properties in different directions, it follows that an aggregate having preferred orientation must also be anisotropic to a greater or lesser degree [27]. Such properties may or may not be beneficial, depending on the intended use of the material. For example, if a steel sheet was to be formed into a cup by deep drawing, a texture with (111) planes parallel to the surface of the sheet would make the steel less likely to crack during the severe deformation of deep drawing. However, if the part to be formed by deep drawing has an unsymmetrical shape, a different texture, or none at all, might yield better results [27].

Most of the problems that arose in this project were due to specimen preparation. Great care must be taken when sectioning the specimen to

ensure that its surface is precisely perpendicular to its axis. After much trial and error using a wafering saw, this process was eventually performed to the precision needed. Another barrier to overcome was the polishing technique. Great care is also required here, to ensure that plane surfaces remain plane. Otherwise, the fiber texture will be obscured in the pole figure plot. Repeated attempts were required before this process was carried out acceptably.

#### CONCLUSIONS

Pole figures can be obtained from suitably equipped x-ray diffraction units. To simplify the pole map, contours are drawn around intensities in gradation from the lowest intensity to the highest intensity, so that the result resembles a topographical map with peaks or mountains appearing in areas that can be attributed to certain poles. Extreme care must be taken when preparing samples for pole figure analysis to ensure known orientations. During the pole figure procedure data files are produced which can be used in subsequent theoretical modeling of the material anisotropy.

Texture measurement is extremely significant because texture control is potentially an important tool in modern metallurgy. Often a certain texture can enhance the formability of the material. This necessitates measurement and evaluation. Metallurgists are concerned with modifying production processes to produce textures that endow metals with a set of required properties. Modern application of this research focuses on problems such as deep drawing of steel, ridging phenomena in stainless

steel, cohesion along grain boundaries, and the production of oriented eutectics to achieve improved properties [26].

#### ACKNOWLEDGMENTS

The author would like to thank Joel House and Thad Wallace at Eglin Air Force Base, Florida and Dr. Peter P. Gillis, Kenny Boggs and Larry Rice at the University of Kentucky for their assistance in compiling this report.

## Classic Taylor Test

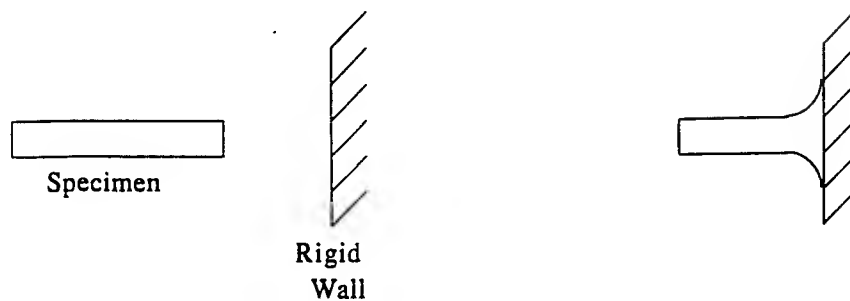


FIGURE 1a: Schematic Diagram of the Classic Taylor Test.  
ref [25]

## Symmetric Rod Impact Test

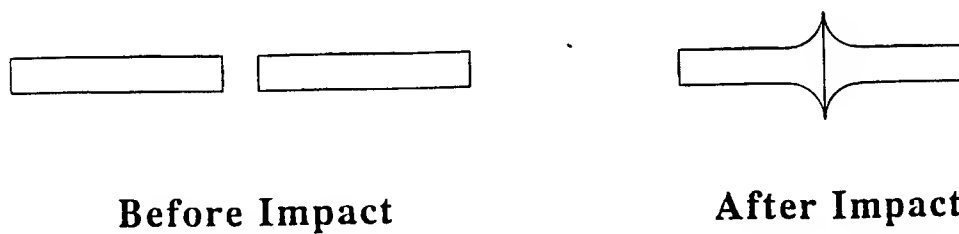


FIGURE 1b: Schematic Diagram of the Symmetric Rod (Rod-on-Rod) Impact  
Test. ref [25]

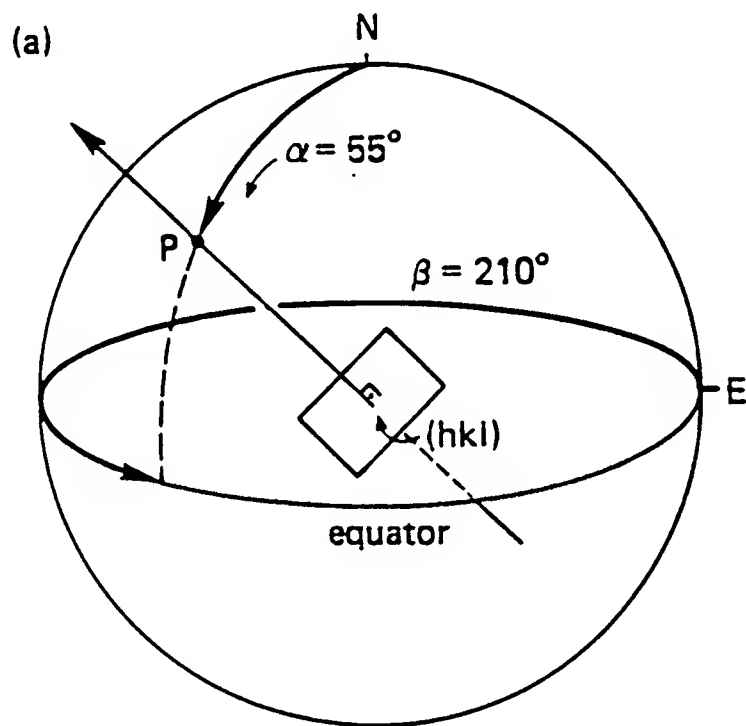


FIGURE 2: Spherical Coordinates for a Point P.  
ref [26]

Z00001.RAW  
CU POWDER STANDARD2;38-78,5,.05

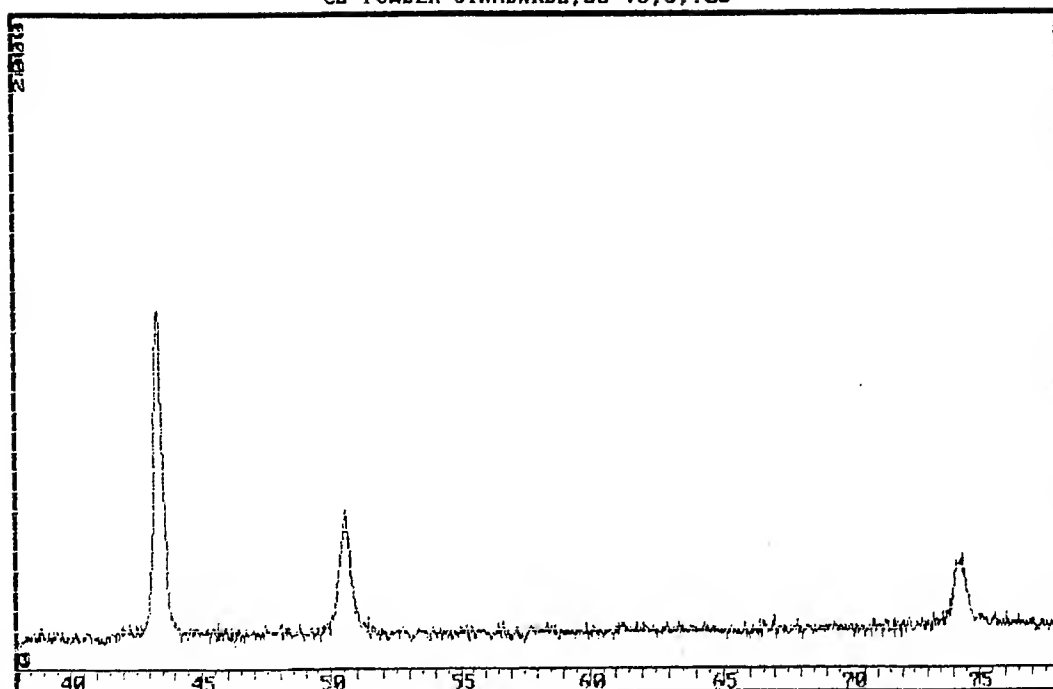


FIGURE 3:  $2\theta$  scan for a Copper Standard.

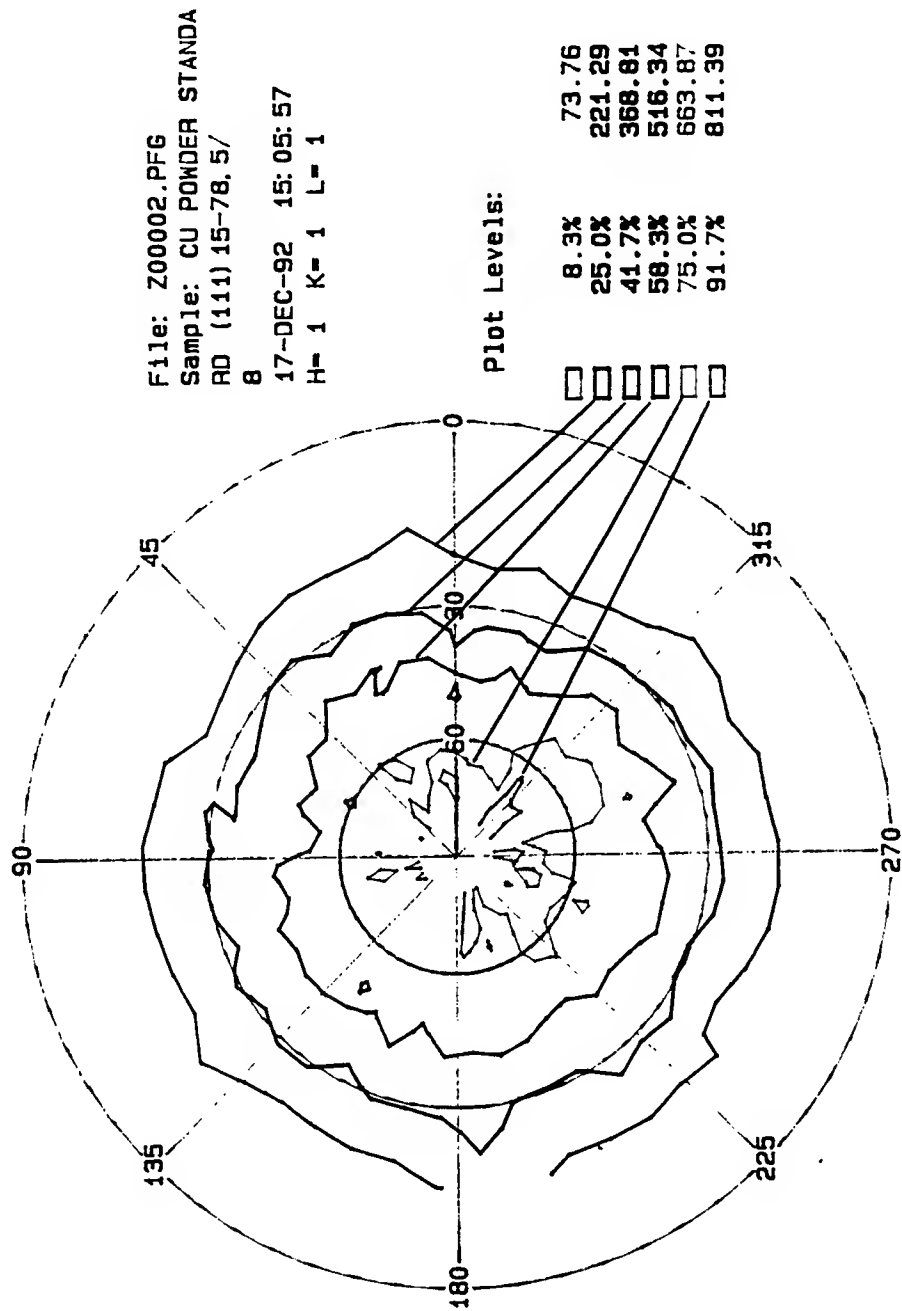


FIGURE 4: (111) Pole Figure for a Copper Powder Standard  
Showing a Random Orientation of Grains.

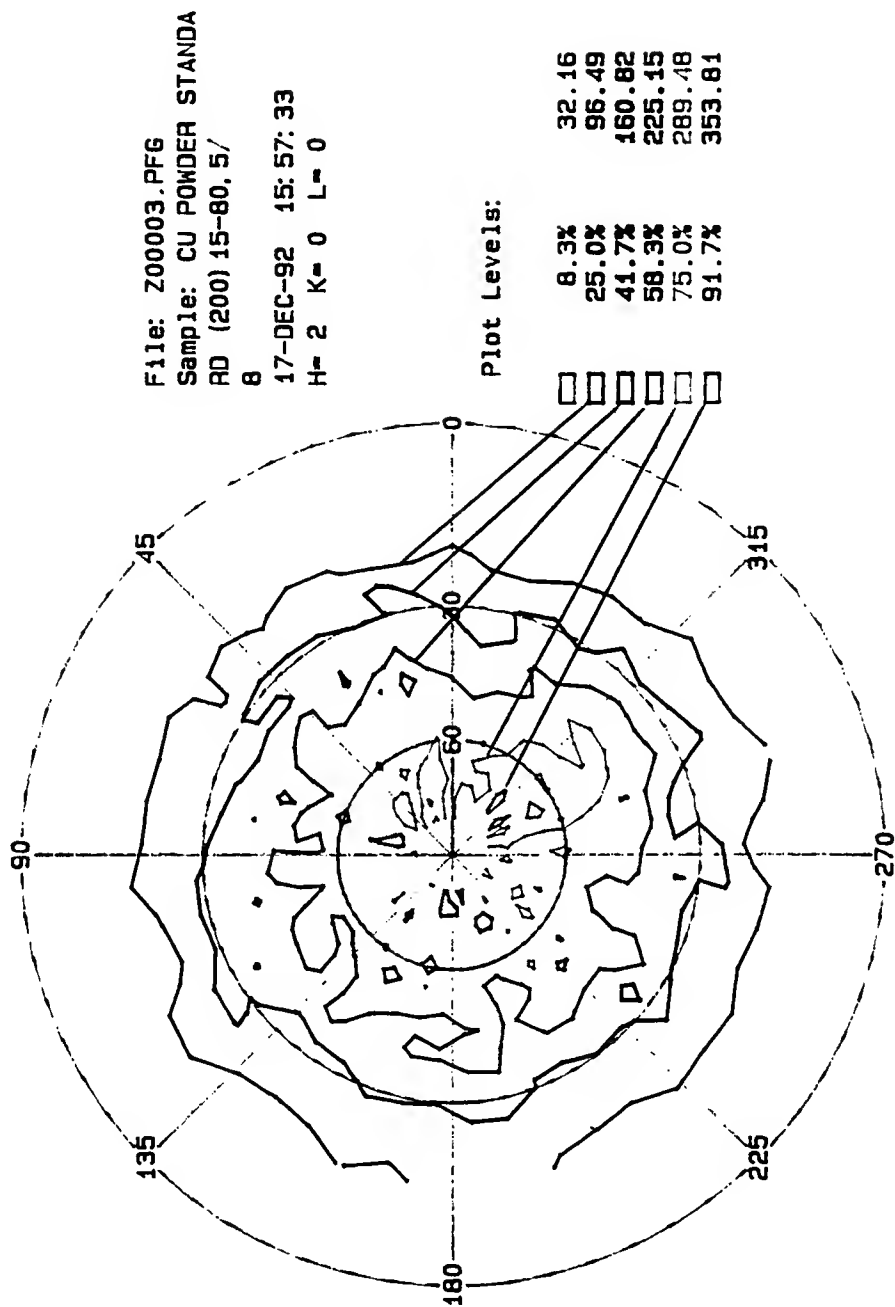


FIGURE 5: (200) Pole Figure for a Copper Powder Standard  
Showing a Random Orientation of Grains.



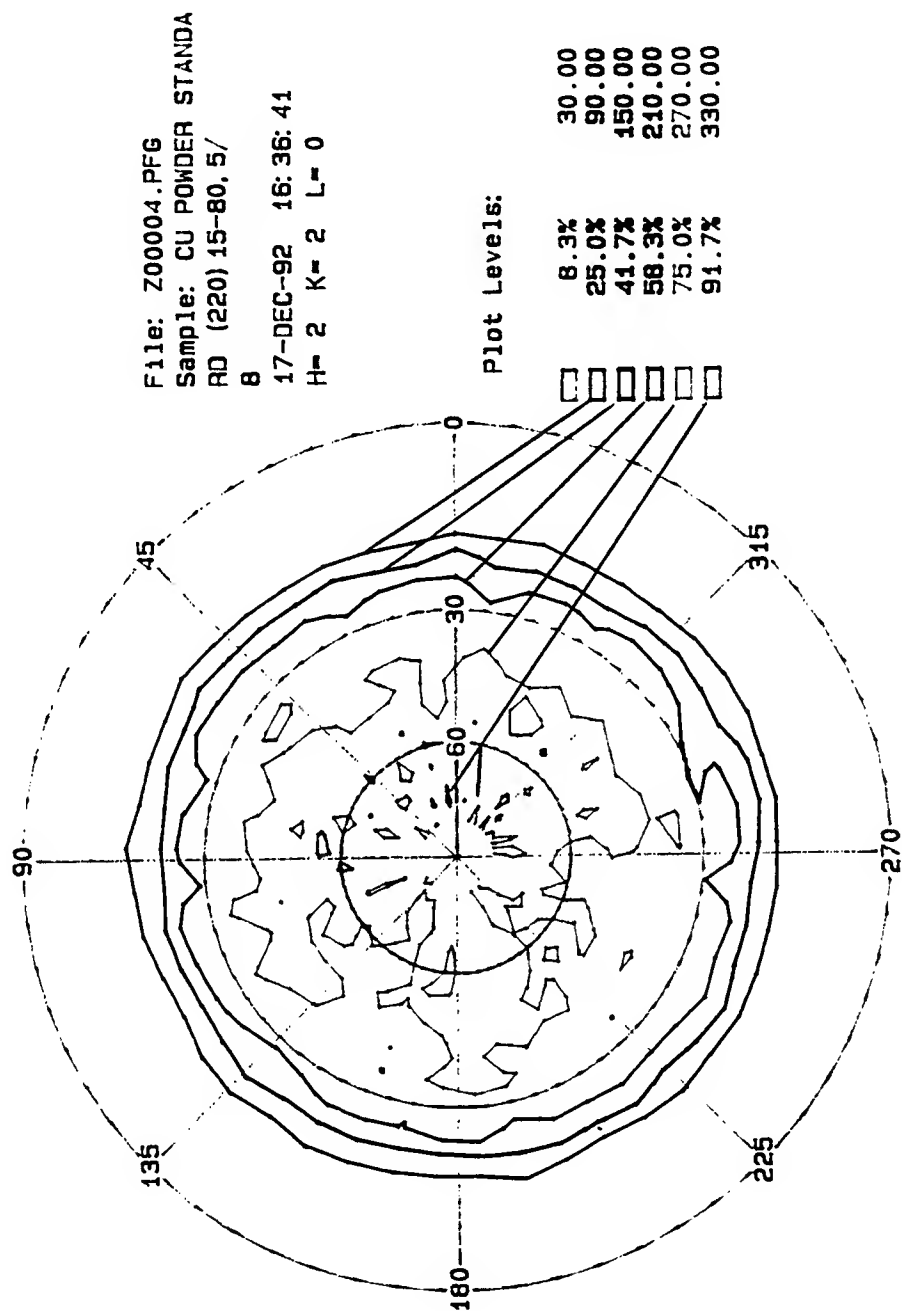


FIGURE 6: (220) Pole Figure for a Copper Powder Standard  
Showing a Random Orientation of Grains.

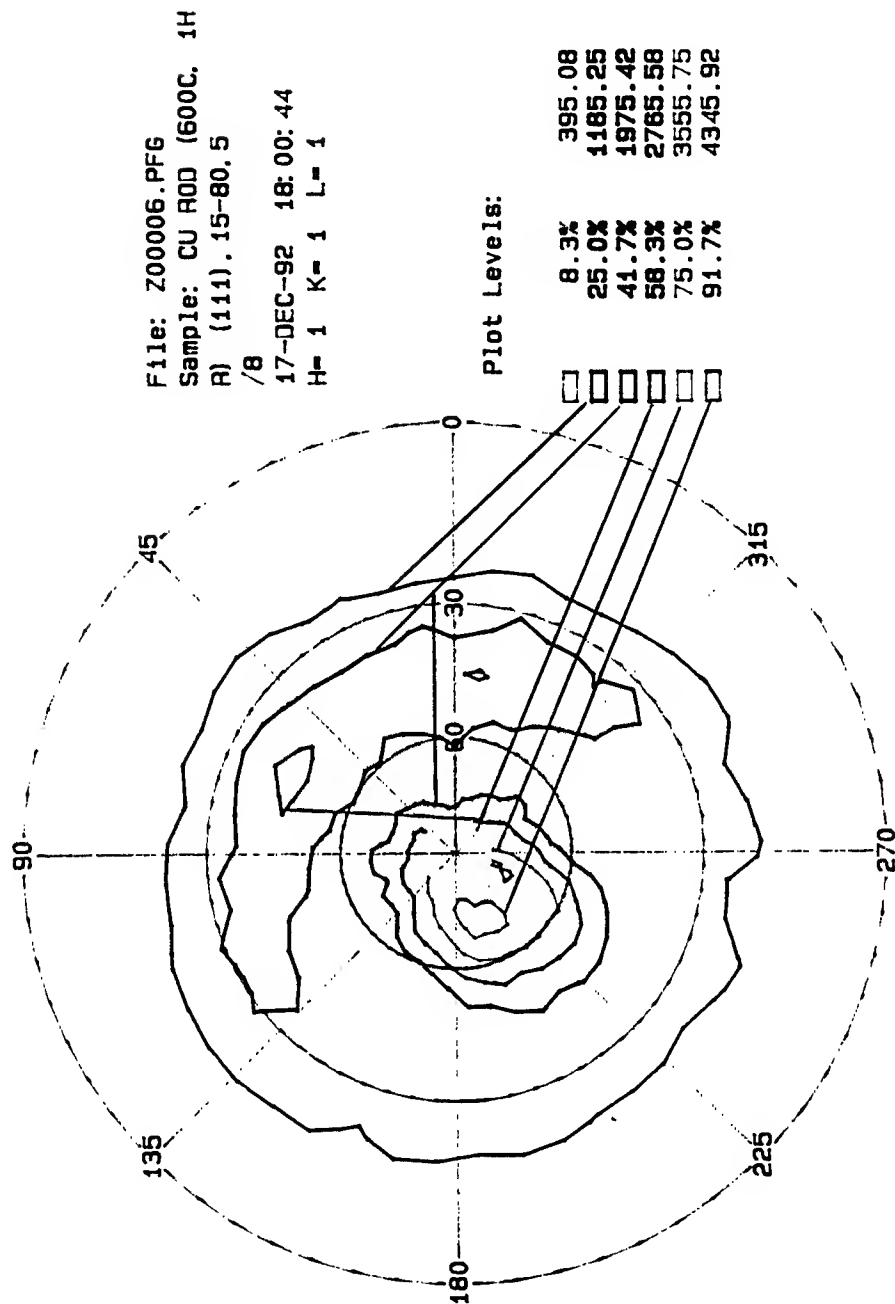


FIGURE 7: (111) Pole Figure Describing the Texture of a Cross-Section Perpendicular to the Axis of the Undeformed Copper Rod.

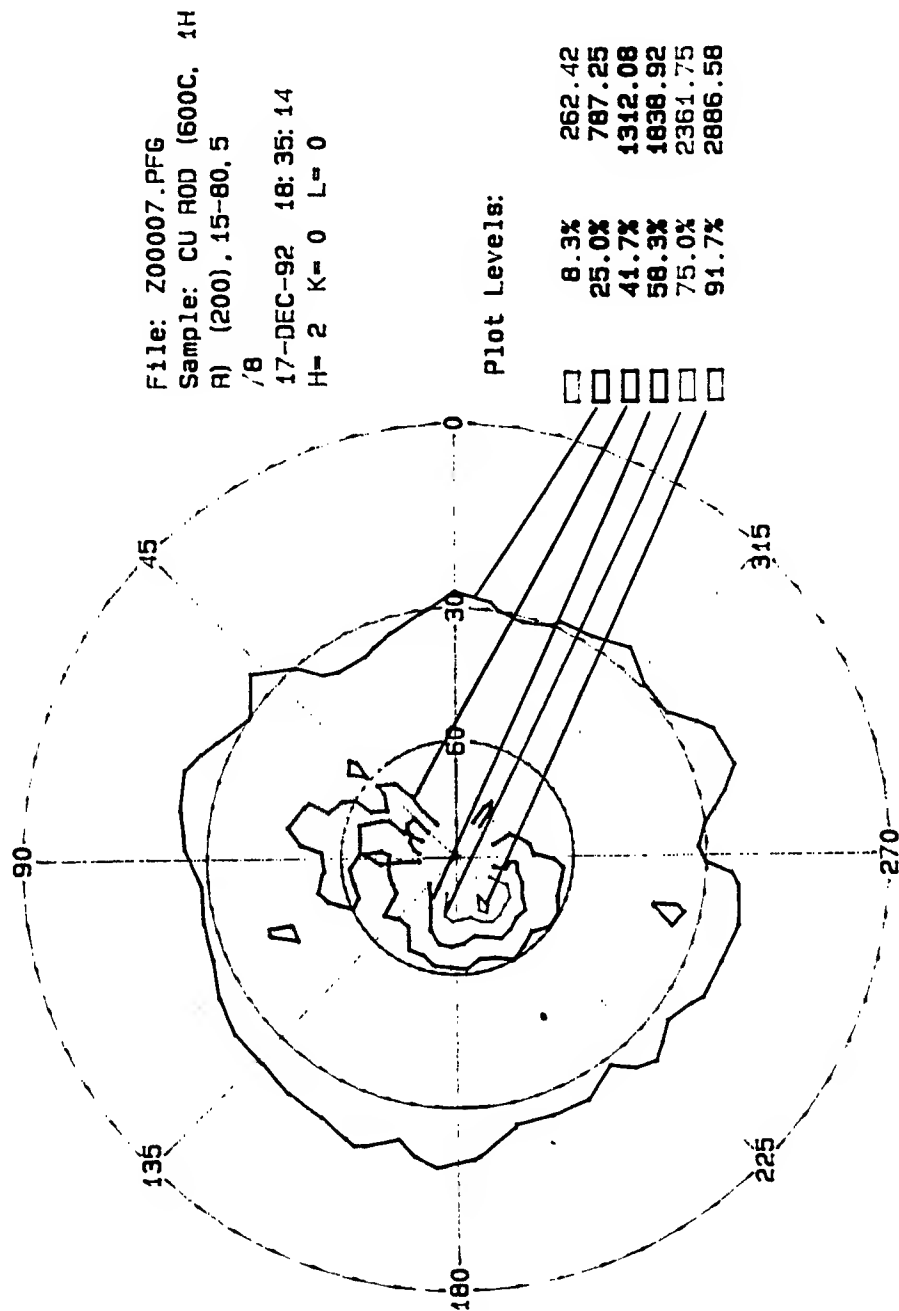


FIGURE 8: (200) Pole Figure Describing the Texture of a Cross-Section Perpendicular to the Axis of the Undeformed Copper Rod.

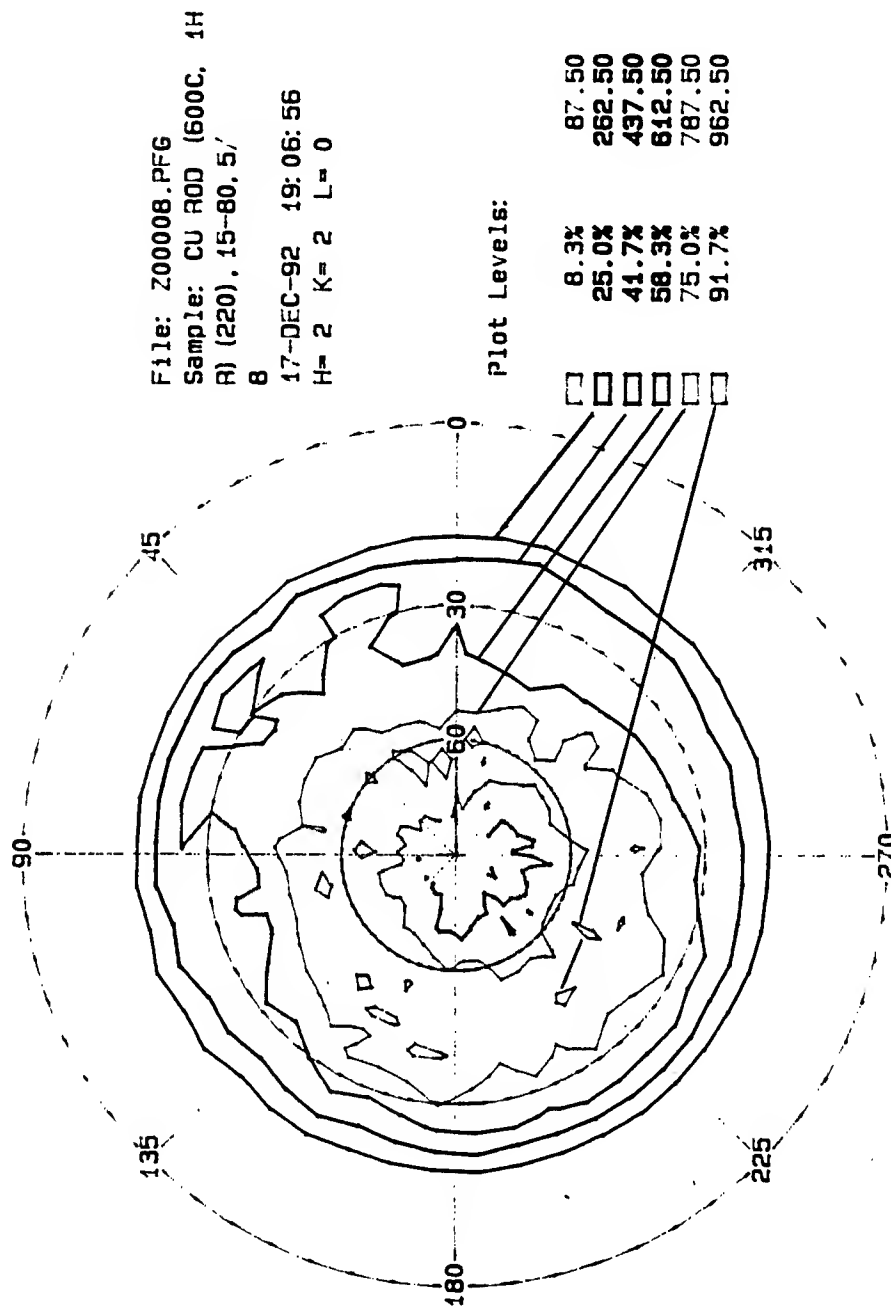


FIGURE 9: (220) Pole Figure Describing the Texture of a Cross-Section Perpendicular to the Axis of the Undeformed Copper Rod.

#### REFERENCES

1. G. E. Dieter, Mechanical Metallurgy, McGraw-Hill, 3rd edition, 1986, p.322.
2. B. Paul, "Prediction of Elastic Constants of Multiphase Materials". AIME Trans. 218 36 (1960).
3. L. B. Greszczuk, "Elastic Constants and Analysis Methods for Filament Wound Shell Structures," Douglas Aircraft Missile & Space Systems Division Report SM-45849, 1964.
4. S. G. Lekhnitskii, Theory of Elasticity of an Anisotropic Elastic Body, Holden-Day, 1963.
5. J. E. Ashton, J. C. Halpin and P. H. Petit, Primer on Composite Materials, Technomic, 1969.
6. R. Hill, "A Theory of the Yielding and Flow of Anisotropic Plastic Metals", Proc. Roy. Soc. London A193 281 (1948).
7. R. Hill, "Theoretical Plasticity of Textured Aggregates", Proc. Camb. Phil. Soc. 85 179 (1979).
8. R. Hill, "Constitutive Modeling of Orthotropic Plasticity in Sheet Metals", J. Mech. Phys. Solids 38 405 (1990).
9. W. F. Hosford, "On Yield Loci of Anisotropic Cubic Metals", Proc. 7th North American Metalworking Conference, SME, Dearborn MI, 1980, p. 191.
10. W. F. Hosford, "Comments on Anisotropic Yield Criteria", Int. J. Mech. Sci. 27 423 (1985).
11. W. F. Hosford and R. M. Caddell, Metal Forming: Mechanics and Metallurgy, Prentice Hall, 1983.
12. A. Grof and W. F. Hosford, "The Effect of R-Value on Calculated Forming Limit Curves", Forming Limit Diagrams: Concepts, Methods and Applications, R. F. Wagoner, K. S. Chan and S. P. Keeler, Eds., TMS-AIME, (1989) p. 153.
13. G. I. Taylor, "Plastic Strain in Metals", J. Inst. Met. 62 307 (1938).
14. J. F. W. Bishop and R. Hill, "A Theory of the Plastic Distortion of a Polycrystalline Aggregate Under Combined Stresses" and "A Theoretical Derivation of the Plastic Properties of a Polycrystalline Face-Centered Metal", Phil. Mag. 42 414 and 1298 (1951).

15. G. Y. Chin and W. L. Mammel, "Generalization and Equivalence of the Minimum Work (Taylor) and Maximum Work (Bishop-Hill) Principles for Crystal Plasticity", Trans. Metall. Soc. AIME 245 1211 (1969).
16. A. D. Rollett, M. G. Stout and U. F. Kocks, "Polycrystal Plasticity as Applied to the Problem of In-Plane Anisotropy in Rolled Cubic Metals", Advances in Plasticity '89, A. F. Khan, Ed., Pergamon, 1989, p. 69.
17. ASTM Standard E8-89b
18. ASTM Standard E81-89
19. J. L. Mayes, "Material Characterization and Evaluation for Penetration Applications: Physical Properties", Report to AFOSR RDL Summer Research Program Office dated 16 August 1991.
20. S. L. Hatfield, "Material Characterization and Evaluation for Penetration Applications: Mechanical Properties", Report to AFOSR RDL Summer Research Program Office dated 16 August 1991.
21. J. S. Kallend, U. F. Kocks, A. D. Rollett and H. R. Wenk, "Operational Texture Analysis", Matls. Sci. Eng. A132 (1991).
22. A. D. Rollett, private communications.
23. G. I. Taylor, "The Use of Flat-Ended Projectiles for Determining Dynamic Yield Stress", Proc. Roy. Soc. (London), 194 289 (1948)
24. D. Erlich, D. A. Shockey and L. Seaman, "Symmetric Rod Impact Technique of Dynamic Yield Determination", AIP Conference Proceedings, No. 78, Second Topical Conference on Shock Waves in Condensed Matter, Menlo Park, CA, 1981, pp. 402-406.
25. J. L. Mayes, S. L. Hatfield, P. P. Gillis and J. W. House, "Void Formation in OFE Copper", accepted for publication on the Journal of Impact Engineering
26. H. R. Wenk, Preferred Orientation in Deformed Metals and Rocks: An Introduction to Modern Texture Analysis, Harcourt, Brace and Jovanovich (1985)
27. B. D. Cullity, Elements of X-Ray Diffraction, Addison-Wesley, 2nd ed. (1978).

INVESTIGATION OF THE COMBUSTION CHARACTERISTICS OF CONFINED  
COANNULAR SWIRLING JETS WITH A SUDDEN EXPANSION  
[TASK 150 COMBUSTOR]

Paul O. Hedman, Professor  
Department of Chemical Engineering

David K. Pyper and David L. Warren, Master Candidates  
Department of Mechanical Engineering

Brigham Young University  
Provo, Utah 84602

Final Report for:  
Research Initiation Program  
Aero Propulsion and Power Laboratory  
Wright-Patterson AFB, OH 45433

Sponsored by:  
Air Force Office of Scientific Research  
Boiling Air Force Base, Washington D.C.,

December 1992

# INVESTIGATION OF THE COMBUSTION CHARACTERISTICS OF CONFINED COANNULAR SWIRLING JETS WITH A SUDDEN EXPANSION [TASK 150 COMBUSTOR]

Paul O. Hedman, Professor  
David K. Pyper and David L. Warren, Master Candidates  
Departments of Chemical and Mechanical Engineering  
Brigham Young University

## ABSTRACT

This report contains a brief summary of work done during the 1992 AFOSR Research Initiation Program to investigate a burner designed to "specifically reproduce recirculation patterns and LBO processes that occur in a real gas turbine combustor." Measurements in both The Pratt & Whitney Task 100 and 150 Combustor were made. The Task 150 combustor uses a swirling fuel injector from an actual turbojet engine installed in a sudden expansion chamber. The Task 100 and 150 burners have been configured to be as axisymmetric as possible and still allow optical measurements to be made.

The primary efforts of this AFOSR research initiation program were: 1) modification of the burner facility to allow independent air flow partitioning between the primary and secondary swirlers in the task 150 burner and the evaluation of that flow partitioning on flame structure; 2) collection of MIE scattered images from a seeded flow; and 3) further evaluation of geometry and operating conditions on the lean blow-out of the Task 100 burner and the Task 150 burners. This data complements work done during the 1991 and 1992 summer faculty research programs (Hedman and Warren, 1991 and 1992).

During this study, work has been done on the flow partitioning in the low and high swirl nozzles. The flow partitioning was evaluated over wider ranges than was done previously (Hedman and Warren, 1991). The facility was also modified to independently control the air flow rates to various injector passages, and limited data on the effect on flame structure and lean blow out on this characteristic was obtained.

Additional insights were obtained regarding the general structure of the flames associated with the air flow rate and fuel overall fuel equivalence ratio. Photographs of laser sheet lighted images of MIE scattering from a seeded flow were made to better understand the flame fronts locations and the turbulent structures.

Additional lean blow out measurements were made quantifying the effects of chimney extension and size of exit orifice plate. In addition, a nitrogen diluent and supplemental oxygen were added in an effort to determine the effect of oxygen partial pressure (altitude) on lean blow out. Work still needs to be done to quantify the volume of a flame that is attached to the burner and the amount of air and fuel that is actually entering the flame zone. This data is necessary in order to better determine the actual fuel equivalence ratio in the "well mixed" flame zone, and to correlate the LBO data in terms of the "loading parameter"



# INVESTIGATION OF THE COMBUSTION CHARACTERISTICS OF CONFINED COANNULAR SWIRLING JETS WITH A SUDDEN EXPANSION [TASK 150 COMBUSTOR]

Paul O. Hedman, David K. Pyper and David L. Warren

## INTRODUCTION

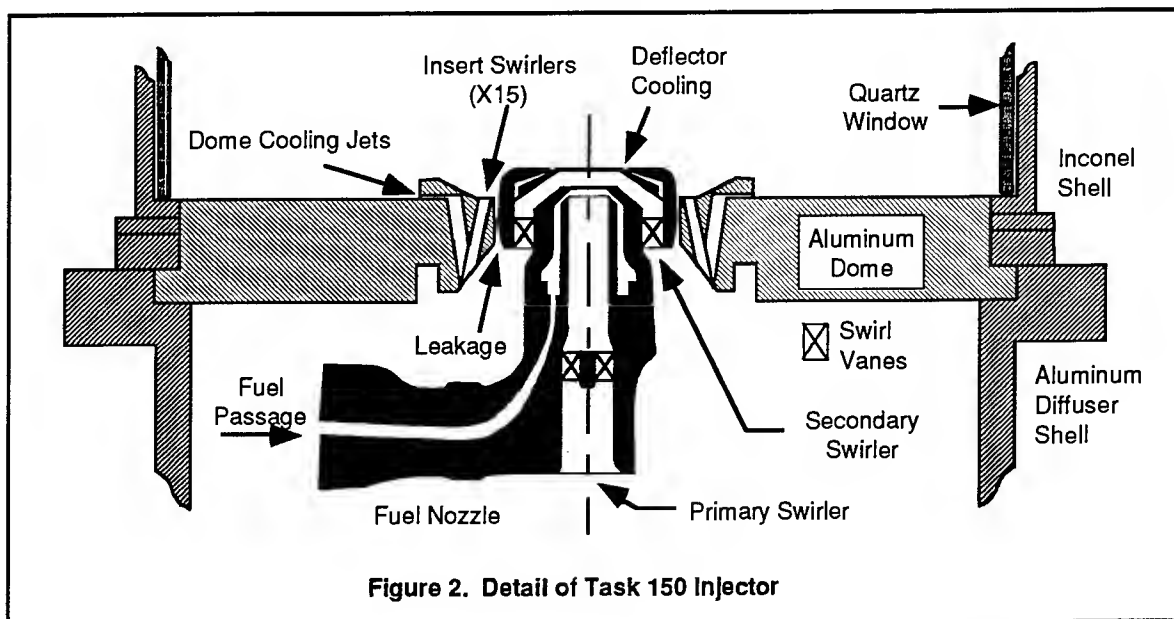
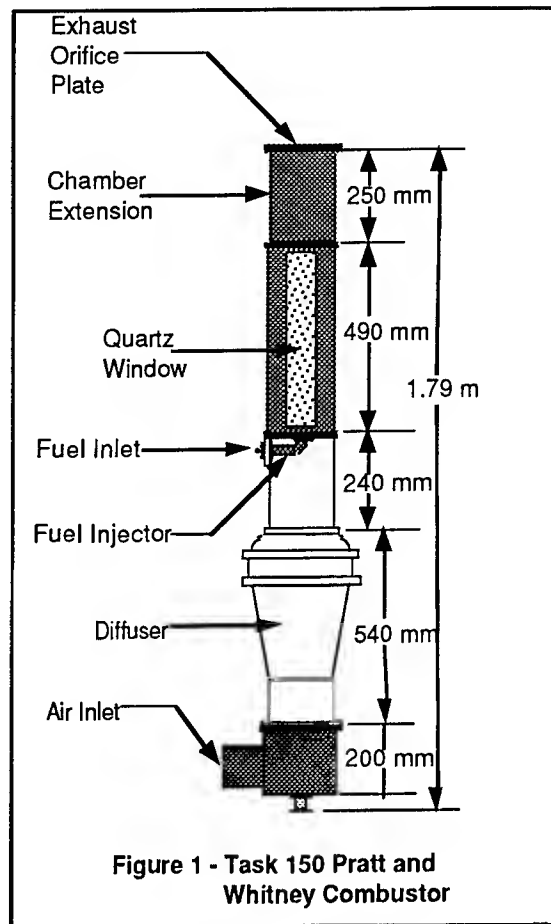
This study has continued the investigation of the operational characteristics of a burner that was designed to "specifically reproduce recirculation patterns and LBO processes that occur in a real gas turbine combustor" (Sturgess, et al., 1990). The study has continued efforts by the principal investigator while participating in Summer Faculty Research Programs at the Aero Propulsion and Power Laboratory, Wright-Patterson Air Force Base during the summers of 1990, 1991, and 1992 (Hedman, 1990; Hedman and Warren, 1991; and Hedman and Warren, 1992) and work done at Brigham Young University that was supported under a previous AFOSR/UES Research Initiation Grant (Hedman and Pyper, 1991).

The Pratt & Whitney Task 100 and 150 combustors, which were provided to BYU by the Aero Propulsion and Power Laboratory at Wright-Patterson Air Force Base, have been specifically developed to study the combustion phenomenon of modern annular aircraft gas turbine combustors. Combustion studies are also being conducted at Aero Propulsion and Power Laboratory at Wright-Patterson Air Force Base in the Pratt & Whitney Task 200 combustor. The investigation of the Task 100 and 150 combustors either at Wright-Patterson AFB during summer faculty research programs by the principal investigator or at BYU in the research initiation programs complements the work being conducted by the Air Force in the Task 200 burner. The Task 100, 150, and 200 combustors allow the characteristics of a jet engine combustor to be investigated in simple geometries where various diagnostic measurements (primarily laser-based optical measurements) can be more easily made.

The Task 100 combustor consists of a 29 mm diameter central fuel jet surrounded by a 40 mm diameter annular air jet. The jets are located in the center of a 150 mm diameter duct, creating a rearward-facing bluff body with a step height of 55 mm at the exit plane. The combustor test section incorporates flat quartz windows to accommodate laser and other optical access, but uses a metal shell with metal corner fillets to reduce the vorticity concentration and its effect on the bulk flow field in the combustor. This box-section combustor with corner fillets allows reasonable optical access while providing a cross section that approximates a two-dimensional axisymmetric cross section. The bluff body provides a recirculation region which stabilizes the flame.

The Task 150 combustor configuration utilizes the basic Task 100 hardware, but replaces the confined, coannular jets with an insert and a swirling fuel injector from a Pratt & Whitney jet engine. A schematic drawing of the Task 150 Combustor is shown in Figure 1. A drawing showing the installation of the fuel injector in greater detail is presented in Figure 2.

Two different fuel injectors were used for this study, a high swirl injector, and a low swirl injector. The high swirl injector used in this study was referred to by representatives of Pratt & Whitney as a "bill of materials injector" used in production engines. The low swirl injector was reported to match the characteristics of the injectors supplied by Pratt & Whitney for use in the Task 200 combustor. The Pratt-Whitney Task 150 combustor was installed in the Combustion Laboratory at Brigham Young University during a previous research initiation grant (Pyper and Hedman, 1991). Figure 3 presents a schematic drawing of the Task 150 Combustor as it has been installed in the Brigham Young University Combustion Laboratory.



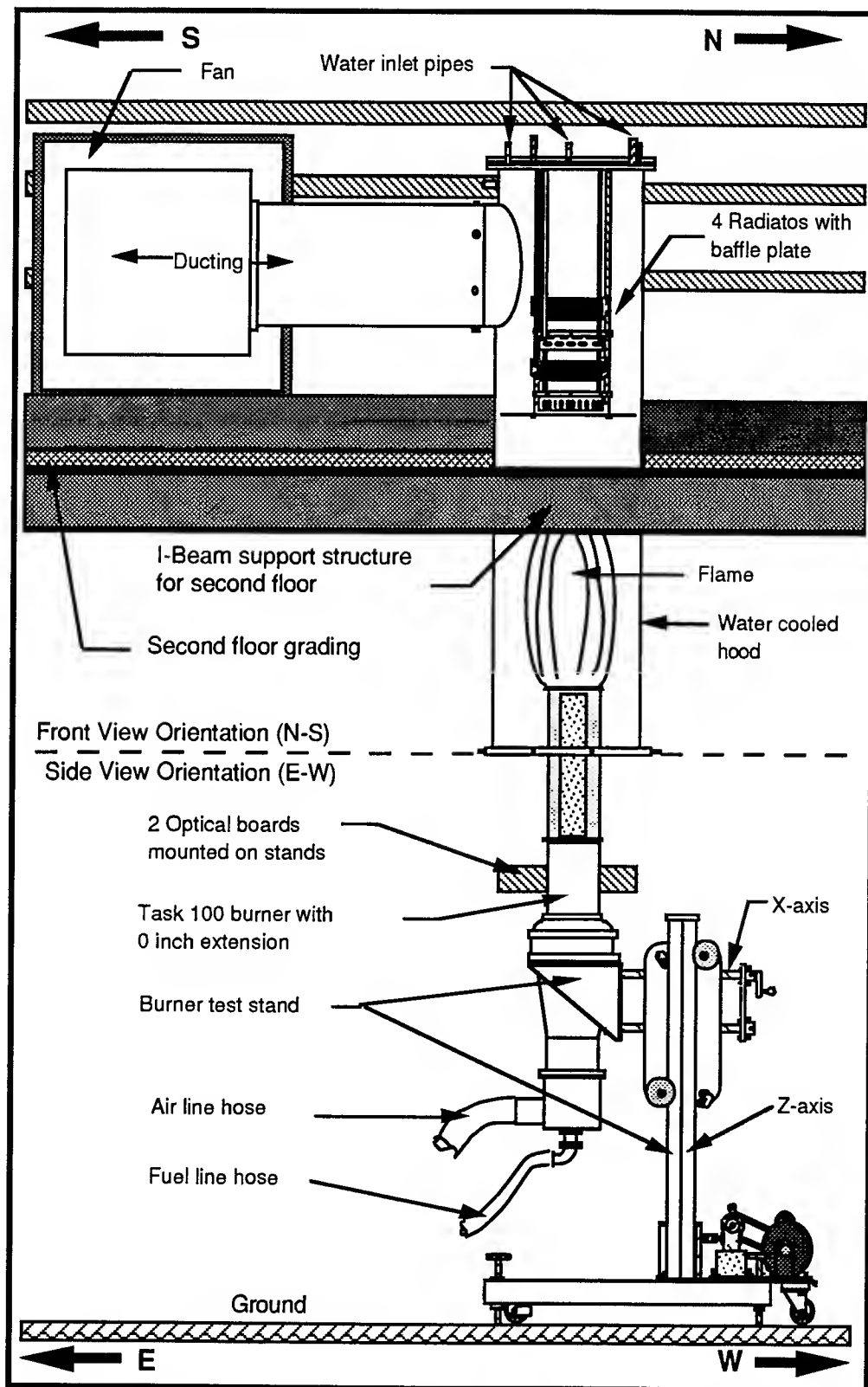


Figure 3. Schematic of the Pratt-Whitney Burner Installation at BYU

The overall objectives of the summer faculty research programs and the research initiation grants has been to determine the combustion and flow characteristics of the Task 100 and 150 burners over a range of operating conditions. Specifically, the objective of the continuing studies has been to characterize the broad operating characteristics of the Task 100 burner and the Task 150 burner with both high and low swirl injectors. A secondary objective has been to collect data that can be used in validating a computer code which predicts the flame phenomena and blowout limits (Sturgess, et al. 1990).

Several tasks were completed during this research initiation program. The effect of swirl on injector performance on flow partitioning, flame structure, and lean blow out were investigated by comparing results from the high swirl (HS) and low swirl (LS) fuel injectors made available to the project by Wright-Patterson AFB and Pratt-Whitney Aircraft Co. Limited experiments were also conducted with the Task 100 burner. Specific tasks that were performed are summarized below.

The evaluation of air flow partitioning through the various burner passages was determined in Task 1. In this task, the pressure drop in the dome jets, the insert jets, the gap between insert and injector, the secondary swirler passages, and the primary air swirler passages was measured as a function of air flow rate. This data has allowed the percent flow in each of the burner air passages to be determined. In addition, the test facility was modified to allow independent delivery of air to the primary air swirler and a combination of secondary air swirler, gap between injector and insert, insert jets, and dome jets. This has permitted the effect of varying air flow partitioning on flame structure to be determined.

In Task 2 various experimental procedures were used to evaluate the effects of operating condition on flame structure. The general flame structure was determined with film photographs and video movies as a function of air flow rate and fuel equivalence ratios that varied from fuel rich to lean blow out. The fuel rich limit was set by the limits imposed by the ability of the facility to deliver propane fuel through the fuel injector. The flow restrictions of the fuel injector prevent propane flow rates beyond about 50 to 55 slpm ( $0\text{ }^{\circ}\text{C}$ ) at propane delivery pressures of about 40 to 50 psig. This fuel flow rate corresponds roughly to the lean blow out limit determined previously (Hedman and Warren, 1991) at an air flow rate of about 2500 slpm ( $70\text{ }^{\circ}\text{F}$ ). In order to visualize the flow, it was necessary to incorporate into the experimental facility the capability of seeding the fuel feed system with liquid  $\text{TiCl}_4$  or  $\text{Al}_2\text{O}_3$  powder so that MIE scattering from sheets of laser (532 nm) light from the  $\text{TiO}_2$  or  $\text{Al}_2\text{O}_3$  particles could be used to investigate the more detailed aspects of the flame structure. Film photographs and limited video images of MIE scattered images from sheets of laser (532 nm) light from the  $\text{TiO}_2$  or  $\text{Al}_2\text{O}_3$  particles at various air flow rates and fuel equivalence ratios were made to identify important flame structures, eddies, and other flame features that have importance in helping to develop an understanding of the behavior of the burner at different operating conditions. Operating conditions were selected so that representative

images for each of the different operating modes (rich attached, rich lifted, funnel cloud, tornado, debris cloud, lean lifted, lean separated) were obtained.

Considerable effort has been expended in the Task 100, 150, and 200 Pratt & Whitney burners to determine the effect of burner geometry and air flow rate on lean blow out. Nevertheless, there are several effects that have not been fully determined. In Task 3, additional lean blow out measurements were made in order to systematically quantify the effects of extension length, exit orifice size, and nitrogen dilution and oxygen addition (reduced or enhanced oxygen partial pressure). Measurements were made in the Task 100 and Task 150 burner with both high and low swirl injectors. In addition, the volume of the flame zone was determined from film photographs and video movies at each of the operating conditions, particularly when the flame is attached to the central part of the burner just prior to lean blow out. This allows the amount of air entering the combustion zone to be estimated. The volume and mass flow of air estimates entering into the "well mixed" flame zone can be used to calculate the "loading parameter" for these lean blow out experiments. The LBO data should correlate with the similar "loading parameter" correlations developed for the Task 100 combustor (Longwell et al., 1953; and Longwell and Weiss, 1955).

The page constraints of this report prevent a detailed summary and discussion of all of the experimental results obtained. Consequently, only example results are presented. However, the work on the study is being continued in an additional AFOSR sponsored Summer Research Extension Program (Subcontract No. 93-30, AFOSR # F49620-90-C-09076). In this program extension, the data obtained during the 1991 and 1992 summer research programs (Hedman, and Warren, 1991; Hedman, and Warren, 1992) and the data collected in this study and a previous AFOSR research initiation grants (Pyper and Hedman, 1991) will be analyzed in detail and reported in the Master of Science theses of Mr. David L. Warren (Warren, 1993) and Mr. David K. Pyper (Pyper, 1993). Additional data will be taken in this program extension as needed to complete the data sets for the Task 100 and 150 burners. This will include CARS gas temperature measurements to further investigate the combustion characteristics of the Task 100 and 150 burners, and to collect specific data that could be used to validate computer codes, such as are being created by Pratt & Whitney Aircraft or Wright-Patterson AFB.

## RESULTS

Basic combustion measurements to further characterize the various structures of the swirling flame as a function of air flow rate and fuel equivalence ratio have been performed. The effect of various operating parameters on lean blow out have also been determined. Additionally, laser sheet lighting was used to obtain film images of MIE scattering from  $\text{TiCl}_4$  and  $\text{Al}_2\text{O}_3$  seeded flows. These film images are being used to locate the major flow structures in the swirling flows and various recirculation zones associated

with the flame fronts. Example results for each of these measurements are presented in the following sections.

#### Task 1: Effects of Injector Flow Partitioning.

Additional work has been done on the flow partitioning in the low and high swirl nozzles, and the effect that this partitioning has on flame stability. The flow partitioning was evaluated at higher flow and pressure drop ranges than was done during the summer of 1991 (Hedman and Warren, 1991). The partitioning of the air flow rates to the primary and secondary swirlers was found to have a major impact on the operation of the combustor. The facility was modified so that the air flow rates to the various injector passages could be independently controlled, and limited data on the effect on flame structure and lean blow out on this characteristic was obtained.

An essential element to understanding the combustion characteristics of the Task 150 burners lies in the flow partitioning, or the amounts of air which flow through the various passages of the fuel injectors. Not only is this information important from a design viewpoint, it will also be required to properly account for the amount of air actually involved in the combustion process, affecting both fuel equivalence ratios and loading parameters.

The process of determining these flow splits is conceptually simple. Three of the four passages were blocked, or plugged, leaving one passage open and unobstructed. Measurements were then made to determine the relationship between air flow and pressure drop for the open passage. This procedure was repeated for each of the four passages, providing a separate equation for each of the four passages for both the low and high swirl injectors. These equations were then summed to provide a total air flow rate, which in turn, provided the percentage flow through each injector passage.

One of the most useful equations of fluid mechanics is Bernoulli's equation. This equation assumes a steady, incompressible, frictionless flow along a single streamline with no work. The swirling injectors are very much like obstruction flow nozzles, employing various flow passages that look somewhat like sharp edged orifice plates (insert jets and dome jets) and flow nozzles (gap between injector and insert). The flow in the primary and secondary swirlers is somewhat a cross between flow in a sharp edged orifice plate and in a flow nozzle. It has been assumed that conventional theory through an obstruction flow instrument can be applied to model the flow through the entire injector. Once this assumption is made, and the continuity equation applied, the flow rate (Q) through an obstruction (flow nozzle) can be expressed as:

$$Q = C_d A_t \sqrt{\frac{2 \Delta p_t}{\rho [1 - (A_t / A_1)^2]}}$$

or assuming constant areas and combining the constant terms into a single coefficient (c)

$$Q = c\sqrt{\Delta p_z}$$

It was expected, therefore, that pressure drop would be a linear function of the flow rate squared.

Figures 4 and 5 present the pressure drop as a function of flow rate across each of the various passages and the pressure drop for the entire injector for the Task 150 high and low swirl burners respectively. The data for each passageway was fitted using a least squares method to the simplified equation above. As can be seen in Figures 4 and 5, these curve fits are quite good for both injectors. As a consequence of being a single variable function, the amount of flow through a given passage will be proportional to the total air flow. These flow splits are presented in Table 1.

**Table 1. Flow Splits**

This table presents the amount of air flowing through each of the injector passages as a percent of the total air flow. Note the gap is included twice, once each with both the primary and secondary swirlers. This results in a slight error in the total flow rate and hence also the flow splits themselves.

	High Swirl Nozzle	Low Swirl Nozzle
Primary and Gap	14%	19%
Secondary and Gap	41%	43%
Insert Jets	19%	16%
Dome Jets	26%	22%

The main source of error for these results is from leaks present in the system. Leaks present in the system after the flow measurements were counted as part of the flow relationship being measured for a given passage. The gap between the injector and the dome, for example, was left unplugged during tests of both the primary and secondary passages. This leakage increased the flow through the respective passages for a given pressure drop. A measure of the leakage can be calculated by adding the flows for the individual passages and comparing this composite flow relationship to that of the total flow relationship. For each injector, the composite flows were 10 percent greater than the total flow. However, a test involving just two passages (HS primary, gap, and insert jets), had a composite error of just 2 percent.

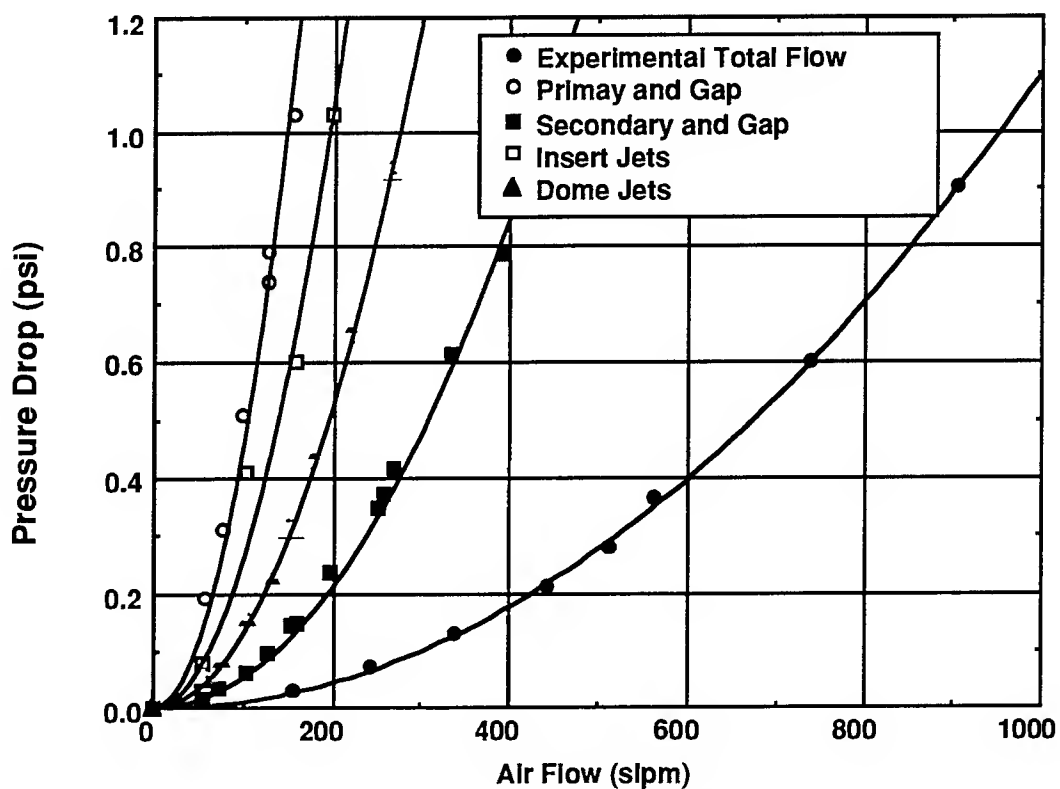


Figure 4.. Flow Partitioning in Task 150 High Swirl Nozzle

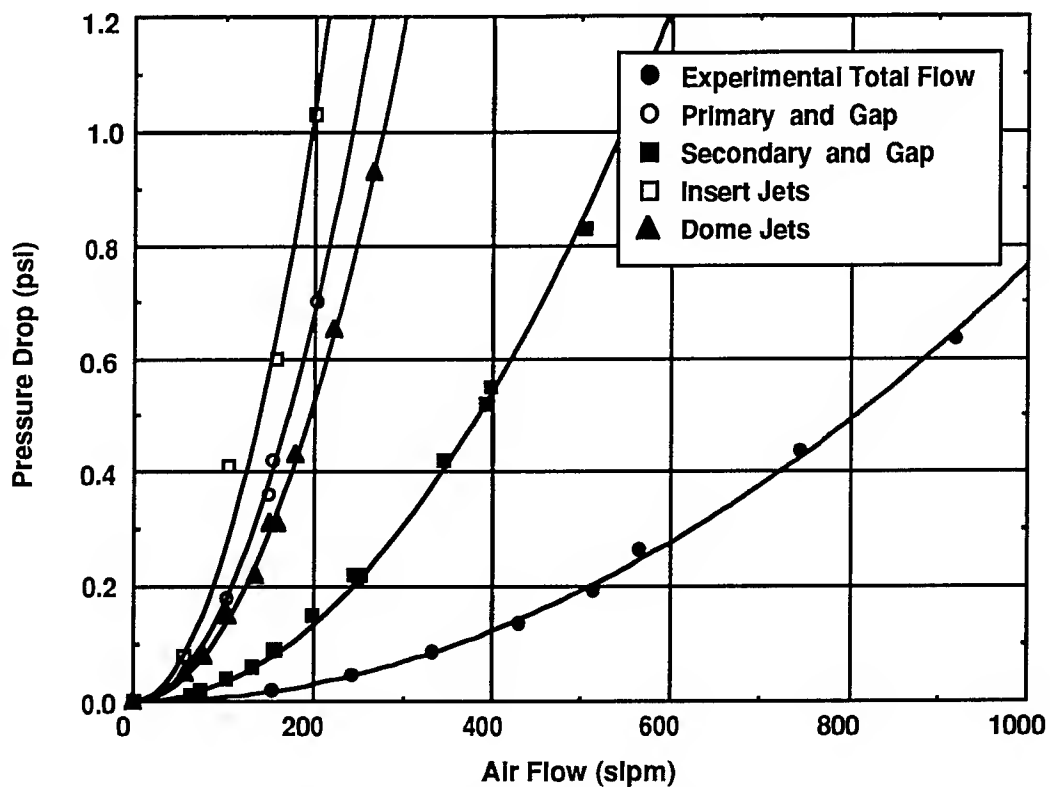


Figure 5. Flow Partitioning in Task 150 Low Swirl Nozzle



Previous experiments (Hedman and Warren, 1991) have produced similar results, differing only slightly in the partitioning between the dome and insert jets. In the previous experiments, however, the flow partitioning was slightly dependent upon the total air flow rate. It is felt the present study is the more accurate of the two.

#### Task 2: Images of Flame Structure.

Additional insights were obtained during this research initiation program regarding the general structure of the flames associated with the air flow rate and overall fuel equivalence ratio. Film photographs of laser sheet lighted images of MIE scattering from a seeded flow were made and used to provide mappings of the flow fields. This information is essential in order to better understand where the flame fronts are located, and the characteristics of the eddies and other turbulent structures. Limited images were taken with a video camera to record the effects in flame structure as the air flows were partitioned between the primary and secondary swirl passages in the fuel injector. Additional flow partitioning studies will be conducted in the follow-on AFOSR Grant (1993 Summer Research Extension Program Subcontract No. 93-30; United States AFOSR Contract Number F49620-90-C-09076).

The laser sheet lighting was created using a Q-switch Nd-Yag laser pulsed at 10 Hz. The flow was seeded with  $\text{Al}_2\text{O}_3$  particles after  $\text{TiCl}_4$  failed to produce satisfactory images. The  $\text{Al}_2\text{O}_3$  particles were introduced into the air flowing through the secondary swirler, insert jets, and dome jets. The flow through the primary air swirler was independently controlled and unseeded. The film images obtained with the  $\text{Al}_2\text{O}_3$  particles have provided insights into the structure of the swirling flow as they exit the injectors.

Examples of digitized film images obtained in the high and low swirl injectors at a fuel equivalence ratio ( $\phi$ ) of about 0.6 are shown in Figures 6 and 7 respectively. The particles as they exit the injector appear to be centrifuged to the outside edge of the secondary swirler with both the high and low swirl injectors (Figures 6 and 7 respectively). A cloud of well mixed particles is observed near the injector with the high swirl burner, Figure 6. In the case of the low swirl burner, Figure 7, a similar cloud is observed, but at a distance much displaced above the burner. While the air flow rates and the percent of air discharged through the primary swirler in the two cases are slightly different, the major effect that is observed is thought to be caused by the different swirl rates between the two injectors. In both of these cases, the air flow rate through the primary swirler (18% and 21% for the high and low swirl injectors respectively) has been forced to be just slightly above the flows that would occur naturally (Table 1), with out the imposition of flow partitioning.



**Figure 6. Sheet Lighting of High Swirl Injector.**  
**Phi 0.6, Air Flow 375 slpm, 18% Air Flow through Primary**

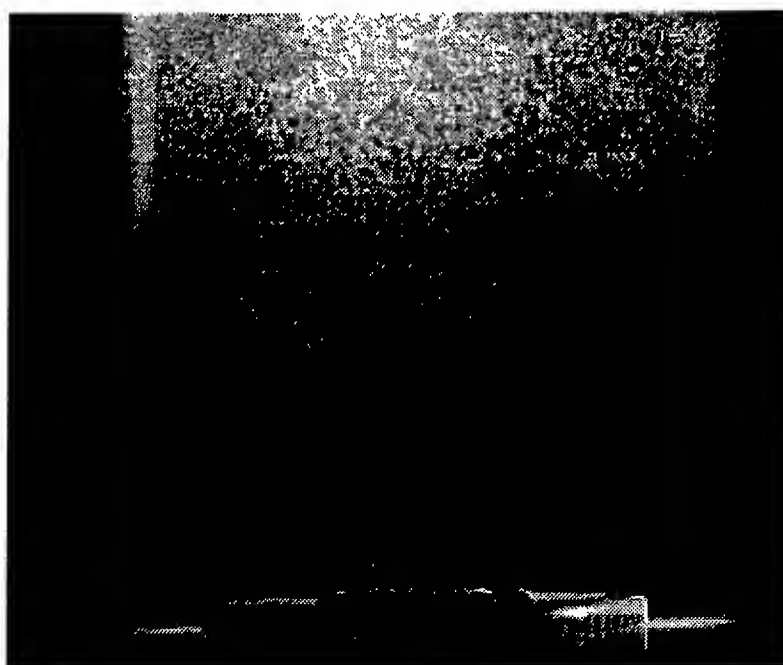


**Figure 7. Sheet Lighting of Low Swirl Injector.**  
**Phi 0.6, Air Flow 500 slpm, 21 % Air Flow through Primary**

Two additional examples of laser imaging are presented in Figures 8 and 9 for a fuel rich ( $\phi = 1.6$ ) high swirl case, and for a near stoichiometric low swirl case. The apparent centrifuging of the particles at the exit of the secondary swirler is also apparent in both cases. Comparing Figures 6 and 8, both high swirl cases, that the flow structures seen are nearly the same inspite of considerable differences in the flow conditions ( $\phi = 0.6$  versus 1.6; and primary air = 18% versus 25% for Figures 6 and 8 respectively). The flow structure shown in Figure 9 is very different from that observed in Figure 7. There appears to be a very well mixed zone in the near field of the injector.

Additional analysis of the images taken will be made in the theses of Warren (Warren, 1993) and Pyper (Pyper, 1993). These theses will compare the images obtained to the LBO data, OH- LIF images, LDA velocity data, and CARS temperature data to investigate the flow structures, and mechanisms of the combustion process in the Pratt and Whitney burner.

### Task 3: Lean Blow-Out Measurements.

Additional lean blow out measurements were made during this study. The effects of chimney extension and size of exit orifice pale were quantified. In addition, a nitrogen diluent and supplemental oxygen were added to the air stream in an effort to determine the effect of oxygen partial pressure (altitude) on lean blow out. Work still needs to be done to quantify the volume of a flame that is attached to the center of the burner and the amount of air and fuel that is actually entering the flame zone. This data is necessary in order to better determine the actual fuel equivalence ratio in the "well mixed" flame zone, and to correlate the LBO data in terms of the "loading parameter". This additional analysis will be performed and reported in the thesis of Pyper ( Pyper, 1993).

LBO with Varying Geometric Configurations. An extensive set of LBO tests were conducted on the Task 100 burner with different extension heights (0 inch and 10 inch) and varying percent orifice plates (0 %, 23 %, 45 %, and 62 % exit blockage). Figure 10 illustrates the effects of the orifice plates on the Task 100 burner with no exhaust extension. Even though there is considerable variability in the data, there is a distinct trend. The quadratic curve fits through each set of data show that the LBO decreases with increasing exit blockage. This effect may be due to the different recirculation patterns associated with the relatively short combustion chamber, or may be caused by the slightly higher pressures associated with the restricted exhaust flow, or a combination of both. Figure 11 shows the effects of the orifice plates on the Task 100 burner with the 10 inch extension. With the 10 inch extension, there is no apparent difference in LBO with increased exit blockage (increasing orifice plate %). The quadratic fits through each set of data are not substantially different, and are well within the data scatter. The effect of the 10 inch extension has been to eliminate the effect of the exhaust orifice on the measured fuel equivalence ratio at lean blow out ( $\phi_{LBO}$ ).

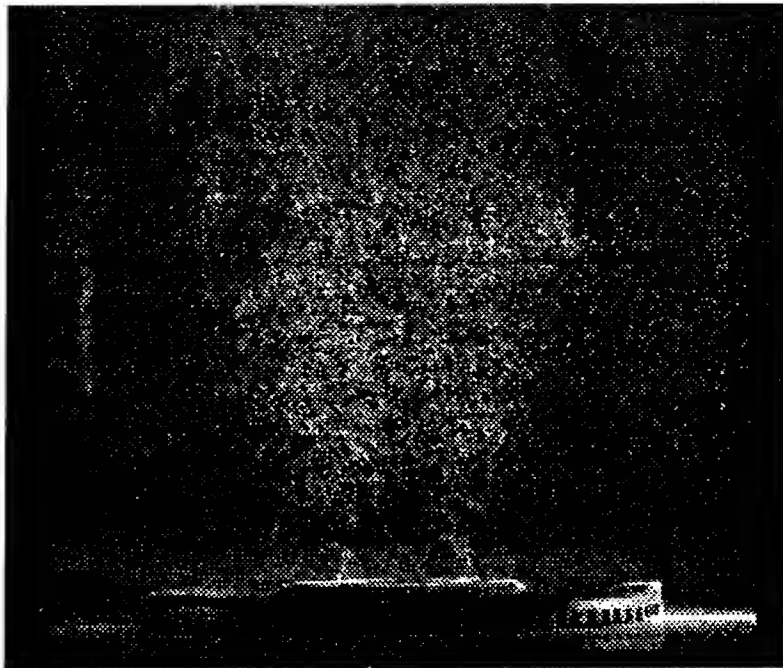


**Figure 8. Sheet Lighting of High Swirl Injector.**  
 **$\Phi$  1.6, Air Flow 350 slpm, 25% Air Flow through Primary**

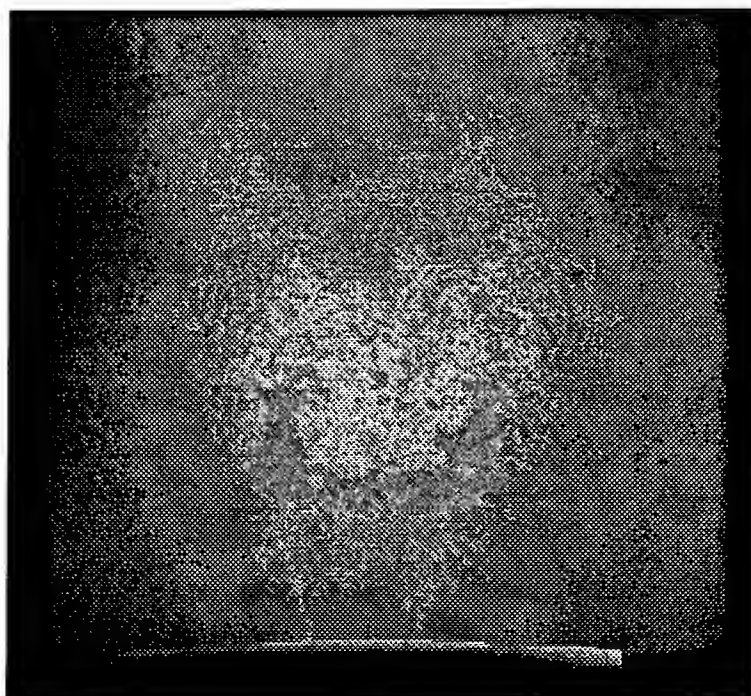


**Figure 9. Sheet Lighting of Low Swirl Injector.**  
 **$\Phi$  1.0, Air Flow 500 slpm, 18% Air Flow through Primary**

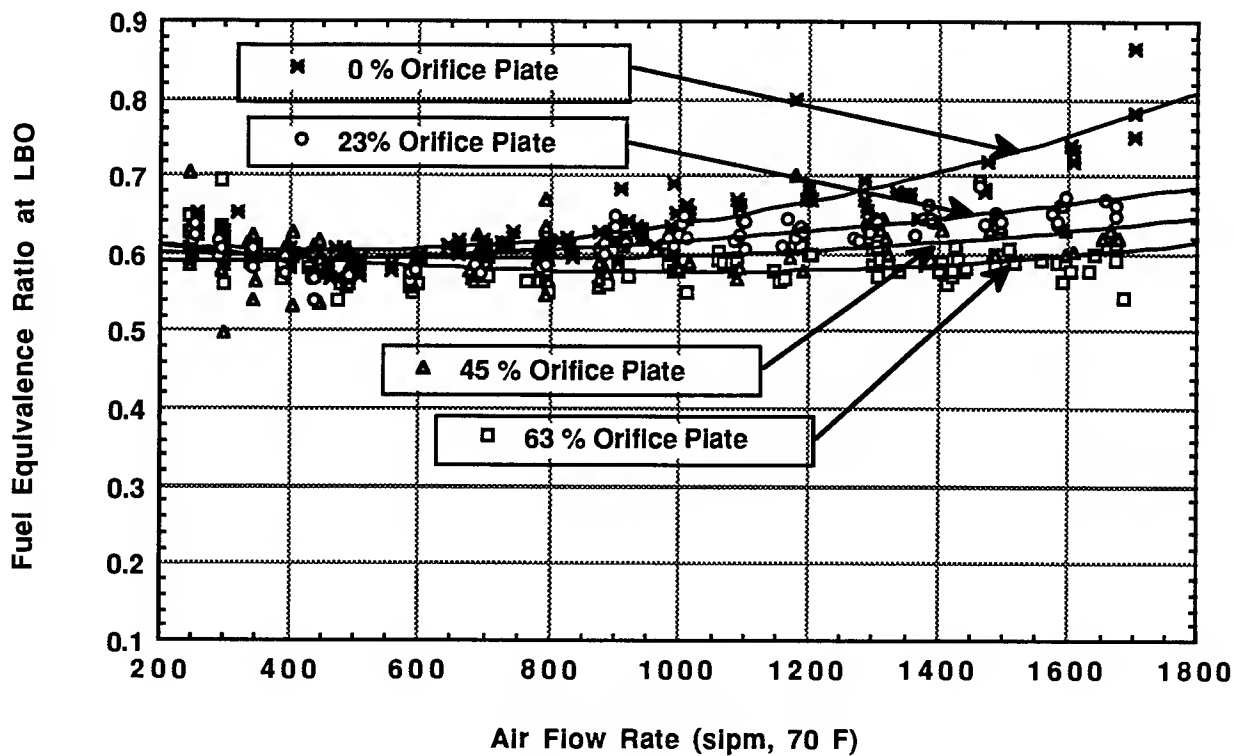


Figure 10. Effect of Exit Orifice on Lean Blow Out for the Task 100 Burner with no Extension

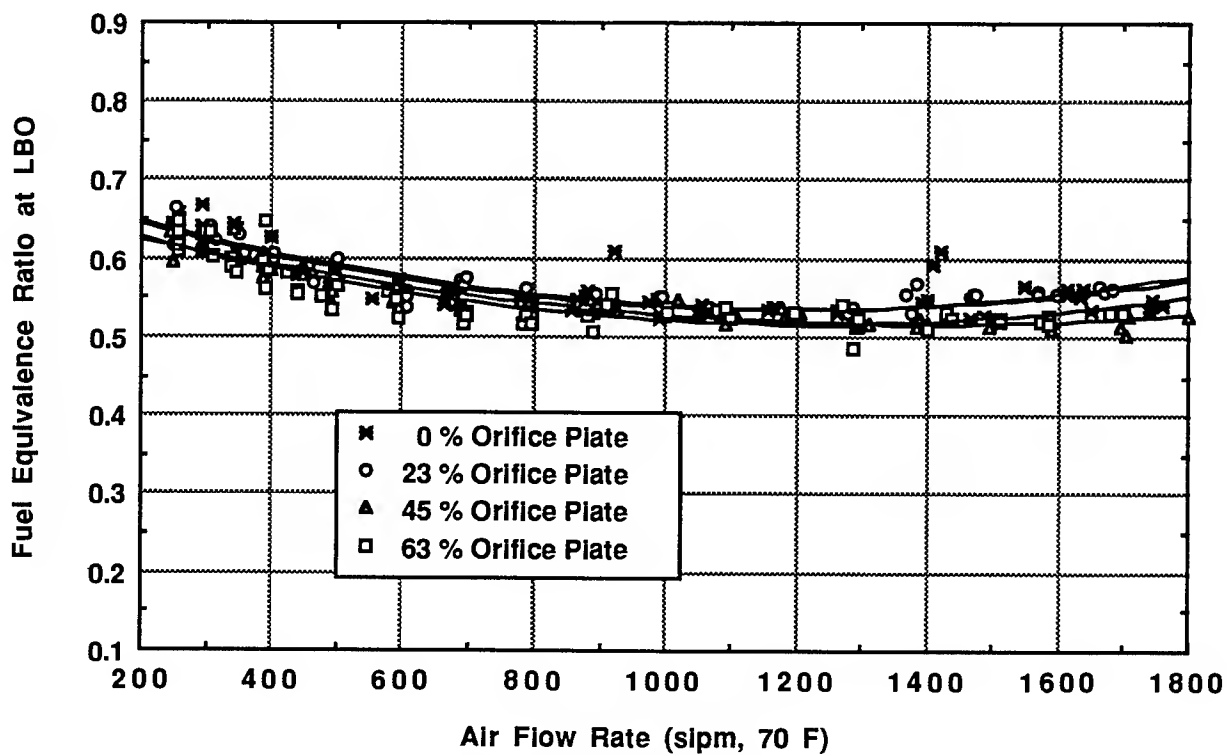


Figure 11. Effect of Exit Orifice on Lean Blow Out for the Task 100 Burner with 10 inch Extension

The results from these Figures suggests that in the Task 100 the flame stability (lower  $\phi_{LBO}$  at LBO) may be enhanced by increased exit blockage and the addition of 10 inch extension. Both of these effects will alter the recirculation flow patterns within the combustor, which likely influence the  $\phi_{LBO}$ . The increased pressure in the combustor associated with increased flow blockage is not likely to significantly affect the  $\phi_{LBO}$ , although some differences in  $\phi_{LBO}$  have been seen between measurements taken at BYU (altitude near 5000 ft) and at Wright Patterson AFB (altitude near 1000 ft). It probably can be concluded that the recirculation patterns are being altered by the different geometric configurations, and these different mixing patterns are affecting the  $\phi_{LBO}$ . Additional understanding will be obtained through analysis of the flow field imaging, LDA velocity data, and CARS temperature data.

Limited sets of LBO tests were conducted on the Task 150 burner with both high and low swirl burners with varying geometric configurations at air flow rates of up to 1000 slpm (70 F). Again LBO tests were done with two extension heights (0 inch and 10 inch), but only for the 0 % and 45 % percent blockage orifice plates. Figure 12 illustrates the effects of the two orifice plates on the Task 150 -HS burner with no exhaust extension. Figure 13 shows the effects of the two orifice plates on the Task 150-HS burner with the 10 inch extension. In both high swirl burner cases, the flame would "blow out" in two different modes. At lower air flow rates, the flame would blow out from an attached position to the burner. At higher air flow rates, the flame would lift and stabilize on a down stream recirculation zone prior to blow out. In an intermediate air flow range, both modes of blow out were observed. Consequently, Figure 12 shows sets of data for both modes of blow out, including an overlapped set where both modes of blow out would occur. While the set of data presented in Figure 13 for the case with the 10 inch extension are more limited, the same trend seems to exist. In both cases shown, the levels of  $\phi_{LBO}$  are at about the same levels at the same air flow rates. It appears that the 10 inch extension and the differences in exit blockage have had little or no effect on the  $\phi_{LBO}$  for the high swirl burner.

LBO tests were also conducted for the Task 150-LS burner. Figure 14 illustrates the effects of the two orifice plates on the Task 150-LS burner with no extension, and Figure 15 shows the effects of the two orifice plates on the Task 150-LS burner with the 10 inch extension. It is interesting to note that there is an effect of exhaust restriction on the  $\phi_{LBO}$  for the data set no exhaust extension. In this case, the increased exhaust restriction (45% versus 0%) caused the  $\phi_{LBO}$  to increase. This is opposite to the effect observed on the Task 100 burner, Figure 10, where increased exit blockage caused a decrease in  $\phi_{LBO}$ . However, when the 10 inch extension was added to the Task 150-LS burner, no real effect on the  $\phi_{LBO}$  for the two different orifice plates was observed. This trend was more like that observed with the high swirl burner where no effect of extension or exhaust blockage was seen.

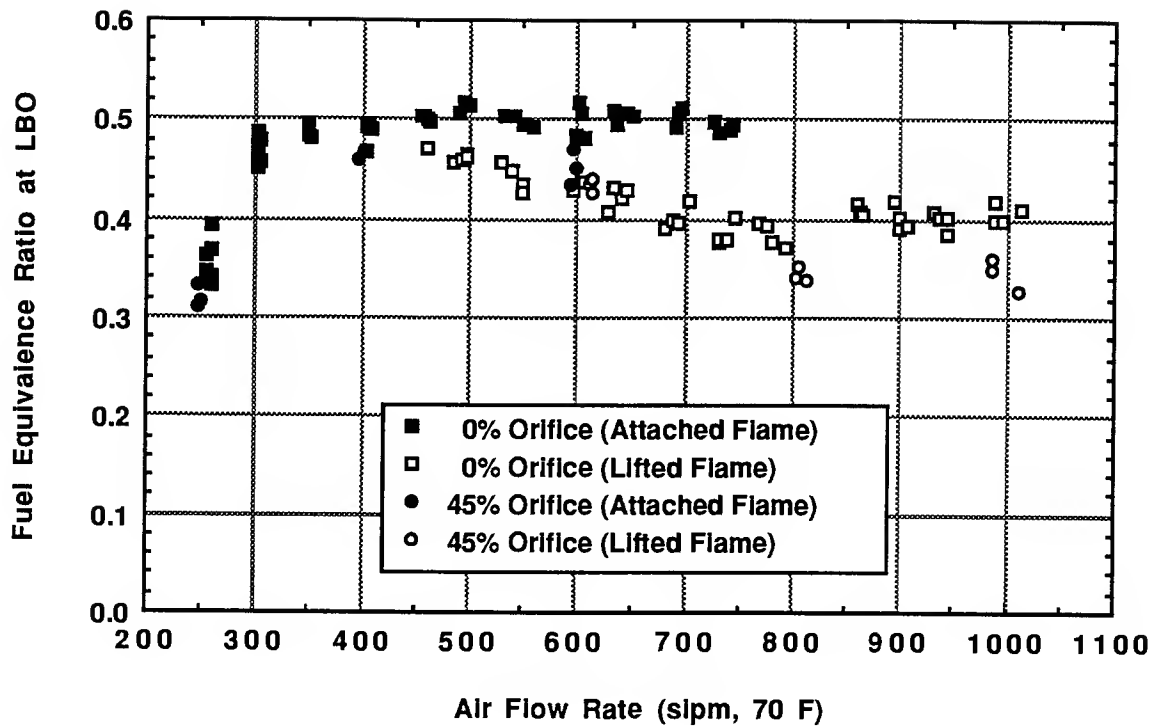


Figure 12. Effect of 0% & 45 % Orifice Plates on LBO for the Task 150 HS Burner with no Extension.

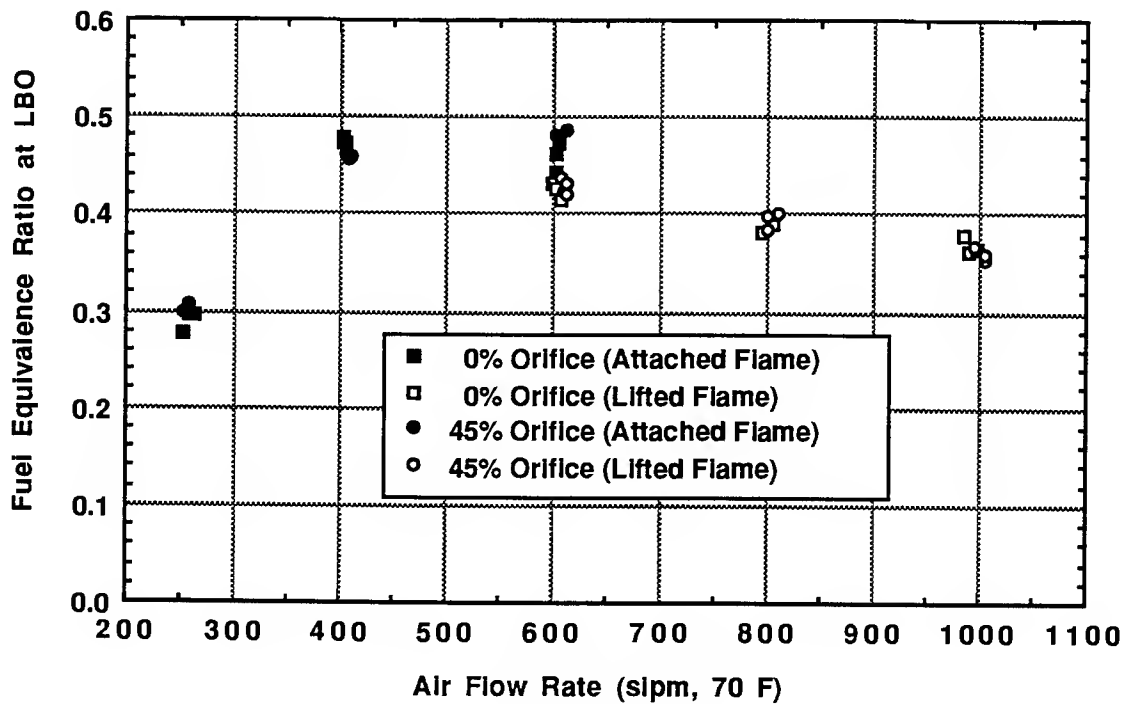


Figure 13. Effect of 0% & 45 % Orifice Plates on LBO for the Task 150 HS Burner with 10 in. Extension.

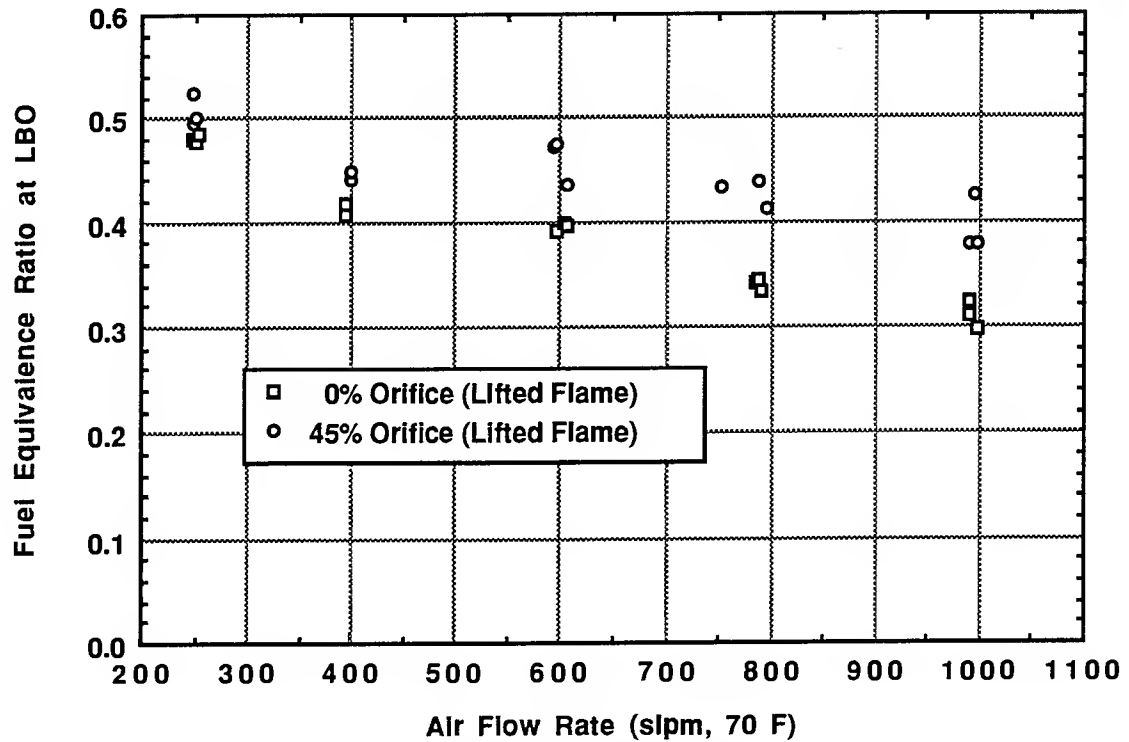


Figure 14. Effect of 0% & 45% Orifice Plates on LBO for the Task 150 LS Burner with no Extension.

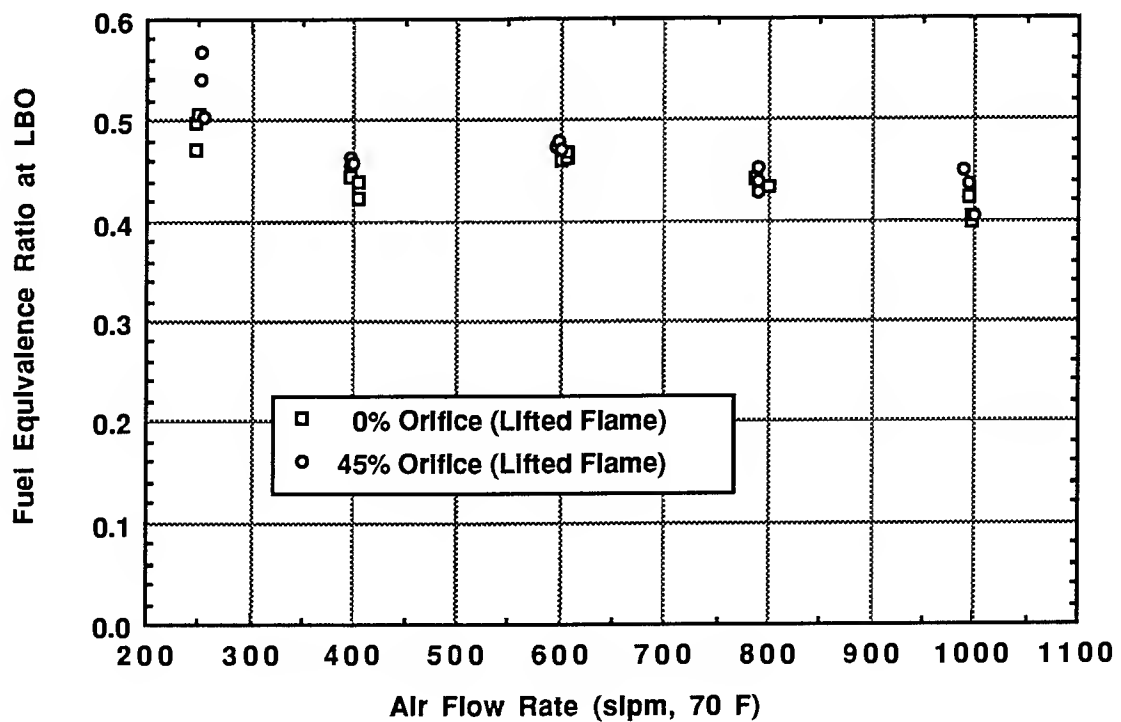


Figure 15. Effect of 0% & 45% Orifice Plates on LBO for Task 150 LS Burner with 10 inch Extension.



It should be noted that the  $\phi_{LBO}$  at very low air flow rates for both the high and low swirl burners depart from expected values. The values of  $\phi_{LBO}$  for the high swirl burner drop to levels of about 0.3 while the  $\phi_{LBO}$  for the low swirl burner increase to levels of about 0.5-0.6. At these very low air flow rates, the burners may no longer be fully turbulent. Further investigation at these low air flow rates is probably not warranted, since these flows are not representative of actual jet engine combustion conditions.

LBO with Varying Partial Pressure of  $N_2$  and  $O_2$ . Preliminary tests were conducted on the Task 100 and the Task 150 high and low swirl burners to determine the effects of partial pressure of oxygen on lean blow out. The tests were run at a nominal air flow rates of 500 slpm (70 F) for the Task 150 high and low swirl burners and 1000 slpm (70 F) for the Task 100 burner. The 10 inch extension was used in each test with either the 0 % or the 45 % orifice plate. The main objective for this experiment was to obtain some understanding for the observed differences in  $\phi_{LBO}$  for the Task 100 LBO data taken at BYU when compared to the comparable LBO taken at Wright-Patterson AFB. The  $\phi_{LBO}$  data were obtained at various flow conditions where supplemental amounts of nitrogen or oxygen were added to the combustion air stream in order to modify the mole fraction of oxygen (partial pressure) in the "air". The tests were intended to maintain an overall total air flow rate (normal air plus added gas) although at times the actual total air flow varied from the nominal total air flow by as much as 150 slpm (70 F).

The atmospheric pressure at WPAFB, Ohio is approximately 14.6 psi while BYU, located in Provo, Utah, averages about 12.6 psi. These two atmospheric pressures correspond to a partial pressure of oxygen at WPAFB of about 3.07 psi at WPAFB and about 2.65 psi at BYU. Figure 16 illustrates the effect of oxygen partial pressure on the  $\phi_{LBO}$  for the Task 100 and Task 150 Burners with the 10 inch extension. As the oxygen concentration (partial pressure) is decreased from normal air there is a steady increase in the  $\phi_{LBO}$ . At higher oxygen mole fractions, the  $\phi_{LBO}$  shows a gradual decrease. This trend supports the general observations made since the  $\phi_{LBO}$  measured at BYU is generally higher, at least for the Task 100 burner, than measured at WPAFB. This data analysis is preliminary, and further investigation will be conducted and reported in the MS thesis of Pyper (Pyper, 1993).

A complete analysis of all of the LBO data obtained at WPAFB and BYU will be made and will be reported by Pyper (Pyper, 1993).

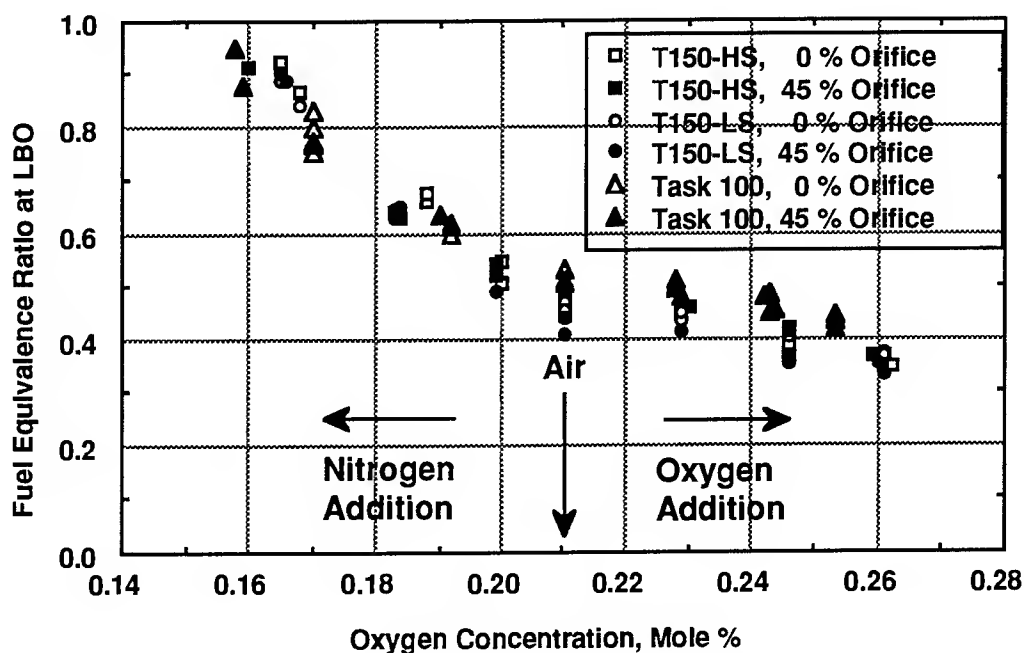


**Figure 16. Effect of Oxygen Partial Pressure on LBO for the Task 100 and 150 Burners with 10 inch Extension**

#### ACKNOWLEDGMENTS

We wish to thank the Aero Propulsion and Power Laboratory, Wright Patterson Air Force Base, and the Air Force Office of Scientific Research for sponsorship of this research initiation program. The very successful experience gained during this Summer Research Extension Program (SREP) is in large measure due to the very excellent support of my sponsor, Dr. W. M. (Mel) Roquemore (WRDC/POSF). The timely help of Mr. Gary Moore and other individuals at Research and Development Laboratories, Inc. is greatly appreciated. The help of Scott Blackham and Jenai Christensen in making many of the measurements is gratefully acknowledged. Special thanks are also given to Mr. Dale Shouse and Mr. Melvin Russell who provided much needed support with instrumentation and the burner and facility modifications. The help received from the very well-qualified research staff at Systems Research Laboratory, Inc. (SRL) is gratefully appreciated. Special thanks are in order for Dr. Larry Goss, Mr. Benjamin Sarka, and Mr. Daryl Trump of SRL. Their willingness to help, to answer questions, and the help they provided have proven very valuable.

## REFERENCES

- Hedman, Paul O., "Investigation of the Combustion Characteristics of a Confined Coannular Jet with a Sudden Expansion," Final Report, Contract No. F49620-88-C-0053, 1990 USAF-UES Summer Faculty Research Program, for Universal Energy Systems, Inc. (July 20, 1990)
- Hedman, Paul O., and Warren, David L., "Investigation of the Combustion Characteristics of Swirled Injectors in a Confined Coannular System with a Sudden Expansion," Final Report, 1991 USAF-RDL Summer Faculty Research Program, for Research Development Laboratories, Inc. (September 11, 1991)
- Hedman, Paul O., and Warren, David L., "Investigation of the Combustion Characteristics of Swirled Injectors in a Confined Coannular System with a Sudden Expansion," Final Report, 1992 USAF-RDL Summer Faculty Research Program, for Research Development Laboratories, Inc. (September, 1992)
- Longwell, J.P., E.E. Frost, and M.A. Weiss, "Flame Stability in Bluff Body Recirculation Zones", Industrial and Engineering Chemistry, 45(8), pp 1629-1633 (August 1953)
- Longwell, J.P., and M.A. Weiss, "High Temperature Reaction Rates in Hydrocarbon Combustion", Industrial and Engineering Chemistry, 47(8), pp 1634-1643 (August 1955)
- Pyper, D.K. and Hedman, P.O., "Investigation of the Combustion Characteristics of Confined Coannular Swirling Jets with a Sudden Expansion," Final Report, 1990 AFOSR Research Initiation Program, Universal Energy Systems, Inc., Dayton, Ohio (1991)
- Pyper, D.K., Master of Science Thesis, Mechanical Engineering Department, Brigham Young University, Provo, Utah (in progress) (1993)
- Sturgess, G.J., D.G. Sloan, A.L. Lesmerises, S.P. Henneghan and D.R. Ballal, "Design and Development of a Research Combustor for Lean Blowout Studies", 35th International Gas Turbine and Aeroengine Congress and Exposition. Brussels, Belgium.(June 1990)
- Warren, D.L., Master of Science Thesis, Mechanical Engineering Department, Brigham Young University, Provo, Utah (in progress) (1993)

TWO DIMENSIONAL SIMULATION OF ARC PLASMAS  
IN ELECTROMAGNETIC RAIL LAUNCHERS

Principal Investigator: Dr. Manuel A. Huerta  
Professor of Physics  
Soc. Sec. No. 262-70-9459  
Telephone No. (305) 284-2323, Ext. 8

Institution: University of Miami  
Physics Department  
Coral Gables, FL 33124

Final Report for:  
Research Initiation Program

Summer 91 Research Location: WL/MNSH  
Eglin AFB, FL 32542-5000

Sponsored by:  
Air Force Office of Scientific Research  
Bolling Air Force Base, Washington, D. C.  
and  
University of Miami  
Under  
1991 USAF-RDL Summer Research Program

December 1992

# TWO DIMENSIONAL SIMULATION OF ARC PLASMAS IN ELECTROMAGNETIC RAIL LAUNCHERS

Manuel A. Huerta  
Professor of Physics  
University of Miami

## Abstract

We have developed a fully heat conducting two dimensional MHD code to simulate the internal dynamics of a railgun plasma armature. We use the equations of resistive MHD, with an energy equation that includes Ohmic heating and heat transport in the radiation diffusion approximation. We use an explicit Flux Corrected Transport code to advance all quantities in time. During the minigrant period we completed the incorporation of rail ablation into our computer simulation. We did several runs and obtained interesting results. The main new result is that our simulation is the first one to show the growth of a strong secondary arc. This is important because secondary arcs are believed to be significant in degrading the performance of these launchers. We also made progress in developing a model for projectile viscous drag. Both of these pieces of work have been accepted for publication in IEEE Transactions on Magnetics.

# TWO DIMENSIONAL SIMULATION OF ARC PLASMAS IN ELECTROMAGNETIC RAIL LAUNCHERS

Manuel A. Huerta

## I. INTRODUCTION

The work under this minigrant was a followup to the work that my graduate student, Mr. G. C. Boynton, and I did at WL/MNSH of Eglin AFB under the 1991 RDL-USAF Summer Faculty Research Program.

Our work is centered on developing a two dimensional time dependent simulation of plasma armatures found in electromagnetic rail launchers. Our intention is to understand why electromagnetic rail launchers with plasma armatures fail to perform according to their design goals.

We model the plasma with the equations of resistive MHD and we use a two dimensional fully explicit flux corrected transport code to advance all quantities in time. Before the work in this minigrant the physical effects that we included in our model were the same as in the steady, one dimensional model of Powell and Batteh<sup>1</sup>. Therefore we had left out ablation, viscosity and other effects that can be important in a boundary layer. Our papers Boynton and Huerta<sup>2,3,4</sup> have reported on this previous work.

There are several mechanisms for the loss of performance of rail launchers and there is not complete agreement in the research community on their relative importance. Three important ones are ablation, projectile-rail viscous drag, and plasma armature-rail viscous drag.

## II. RESULTS

Ever since the work of Parker<sup>5,6</sup> it has been recognized that rail ablation, secondary arc formation or restrike, and viscous drag, represent important mechanisms in degrading launcher performance. Hawke<sup>7</sup> et al. have reported on the effects believed to prevent the attainment of high velocities in the HELEOS rail launcher. These effects were discussed intensively at the Workshop on Secondary Arcs and Hybrid Armatures organized by Keith

Jamison and Dennis Keefer, held at the College of Engineering of the University of New Mexico in Albuquerque, N. M., during September 12 and 13, 1989.

During the period of this minigrant we were able to include a model of rail ablation into the simulation. We obtained interesting results. Our simulation is the first one to produce a secondary arc similar to those found in the experiments. Our work has been accepted for publication in the IEEE Transactions on Magnetics with the title "2-D MHD Numerical Simulations of EML Plasma Armatures with Ablation". Rather than repeating the details we attach a preprint of this paper.

We also made progress on developing a model for projectile drag. Some of this work appears in a paper of ours, with the title "The Projectile Wall Interface in Rail Launchers", that has also been accepted for publication in the IEEE Transactions on Magnetics. A preprint of this paper is also attached. This drag effect has not yet been put into the code, however. The effects of armature-rail viscous drag have not been put into the code yet either. These further improvements are left for future work.

## REFERENCES

1. Powell, J. D., and Batteh, J. H., "Plasma Dynamics of an Arc-Driven Electromagnetic Projectile Accelerator," J. Appl. Phys., vol. 52, 2717 (1981)
2. M. A. Huerta and G. C. Boynton, "Two-dimensional time dependent MHD simulation of plasma armatures", IEEE Trans. MAG., vol. 25, pp. 238-242, Jan. 1989.
3. G. C. Boynton and M. A. Huerta, "Two-dimensional MHD simulation of isothermal plasma armatures", IEEE Trans. Plasma Sci., vol. 17, pp. 468-475, June 1989.
4. M. A. Huerta and G. C. Boynton, "Two-Dimensional Heat Conducting simulation of plasma armatures", IEEE Trans. MAG., vol. 27, pp. 261-265 (1991).
5. J. V. Parker, "Why Plasma Armature Railguns Don't Work (and what can be done about it)", IEEE Trans. MAG., vol. 25, pp. 418-424, Jan. 1989.
6. J. V. Parker, "Experimental measurement of ablation effects in plasma armature railguns", IEEE Trans. Mag., 22, 1633 (1986).
7. R. S. Hawke, et al., "Armature Formation in a Railgun Using a Two-Stage Light Gas Gun Injector", IEEE Trans. Plasma Sci. 17, 378 (1989).



# 2-D MHD NUMERICAL SIMULATIONS OF EML PLASMA ARMATURES WITH ABLATION

G. C. Boynton, M. A. Huerta, and Y. C. Thio  
Physics Department, University of Miami  
Coral Gables, FL 33124

**Abstract**—We use a 2-D resistive MHD code to simulate an EML plasma armature. The energy equation includes Ohmic heating, radiation heat transport and the ideal gas equation of state, allowing for variable ionization using the Saha equations. We calculate rail ablation taking into account the flow of heat into the interior of the rails. Our simulations show the development of internal convective flows and secondary arcs. We use an explicit Flux Corrected Transport algorithm to advance all quantities in time.

## I. INTRODUCTION

In a previous paper<sup>1</sup> we reported the results of our two-dimensional numerical simulations of the plasma armatures found in electromagnetic rail launchers. We considered the same effects as the Powell-Battch<sup>2</sup> model, including heat transport in the radiation diffusion approximation, and variable ionization from the Saha equation, but neglected viscosity and rail ablation. In this paper we report the result of including rail ablation in the simulations. Of the mechanisms believed to be mainly responsible for the deficient performance of rail launchers, the ablation effect, specially pointed out by Parker<sup>3</sup>, has received the most attention. Most of the ablated material tends to be left behind the main plasma armature. The actual ablation drag is caused by the entrainment of some the ablated material into the forward motion of the armature. Secondary arcs that develop in the rear of the armature seem to be specially important in entraining ablated material, and degrading the accelerating force. This is clearly shown in experiments, and in our simulation, which show a drop in acceleration accompanied by the formation of a secondary arc.

## II. MODEL

The MHD model to describe the plasma and the geometry are the same as in Ref. [1] except that here we include rail ablation. We consider variations

along the  $x$ -axis, which we choose along the rail direction, from the projectile back toward the breech, and along the  $y$ -axis, which goes from rail to rail, opposite to the direction of the current in the armature. All quantities are taken independent of  $z$  in our two dimensional model (translational invariance along the  $z$  axis,  $0 = \partial/\partial z$  as for infinitely tall rails). The magnetic field only has a  $z$  component, but the fluid velocity, and the current do not have  $z$  components. Behind the armature, where there is no current, the magnetic field between the rails is uniform along the  $z$  axis with the value

$$B_z(t) = \mu_0 \frac{I(t)}{h}, \quad (1)$$

where  $I$  is the rail current and  $h$  is the rail height.

With ablation the mass conservation equation becomes

$$\frac{\partial \rho}{\partial t} + \nabla \cdot (\rho \mathbf{v}) = s_a, \quad (2)$$

where  $s_a$  represents the rate of density increase due to ablated material. As in Ref. [1] our coordinate system is fixed to the projectile, whose speed is  $v_p$ . When we speak of the fluid velocity  $\mathbf{v}$ , the magnetic field  $\mathbf{B}$ , or any other quantity, we mean it as measured in the frame of reference that moves with the projectile, unless otherwise specified. The momentum equation is

$$\frac{\partial(\rho \mathbf{v})}{\partial t} + \nabla_j(\rho v_j \mathbf{v}) = -\nabla p + \mathbf{J} \times \mathbf{B} + \rho \mathbf{g} + s_a \mathbf{v}_a, \quad (3)$$

with  $\mathbf{g} = g \hat{\mathbf{x}} = \frac{dv_p}{dt} \hat{\mathbf{x}},$

where  $g$  is due to the accelerated frame, and the term  $s_a \mathbf{v}_a$  represents the momentum added by the ablated material. The energy equation is

$$\frac{\partial(\rho e)}{\partial t} + \nabla \cdot (\rho e \mathbf{v}) = -p \nabla \cdot \mathbf{v} - \nabla \cdot \mathbf{q} + \frac{J^2}{\sigma} + e_a s_a, \quad (4)$$

where we take the ideal gas form for  $e$  as in Ref. [1], and the term  $e_a s_a$  represents the added energy

brought in with the ablated material.  $e_a$  is taken at the vaporization temperature of the rail. In Eq. (4)  $q$  is the heat flow vector in the radiation diffusion approximation and  $\sigma$  is the Spitzer conductivity as in Refs. [1] and [2].

All electrical quantities except  $B_z$  are eliminated from the problem using Ohm's, Ampere's, and Faraday's laws.  $B_z$  obeys the equation

$$\frac{\partial B_z}{\partial t} + \nabla \cdot (B_z \mathbf{v}) = \frac{\partial}{\partial x} \left( D \frac{\partial B_z}{\partial x} \right) + \frac{\partial}{\partial y} \left( D \frac{\partial B_z}{\partial y} \right),$$

with  $D = \frac{1}{\mu_0 \sigma},$  (5)

where  $D$  is the magnetic diffusion coefficient. When  $D$  is small (large  $\sigma$ ), the magnetic field tends not to diffuse, but rather to be convected along with the fluid. When  $D$  is large (small  $\sigma$ ), the magnetic field diffuses through the conducting fluid. We have neglected fluid viscosity in our model. This is important in a boundary layer located at the boundary walls, and is responsible for a large part of the drag force that robs momentum from the projectile. Its inclusion in the simulation is left for future work. We also use the tall rail idealization which results in an acceleration that is about three times higher than real devices for the same current.

As in Ref. [1] we use an explicit flux corrected transport (FCT) finite difference scheme to advance all our quantities in time.

### III. ABLATION

We divide each rail into  $R$  cells of length  $\Delta x_r$ . We calculate the heat flux into the  $r$ th rail cell  $q(r, t)$  from

$$q(r, t) = (1 - \alpha) q_{rad}, \quad \text{with} \quad q_{rad} = \frac{16}{3} \sigma_{SB} \lambda T^3 \frac{\partial T}{\partial y_n},$$

where  $\alpha$  is the reflectivity of the rail and  $q_{rad}$  is the radiation diffusion heat flux into the rail, evaluated 1/4 of a cell inward from the boundary of the computational region. Here  $y_n$  is the coordinate normal to the rail and  $\lambda$  is the Rosseland mean free path for radiation, as in Ref. [2]. Of course one must be careful that each rail cell gets heat from the plasma cell that is actually in front of it. The rails need to be heated from their initial temperature  $T_0$  to the ablation temperature  $T_v$ , which we take equal to the vaporization temperature of the rail material. We

need the solution for the rail temperature at a depth  $y$  from the surface of the  $r$ th cell, given the heat flux  $q(r, t)$  at the  $y = 0$  surface. Neglecting heat diffusion along the rails, the solution for the temperature is

$$T(y, r, t) = T_0 + \frac{2}{\pi c_r \rho_r} \int_0^t \sqrt{\frac{\pi}{4\nu(t-t')}} \times \exp\left[-\frac{y^2}{4\nu(t-t')}\right] q(r, t') dt', \quad (6)$$

where  $c_r$  is the specific heat,  $\rho_r$  the density,  $\nu = \kappa_r / c_r \rho_r$  the heat diffusivity, and  $\kappa_r$  is the heat conductivity of the rails. At the  $y = 0$  rail surface this is

$$T(r, t) = T_0 + \frac{2}{\pi c_r \rho_r} \int_0^t dt' q(r, t') \sqrt{\frac{\pi}{4\nu(t-t')}}.$$

Unfortunately this quantity is a convolution integral that at each time step requires us to do an integral that goes back to the beginning of time. This is too burdensome in terms of CPU time. Therefore we devised an approximation based on the result

$$T(r, t) = T_0 + \frac{q(r, av)}{\kappa_r} \sqrt{\frac{4\nu t}{\pi}},$$

where  $q(r, av)$  is the average heat flux into the rail, which is exact if  $q(r, t)$  is constant in time. We define

$$q(r, av) = \frac{1}{t} \int_0^t q(r, t') dt' \equiv \frac{1}{t} E(r, t), \quad (7)$$

where  $E(r, t)$  is the total heat input into the rail element. New cells appear as the projectile passes and others disappear as they reach the end of our computational region. They are managed in such a way that the heat deposited in each cell is properly accounted for. We decide ablation begins when the rail surface reaches the vapor temperature. Based on the approximation of Eq. (7) we test when

$$E(r, t) \geq [c_s \rho_s (T_m - T_0) + L_m \rho_m + c_m \rho (T_v - T_m)] \left( \sqrt{\frac{\pi \nu t_{ex}(r)}{4}} \right), \quad (8)$$

where  $t_{ex}(r)$  is the time that cell  $r$  has been exposed to the plasma, and the subscripts  $s$ ,  $m$ , and  $v$  refer to solid, molten, and vapor. We do not treat the

change in the heat conductivity of solid to liquid. After Eq. (8) is satisfied, at time  $t = t_v$ , we let ablation begin. Not all the heat flux  $q(r, t)$  goes to ablate material because some heat flux  $q_l(r, t)$  is lost by diffusion into the rail. The temperature at the rail surface stays at  $T_v$  and the solution in the interior is

$$T(y, r, t) = \frac{2T_v}{\sqrt{\pi}} \int_s^\infty du e^{-u^2}, \quad s = \frac{y}{\sqrt{4\nu(t - t_v)}}. \quad (9)$$

From Eq. (9) we calculate that

$$q_l(r, t) = -\kappa_r \frac{\partial T}{\partial y} \Big|_{y=0} = \kappa_r \frac{T_v - T_0}{\sqrt{\pi\nu(t - t_v)}}.$$

This approximation overestimates  $q_l(r, t)$  at early times. Then we calculate that an element of rail of area  $A$  ablates mass at the rate

$$\frac{\Delta m}{\Delta t} = A \frac{q(r, t) - q_l(r, t)}{L_v} \equiv s_a A \Delta y, \quad (10)$$

where  $L_v$  is the latent heat to vaporize, and  $s_a$  is the ablated mass density rate to be added as a source to the plasma cell of thickness  $\Delta y$  adjacent to the wall.

#### IV. RESULTS

This simulation was run on a Vaxstation 3100 at a rate of about 56 minutes of CPU time per 1000 time steps. The rail to rail distance of 1 cm is covered by 10 cells of 1 mm each. We have assumed solutions that are symmetric about the midpoint of the rail to rail dimension. This enables us to simulate a region twice as large as what we actually compute. Other simulations in which we do the entire region maintain their symmetry rather well when we take symmetric initial conditions. Due to our symmetry restriction we compute over only 5 cells in the  $y$  direction. The symmetry is needed to understand many of the figures that follow, which only show 5 cells, one half of the rail to rail dimension. The figures show four boxes rail to rail but this is due to a peculiarity of our graphics. The center of the actual computational cells appear in the figures at the crossings of the grid lines.

Fig. 1 shows the time trace of the rail current generated by a sequentially fired multiple capacitor bank provided to us by E. Clothiaux<sup>5</sup>. We have incorporated this current into our simulation. The varying rail current enters the model as a varying

magnetic field at the rear. The plasma is initiated by the explosion of a metal foil that initially shorts the rails. The initiation process lasts about  $10^{-4}$  sec as evidenced by muzzle voltage traces.

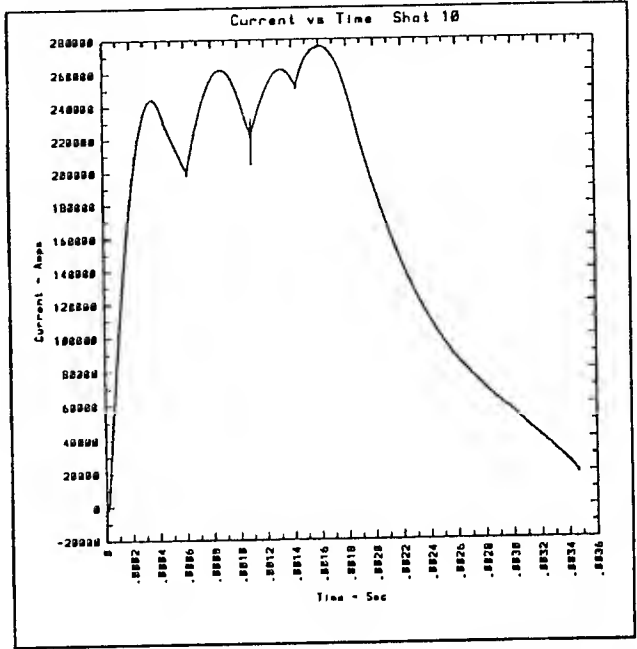


Figure 1: Current profile from a sequentially fired multiple capacitor bank.

For this reason we take  $t = 10^{-4}$  sec to be the initial time of our plasma simulation. The initial temperature, density, and current density are taken uniform over a plasma that is only two cells long. Except for ablation, the boundary conditions are the same as in Ref. [1]. At the rear of the computational region we take  $\frac{\partial}{\partial x} = 0$  for everything, which requires no current at that boundary, thus no conductivity. If the cells adjacent to the boundary become conducting, the simulation stops.

Ohmic heat causes the plasma to expand rapidly. Fig. 2 shows the plasma has lengthened to about 90 cells in 40,000 time steps,  $2.49 \times 10^{-4}$  sec ETIME ( $1.49 \times 10^{-4}$  sec actual simulation time, so average time step  $\approx 3.72 \times 10^{-9}$  sec). The explicit algorithm requires such short time steps to satisfy the Courant criteria and preserve numerical stability. We impose upper bounds on the heat diffusion coefficient calculated in our model to keep the required time step from becoming too short. Regions where the magnetic diffusion is too great are assigned a uniform magnetic field as, in Ref. [1].

Fig. 3 (note that this figure is symmetric and contains the full 10 cells rail to rail) shows the development of a strong secondary arc at the rear of the main plasma after 82,000 time steps, around  $3.05 \times 10^{-4}$  sec, an elapsed time typical of many experiments. secondary arcs.

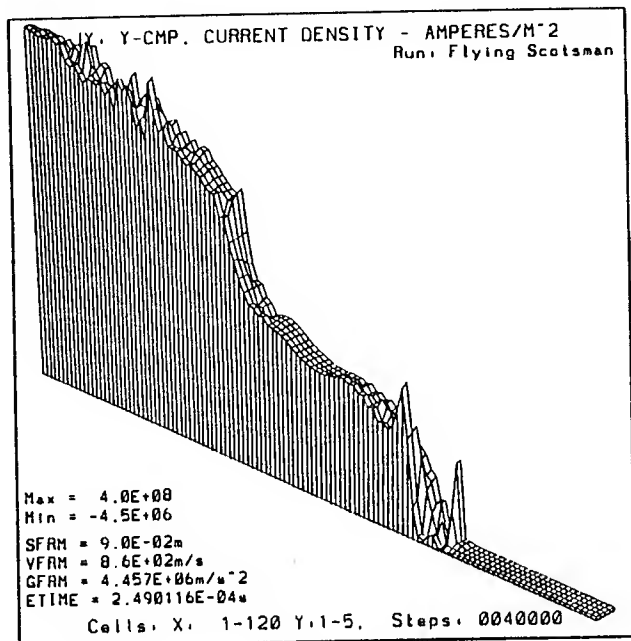


Figure 2: y component of Current density,  $J_y$ , showing near equilibrium profile.

This arc has a peak current density almost as large as the maximum current density in the main arc, although the total current is less than 10 per cent of the total. The peak current value in the secondary arc in the simulation is strongly influenced by the ablated material. Secondary arcs without ablation were obtained in Ref. [1], but the peak current was only about 5 per cent of the peak in the main arc, and the total current in the secondary was less than one per cent of the total. In this simulation the last cell is forced to have the vacuum value of the rear magnetic field. Once a sizable current reaches the last cell a spurious arc develops there and the simulation is stopped. We made the computational region 120 cells long, enough to give us time to develop secondary arcs in the plasma before a sizable current reached the rear boundary but this happened not long after the time of Fig. 3.

There is a feature in Fig. 3 centered near cell 43. This seems to be associated with the turn around point in the convective flows set up in the plasma.

The convective flow near the rear of the projectile is shown in Fig. 4.

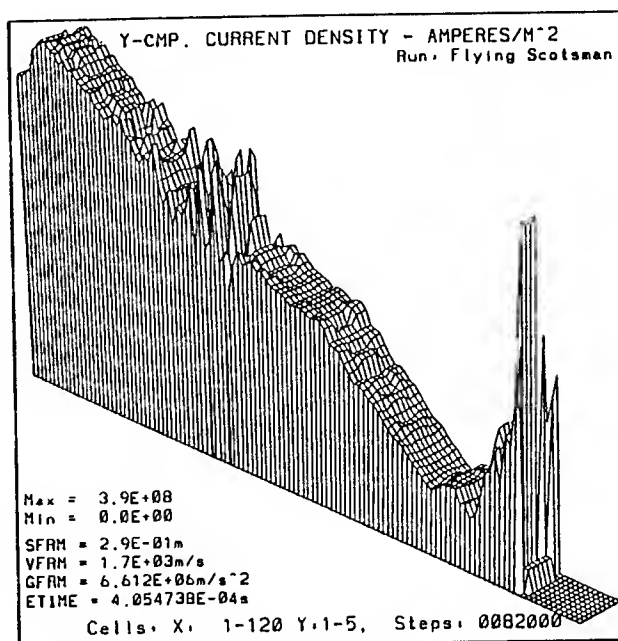


Figure 3: y component of Current density,  $J_y$ , showing fully developed secondary arc.

It shows the velocity vector flow field from cells 1 to 30, for the whole rail to rail width, after 82,000 time steps. This vector field shows a big convection cell.

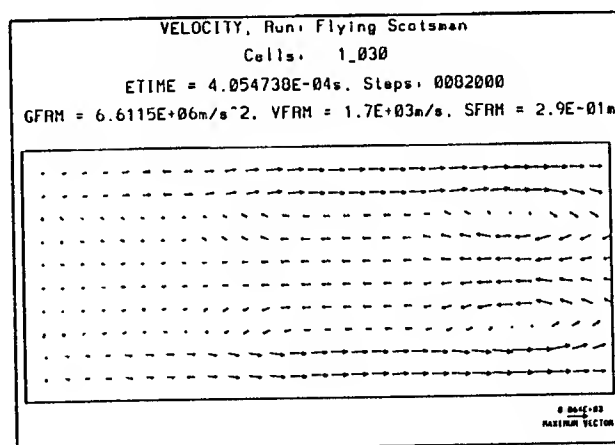


Figure 4: Velocity vector flow field.

The convective flow is driven by two effects. First there is the ablated material which is produced at rest relative to the rails. In the frame of the projectile it has a strong velocity toward the rear. Near the center of the plasma the flow is toward the front due

to the buoyancy force felt in the accelerated frame by the hot, relatively low density, plasma near the center. Fig. 5 shows the velocity field from cells 30 to 60. It contains another convection cell. The current feature lies near the point of stagnation of this cell. The largest velocity vectors in Fig. 5 have a magnitude of  $.139 \times 10^4$  m/sec, which is nearly as large as the projectile velocity at this time.

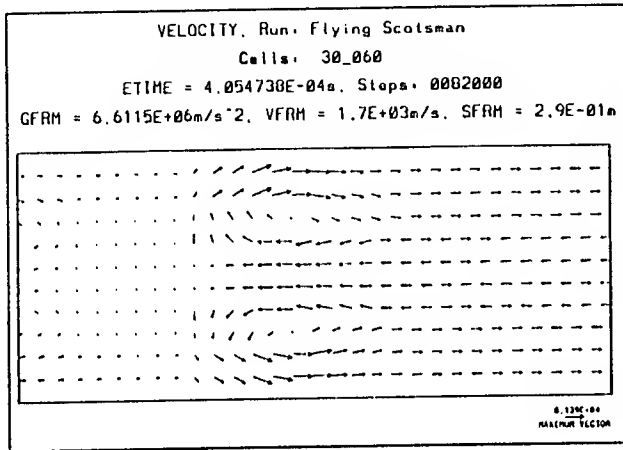


Figure 5: Velocity vector flow field.

Clothiaux<sup>8</sup> et al. have observed a low current buffer zone right behind the projectile that might be related to these convective flows. The velocity vector fields from cells 60 to 120 show a flow mostly toward the rear due to the ablated material that is being left behind.

## V. CONCLUSIONS

We postulate a simple theoretical model to explain the initiation of secondary arcs in terms of Ohmic heating in a medium where the electrical conductivity increases with temperature. A current increase at a point raises the electrical conductivity which tends to increase the current even further. The growth of the current is opposed by the diffusion of heat away from the hot spot. Our model is based upon the one-dimensional version of Eqs. (4) and Eq. (5) neglecting body motions and density changes, so  $v_x = 0$ ,  $\rho = \text{constant}$ . We introduce the temperature  $T$  by using for the plasma a simple ideal gas energy equation for  $e$  and  $q_x$  component of the heat flow vector

$$e = \frac{3k_B T}{2m_a} = cT, \quad \text{and} \quad q_x = -\kappa \frac{\partial T}{\partial x},$$

where  $m_a$  is the mass of a plasma atom,  $c$  is the specific heat, and  $\kappa$  is the heat conductivity of the plasma (mostly by radiation), which depends on  $T$ . We rewrite the energy equation as

$$\frac{\partial T}{\partial t} = \frac{\partial}{\partial x} \left( D_T \frac{\partial T}{\partial x} \right) + \frac{J^2}{\rho c \sigma(T)} \quad \text{with} \quad D_T = \frac{\kappa(T)}{\rho c}, \quad (11)$$

where  $D_T$  is the temperature diffusion coefficient of the plasma. We rewrite the magnetic field equation in terms of the current density as

$$\frac{\partial J_y}{\partial t} = \frac{\partial^2}{\partial x^2} (D J_y) \quad \text{with} \quad J_y = -\frac{1}{\mu_0} \frac{\partial B_z}{\partial x}, \quad (12)$$

where  $D$ , defined in Eq. (5), depends on  $T$  via  $\sigma(T)$ . The temperature dependence of  $\sigma(T)$  is an essential factor of the model, as will be shown below. We do a linear analysis of Eqs. (11) and (12) by seeking the usual type of solutions

$$T = T_0(x) + T_1(x, t) \quad \text{and} \quad J = J_0(x) + J_1(x, t),$$

where  $T_0(x)$  and  $J_0(x)$  are equilibrium profiles and  $T_1(x, t)$  and  $J_1(x, t)$  are small perturbations. For brevity the differential equations for  $T_0, T_1, J_0$ , and  $J_1$  will not be given here. The simplest case, for which we can give results in closed form, is where the  $x$  dependence of the equilibrium profiles can be neglected compared to that of the perturbations. This is a form of local analysis valid for perturbations of much shorter wavelength than the length scales of the equilibrium. The perturbations have the form

$$T_1(x, t) = T_1 e^{ikx} e^{\Gamma t} \quad \text{and} \quad J_1(x, t) = J_1 e^{ikx} e^{\Gamma t},$$

where the growth rate  $\Gamma$  is given by

$$\Gamma = \frac{k^2 D_T}{2} \left[ -\left(1 + \frac{D}{D_T} + H\right) + \sqrt{\left(1 + \frac{D}{D_T} + H\right)^2 - 4 \frac{D}{D_T} (1 - H)} \right],$$

$$\text{with} \quad H = \left( \frac{J_0}{\sigma(T_0)} \right)^2 \frac{d\sigma}{dT_0} \frac{1}{k^2 \kappa}, \quad (13)$$

where  $D$  and  $D_T$  are evaluated at  $T_0$ . The criterion for instability is that  $H > 1$ , or

$$E_0^2 \frac{d\sigma}{dT} > k^2 \kappa_p, \quad \text{where} \quad E_0 = \frac{J_0}{\sigma(T_0)}. \quad (14)$$

$E_0$  is the electric field in the frame of the plasma. This is the same result given by Huerta<sup>7</sup>. Clearly the Ohmic heating due to the electric field drives the instability when  $\frac{d\sigma}{dT} > 0$ . We may use the Spitzer conductivity to write

$$\frac{d\sigma}{dT} \approx \frac{3\sigma}{2T} \quad \text{and} \quad \sigma E_0^2 = \frac{J_0^2}{\sigma} > \frac{2}{3} k^2 \kappa T \quad (15)$$

for Eq. (14), which can be interpreted in terms of Joule heating overcoming heat diffusion. To get a rough guide it makes sense to let the length  $L$  of the plasma set a lower limit to the allowed wavevector  $k_{low} = 2\pi/L$ . Then Eq. (15) yields an approximate criterion for arc growth

$$\sigma E_0^2 L^2 > \frac{8\pi^2}{3} \kappa T. \quad (16)$$

Therefore longer plasmas are more prone to show the instability because they allow longer wavelength modes to fit in the plasma. The qualitative information contained in Eq. (16) agrees well with experiments. As the plasma tail becomes longer, due to ablation, viscous drag, etc., it reaches a threshold value where the electric field is able to trigger the instability. There are several important quantities in understanding this result. Let  $V_m$  be the muzzle voltage, which is approximately equal to the resistive drop in the armature right behind the projectile,  $v_p$  be the speed of the projectile and  $v_t$  be the speed of the plasma at a point in the tail. The electric field  $E_{0t}$  in the frame of the plasma at that point in the tail is

$$E_{0t} \approx \frac{V_m}{w} + B_t(v_p - v_t), \quad (17)$$

where  $B_t$  is the magnetic field at the tail. Eqs. (16) and Eq. (17) explain why the instability increases as the tail velocity falls behind the projectile velocity due to drag. The picture is that as the tail gets longer and slows down both  $L$  and  $E_0$  increase leading to the formation of the secondary arcs. A drop in the driving current can also lead to a lengthening of the arc, and we note that the arc begins during the time that the rail current is dropping in Fig. 1. Using the radiation diffusion approximation for  $\kappa$  and the Spitzer conductivity for  $\sigma$ , Eqs. (13), (16), and (17) give values that show good agreement with the simulation and with experiment.

Our code is somewhat validated by the fact that previous isothermal and adiabatic simulations, using essentially the same code, did not show secondary arcs. The simulation reported in Ref. [1] did show features that looked like small secondary arcs. In this simulation the arcs are enhanced by the ablation.

Our explicit numerical scheme forced us to use short time steps to preserve numerical stability. This had the benefit that the simulation captured the fast time scale phenomena associated with secondary arc formation. The paper by Frese<sup>8</sup> presented a very similar simulation using an implicit numerical scheme that did not show the formation of secondary arcs. The implicit scheme of Ref. [8] allowed long time steps, with the benefit of reduced CPU time, but in our opinion the time steps were too long to see the secondary arcs.

## VI. REFERENCES

- [1] M. A. Huerta and G. C. Boynton, "Two dimensional Heat Conducting Simulation of plasma armatures", *IEEE Trans. MAG.*, vol. 27, pp.261-265 (1991).
- [2] J. D. Powell and J. H. Batteh, "Plasma Dynamics of an Arc-Driven Electromagnetic Projectile Accelerator," *J. Appl. Phys.*, vol. 52, p. 2717 (1981).
- [3] J. V. Parker, "Why Plasma Armature Railguns Do not Work (And What Can Be Done About It)," *IEEE Trans. MAG.*, vol. 27, pp.418-424 (1991).
- [5] E. Clothiaux, K. A. Thomas, and J. Rogers, Auburn University, Physics Department, private communication, July, 1991.
- [6] E. J. Clothiaux R. A. Villecco, and K. K. Cobb, "Experimental Indication of a Buffer Zone between the Plasma Armature of an EML and the Projectile", *IEEE Trans. MAG.*, vol. 27, pp.294-297 (1991).
- [7] M. A. Huerta, "Spot Formation and Temperature Instabilities driven by Joule Heating", in *IEEE Conference Record-Abstracts, 1985 IEEE International Conference on Plasma Science, June 3-5, 1985, Pittsburgh, Pennsylvania.*
- [8] Frese, M. H., "The Internal Structure and Dynamics of the Railgun Plasma Armature between Infinitely Wide Ablating Rails", *IEEE Trans. MAG.*, vol. 27, pp.233-239, Jan. 1991.

# THE PROJECTILE-WALL INTERFACE IN RAIL LAUNCHERS

Y. C. Thio, M. A. Huerta, G. C. Boynton  
Physics Department, University of Miami, Coral Gables, FL 33124

D. A. Tidman, S. Y. Wang, N. K. Winsor  
GT-Devices, Inc., Alexandria, VA 22322.

**Abstract** -- At sufficiently high velocity, an energetic gaseous interface is formed between the projectile and the gun wall. We analyze the flow in this interface in the regime of moderately high velocity. The effect of this gaseous interface is to push the gun wall radially outward and shrink the projectile radially inward. Our studies show that significant plasma blow-by can be expected in most experimental railguns in which organic polymers are used as insulators. Since plasma leakage may result in the reduction of propulsion pressure and possibly induce the separation of the primary, the results point to the importance of having sufficiently stiff barrels and structurally stiff but 'ballistically compliant' projectile designs.

## 1. INTRODUCTION

Projectile wall interactions have been studied extensively in conventional guns in which a relatively stiff projectile slides in a relatively stiff gun tube [1]. This contrasts with many railgun experiments in which relatively soft insulating barrel liner and projectile/sabot materials are used. The effects of the gaseous interface between the projectile and the gun wall in these environments can be quite different and have not been discussed before except for the case of extremely high projectile velocities ( $> 10$  km/s) [7].

Our purpose in this paper is to discuss some of the salient features of this interface at the lower velocity range (2 - 8 km/s) as problems continue to defy experimental attempts to reach velocity above this range, and to lay the groundwork for further studies of this interface. For concreteness, we treat the case of organic polymers (e.g. polycarbonate) sliding against each other. For further simplification, we assume that all surfaces of interest have been machined (honed) to have smoothness better than  $.25 \mu\text{m}$ , i.e. any surface irregularities would have dimensions less than  $0.25 \mu\text{m}$ . This provides nearly mirror-finished surfaces.

## 2. HYPERVELOCITY SLIDING: THE PHENOMENOLOGY

The phenomenology of hypervelocity sliding is extremely complex, while experimental information is relatively scant. We propose here a theoretical description of the phenomenology as follows, starting with the projectile at rest. The projectile is assumed to have a tight fit with the bore initially. Acceleration of the projectile begins with overcoming any static friction which may be present. For

projectile velocity up to one or two hundred m/s, friction between the projectile and the wall arises essentially due to solid-to-solid collisions of surface asperities. Once past this regime of 'solid-to-solid' sliding, a thin film of fluid begins to fill the void between the projectile and the wall.

Due to viscosity and the high velocity shear, significant viscous dissipation occurs and this film of fluid rapidly evolves into a gaseous state forming what might be called a gaseous bearing. The rate of this viscous dissipation is approximately given by  $\nu \rho U^2 / h$  and increases rapidly with velocity, where  $\nu$  is the kinematic viscosity,  $\rho$  the density,  $U$  the sliding velocity, and  $h$  is the thickness of the gaseous film.

Some of the heat generated in the gaseous bearing escapes through the rear of the bearing with any backward flow from the bearing into the region behind the projectile. Some of this heat is trapped in the bearing and goes to heat up the projectile surface as well as the "counter surface" of the wall. The counter surface is defined here as that part of the gun wall directly opposing the projectile.

The counter surface is heated only during the transit of the projectile and is therefore cooler than the projectile surface, at least during the early phase of this regime. Because of the smallness of the gap at this point, a small temperature difference can lead to a large thermal gradient and therefore a significant heat flux towards the counter surface. The wall thus acts as a heat sink and helps to keep the projectile surface relatively cool.

As the projectile velocity increases, the rate of viscous heat dissipation in the interface increases. The thermal gradient in the interface tries to adjust itself to produce the higher heat flux necessary to drain away the heat generated. It does so by increasing the surface temperature of the projectile, until a point is reached when the projectile surface begins to ablate and contributes rapidly to the interfacial matter. At some operating point (which is a complicated function of velocity and total elapsed time of projectile motion) the thin gaseous film becomes sufficiently thick to allow the plasma armature at the base of the projectile to drive a flow through the interface. This is the onset of the leaky gaseous bearing regime and is often associated with moderately high velocity.

In this regime, gaseous matter from the plasma armature



flows into the gaseous interface rapidly transferring thermal and kinetic energy into the interface, resulting in further ablation of the projectile, and possibly the counter surface, and widening of the interface. If the pressure gradient in the interface is sufficiently large, plasma leakage (blow-by) can occur. The occurrence of leakage may result in some reduction in the propulsive pressure or interfering with the physics of the plasma armature. Recent experimental evidence has indicated that such leakage can initiate the growth of a buffer zone ("separation of the primary") [2, 3].

The pressure and temperature distribution of the gaseous interface is now determined by the gasdynamics of the flow through the interface and the mechanical response of the projectile and the counter surface. The pressure in the bearing will tend to shrink the projectile and push the gun wall away from the projectile radially, thus increasing the size of the bearing and the rate of leakage through it. On the other hand, ablation, inertia and viscous forces work to block the leakage flow.

As the velocity increases even further, the rate of viscous dissipation continues to increase rapidly. A point is reached at which the rate of viscous dissipation is so high that it is possible for the viscous dissipation alone to produce sufficient pressure to block any forward flow from the plasma armature. We now enter the regime of extremely high velocity sliding [7] and a self-sealing plasma bearing, with the possibility of highly energetic reverse flow from the interface into the plasma armature. The pressure in the plasma bearing is now maintained as a thermodynamic balance between the volume of the bearing and the thermal energy trapped in the interface. In this highly pressurized state, the plasma bearing can provide a cushioned ride for the projectile.

The above model of the tribological phenomenology applies under more or less ideal conditions where the projectile and the gun wall have mirror polished surfaces, and in which the geometries and the propulsive pressure are perfectly axially symmetrical. In practice these conditions are seldom realized. The result is that the processes from the various regimes often can and do occur simultaneously, making the phenomena considerably more complicated. For example, in the case of an imperfectly machined projectile or a rough gun wall, severe gouging caused by collisions of solid asperities of the projectile surface and the wall can occur. This leads to uneven projectile deformation and accentuate the erratic nature of the flow through the interface.

In the present communication, we shall restrict our discussion of the interfacial dynamics to the regime of the leaky gaseous bearing at moderately high velocity. The regime of self-sealing plasma bearing at extremely high velocity is not treated here and is a subject for future

investigations.

### 3. PROJECTILE BEHAVIOR

In conventional guns which use a steel gun tube and a metallic projectile, both the gun wall and the projectile are relatively stiff. Consequently the bore dilation and the projectile shrinkage are minimal, and the presence of the gaseous interface presents much less of a problem as far as the leakage effect is concerned. In the case of railguns, the gun wall and the projectile usually contain insulating materials which have lower stiffness. It becomes necessary to examine closely the deformation of the projectile and the gun wall.

We begin by considering a simple regular cylindrical projectile with a rounded nose made of polycarbonate as shown in Fig. 1a. A typical length-to-diameter ratio of 1 is assumed. There is not much experimental or theoretical data on the pressure distribution in projectile-wall interface. To make progress, we assume that the pressure in the interface starts at the same pressure as the plasma armature pressure at the projectile base and decays linearly to one half this value at the nose. This pressure profile is appropriate for the leaky gaseous regime for moderately high projectile velocity, and is almost the opposite of the ordinary lubrication flow profile when the projectile velocity is much lower.

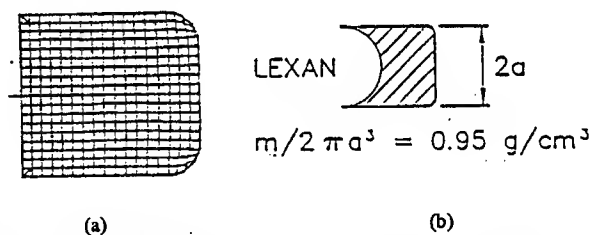


Fig. 1. Projectile geometries: (a) Simple cylinder. (b) With obturating geometry

A finite-element, linear elastic, 2-D static, axially symmetric model is used to calculate the deformation of the projectile. The computation is performed with SUPERSAP [4]. A result of the calculation for the case of a regular cylindrical projectile is shown in Figure 2, which displays the isocontours of radial displacement. The displacements are shown in inches and have negative values since they are inwards towards the axis of projectile. The base pressure used is 4 kilobars (400 MPa), and the gaseous interface pressure is assumed to decrease linearly to 2 kilobars at the nose. The deformation due to the body force resulting from its acceleration by the base pressure is included and tends to reduce the displacement at the rear. However, due to the larger interface pressure towards the rear, the largest shrinkage, as much as 0.014 inch (356  $\mu\text{m}$ ), occurs at a point rearward from the nose. Since the analysis is a linear elastic calculation, we may interpret the results as giving a radial



shrinkage of 0.0035 inch (89  $\mu\text{m}$ ) per kilobar of driving pressure at the projectile base.

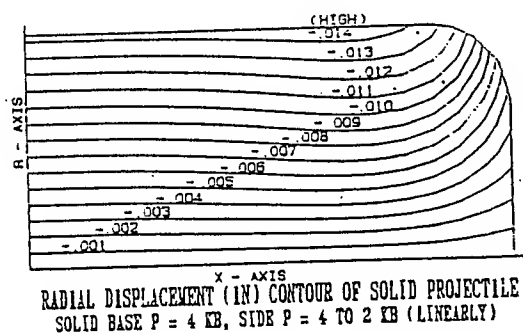


Fig. 2. Radial displacements of a simple regular cylindrical projectile subject to the energetic gaseous interface.

The relatively large radial shrinkage is a result of the low stiffness of the polycarbonate material used for the projectile and also of not having any ballistics feature in its design. The effective stiffness of the projectile can be enhanced by using an obturating geometry as depicted in Figure 1(b).

Assuming the same pressure distribution in the gaseous interface, we perform a similar finite-element analysis on this geometry. Figure 3 shows the corresponding isocontours of the radial displacements in the projectile. We see that, though the maximum radial shrinkage is approximately the same (0.012 inch), a position of minimum shrinkage occurs towards the rear end of the projectile where the shrinkage is reduced to 0.007 inch. The interface converges to a 'throat' and then diverges towards the nose. The constriction in the interface should serve to obstruct the forward flow and thus reducing the leakage rate.

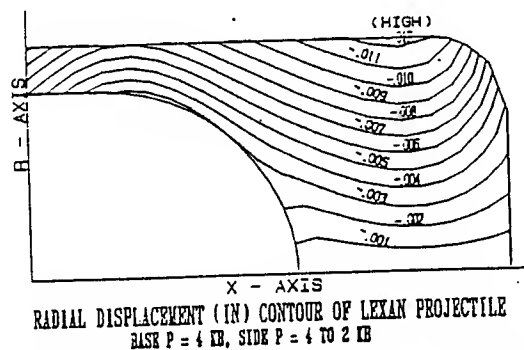


Fig. 3. Radial displacements of a cylindrical projectile ballistically enhanced by an obturating cavity.

#### 4. THE BARREL BEHAVIOR

To make the present discussion self-contained and consistent, we provide below an analysis of the barrel response to the energetic gaseous interface between the projectile and the gun wall in a form general enough that the result is relevant to current railgun experiments.

The main difficulty in doing this is that there are almost as many railgun barrel designs as there are railgun experimenters. After some considerations we decided to use a 'generic' railgun barrel design for the purpose of this study. It is generic in the sense that it contains many of the features common to or underlying many of the railgun barrel designs which have been devised. Such a generic design is illustrated in Figure 4. The bore diameter again is 16 mm.

The design embodies a stiff outer containment structure made of such materials as steel or graphite fiber composite. This outer containment structure is insulated from the rails by insulators which are typically of the glass fiber composite variety (e.g. G-11). The rails and the inter-rail insulating inserts (polycarbonate) comprise the inner structure.

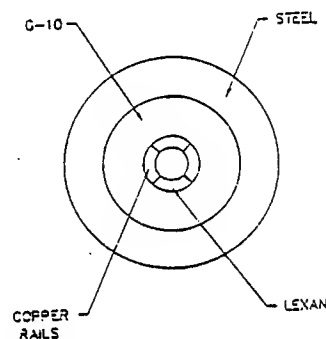


Figure 4. A typical railgun barrel cross section

The pressure loading on the gun wall by the gaseous bearing is impulsive. As the gaseous bearing flies past, a compressive wave is produced in the barrel wall propagating radially outward at approximately the acoustic wave speed. As the compressive wave travels past a given point, it induces material motion, and in particular, causes the gun wall to recede.

For a bore size of 16 mm and a projectile L/D ratio of 1, the projectile length is 16 mm. Let the projectile have a velocity of say 3 km/s. Then the passage of the plasma bearing takes approximately 5  $\mu\text{s}$ . The acoustic compressive wave speed in polycarbonate is about 2 km/s. In 5  $\mu\text{s}$ , such a wave travels 10 mm. Referring to Figure 4, the polycarbonate inter-rail insulator has a thickness of 4.8 mm. Therefore, during the passage of the projectile, we expect that the radial displacement of the projectile and some of the G-10 backing plate within a short distance from the boundary of the polycarbonate liner.

The dynamic displacement of the polycarbonate liner subjected to a linear pressure ramp may be determined using the method of the Duhamel's integral [5]. According to this method, the dynamic displacement,  $x_d$  at a given time  $t$  is

related to the static displacement,  $x_s$ , through the dynamic load factor as,

$$x_d = x_s D_p(t/T) \quad (4.1)$$

where the dynamic load factor,  $D_p$ , is a function of the pulse shape and of the relative time  $t/T$  (where  $T$  is the resonant period of the structural member). The function  $D_p$  for three typical pulse shapes is shown in Figure 5.

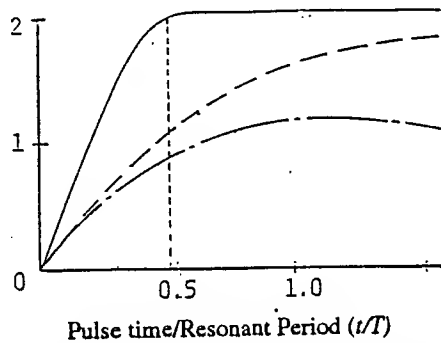


Fig. 5. The Dynamic Load Factor According to the Duhamel's Integral: (a) A Heaviside step function in loading, (b) A decreasing linear ramp in loading, (c) An increasing linear ramp in loading

To use the method, we first perform a static finite-element linear elastic computation for the barrel whose cross sectional geometry is shown in Figure 4. The resultant radial displacement is shown in Figure 5. The maximum static radial deflection is experienced by the polycarbonate insulators. At the bore, the radial displacement is 0.015" (381  $\mu$ m). At its boundary with the G-10 backing plate, the displacement is 0.002" (50  $\mu$ m).

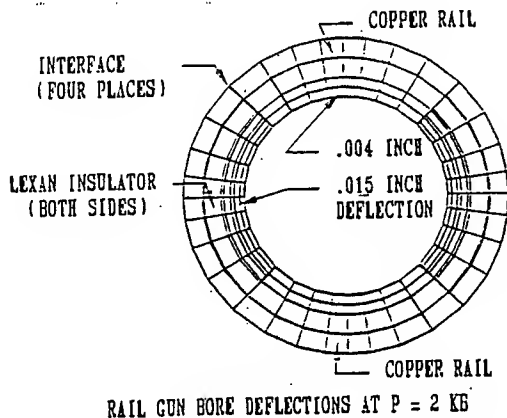


Figure 6. Typical railgun bore deflections

The net compression of the insulator is 0.013" for a pressure of 2 kb applied to the face of the insulator. Thus the force required to produce unit compression per unit length of the insulator can be calculated to be 7.56 GN/m/m. This is the equivalent spring constant 'k' per unit length of the polycarbonate insulator. The mass per unit length of the insulator can be calculated to be 0.0925 kg/m. This gives a

resonant period of 22  $\mu$ s. Referring to Figure 6, for a linear ramp, the dynamic load factor  $D_p$  at 5  $\mu$ s ( $t/T = 2.3$ ) is approximately 0.5. Using expression (4.1), the maximum dynamic radial displacement can be determined to be 0.0075" for 2 kb or 0.0038" per kb during the passage of the projectile. This occurs at the rear end of the projectile. The displacement tapers towards the nose of the projectile.

## 5. THE FLOW THROUGH THE INTERFACE

For pipe flows the critical Reynolds number for laminar to turbulence transition may be as low as 2300 depending on the surface conditions of the pipe and the initial condition of the flow entering the pipe. Carefully controlled experiments have produced critical Reynolds numbers for the transition as high as 40,000[6]. For this study, we assume a critical Reynolds number of about 3000.

Ablation from the surface of the projectile and/or from the gun wall would considerably complicate the flow in the interface, its effects are not included in the present discussion. Also assumed in the present analysis is incompressibility of the flow. Thus the results of the present analysis are valid only for subsonic flows, when the projectile velocity is not too high. Both these assumptions are made for purely mathematical convenience. The flow is essentially 2-D. In what follows, the  $x$ -axis is taken to be parallel to the interface and directed towards the nose of the projectile, and the  $y$ -axis is oriented towards the gun wall.

In the laminar regime the flow in the interface corresponds to the case of the classical Couette flow [6] if we ignore the effects of the entrance and exit flows. The net mass flow rate through the gap is given by,

$$Q = \pi p U R h \left[ -\frac{h^2}{6\nu U} \frac{\partial p}{\partial x} - 1 \right] = \pi R U \rho p_2 \chi \left[ \frac{\chi^2 p_2^3}{6\ell_{proj} \nu U} - 1 \right], \quad (3.1)$$

where  $R$  is the bore radius,  $\ell_{proj}$  the projectile length,  $p_2$  the rear pressure (pressure at the projectile base), and  $\chi = h/p_2$  which we call the gap separability. The result (3.1) assumes that the fluid is incompressible and becomes invalid when the flow velocity approaches that of the fluid sound speed. The leakage rate at the sound speed ( $c$ ) limit is given by,

$$Q_L = 2\pi R h p c = 2\pi R \chi p p_2 c, \quad (3.2)$$

The laminar leakage rate is estimated as the minimum of the two expressions (3.1) and (3.2).

For the turbulent regime, we have not been able to find a reference for an analytical solution for the flow field. A derivation is provided here as follows. Following Schlichting [6], (pg. 545), an approximate form of the 2-D, incompressible Navier-Stokes equations for turbulent flow, expressed in terms of the mean flow velocity  $\bar{w} = (\bar{u}, \bar{v})$  and an eddy ('apparent') viscosity may be written as

$$\frac{\partial \bar{u}}{\partial x} + \bar{w} \cdot \nabla \bar{u} = -\frac{1}{\rho} \nabla p + \nabla \cdot (\nu + \varepsilon) \nabla \bar{u} \quad (3.3)$$

and  $\nabla \cdot \bar{w} = 0$ ,

where  $\varepsilon$  is the eddy viscosity which is due to momentum transfer between different fluid elements caused by turbulence, and  $\nu$  is the usual fluid kinematic viscosity.

For steady state and parallel flow, and assuming that the density and pressure gradient is independent of  $y$  (for a long channel and ignoring the effect of ablation on the flow), the above equations can be integrated to give

$$(\nu + \varepsilon) \frac{\partial \bar{u}}{\partial y} = \frac{1}{\rho} \frac{\partial p}{\partial x} y + c, \quad (3.4)$$

where  $c$  is a constant of integration.

To make further progress with (3.4), we need some information on the eddy viscosity coefficient. The eddy viscosity depends on the mean velocity of the flow. Measured data and theoretical analysis based upon the flow resistance coefficients indicate that the eddy viscosity is approximately proportional to the first power of the mean velocity, thus [6],

$$\varepsilon = \beta \bar{u}, \quad (3.5)$$

where  $\beta$  is a constant of proportionality. Then equation (3.4) can be integrated subject to the boundary conditions at  $y = 0$  and  $y = h$  to give:

$$\bar{u}(1 + \beta \bar{u}/2) = U(1 + \beta U/2) \xi - \frac{p'(x)h^2}{2\rho\nu} (1 - \xi)^2, \quad (3.6)$$

$$\xi = y/h.$$

We see that, if  $\beta = 0$ , then the solution reduces to the classical solution for laminar Couette flow as it should be. For the case in which the eddy viscosity dominates the viscous forces in the flow, then  $\beta \bar{u} \gg 1$ . This is the case we consider here. In this case, the above expression can be reduced to,

$$\bar{u}^2 = U^2 \xi + b(1 - \xi)^2, \quad (3.7)$$

where

$$b = -\frac{p'(x)h^2}{\beta\nu\rho}. \quad (3.8)$$

In terms of a flow resistance coefficient  $\lambda$ , which is related to the net viscosity as  $\lambda = 32\varepsilon/Ru$ , and assuming that the net viscosity is dominated by kinematic eddy viscosity, we may write the parameter  $b$  in terms of the flow resistance coefficient as

$$b = -\frac{64p'(x)h}{\rho\lambda}. \quad (3.9)$$

In this form practical applications of the solution are more convenient as vast amount of data on the flow resistance coefficient are available for a wide range of Reynolds number and for a wide variety of surfaces, from hydraulically

smooth to completely rough.

The mass flow rate through the plasma bearing in the turbulent regime may be calculated from the mass flux integral to be

$$Q_{turb} = \frac{\pi}{4} \rho R h \sqrt{b} \left\{ 2(1-a)a + (1+a)^2 \left[ \sin^{-1} \left( \frac{1-a}{1+a} \right) + \frac{\pi}{2} \right] \right\}, \quad (3.10)$$

where  $a = U^2/b$ . Again, the flow rate will be limited by the sound speed and the turbulent leakage rate is estimated by taking the minimum of the two expressions (3.10) and (3.2). For  $\lambda$ , the flow resistance coefficient, a semi-empirical fit to extensive data on pipe flows for completely hydraulically rough surfaces is given in [6] as,

$$\lambda = \left\{ 2 \log_{10} (a/\delta a) + 1.74 \right\}^{-2}, \quad (3.11)$$

where  $a$  may be taken here as the gap size and  $\delta a$  is the surface roughness ( $0.25 \mu\text{m}$  in our discussion).

## 6. MASS LEAKAGE RATES

For concreteness, we consider a plasma armature driving and filling the interface with a partially ionized lithium plasma. The sound speed  $c_s$  and the generalized  $\gamma$ , of this plasma can be obtained from the SESAME code of LANL[8], and are shown in Fig. 7 in the range of temperatures and pressures of interest.

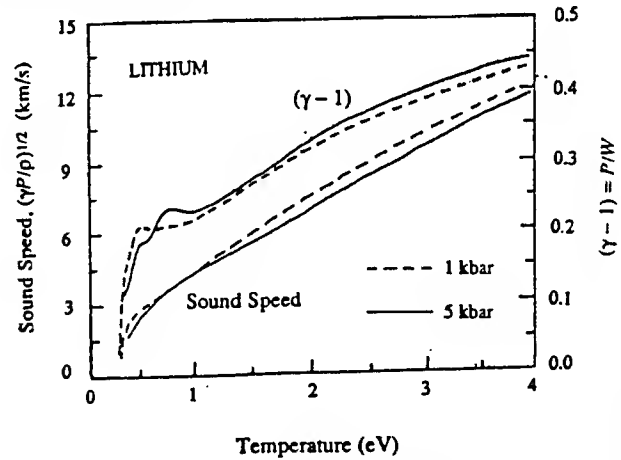


Fig. 7. Sound speed  $c_s$  and  $(\gamma - 1)$  vs temperature for lithium from SESAME

From the analysis of Sections 3 and 4 on projectile and barrel behavior in a typical railgun with a bore size of 16 mm, we see that practical values for the gap separability  $\chi$  may be as high as  $100 \mu\text{m}/\text{kb}$ . For these guns and projectiles, we estimate that the flow is laminar only for drive pressure below 1 kb. In this regime the leakage rate may be estimated from (3.1) and (3.2). Some numerical results are shown versus the drive pressure  $p_2$  for this regime in Figure 8, for the case in which the projectile velocity is 2.5 km/s and the

gaseous interface has a temperature of 1 eV. The curves (a) to (e) are for five different values of gap separability: 20, 30, 40, 50 and 60  $\mu\text{m}/\text{kb}$ . For curves (a) to (d), the sound speed limiting leakage rates are not reached within the range of the drive pressures shown. The sound speed limit is attained in case (e) where a kink in the curve can be seen.

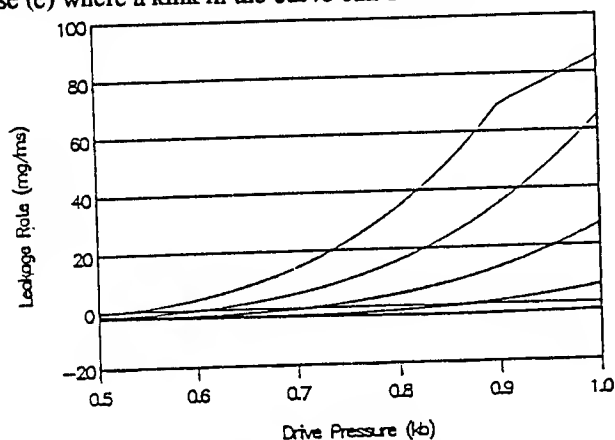


Fig. 8. Laminar leakage rates for a projectile moving at 2.5 km/s, in a bore of 16 mm diameter, for five different gap separabilities: (a) 20, (b) 30, (c) 40, (d) 50, and (e) 60  $\mu\text{m}/\text{kb}$ . A temperature of 1 eV is assumed for the interface

The result shows that for gap separabilities less than 40  $\mu\text{m}/\text{kb}$  and for drive pressure less than 1 kb the leakage rates are small and below 20 mg/ms. However, for gap separability above 60  $\mu\text{m}/\text{kb}$ , the leakage rate easily exceeds 90 mg/ms at the same pressure.

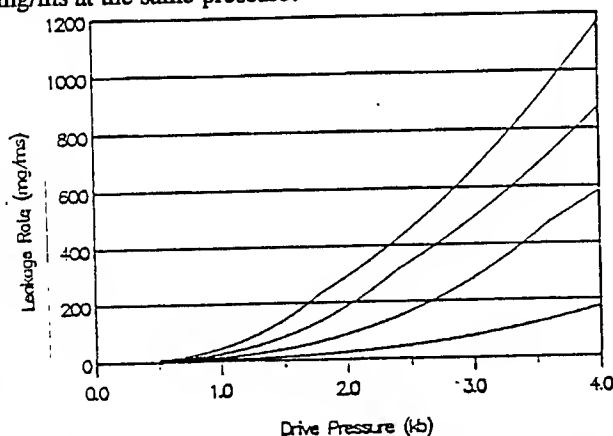


Fig. 8. The leakage rates in the turbulent regime for a projectile moving at 2.5 km/s, in a bore of 16 mm diameter, for four different gap separabilities: (a) 20, (b) 40, (c) 60, and (d) 80  $\mu\text{m}/\text{kb}$ . A temperature of 2 eV is assumed for the interface.

For the generic gun and projectiles considered, the interfacial flow is estimated to be turbulent for drive pressures exceeding 2 kb. The leakage rate calculated for an exemplary case of a turbulent interface is shown in Figure 8. The case shown is for a projectile moving at 2.5 km/s, and a gaseous interface with a temperature of 2 eV in a bore of 16 mm as assumed in Sections 3 and 4. Four different values of

gap separability are considered: 20, 40, 60, and 80  $\mu\text{m}/\text{kb}$ . The cross-overs from the turbulence viscous flow to the sound speed limit may be seen in these figures as gentle kinks in the curves. The leakage rates increase rapidly with the drive pressures and gap separability. At 2 kb, the leakage rates range from a low value of about 20 mg/ms for a gap separability of 20  $\mu\text{m}/\text{kb}$  to about 300 mg/ms for a gap separability of 80  $\mu\text{m}/\text{kb}$ . When the drive pressure increases to 4 kb, the leakage rate reaches a value as high as 1000 mg/ms for a gap separability of 80  $\mu\text{m}/\text{kb}$ .

## 7. CONCLUSION

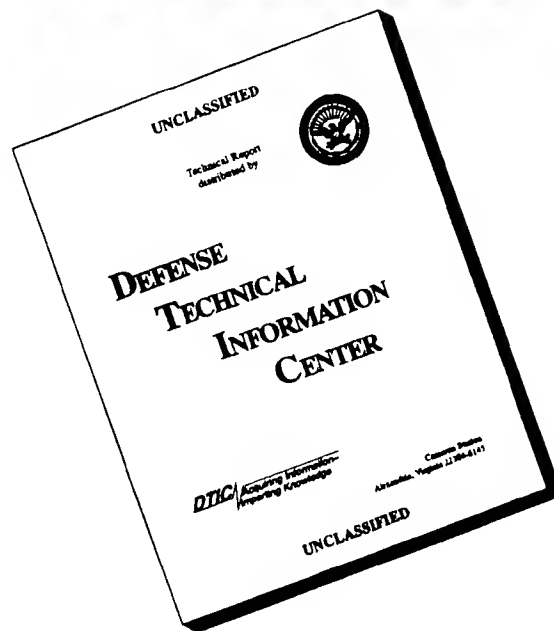
Our studies show that significant plasma blow-by can be expected in most experimental railguns in which organic polymers are used as insulators. Since plasma leakage may result in reduction of propulsion pressure and possibly induce the separation of the primary, the studies points to the importance of having sufficiently stiff barrels and structurally stiff but 'ballistically compliant' projectile designs.

The present flow analysis is subsonic and 1-D. At higher projectile velocities, the flow in the interface is essentially supersonic. Higher dimensionality effects can also be important. The results obtained in the present studies beckon for more studies to extend the present analysis to the case of hypersonic and supersonic flows in the interface with higher dimensionality. Experimentally, more sensitive and precise diagnostics are required to detect and observe the dynamical effects of this energetic interface. Accurate projectile position sensors are crucial. Data on the pressure distribution in the interface will be very useful, so also will be the details of the flow just behind and ahead of the projectile.

## REFERENCES

- [1] L. M. Barker, T. G. Trucano and J. W. Munford, *Surface Gouging by Hypervelocity Sliding Contact Between Metallic Materials*, Sandia National Laboratory Report SAND87-1328, Sept., 1987.
- [2] E. J. Clothiaux, private communication, October, 1991, Physics Department, Auburn University, Auburn, Alabama.
- [3] E. J. Clothiaux, R. A. Villecco, and K. K. Cobb, "Experimental indication of a buffer zone between the plasma armature of an EML and the projectile," *IEEE Trans. Magn.*, vol. 27, pp. 294-297, 1991.
- [4] *SUPERSAP - A Finite Element Computer Modelling Code*, Algor Interactive Systems, Inc., 260 Alpha Drive, Pittsburg, Pa. 15238.
- [5] G. R. Abrahamson and H. E. Lindberg, "Peak load-impulse characterization of critical pulse loads in structural dynamics," in *Dynamic Response of Structure*, G. Hermann and N. Perrone, Eds., 1972.
- [6] H. Schlichting, *Boundary Layer Theory*, McGraw-Hill, 1968.
- [7] D. A. Tidman, S. A. Goldstein, and N. K. Winsor, "A Railgun Plasma Armature Model," *IEEE Trans. Magn.* vol. 22, pp.1763-1771, 1Nov. 1986.
- [8] *Equation-of-State Data Listing, SESAME Tables*, Los Alamos Science Liaison Company, 253 Rio Bravo, Los Alamos, NM 87544.

# DISCLAIMER NOTICE



**THIS DOCUMENT IS BEST QUALITY AVAILABLE. THE COPY FURNISHED TO DTIC CONTAINED A SIGNIFICANT NUMBER OF PAGES WHICH DO NOT REPRODUCE LEGIBLY.**